Synthesis of γ-Fe$_2$O$_3$-SiO$_2$ composite nanoparticles targeting magnetic resonance imaging and magnetic hyperthermia applications

PhD Thesis

Author: Elena Taboada Cabellos

Supervisor: Dr. Anna Roig Serra

Departament de Física, Facultat de Ciències

Universitat Autònoma de Barcelona

October 2009

ICMAB CSIC

UAB
Universitat Autònoma
de Barcelona

Anna Roig Serra, Investigadora del CSIC a l'Institut de Ciència de Materials de Barcelona,

CERTIFICA

Que Elena Taboada Cabellos, Llicenciada en Ciències Químiques per la Universidad Autónoma de Madrid, ha dut a terme sota la seva direcció el treball que porta per títol "Synthesis of γ-Fe$_2$O$_3$-SiO$_2$ composite nanoparticles targeting magnetic resonance imaging and magnetic hyperthermia applications", i queda recollit en aquesta memòria per optar al grau de Doctor en Ciència de Materials.

I perquè així consti, signa el present certificat.

Dra. Anna Roig Serra

Bellaterra, 14 de setembre de 2009

Para Anna y David

Com sempre diu l'Eli,

paciència, que és la mare de la ciència

Agradecimientos (Acknowledgements)

I want to express my most sincere gratitude to many people. For that, I will use the languages closer to them.

First of all, I am grateful to Anna. Dr. Anna Roig has supervised this PhD Thesis. From the very first day she encouraged me to do it, she has always trusted me and this is the reason why this thesis is especially dedicated to her. Thank you. Ha sigut un camí llarg, però amb esforç i molta feina hem arribat fins aquí. Moltes gràcies per tots els ensenyaments que m'has donat a tots els nivells. Finalment he d'admetre que tenies raó en més d'un parell de coses...

I am also grateful to Prof. Elies Molins for recruiting me to pursue a PhD as well as for his scientific advice and for choosing me to collaborate with Dr. Jordi Llorca and Montse Domínguez of the UPC. Ha sigut molt satisfactori treballar amb tots tres, i a més a més aconseguir tan bons resultats!

It is been a pleasure to be able to work at the ICMAB for the facilities. In particular I would like to mention the support that I have always received from Prof. Carles Miravitlles.

I would like to thank Dr. Josep Nogués for agreeing to be my tutor at the UAB and to Prof. Markus Antonietti (Max Planck Institute of Colloids and Interfaces, Germany) and Prof. Anna Slawska (Institute of Physics, Polish Academy of Sciences) for kindly accepting to be the foreign examiners to apply for the European Doctorate Mention.

The economic support is always essential. I am very grateful to all the institutions that have funded this research: the Ministerio de Ciencia e Innovación for the FPU grant (AP-2004-2447) and the projects: MAT2003-01052, MAT2006-13572-C02-01 and Consolider-Nanoselect CSD2007-00041. Besides, the European Commission for the NoE FAME.

About the scientific aspect of the thesis, I preferred to express my gratitude to all the people who has directly contributed to the thesis by elaborating a list of Attributions (page xv). Other collaborators of parallel projects have been added in the Annexes. To all of them, I am very grateful for their contributions and their knowledge.

I would like to acknowledge the laboratory facilities of MATGAS which have been essential for the experimental work of this thesis.

I have also to acknowledge for profiting from short stages at foreign labs where I have learnt new techniques. Those labs are: Institute de la Chimie de la Matière Condenseé de Bordeaux, France (ICMCB-CNRS), under the supervision of Prof. Etienne Duguet, Max Planck Institute of Colloids and Interfaces in Potsdam, Germany, under the supervision of

A Madriz. A Sanse… mi Sanse…

Foreword and Scope of the Thesis

My interest in materials science was born from the curiosity to know why two materials that at first glance looked alike, had different properties. It seemed amazing how something could be modified at the atomic or molecular level to produce huge changes at the macroscopic level.

In 2004 I applied for a scholarship linked to a project to investigate porous silica composites offered by Prof. Elies Molins at the Institut de Ciència de Materials de Barcelona (ICMAB-CSIC). After one year I secured a FPU scholarship and began my doctoral thesis under the supervision of Dr. Anna Roig. My first tasks in the group were directed to the synthesis of silica aerogel and xerogel nanocomposites with magnetic nanoparticles. We also dedicated some initial efforts to the synthesis of aerogels with dispersed fct-$Fe_{0.5}Pd_{0.5}$ nanoparticles. This phase presents some interesting magnetic properties for applications of magnetic data recording. However, initial results were not entirely satisfactory since metallic iron easily oxidizes. At that time, Elisenda Rodriguez was a doctoral candidate in the group. She was pursuing her thesis on a molecular complex of iron (Fe_8) for its use as a positive contrast agent for magnetic resonance imaging (MRI). The iron oxide nanoparticles (γ-Fe_2O_3 and Fe_3O_4) are used as negative contrast agents in magnetic resonance imaging. Taking advantage of the knowledge in the group on iron oxide nanoparticles and Elisenda's knowledge on MRI, we decided to change the scientific objectives of the thesis to the development of a new synthetic protocol for iron oxide-silica composite nanoparticles useful in MRI and magnetic hyperthermia. Collaboration with Elisenda has been constant over the years that has lasted this work. Our approximation combines the sol-gel chemistry and supercritical fluids to obtain biocompatible, spherical composite particles, with narrow particle size distribution. For that, we were inspired in the drying procedure of silica aerogels under supercritical conditions and also in the synthetic protocol developed by Magda Moner Girona to obtain silica microparticles. The composite particles showed very high values of relaxivity. We have also studied the dependence of the specific absorption rate with iron concentration.

This manuscript is organized into seven chapters. **Chapter 1** provides a general introduction to magnetic nanoparticles, their properties, synthesis, stabilization and applications, with special interest in the biomedical field. The aim of the chapter is to place the reader in the scientific context of the thesis.

Chapter 2 describes the synthesis of nanoparticles by thermal decomposition of an iron complex, $Fe(CO)_5$, and their characterization in solid and colloidal dispersion.

Silica coating is a convenient approach to stabilize nanoparticles in a biocompatible way. In this thesis we have developed a new synthetic protocol to coat iron oxide nanoparticles with silica that combines the sol-gel chemistry and supercritical fluids. To understand and control the details of this procedure, we first synthesized nano- and microparticles of silica. They are described in **Chapter 3.**

Chapter 4 includes the synthesis of the composite γ-Fe$_2$O$_3$@SiO$_2$ nanoparticles. The core is composed of clustered iron oxide nanoparticles (described in Chapter 2) surrounded by a silica shell. Chapter 4 also describes the material characterization, with special emphasis on the magnetic properties, which will be exploited in the biomedical applications. We also succeeded in synthesizing composite ε-Fe$_2$O$_3$@SiO$_2$ nanospheres from the previous γ-Fe$_2$O$_3$@SiO$_2$ particles.

The evaluation of the materials described in Chapters 2 and 4 as contrast agents for magnetic resonance imaging and as mediators for magnetic hyperthermia is included in **Chapter 5**.

Chapter 6 lists the main conclusions derived from the present thesis.

Finally, **Chapter 7** gathers the annexes. It includes four publications arising from the main subject of this thesis, as well as five other publications and a patent on projects that I worked during the time that has lasted my doctoral thesis. The annexes also include a brief description of the experimental techniques used and protocols for sample preparation.

Presentación y Objetivos de la Tesis

Mi interés por la ciencia de materiales nació de la curiosidad de saber por qué dos materiales que a simple vista parecían iguales, tenían propiedades diferentes. Me parecía fascinante cómo se podía modificar algo a nivel atómico o molecular y obtener grandes cambios a nivel macroscópico. ¿Por qué un estropajo raya la vitrocerámica y otro no, cuando no veo ninguna diferencia entre ellos y tienen el mismo tacto…?

En el año 2004 el Prof. Elies Molins del Institut de Ciència de Materials de Barcelona (ICMAB-CSIC) ofrecía una beca asociada a proyecto para investigar materiales porosos de sílice compuestos con nanopartículas. Un año después obtuve una beca FPU y comencé mi tesis doctoral bajo la dirección de la Dra. Anna Roig. Mis primeros trabajos en el grupo se dirigieron hacia la síntesis de aerogeles y xerogeles de sílice nanocompuestos con partículas magnéticas. Dedicamos también algunos esfuerzos a la síntesis de nanopartículas $Fe_{0.5}Pd_{0.5}$ en aerogeles con el objetivo de tener partículas dispersas en una matriz sin que se agregasen durante el tratamiento térmico necesario para obtener la fase fct-$Fe_{0.5}Pd_{0.5}$. Esta fase presenta unas propiedades magnéticas interesantes para aplicaciones de grabación magnética de datos. Sin embargo, los resultados no fueron del todo satisfactorios por la tendencia del hierro metálico a oxidarse. Elisenda Rodríguez, entonces doctoranda del grupo, desarrollaba su tesis sobre un complejo molecular de hierro (Fe_8) para utilizarlo como agente de contraste positivo de resonancia magnética de imagen (RMI). Las nanopartículas de óxido de hierro (γ-Fe_2O_3, Fe_3O_4) son materiales utilizados como agentes de contraste negativo en resonancia magnética de imagen. Aprovechando los conocimientos del grupo en nanopartículas de óxido de hierro y el conocimiento de Elisenda en RMI cambiamos el rumbo de los objetivos científicos de la tesis. Comenzamos entonces el desarrollo de una nueva metodología sintética de esferas nanocompuestas de sílice y óxido de hierro útiles en dos aplicaciones biomédicas como son la resonancia magnética de imagen y la hipertermia magnética. La colaboración con Elisenda ha sido constante durante los años que ha durado este trabajo. Nuestra aproximación ha consistido en combinar la química sol-gel y los fluidos supercríticos para obtener nanoesferas biocompatibles de sílice con una distribución de tamaños estrecha. Para esto nos hemos inspirado en el procedimiento de obtención de aerogeles a partir del secado de geles en condiciones supercríticas y también en el método de obtención de micropartículas de sílice desarrollado por Magda Moner Girona. Las partículas compuestas mostraron valores de relajatividad muy altos. Hemos estudiado también la dependencia de la velocidad de absorción específica con la concentración de hierro.

El presente manuscrito se ha organizado en siete capítulos. El **Capítulo 1** recoge una introducción general sobre nanopartículas magnéticas, sus propiedades, síntesis, estabilización y aplicaciones, con especial interés en el campo biomédico. El capítulo pretende situar al lector en el contexto científico de la tesis.

El **Capítulo 2** describe la síntesis de nanopartículas de γ-Fe_2O_3 por descomposición térmica de un complejo de hierro (0), el $Fe(CO)_5$, así como su caracterización en estado sólido y en dispersión coloidal.

El recubrimiento de nanopartículas con sílice es un método muy útil de estabilización de forma biocompatible. En esta tesis hemos desarrollado un nuevo método sintético para recubrir nanopartículas de óxido de hierro con sílice que combina la química sol-gel con fluidos supercríticos. Para entender y controlar los detalles del procedimiento, primero sintetizamos nano- y micropartículas de sílice. Están descritas en el **Capítulo 3.**

El **Capítulo 4** incluye la síntesis de partículas magnéticas compuestas con sílice (γ-Fe_2O_3@SiO_2). El núcleo magnético está formado nanopartículas de γ-Fe_2O_3 (descritas en el capítulo 2) agrupadas en el centro y rodeadas de una capa de sílice. También se incluye su caracterización, con especial interés sobre las propiedades magnéticas, que serán las explotadas en las aplicaciones biomédicas. Conseguimos también sintetizar nanoesferas compuestas ε-Fe_2O_3@SiO_2 a partir de las partículas compuestas γ-Fe_2O_3@SiO_2.

La evaluación de los materiales descritos en los Capítulos 2 y 4 como agentes de contraste para resonancia magnética de imagen y como mediadores de hipertermia magnética se explica en el **Capítulo 5**.

El **Capítulo 6** recoge las conclusiones generales de la tesis.

Para acabar, el apartado de **Anexos (Capítulo 7)** incluye las cuatro publicaciones derivadas del tema principal de esta tesis, así como otras cinco publicaciones y una patente sobre proyectos en los que he colaborado durante el tiempo que ha durado la tesis doctoral. Los anexos incluyen también una breve descripción de las técnicas experimentales usadas, así como protocolos de preparación de muestras.

Presentació i Objectius de la Tesi

El meu interès per la ciència de materials va néixer de la curiositat de saber per què dos materials que a primera vista semblaven iguals, tenien propietats diferents. Em semblava fascinant com es podia modificar una cosa a nivell atòmic o molecular i obtenir grans diferències a nivell macroscòpic. Per què un fregall ratlla la vitrocerámica i un altre no, quan no veig cap diferència entre ells i tenen el mateix tacte...?

A l'any 2004 el Prof. Elies Molins de l'Institut de Ciència de Materials de Barcelona (ICMAB-CSIC) oferia una beca associada a projecte per a investigar materials porosos de sílice composats amb nanopartícules. A l'any vaig obtenir una beca FPU començant la meva tesi doctoral sota la direcció de la Dra. Anna Roig. Així, els meus primers treballs en el grup van dirigir-se cap a la síntesi d'aerogels i xerogels de sílice nanocomposats amb partícules magnètiques. També vam dedicar esforços cap a la síntesi de nanopartícules $Fe_{0.5}Pd_{0.5}$ en aerogels amb l'objectiu de tenir partícules disperses a una matriu sense que s'agreguessin durant el tractament tèrmic necessari per a aconseguir la fase $fct-Fe_{0.5}Pd_{0.5}$. Aquesta fase presenta unes propietats magnètiques interessants per a aplicacions de gravació magnètica de dades. No obstant això, els resultats no van ser del tot satisfactoris per la gran tendència del ferro metàl·lic a oxidar-se. En aquell moment Elisenda Rodríguez desenvolupava la seva tesi doctoral al grup sobre un complex molecular de ferro (Fe_8) per a avaluar-lo com agent de contrast positiu en ressonància magnètica d'imatge (RMI). Les nanopartícules d'òxid de ferro ($\gamma-Fe_2O_3$, Fe_3O_4) són materials utilitzats com agents de contrast negatiu en ressonància magnètica d'imatge. Aprofitant els coneixements del grup en nanopartícules d'òxid de ferro i el coneixement d'Elisenda en RMI, vam canviar els objectius científics de la tesi. Vam començar, aleshores, el desenvolupament d'una nova metodologia sintètica d'esferes nanocomposades de sílice i òxid de ferro, útils en dues aplicacions biomèdiques: RMI i hipertèrmia magnètica. La col·laboració amb l'Elisenda ha sigut constant durant la durada d'aquesta tesi. La nostra aproximació ha consistit en combinar la química sol-gel amb els fluids supercrítics per a obtenir nanoesferes biocompatibles de sílice amb una distribució de mida estreta. Per a això, ens hem inspirat en el procediment d'obtenció d'aerogels a partir de l'assecatge en condicions supercrítiques i també en el mètode d'obtenció de micropartícules de sílice desenvolupat per Magda Moner Girona durant la seva tesi. Les partícules composades van mostrar uns valors de relaxativitat molt grans. Hem estudiat també la dependència de la velocitat d'absorció específica amb la concentració de ferro.

El present manuscrit està organitzat en set capítols. El **Capítol 1** recull una introducció general sobre nanopartícules magnètiques, les seves propietats, síntesi, estabilització i aplicacions, amb especial interès en l'aspecte biomèdic. El capítol pretén situar al lector al context científic de la tesi.

El **Capítol 2** descriu la síntesi de nanopartícules de γ-Fe$_2$O$_3$ per descomposició tèrmica d'un complex de ferro (0), el Fe(CO)$_5$, així com la seva caracterització en estat sòlid i en dispersió col·loïdal.

El recobriment de nanopartícules amb sílice és un mètode molt útil d'estabilització biocompatible. En aquesta tesi hem desenvolupat un nou mètode sintètic per a recobrir nanopartícules d'òxid de ferro amb sílice que combina la química sol-gel amb fluids supercrítics. Per a entendre i controlar els detalls del procediment, primer hem sintetitzat nano- i micropartícules de sílice. Es descriuen al **Capítol 3**.

El **Capítol 4** inclou la síntesi de partícules magnètiques composades amb sílice (γ-Fe$_2$O$_3$@SiO$_2$). El nucli magnètic està format per nanopartícules de γ-Fe$_2$O$_3$ (descrites al capítol 2) agrupades al centre i envoltades d'una capa de sílice. També s'inclou la seva caracterització, amb especial interès en les propietats magnètiques, que seran les explotades a las aplicacions biomèdiques. També hem aconseguit sintetitzar nanoesferes compostes ε-Fe$_2$O$_3$@SiO$_2$ a partir de les partícules compostes γ-Fe$_2$O$_3$@SiO$_2$.

L'avaluació dels materials descrits als capítols 2 i 4 com a agents de contrast per a ressonància magnètica d'imatge i com mediadors de hipertèrmia magnètica s'explica al **Capítol 5**.

El **Capítol 6** recull les conclusions generals de la tesi.

Per acabar, l'apartat d'**Annexes** (**Capítol 7**) inclou les quatre publicacions derivades del tema principal d'aquesta tesi, així com altres cinc publicacions i una patent sobre projectes en els que he col·laborat durant el temps de la tesi. Els annexes inclouen també una breu descripció de les tècniques experimentals utilitzades i els protocols de preparació de mostres.

Table of contents

x

Abbreviations, acronyms and symbols

$\varnothing$	Diameter (also d)
α-Fe_2O_3	Hematite
χ	Magnetic susceptibility (adimensional in cgs and SI units)
ε-Fe_2O_3	Epsilon-iron oxide
γ-Fe_2O_3	Maghemite
ρ	Density
ζ	Zeta potential
CTAB	Cetyltrimethylammonium bromide
CO_2	Carbon dioxide
CSIC	Consejo Superior de Investigaciones Científicas
DLS	Dynamic light scattering
ED	Electron diffraction
$Fe(CO)_5$	Iron pentacarbonyl
Fe_3O_4	Magnetite
FM	Ferromagnetic
H^+	Proton
H	Magnetic field (T $\equiv$ 10 kOe)
H_C	Coercitive field
ICMAB	Institut de Ciència de Materials de Barcelona
IEP	Isoelectric point
IUPAC	International Union of Pure and Applied Chemistry
i.v.	Intravenously
K_{eff}	Effective anisotropy constant (J/m^3)
m	Magnetic moment (emu)
M	Magnetization (emu/g $\equiv$ A $\cdot m^2$/kg)
M_R	Remanence magnetization (emu/g $\equiv$ A $\cdot m^2$/kg)
MRI	Magnetic resonance imaging
M_S	Saturation magnetization (emu/g $\equiv$ A $\cdot m^2$/kg)
NP	Nanoparticle
OH^-	Hydroxyl ion
PM	Paramagnetic
Rf	Radiofrequency
r_i	Relaxivity ($s^{-1}mM^{-1}$)
SAR	Specific absorption rate (W/g)
SI	Système International
SPM	Superparamagnetic
T_B	Blocking temperature (K)
TEOS	Tetraethoxysilane

TMAOH	Tetramethylammonium hydroxide
TMOS	Tetramethoxysilane
UAB	Universitat Autònoma de Barcelona

Attributions

Here, I would like to acknowledge the people who have contributed to this thesis. Other collaborators of projects outside the scope of the thesis and outlined in the Annexes are acknowledged there.

- **Elisenda Rodríguez** (ICMAB-CSIC, University of Mons, Belgium, and Cambridge University, USA) performed the toxicity experiments and the relaxivity measurements for the maghemite and the composite particles and other magnetic measurements. She collaborated with us during all these years.

- **Martí Gich** (ICMAB-CSIC, Saint-Gobain Recherche) collaborated with us in the development of epsilon-iron oxide-silica nanospheres.

- The synthetic protocol of the composite iron oxide@silica particles was inspired in the results obtained by **Magda Moner Girona** during her Thesis at the ICMAB-CSIC.

- SAXS measurements were done at the Max Planck Institute of Colloids and Interfaces in Potsdam, Germany, at the group of **Markus Antonietti**. **Bernd Smarsly** trained me to operate the instrument as well as to perform the data fittings and interpretations.

- **Anna Slawska-Waniewska** from the Institute of Physics at the Polish Academy of Science performed part of the magnetic characterisation of the materials. The rest were done at the low temperature lab of the ICMAB, carried out by **Bernat Bozzo** and **Jose Manuel Pérez Falcón.**

- **Du Xing Chen** and **Alvaro Sánchez** (UAB) performed specific magnetic measurements and developed a model to calculate the size of magnetic nanoparticles from the magnetization curves.

- **Robert N. Muller** and **Alain Roch** (University of Mons, Belgium) contributed to the evaluation and understanding of the relaxivity results.

- **Etienne Duguet**, **Lydia Raison** and **Lucile Hardel** (Institut de Chimie de la Matière Condenseé de Bordeaux, France) trained me and also performed hyperthermia measurements. **Marie Helene Delville** (Institut de Chimie de la Matière Condenseé de Bordeaux, France) is acknowledged for early discussion and inspiration on the design of the silica nanocomposite material.

- **Susagna Ricart** and **Josep Maria Moretó** (ICMAB-CSIC) contributed with valuable chemical advice at the beginning of the work and participated in the set-up of the vacuum/inert gas line for the synthesis of iron oxide nanoparticles.

- **Jaume Gazquez** (Oak Ridge National Laboratory, USA) performed STEM and EELS analyses of the composite samples.

- **Judit Oró** (ICMAB-CSIC) performed the TEM images and electron diffraction analyses during the first three years of the thesis and trained me to use the scanning electron microscope.

- **Raul Solanas** is the engineer responsible for the supercritical fluid laboratory at MATGAS where the experiments at high temperature and high pressure were carried out; he was in charge of all the technical manipulations. Besides, he participated in fruitful discussions about technical and synthetic aspects of the composite particles.

- Atomic force microscopy images were performed by **Marcos Paradinas** in **Carmen Ocal's** group (ICMAB-CSIC).

- X-ray diffraction analyses were done at the XRD lab of the ICMAB. **Francisco Javier Campos** and **Joan Esquius** (ICMAB-CSIC) performed the x-ray diffractograms in powder form. **Anna Crespi** (ICMAB-CSIC) performed the diffractograms in colloidal dispersion.

- **Julio Fraile** (ICMAB-CSIC) participated in fruitful discussions about technical and fundamental aspects of the nitrogen adsorption/desorption technique.

- **Amable Bernabé** (ICMAB-CSIC) performed most of the infrared spectra.

- Thermal gravimetric analyses were done by **Ana Bea** (ICMAB-CSIC).

- **Neus Romà** (ICMAB-CSIC) assisted us to carry out the contact angle measurements.

- **Pau Solsona** performed some nitrogen adsorption/desorption analyses at MATGAS.

- Chemical analyses were performed at the Universitat Autònoma de Barcelona by **Ignasi Villarroya**.

- **Self use** of the following characterization techniques:

    o DLS and zeta potential measurements at MATGAS.
    o SEM at the ICMAB.
    o TEM: two last years at the Servei de Microscopia of Universitat Autònoma de Barcelona.
    o Nitrogen adsorption/desorption isotherms at the ICMAB.
    o Magnetic hyperthermia measurements at the ICMCB-CNRS in Bordeaux, France.
    o SAXS measurements and fittings at the MPI-Colloids and Interfaces in Potsdam, Germany.

Figure captions for the opening images in each chapter

The images introducing every chapter were obtained along the thesis. They will be briefly explained below.

Chapter 1. Amazonian grey goo...? TEM image of iron oxide nanoparticles (darker spots) 6-7 nm in diameter, dispersed in an organic TTF gel. The resulting spontaneous shape reminds the Amazon. Grey goo is a hypothetical end-of-the-world scenario involving molecular nanotechnology in which out-of-control self-replicating robots consume all matter on Earth while building more of themselves.

Chapter 2. TEM image of iron oxide nanoparticles stabilized with oleic acid and self-arranged in a hexagonal compact packing due to their narrow particle size distribution. The colour has been modified.

Chapter 3. Lid of the autoclave used for the syntheses of silica particles at the end of experiment Si_07_13. The material was dispersed all over the autoclave, including the lid.

Chapter 4. Cartoon image of composite particles showing the iron oxide nanoparticles clustered in the centre and surrounded by a silica shell.

Chapter 5. Photograph of fibroblast cells with fluorescent dye (from Invitrogen). Cytotoxicity tests were performed with this type of cells.

Chapter 6. Illustrating scheme of the main conclusions of the thesis. From left to right: a) Synthesis and characterization of maghemite nanoparticles, b) Coating of maghemite nanoparticles with silica by sol-gel chemistry under supercritical conditions and c) Evaluation of the maghemite nanoparticles before and after the silica coating as contrast agents for magnetic resonance imaging and as mediators for magnetic hyperthermia.
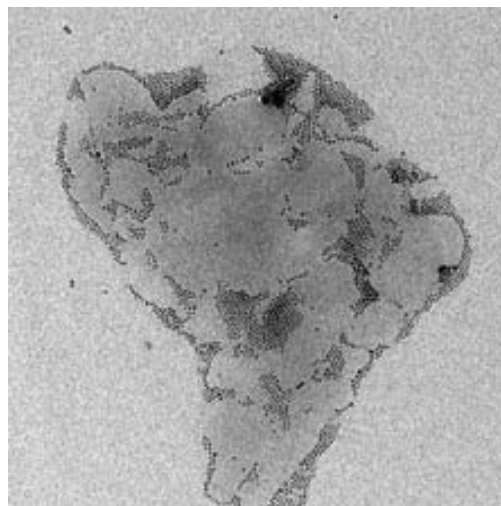
Amazonian grey goo...?!

1. INTRODUCTION AND SCOPE OF THE THESIS

1.1. Introduction

1.1.1. Nanoscience and nanotechnology

Nanoscience and nanotechnology have constantly gained in importance since they were first introduced in 1959 by Nobel Prize-winning physicist Richard Feynman. He gave a lecture to the American Physical Society entitled "There's plenty of room at the bottom: an invitation to enter a new field of physics".[1] He exposed the idea of building tiny devices and machines at a very small scale with remarkable new properties such as high density in storage of information or the ability to sequence genes by reading DNA molecules. He also emphasized the idea of building new mechanical machines to make smaller ones with increased precision. Many of his predictions have come true in the current context of "nanotechnology", although he didn't coined the term himself. It was Norio Taniguchi of

Tokyo Science University who first used the term "nanotechnology" in 1974 to describe the precision of achieving low-dimensional devices at that time. But the term did not become popular until the publication of a seminal work entitled "Engines of Creation: The Coming Era of Nanotechnology", by engineer K. Eric Drexler. The prefix "nano" comes from the Greek word "nanos (νανo)" meaning "dwarf". The Royal Society defines *Nanoscience* and *Nanotechnology* in the following manner:[2]

"*Nanoscience* is the study of phenomena and manipulation of materials at atomic, molecular and supramolecular scales, where properties differ significantly from those at larger scale."
"*Nanotechnologies* involve the design, characterization, production and application of structures, devices and systems controlling shape and size at nanometre scale."

The key point of nanoscience is the fact that the physico-chemical properties of materials with sizes in the nanometric scale hugely differ from those of the same bulk materials. For example, gold is a noble metal which had always been considered to be non active as a catalyst.[3,4] However, Haruta first demonstrated that gold nanoparticles are very good catalysts for oxidation of carbon monoxide (CO), even better than platinum.[5] They are also very good catalysts for the hydrogenation of nitrocomposites.[6] Semiconductors are another interesting example. When bulk, their band gap is fixed but when their dimensions are reduced to the nanometric range it is possible to modulate their band energies by changing their particle size. This property is very valuable to synthesize solar cells with control over the photoresponse and photoconversion efficiency.[7] These new properties of old and well-known materials occurring at their novel smaller size have opened new dimensions of science. And why are these big differences originated? They are mainly due to the high proportion of surface atoms and to quantum effects. When considering the ratio of surface atoms to inner atoms in a macroscopic cube of iron of 1 cm^3 it is only 10^{-5}%. If the cube is reduced to 10 nm^3 the percentage increases up to 10%, and if it is further reduced to 1 nm^3 all the atoms are located at the surface.[8] **Figure 1.1** illustrates this concept with another material, palladium clusters: 100 nm downwards the amount of surface atoms increases exponentially.[9] Therefore nanostructures bear high surface energy for what they are thermodynamically metastable. To compensate the excess of surface energy, the nanoentities tend to aggregate to bigger structures, thus changing their properties. The stabilization of nanometric materials is one of the most challenging problems in nanotechnology.

The nanoengineered devices are already present all over many of the everyday scenes of life. Since they were first thought in 1959 until our days, a great deal of scientific research has been invested in this area and many technological applications are now real. For their synthesis two main approximations are followed: the top-down and the bottom-up approaches. Top-down methods start from bulk materials, which are progressively

miniaturized up to the desired size. By using these protocols it is difficult to achieve nanometric particles under 100 nm with high degree of homogeneity and good stability. The opposite method, the bottom-up approximation, begins from atoms or molecules to end up with nanometric products. The control over the desired size, the homogeneity of the product and its stability is superior. For this approximation, chemical methods are the easiest and most widely applied. As G. Whitesides says: "In a sense, chemistry is (and has always been) the ultimate nanotechnology: chemists make new forms of matter (and they are really the only scientists to do so routinely) by joining atoms and groups of atoms together with bonds".[10]
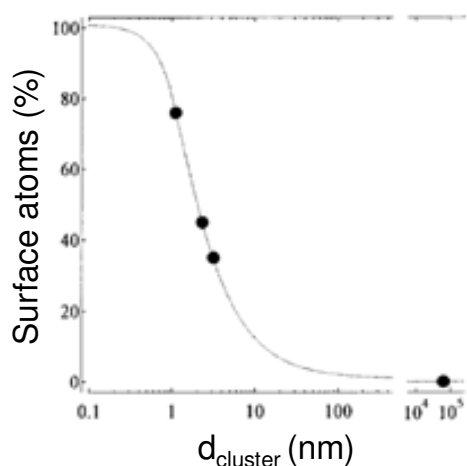
Figure 1.1 Percentage of surface atoms vs. the palladium cluster diameter.

Roger W. Whatmore pointed out in a publication in 2005[11] that the main periods of human history are named after the dominant technology of the moment: the stone age, the bronze age, the iron age, the industrial age and the computer age. But, at each of those moments, people were not conscious of the huge impacts that those technologies would generate ever after on the whole planet. Nowadays, perhaps it is the first time in human history in which we can anticipate the impacts of this new technological era and try to model it to improve the living conditions of all the inhabitants on the Earth.

1.1.2. Magnetic nanoparticles: properties, synthesis and applications

Properties of magnetic nanoparticles

Nanometric materials are those with any of their dimensions between 1 and 100 nm in length. Depending on how many dimensions are nanometric we find nanoparticles (NPs), as zero-dimensional materials (0D); nanorods, nanotubes or chains of NPs (1D); monolayers with nanometric width or with an assembly of 0D or 1D nanomaterials on

one plane (2D); and three-dimensional arrangements of nanometric entities (3D). Preparing samples with narrow size distribution[12] is critical to achieve long-range order in NP assemblies and controlled properties: for size distributions of 7% short- to medium-range order is observed; reducing the distribution to 5% enables the formation of assemblies with long-range order, known as colloidal crystals or superlattices.[13]

As already mentioned, the physico-chemical properties of nanomaterials differ from their bulk counterparts because of their high surface to volume ratio, their spatial confinement and their reduced imperfections.[8] Examples can be found reporting melting point or phase transition temperature decrease; they have reduced lattice constants; the mechanical strength is enhanced due to the reduced probability of defects; optical properties like absorption can change because of the discretization of the energetic levels; the colour of metallic nanoparticles may depend on their size due to surface plasmon resonance; electrical conductivity decreases with a reduced dimension due to increased surface scattering; ferromagnetism of bulk materials transfers to superparamagnetism in the nanometre scale; there is a higher diffusion of impurities and defects to the surface with thermal treatments, etc. Many of these properties depend significantly on particle size.

This thesis focuses on magnetic zero-dimensional nanoparticles, whose properties depend on their nanometric size and also on the interactions with neighbouring nanoparticles. It is important to keep in mind that 1D to 3D assemblies of nanoparticles can alter their individual behaviour. For example, magnetic nanoparticles can be superparamagnetic at a defined temperature under a critical size when they are dispersed, but if there are interparticle interactions they can increase the effective anisotropy constant, increasing the blocking temperature.[14]

Magnetism at the nanoscale differs significantly from the bulk. Hereafter, a brief introduction to the basis of magnetism will be given, trying to underline the magnetic differences among both dimensions.

The word "magnetism" is derived from Magnesia, a town in Turkey. Its discovery was done by the shepherd Magnes around 1000 BC when, while walking in the mountains, he was drawn to the earth by the tacks in his sandals. He looked for the origin of the attraction and found out that it was the loadstone, a magnetic iron oxide which was later called magnetite. All materials are magnetic to some extent; their response depends on their atomic structure and temperature. They can be classified according to their magnetization (*M*) induced by an external magnetic field (*H*), i.e. their magnetic susceptibility (χ):

Equation 1.1
$$\chi = \frac{M}{H}$$

4

In SI units (Système Internationale) χ is dimensionless and M and H have units of A/m. Diamagnetic and paramagnetic materials display very little magnetization and only in the presence of a magnetic field, with χ within the ranges -10^{-6} to -10^{-3} and 10^{-6} to 10^{-1}, respectively. Other materials have ordered magnetic states and they are magnetic even in the absence of an external magnetic field: ferro-, ferri- and antiferromagnets. They differ in the coupling of their magnetic moments: parallel alignment with net magnetic moment ($\chi = 50$ to 10^4), uncompensated antiparallel alignment with net magnetic moment ($\chi = 50$ to 10^4), and antiparallel alignment without net magnetic moment ($\chi = 10$ to 1000), respectively. Ferro- and ferrimagnets have permanent magnetic moment, i.e. they have remanence magnetization (M_R) without the presence of an external magnetic field. The external field required to bring this magnetization to zero is called coercivity (H_C). These values are represented in a typical magnetization curve with hysteresis cycle in **Figure 1.2**. When all the magnetic moments are aligned with the external magnetic field the material reaches its maximum magnetization, called saturation magnetization (M_S), which is an intrinsic value of the material.
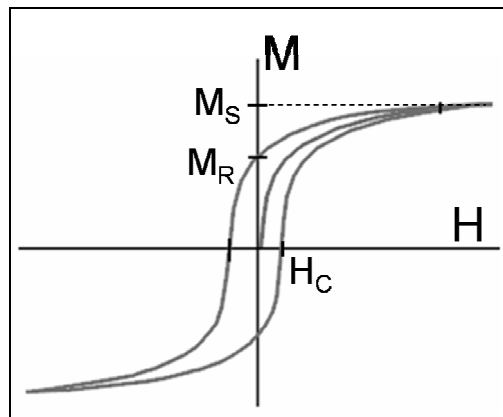
Figure 1.2 A typical magnetization curve of a ferro- or ferrimagnetic material. M_S stands for saturation magnetization; M_R is the remanence magnetization and H_C is the coercivity.

Ferromagnetic materials are made up of magnetic domains; each domain contains parallel magnetic moments separated by domain walls. These domains are created to reduce the magnetic free energy. If the material is reduced up to nanometric dimensions, there is a critical size below which the energy necessary to create domain walls is higher than the magnetic free energy (or magnetostatic energy). The critical size of a spherical particle (D_C) below which it is a single-domain particle fulfils the condition E(domain wall) = E(magnetostatic energy)[15] which implies:

Equation 1.2
$$D_C \approx 18 \cdot \frac{\sqrt{A \cdot K_{eff}}}{\mu_0 \cdot M_S^2}$$

where A is the exchange constant, K_{eff} is the anisotropy constant, μ_0 is the vacuum permeability and M_S is the saturation magnetization. For example, maghemite spherical

particles are expected to be single-domain below 166 nm in diameter[16] and fcc cobalt particles only below 7 nm.[15] The smaller critical size of cobalt is due to its higher effective anisotropy constant. This value depends on the magnetocrystalline energy, shape, exchange interactions and surface energy. That is why, for instance, a nanorod will have higher anisotropy and consequently a higher critical size than a spherical particle of the same material, since the nanorod has a higher surface to volume ratio.

In a paramagnetic (PM) material the individual atomic spins are independent from each other and randomly oriented. In contrast, the atomic spins in ferromagnetic domains are coupled and align parallel. The magnetic anisotropy energy in monodomain FM particles is responsible for holding the magnetic moments along a certain direction:

Equation 1.3 $$\Delta E = K_{eff} \cdot V$$

This is the simplified equation for uniaxial anisotropy, where V is the volume of the particle. The energy barrier $K_{eff} \cdot V$ separates the two energetically equivalent easy directions of magnetization, as exemplified in **Figure 1.3**.
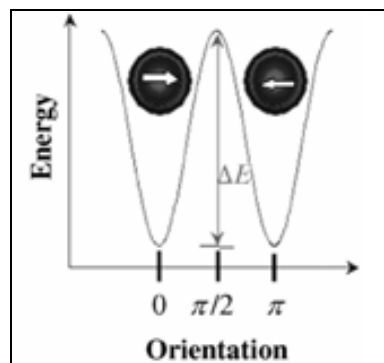
Figure 1.3. Energy dependence on the magnetic moment orientation in monodomain particles. ΔE represents the energy barrier to the rotation of the magnetization. The left and right arrows represent spin states.[13]

When monodomain particles are further reduced, the thermal energy becomes larger than the energy barrier and the magnetic moment of the particles fluctuates:

Equation 1.4 $$k_B \cdot T > K_{eff} \cdot V$$

where k_B is the Boltzmann constant and T is the temperature. The material behaves then like a paramagnet but bearing a giant moment inside each particle: it is called a superparamagnet (SPM). As schemed in **Figure 1.4** SPM materials share the lack of remanence magnetization and coercivity with paramagnets, but their susceptibility and saturation magnetization values are similar to those ones of ferromagnets. The magnetization of an ideal SPM system obeys a Langevin function:[17]

Equation 1.5 $$M = M_S \cdot (\coth \alpha - \frac{1}{\alpha})$$

6

where $\alpha = \dfrac{m_0 \cdot H}{k_B \cdot T}$ and $m_0 = M_S \cdot V_{ptle}$, where the saturation magnetization is expressed in

volume units. Their magnetization curves at different temperature superimpose onto a universal curve of M vs. H/T.
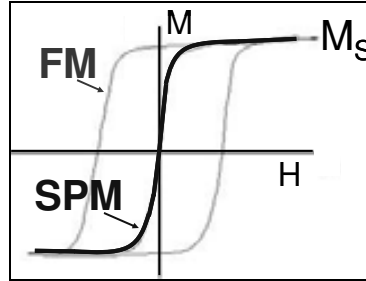
Figure 1.4. Comparison between a typical magnetization curve of a ferromagnet (FM) and a superparamagnet (SPM). The SPM curve obeys a Langevin function.

Figure 1.5 summarizes the previous concepts. Ferromagnets, when bulk, are multi-domain materials with coercivity but, as the size is reduced, the energy to build domain walls becomes comparable to the magnetic free energy and monodomain particles are stabilized. The coercivity increases because of the lack of domain walls. If the size is further reduced there is a critical size below which the thermal energy is higher than the magnetic energy and the magnetic moment of the particles fluctuate freely: coercivity disappears.
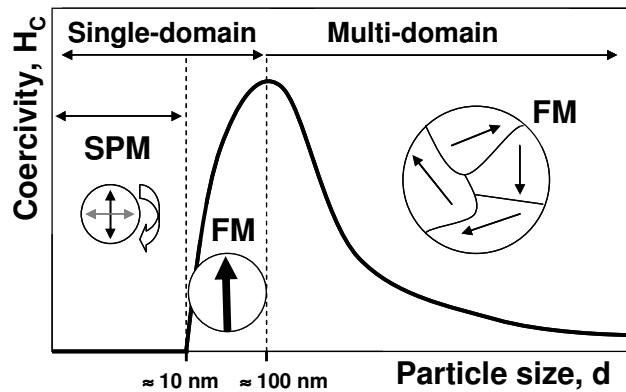
Figure 1.5. Coercivity vs. particle size. The numerical values of particle size are a reference of the order of magnitude for the critical size values at room temperature; they vary for each material.

The relaxation time of the moment of a single-domain particle can be approximated by the Néel-Brown expression: [15]

Equation 1.6 $$\tau = \tau_0 \cdot \exp \dfrac{K_{eff} \cdot V}{k_B \cdot T}$$

where $\tau_0 \approx 10^{-9}$ s is usually assumed. The observation of the transition temperature between ferro- and superparamagnetic behaviour depends not only on the temperature

but also on the chosen technique and its characteristic measuring time, τ_m. If $\tau << \tau_m$ the particles will appear SPM and if $\tau >> \tau_m$ the particles will display coercivity. The blocking temperature (T_B) is defined as the temperature of the FM-SPM transition. It depends on the magnetocrystalline anisotropy of the material, its particle size, the applied magnetic field and the experimental measuring time.

In most of real systems, the saturation magnetization in SPM particles (proportional to the particle size) is lower than the intrinsic bulk value. A general accepted explanation, mostly for oxide systems, is the high surface to volume ratio in nanoparticles: the spins at the surface are canted and do not contribute to the total magnetic moment of the particle.[18-21] This non-magnetic surface mantle is called dead layer. Then, the magnetization can be written as a sum of the superparamagnetic core contribution plus the paramagnetic shell contribution:[22]

Equation 1.7
$$M(H) = \int_0^\infty p(v; \eta, \sigma) v^{-1} \left[M_S v_C L(x) + v_S \chi_{pm} H \right] dv$$

where $p(v, \eta, \sigma)$ is the particle volume distribution, $M_S \cdot v_C \cdot L(x)$ is the superparamagnetic core contribution (M_S = bulk saturation magnetization, v_C = core volume and $L(x)$ corresponds to the Langevin function (**Equation 1.5**)) and $v_S \chi_{Pm} \cdot H$ is the paramagnetic shell contribution (v_S = shell volume, χ_{pm} = PM susceptibility and H = applied field). I have recently co-authored a publication on "Size determination of superparamagnetic nanoparticles from magnetization curve" where the particles described in this thesis were used to check the model proposed in the publication (see annex 7.1).[22] Currently, it is still a challenge to synthesize magnetic monodomain nanoparticles presenting the saturation magnetization equal to the bulk saturation magnetization.

For many applications an advantage of superparamagnetic materials is the lack of coercivity because when the magnetic field is switched off, the thermal energy is large enough to fluctuate the particle magnetic moment. A potential aggregation of particles is avoided and no extra energy is necessary to demagnetize the system. In the biomedical field it is a major benefit when magnetic colloidal dispersions are injected intravenously: the risk of embolism is diminished.

Synthesis of magnetic nanoparticles

There is a large number of publications regarding synthesis and potential uses of magnetic nanoparticles.[23] In general terms, physical techniques like physical vapour deposition,[24,25] evaporation/condensation,[26,27] sputtering deposition,[28,29] mechanical alloying or ball milling,[30] lithography[31,32] and ionic implantation,[33] are top-down methods which produce nanoparticles with good crystallinity; however, many of these techniques need a substrate to deposit the particles. Furthermore, the economical costs are high and the product yield is low. Aggregation of particles is an unresolved issue for most of those

techniques. On the contrary, chemical methods like reactions in supercritical fluids,[34] aerosol pyrolysis[35] and specially wet chemistry methods,[36-38] are bottom-up approaches which can reach higher product yields, they can be much more economical and the particles can be handled in an easier way since they are obtained in liquid or gaseous media: no substrate is necessary and particle aggregation is easier to handle.

There are many wet chemistry methods reported in the literature, some of them being easy and cheap. Several iron oxide crystalline phases like magnetite (Fe_3O_4), maghemite (γ-Fe_2O_3), hematite (α-Fe_2O_3), FeO, etc, have been successfully synthesized. Metallic nanoparticles such as Fe, Co and Ni, metal alloys like FePt and CoPt, metal oxides or ferrites such as $MgFe_2O_4$, $MnFe_2O_4$ and $CoFe_2O_4$, are also interesting magnetic materials with many applications. The following paragraphs will summarize the most used synthetic bottom-up pathways of wet chemistry with illustrating examples.

The *co-precipitation method* is a simple and convenient route to synthesize iron oxide nanoparticles (magnetite, Fe_3O_4, and maghemite, γ-Fe_2O_3) from aqueous Fe^{2+}/Fe^{3+} salt solutions. This method was broadly developed by Massart et al in 1987.[39] Briefly, a mixture of ferrous and ferric salts like acetate, acetylacetonate, chloride, etc. dissolved in water yield the precipitation of iron oxide nanoparticles after the addition of sodium hydroxide or ammonia. A mixture of magnetite and maghemite is often obtained. Maghemite is the most stable phase under ambient conditions since magnetite can be easily oxidized.[15] The synthesis is reproducible but the particle size dispersion is generally broad (see **Figure 1.6**). Reaction parameters such as the type of iron salts, Fe^{2+}/Fe^{3+} ratio, pH and temperature determine the size, shape and crystalline phase.[40] They can be stabilized either electrostatically or sterically with organic ions such as carboxylate or hydroxyl ions. Among those, oleic acid has been defined as the best candidate.[15]
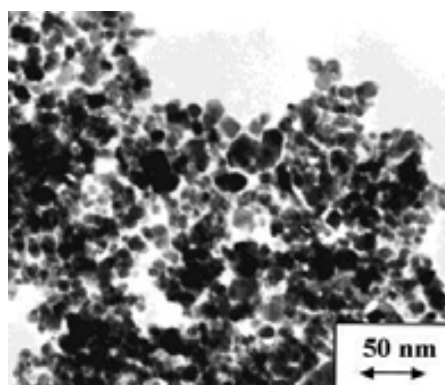
Figure 1.6. Iron oxide polydisperse nanoparticles synthesized by the co-precipitation method.[18]

Thermal decomposition is another method to synthesize oxides, metallic and alloy particles. The reactants are organometallic compounds which decompose at high temperature in an organic solvent with high-boiling point in the presence of a surfactant. This method allows the reaction to follow the LaMer mechanism,[41] i.e. the temporal separation between

a short burst of nucleation from a supersaturated solution and the subsequent slow controlled growth of the particles. LaMer mechanism leads to monodisperse systems. The precursors can be metal acetylacetonates [$M(acac)_n$] (M = Fe, Mn, Co, Ni, Cr), metal cupferronates [M^xCup_x] (Cup = N-nitrosophenylhydroxylamine, $C_6H_5N(NO)O^-$) or carbonyls [$M^0(CO)_n$], among others. Fatty acids and organic amines are often used as surfactants and consequently the particles are dispersible in organic solvents such as toluene or hexane.

Hyeon and co-workers have used the thermal decomposition method at 240-320°C with an iron salt, $FeCl_3$, and sodium oleate in different solvents like 1-hexadecene, octyl ether, 1-octadecene, etc., and have succeeded in the synthesis of monodisperse particles with controlled size from 5 to 22 nm.[42] Hyeon's group has also succeeded in synthesizing iron oxide nanoparticles by decomposition of iron pentacarbonyl ($Fe(CO)_5$, a very versatile compound) at 300°C in octyl ether in the presence of oleic acid or lauric acid. No size-selection process was necessary to obtain monodisperse spherical maghemite nanoparticles ranging from 4 to 16 nm (see **Figure 1.7**).[43] Other particle shapes including diamonds, triangles and plates have been obtained by decomposition of $Fe(CO)_5$ in o-dichlorobenzene (ODCB) at 180°C with dodecylamine (DDA) as the capping agent. By changing the surfactant/iron precursor molar ratio the shape was controlled.[44]

In order to use iron oxide nanoparticles for biomedical applications aqueous dispersions are required and therefore an extra step to exchange the solvent has to be added to the previous synthesis. To avoid this step, Li et al. have prepared water-dispersible Fe_3O_4 nanoparticles using $FeCl_3$ and 2-pyrrolidone under reflux at 245°C.[45,46]
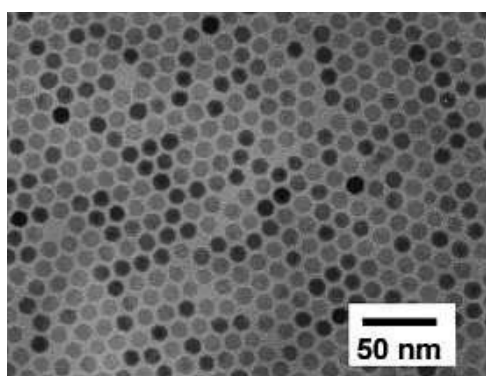
Figure 1.7. TEM image of 11 nm iron oxide nanoparticles synthesized by thermal decomposition of $Fe(CO)_5$.[43]

Metallic nanoparticles of Fe, Co and Ni can be also prepared through thermal decomposition of metal carbonyls under inert atmosphere to avoid the formation of metal oxides.[13] In 1979 Griffiths et al. succeeded in synthesizing 5 to 20 nm in diameter iron nanoparticles from the decomposition of iron pentacarbonyl.[47] Puntes et al. reported the synthesis of the ε-phase of Co nanoparticles through decomposition of dicobalt

octacarbonyl, $Co_2(CO)_8$, in the presence of different surfactants.[48,49] Reducing agents like molecular hydrogen[50] or superhydrides[51] are sometimes necessary. However, another strategy to stabilize the metallic particles is to gently oxidize the particle surface with synthetic air.[52]

Alloys such as FePt, CoNi and CoPt are very interesting for their high magnetic anisotropy.[53-55] Sun et al. reported the first synthesis of monodisperse FePt nanoparticles through the thermal decomposition of $Fe(CO)_5$ and the simultaneous reduction of platinum acetylacetonate.[36] The as-synthesized alloy had a disordered face centred cubic (fcc) crystal structure and did not bear the most interesting magnetic properties of the fct polymorph (face centred tetragonal or $L1_0$ phase). Annealing at 500ºC was necessary, but sintering of nanoparticles could not be avoided. Jeyadevan et al. reported the first direct synthesis of fct FePt phase using a wet-chemistry method.[56]

The third method to be mentioned is the *microemulsion* technique. A microemulsion is a thermodynamically stable isotropic dispersion of two immiscible liquids. The minor or dispersed phase is formed of nanodroplets (between 1 and 50 nm in diameter) stabilized by an interfacial film of surfactant molecules, which are immersed in the major or continuous phase. The droplet size depends on the molar ratio of both phases.[57,58] These droplets are used as nanoreactors for the synthesis of metal, alloy or oxide nanoparticles. Depending on the individual synthesis, the microemulsion will be water-in-oil (water droplets dispersed in an organic continuous phase) or the opposite, oil-in-water.

Zhang et al. reported on the synthesis of ferrite nanoparticles, $MnFe_2O_4$, using a water-in-oil microemulsion.[59] Briefly, metal salts ($Mn(NO_3)_2$ and $Fe(NO_3)_3$) are first dissolved in water; then an aqueous solution of surfactant, sodium dodecylbenzenesulfonate (NaDBS), is added to the previous solution. To form the micelles, a large amount of toluene is added and the whole mixture is stirred overnight. Next, sodium hydroxide is added to induce the formation of ferrite nanoparticles inside the micelles. By controlling the water/toluene ratio the particle size could be tuned from 4 to 15 nm. This group used the same approach to synthesize $CoCrFeO_4$ nanoparticles from $CoCl_2$, $CrCl_3$ and $Fe(NO_3)_3$ with sodium dodecyl sulfate (SDS). The particle size could be tuned from 6 to 16 nm.[60]

In spite of the good reproducibility of the particles synthesized by microemulsion technique, the particle size and shape dispersions are not narrow and the product yield is very low, such that large amounts of solvents are required to obtain appreciable amounts of material. Besides, the scaling-up of the processing seems to be rather difficult.[15]

Hydrothermal synthesis is another synthetic method that allows for the fabrication of different crystalline phases. Li et al. reported a generalized hydrothermal method based on a liquid-solid-solution reaction: a phase transfer and separation mechanism takes place at the interfaces of the liquid (ethanol-linoleic acid), solid (metal linoleate) and solution

phases (water-ethanol).[61] The resulting particles, Fe_3O_4 and $CoFe_2O_4$, among others, are monodisperse and well crystallized. Surfactants or electrolytes as polyethylene glycol or sodium acetate are also necessary to avoid particle agglomeration.

The main characteristics of the four introduced methods for the synthesis of magnetic nanoparticles are summarized in **Figure 1.8**.[15] Co-precipitation seems to be the simplest method since the syntheses take place in a few minutes, at soft conditions of temperature (20-90°C) and pressure (P_{atm}), being water the solvent. Nevertheless, the resulting particles are polydisperse with poor control over the shape. Microemulsion method leads to spherical well-crystallized particles with relatively narrow size distribution. However, the method is not trivial, but rather complicated, and neither efficient, since high amounts of solvents are necessary to get small quantities of particles. Furthermore, the particle purification to get rid of the high amount of surfactants is not trivial. Hydrothermal synthesis has not yet been widely exploited although its technical conditions are easily attained and the quality of the resulting particles is quite good.

The most profitable method is certainly the thermal decomposition one since it produces particles with controlled size, narrow particle size distribution with no size-selection process, reasonable product yield and potential scalability. The control over the particle characteristics enables the control over their properties, essential for their successful applications. **This is the method chosen as the synthetic path to obtain iron oxide nanoparticles in this thesis.**

Synthetic method	Synthesis	Reaction temp. [°C]	Reaction period	Solvent	Surface-capping agents	Size distribution	Shape control	Yield
co-precipitation	very simple, ambient conditions	20–90	minutes	water	needed, added during or after reaction	relatively narrow	not good	high/ scalable
thermal decom-position	complicated, inert atmosphere	100–320	hours–days	organic compound	needed, added during reaction	very narrow	very good	high/ scalable
microemulsion	complicated, ambient conditions	20–50	hours	organic compound	needed, added during reaction	relatively narrow	good	low
hydrothermal synthesis	simple, high pressure	220	hours ca. days	water-etha-nol	needed, added during reaction	very narrow	very good	medium

Figure 1.8. Main characteristics of the synthetic methods to obtain magnetic nanoparticles.[15]

Applications of magnetic nanoparticles

The applicability of magnetic nanoparticles is very broad. They are being used in a number of industrial processes and their potentiality is growing. An especially interesting fact is the diversity of areas of application, from nuclear waste separation to electronic devices or biomedical applications.

Ferrofluids are magnetic fluids made up of superparamagnetic nanoparticles dispersed in a liquid, i.e. magnetic colloidal dispersions, with amazing properties.[21] They were first developed at the National Aeronautical and Space Administration (NASA) in the 1960s to control fluids in space.[62] They can be used as lubricants due to their high degree of sealing, no leaking out and lower friction than conventional seals. They can be also used to separate nonmagnetic objects according to the density. This property derives from the magnetostatic repulsion, which can push nonmagnetic objects immersed in a ferrofluid out of the region of a strong magnetic field. By adjusting the strength of the magnetic field it is possible to only float particles with a specific density.[63] And a third example is the generation of heat when a ferrofluid is exposed to an alternating magnetic field. The particles rotate to align with the external field and relax when the field is over: the magnetic energy is transformed in thermal energy. **Figure 1.9** is an example of a ferrofluid.

Chemical catalysis has found important advantages in nanometric materials, especially in the magnetic ones. When the nanometric entities are not only catalytically active but also magnetic, they can be much more easily recovered from the reaction solutions by external magnets. This is the case of a chiral catalyst immobilized through a ruthenium(II) complex on magnetite nanoparticles.[64] Another smart example is the coating of a magnetic nanoparticle such as cobalt with a highly active catalyst, such as platinum.[65] The mass of the highly expensive noble metal is decreased since only a monolayer of platinum atoms is necessary and the recovery of the particles is simplified by the magnetic properties of cobalt. Superparamagnetism is a useful property for these systems. The catalytic reaction takes place with no external magnetic field: the magnetic moment of each particle fluctuates with thermal energy and therefore, the particles act as non-magnetic particles, just as catalysts. After the reaction, an external magnetic field is applied to magnetize the particles and collect them from the solution. Once they are collected, they can be redispersed in a new solution when the external magnetic field is removed.
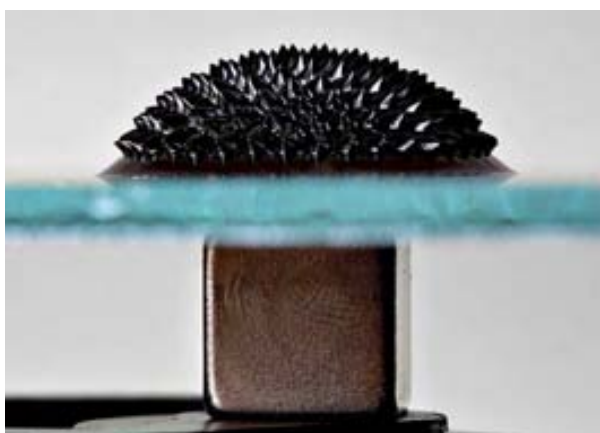
Figure 1.9. Ferrofluid on a glass substrate, with a magnet underneath.

Nuclear waste separation also takes profit of magnetic nanoparticles.[66] For example, Nuñez et al. have efficiently separated radionuclides such as plutonium, americium and uranium from acidic solutions by adsorption of alkylphosphates onto superparamagnetic magnetite nanoparticles.[67] They have a promising potential for metal removal and environmental applications.

In the field of computing, superlattice assemblies of ferromagnetic nanoparticles with high coercivity can act as high density magnetic recording media. FePt nanoparticles are a good example since they bear a high uniaxial magnetocrystalline anisotropy ($K \approx 7 \cdot 10^6$ J/m^3) and good chemical stability.[36] These nanometric ferromagnets could store information given that their spins do not fluctuate in the absence of an external magnetic field. For this particular application superparamagnetic particles are not useful.

To end this selection on applications of magnetic properties, their use in biomedicine cannot be excluded. In the last few years several reviews have been published on their synthesis, stabilization and detailed applications.[15,68-72] Drug delivery, ultrasensitive detection and separation of biomolecules, cell tagging, tracking and imaging, hyperthermia, etc. These and other biomedical applications will be later explained in section 1.1.4.

1.1.3. Stabilization of nanoparticles as colloidal dispersions

1.1.3.1. Brief introduction to colloid science

The concept of colloid was first introduced by Thomas Graham in 1861.[73] He described it as a viscous solution, with low diffusivity, unable to pass through common filters. The word "colloid" comes from the Greek noun "κολλώδης" which means sticky or viscous.

The IUPAC (International Union of Pure and Applied Chemistry) definition for colloidal dispersion states: a system with particles of colloidal size (1-1000 nm) of any nature (solid, liquid or gas) dispersed in a continuous phase of a different composition or state.[74] Smaller entities like atoms or molecules constitute true solutions, their diameters being lower than 0.5 nm. Both the solute and solvent molecule diameters are comparable in true solutions, but in colloidal dispersions the particles are much larger than the solvent molecules (among 1 and 4 orders of magnitude). This fact implies important differences in the interactions with light. On the other end of the colloidal range, particles larger than 1000 nm form suspensions. Some examples of everyday colloidal dispersions are fog, milk, mayonnaise, gelatine, lubricants, catalysts, cosmetics, foams, aerosols, etc.

A stable dispersion of solid particles in a liquid is called a sol. It is said to be stable when the particles do not aggregate at a significant rate.[74] These systems are not thermodynamically stable like true solutions, but kinetically stable for a given time-span.

Their stability depends on the degree of dispersion of the discrete phase, affinity between both phases, viscosity of the solvent, electrical charge onto the surface of the discrete particles and temperature. The colloidal dispersions can be purified by dialysis, ultrafiltration, ionic exchange and sedimentation/centrifugation.

Nanostructures like colloids have very high surface energy due to their high percentage of surface atoms. To minimize this excess of energy they tend to follow different mechanisms such as surface reorganization (new stressed bonds are created between the surface atoms), physical or chemical adsorption of surrounding molecules, sintering of particles (when the temperature is high), Ostwald ripening or particle agglomeration. Particle agglomeration is the association of groups of particles through physical or chemical bonds to form larger entities with lower surface energy. Consequently, the individual properties of single particles are sacrificed and the stability of the nanoparticulated system may be destroyed. Most of the physical methods need a substrate to deposit the particles in order to avoid their agglomeration.[24-33] The resulting particles are fixed, they have no individual mobility. On the contrary, wet chemistry methods can synthesize and stabilize the particles individually in a liquid dispersant. The first reported example of a colloidal dispersion, colloidal gold, was first described by Michael Faraday more than a century ago, in 1887,[75] and it is said that the dispersion is nowadays still stable.

Colloidal stabilization is divided in *electrostatic* and *steric stabilization*. The *electrostatic stabilization* arises from the surface charge density created onto a particle when it is immersed in a polar solvent or an electrolyte solution. Two equivalent particles will repel each other because they bear the same surface charge. The charge is originated from the dissociation of surface charged species, isomorphic substitution of ions onto the surface, accumulation or depletion of electrons at the surface or physical adsorption of charged species onto the surface. Therefore, the surface potential of a solid depends not only on the chemical composition of the particle but also on the kind and concentration of ions in the surrounding solution. It can be either positive or negative.

From now on the discussion will be centred on non-conductive materials or dielectrics, more specifically on oxides. The electric charge on oxides is mainly due to the dissociation of surface ions or to the adsorption of surrounding ions (defined as charge determining ions), mainly protons, H^+, and hydroxyl ions, OH^-. The adsorbed species are called surface charge determining ions. Consequently, the surface charge will vary with pH from positive values (acidic medium, high concentration of protons) to negative values (basic medium, high concentration of hydroxyl ions). The pH at which the surface charge is zero is called the isoelectric point (IEP).

The charge determining ions are anchored to the surface through electrostatic forces. Associated to them there are always counter ions with opposite charge, as depicted in

Figure 1.10. Although the whole system must be electrically neutral, there are differences in charge density near the particle surface due to the different distribution of charge determining ions and counter ions. The result is the formation of an electrical double layer, schematized in **Figure 1.10**. Between the particle surface and the Helmholtz plane there is the Stern layer, where the electric potential drops linearly. From the Helmholtz plane to the bulk solution the Gouy layer or diffuse double layer expands with an exponential decay of the potential.

The slip plane separates the bulk solution from the area where the electrolytes are tightly bound to the particle and move with it due to the Brownian motion. The potential at this plane is called the zeta potential (ζ) and it is used as a reference value to measure the stability of the electrostatically stabilized colloidal particles. When two particles approach one another, double layers overlap and a repulsive force develops. The higher the absolute value of zeta potential, the stronger the electric repulsion between particles and therefore, the higher the stability of the colloid. Consequently, the colloid will be completely unstable at the isoelectric point. The zeta potential decreases with the concentration and valence state of the counter ions and increases with the solvent dielectric constant. The repulsion originated when two electrical double layers overlap is not only due to the repulsion of ions of the same charge but also due to an osmotic force. The concentration of ions in the region of overlapping becomes very high; a flow of solvent restores the initial equilibrium of concentration profiles.
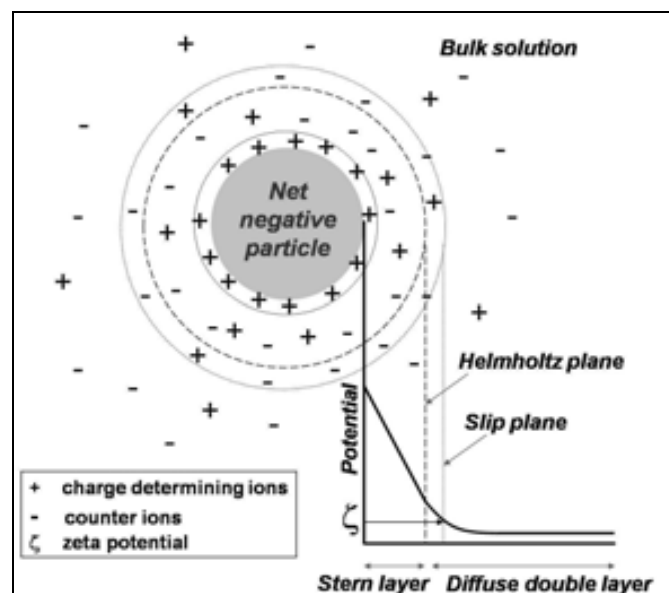
Figure 1.10. Scheme of the diffuse double layer and the electric potential for a negatively charged particle.

Electrostatic forces induce particles to repeal from each other. But, which are the forces responsible for the agglomeration of colloidal particles? They are the Van der Waals attraction forces. At the nanometric scale, gravitational forces are negligible and as a

result, Brownian motion and Van der Waals forces gain in importance. The particles collide with each other constantly due to the Brownian motion, increasing the attraction force as the distance between them is reduced. The Van der Waals interaction between two particles depends on the particle radius (r), the distance between particles (S) and the Hamaker constant, A:

Equation 1.8 $$V_A = -\frac{A}{12} \cdot f(r,S)$$

The Hamaker constant is a positive value which depends on the polarization properties of the molecules constituting the two particles and on the dispersion medium. Electrostatic or steric stabilization is thus essential to avoid the destabilization of the colloid by Van der Waals forces.

Just before World War II, Derjaguin and Landau[76] on the one hand, and Verwey and Overbeek[77] on the other hand, simultaneously formulated an initial theory of electrostatic stabilization of particles in a suspension, which was named after all of them as DLVO theory. Although it has important assumptions which are not fulfilled by colloids (i.e. infinite flat solid surface) the theory works well in explaining the interactions between two particles and thus it is widely accepted in the research community of colloidal science.[8] It states that the total interaction between two particles (V) which are electrostatically stabilized is the sum of the Van der Waals attraction (V_A) and the electrostatic repulsion (V_B): $V = V_A + V_R$ (see **Figure 1.11**). A minimum of potential is found near the particle surface due to the attraction forces and a maximum is found a little further originated from the electrostatic repulsion. Since the Van der Waals forces are almost independent of the counter ions concentration and of their valence state, as the electrostatic potential does, the increase of any of those parameters will decrease the repulsion potential. Then, the particles agglomerate. Therefore, the total potential is highly dependent on the concentration and valence state of the counter ions.
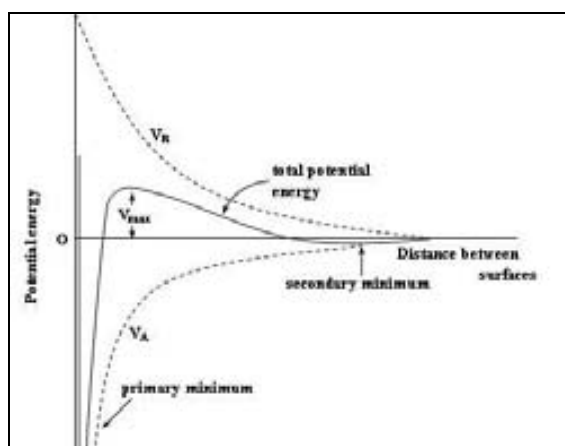
Figure 1.11. Scheme of DLVO potential: V_A = attractive Van der Waals potential; V_B = repulsive electrostatic potential.

As it was noticed before, the DLVO theory establishes some assumptions which are not satisfied in real colloidal systems. Nevertheless, it has been widely applied in practice, as far as the following conditions are met:

- Highly diluted dispersions: the electric potential of one particle does not influence other particle potential.
- Only Van der Waals and electrostatic forces are present in the system: gravitational forces are negligible, there are no magnetic forces, etc.
- The surface properties are the same over the entire particle surface.
- The double layer is purely diffusive.
- The solvent is a structureless dielectric medium.

Summarizing, the main ideas regarding *electrostatic stabilization* are:

- It is a kinetic stabilization method.
- It is only useful for dilute systems.
- It is not applicable to electrolyte sensitive systems. The stability of electrostatically stabilized colloids highly depends on pH.
- When particles agglomerate, it is almost impossible to redisperse them.
- It is not applicable to multiphase systems where different particles show different surface charge distributions.

The other main strategy to stabilize colloidal systems is by *steric stabilization*. It is not so well understood as the electrostatic approach but it has several advantages over it:

- It is a thermodynamic stabilization method.
- It is useful for the whole range of particle concentrations, even without solvent.
- It does not depend on electrolyte concentration or pH.
- The particles are always redispersible due to the thermodynamic character of the stabilization and also due to the steric impediment onto each particle surface.
- It is suitable for multiphase systems.
- It is used to control the particle size and particle size distribution during the synthesis of nanoparticles.

The steric stabilization can be used both during and after the synthesis of nanoparticles. The steric stabilizers can be polymeric or non-polymeric (surfactants). They must be soluble in the colloid solvent and must adsorb physically or chemically onto the particle surface. The repulsion between two particles arises from the interaction between their polymer layers (see **Figure 1.12**). If there is a low coverage of polymer onto the solid surface, as the particles approach each other the polymer chains will interpenetrate. The entropy decreases and therefore the Gibbs free energy increases. Consequently, the particles repel each other to lose this excess of Gibbs free energy. On the other hand, if there is a high coverage of polymer onto the solid surface, the particles will repel when

they get close because the polymer chains will be compressed, what is energetically unfavourable since their Gibbs free energy increases.
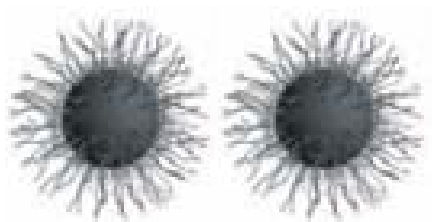
Figure 1.12. General representation of sterically stabilized nanoparticles with surfactant or polymer molecules adsorbed onto the surface.

The osmotic effect is also present in the steric stabilization mechanism. When two particles approach each other, the concentration of polymers in between the particles will increase over the equilibrium value and a flow of solvent will be pumped into the interparticle space to push them away and recover the initial value of polymer concentration.

The previous considerations on colloidal stability include only particles whose attractive interactions are Van der Waals forces and whose repulsive interactions are electrostatic or steric ones. But our main interest focalizes on **iron oxide magnetic nanoparticles**: there is an extra attractive interaction due to the magnetic forces. Thus, the electrostatic or steric stabilization becomes even more important, it must be strengthened to avoid agglomeration processes.

1.1.3.2. Stabilization strategies for iron oxide magnetic nanoparticles

Undoubtedly, the synthesis of stable monodisperse colloidal systems is a major aim for professionals developing nanomaterials. Common stabilization methods for iron oxide nanoparticles are *electrolyte adsorption*, *surfactant and polymer coating* and *silica coating*.

Electrolyte adsorption is the easiest method to stabilize magnetic nanoparticles in restricted conditions. It is directly obtained when the particles are synthesized by co-precipitation method in a basic medium (section 1.1.2). The resulting particles have hydroxyl ions on the particle surface. If the solution is acidified the particle surface will be covered by protons, but at neutral pH the system will be unstable. By choosing two electrolytes like tetramethylammonium hydroxide (TMAOH)[78] and sodium citrate[79] the pH range of stability can be tuned. Cheng et al. obtained magnetite nanoparticles by the co-precipitation of iron salts with TMAOH in an aqueous solution. The *in vitro* cytotoxicity tests revealed that the particles were biocompatible.[78] Another strategy is to synthesize the particles by thermal decomposition in the presence of a surfactant, such as oleic acid, to obtain monodisperse nanoparticles and exchange the oleic acid by an electrolyte.[80] The second pathway improves the particle size distribution of the system.

To avoid stability variations with pH organic species like *surfactants and polymer coatings* are used. They are amphiphilic molecules with an organic chain and polar groups which anchor to the iron oxide surface. A general classification would differentiate:

- Surfactants (non-polymeric organic stabilizers): carboxylic acids like oleic, lauric, dodecylphosphonic acid, etc.; organic amines like oleilamine; alkyl phosphonates and phosphates, sulfonates, etc.
- Polymers:
  - Natural origin: gelatin, dextran, chitosan, pullulan, etc.
  - Synthetic origin: poly(vinylpyrrolidone) (PVP), poly(ethyleneglycol) (PEG), poly(vinyl alcohol) (PVA), polystyrene (PS), etc.
  - Inorganic polymers: oxides such as silica, titania, etc.

These molecules are used during or after the synthesis of iron oxide nanoparticles. When surfactants or polymers are added to the reaction medium they adsorb onto the primary nuclei and act as a diffusion barrier between these nuclei and the precursor molecules, which limits the growth of the particles. The resulting system has a narrow particle size distribution which is indispensable to control the properties of the colloid.[63,81] Hyeon et al. synthesized the nice magnetite nanoparticles showed in **Figure 1.7** with oleic and/or lauric acid through thermal decomposition of iron pentacarbonyl. Post-functionalization of magnetic nanoparticles with polymers is also widely used to increase their stability. Thünemann et al., for instance, synthesized the nanoparticles by co-precipitation of iron chlorides ($FeCl_2$ and $FeCl_3$) and stabilized them at pH 2. Afterwards, they were coated with a first layer of poly(ethylene imine) (PEI) and a second one of poly(ethyleneoxide)-b-poly(glutamic acid) (PEO-PGA). The authors claim that all the process is organic solvent free, only water was used as a solvent.[82] On the other hand, Euliss et al. synthesized the magnetic nanoparticles through thermal decomposition of $Fe(CO)_5$ in octyl ether with oleic acid and then transferred them to water with TMAOH. Next they were coated with a block copolypeptide, $poly(EG_2\text{-}lys)_{100}\text{-}b\text{-}poly(asp)_{30}$, which induced the particles to assemble into uniform clusters of approximately 20 nanoparticles.[37] Poly(ethylene glycol) (PEG) is commonly used to improve the biocompatibility of the particles.[83,84]

A drawback of polymer coatings is their low stability at high temperatures. Thermal treatments to improve the crystallinity properties of the magnetic core or to transform the crystalline phase without changing the particle size, for instance, are difficult to carry out when the particles are coated with organic stabilizers.

Another stabilizing method is the *silica coating*. It has several advantages compared to the previous methods. It is the chosen one for the stabilization of the iron oxide nanoparticles synthesized in the present thesis. For this reason, the strategies to coat nanoparticles with

silica will be explained in more detail, emphasizing their relevant benefits and weaknesses.

The advantages of silica coating over electrolytes, surfactants and polymers encircle chemical and physical aspects: its stability in aqueous media does not depend significantly on the electrolyte concentration or pH (as far as it is not highly basic), it can be functionalized through the reaction of surface silanol groups with alcohols and silane coupling agents, the magnetic interparticle interactions of the coated particles can be modulated by the thickness of the silica shell, it shows stability at high volume fractions, stability at high temperature and biocompatibility. A short description of the main sol-gel processing methods by the *Stöber method*, *reverse microemulsion* and *aerosol pyrolysis* to coat magnetic nanoparticles with silica is included.

The *Stöber method* was first reported in 1968 by Stöber et al.[85] and described the synthesis of monodisperse silica microparticles. It consists of the sol-gel process of hydrolysis and condensation reactions of a silicon alkoxyde diluted at very low concentrations in water and a co-solvent (acetone, ethanol, etc.). After the addition of ammonia, silica particles are formed instead of a bulk gel network because of the high dilution of the silicon precursor. The resulting silica is compact, with no intrinsic porosity. The particle size can be tuned from 50 nm to 2 microns by varying the concentration of ammonia and the ratio of alkoxyde to water.

When iron oxide nanoparticles are dispersed in the reaction solution they are directly coated with a silica shell. There is no need to functionalize them to promote the deposition and adhesion of silica onto the iron oxide surfaces since there is a strong affinity between both chemical compounds. The silica surface has negatively charged silanol groups which are responsible for the redispersibility of the composite particles (iron oxide core-silica shell) in water without the need of adding other stabilizers.

The chemical reaction that takes place in the reverse *microemulsion* and *aerosol pyrolysis* methods is also based on the hydrolysis and condensation of a silicon alkoxyde in basic medium and the obtained silica has the same chemical properties. The difference between the three methods resides on the processing of the initial common reactants: in the original Stöber method the reactants are dissolved in an alcoholic solution at very low concentration and they are allowed to react with basic catalysis; in the microemulsion technique the reactants are encapsulated in the dispersed droplets; and in the aerosol pyrolysis the reactant solution is heated up to let the solvent evaporate and force the formation of silica.

There are plenty of examples of the Stöber process.[86-90] Lu et al. have successfully coated commercially available ferrofluids by the hydrolysis and condensation of tetramethoxy silane (TEOS) in 2-propanol with water and ammonia.[88] The silica shell can be tuned by

controlling the TEOS concentration. **Figure 1.13** shows a batch of these nicely structured composite particles. Zhao et al. initially coated magnetite nanoparticles with a thin layer of silica by the Stöber method and later they grew another silica shell with a template, CTAB (cetyltrimethylammonium hydroxide). After the synthesis the template was removed by acetone extraction resulting in a triple system of magnetic core-compact silica shell-mesoporous silica shell (see **Figure 1.14**).[90]
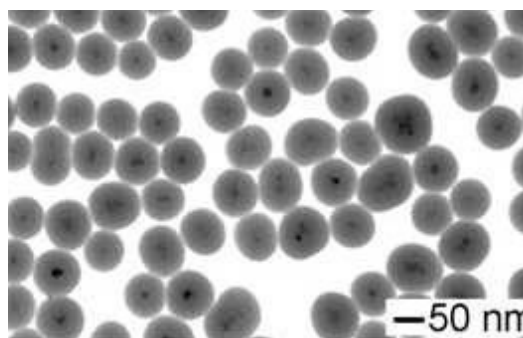
Figure 1.13. TEM image of iron oxide nanoparticles individually coated with silica shells by the Stöber method.[88]

To sum up, Stöber method allows for the synthesis of silica shell onto magnetic nanoparticles with control over the shell thickness and with high monodispersity of the resulting composite particles without the need of size-selection procedures. The final particle shape depends directly on the shape of the iron oxide particle for what it is very important to start up from a monodispersed system of magnetic particles. The shell is compact unless a porogenic agent is used to induce the porosity. The reactions take from several hours to some days, with high final yields. Organic solvents are needed for the synthesis and therefore, a subsequent step of purification is crucial if the particles are to be used for biomedical applications.
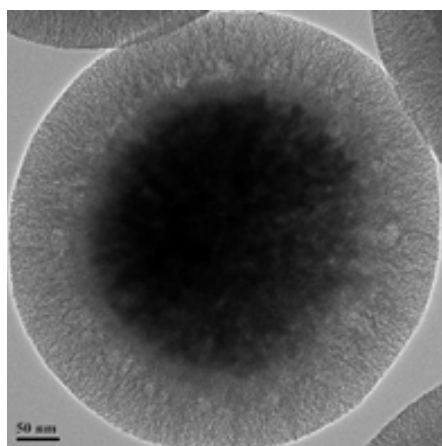
Figure 1.14. TEM image of a magnetite nanoparticle coated with a compact silica shell and a second mesoporous silica shell by the Stöber method.[90]

The bases of the *microemulsion* technique to coat nanoparticles are the same as the ones explained in paragraph 1.1.2 to synthesize nanoparticles. There are two approaches: the first one, the co-precipitation of silica and iron precursors, followed by thermal annealing at high temperature,[91] and the second one, the silica encapsulation of pre-formed magnetic nanoparticles.[92] In both of them a Stöber mechanism takes place inside or at the interface of the dispersed droplets investing the same reaction times as in a classical Stöber reaction. Santra et al. managed to coat iron oxide nanoparticles with silica by the second method using three different non-ionic surfactants for the preparation of the microemulsions.[93] The bare magnetic particles are enclosed inside the droplets of the dispersed phase together with the silicon precursor and the water. The silica shell spherical shape and thickness is restricted to the droplet size and shape. Anderson et al. used a water in oil (w/o) emulsion combined with solvent evaporation.[94] The reaction of formation of mesoporous silica and its deposition onto the magnetic nanoparticles takes place inside the water droplets at the same time of evaporation of the continuous organic solvent. The authors claim these particles to be potentially useful for catalytic or waste removal applications. Summarizing the microemulsion technique description, different approaches have been developed with successful results on the control of particle size and sequential deposition of layers. Inconveniently, as it was mentioned in paragraph 1.1.2, large amounts of solvents are needed for getting low product yields and the preparation of the microemulsion is not trivial. Furthermore, the method requires much effort to separate the synthesized composite particles from the large amount of surfactants used to prepare the microemulsion system.[95] The obtained particles are submicronic in size.

The third method to be mentioned is the *aerosol pyrolysis*. Aerosol or spray pyrolysis is a process in which a solid is obtained by spraying a solution into a series of reactors heated at a given temperature where the aerosol droplets undergo evaporation of the solvent and consequently solute condensation. Afterwards, the particles are dried and thermolysed in another reactor at higher temperature.[96] Tartaj et al. prepared submicronic silica-coated maghemite hollow and dense spheres with a high loading of magnetic material.[97] Duguet et al. have synthesized similar composite particles for biomedical applications.[98] Experimentally it is not as simple as the previous methods since a specific set-up consisting of an atomizer and reactors is necessary. Besides, the particle size and size distribution is very difficult to control since it depends on the sprayed droplets whose formation is kinetically controlled. However, the reaction time is importantly reduced to some minutes and the total process is simple, easy to scale up and the reaction yield is high.

Peculiarities of silica colloidal particles

Silicon dioxide (SiO_2) is the main component of the crust of the earth, which is present in the rocks and soil. It also plays an important role in many forms of life like the skeleton of

diatoms, some needles and stems in plants, and bones in the human beings (each one of us contains about half a gram of silica, which is essential for our life). Colloidal silica is interesting from a technological point of view since it has many industrial applications: in the industry of paints as thickener, pharmacy as an excipient, food additive in food industry, abrasive in toothpaste, water purification, photography, catalysis, fine abrasive in microelectronic industry, etc.[99] Very recently a method to protect teeth from cavities by ultrafine polishing with silica nanoparticles has been reported.[100]

A simplified schematic representation of a colloidal non-porous silica particle is shown in **Figure 1.15**. The inner part has only siloxane bonds, Si-O-Si, and the outer surface bear both siloxane and silanol groups (Si-OH), the last ones being able to ionize. Therefore, the surface is negatively charged, conferring stability to the colloidal particles. The silanol bonds constitute the reactive sites for surface functionalization. Water is strongly adsorbed onto the surface.

The colloidal stability of silica does not conform to DLVO theory. In contrast to other colloidal systems (see page 17) it is stable in conditions where the theory predicts minimum stability, as for example, around its isoelectric point[8] (pH 2.5 for silica); it is unstable in alkaline solutions, in which their electrical surface charge is high and should therefore increase their stability; the forces between particles are repulsive up to a few angstroms of separation; the stability is maintained at high electrolyte concentration near neutral pH and, in some cases, it even improves when the ionic strength increases.[101]
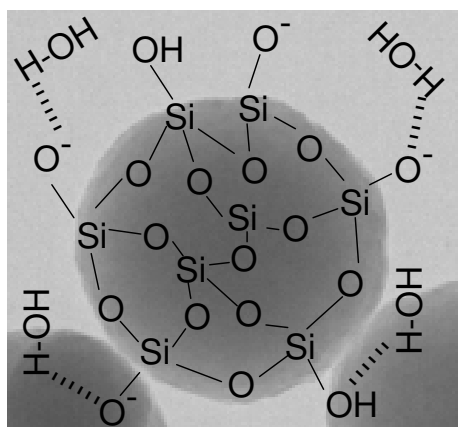
Figure 1.15. Simplified schematic representation of siloxane and silanol bonds in a compact silica particle.

There is no unified explanation for such behaviour at the moment but it seems that the hydrogen bonds between silanol groups and water might be responsible for that. The electrical double layer in silica consists of electrolytes and water molecules, tightly associated or bound to the surface, sometimes called hydration or solvation stabilization. It is estimated that this double layer is about 2 nm thick, i.e. among 6 and 8 water molecules thick.[101] It is also thought that silica particles have oligomeric or polymeric

silicate species at the silica-water interface and that steric repulsion results from the overlap of such layers. These oligomeric-polymeric coatings are electro-steric stabilization barriers. It is hypothesized that a 2 nm steric silicate oligomer-polymer barrier protects a silica sol at pH 8.0 in 0.15 M salt.[99] A new kind of short-range forces, known as structural forces, were discovered experimentally in silica particles. It was also observed that the Hamaker constant (proportional to the Van der Waals attraction potential; see page 17) is much smaller than for other materials like titania ($0.651 \cdot 10^{-20}$ vs. $23.27 \cdot 10^{-20}$ J). Since Van der Waals potential depends, besides on the Hamaker constant, only on the particle size and interparticle distance, this means that the attraction energy between two silica particles is 35 times smaller than the one between two titania particles of the same size.[101] This small Hamaker constant is attributed to the hydration-polysilicic acid formation at silica-water interfaces.

In conclusion, the anomalous colloidal stability of silica is thought to be due to:

- A very small Hamaker constant, responsible for weak Van der Waals forces.
- A strong association between water molecules, electrolytes near the surface and surface silanol groups through hydrogen bonding. The resulting structured water layer exerts a hydration or solvation stabilization.
- A layer of oligomeric or polymeric silicate species at the silica-water interface acting as an electrostatic stabilizer.

The origin of the anomalous colloidal silica stability is still being debated, no unified explanation has still been found. Nevertheless, the better colloidal stability of silica compared to other colloidal systems is a fact and we took profit from it.

1.1.4. Biomedical applications of iron oxide nanoparticles

Nanoparticles are to be biocompatible when used *in vivo*. Therefore, magnetic materials like cobalt, nickel, iron platinum alloy or chromium ferrites are left aside because of their toxicity and other magnetic materials like iron oxides gain relevance thanks to their biocompatibility. Still others, as manganese ferrites should be further explored. The biocompatibility of a material is defined as its capability of coexistence with living tissues or organisms without causing harm. They can be evaluated *in vitro* via cytotoxicity tests which assess the percentage of cell death when exposed to the material. The toxicity of nanoparticles is an emerging field of study since they can reach sub-cellular entities while bigger particles cannot.[102]

From now on the attention will be focussed on biomedical applications of iron oxide nanoparticles. In general, they can be classified according to their application inside (*in vivo*) or outside (*in vitro*) the body. *In vivo* applications can be therapeutic (hyperthermia and drug delivery) or diagnostic (magnetic resonance imaging, MRI), while for *in vitro*

applications the main use is in diagnosis and as a routine tool in a biological lab (magnetic selection and separation and cell tracking).

Magnetic separation is a very useful technique to separate biological entities (biomolecules, cells, etc.) from their solutions in order to be concentrated and later to be analysed or, on the contrary, to be discarded so as to purify the mother solution. Since it is an *in vitro* technique, biocompatibility of the magnetic nanoparticles is not first priority. However, whichever the used material it is essential to be stabilized in colloidal state. Separation technique comprises two steps: first, anchoring of the biomolecule to the nanoparticle and second, separation of the nanoparticles with magnetic field gradients. The nanoparticles have to be functionalized with antibodies or other biomolecules which bear specific functional groups like folic acid, hormones, etc., that react specifically with the active sites on cell surfaces or functional groups of the biomolecules to be separated.[103] The separation step can be static of dynamic. The first one is as simple as placing a magnet near the walls of the test tube that contains the solution (see **Figure 1.16**). The magnetic nanoparticles are immobilized onto the wall and the supernatant solution is removed. Unfortunately, it takes long time for the separation. The dynamic mode, however, is faster and can fractionate the particles regarding their magnetic strength. Briefly, a flow column is loosely packed with a magnetisable matrix of wires or beads. The magnetically tagged fluid is pumped through the column while a magnetic field is applied. The magnetic particles are retained in the column until they are recovered once the magnetic field has been removed. By applying fields with different intensities the magnetic particles can be fractionated.[68]
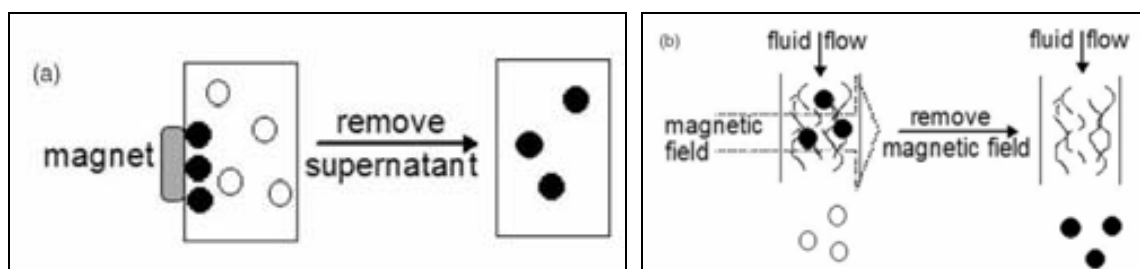
Figure 1.16. Schematic representation of the static (a) and dynamic (b) magnetic separation processes.[68]

Recently, a star-up company, Sepmag Tecnologies,[104] has been set up in the Vallés Technological Park, near Barcelona. They develop, manufacture and market Precision Magnetophoresis systems for the Biotechnology industry. In the course of this thesis, I have duly collaborated with them together with Jordi Faraudo and Juan Camacho (from ICMAB) using the Sepmag Precision Magnetophoresis systems to study the magnetophoretic properties of some materials I have synthesized (see **Figure 1.17**).

Figure 1.17. Lab-scale Precision Magnetophoresis system by Sepmag (left image) and one of our samples magnetically separated by the previous instrument (right image).[104]

Drug delivery comprises the transport of drugs to a specific place inside the body. The main aim is to concentrate the drug in the pathological tissue avoiding a general systemic distribution of the drug all over the body, what implies unnecessary side-effects in healthy cells. Furthermore, the dosage of drug is reduced due to a higher efficiency. Biocompatible magnetic nanoparticles, particularly iron oxides, are ideal candidates to anchor the drug onto their surface and be directed to the target by external magnetic fields. Magnetic resonance imaging can be used to localize the particles in the body.[105] Once they are concentrated in the targeting place, the drug can be released from the nanoparticles by changes in physiological conditions such as pH and temperature or they can be up-taken by tumour cells. The magnetic forces are to be higher than the forces exerted by the blood flow, although care against embolization must always be kept in mind. The drugs can be loaded in the pores of the coating, either silica or a polymer (see **Figure 1.18**), inside micelles or vesicles or be chemically anchored to an appropriate functional group of the particle coating. This strategy has already had positive results in targeting sarcoma and brain tumours and performing gene therapy.[68]
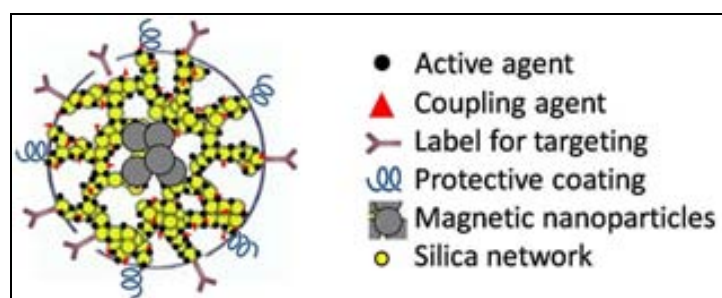
Figure 1.18. Scheme of a magnetic biomedical multifunctional platform.

The treatment of diseases with heat is called *hyperthermia*, a word that comes from the Greek word for "overheating". There are different kinds regarding the origin of the heat, but only *magnetic hyperthermia* will be considered. Hyperthermia is a promising cancer therapy since it is well-known that cancerous cells are more sensitive to high temperatures than healthy cells (cancerous cells are destroyed around 41-48°C). It is thought that the high temperature induces a modification of many structural and enzymatic functions within cells, which can induce apoptosis.[106] This technique is usually

complemented with chemo- or radiotherapy. In magnetic hyperthermia, the heat is generated when an alternating magnetic field (ac) is applied to a material with net magnetization. The magnetic material is usually prepared as a colloidal dispersion. The amount of generated heat depends on the size and the magnetic properties of the particles. For multidomain ferro- or ferrimagnetic materials, heating is due to hysteresis losses. The orientation of the magnetic moments inside the material takes place through the displacements of the domain walls. High magnetic field amplitudes are necessary to saturate ferromagnetic materials. In single-domain superparamagnetic nanoparticles the heating is due to two relaxation mechanisms: Neél relaxation and Brownian relaxation. The former one transforms magnetic energy into thermal one when the magnetized particles come back to their equilibrium state. The second relaxation mechanism involves the physical movement of the whole particle in the carrier liquid due to the rotational Brownian motion. It depends on the hydrodynamic size of the particles, the viscosity of the solvent and the temperature. The efficiency of a magnetic material as a hyperthermia mediator is defined as the specific absorption rate (SAR), the power of heating of a magnetic material per gram:

Equation 1.9 $$SAR = C \cdot \frac{\Delta T}{\Delta t}$$

where C is the specific heat capacity of the material (J $\cdot$g^{-1} $\cdot$K^{-1}) and $\Delta T/\Delta t$ is the initial slope of the temperature vs. time curve. The heat generation from the transformation of magnetic energy into thermal energy can be directly related to the out-of-phase component of susceptibility, χ'', i.e. the de-phasing between M (magnetization) and H (external field). The ac magnetic field used to generate the heating is limited by deleterious physiological effects of high frequency magnetic fields, i.e. stimulation of skeletal muscles, possible arrhythmia, etc. The useable frequency range is 0.05 - 1.2 MHz and the intensity range is 0 - 15 kA $\cdot$m^{-1} (0-0.02 T).[68,107] Hergt et al. estimated that exposure to fields where the product (*H* $\cdot$*f*) exceeds 5 $\cdot$10^9 Am^{-1} $\cdot$s^{-1} can be harmful to humans.[108]

Superparamagnetic nanoparticles are a better choice for magnetic hyperthermia than ferromagnetic ones since FM materials need high magnetic field amplitudes to fully saturate (around 100 kA $\cdot$m^{-1}). Since hyperthermia set-ups use small amplitudes (0 - 15 kA $\cdot$m^{-1}), the SAR values obtained with SPM particles are considerably higher. Furthermore, they can be directed to a specific target within the body with external magnetic fields avoiding potential embolism when the external field is removed.

1.1.4.1. Magnetic resonance imaging (MRI)

Magnetic resonance imaging is a medical technique to obtain tomographic images of any part of the body, taking profit of radiofrequency (rf) energy and enabling the differentiation of tissues according to their water content. Consequently, it allows for

distinguishing ill tissues from healthy ones. Significantly, no ionization radiation neither x-ray energy is involved; it is considered biologically safe. **Figure 1.19** shows an example of a magnetic resonance image.

The physical basis of MRI relies on the nuclear magnetic resonance (NMR): *nuclear* because it is only the nuclei of the atoms that are involved in the energetic changes; *magnetic* because it happens in a magnetic field; and *resonance* because there is a direct dependence on strength and field frequency. When NMR resonance was introduced to clinical imaging, the adjective *nuclear* was eliminated for marketing reasons, not to raise the alarm of the general public. Therefore, this technique is known as magnetic resonance imaging (MRI).[109]
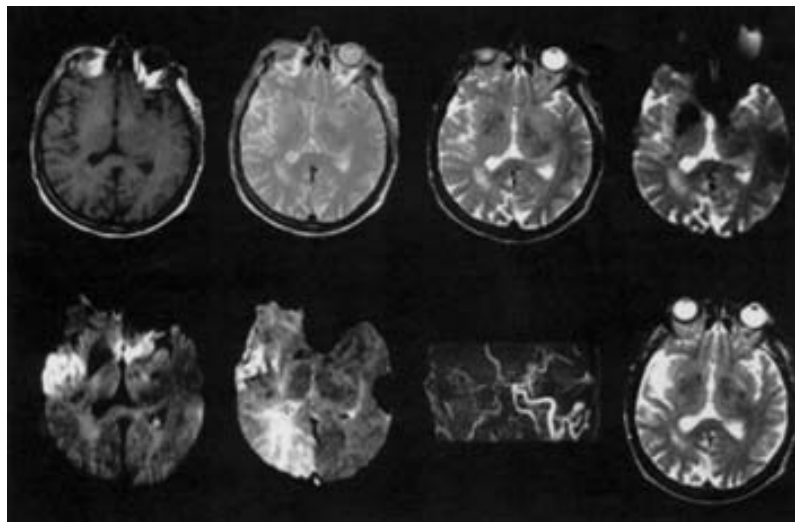
Figure 1.19. Multimodality magnetic resonance imaging of acute ischemic stroke. The magnetic resonance angiograph reveals extremely poor flow in the right internal carotid artery.[110]

When an atom with uneven number of protons is placed in a magnetic field it produces magnetic resonance signals. The most interesting nuclei for MRI are ^{1}H, ^{13}C, ^{19}F, ^{23}Na and ^{31}P because all of them occur naturally in the body. The most commonly used is the proton, since it appears in the major components of the body: water and fat. A proton in a magnetic field precesses around the field direction with the Larmor frequency (ω, unit MHz):

Equation 1.10 $\omega = \gamma \times B_0$

where γ is the gyromagnetic ratio (unit MHz/T; unique for every nucleus) and B_0 is the external magnetic field (unit T for Tesla). The resonance phenomenon occurs when an electromagnetic wave with a frequency similar to the Larmor one reaches the nuclei: the nuclei absorb that energy and relax afterwards by the emission of a radiofrequency signal. In a typical MRI experiment the protons are placed in a magnetic field (B_0) parallel to z axis and precess around this axis. They show a net magnetization in z direction. Then, a radiofrequency pulse with equal or similar frequency to the Larmor frequency is applied

perpendicularly to B_0, inducing the coherent precession of the protons in the *x-y* plane. At this point there is no net magnetization in *z* axis (see **Figure 1.20**).

When the rf pulse ends, the protons relax to their equilibrium state (back to position *a* in **Figure 1.20**), by losing their coherence in the *x-y* plane (transversal relaxation) and by recovering the net *z* magnetization (longitudinal relaxation). **Figure 1.21** shows the free induction decay (FID) schemes: the magnetization intensity vs. time in the *z* axis (lower graph) and *x-y* plane (upper graph) after removal of rf pulse.
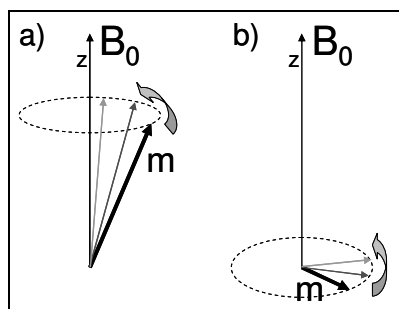
Figure 1.20. Scheme of proton magnetic moments which precess around the direction of an external magnetic field (a), and their precession in the *x-y* plane while excited with a perpendicular radiofrequency pulse (b).

By applying a Fourier transformation to the FID, information about the frequencies of the sample protons is obtained, which can be then related to the kind of protons and its environment. This information is used to build up the images. The longitudinal or spin-lattice relaxation is the recovery of the magnetization along the *z*-axis. It is characterized by T_1 time, which is the time needed to recover the 63% of the initial magnetization after the exposure to a 90° rf pulse (see lower graph in **Figure 1.21**). It depends on the kind of nucleus, resonance frequency, field strength, temperature, presence of macromolecules in the medium and presence of paramagnetic ions or molecules. Different pulse sequences are used to measure T_1 values, such as the partial saturation pulse sequence (sequence of equidistant 90° pulses) and the inversion-recovery pulse sequence (180-90° pulse sequence).

The transversal relaxation consists in the de-phasing, lost of coherent movement, of the moments in the *x-y* plane (see **Figure 1.20.b** and upper graph in **Figure 1.21**) and therefore the loss of net magnetization in this plane. It is also called spin-spin relaxation. Its typical time, T_2, is the time needed to lose 63% of transversal magnetization. T_2 is always much shorter than T_1. It depends on the resonance frequency, the field strength, temperature, presence of macromolecules and magnetic atoms or molecules. T_2 does not only depend on the magnetic inhomogeneities produced by nearby atoms, but also on the inhomogeneities due to the imperfections of the external magnetic field. These influences are reflected in the following relationship: $1/T_2^* = 1/T_2 + 1/T_2(inh)$, where T_2^* is the observed relaxation time, T_2 is the true relaxation time and $T_2(inh)$ is the one induced by

the field inhomogeneities. To eliminate $T_2(inh)$ a spin-echo pulse sequence is used ($90-180^{\circ}_n$). The spin echo sequence is the chosen one for standard MRI experiments or diagnosis.
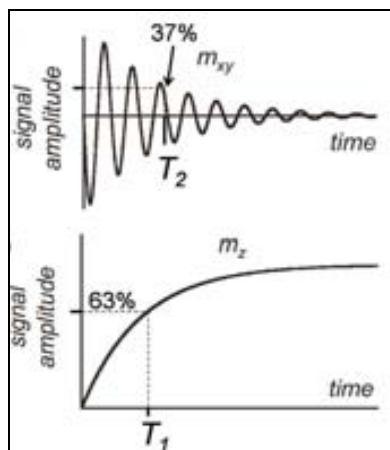
Figure 1.21. Magnetic moment vs. time after removal of the rf pulse. Upper figure: *x-y* plane values; lower figure: *z* values.

How is it possible to get body images from the relaxation time (T_i) values? In the instrument set-up at least one of the two fields (B_0 and rf field) has to vary over space. Then, relaxation data are collected by a computer which applies a two-dimensional Fourier transform to give the amplitudes of NMR signals and permits reconstruction of the 3D images. The better the contrast between different nucleus signals, the better the interpretation of the images. T_1 weighted images have bright contrast and T_2 ones show dark contrast, similar to the areas without signal (see **Figure 1.22**).[111] The current clinical fields used for proton MRI are up to 3 T in strength, although pre-clinical investigations are using fields up to 9 T.[112] Relaxivity measurements to evaluate materials as contrast agents are normally performed at 0.47 T.

More than 65 millions clinical imaging procedures worldwide are being performed each year. About 35% of those make use of contrast agents. Contrast agents are magnetic ions, molecules or particles which accelerate the relaxation rates and, therefore, increase the contrast allowing for a better discernment between healthy and pathological tissues. The presence of paramagnetic ions or molecules reduces T_1 values since the electrons produce a larger window of different frequencies to induce a faster relaxation than the nuclei (paired electrons show almost no net magnetization). Paramagnetic ions such as Gd^{3+}, Fe^{2+}, Fe^{3+}, Mn^{2+} and Cu^{2+} are known as *T_1 or positive contrast agents*. Positive contrast agents have to be in contact with the water molecules to reduce the longitudinal relaxation time (T_1). Since they are highly toxic they have to be complexated with organic ligands when used *in vivo*. Despite its toxicity, they have been the first contrast agents to be used in clinical tests and gadolinium complexes are still the most used in routine medical diagnosis with MRI.

Ferro-, ferri- and superparamagnetic compounds are called *T₂ or negative contrast agents* since they especially shorten the transversal relaxation time (T_2). The magnetic compounds produce local magnetic field gradients; T_2 is reduced due to the diffusion of protons through these gradients affecting the coherence of the hydrogen spin movement. Therefore, no direct contact between the contrast agents and water molecules is necessary. The effect is also called susceptibility effect.
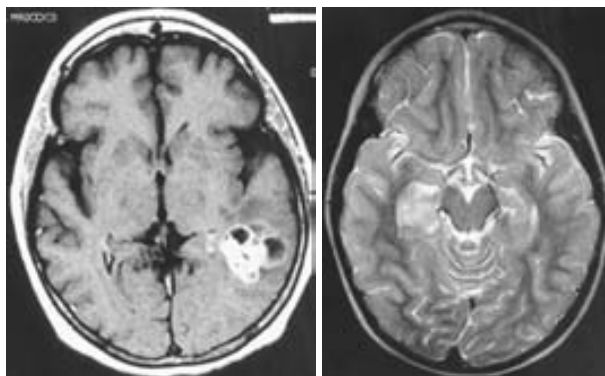
Figure 1.22. Magnetic resonance imaging of the brain after *i.v.* injection of two different kinds of contrast agents: positive (left image) and negative (right image).

Iron oxide nanoparticles are mostly used as negative contrast agents due to their high susceptibility, their tuneable size and the possibility to functionalize them to be tissue specific. Nevertheless, if particle size is reduced down to 5 nm and the system is highly monodisperse they can also act as positive contrast agents as we have observed.[80] When used *in vivo* their superparamagnetic character is essential to avoid embolization once the MRI test is finished.

Passive and active targeting of iron oxide nanoparticles for biomedical applications

It has been already proved that iron oxide nanoparticles can be synthesized by multiple methods, as well as functionalized with different coatings in order to guarantee their colloidal stability and widen their functionality. The control over their particle size and particle size distribution can also be achieved. But if they are to be used for *in vivo* biomedical applications, via intravenous administration, they must fulfil some extra requirements regarding the half-life in the blood compartment and their final biodistribution. Even the most active compound *in vitro* is useless for *in vivo* applications if it does not reside in the blood compartment long enough to reach its target.

The function of the mononuclear phagocyte system (MPS), also known as the reticuloendothelial system (RES), is to recognize and clear any senescent cell, invading micro-organism or particle. The cells which carry out this task are the bone marrow progenitors, blood monocytes and tissue macrophages, which are strategically placed in

different tissues of the body. When an invading entity enters the blood stream, different circulating plasma proteins, called opsonins, adsorb onto its surface. These opsonins interact with the specialized plasma membrane receptors on the circulating monocytes or on the fixed macrophages, thus allowing these RES cells to recognize the invading particle. Afterwards, endocytosis or phagocytosis takes place leading to the elimination of the particle from the blood stream and to its concentration in organs with high phagocytic activity: liver, spleen and bone marrow. In this context, half-life in blood stream of any invading particle will be very short and RES-mediated clearance will determine its bio-distribution. The blood residence time depends directly on the circulating particle size and coating (see **Figure 1.23**). Nevertheless, if the target tissue or organ belongs to RES this will be a successful targeting of nanoparticles; it is called the *passive targeting*.[111]
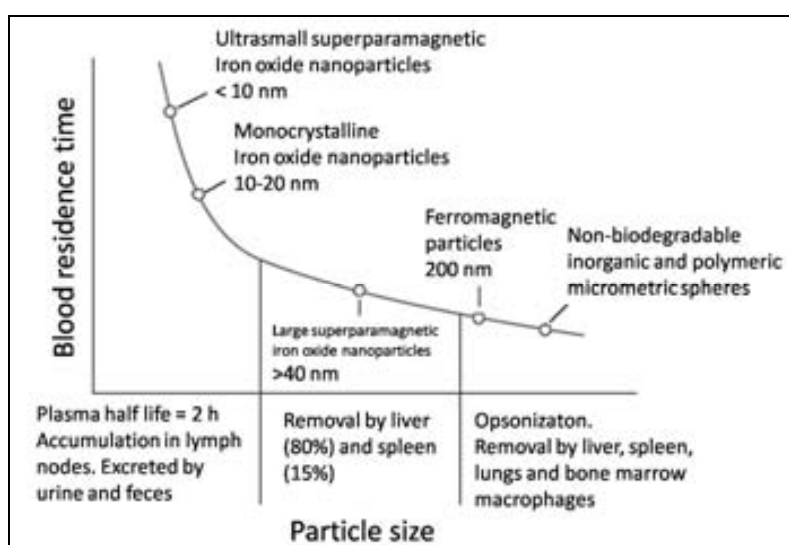
Figure 1.23. Qualitative diagram showing the evolution of blood residence time with particle size.[113]

But if the RES cells are not the desired target, then a strategy of *active targeting* has to be developed. The first requirement is minimizing the adsorption of opsonins onto the invading particle and therefore delaying its recognition and clearance by the RES. Such long circulating particles are defined as stealth. Looking at Nature, healthy erythocytes (red blood cells) evade the macrophages and live for 110 - 120 days long in the blood stream. Many factors are thought to be involved in their stealthiness, particularly important is their surface protection by a barrier of hydrophilic oligosaccharaide groups. This barrier could be responsible for the prevention of opsonin adsorption.[111] The main physico-chemical factors which are known to be involved in the opsonization process are the size, the surface charge density and the hydrophilicity/hydrophobicity balance. It has been concluded that the particles with the longest circulation times are the smallest in size, non-electrically charged and the most hydrophilic at the surface. Furthermore, magnetism can increase the blood half-life of nanoparticles with the help of external magnetic fields. These long-circulating particles can be used for blood-pool imaging or

can escape from the circulation through opened fenestrations in capillaries (damaged endothelial barriers due to inflammatory processes like arthritis or infections, tumours, etc.).

A second stage in active targeting consists of conjugating ligands to direct the particles to a specifically desired target with unique epitopes or receptors. Examples of these ligands include oligosaccharides, oligopeptides, folic acid and antibodies. Folic acid could be grafted onto iron oxide nanoparticles in order to adsorb specifically onto cancer cells due to the over expression of folate receptors. It may be equally useful to target inflammatory sites. The folate receptor has been found to be over expressed on the surface of several cancer cells. It has been recently reported the development of a library of iron oxide nanoparticles.[114] Using a robotic system, several molecules have been conjugated to iron oxide nanoparticles and have been screened against different cell lines. In a relative rapid way, the creators have discovered a series of nanoparticles with high specificity for endothelial cells, activated human macrophages and pancreatic cells.

Concluding, a combination of crystalline and magnetic properties, particle size and size distribution, coating and functionalization are indispensable properties to be considered for the successful synthesis and performance of a magnetic carrier to be used for *in vivo* techniques.

The **purpose of this introduction** has been to explain some general concepts to frame the work presented in this thesis. Namely, the implications of nanometric dimensions in material properties, some basics on colloidal science and magnetism at the nanoscale, synthetic methods of magnetic nanoparticles along with strategies to stabilize them in fluids, and finally, their broad range of applications, especially in biomedicine. Magnetic resonance imaging and magnetic hyperthermia have been underlined because of their special significance in this thesis.

1.2.   Scope of the thesis

The main scope of this thesis is the chemical synthesis and physicochemical characterization of biocompatible iron oxide-based nanoparticulated systems with optimised properties to act as contrast agents for magnetic resonance imaging (MRI) and as mediators for magnetic hyperthermia.

This main goal can be divided into several objectives:

- Synthesis of maghemite nanoparticles with control over the particle size and narrow particle size distribution.

- Stabilization of the maghemite nanoparticles in organic and aqueous colloidal dispersions with different stabilizing agents.

- Physicochemical characterization of the maghemite nanoparticles in powder form and in colloidal dispersions.

- Synthesis of composite particles (γ-Fe_2O_3@SiO_2) by coating the maghemite nanoparticles with silica by a novel method combining sol-gel chemistry and supercritical fluids.

- Synthesis of pure silica particles by sol-gel chemistry using supercritical fluids to study the optimum conditions to achieve the previous point.

- Physicochemical characterization of the silica and composite particles; evaluation of their similarities and differences.

- Synthesis of composite ε-Fe_2O_3@SiO_2 particles from γ-Fe_2O_3@SiO_2 particles.

- Evaluation of the maghemite colloidal systems as contrast agents for MRI and mediators for magnetic hyperthermia

I have also participated in several collaborations to exploit the properties of magnetic nanoparticles for other applications, such as magnetic photonic crystals and catalysts for hydrogen generation. The results are reported in the form of several publications included in annex 7.2.

1.3.   Bibliography and notes of Chapter 1

1.   Feynman, R., There is plenty of room at the bottom: an invitation to enter a new field of physics. *California Institute of Technology Engineering and science magazine* **1960,** 23.

2.   *Nanoscience and nanotechnologies: opportunities and uncertainties. RS Policy Document 29/04*; Royal Society: London, **2004**.

3.   Bond, G. C., Gold: a relatively new catalyst. *Catalysis Today* **2002,** 72, (1-2), 5-9.

4.   Grisel, R.; Weststrate, K. J.; Gluhoi, A.; Nieuwenhuys, B. E., Catalysis by gold nanoparticles. *Gold Bulletin* **2002,** 35, (2), 39-45.

5.   Haruta, M., Size- and support-dependency in the catalysis of gold. *Catalysis Today* **1997,** 36, (1), 153-166.

6.   Corma, A.; Serna, P., Chemoselective hydrogenation of nitro compounds with supported gold catalysts. *Science* **2006,** 313, (5785), 332-334.

7.   Kamat, P. V., Quantum Dot Solar Cells. Semiconductor Nanocrystals as Light Harvesters. *Journal of Physical Chemistry C* **2008,** 112, (48), 18737-18753.

8.   Cao, G., *Nanostructures and nanomaterials. Synthesis, properties and applications*. London, **2004**.

9.   Nutzenadel, C.; Zuttell, A.; Chartouni, D.; Schmid, G.; Schlapbach, L., Critical size and surface effect of the hydrogen interaction of palladium clusters. *European Physical Journal D* **2000,** 8, (2), 245-250.

10.   Whitesides, G. M., Nanoscience, nanotechnology, and chemistry. *Small* **2005,** 1, (2), 172-179.

11.   Whatmore, R. W., Nanotechnology - what is it? Should we be worried? *Occupational Medicine-Oxford* **2006,** 56, (5), 295-299.

12.   The size distribution is defined as the percentage of the standard deviation (σ) related to the mean value (100*σ/mean). The standard deviation is defined as the root of the average of the squares of the differences of all the observations from their mean: $\sigma = \sqrt{\dfrac{\sum(value_i - meanvalue)^2}{meanvalue}}$.

13.   Murray, C. B.; Sun, S. H.; Doyle, H.; Betley, T., Monodisperse 3d transition-metal (Co, Ni, Fe) nanoparticles and their assembly into nanoparticle superlattices. *Mrs Bulletin* **2001,** 26, (12), 985-991.

14.   Dormann, J. L.; Spinu, L.; Tronc, E.; Jolivet, J. P.; Lucari, F.; D'Orazio, F., Effect of interparticle interactions on the dynamical properties of gamma-Fe_2O_3 nanoparticles. *Journal of Magnetism and Magnetic Materials* **1998,** 183, (3), L255-L260.

15.   Lu, A. H.; Salabas, E. L.; Schuth, F., Magnetic nanoparticles: synthesis, protection, functionalization, and application. *Angewandte Chemie-International Edition* **2007,** 46, (8), 1222-1244.

16.   Pelecky, D. L.; Rieke, R. D., Magnetic properties of nanostructured materials. *Chemistry of Materials* **1996,** 8, (8), 1770-1783.

17.   Blundell, S. *Magnetism in Condensed Matter*, **2001,** Oxford master Series in Condensed Physics, Oxford University Press.

18.   Morales, M. P.; Veintemillas-Verdaguer, S.; Montero, M. I.; Serna, C. J.; Roig, A.; Casas, L.; Martinez, B.; Sandiumenge, F., Surface and internal spin canting in gamma-Fe_2O_3 nanoparticles. *Chemistry of Materials* **1999,** 11, (11), 3058-3064.

19.   Parker, F. T.; Foster, M. W.; Margulies, D. T.; Berkowitz, A. E., Spin canting, surface magnetization and finite-size effects in gamma-Fe_2O_3 particles. *Physical Review B* **1993,** 47, (13), 7885-7891.

20.   Kaiser, R.; Miskolcz.G, Magnetic properties of stable dispersions of subdomain magnetite particles. *Journal of Applied Physics* **1970,** 41, (3), 1064-&.

21.   Rosensweig, R. E., *Ferrohydrodynamics*. Cambridge, **1985**.

22.   Chen, D.-X.; Sanchez, A.; Taboada, E.; Roig, A.; Sun, N. and Gu, H.-C. Size determination of superparamagnetic iron oxide nanoparticles from magnetization curve, *Journal of Applied Physics* **2009**, 105, 083924.

23.   Bibliographic search in ISI Web of knowledge with topic "magnetic nanoparticles" gives more than 13,000 results.

24.   Groshens, T. J.; Klabunde, K. J., Heated inlet system for co-condensation metal atom reactor. Acs Symposium Series **1987**, 357, 190-192.

25.   Takahashi, Y. K.; Koyama, T.; Ohnuma, M.; Ohkubo, T.; Hono, K., Size dependence of ordering in FePt nanoparticles. *Journal of Applied Physics* **2004,** 95, (5), 2690-2696.

26.   Birringer, R.; Gleiter, H.; Klein, H. P.; Marquardt, P., Nanocrystalline materials; an approach to a novel solid structure with gas-like disorder. *Physics Letters A* **1984,** 102, (8), 365-369.

27.   Siegel, R. W.; Ramasamy, S.; Hahn, H.; Li, Z. Q.; Lu, T.; Gronsky, R., Synthesis, characterization and properties of nanophase TiO_2. *Journal of Materials Research* **1988,** 3, (6), 1367-1372.

28.   Shima, T.; Takanashi, K.; Takahashi, Y. K.; Hono, K., Coercivity exceeding 100 kOe in epitaxially grown FePt sputtered films. *Applied Physics Letters* **2004,** 85, (13), 2571-2573.

29.   Falicov, L. M.; Pierce, D. T.; Bader, S. D.; Gronsky, R.; Hathaway, K. B.; Hopster, H. J.; Lambeth, D. N.; Parkin, S. S. P.; Prinz, G.; Salamon, M.; Schuller, I. K.; Victora, R. H., Surface, interface and thin-film magnetism. *Journal of Materials Research* **1990,** 5, (6), 1299-1340.

30.   Koch, C. C., The synthesis and structure of nanocrystalline materials produced by mechanical attrition: A review. *Nanostruct. Mater.* **1993,** 2, 109.

31.   Schift, H., Nanoimprint lithography: An old story in modern times? A review. *Journal of Vacuum Science & Technology B* **2008,** 26, (2), 458-480.

32.   Kim, P.; Kwon, K. W.; Park, M. C.; Lee, S. H.; Kim, S. M.; Suh, K. Y., Soft lithography for microfluidics: a review. *Biochip Journal* **2008,** 2, (1), 1-11.

33.   White, C. W.; Withrow, S. P.; Budai, J. D.; Boatner, L. A.; Sorge, K. D.; Thompson, J. R.; Beaty, K. S.; Meldrum, A., Ferromagnetic FePt nanoparticles formed in Al_2O_3 by ion implantation. *Nuclear Instruments & Methods in Physics Research Section B-Beam Interactions with Materials and Atoms* **2002,** 191, 437-441.

34.   Reverchon, E.; Adami, R., Nanomaterials and supercritical fluids. *Journal of Supercritical Fluids* **2006,** 37, (1), 1-22.

35.   Martinez, B.; Roig, A.; Molins, E.; Gonzalez-Carreno, T.; Serna, C. J., Magnetic characterization of gamma-Fe_2O_3 nanoparticles fabricated by aerosol pyrolysis. *Journal of Applied Physics* **1998,** 83, (6), 3256-3262.

36. Sun, S. H.; Murray, C. B.; Weller, D.; Folks, L.; Moser, A., Monodisperse FePt nanoparticles and ferromagnetic FePt nanocrystal superlattices. *Science* **2000,** 287, (5460), 1989-1992.

37. Euliss, L. E.; Grancharov, S. G.; O'Brien, S.; Deming, T. J.; Stucky, G. D.; Murray, C. B.; Held, G. A., Cooperative assembly of magnetic nanoparticles and block copolypeptides in aqueous media. *Nano Letters* **2003,** 3, (11), 1489-1493.

38. Yin, M.; Willis, A.; Redl, F.; Turro, N. J.; O'Brien, S. P., Influence of capping groups on the synthesis of gamma-Fe_2O_3 nanocrystals. *Journal of Materials Research* **2004,** 19, (4), 1208-1215.

39. Massart, R.; Cabuil, V., Effect of some parameters on the formation of colloidal magnetite in alkaline medium; yield and particle size control. *Journal De Chimie Physique Et De Physico-Chimie Biologique* **1987,** 84, (7-8), 967-973.

40. Alibeigi, S.; Vaezi, M. R., Phase Transformation of Iron Oxide Nanoparticles by Varying the Molar Ratio of Fe^{2+}:Fe^{3+}. *Chemical Engineering & Technology* **2008,** 31, (11), 1591-1596.

41. Lamer, V. K.; Dinegar, R. H., Theory, production and mechanism of formation of monodispersed hydrosol. *Journal of the American Chemical Society* **1950,** 72, (11), 4847-4854.

42. Park, J.; An, K. J.; Hwang, Y. S.; Park, J. G.; Noh, H. J.; Kim, J. Y.; Park, J. H.; Hwang, N. M.; Hyeon, T., Ultra-large-scale syntheses of monodisperse nanocrystals. *Nature Materials* **2004,** 3, (12), 891-895.

43. Hyeon, T.; Lee, S. S.; Park, J.; Chung, Y.; Bin Na, H., Synthesis of highly crystalline and monodisperse maghemite nanocrystallites without a size-selection process. *Journal of the American Chemical Society* **2001,** 123, (51), 12798-12801.

44. Cheon, J. W.; Kang, N. J.; Lee, S. M.; Lee, J. H.; Yoon, J. H.; Oh, S. J., Shape evolution of single-crystalline iron oxide nanocrystals. *Journal of the American Chemical Society* **2004,** 126, (7), 1950-1951.

45. Li, Z.; Sun, Q.; Gao, M. Y., Preparation of water-soluble magnetite nanocrystals from hydrated ferric salts in 2-pyrrolidone: Mechanism leading to Fe3O4. *Angewandte Chemie-International Edition* **2005,** 44, (1), 123-126.

46. Li, Z.; Wei, L.; Gao, M. Y.; Lei, H., One-pot reaction to synthesize biocompatible magnetite nanoparticles. *Advanced Materials* **2005,** 17, (8), 1001.

47. Griffiths, C. H.; Ohoro, M. P.; Smith, T. W., Structure, magnetic characterization and oxidation of colloidal iron dispersios. *Journal of Applied Physics* **1979,** 50, (11), 7108-7115.

48. Puntes, V. F.; Krishnan, K. M.; Alivisatos, A. P., Colloidal nanocrystal shape and size control: the case of cobalt. *Science* **2001,** 291, (5511), 2115-2117.

49. Puntes, V. F.; Zanchet, D.; Erdonmez, C. K.; Alivisatos, A. P., Synthesis of hcp-Co nanodisks. *Journal of the American Chemical Society* **2002,** 124, (43), 12874-12880.

50. Dumestre, F.; Chaudret, B.; Amiens, C.; Renaud, P.; Fejes, P., Superlattices of iron nanocubes synthesized from Fe[N(SiMe₃)₂]₂. *Science* **2004,** 303, (5659), 821-823.

51. Sun, S. H.; Murray, C. B., Synthesis of monodisperse cobalt nanocrystals and their assembly into magnetic superlattices. *Journal of Applied Physics* **1999,** 85, (8), 4325-4330.

52. Bönnemann, H.; Brijoux, W.; Brinkmann, R.; Matoussevitch, N.; Waldoefner, N.; Palina, N.; Modow, H., A size-selective synthesis of air stable colloidal magnetic cobalt nanoparticles *Inorg. Chim. Acta* **2003,** 350, 617.

53.   Vazquez, M.; Luna, C.; Morales, M. P.; Sanz, R.; Serna, C. J.; Mijangos, C., Magnetic nanoparticles: synthesis, ordering and properties. *Physica B-Condensed Matter* **2004,** 354, (1-4), 71-79.

54.   Ely, T. O.; Pan, C.; Amiens, C.; Chaudret, B.; Dassenoy, F.; Lecante, P.; Casanove, M. J.; Mosset, A.; Respaud, M.; Broto, J. M., Nanoscale bimetallic Co_xPt_{1-x} particles dispersed in poly(vinylpyrrolidone): synthesis from organometallic precursors and characterization. *Journal of Physical Chemistry B* **2000,** 104, (4), 695-702.

55.   Hyeon, T., Chemical synthesis of magnetic nanoparticles. *Chemical Communications* **2003**, (8), 927-934.

56.   Jeyadevan, B.; Urakawa, K.; Hobo, A.; Chinnasamy, N.; Shinoda, K.; Tohji, K.; Djayaprawira, D. D. J.; Tsunoda, M.; Takahashi, M., Direct synthesis of fct-FePt nanoparticles by chemical route. *Japanese Journal of Applied Physics Part 2-Letters* **2003,** 42, (4A), L350-L352.

57.   Langevin, D., Micelles and microemulsions. *Annual Review of Physical Chemistry* **1992,** 43, 341-369.

58.   Paul, B. K.; Moulik, S. P., Uses and applications of microemulsions. *Current Science* **2001,** 80, (8), 990-1001.

59.   Liu, C.; Zou, B. S.; Rondinone, A. J.; Zhang, Z. J., Reverse micelle synthesis and characterization of superparamagnetic $MnFe_2O_4$ spinel ferrite nanocrystallites. *Journal of Physical Chemistry B* **2000,** 104, (6), 1141-1145.

60.   Rondinone, A. J.; Samia, A. C. S.; Zhang, Z. J., Superparamagnetic relaxation and magnetic anisotropy energy distribution in $CoFe_2O_4$ spinel ferrite nanocrystallites. *Journal of Physical Chemistry B* **1999,** 103, (33), 6876-6880.

61.   Wang, X.; Zhuang, J.; Peng, Q.; Li, Y. D., A general strategy for nanocrystal synthesis. *Nature* **2005,** 437, (7055), 121-124.

62.   Berger, P.; Adelman, N. B.; Beckman, K. J.; Campbell, D. J.; Ellis, A. B.; Lisensky, G. C., Preparation and properties of an aqueous ferrofluid. *Journal of Chemical Education* **1999,** 76, (7), 943-948.

63.   Jeong, U.; Teng, X. W.; Wang, Y.; Yang, H.; Xia, Y. N., Superparamagnetic colloids: controlled synthesis and niche applications. *Advanced Materials* **2007,** 19, (1), 33-60.

64.   Hu, A. G.; Yee, G. T.; Lin, W. B., Magnetically recoverable chiral catalysts immobilized on magnetite nanoparticles for asymmetric hydrogenation of aromatic ketones. *Journal of the American Chemical Society* **2005,** 127, (36), 12486-12487.

65.   Jun, C. H.; Park, Y. J.; Yeon, Y. R.; Choi, J. R.; Lee, W. R.; Ko, S. J.; Cheon, J., Demonstration of a magnetic and catalytic Co@Pt nanoparticle as a dual-function nanoplatform. *Chemical Communications* **2006**, (15), 1619-1621.

66.   Ngomsik, A. F.; Bee, A.; Draye, M.; Cote, G.; Cabuil, V., Magnetic nano- and microparticles for metal removal and environmental applications: a review. *Comptes Rendus Chimie* **2005,** 8, 963-970.

67.   Nuñez, L.; Kaminski, M. D., Transuranic separation using organophosphorus extractants adsorbed onto superparamagnetic carriers. *Journal of Magnetism and Magnetic Materials* **1999,** 194, (1-3), 102-107.

68.   Pankhurst, Q. A.; Connolly, J.; Jones, S. K.; Dobson, J., Applications of magnetic nanoparticles in biomedicine. *Journal of Physics D-Applied Physics* **2003,** 36, (13), R167-R181.

69. Tartaj, P.; Morales, M. D.; Veintemillas-Verdaguer, S.; Gonzalez-Carreno, T.; Serna, C. J., The preparation of magnetic nanoparticles for applications in biomedicine. *Journal of Physics D-Applied Physics* **2003,** 36, (13), R182-R197.

70. Berry, C. C.; Curtis, A. S. G., Functionalisation of magnetic nanoparticles for applications in biomedicine. *Journal of Physics D-Applied Physics* **2003,** 36, (13), R198-R206.

71. Gupta, A. K.; Gupta, M., Synthesis and surface engineering of iron oxide nanoparticles for biomedical applications. *Biomaterials* **2005,** 26, (18), 3995-4021.

72. Duran, J. D. G.; Arias, J. L.; Gallardo, V.; Delgado, A. V., Magnetic colloids as drug vehicles. *Journal of Pharmaceutical Sciences* **2008,** 97, (8), 2948-2983.

73. Graham, T., Liquid Diffusion Applied to Analysis. *Phil. Trans. Roy. Soc.* **1861,** 151, 183.

74. McNaught, A. D.; Wilkinson, A., *IUPAC. Compendium of chemical terminology, 2nd Ed (the "Gold Book")*. Oxford, **1997**.

75. Faraday, M., *Philosophical Transactions of the Royal Society London A* **1887,** 147, 145.

76. Derjaguin, B. and Landau, L. Theory of the stability of strongly charged lyophobic sols and of the adhesion of strongly charged particles in solution of electrolytes. *Acta physicochim. URSS* **1941** 14:633-62.

77. Verwey, F., Overbeek, J. and Nes, K. *Theory of the stability of liophobic colloids: the interaction of sol particles having an electric double layer*, **1948**, New York, Elsevier.

78. Cheng, F. Y.; Su, C. H.; Yang, Y. S.; Yeh, C. S.; Tsai, C. Y.; Wu, C. L.; Wu, M. T.; Shieh, D. B., Characterization of aqueous dispersions of Fe_3O_4 nanoparticles and their biomedical applications. *Biomaterials* **2005,** 26, (7), 729-738.

79. Bulte, J. W. M.; Brooks, R. A.; Moskowitz, B. M.; Bryant, L. H.; Frank, J. A., Relaxometry and magnetometry of the MR contrast agent MION-46L. *Magnetic Resonance in Medicine* **1999,** 42, (2), 379-384.

80. Taboada, E.; Rodriguez, E.; Roig, A.; Oro, J.; Roch, A.; Muller, R. N., Relaxometric and Magnetic Characterization of Ultrasmall Iron Oxide Nanoparticles with High Magnetization. Evaluation as Potential T_1 Magnetic Resonance Imaging Contrast Agents for Molecular Imaging. *Langmuir* **2007,** 23, (8), 4583-4588.

81. Pellegrino, T.; Manna, L.; Kudera, S.; Liedl, T.; Koktysh, D.; Rogach, A.; Keller, S.; Rädler, J.; Natile, G. and Parak, W. Hydrophobic nanocrystals coated with an amphiphilic polymer shell: a general route to water soluble nanocrystals. *Nanoletters* **2004** 4 (4) 703-707.

82. Thunemann, A. F.; Schutt, D.; Kaufner, L.; Pison, U.; Mohwald, H., Maghemite nanoparticles protectively coated with poly(ethylene imine) and poly(ethylene oxide)-block-poly(glutamic acid). *Langmuir* **2006,** 22, (5), 2351-2357.

83. Bonder, M. J.; Gallo, D.; Srinivasan, B.; Hadjipanayis, G. C., Size dependent in-vitro heating with polyethylene glycol coated magnetic nanoparticles. *Ieee Transactions on Magnetics* **2007,** 43, (6), 2457-2458.

84. Flesch, C.; Unterfinger, Y.; Bourgeat-Lami, E.; Duguet, E.; Delaite, C.; Dumas, P., Poly(ethylene glycol) surface coated magnetic particles. *Macromolecular Rapid Communications* **2005,** 26, (18), 1494-1498.

85. Stober, W.; Fink, A.; Bohn, E., Controlled growth of monodisperse silica spheres in micron size range. *Journal of Colloid and Interface Science* **1968,** 26, (1), 62-69

86.   Zhao, W. R.; Gu, J. L.; Zhang, L. X.; Chen, H. R.; Shi, J. L., Fabrication of uniform magnetic nanocomposite spheres with a magnetic core/mesoporous silica shell structure. *Journal of the American Chemical Society* **2005,** 127, (25), 8916-8917.

87.   Wu, P. G.; Zhu, J. H.; Xu, Z. H., Template-assisted synthesis of mesoporous magnetic nanocomposite particles. *Advanced Functional Materials* **2004,** 14, (4), 345-351.

88.   Lu, Y.; Yin, Y. D.; Mayers, B. T.; Xia, Y. N., Modifying the surface properties of superparamagnetic iron oxide nanoparticles through a sol-gel approach. *Nano Letters* **2002,** 2, (3), 183-186.

89.   Deng, Y. H.; Wang, C. C.; Hu, J. H.; Yang, W. L.; Fu, S. K., Investigation of formation of silica-coated magnetite nanoparticles via sol-gel approach. *Colloids and Surfaces a-Physicochemical and Engineering Aspects* **2005,** 262, (1-3), 87-93.

90.   Deng, Y.; Qi, D.; Deng, C.; Zhang, X.; Zhao, D., Superparamagnetic high-magnetization microspheres with a $Fe_3O_4@SiO_2$ core and perpendicularly aligned mesoporous SiO_2 shell for removal of microcystins. *Journal of the American Chemical Society* **2008,** 130, (1), 28.

91.   Tartaj, P.; Serna, C. J., Synthesis of monodisperse superparamagnetic Fe/silica nanospherical composites. *Journal of the American Chemical Society* **2003,** 125, (51), 15754-15755.

92.   Vestal, C. R.; Zhang, Z. J., Synthesis and magnetic characterization of Mn and Co spinel ferrite-silica nanoparticles with tunable magnetic core. *Nano Letters* **2003,** 3, (12), 1739-1743.

93.   Santra, S.; Tapec, R.; Theodoropoulou, N.; Dobson, J.; Hebard, A.; Tan, W. H., Synthesis and characterization of silica-coated iron oxide nanoparticles in microemulsion: The effect of nonionic surfactants. *Langmuir* **2001,** 17, (10), 2900-2906.

94.   Andersson, N.; Kronberg, B.; Corkery, R.; Alberius, P., Combined emulsion and solvent evaporation (ESE) synthesis route to well-ordered mesoporous materials. *Langmuir* **2007,** 23, (3), 1459-1464.

95.   Lu, Y.; Yin, Y.; Mayers, B. and Xia, Y. Modifying the surface properties of superparamagnetic iron oxide nanoparticles through a sol-gel approach, *Nanoletters* **2002**, 2 (3) 183-186.

96.   Tartaj, P.; Morales, M. P.; Gonzalez-Carreno, T.; Veintemillas-Verdaguer, S.; Serna, C. J., Advances in magnetic nanoparticles for biotechnology applications. *Journal of Magnetism and Magnetic Materials* **2005,** 290, 28-34.

97.   Tartaj, P.; Gonzalez-Carreno, T.; Serna, C. J., Single-step nanoengineering of silica coated maghemite hollow spheres with tuneable magnetic properties. *Advanced Materials* **2001,** 13, (21), 1620.

98.   Julian-Lopez, B.; Boissiere, C.; Chaneac, C.; Grosso, D.; Vasseur, S.; Miraux, S.; Duguet, E.; Sanchez, C., Mesoporous maghemite-organosilica microspheres: a promising route towards multifunctional platforms for smart diagnosis and therapy. *Journal of Materials Chemistry* **2007,** 17, (16), 1563-1569.

99.   Iler, R. K., *The Chemistry of Silica*. New York, 1979.

100.   Gaikwad, R.M. and Sokolov, I. Silica nanoparticles to polish tooth surfaces for caries prevention. *Journal of Dental Research* **2008** 87 (10) 980-983

101.   Bergna, H. E.; Roberts, W. O., *Colloidal Silica. Fundamentals and applications.* **2006**; Vol. 131. Taylor and Francis.

102. Hussain, S.; Braydich-Stolle, L.; Shrand, A; Murdock, R.; Yu, K.; Mattie, D.; Schlager, J. And Terrones, M. Toxicity evaluation for safe use of nanomaterials: recent achievements and technical challenges. *Advanced Materials* **2009**, 21, 1-11.

103. Parak, W. J.; Gerion, D.; Pellegrino, T.; Zanchet, D.; Micheel, C.; Williams, S. C.; Boudreau, R.; Le gros, M. A.; Larabell, C. A. and Alivisatos, A. P. Biological applications of colloid nanocrystals, *Nanotechnology*, **2003**, 14 (7) R15-R27.

104. Sepmag Technologies: http://www.sepmag.eu/home.php

105. Liong, M.; Angelos, S.; Choi, E.; Patel, K.; Stoddart, J. and Zink, J. Mesostructured multifunctional nanoparticles for imaging and drug delivery, *J. Mater. Chem.* **2009**, 19, 6251-6257.

106. Moroz, P.; Jones, S. K.; Gray, B. N., Status of hyperthermia in the treatment of advanced liver cancer. *Journal of Surgical Oncology* **2001,** 77, (4), 259-269.

107. Atkinson, W. J.; Brezovich, I. A.; Chakraborty, D. P., Usable frequencies in hyperthermia with thermal seeds. *Ieee Transactions on Biomedical Engineering* **1984,** 31, (1), 70-75.

108. Hergt, R. and Dutz, S. Magnetic particle hyperthermia-biophysical limitations of a visionary tumour therapy. *J. Magn. Magn. Mater.* **2007**, 311, 187-192.

109. Rinck, P. A., *Magnetic Resonance in Medicine*. Vienna **2001**. Blackwell Science.

110. Baird, A. and Warach, S. Magnetic resonance imaging of acute stroke, *J. Cerebral Blood Flow and Metabolism* **1998**, 18, 538-609.

111. Mornet, S.; Vasseur, S.; Grasset, F.; Duguet, E. Magnetic nanoparticle design for medical diagnosis and therapy. *J. Mater. Chem.* **2004**, 14, 2161-2175

112. Karpowicz, J.; Hietanen, M.; Gryz, K., Occupational risk from static magnetic fields of MRI scanners. *Environmentalist* **2007**, 27, 533-538

113. Arruebo, M.; Fernández-Pacheco, R.; Ibarra, M. R. and Santamaría, J. Magnetic nanoparticles for drug delivery *Nanotoday* **2007** 2, 22.

114. Weissleder, R.; Kelly, K.; Sun, E.; Shtatland, T. and Josephson, L. Cell-specific targeting of nanoparticles by multivalent attachment of small molecules. *Nature Biotechnology* **2005,** 23, 1418 – 1423.
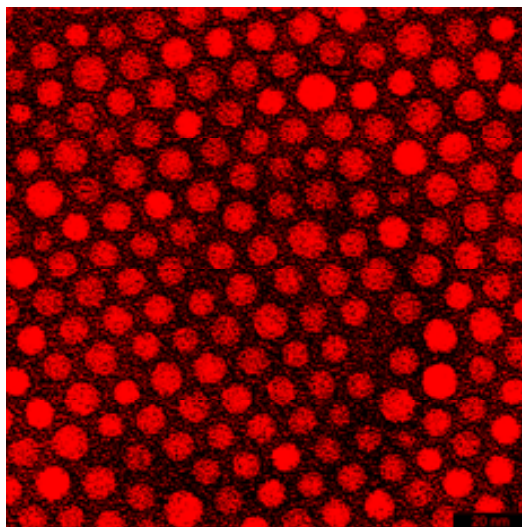
2. COLLOIDAL DISPERSIONS OF MAGHEMITE NANOPARTICLES

Chapter 2 describes the synthetic procedure to obtain iron oxide nanoparticles as well as their properties in solid form and in colloidal dispersions. The complete set of results is gathered in my M. Sc. Thesis.[1] Representative results, as well as some new data on the characterization of the particles, are included here.

Iron oxide compounds are present in almost all of the different compartments of the earth system: atmosphere, biosphere, hydrosphere and lithosphere. They have been used since the prehistoric era as pigments for paintings. Nowadays, the uses of iron oxides comprise not only the pigments, but also glazing in ceramic applications, hydrogen production, anticorrosion paints, magnets, magnetic data storage and water remediation, among others. Of special relevance for this thesis is the increasing number of applications of iron oxides in nanomedicine.

There are 16 known iron oxides which include oxides, hydroxides and oxide-hydroxides.[2] The difference between the iron oxides lies on the iron oxidation state: iron (II) oxide (FeO) is known as wüstite, iron (II, III) oxide (Fe_3O_4) is the magnetite and iron (III) oxide (Fe_2O_3) has four polymorphs: α-Fe_2O_3 (hematite), β-Fe_2O_3, γ-Fe_2O_3 (maghemite) and ε-Fe_2O_3. Hematite is the most stable iron (III) oxide polymorph in bulk form. However, at nanometric level maghemite is the most stable one due to its lowest surface energy.

Especially remarkable, owing to their interest in the present thesis, are magnetite, maghemite and epsilon compounds (see **Table 2.1**). The crystal structure of magnetite and maghemite corresponds to an inverse spinel and they show similar magnetic behaviour: they are ferrimagnets (FI). Both of them behave as soft magnets, with high magnetization and a relatively low anisotropy constant. Those similarities constitute a hindrance to differentiate them when they are at the nanoscale. The Verwey transition which is a first order transition from resistive to conductive state, at $T_w \approx 110K$, constitutes a fingerprint to identify magnetite. Such transition is, however, very sensitive to iron vacancies and particle size.

Table 2.1. Crystalline and magnetic properties of selected iron oxides. Fe^{n+} = iron cations, M_S = saturation magnetization of bulk material at room temperature and at 5K, K_{eff} = anisotropy constant.

Phase	Fe^{n+}	Crystalline structure	Cell parameter (Å)	Magnetic behaviour	M_S (emu/g) RT-5K	K_{eff} (J/m³)	Colour
Fe_3O_4	$Fe^{2+}/$ Fe^{3+}	Inverse cubic spinel (Fd-3m)	a = 8.394	Ferrimagnetic	90-100	$\approx 10^5$	Black
γ-Fe_2O_3	Fe^{3+}	Inverse cubic spinel (Fd-3m)	a = 8.346	Ferrimagnetic	60-80	$\approx 10^5$	Reddish-brown
α-Fe_2O_3	Fe^{3+}	Corindon Hexagonal (R-3c)	a = b = 5.034 c = 13.752	Anti-ferromagnetic	0.4	$\approx 3 \cdot 10^4$	Bright red
ε-Fe_2O_3	Fe^{3+}	Rhombic ($Pna2_1$)	a = 5.087 b = 8.784 c = 9.469	Ferrimagnetic	15-20	$\approx 5 \cdot 10^5$	Reddish

Maghemite at the nanometric scale is a very stable crystalline phase. Nevertheless, if it is heated over 400°C (approximate value)[3] it transforms to hematite. This temperature can be shifted to higher values, even up to 1000°C, when the particles are confined in solid matrixes.[4] In fact, maghemite nanoparticles confined in silica transform to the epsilon polymorph. Epsilon-iron (III) oxide is a metastable phase that presents difficulties to be stabilized in pure form. This polymorph, also ferrimagnetic, presents an uncommon high coercivity of 2 Tesla (20 kOe) and low saturation magnetization (15-20 emu/g) at room temperature, for what it could be an interesting material for magnetic data storage. An important part of the PhD Thesis of Martí Gich,[4] former component of the group, was

dedicated to the synthesis and characterization of this polymorph. I participated in some parts of such work. Section 4.5 describes the synthesis of ε-Fe$_2$O$_3$@SiO$_2$ nanospheres developed in this thesis.

2.1. Synthesis of maghemite nanoparticles

Since we aim at fabricating colloidal dispersions of maghemite nanoparticles to be used as contrast agents for magnetic resonance imaging (MRI) as well as mediators for magnetic hyperthermia, a control over the appropriate magnetic properties, like high magnetic susceptibility, high magnetization and superparamagnetic behaviour at room temperature is desirable. The possibility to tune the particle size and the particle size distribution were the main criteria considered when choosing the most suitable synthetic pathway since the magnetic properties of the dispersion will strongly depend on the mean particle size. Thermal decomposition of organometallic compounds in organic solvents was the method of choice since it enables good crystallinity of the nanoparticles, high control over the particle size and very narrow particle size distributions. We adapted the synthesis for FePt nanoparticles reported by Sun et al.[5] to synthesize monodisperse maghemite NPs. The method is very similar to another one for γ-Fe$_2$O$_3$ nanoparticles reported by Hyeon et al.[6]

Figure 2.1 shows the experimental set-up put in place. A typical experimental procedure reads as follows: the oleic acid (cis-9-octadecenoic acid, CH$_3$(CH$_2$)$_7$CH=CH(CH$_2$)$_7$COOH), which plays the role of surfactant, was dissolved in 40 ml of octyl ether (an organic solvent with high boiling point, 360°C). The reaction proceeded under inert atmosphere, preferably under argon. The solution was heated up to 100°C and the iron precursor (Fe(CO)$_5$) was quickly added to the flask; the colourless solution turned yellow (the reactant concentrations are listed in **Table 2.2**). Shortly afterwards, the formation of the first nuclei was identified by another colour change, from yellow to black. The system was heated up further to let it reflux for a given time. Next, it was cooled down to room temperature. The particles were then collected from the reactant solution by precipitating them with the addition of an antisolvent, ethanol or acetone, and centrifuging them for 15 minutes at 4400 rpm. The brown supernatant solution containing the octyl ether and the unreacted precursors was discarded. The black precipitate, i.e. the iron oxide nanoparticles, was redispersed in hexane. Repetition of the cycle of precipitation with an antisolvent and redispersion in a good solvent constitutes a purification method. Some amount of oleic acid is desorbed from the particle surfaces in this cycle, thus, it is advisable to add 100-300 µl of the surfactant to the hexane dispersion to ensure its long term stability. Finally, the hexane dispersion was centrifuged 5 more minutes to precipitate any solid impurities; this centrifugation was repeated until no precipitates were obtained. The supernatant solution was collected and stored. Its colour could vary

from reddish-brown to black. The amount of nanoparticles obtained in each batch was of 100-120 mg Fe_2O_3 (80-100% yield).
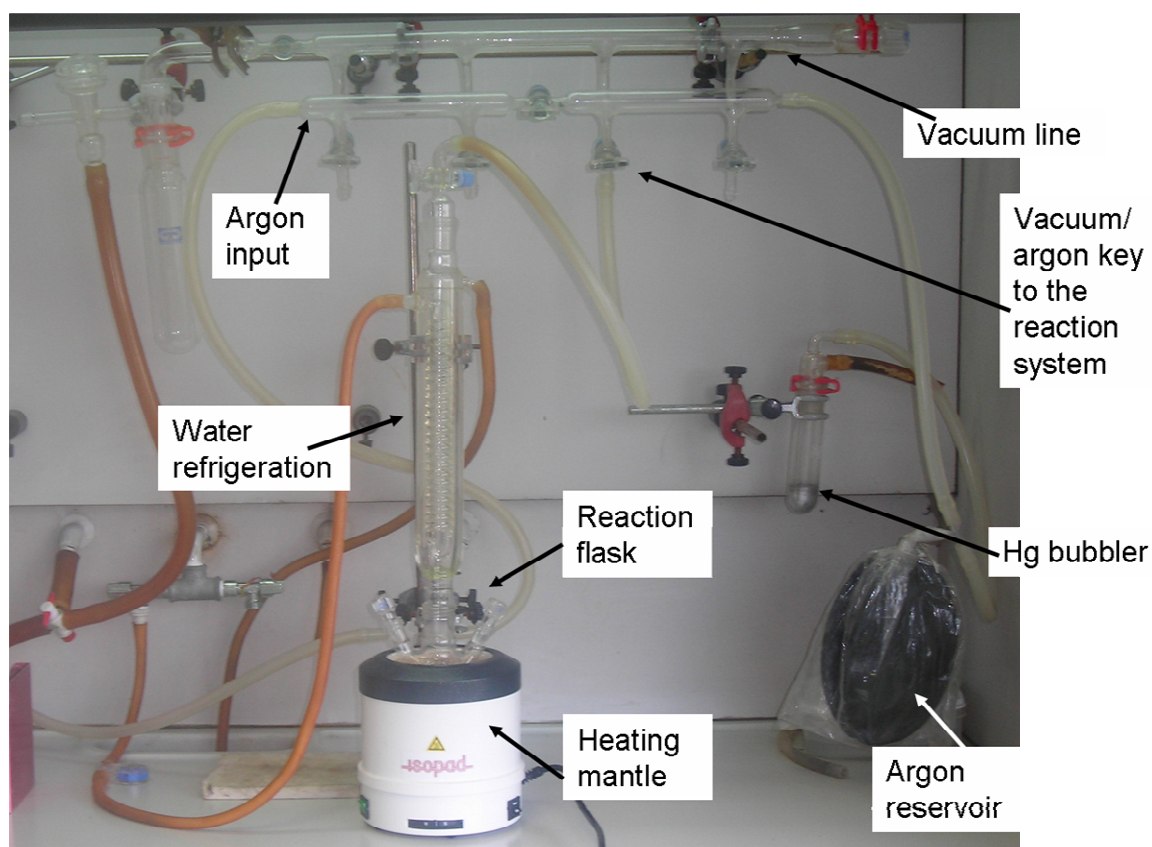
Figure 2.1. Experimental set-up for the synthesis of iron oxide nanoparticles by thermal decomposition of iron pentacarbonyl.

Different experimental parameters as the oleic acid quantity, reaction temperature and reaction time were varied to study their influence on the final particle size and size distribution (see **Table 2.2**). The thermal decomposition method allows the reaction to follow the LaMer mechanism which leads to monodisperse systems.[7] This mechanism is based on the temporal separation between a first short burst of nucleation from a supersaturated solution and the subsequent slow controlled growth of the particles. In our case, the short burst of nucleation was achieved by adding the iron pentacarbonyl around 100ºC while heating up the solution instead of adding it at room temperature. After the first nuclei were formed, a big amount of precursor was spent and thus, the remaining amount of iron pentacarbonyl was not concentrated enough to form more nuclei, so it was expended for the growth of the particles. In this way, all the particles grew at the same rate and had the same final size. This synthetic route was repeated around 100 times during the thesis.

The complete process took around 4 hours. There are several details to be taken into account if to obtain high quality products. The first consideration is the condition of the

iron pentacarbonyl. This compound is sensitive to air and humidity. It is highly flammable and very toxic, since it partly decomposes in carbon monoxide (CO). Although the commercial product is sealed under nitrogen atmosphere, it oxidizes with time and a precipitate of iron oxide is deposited at the bottom of the bottle. It is convenient to check its quality before using it. In case of precipitate, the pentacarbonyl should be filtrated under inert atmosphere or replaced by a new batch.

Table 2.2. Experimental conditions for different synthesis of iron oxide nanoparticles. T_R: temperature at reflux conditions, t_R: reaction time under reflux conditions.

Synthesis ID	[Fe(CO)$_5$] (mM)	[oleic acid] (mM)	T_R (°C)	t_R (min)
A	37.5	50	**320**	30
B	37.5	50	300	30
C	37.5	**50**	300	**120**
D	37.5	**133**	300	30
E	37.5	**200**	300	30

Another difficulty of the process is the use of inert atmosphere. Due to the toxicity and flammability of the precursor it is indispensable to avoid a violent reaction and also to ensure a correct oxidation to nanometric entities. It has been reported that the lack of oxygen also avoids the undesirable formation of hematite.[8] A third aspect to consider is the stirring method. Magnetic stirring is not the best option for the particle growth step since the magnetic nanoparticles can stick to the magnet and aggregate. Besides, the solvent reflux has to be controlled with a homogenizing agent to avoid abrupt boiling which would induce inhomogeneities in the final product. For that purpose, two possible solutions are mechanical stirring with a material withstanding more than the reflux temperature (> 320°C) or using pumice pieces. We chose the combination of magnetic stirring to homogenize the reactant solution before the nucleation step (until the addition of Fe(CO)$_5$) and the pumice pieces to control the boiling of the solvent and the growing of the particles. The last aspect to be underlined is the heating ramp. As it was mentioned before, to follow a LaMer mechanism the iron precursor is to be added at 100°C and the faster the heating rate, the better the monodispersity of the particles. The process to obtain spherical nanoparticles is kinetically controlled; a slow reaction would lead to a thermodynamic process and thus, to faceted and bigger particles.

The resulting nanoparticles are sterically stabilized with oleic acid in hexane, an organic apolar solvent (see **Figure 1.12** for a schematic illustration). The stability of these dispersions was maintained for months and even years. Unfortunately, hexane is not a biocompatible solvent. In this thesis, two different approaches have been developed to coat the particles with biocompatible materials: first, the exchange of the oleic acid with a molecular electrolyte, and second, the coating of the particles with silica gel under supercritical conditions. The first approach will be explained below and the second one will be described in Chapter 4.

The exchange of stabilizers was accomplished by mixing the organic dispersion of nanoparticles with an aqueous solution of tetramethylammonium hydroxide (TMAOH, $[(CH_3)_4N]^+[OH]^-$). Different Fe_2O_3/TMAOH molar ratios were tested; the optimal one was 1/10. The iron oxide concentration was measured by titration with potassium dichromate (see annex 7.3.1 for details). With vigorous stirring the immiscible phases form an emulsion where the TMAOH molecules displace the oleic acid from the particle surface. After 2 to 5 hours the particles were completely transferred to the aqueous phase (see **Figure 2.2**). They were collected by precipitation with the addition of acetone and centrifugation. The precipitate was dispersed in water. Sometimes it was necessary to repeat the precipitation/centrifugation cycle two or three times. The solvent exchange process yield was close to 100%.
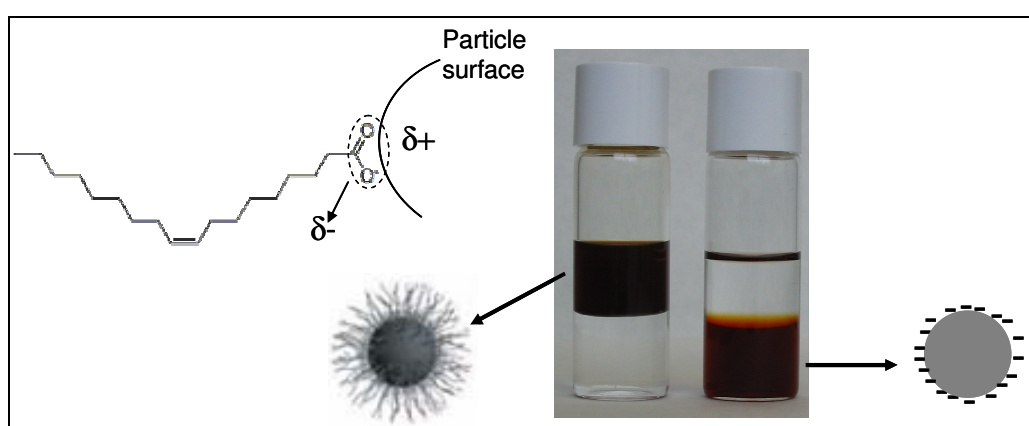
Figure 2.2. Stable dispersions of iron oxide nanoparticles in hexane (left vial; upper phase) and in water with hydroxyl ions (right vial; lower phase). The particles in the left vial are totally undispersible in water. In the right vial, they are totally undispersible in hexane.

At this point, the right vial in **Figure 2.2** contained an aqueous dispersion of iron oxide nanoparticles at basic pH (12-13). Electrostatic stabilization highly depends on pH, as it was explained in section 1.1.3.1. In this way, the electrostatic barrier with TMAOH at the particle surface is neutralized when pH is around 7, and therefore, another electrolyte had to be added to ensure the stability at the physiological pH (7-7.5). The polyvalent anion sodium citrate was chosen for that ($HOC(COONa)(CH_2COONa)_2 \cdot 2H_2O$, pk_1, pk_2 and pk_3 = 3.13, 4.76 and 6.4, respectively; thus, at neutral pH it is completely ionized). Sodium citrate was added to the basic dispersion and the pH was decreased to 7 with nitric acid while magnetically stirring. Different iron oxide/sodium citrate molar ratios were studied (3 to 0.2); the optimum ratio was found for 1/2. Finally, the sample was ultrasonified for 5 minutes to avoid aggregation of the particles. Long-term stable aqueous dispersions of iron oxide nanoparticles at neutral pH could be achieved in this way. The amount of iron was measured by titration with potassium dichromate before and after the stabilizers exchange in order to control the efficiency of the process. The transfer resulted to be complete.

2.2.   Characterization of the nanoparticles in powder form and in colloidal dispersion

Iron oxide nanoparticles in solid form and in colloidal dispersion were reddish-brown to black (see **Figure 2.3**). The stable dispersions had bright clear colour which changed to cloudy if the particles began to aggregate. In case of further aggregation, the particles finally precipitate.

Figure 2.3. Photographs of several iron oxide colloidal dispersions.

The stabilization in water with TMAOH and sodium citrate was pH dependent, as expected for electrolytes (see **Figure 2.4**).
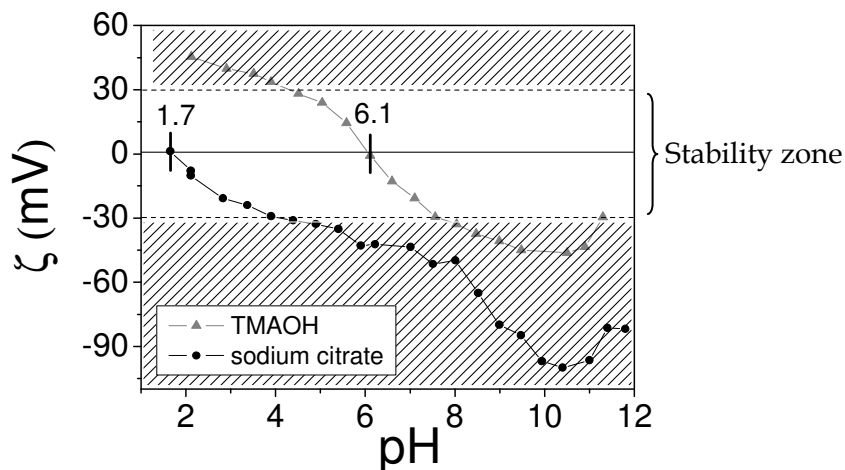
Figure 2.4. Zeta potential (ζ) of the electrostatically stabilized dispersions with TMAOH (full grey triangles) and with TMAOH + sodium citrate (full black circles). The isoelectric points are noted down.

The stability of iron oxide nanoparticles in water matched the predictions from DLVO theory and therefore could be estimated by measuring the zeta potential (see sections 1.1.3.1. and 7.3.2). The isoelectric point (pH at which there is no net surface charge) corresponded to the pH of lower stability of the system: 6.1 for TMAOH and 1.7 for sodium citrate. Particles stabilized with the former electrolyte precipitate between

pH 4.5 and 7.5. Particles stabilized with further addition of sodium citrate were stable above pH 4.

2.2.1. Particle size determination

A big effort was directed to the determination of the mean particle size and size distribution. Several techniques were used: transmission electron microscopy (TEM), X-ray diffraction (XRD), small angle X-ray scattering (SAXS), dynamic light scattering (DLS), magnetometry and relaxivity. Each of these techniques measures a different property of the sample and from that, a mean diameter can be derived. The narrower the particle size distribution, the more similar will be the average size values resulting from the different techniques. The averages sizes values obtained are listed in **Table 2.3**.

Table 2.3. Average particle size from different characterization techniques. d stands for diameter, $d_{DLS} \equiv$ hydrodynamic diameter at basic pH. SAXS results are analyzed separately.

Synthesis ID	d_{TEM} (nm)	d_{XRD} (nm)	d_{MAG} (nm)	d_{DLS} (nm)
A	5.5	7	5.8	8.5
B	7.0	12	7.1	10.0
C	5-12	12	9.2	17.0
D	10.0	9	10.0	21.0
E	22.0	-	-	43.0

Transmission Electron Microscopy (TEM)

The main results obtained from the direct observation of the particles with TEM concern the particle morphology, *physical size* and size distribution of the solid particles, independently of their colloidal state (details on sample preparation for TEM analysis can be found in annex 7.3.3). The TEM particle size is the diameter of the particles directly measured in the TEM images. The size distribution was calculated by fitting the size histogram of at least 200 nanoparticles with a Gaussian function. The standard deviation (σ) is defined as the root of the average of the squares of the differences of all the observations from their mean value, and the polidispersity of the distribution (P) is defined as the percentage of the standard deviation (σ) related to the mean value.

Equation 2.1 $$\sigma = \sqrt{\frac{\sum(\text{value}_i - \text{mean} \cdot \text{value})^2}{\text{mean} \cdot \text{value}}} \qquad P = \frac{\sigma}{mean \cdot value} \cdot 100$$

Table 2.4 summarizes the synthetic conditions, the morphology and mean size of the resulting nanoparticles. The particle shape and size depend on the reaction time. Synthesis of only 30 minutes yielded spherical particles (syntheses A, B, D and E), whereas longer reaction times, 120 minutes, produced faceted particles with cubic shape (synthesis C). This difference is attributed to the oxide anisotropic structure, i.e., every

crystalline plane has a different surface energy. Then, when the synthesis is thermodynamically controlled (long reaction time), the particles are faceted, being the outer planes the ones with the lowest surface energy. On the contrary, if the process is kinetically controlled (short reaction time), there is no preferential shape. In our case, the final shape was spherical but other shapes such as triangular, rhombohedral, star-like, rod-like, etc. have been reported by controlling the kinetics.[9,10] Therefore, a short reaction time (30 minutes) enabled a kinetic control of the synthesis, resulting in spherical particles with narrow particle size distribution (see **Figure 2.5**).

Table 2.4. Synthetic conditions, average particle size measured by TEM (d_{TEM}) and size polidispersity (P) for each set of experimental parameters.

| Synthesis ID	[Fe(CO)$_5$] (mM)	[oleic acid] (mM)	T_R (°C)	t_R (min)	Shape	d_{TEM} (nm)	P (%)
A	37.5	50	**320**	30	**Spherical**	**5.5**	$\approx$ **11**
B	37.5	**50**	**300**	**30**	**Spherical**	**7.0**	$\approx$ **11**
C	37.5	50	300	**120**	**Faceted**	**5-12**	$\approx$ **29**
D	37.5	**133**	300	30	**Spherical**	**10.0**	$\approx$ **8**
E	37.5	**200**	300	30	**Spherical**	**22.0**	$\approx$ **10**

Longer reaction time (120 minutes) favoured the thermodynamic control of crystal growth and thus cubic particles with broader size distribution were obtained (see **Figure 2.6**). The broadening of the size distribution might be due to an incomplete process of Ostwald ripening (the smaller particles dissolve and re-precipitate onto the bigger ones). If the Ostwald ripening process would have been completed, the final particle size would have been larger and the size distribution narrower.

The oleic acid concentration was also responsible for the final particle size due to its role on particle nucleation and growth, as it was described by Yin et al.[11] The surfactant molecules coordinate to the iron atoms and stabilize them after decomposition of the iron pentacarbonyl. Then, these iron-oleic acid complexes react to form the iron oxide nuclei. Later, the growth of the particles is controlled by diffusion. As the oleic acid concentration increases (synthesis B, D and E), the stability of the first iron-oleic acid complexes increases and consequently the nucleation is hindered, resulting in a lower number of nuclei and therefore a lower number of particles, but larger in size, since the concentration of iron precursor is constant (see **Figure 2.7**). Unfortunately, particles from synthesis E ($\varnothing \approx 22$ nm) were unstable as colloids.
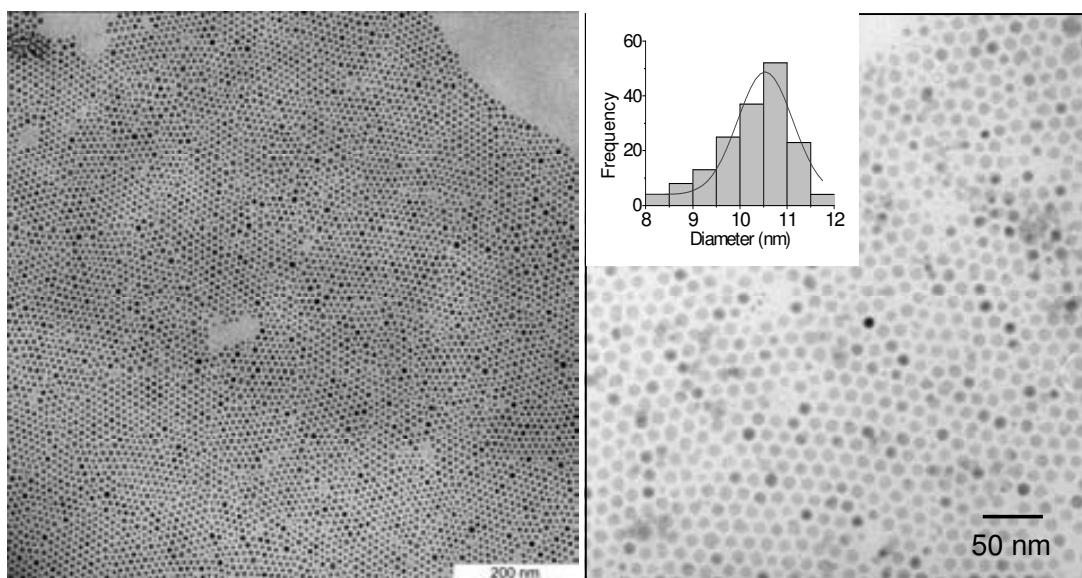
Figure 2.5. TEM images of spherical particles (synthesis B (left) and D (right); 30 minutes of reaction time). Notice the almost complete coverage of 1 micron² in the left image. The inset in the right image corresponds to the particle size histogram fitted to a Gaussian function.
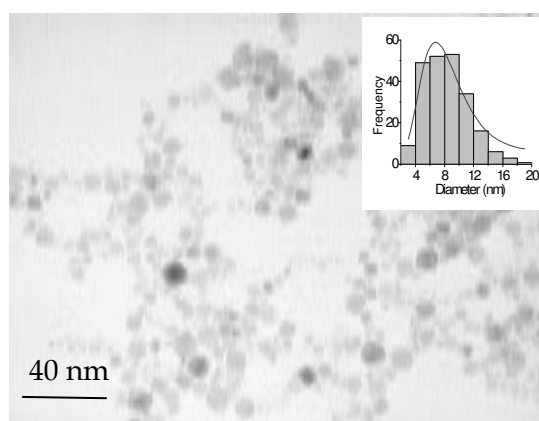

Figure 2.6. TEM images of faceted particles with broad particle size distribution obtained in a long reaction time synthesis and the corresponding particle size histogram fitted to a Gaussian function (inset) (synthesis C; 120 minutes of reaction time).

Oleic acid:	50 mM	133 mM	200 mM
$<\varnothing> \pm \sigma$ (nm):	7.0 ± 0.8	10.0 ± 0.8	22.0 ± 2.2
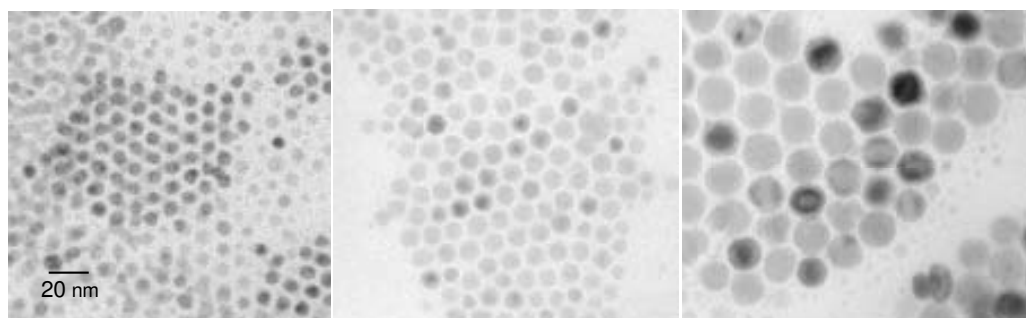
Figure 2.7. TEM images of syntheses B, D and E (from left to right, respectively) with increasing oleic acid amount. Bar scale = 20 nm for the three images.

The smallest particles (synthesis A, 5 nm in diameter) were obtained combining a short reaction time (30 minutes), low concentration of oleic acid (50 mM) and high reaction temperature (320°C). They are spherical in shape with narrow particle size distribution (see **Figure 2.8**).
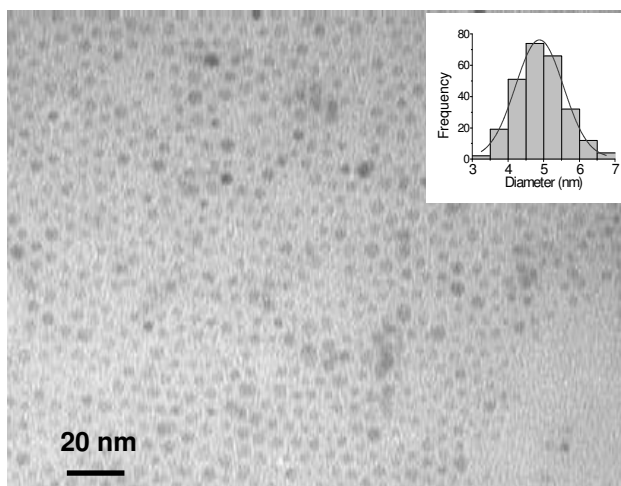
Figure 2.8. TEM image and size histogram fitted to a Gaussian function of the smallest particles, 5 nm in diameter (synthesis A).

X-Ray diffraction (XRD)

Diffraction intensity is proportional to the volume of the particles. Besides, the width of the diffraction peaks depends on the *crystallite size* of the sample analyzed in powder form. By fitting the experimental diffractograms with the MAUD program through the Rietveld method the crystallite sizes of the iron oxide nanoparticles were obtained (see annex 7.3.5). The values are summarized in **Table 2.3**. **Figure 2.9** shows an example of this fitting procedure. Values of the crystallite sizes match those obtained by TEM, indicating that the particles are monocrystalline.
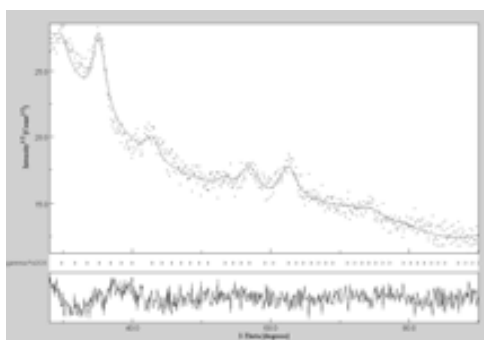
Figure 2.9. Experimental diffraction of one sample type A (dots) and its corresponding fitting curve using the MAUD program (continuous line).

Small angle x-ray scattering (SAXS)

Small angle x-ray scattering is a non-destructive analytical technique for the structural characterization of solid and fluid materials at the nanometre range. By fitting the scattering curves with different fitting models, the particle size, interparticle distance and particle packing can be obtained (see annex 7.3.6). Especially interesting is the possibility of analyzing the iron oxide particle size in colloidal state (without the contribution of the stabilizers) since this information, compared to the one obtained from TEM, can help identifying the degree of aggregation of the particles in a given solvent.

SAXS measurements were performed at the Max Planck Institute of Colloids and Interfaces, in Potsdam, Germany. The analyzed samples were synthesized at this institution as well as the TEM characterisation. For the batches synthesized in Germany, using the same synthetic conditions as in Barcelona, it was found that the average particle size was shifted to slightly larger values and the particles were more faceted, although the size distribution was also narrow. This is an indication of how extremely sensible are the nanometric products to the synthetic conditions. For that reason a different labelling to identify the materials was used.

Several aqueous and organic colloidal samples with different iron oxide concentrations (from 10 to 100 mM) were analyzed, as well as dried particles in powder form. Sodium citrate was chosen as the electrolyte for the aqueous dispersions. **Table 2.5** shows the numerical results for some of the analyzed samples. The average particle sizes resulting from SAXS were identical in water and hexane at different concentrations, as well as in powder form. Among the available models, the best fit for the colloidal samples was obtained with the model of non-interacting particles. The powder samples were best fitted with the Percus-Yevick model of short-range interacting particles with no crystalline order.

In all cases, particle sizes calculated by SAXS are almost identical to the ones observed by TEM. It can be then concluded that the iron oxide nanoparticles were individually stabilized in aqueous and organic colloidal state up to, at least, 100 mM Fe_2O_3 and that SAXS is a very convenient technique to measure particle sizes and polydispersity indexes in colloidal dispersions.

Figure 2.10 shows three scattering curves of sample Fe.06.25 stabilized in hexane at 25, 50 and 100 mM, respectively. The scattering intensity increases with increasing iron oxide concentration, but the minimum and maximum do not shift along the x-axis indicating that the particle size neither the interaction distance between particles change. Consequently, there is no aggregation when concentrating the sample up to 100 mM Fe_2O_3.

Table 2.5. Average particle size calculated by SAXS compared to particle size determined by TEM of samples synthesized at MPI-Colloids and Interfaces, Germany. *Percus-Yevick approximation corresponds to short-range interacting spheres without crystalline order.

Sample	$[Fe_2O_3]$ (mM)	d_{TEM} (nm) (P)	d_{SAXS} (nm) (P)	$d_{SAXS}/$ d_{TEM}	Fitting model*
Fe.06.8_hexane	25	10.5 (8%)	10.6 (15%)	1.01	Non-interacting spheres
	50		10.4 (15%)	0.99	
	100		10.5 (15%)	1.00	
Fe.06.8	Powder		10.8 (16%)	1.03	Percus-Yevick
Fe.06.22	Powder	9.6 (11%)	10.2 (18%)	1.06	Percus-Yevick
Fe.06.24	Powder	7.6 (9%)	8.6 (15%)	1.13	Percus-Yevick
Fe.06.25_hexane	25	14.3 (11%)	13.8 (16%)	0.97	Non-interacting spheres
	50		13.9 (16%)	0.97	
	100		14.0 (16%)	0.98	
Fe.06.25_citrate	25		14.0 (15%)	0.98	
Fe.06.25	Powder		14.6 (12%)	1.02	Percus-Yevick
Fe.06.26_citrate	25	11.9 (23%)	11.8 (24%)	0.99	Non-interacting spheres
Fe.06.27_citrate	25	12.5 (11%)	12.0 (17%)	0.96	Non-interacting spheres
Fe.06.29_hexane	25	10.5 (10%)	10.7 (14%)	1.02	Non-interacting spheres
Fe.06.29_citrate	25		10.7 (13%)	1.02	
Fe.06.31_citrate	25	10.9 (18%)	10.8 (15%)	0.99	Non-interacting spheres
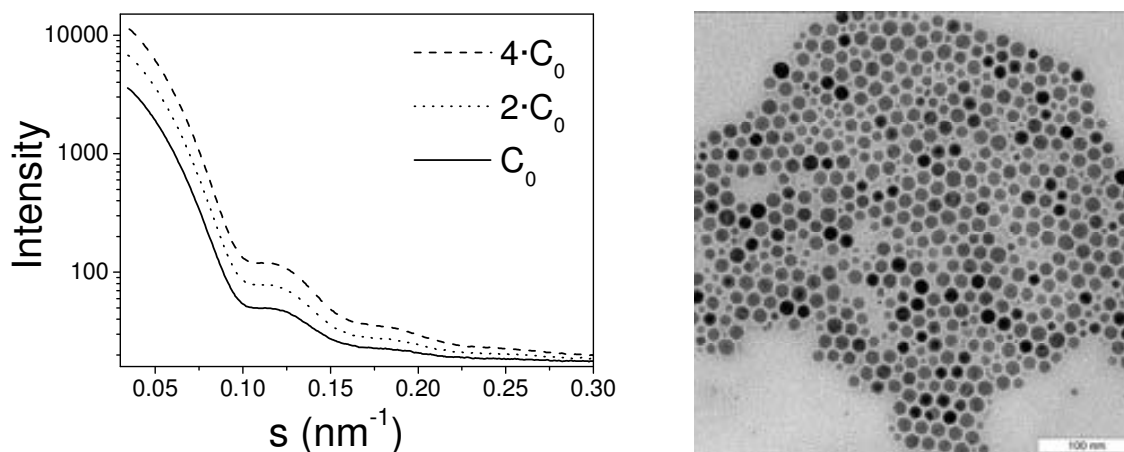
Figure 2.10. SAXS curves of sample Fe.06.25_hexane at different concentrations (C_0 = 25mM) (left graph) and TEM image of the particles showing the hcp ordering of the particles (the white bar corresponds to 100 nm).

Figure 2.11 shows the good fitting obtained by using the model of non-interacting particles to the scattering curve of sample Fe.06.25_hexane (100 Mm). All the fittings performed to the scattering curves of colloidal samples showed the same accuracy.
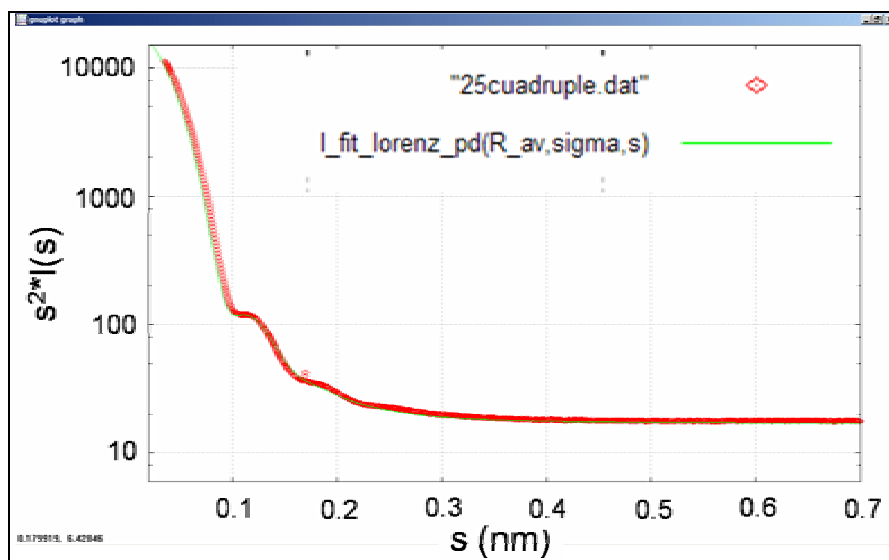
Figure 2.11. SAXS curve of sample Fe.06.25_hexane (100 mM; red dots) and its fitting curve using the model of non-interacting particles (green line).

Magnetometry

The magnetic particle size was calculated by fitting the magnetization curves to a Langevin equation (**Equation 1.5**). An example is shown in **Figure 2.12**. Results are listed in **Table 2.3**. Values are consistent with those obtained by TEM and XRD.

Equation 1.5 $\qquad$ $M = M_S \cdot (\coth \alpha - 1/\alpha) \qquad \alpha = \dfrac{m_0 \cdot H}{k_B \cdot T} \qquad m_0 = M_S \cdot V_{ptle}$
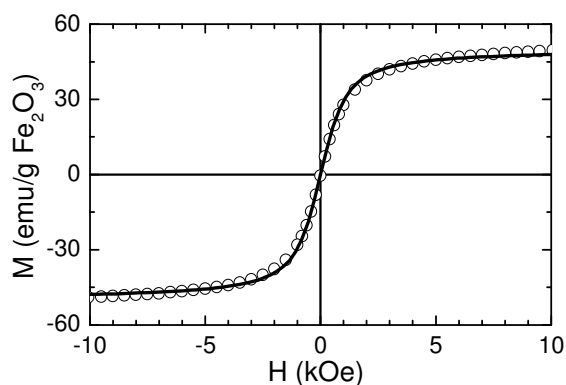

Figure 2.12. Experimental data on magnetization vs. external magnetic field (empty circles) and fitting curve by the Langevin equation (straight line).

The size determination of superparamagnetic nanoparticles from magnetization curves was studied more accurately by Prof. Chen; results are reported in reference 12. Two fitting models were considered: first, a core-shell model with a ferrimagnetic core (with bulk saturation magnetization) and a paramagnetic shell (with a given paramagnetic susceptibility; see **Equation 1.7**), and second, a uniform model with a homogeneous

magnetic particle and with homogeneous saturation magnetization lower than the bulk one. Both models are based on the Langevin function and consider a log-normal particle volume distribution. It is found that the magnetically determined average size by the core-shell model, which is physically sounder, is in agreement with the results from TEM and XRD. The fitting model also allows for the determination of the shell dimensions (for particles of mean diameter around 6 nm, the surface layer was determined to be around 0.3 nm). Moreover, the method allows extracting different mean values that can be compared in a straightforward manner with the values obtain by other techniques (d_{XRD}, d_{TEM}, etc.).

Dynamic light scattering (DLS)

Dynamic light scattering measures the Brownian motion and relates it to the *hydrodynamic diameter* of the particles. The hydrodynamic diameter includes not only the physical particle but also the coating onto the surface and the shell of solvent strongly anchored to the surface which moves together with the particle. This technique is only useful for stable colloidal dispersions. DLS is very sensitive to any particle in suspension, such as dust. Therefore, it is very important to have a well purified sample to obtain reliable data (see annex 7.3.2). The hydrodynamic size is always higher than the size observed by TEM (data are listed in **Table 2.3**) and it depends on the nature of the coating onto the particle surface, the solvent, temperature and in some cases, on the pH of the medium. As an example, **Figure 2.13** shows the different hydrodynamic diameters of sample A dispersed in hexane with oleic acid, in water with TMAOH (basic pH) and in water with sodium citrate (neutral pH).
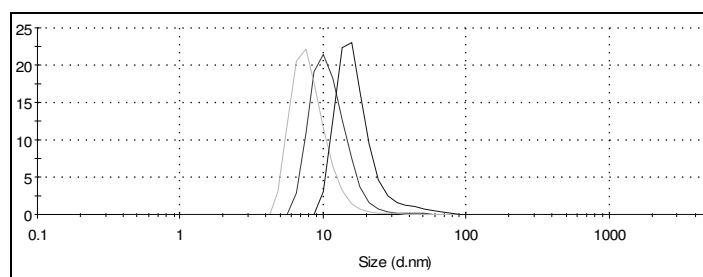
Figure 2.13. Hydrodynamic size distribution by number of sample A dispersed in basic aqueous medium (left curve; mean size = 8.4 nm), in organic medium with oleic acid (central curve; mean size = 11.6 nm) and in neutral aqueous media (right curve; mean size = 17.8 nm).

Particles stabilized with oleic acid (middle curve) were 11.6 nm in diameter. This value is close to the expected one for a 5.5 nm particle (observed by TEM) and two layers of oleic acid (2x2.3 nm). When stabilized in TMAOH the hydrodynamic diameter became smaller (left curve). Since the particle size does not change, this means that the TMAOH coating (including the water molecules adsorbed onto the particle and the electrolyte) has a thickness of (8.4 - 5.5)/2 ≈ 1.5 nm. Finally, the right curve shows the hydrodynamic

diameter of particles stabilized at neutral pH with TMAOH and sodium citrate. The mean size is 17.8 nm, almost double than the TMAOH value. This size could only be interpreted by, first, a coating thickness of (17.8-5.5)/2 = 6.15 nm, or second, a small degree of aggregation in dimmers or small clusters. The first one seems to be impossible, since the sodium citrate molecule is no larger than 1 nm. The second option seems to be the most plausible since relaxivity measurements also point out to a certain degree of clustering (see section 5.2).

### 2.2.2. Crystalline phase determination

X-Ray diffraction in powder

Magnetite and maghemite belong to the family of the cubic ferrites. Their crystalline structure, an inverse spinel, belongs to the Fd-3m symmetry group. It is illustrated in **Figure 2.14**: the oxygen atoms arrange in a face centred cubic packing whose tetrahedral sites are occupied by half of the trivalent cations and the octahedral sites are occupied by the divalent cations and the second half of the trivalent ones. In the case of maghemite, the lack of divalent cations is compensated by vacancies.
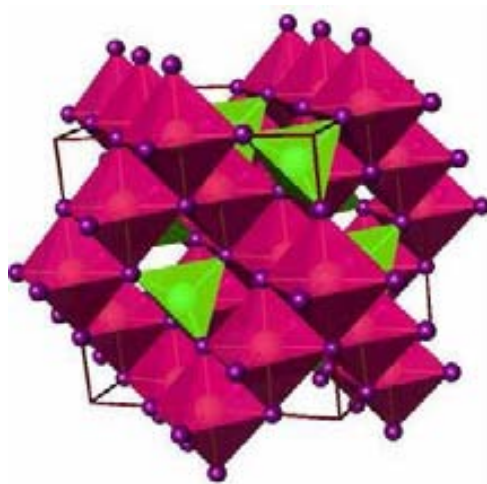
Figure 2.14. Crystalline structure of an inverse spinel.

X-Ray diffraction allows for the identification of the crystalline phases (see annex 7.3.5). The diffractograms for samples A to D showed only the presence of one crystalline phase which could be indexed to maghemite and magnetite. Due to the similar crystalline structure of these iron oxides, the position and intensity of the diffraction peaks is almost identical: the interplanar distances (d) differ only in few hundredths of angstroms (cell parameter for Fe_3O_4 and γ-Fe_2O_3 are 8.394 and 8.346 Å, respectively). Furthermore, the diffraction peaks broaden as the crystallite size is reduced to the nanometric range, making even more difficult the precise localization of the peak centre. In addition, the quality of the diffractogram also depends on the amount of available sample and the

signal to noise ratio is lowered when the glass holder is not completely covered (see **Figure 2.15**). From XRD we could not differentiate between maghemite and magnetite but we could conclude that no other phase, such as hematite, was present. Nevertheless, we assumed our particles to be γ-Fe_2O_3 since the synthetic route we adopted is very similar to the one first reported by Hyeon et al. where they obtained maghemite.[6] Moreover, maghemite is the most stable phase at nanometric dimensions under ambient conditions since it is completely oxidized.[13] We did not use any special storage conditions for the samples and we did not detect any change of properties with time evidencing oxidative processes. In addition, no evidence of the Verwey transition was found in the ZFC-FC curves of our particles whichever their size was.
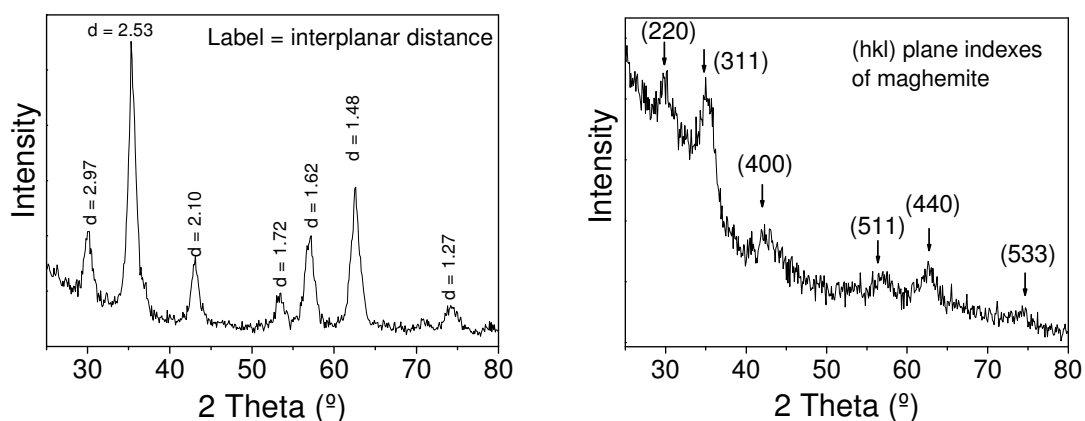

Figure 2.15. X-Ray diffractogram of representative samples. Left graph: good signal to noise ratio due to high degree of holder coverage with sample. Right graph: poor signal to noise ratio due to the small amount of powder and the irregular background signal coming from the glass holder.

X-Ray diffraction of colloidal dispersions

The amount of powder necessary to perform a XRD analysis with high signal to noise ratio (see **Figure 2.15_left**) corresponds approximately to the total amount of material synthesized in one batch of particles (100-120 mg). A solid sample is often difficult to be re-dispersed and if the amount of sample is too small, the signal to noise ratio may be very poor (see **Figure 2.15_right**). We overcame those difficulties analyzing the samples directly in colloidal state using a microdiffractometer D8 Advance (see details in annex 7.3.5). The technique could be routinely used to check that a single phase was present in our colloidal dispersions. The main advantage is the small amount of sample needed, just few hundred microlitres, and the possibility of directly measuring in colloidal state, avoiding the time consuming process of particle precipitation and drying. The low signal to noise ratio is due to the iron fluorescence. The analyses of samples without fluorescence gives better defined diffractograms, as tested with nickel nanoparticles. The quality of the diffractogram in colloidal state was similar to that one in powder form.

Electron diffraction

Electron diffraction also allows for the study of the crystalline structure of solids. It is done with a transmission electron microscope by directing an electron beam through the sample (see details in annex 7.3.3). Two examples of electron diffractograms from samples A and C are shown in **Figure 2.16**. The diffraction rings are indexed to maghemite. Sample A shows only diffraction rings while in sample C there is a mixture of discrete spots and rings. These results are in accordance with the smaller size of the monocrystalline nanoparticles in the sample A (responsible for multiple weak spots randomly oriented which appear as diffuse rings) and the broad size distribution with bigger particles in sample C (weak spots (diffuse rings) and more intense ones attributed to the bigger crystallites) ($\varnothing_A$ = 5.5 nm vs. $\varnothing_C$ = 5-12 nm).
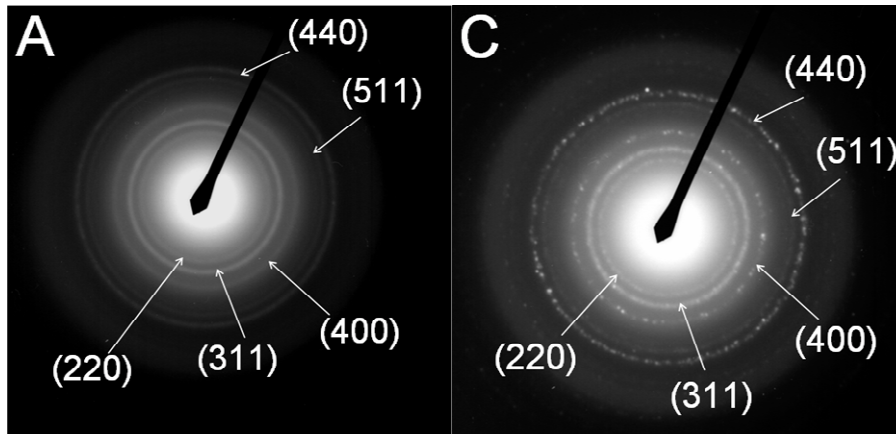
Figure 2.16. Electron diffractograms of samples A and C, respectively. The diffraction rings are indexed to the maghemite hkl planes.
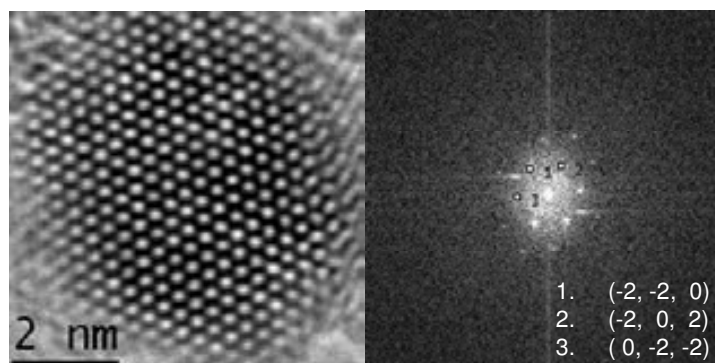
Figure 2.17. HRTEM image of one single iron oxide nanoparticle (left) and its corresponding fast Fourier transform (FFT) image with identification of the crystalline planes (right).

Selected samples were also characterized with high resolution TEM (HRTEM). The left image in **Figure 2.17** shows one single particle 5 nm in diameter. The spots represent the position of the atoms. The crystallinity of the nanoparticles is undoubtedly confirmed with this image and with its corresponding fast Fourier transform (FFT) (right image).

Iron titration with potassium dichromate

The iron content in a sample can be determined by titration of ferrous ions (Fe^{2+}) with potassium dichromate. First, hydrochloric acid (HCl) dissolves the solid species to iron ions and then tin chloride ($SnCl_2$) is added to convert the ferric ions to ferrous ones ($Fe^{3+} \rightarrow Fe^{2+}$). Once the sample is prepared to be titrated (see annex 7.3.1 for the complete details) potassium dichromate is added until the solution changes from green to violet. This method was used in my M. Sc. Thesis[1] to prove the presence of maghemite. At that moment, we assumed that the addition or not of $SnCl_2$ before the titration would enable to differentiate between Fe^{3+} and Fe^{2+} ions, and therefore, would enable the determination of the presence of maghemite (Fe^{3+}) or magnetite ($Fe^{3+} + Fe^{2+}$). Unfortunately, we did not consider that the high acidic environment created after the addition of the hydrochloric acid would oxidize all the iron atoms to ferric ions (Fe^{3+}). At present we consider that this method is not reliable to determine the presence or not of ferrous ions although it is still useful to measure the total amount of iron atoms of a sample.
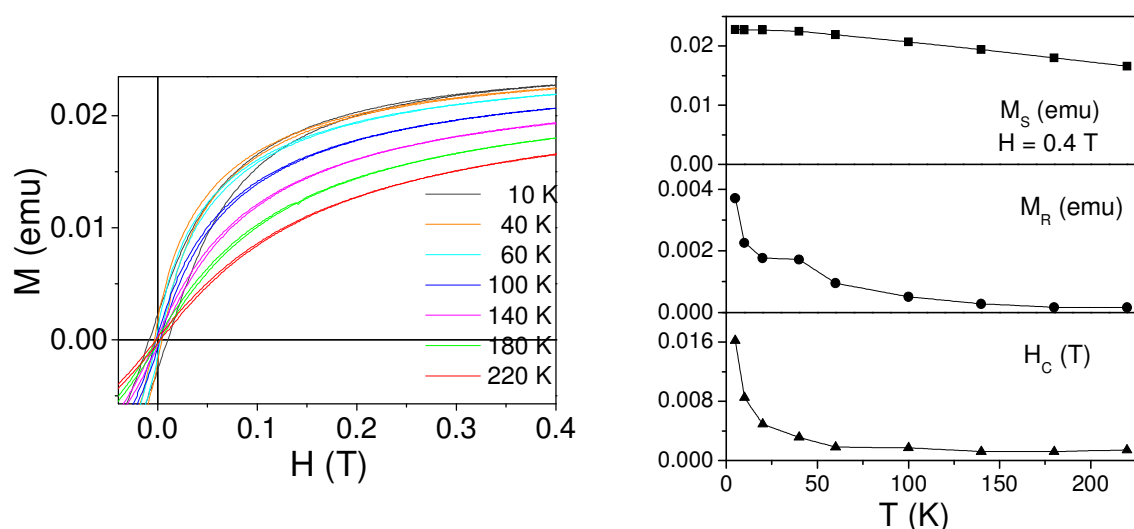
2.2.3. Magnetic properties

The magnetic properties are the most interesting for our purposes since we intend to exploit them for biomedical applications. As it was explained in section 1.1.4.1, superparamagnetic particles with high magnetic susceptibility and high magnetization are pursued. The saturation magnetization is an intrinsic property of a material. It depends on the atomic nature and the crystalline structure. However, at the nanometric scale it is significantly reduced due to the large proportion of surface atoms which are not totally coordinated and create an outer layer of lower symmetry (referred to as dead layer).[14,15] Therefore, it is expected that the smallest particles show the lowest saturation magnetization values due to their higher surface to volume ratio. This section is focussed in introducing the simplest magnetic aspects of the iron oxide nanoparticles but a more in-depth discussion of magnetic properties is included in Chapter 4. **Table 2.6** summarizes some magnetic properties of iron oxide nanoparticles synthesized by routes A-D.

Figure 2.18 collects magnetization curves at different temperatures of a sample type A (left graph) and some magnetic data extracted from them (right panel). The qualitative behaviour is common to samples B-D; they differ in the quantitative values, as shown in **Figure 2.19**. Regarding qualitative behaviour, all the samples are superparamagnetic at room temperature, as shown in **Figure 2.18** up to **Figure 2.20**. The magnetization of each sample decreases as the temperature increases (upper graph in **Figure 2.18_right**). The remanent magnetization and coercivity field are coupled values: either both are zero (approximately over 100 K in sample A) or both increase with decreasing temperature (below 100 K in sample A) (mid and lower graphs in **Figure 2.18_right**).

Table 2.6. Average values of main magnetic data for each synthetic route. A* followed the same experimental route as A, but it showed unexpected high magnetization values. M_S: magnetization at 5K, H_C: coercivity.

| Synthesis ID	d_{TEM} (nm)	M_S at 298 K (emu/g Fe_2O_3)	M_S at 5 K (emu/g Fe_2O_3)	H_C at 5 K (Oe)
A	6.0	23	28	412
B	7.0	42	-	-
C	5-12	29	47	285
D	10.0	43	-	-
A*	5.5	**68**	74	95

Figure 2.18. Magnetization curves at different temperatures of sample type A (left panel) and some selected magnetic data vs. temperature (right panel). M_S: saturation magnetization, M_R: remanent magnetization, H_C: coercive field.

The magnetization increases with particle size (see **Table 2.6** and **Figure 2.19**) as expected from the consideration of a magnetic dead layer. However, there is one type of particles, called A*, which do not follow the expected magnetic behaviour. Although all the experimental conditions corresponded to the synthetic pathway A (320ºC and 30 minutes of reaction, 133 mM oleic acid) and the resulting particles were the same size (only 5-6 nm in size) their magnetization was the highest of all the studied samples, and furthermore, it was very close to the bulk saturation magnetization (76 emu/g Fe_2O_3 at 298K).[16] We ascribe the improvement of the magnetic properties in samples A* to a better crystallinity of the particles and a lower contribution of the outer layer of low symmetry compared to its counterpart sample A. Actually, it was experimentally observed that the nucleation step in these synthesis (the change of colour from yellow to black; see section 2.1) took a shorter time than in the other syntheses, and the resulting particles had a narrower size distribution and higher magnetization. It could be thought that these particles were magnetite, which bears a higher magnetization (see **Table 2.1**). However,

they are more red than samples B to D (see **Figure 2.3**), implying that they are more likely to be maghemite than the rest.
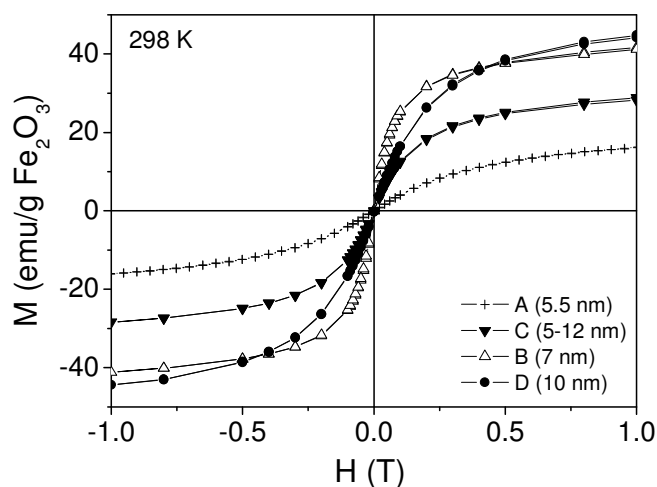
Figure 2.19. Magnetization curves of samples A to D. Mean particle sizes are included in brackets.

Figure 2.20 shows M(H) and zero field cooling-field cooling curves (ZFC-FC) of a sample type A* (see annex 7.3.7 for details on the measurement protocol). The shape is typical of a superparamagnetic system. The zero-field cooling curve (full circles) has a maximum at 15 K, defined as the blocking temperature. Below this temperature the system behaves as a ferromagnet with net coercivity and remanent magnetization. Above it, the thermal energy is higher than the energy barrier related to the effective anisotropy so the magnetic spins fluctuate: the system is then superparamagnetic (see **Figure 1.3** and **Equation 1.4**). Since the maximum is a sharp peak and the field-cooling curve separates from the zero-field-cooling one just above the blocking temperature, it is confirmed that the system is magnetically monodisperse and consequently monodisperse in size.
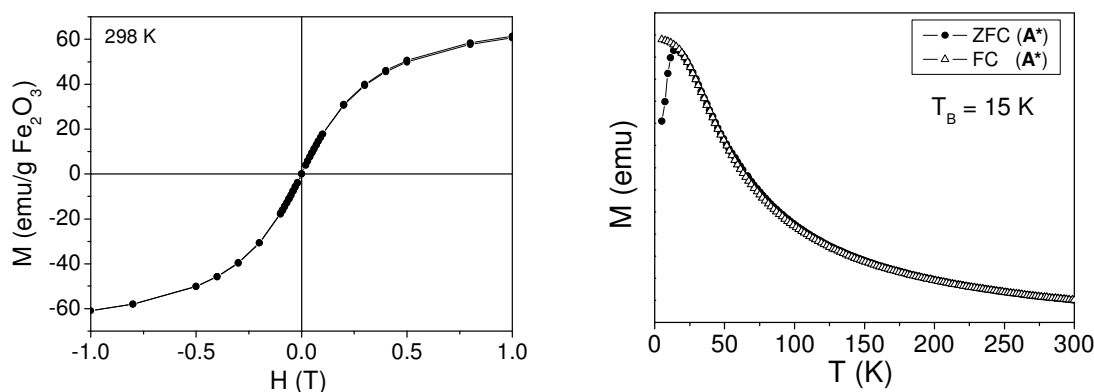

Figure 2.20. Magnetization curve vs. field (left graph) and ZFC-FC curves (full circles-triangles) at 100 Oe (right graph) of a sample type A*.

2.2.4. Superlattice assemblies

Although the ordering of the nanoparticles in superlattice assemblies was not the purpose of this work, it was observed by TEM that, resulting from their narrow size distribution, the nanoparticles tended to form ordered spontaneous arrangements. The protocol to prepare a sample for TEM analysis is very simple: a drop of a highly diluted colloidal dispersion is deposited onto a TEM grid allowing the solvent to evaporate (see annex 7.3.3 for more details). The interparticle interactions change since there is no solvent anymore. The repulsive forces between particles due to osmotic effects disappear and the particles attract each other creating a spontaneous ordering between them. The resulting order differs with the solvent, the evaporation time and the stabilizing agent.

Electrostatic stabilizers

The particles electrostatically stabilized in water arranged in chains after the solvent evaporation (see **Figure 2.21**), probably due to dipolar interactions (either magnetic o electrostatic). On the contrary, if the particles were first precipitated by centrifugation solution and then deposited onto the TEM grid, they were agglomerated in big clusters, with no chain formation.
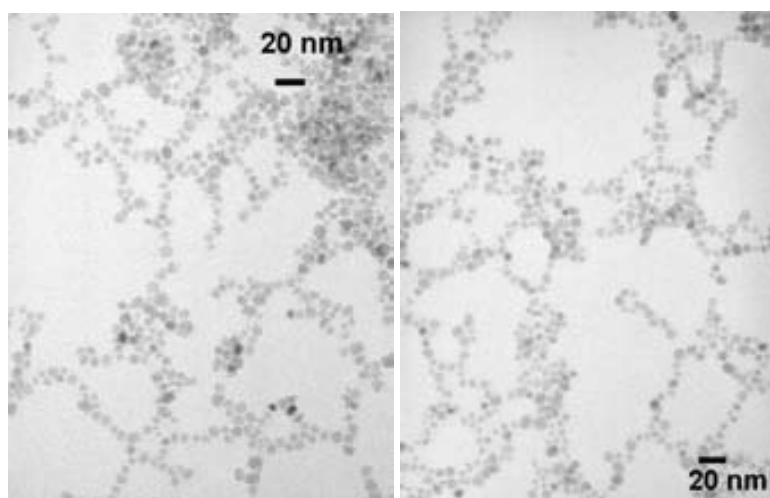

Figure 2.21. TEM image of electrostatically stabilized particles arranged in chains.

Steric stabilizer

When the particles were sterically stabilized in hexane they also got closer as the solvent evaporated due to the Van der Waals forces. The steric barrier fixes a minimum interparticle distance. The resulting arrangement is a two dimensional hexagonal close packing (hcp) which can extend up to three or four layers. The main parameter to obtain long-range ordering is the particle size distribution: the narrower distribution, the better

ordering.[17] **Figure 2.22** shows a micrograph where the hcp arrangement is observed in one, two and up to three layers.
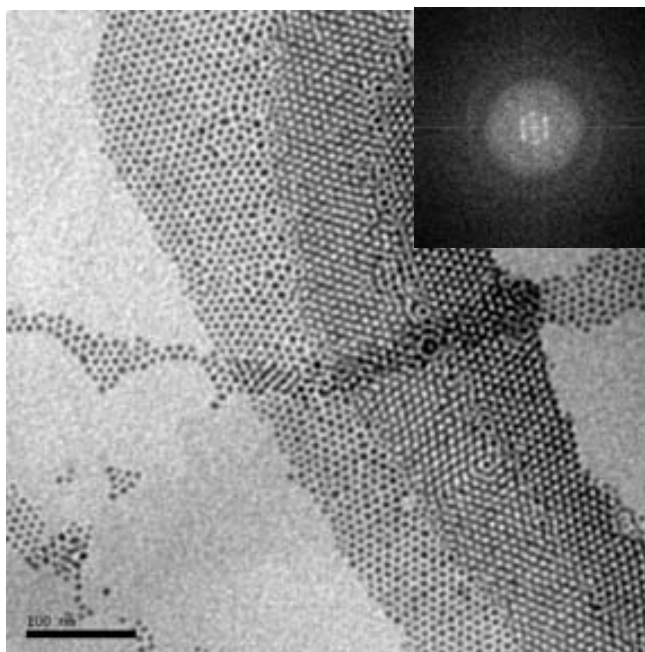
Figure 2.22. TEM image of iron oxide nanoparticles stabilized with oleic acid and ordered in a hexagonal close packing. The inset corresponds to the fast Fourier transform (FFT) showing the hcp ordering. The order can be two- and three-dimensional (bar scale = 100 nm).

The ordering of the oleic acid-coated particles was studied by small angle x-ray scattering (SAXS). The samples were deposited onto silicon substrates and heat treated at different temperatures. Only results of one representative sample are presented. Details on the calcination protocol and the data fitting are explained in annex 7.3.6.

Sample Fe.06.8 (described in section 2.2.1_SAXS) was analyzed in hexane colloidal dispersion and as a dry powder (after deposition of the colloidal dispersion onto a silicon substrate at room temperature, see **Figure 2.23**). The scattering curve of the dispersed particles (full circles) was successfully fitted to a model of non-interacting particles with a mean size 10.5 ± 1.6 nm. But the scattering curve of the dried particles (empty triangles) showed a new peak at low values of the scattering vector (≈ 0.8 nm^{-1}) which indicates that there is a new interparticle interaction at a constant distance of 12 nm. The first minimum (0.13 nm^{-1}) is related to the particle size and did not shift after the drying of the particles. The calculated mean size was 10.8 ± 1.7 nm, which matched the mean size of the colloidal dispersion. Then, the short-range ordering of the nanoparticles observed by TEM was confirmed by SAXS.
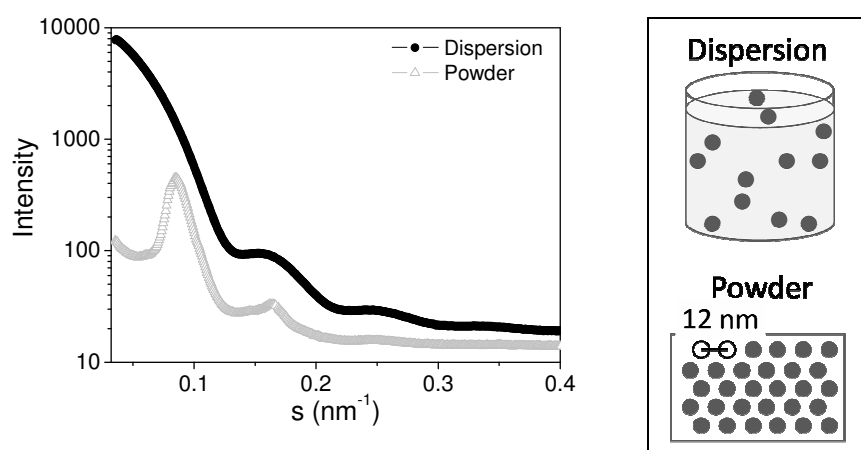
Figure 2.23. Left panel: SAXS curves for sample Fe.06.8 dispersed in hexane (full grey circles) and for the same dried sample deposited onto a silicon substrate (empty black triangles). Right panel: schematized cartoon.

Figure 2.24 shows the scattering curves of the sample Fe.06.8 deposited onto a silicon substrate and calcined at different temperatures up to 450ºC. As the calcination temperature increased up to 350ºC, the first maximum shifted to higher values of scattering vector (see also **Figure 2.25**), indicating that the interparticle distance decreased. Then, from 400ºC on, the first maximum and the other peaks almost disappeared, what is attributed to the loss of order between particles. This behaviour matches the desorption and/or calcination of the oleic acid since its boiling point is 360ºC. Over 400ºC there was no surfactant anymore, the particles came into contact and began to sinter. Thus, size monodispersity and long-range ordering was lost.
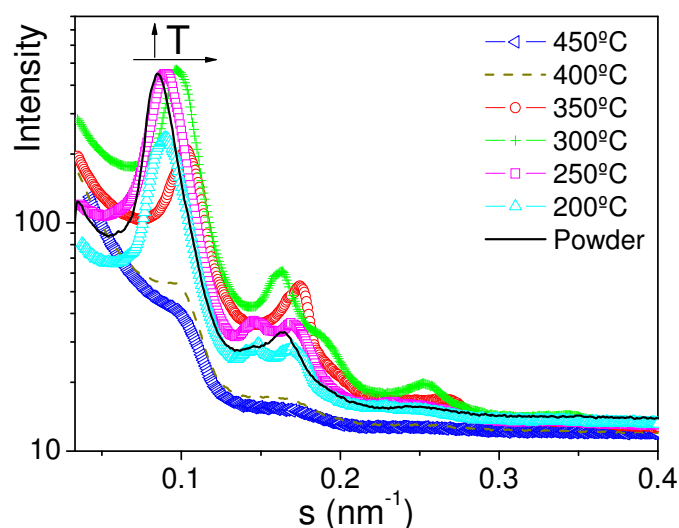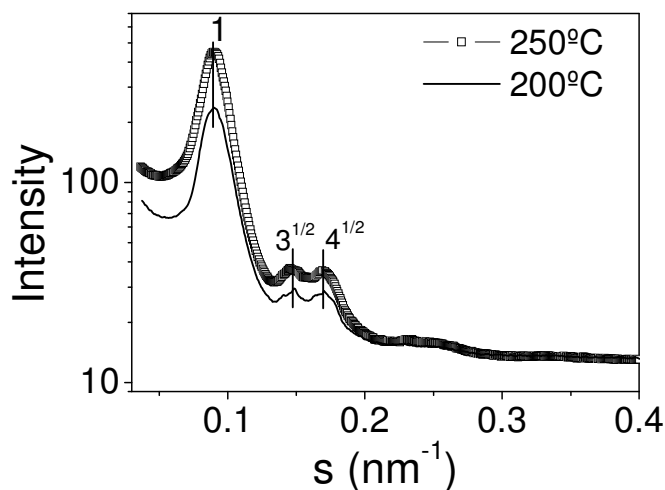

Figure 2.24. SAXS curves for sample Fe.06.8 deposited onto a silicon substrate (continuous line) and calcined at different temperatures.
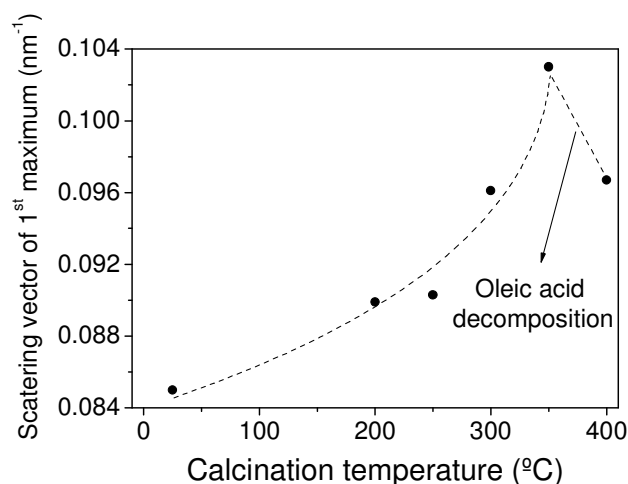
Figure 2.25. Scattering vector values of the first maximum in **Figure 2.24** vs. calcination temperature.

If we focus our attention on samples calcined at 200 and 250ºC (see **Figure 2.26**) a new peak at 0.15 nm⁻¹ is clearly observed, compared to the powder curve. This peak implies a new ordering between the particles. The ratio existing between the scattering vector of the three main peaks, 0.089:0.147:0.170 nm⁻¹ = $1:\sqrt{3}:\sqrt{4}$, is characteristic of hexagonal close packing arrangements. Then, a gentle calcination up to 250ºC of the maghemite nanoparticles coated with oleic acid and deposited onto a silicon substrate favours a better ordering between the particles.

Figure 2.26. SAXS curves of sample Fe.06.8 calcined at 200ºC and 250ºC, respectively. The position of the main peaks fulfils the ratio $1:\sqrt{3}:\sqrt{4}$, which indicates a hcp ordering of the particles.

2.3.   Conclusions of Chapter 2

Iron oxide nanoparticles have been successfully synthesized by thermal decomposition of iron pentacarbonyl in octyl ether in the presence of oleic acid. The particles can be stabilized in aqueous or organic solvents by selecting the appropriate stabilizer. The synthetic parameters temperature, reaction time and amount of oleic acid influence the particle size and shape and size distribution. Several techniques with different physical basis have been used to measure the particle size. The high degree of agreement on the mean particle size of our materials obtained with the different techniques is an evidence of the narrow size distribution. Crystalline structure has also been studied by different techniques: the particles are monocrystalline and are composed of one single crystalline phase, which can be indexed to maghemite and magnetite. The lack of other phases, such as hematite, was confirmed. Nevertheless, considering the chosen synthetic route (starting from $Fe(CO)_5$), we assume the particles to be maghemite since it is a more stable phase than magnetite at nanometric dimensions under ambient conditions and since we have not detected any change of properties with time. Further indications of that are explained in Chapter 4.

The magnetic properties of iron oxide nanoparticles are suitable to target biomedical applications: they are superparamagnetic at room temperature and they bear high magnetization values. The saturation magnetization increases with the particle size, except for one group of samples, which surprisingly have values near the bulk saturation magnetization even though they are only 5 nm in diameter. We ascribe this effect to a better crystallinity of the particles due to a faster nucleation step during the synthetic process.

The iron oxide nanoparticles can spontaneously order after evaporation of the dispersion solvents. When they are electrostatically stabilized in water, they self assemble in chains. On the contrary, the oleic acid-coated particles form hexagonal close packed arrangements in two and even three layers. The higher the monodispersity of the system, the larger the ordering range. A gentle calcination up to 250ºC of the maghemite nanoparticles coated with oleic acid and deposited onto a silicon substrate favours a better ordering between the particles.

2.4.   Bibliography and notes of Chapter 2

1. Taboada, E. Estudio de sistemas coloidales de nanopartículas de maghemita: síntesis, caracterización y aplicaciones biomédicas. *Master Thesis (Trabajo de investigación del plan de doctorado en Ciencia de Materiales)*. **2006**. Institut de Ciència de Materials de Barcelona (ICMAB-CSIC) and Universitat Autònoma de Barcelona (UAB).

2. U. Schwertmann, R. M. Cornell. *Iron oxides in the laboratory: preparation and characterization.* VCH, Weinheim **2000**, page 28.

3. Ayyub, P.; Multani, M.; Barma, M.; Palkar, V. R.; Vijayaraghavan, R. Size-induced structural phase transitions and hyperfine properties of microcrystalline Fe_2O_3. *J. Phys. C: Solid State Phys*.**1998**, 21, 2229-45.

4. Gich, G. Nanopartícules magnètiques en matrius de sílice, *PhD Thesis*, **2006**, Institut de Ciència de Materials de Barcelona, ICMAB-CSIC and Universitat Autònoma de Barcelona (UAB).

5. Sun, S. H.; Murray, C. B.; Weller, D.; Folks, L.; Moser, A., Monodisperse FePt nanoparticles and ferromagnetic FePt nanocrystal superlattices. *Science* **2000,** 287, (5460), 1989-1992.

6. Hyeon, T.; Lee, S. S.; Park, J.; Chung, Y.; Bin Na, H., Synthesis of highly crystalline and monodisperse maghemite nanocrystallites without a size-selection process. *Journal of the American Chemical Society* **2001,** 123, (51), 12798-12801.

7. Lamer, V. K.; Dinegar, R. H., Theory, production and mechanism of formation of monodispersed hydrosol. *Journal of the American Chemical Society* **1950,** 72, (11), 4847-4854.

8. Giersig, M.; Hilgendorff, M., Magnetic nanoparticle superstructures. *European Journal of Inorganic Chemistry* **2005**, (18), 3571-3583.

9. Kwon, S. G.; Hyeon, T. Colloidal chemical synthesis and formation kinetics of uniformly sized nanocrystals of metals, oxides and chalcogenides. *Accounts of chemical research* **2008**, 41 (12) 1696-1709.

10. Redl, F.; Black, C.; Papaefthymiou, G.; Sandstrom, R.; Yin, M.; Zeng, H.; Murray, C.; O-Brien, S. Magnetic, electronic and structural characterization of nonstoichiometric iron oxides at the nanoscale. *Journal of the American Chemical Society* **2004** 126, 14583-14599.

11. Ying, M.; Willis, A.; Redl, F.; Turro, N.; O-Brien, S. Influence of capping groups on the synthesis of γ-Fe_2O_3 nanocrystals. *J. Mater. Res.* **2004** 19 1208-1215.

12. Chen, D.-X.; Sanchez, A.; Taboada, E.; Roig, A.; Sun, N. and Gu, H.-C. Size determination of superparamagnetic iron oxide nanoparticles from magnetization curve, *Journal of Applied Physics* **2009**, 105, 083924.

13. Lu, A. H.; Salabas, E. L.; Schuth, F., Magnetic nanoparticles: synthesis, protection, functionalization, and application. *Angewandte Chemie-International Edition* **2007,** 46, (8), 1222-1244.

14. Parker, F. T.; Foster, M. W.; Margulies, D. T.; Berkowitz, A. E., Spin canting, surface magnetization and finite-size effects in gamma-Fe_2O_3 particles. *Physical Review B* **1993,** 47, (13), 7885-7891.

15. Kaiser, R.; Miskolcz.G, Magnetic properties of stable dispersions of subdomain magnetite particles. *Journal of Applied Physics* **1970,** 41, (3), 1064.

16. Zhang, L.; Papaefthymiou, G. C.; Ying, J. Y. Size quantization and interfacial effects on a novel γ-Fe_2O_3/SiO_2 magnetic nanocomposite via sol-gel matrix-mediated synthesis *J Appl Phys* **1997** 81(10) 6892-6900.

17. Murray, C. B.; Sun, S. H.; Doyle, H.; Betley, T., Monodisperse 3d transition-metal (Co, Ni, Fe) nanoparticles and their assembly into nanoparticle superlattices. *Mrs Bulletin* **2001**, 26, (12), 985-991.

3. SILICA PARTICLES

The synthesis of microporous silica particles combining sol-gel chemistry and supercritical fluids is described in this chapter. Among other advantages, this approach reduces the number of steps compared to other sol-gel processing approaches.

This production route finds the inspiration on the common methodology to obtain aerogels. I profit from the experience of Prof. E. Molins' group producing these materials as well as on the preliminary work on silica microparticles undertaken by Magda Moner during her PhD Thesis.[1,2] Aerogels are obtained by supercritically evacuation of the solvent contained in the pores of a gel, preserving at the same time the fragile solid structure of that gel. Bulk silica aerogels are interesting materials with unique properties: they are extremely porous (between 80 and 99% of their volume is air), reaching densities close to air (0.003–0.5 g/ml), they present very high surface areas (300–1000 m²/g), very low sound speed (80-800 m/s) and

constitute the best thermal insulators known (thermal conductivity in air at 27 °C is 17–21 mW/m·K). Xerogels, on the contrary, do not present such high porous structure and thus, their properties are not so singular. The group has long experience on the synthesis and characterization of pure aerogels and xerogels as well as on their functionalization to improve their properties or to incorporate new ones. Some examples are the synthesis of magnetic aerogels,[2-5] catalyst substrates,[6-8] thin films,[9] superhydrophobic silica aerogels,[10] solid state lasers,[11,12] matrices to synthesize magnetic nanoparticles,[13] characterization of mechanical[14,15] or magneto-optical properties.[16] I participated in some of these projects at the early stages of this thesis, mostly in the synthesis of magnetic nanocomposite aerogels and xerogels (see annex 7.2).

Besides a drying alternative, supercritical fluids are more and more used as a media to produce new particulate materials.[17-19] Material synthesis in conventional solvents is often a multi-step process that needs long processing times. In addition, liquid media transmits temperature or composition changes slowly which may result in a poor control over the particle size. In the case of silica particles, the supercritical fluid will serve as the reaction media as well as a zero tension evacuation fluid.
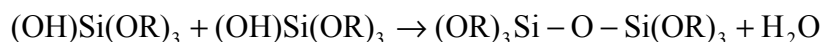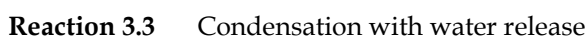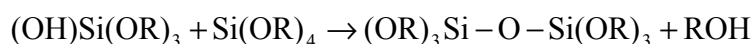
A substance reaches the supercritical phase when the temperature and pressure overcomes the critical point (see **Figure 3.1**). At those conditions, the kinetic energy of the molecules is always higher than the intermolecular attractive forces, in such a way that the fluid becomes incondensable. The properties of supercritical fluids are then in between those of liquids and gases: liquid-like density, thermal conductivity and solubility, and gas-like diffusivity, compressibility and lack of surface tension.
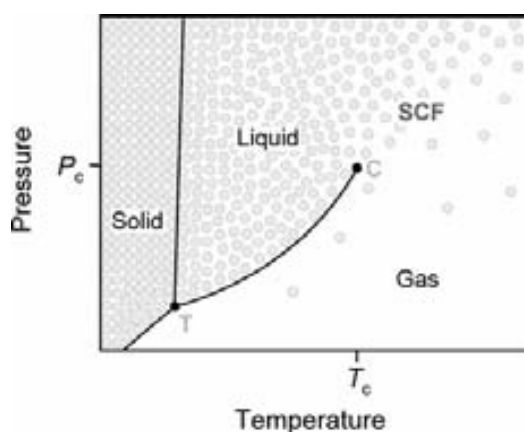
Figure 3.1. General phase diagram. The circles represent molecules whose packaging depends on their state.

3.1. Sol-gel chemistry of silica

The main chemical pathway to synthesize silica materials is by sol-gel chemistry. This process enables obtaining solid products by gelation rather than by crystallization or precipitation. The sol-gel process consists of the hydrolysis and condensation of a silicon precursor, mainly a silicon alkoxyde (see **Reaction 3.1** to **Reaction 3.3**).

Reaction 3.1   Hydrolysis $Si(OR)_4 + H_2O \rightarrow (OH)Si(OR)_3 + ROH$

Reaction 3.2   Condensation with alcohol release

$$(OH)Si(OR)_3 + Si(OR)_4 \rightarrow (OR)_3Si - O - Si(OR)_3 + ROH$$

Reaction 3.3   Condensation with water release

$$(OH)Si(OR)_3 + (OH)Si(OR)_3 \rightarrow (OR)_3Si - O - Si(OR)_3 + H_2O$$
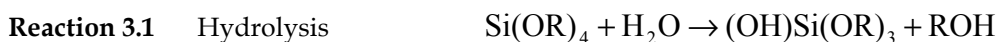
Polycondensation of products in **Reaction 3.2** and **Reaction 3.3** creates new siloxane bonds (Si-O-Si) forming colloidal particles. Although the sol-gel chemistry of silicon alkoxydes as described above seems to be straightforward, the whole picture is much more complex since hydrolysis and condensation reactions compete with each other at any time.

The most commonly used alkoxydes are tetramethoxy silane (TMOS; $Si(OCH_3)_4$) and tetraethoxysilane (TEOS; $Si(OCH_2CH_3)_4$), which are colourless liquids and insoluble in water. Therefore, a common solvent is often used to dissolve both reactants. Methanol and ethanol are usually the selected solvents for TMOS and TEOS, respectively. It is advisable to combine the silicon precursor and the solvent with the same organic radical (R = methyl or ethyl group) in order to avoid transesterification reactions (see **Reaction 3.4**) which may create inhomogeneities in the gel due to the different kinetics of each organic radical.

Reaction 3.4   Example of transesterification reaction

$$(OH)Si(OEt)_3 + MeOH \rightarrow (OH)Si(OMe)(OEt)_2 + EtOH$$
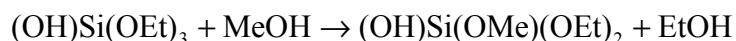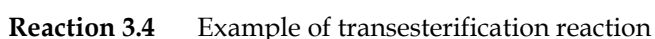
Other solvents with no alkoxy groups and therefore unable to perform transesterification reactions are also appropriate, provided that they dissolve the reactants; for example, acetone. Acid or basic catalysts can be used to accelerate the reaction and modify the mechanism, inducing changes in the structure and properties of the resulting materials. As shown in **Figure 3.2** and **Figure 3.3** acidic pH favours the hydrolysis reaction against condensation, in such a way that many small silica nuclei are formed which condense in a polymeric configuration. The final gel is then formed of small silica particles with small pores. On the contrary, basic conditions favour the condensation reaction; few nuclei are formed which

grow to big particles through the condensation reaction. The final gel is built up of big particles with big pores.
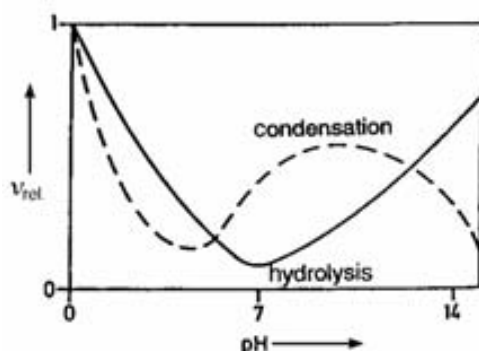
Figure 3.2. Relative speed of condensation and hydrolysis reactions in the sol-gel process vs. pH.[20]
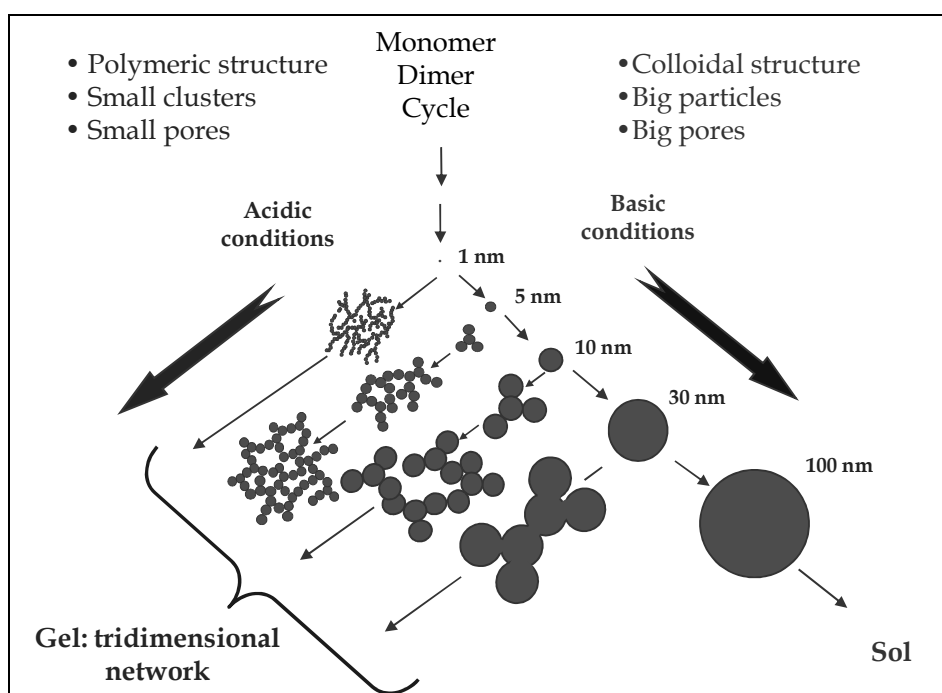
Figure 3.3. Scheme on silica nucleation and growth depending on pH conditions.[20]

Several other parameters also influence the hydrolysis and condensation reactions, and consequently, the properties of the final material. Among them are the type of precursor, the precursor to water ratio, the type of catalyst, the type of solvent, the temperature, the pH and the relative and absolute concentration of the components in the precursor mixtures. **Figure 3.4** summarises the variety of silica-based materials that can be obtained by sol-gel chemistry combined with different drying procedures.
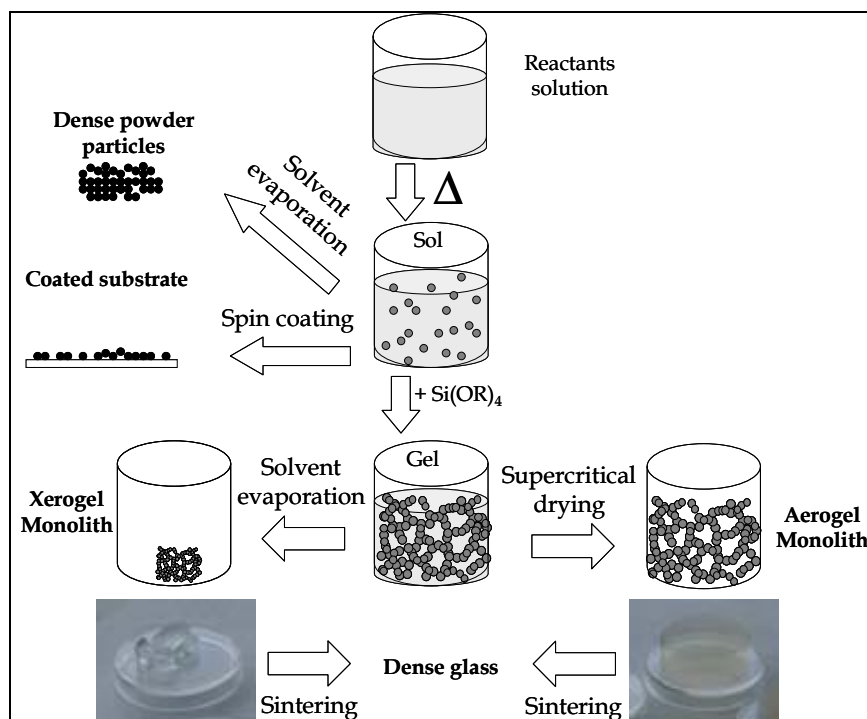
Figure 3.4. Scheme of the sol-gel processing and drying of the silica colloids.

The colloidal dispersion of the first nuclei is called sol. If there is enough amount of silicon precursor these particles will grow and will go on reacting until forming a silica network that will extend all over the container volume, forming a gel. The gel framework is a metastable inorganic polymer with an open pore structure containing the solvent. The gel is named after the filler solvent: alkogel, hydrogel, liogel, etc. If the gel is dried, the properties of the resulting material will drastically depend on the drying procedure. When the solvent is simply evaporated (pathway *a* in **Figure 3.5**), the capillary pressure generated inside the pores induces the collapse of the gel. The resulting material, called xerogel ("xero" means dry), is a low porosity solid that often looses the monolithcity. On the contrary, if the solvent is extracted under supercritical conditions (pathway *b* in **Figure 3.5**), the capillary forces in the pores will be highly reduced and the solid network will not collapse. This process is known as supercritical drying and the resulting product is then a silica aerogel. It is a very porous and light monolith where the liquid filling the pores has been substituted by air.[21] The different degree of porosity between xerogels and aerogels will have a pronounce effect on their different physical properties (optical, thermal, acoustic, etc.).
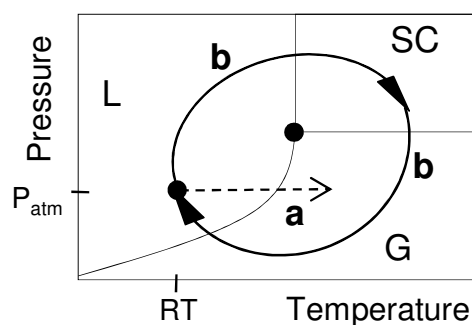
Figure 3.5. Scheme of phase change pathway for gel drying by evaporation (a) and by supercritical drying (b).

The key point for a correct supercritical drying lies in guaranteeing the SC → G phase change avoiding the L → G phase change. The capillary tension created by the liquid during the L → G process inside the silica pores depends inversely on the pore diameter, as defined in **Equation 3.1**. Since the pores in silica gels are nanometric (2-200 nm), the capillary pressure generated in the pore walls (p_c) is very high and can break the silica network destroying the solid structure.

Equation 3.1

$$p_c = \frac{2 \cdot \gamma \cdot \cos \theta}{r}$$

where γ is the surface tension (force per unit length), θ is the wetting angle and *r* is the pore radius.

In this thesis we have investigated the use of supercritical fluids as reaction and as evacuation media to synthesize porous silica particles in one step (see **Figure 3.6**), with the final aim to later apply the same methodology to coat the iron oxide nanoparticles described in Chapter 2. A short description comparing the main synthetic methods to produce silica particles or silica coatings (Stöber method, reverse micro-emulsion and aerosol pyrolysis) was included in Chapter 1.
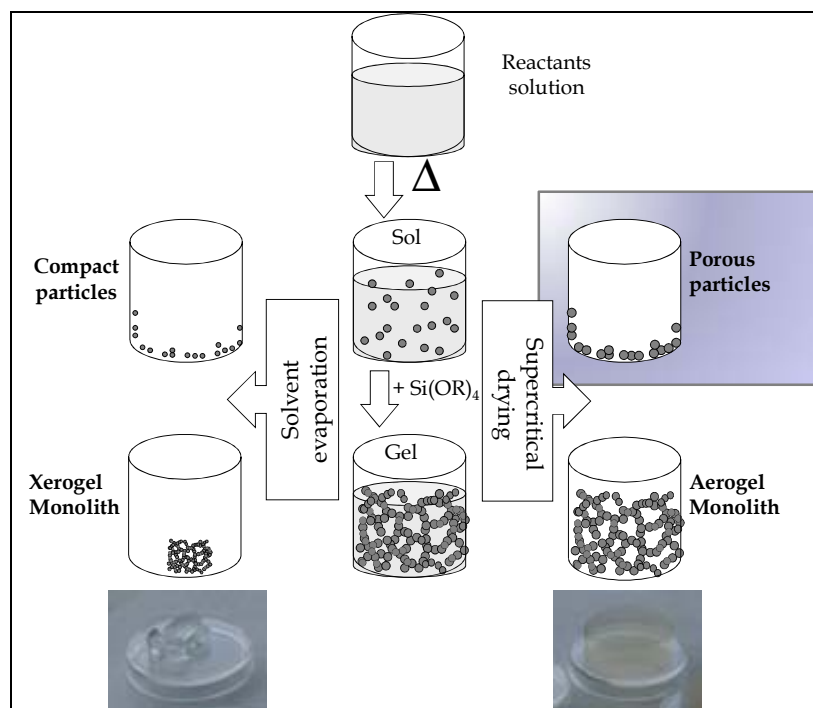
Figure 3.6. Scheme of the silica gel synthesis possibilities together with supercritical fluids, including the porous silica particles.

3.2.   Materials and methods

From Magda Moner's PhD Thesis[1] we selected the parameters which resulted in the smallest and most monodisperse particles ($\approx$ 1 µm): high temperature drying (acetone supercritical conditions), substoichiometric water content ($2 \cdot [SiOR_4]$), the longest depressurization time (90 min) and preparation of one single reactant solution as the starting conditions. New modifications were implemented to decrease the mean particle size from micron to approximately hundred nanometres. **Table 3.2** lists the experimental parameters for representative syntheses of silica particles. A common synthetic procedure reads as follows:

a) Preparation of the reactant solution:

- Reactants:

  ▪ Silicon   precursor: TMOS   ($Si(OMe)_4$)   or   TEOS   ($Si(OEt)_4$).
    $[Si(OR)_4]$ = 0.35-0.05 M (R = OMe or OEt).

  ▪ Water: double   the   molar   concentration   of   silicon   precursor.
    $h = [H_2O]/[Si(OR)_4] = 2$.

  ▪ pH of solutions without catalysts = 5-6.

  ▪ Catalyst (in few experiments): HCl or oleic acid.

▪ Solvent: acetone (for TMOS and TEOS) or ethanol (for TEOS). Volume = 100–500 ml.

▪ It is to be highlighted that no porogenic species were used.

- Preparation protocol: the reactants were added drop-wise to the total volume of solvent while magnetically stirring: first, the silicon precursor, then the water and last, when necessary, the catalyst. The initial solution is defined as a sol. It was prepared just before the supercritical reaction and transferred to a Pyrex vessel which was eventually covered with glass wool. No particles were detected by dynamic light scattering in the sol.

b) The Pyrex vessel was placed inside a 2 litres autoclave (see **Figure 3.7**). No stirring was applied. For details on the supercritical facilities see annex 7.3.8.
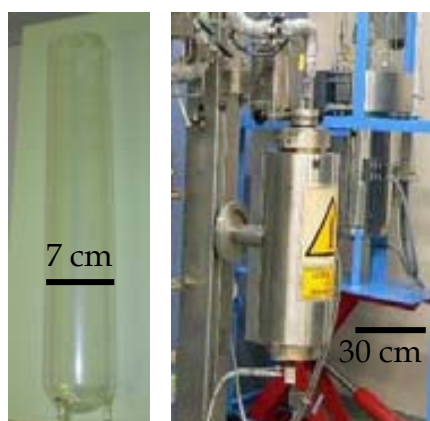
Figure 3.7. Pyrex vessel (left image) and autoclave used during this thesis (right image).

c) The common experimental temperature and pressure pathways are illustrated in **Figure 3.8** and **Figure 3.9** and described below:

- Step i: preparation of the initial sol at room temperature and atmospheric pressure.

- Step ii: pressure was increased up to 50 bar by injecting compressed carbon dioxide (CO_2). The mass of injected CO_2 cannot be accurately controlled with the available pilot plant, but the system pressure was known at any moment. The amount of CO_2 inside the reactor could be approximated using the ideal gas law:

Equation 3.2 $$P \cdot V = n \cdot R \cdot T$$

where P corresponds to pressure (atm), V to volume (l), n to mol number, R is the ideal gas constant (0.082 atm·l/mol·K) and T is temperature (K).

For the calculations out-of-equilibrium state of null solubility of CO_2 in acetone was considered (the gas was not injected directly inside the liquid

solvent and we did not wait till the thermodynamic equilibrium was reached). The calculated CO_2 molar fractions for representative experiments are listed in **Table 3.1**.
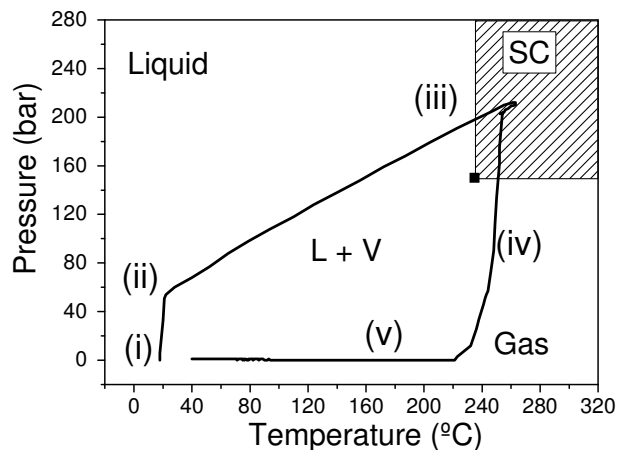
Figure 3.8. Pressure vs. temperature evolution of a representative experiment. The stripped area above 235°C and 150 bar corresponds to the supercritical state for CO_2/acetone and CO_2/ethanol mixtures.
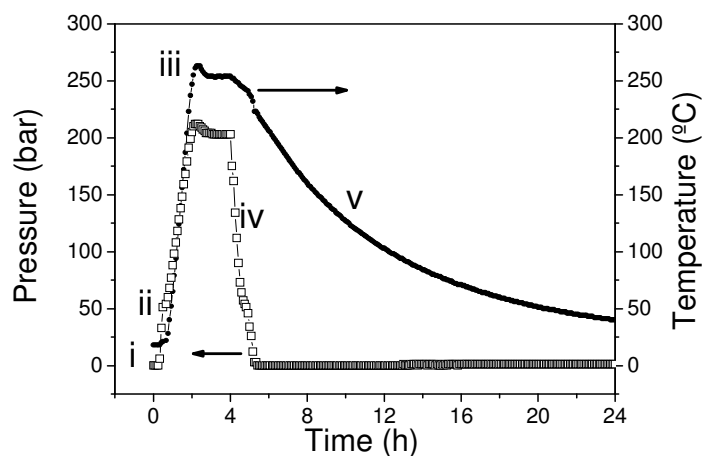
Figure 3.9. Time evolution of pressure and temperature of a representative experiment.

Table 3.1. Calculated molar fraction of CO_2 just after the first pressurization up to 50 bar. The out-of-equilibrium situation of no solubility of CO_2 in the liquid solvent was considered.

Solution volume (l)	Solvent	Solvent amount (mol)	P (atm)	T (K)	CO_2 amount (mol)	CO_2 molar fraction (x)
0.1	Acetone	1.36	50	298	3.70	**0.74**
0.5	Acetone	6.80	50	298	2.92	**0.31**
0.1	Ethanol	1.72	50	298	3.70	**0.69**
0.5	Ethanol	8.58	50	298	2.92	**0.26**

These calculations are important since the critical pressure of CO_2/acetone and CO_2/ethanol binary mixtures cannot be interpolated from the values of the pure substances, as shown in **Figure 3.10** and **Figure 3.11**. On the contrary, the critical temperature of the binary mixtures lies always in between the values of the pure substances. To ensure a correct supercritical solvent evacuation (pathway *b* in **Figure 3.5**) the pressure must be always increased over 120 bar (for carbon dioxide/acetone mixtures) and 150 bar (for carbon dioxide/ethanol mixtures) and the temperature should always be over 250°C.
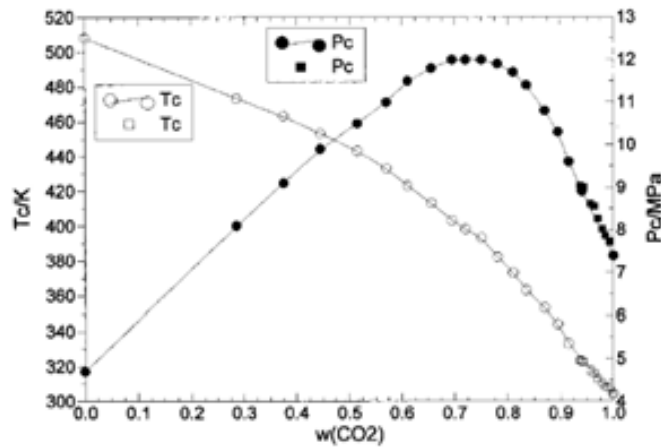
Figure 3.10. Critical temperature and pressure for the binary mixtures carbon dioxide + acetone vs. weight fraction of carbon dioxide (pressure is indicated in megapascal; 1 MPa = 10 bar = 10 atm).[22]
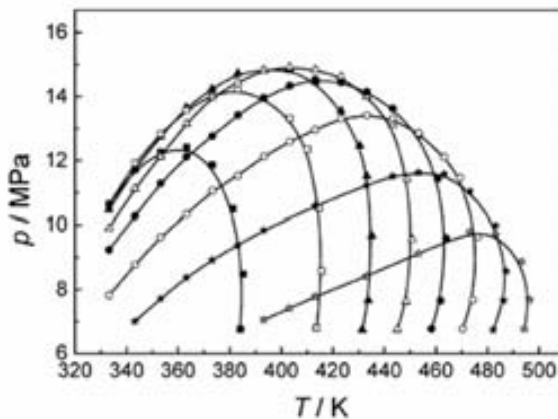
Figure 3.11. Phase boundaries of carbon dioxide and ethanol. Each curve corresponds to a different molar fraction of ethanol (■=0.1, □=0.2, ▲=0.3, (■=0.1, □=0.2, ▲=0.3, □=0.4, ●=0.5, ○=0.6, □=0.7, □=0.8). Approximately, the maximum of each curve corresponds to the critical point.[23]

- Step iii: temperature was increased 30°C every 10 minutes up to 250°C with a consequent increase of pressure up to 200–250 bar. At this point, the system reached the supercritical state. The pressure evolution during the heating was followed carefully. If the pressure did not increase enough, extra compressed

CO$_2$ was injected to ensure a minimum final pressure over 120 or 150 bar. Supercritical conditions were maintained for a given time (called residence time) from 5 minutes to 2 hours.

- Step iv: slow depressurization of the system ($\approx$ 0.5 kg CO$_2$/h). The supercritical solvents together with the unreacted precursors were vented out into another reactor. It is indispensable to maintain the high temperature at this stage to avoid the liquation of the solvents that could cause the collapse of the pore structure. The supercritical solvent must directly change to the gaseous phase. An aliquot of the extracted solvents was kept for analysis. Once at ambient pressure it is advisable to circulate some clean CO$_2$ for 30 minutes to drag out any solvent left.

- Step v: the system was allowed to cool down to room temperature.

Each experiment took 8 hours plus the overnight reactor cooling time, as shown in **Figure 3.9**. Materials are identified as *Si_year_number of experiment*.

In view of the use of these materials for biomedical applications, methanol was avoided because of its higher toxicity (although it is the most appropriate alcohol to dissolve TMOS) and acetone was used instead. Ethanol was not used in combination with TMOS to avoid transesterification reactions (**Reaction 3.4**). The reaction vessel was of Pyrex glass, which stands high temperature and pressure. The vessel was replaced every 3-4 experiments because with time, the silicon precursor also reacted with it favouring the deposition of new silica onto its surface.

Table 3.2. Experimental parameters for selected experiments in supercritical media. *Extra information: Si_08_14: oleic acid 6.3 mM as catalyst; Si_08_15: HCl as catalyst (0.90 ml HCl 35 wt.% instead of water).

| Synthesis ID	Silicon precursor	[Si(OR)$_4$] (M)	Si(OR)$_4$ volume (ml)	Solvent	Solvent volume (ml)	Water volume (ml)	Residence time (min)
Si_07_1	TMOS	0.35	5	Acetone	100	1.23	120
Si_07_2	TMOS	0.35	5	Acetone	100	1.23	120
Si_07_9	TMOS	0.15	2.23	Acetone	100	0.54	120
Si_07_11	TMOS	0.15	2.23	Acetone	100	0.54	120
Si_07_12	TMOS	0.15	2.23	Acetone	100	0.54	5
Si_07_13	TMOS	0.15	11.16	Acetone	500	2.7	120
Si_07_14	TMOS	0.15	4.46	Acetone	200	1.08	30
Si_07_22	TMOS	0.05	1.49	Acetone	200	0.36	15
Si_08_4	TMOS	0.05	3.72	Acetone	500	0.90	120
Si_08_5	TMOS	0.15	11.14	Acetone	500	2.70	120
Si_08_14*	TMOS	0.05	3.72	Acetone	500	0.90	120
Si_08_15*	TMOS	0.05	3.72	Acetone	500	-	120
Si_07_3	TEOS	0.35	7.5	Ethanol	100	1.23	120
Si_07_4	TEOS	0.35	7.5	Ethanol	100	1.23	120
Si_07_5	TEOS	0.05	1.1	Ethanol	100	0.18	120

Synthesis ID	Silicon precursor	$[Si(OR)_4]$ (M)	$Si(OR)_4$ volume (ml)	Solvent	Solvent volume (ml)	Water volume (ml)	Residence time (min)
Si_07_6	TEOS	0.35	7.5	Ethanol	100	1.23	60
Si_07_7	TEOS	0.35	7.5	Ethanol	100	1.23	5
Si_07_8	TEOS	0.15	3.35	Ethanol	100	0.54	120
Si_07_10*	TEOS	0.35	7.5	Ethanol	100	1.23	120
Si_08_16	TEOS	0.15	16.73	Acetone	500	2.7	120

3.3. Results and discussion

The resulting material was a white, very light and dry powder. It was found dispersed all over the autoclave, inside and outside the Pyrex vessel (independently of the presence of glass wool stopper; see **Figure 3.12**).[24] XRD analysis showed only one broad hump around 22º 2θ, typical of amorphous silica.

The results on product mass, yield, particle size, shape and degree of necking are listed in **Table 3.3**. Necking is defined as the growing of silica bridges between two or more particles. It lowers the monodispersity of the system (see **Figure 3.18** for an example).
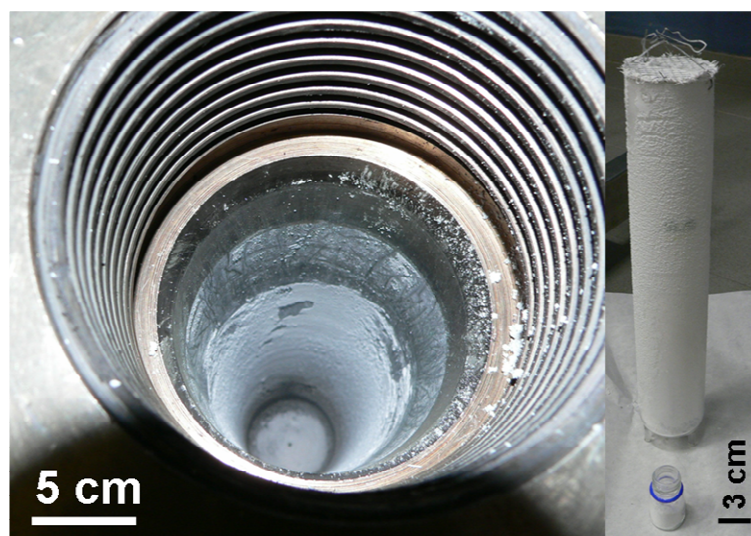
Figure 3.12. Photographs of the supercritical reactor (left image) and the Pyrex vessel (with glass wool cover; right image) just after an experiment.

Table 3.3. Main results on the synthesis of pure silica aerogel particles. *Size values from SEM observations. Size polydispersity (P) is included within parenthesis.

Synthesis ID	Mass (g)	Mass yield (%)	Shape	Size (nm)*	Necking
Si_07_1	0.53	26	Sphere	1720 (17%) 3930 (12%)	No
Si_07_2	0.44	22	Sphere	1700 (27%)	No
Si_07_9	0.06	9	Sphere	2102 (10%)	No

Synthesis ID	Mass (g)	Mass yield (%)	Shape	Size (nm)*	Necking
Si_07_11	0.16	25	Sphere	2250 (50%)	No
Si_07_12	0	0	-	-	-
Si_07_13	2.86	64	Sphere	204 (5%)	No
Si_07_14	0.77	42	Sphere	642 (12%)	No
Si_07_22	0.24	39	Sphere	1000 (50%)	No
Si_08_4	0.96	64	Sphere	2400 (30%)	No
Si_08_5	0.96	22	Sphere	480 (50%)	No
Si_08_14	0.40	27	Sphere	370 (16%)	No
Si_08_15	0.57	38	Sphere	3220 (26%)	No
Si_07_3	0.40	20	Sphere + Sheets	-	Yes
Si_07_4	0.11	5	Sphere + Sheets	-	Yes
Si_07_5	0	0	-	-	-
Si_07_6	0.16	10	Sphere + Sheets	-	Yes
Si_07_7	0.03	2	Sphere + Sheets	-	Yes
Si_07_8	0.01	1	Sheets	-	Yes
Si_07_10	0.28	14	Sphere+ Sheets	7300 (9%)	Yes
Si_08_16	0.50	11	Sphere	660 (22%)	Yes

The mass yield was calculated from the ratio:

Equation 3.3
$$\text{Yield}\% = \frac{\text{grams of product}}{\text{nominal 100\% mass(g)}} = \frac{\text{grams of product}}{\text{mol(TMOS)} \cdot \text{MW(SiO}_2)}$$

where MW(SiO$_2$) is the molecular weight of silica (60.1 g/mol).

Experiments Si_07_9, Si_07_12, Si_07_5, Si_07_7 and Si_07_8 yielded no product or almost none. It is attributed either to the low residence time (5 min; Si_07_12) or to the low amount of silicon precursor (100 ml of volume with concentrations 0.05 and 0.15 M; Si_07_9-5-7-8). The aliquot of the initial solution was checked a few days after the experiments and it was still liquid, no particles were observed neither it had gelified. On the contrary, the extracted solvent had gelified. In these experiments the particles might have nucleated but they might be so extremely small that they were vented out with the solvent during depressurization. Since a high amount of solvent is evaporated after the supercritical extraction, the non-reacted precursor and/or the first silica nuclei were concentrated enough to gelify afterwards.

3.3.1. Size and shape determination

The particle size and shape was analyzed with scanning and transmission electron microscopies (SEM and TEM). It is very important not to disperse the silica particles

in water for TEM observation to avoid further silica hydrolysis and condensation when the material is exposed to the high energy beam of the microscope. For that reason acetone is preferred.

Remarkably, materials produced from TMOS and acetone were composed of spherical particles with no necking between them. Their size ranged from 4 microns to 200 nm in diameter depending mainly on the residence time: longer residence time produced larger particles. Particle size distributions as low as 5% were obtained without the need of any size selection process, as shown in **Figure 3.13** to **Figure 3.15**.
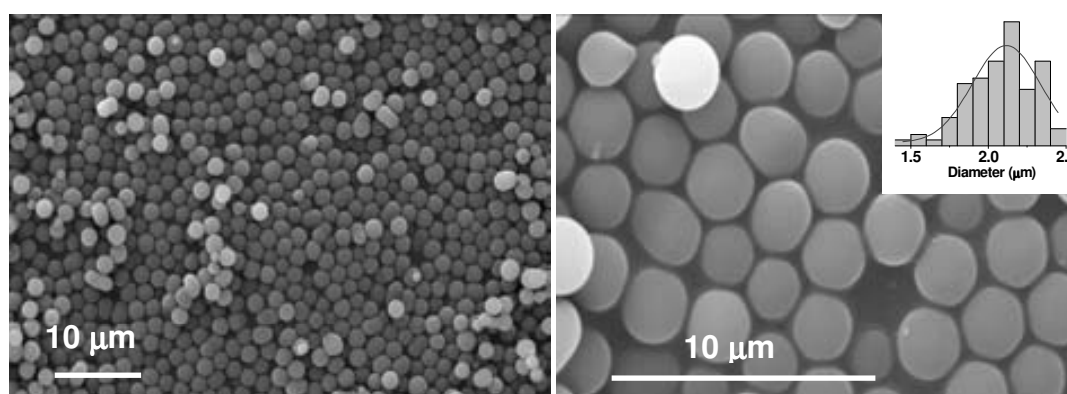
Figure 3.13. SEM images of sample Si_07_9 and particle size histogram fitted to a Gaussian function. Mean diameter = 2.1 microns (P = 10 %).
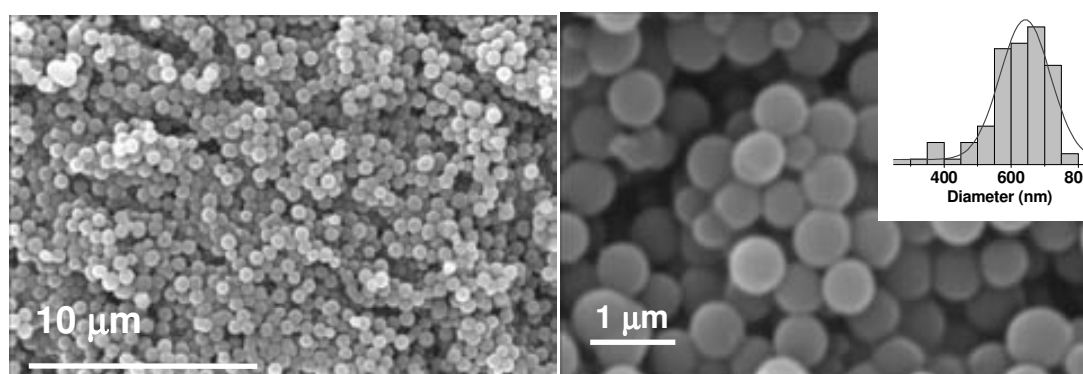
Figure 3.14. SEM images of sample Si_07_14 and particle size histogram fitted to a Gaussian function. Mean diameter = 642 nm (P = 12 %).

On the contrary, all the experiments combining TEOS with ethanol produced mixtures of spherical and irregular particles, which were sometimes agglomerated. Typical products are presented in **Figure 3.16**.
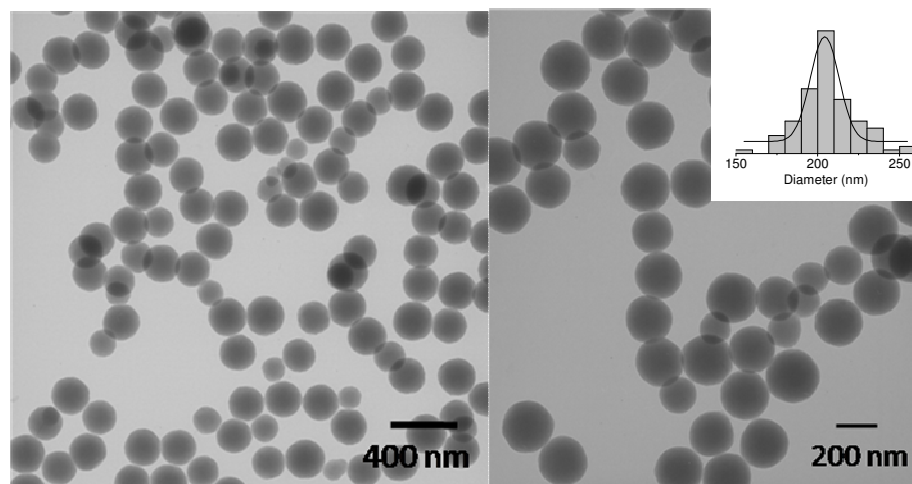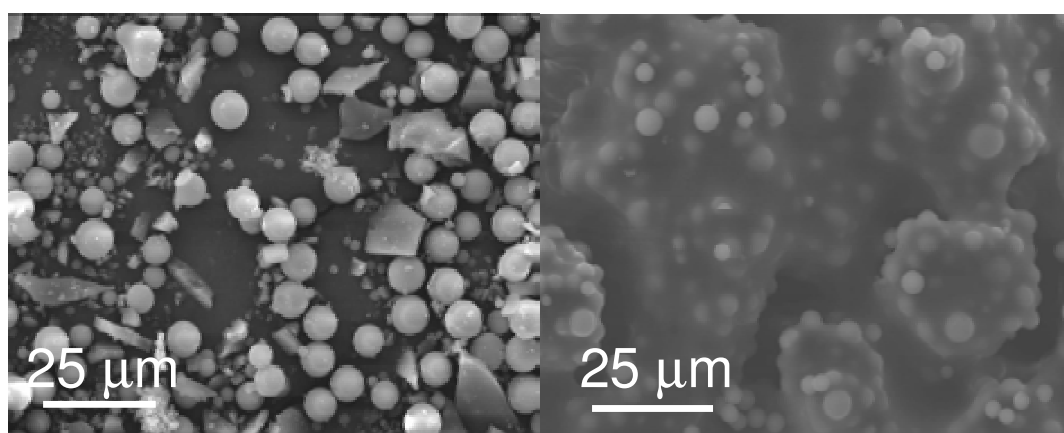
Figure 3.15. TEM images of sample Si_07_13 and particle size histogram fitted to a Gaussian function. Mean diameter = 204 nm (P = 5 %).

Figure 3.16. SEM images of sample Si_07_3 (left image) and sample Si_07_4 (right image).

We believe that the different morphologies obtained when using TMOS or TEOS resulted from the different solubility of acetone and ethanol in CO_2 (see **Figure 3.17**) rather than from the nature of the silicon precursor. The silicon precursor was dissolved more homogeneously in the acetone/CO_2 mixture than in the ethanol/CO_2 one, resulting in more homogeneous final particles.
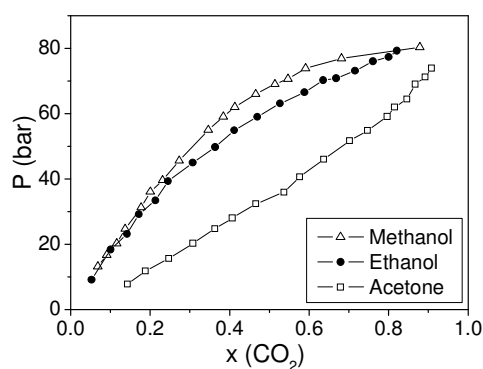
Figure 3.17. Solubility of methanol, ethanol and acetone in CO_2 at 40ºC (pressure vs. molar fraction of CO_2).[26]

Experiment Si_08_16 was performed to test this hypothesis; for that, TEOS was dissolved in acetone. The resulting particles were spherical (see **Figure 3.18**) and no films or aggregates were obtained although some necking between the particles was present.
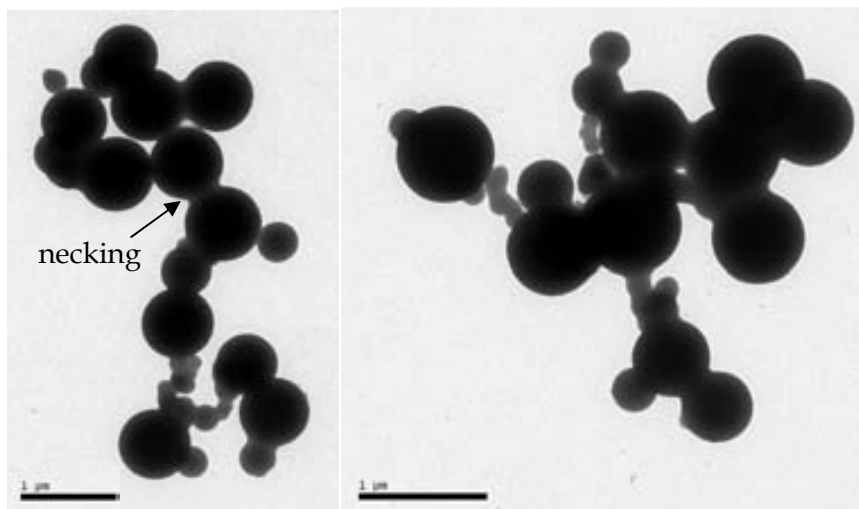
Figure 3.18. TEM images of sample Si_08_16 (TEOS dissolved in acetone): spherical particles with some degree of necking. Bar scales = 1 micron.

Although it was not checked experimentally, the previous results in combination with the data shown in **Figure 3.17** suggest that the particles synthesized with TMOS/methanol might have a higher degree of necking than the ones synthesized in TMOS/acetone. Regarding TMOS/acetone vs. TEOS/acetone, better size monodispersity and homogeneity of the particles obtained with TMOS was attributed to its higher solubility in acetone compared to TEOS.

When using glass wool cover, the particles inside the Pyrex vessel were collected separately from the particles deposited outside. It was observed that the ones inside the vessel were larger with a higher particle size distribution than the particles collected from the autoclave walls. This observation may be related to the silica nucleation and growth times. **Figure 3.19** schematizes a proposed mechanism of the silica processing: after the system is pressurized (step ii) and initially heated (iii_a) the first nuclei are formed, still in liquid phase. With further heating the solvent mixture containing the silica nuclei reaches the supercritical phase and expands all over the autoclave (step iii_b). Then, the particles grow further during the residence time (step iii_c). The circulation of silica particles through the glass wool cover is restricted to the smallest particles and consequently the particle population inside the Pyrex vessel might be enriched in big particles. Another evidence of the particle growing in the supercritical state is the comparison of samples Si_07_9, Si_07_14 and Si_07_12 with residence times 120, 30 and 5 minutes, respectively. The longer the residence time, the larger the particles: the particles nucleate in the liquid phase and then grow further in the supercritical state. No straightforward relationship was

found between the particle size and the silicon precursor concentration. According to the proposed mechanism, the initial sol volume, which expands to the total autoclave volume (2 litres) implying a concentration change, might be also a determining factor for the particle size. Then, for most of the subsequent experiments for the composite particles syntheses (Chapter 4) the initial sol volume was fixed to 500 ml.
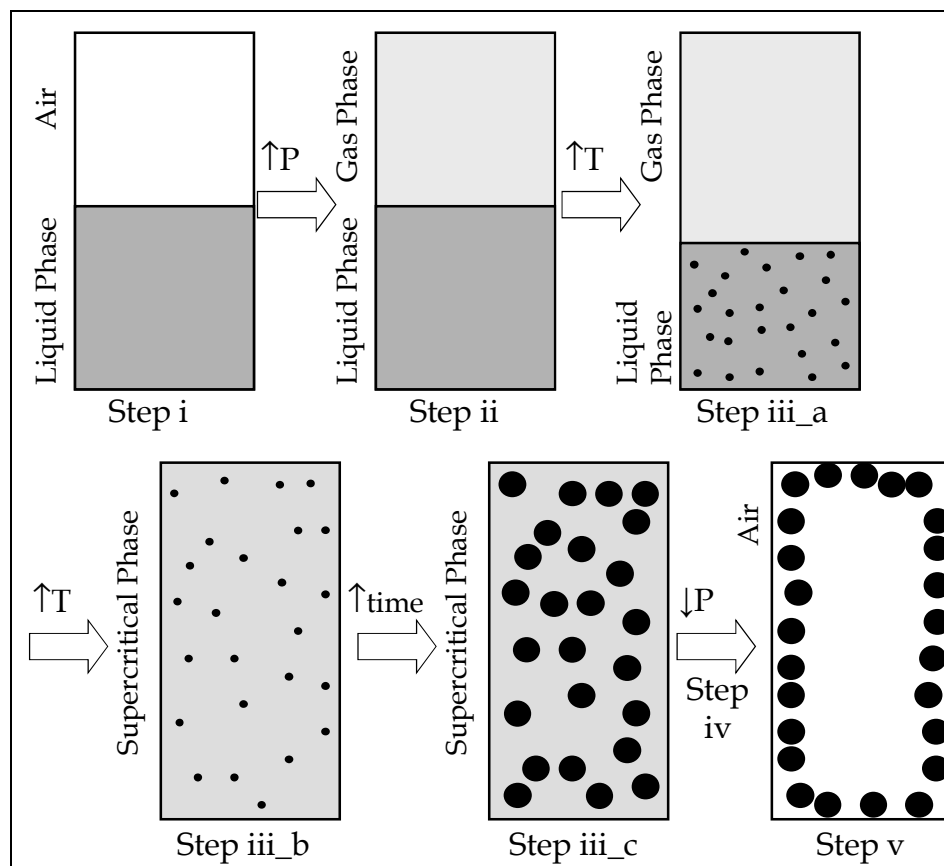
Figure 3.19. Proposed mechanism for the silica particles processing. The steps are defined in the same way as in **Figure 3.8** and **Figure 3.9**. Gas phase is composed of CO_2 + acetone.

3.3.2. Porous structure

The shape of the nitrogen adsorption/desorption isotherms gives general information about the type of porous material. Brunauer assigned numbers to the five first cases (see **Figure 3.20**).[27] Type I isotherms are characteristic of adsorbents having extremely small pores. Types II and IV correspond to either nonporous adsorbents or adsorbents having relatively large pores, and types III and V indicate that the adsorptive molecules have greater affinity for one another than they do for the solid, what is valueless for surface and porosity analysis. The Type VI isotherm, indicative of a nonporous solid with an almost completely uniform surface, is quite rare.[28] According to the IUPAC, the pore size is classified in micro-, meso- and

macropores which are lower than 2 nm, between 2 and 50 nm and higher than 50 nm in diameter, respectively.
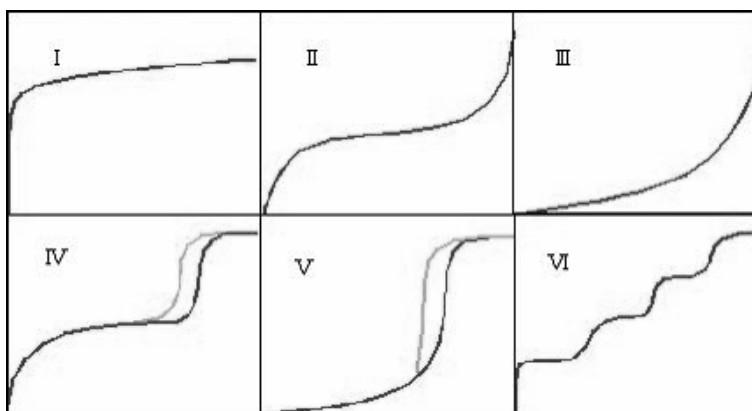
Figure 3.20. The six basic adsorption isotherm types. *X*-axis represents relative pressure (P/P$_0$) and *y*-axis represents the amount of adsorbed nitrogen.[27]

Nitrogen adsorption/desorption isotherms of our silica particles were measured to obtain qualitative information from the curve shape and quantitative data by applying the BET (Brunauer, Emmet and Teller)[29] and BJH (Barret, Joyner and Halenda)[30] models (for the calculation of the surface area and the pore size, respectively). All the analyzed silica particles share the type of isotherms, corresponding to type I which is characteristic of microporous materials. **Figure 3.21** shows two representative isotherms: the steep increase of adsorbed volume at low pressures corresponds to the filling of the micropores and the soft slope for relative pressures between 0.1 and 0.9 is ascribed to the external area of the particles. At P/P$_0$ > 0.99, the steep volume uptake is attributed to the adsorbate (nitrogen in our case) beginning bulk condensation to a liquid inside the meso- and macropores formed by the interparticular voids.[31] Regarding the surface area, the values of our silica particles are on the lower range of those found for bulk silica aerogels (300-200 m^2/g).[21] **Table 3.4** lists these values, which range from 120 to 376 m^2/g. As expected from the isotherm shape, micropore area is predominant with a percentage over 75% in most cases. The value of constant C in the BET model equation is negative for almost all the samples, which is attributed, once more, to the presence of micropores. This constant is related to the heat of adsorption of the first layer and the heat of liquefaction of the adsorptive. The typical range of BET-C values is from about 5 to well over 100. Values much less than 5 imply that the gas-to-gas affinity is competing with the gas-to-solid affinity. C-values much greater than 100 indicate very strong attraction for the surface or preferential adsorption.[28]
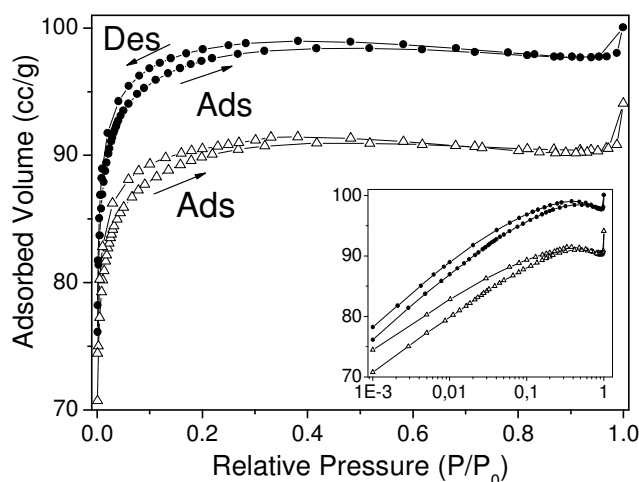
Figure 3.21. Representative nitrogen adsorption/desorption isotherms (full circles: Si_07_1; empty triangles: Si_08_15). The inset shows the same isotherms with logarithmic axis to better illustrate the open cycles.

Table 3.4. Data on porosity analysis by nitrogen adsorption/desorption isotherms using the BET and BJH models. C stands for a constant considered in the BET model.

Synthesis ID	Surface area (m^2/g)	% Micropore area	C	Pore volume (cm^3/g)	Mean pore size (nm)	Open cycle
Si_07_1	322	88	-150	0.151	1.4	Yes
Si_07_13	307	75	-119	0.106	1.8	No
Si_07_14	197	84	-95	0.077	1.6	Yes
Si_07_22	150	52	127	0.031	2.3	Yes
Si_08_4	183	82	-105	0.085	1.4	Yes
Si_08_5	181	80	-101	0.085	1.4	Yes
Si_08_14	120	54	-172	0.057	1.3	Yes
Si_08_15	286	90	-64	0.139	1.4	Yes
Si_07_10	376	88	-67	0.182	1.4	Yes
Si_08_16	286	86	-68	0.139	1.4	Yes
Average	**241**	**78**	**< 0**	**0.105**	**1.5**	**-**

Pore volume is proportional to the surface area. No relationship was found between the surface area and the particle size, neither the TMOS concentration. Nitrogen was used in all cases since our equipment cannot work with argon (smaller molecules than nitrogen) which may be more precise for microporous materials analysis. The pore size is predominantly smaller than 2 nm, i.e. micropores. **Figure 3.22** shows a representative example of the pore size distribution. No significant differences in the pore structure have been found among TMOS and TEOS samples.
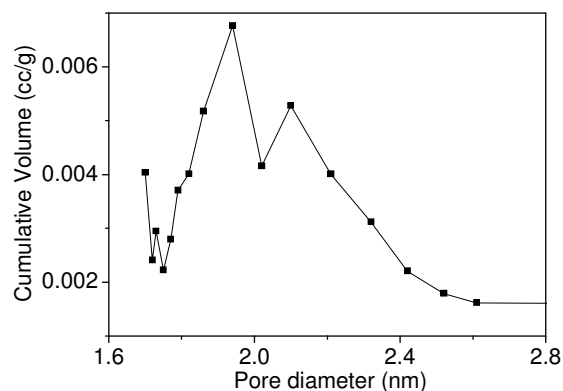
Figure 3.22. Pore size distribution by cumulative volume of a representative sample (Si_07_1). Above 2.8 nm in the *x*-axis there is no relevant info.

A typical isotherm for mesoporous materials has a hysteretic cycle at intermediate pressures, as represented in isotherm type IV (see **Figure 3.20**). It appears because the pore filling by the adsorptive molecules follows a different mechanism compared to the pore emptying. This hysteretic behaviour is restricted to mesopores while both macro- and micropore filling with nitrogen at 77K is a reversible process. The information derived from the desorption branch may be more affected by pore network effects than the adsorption branch. Then, the adsorption branch is preferred for quantitative analysis on pore size.[32]

Although we confirmed our samples to be microporous, the isotherms showed a hysteresis cycle over a wide range of pressures (from 0.001 P/P_0 up to 0.6 and sometimes up to 0.9) and did not close even at the lowest pressures. The last column in **Table 3.4** indicates whether the adsorption/desorption branches show hysteresis. It is illustrated in **Figure 3.21** and more clearly in **Figure 3.23**. Interestingly, the same behaviour was observed by Manuel Hinterstein[33] in micrometric silica samples synthesized under supercritical conditions of carbon dioxide (supercritical drying at low temperature), although no explanation was given. In his case, the C constant in BET analysis was also negative and more than 50% of surface area corresponded to micropore area.

There are several mechanisms that have been reported as responsible for open isotherm cycles, such as activated adsorption arising from a swelling of a polymer matrix,[34] restricted access of nitrogen molecules to pores due to blocking at narrow openings,[31] slit-shaped pores[35] or a fractal structure expected for silica gels dried under supercritical conditions.[36] The two first cases could be probable for our material: the silica network might have some flexibility because it had not totally condensed and could swell up or the pores had narrow openings (it was impossible to check the pore shape by TEM, neither tomography nor AFM). Slit-shaped pores

seem improbable since the primary particles are spherical and their arrangement determines the pore shape. Regarding fractal structure, the question is still open.
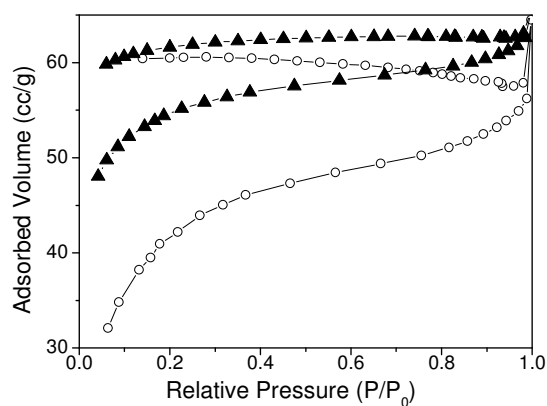

Figure 3.23. Two representative isotherms showing the opened cycles (Si_07_22 in empty circles and Si_08_4 in full triangles).

We took precaution to rule out that the origin of the open cycles was related to the measurement conditions. It has been reported that helium adsorption during the measurement of the dead volume (preliminary step before the isotherm measurement) can generate problems in microporous materials at very low pressures, down to 0.0004 P/P_0, due to incomplete desorption previous to the isotherm analysis.[28] Nevertheless, we expect it not to interfere in our measurements since they begin at 0.001 P/P_0. Another important factor in the preparation protocol for a correct analysis is a thorough pre-degassing of the sample. An insufficient pre-degassing step induces a crossing of the desorption branch below the adsorption one (the sample desorbs the nitrogen adsorbed during the analysis plus the molecules which were not thoroughly degassed). Then, this factor may not be the origin of the hysteresis.

To check if the desorption process was kinetically controlled and whether the reason for the open cycles lied in insufficient equilibration time for the sample desorption, extra analyses with different equilibration times at each relative pressure were performed. First, longer equilibration time was tested (25″ vs. the standard 15″); but the isotherms were still open. Second, the desorption analysis was accelerated and only two points at 0.99 and 0.10 P/P_0 were measured. In an out-of-equilibrium system it would have been expected to obtain a higher adsorbed volume at 0.1 P/P_0 compared to the previous analysis, but our experimental results were identical (see **Figure 3.24**). Thus, the adsorbed nitrogen within the microporous particles was in thermodynamic equilibrium during the tested conditions of the isotherm measurement implying that the origin of the open cycles may lie on the material itself and not on the measurement conditions. Considering once more the results observed in **Figure 3.24** the particle swelling may be also discarded. Perhaps the

pore shape or a potential fractal structure are involved in the issue. Unfortunately we have not been able to give a conclusive explanation to that.
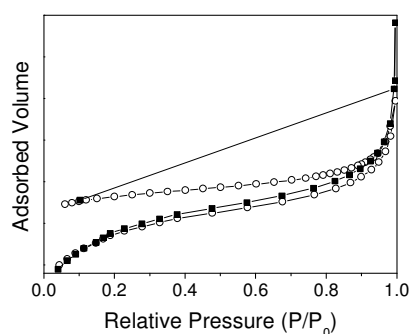
Figure 3.24. Two consecutive isotherms of the same sample. Empty circles: multiple-point desorption branch. Full squares: single-point desorption branch.

3.3.3. Complementary characterization

The particles were further studied by infrared spectroscopy (IR) and thermal gravimetric analysis (TGA). **Figure 3.25** shows an IR spectrum of a representative sample. The bands associated to the silica bonds are found at 1052, 959 and 769 cm^{-1}, respectively. Surface hydroxyl groups and adsorbed water are identified at 3400 and 1635 cm^{-1}, respectively. The absence of C-H bands around 3000 cm^{-1} confirms that the organic solvent has been thoroughly extracted, which is an especially relevant result in view of biomedical applications.
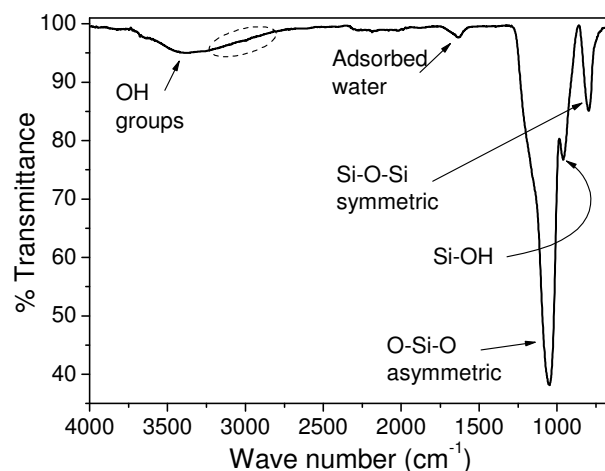
Figure 3.25. Infrared spectrum of a representative sample. The area encircled in the dashed line highlights the absence of C-H bands.

Thermal gravimetric analysis gives information about the relative mass composition of the sample. In amorphous silica the surface silicon atoms tend to maintain their tetrahedral coordination with oxygen through the formation of silanol groups or the coordination of oxygen atoms to water molecules. Water is physically adsorbed whereas hydroxyl groups (OH$^-$) are chemically bonded. The dehydration of silica

should be accomplished at 120ºC, although in highly dispersed and porous silica, water is still present at higher temperatures, up to 300ºC.[37] Between 300 and 500ºC the dehydroxylation of the surface takes place: every two vicinal OH- groups condense into one water molecule and a new siloxane bond (Si-O-Si) is formed. It has been reported that annealing of porous silica above 600ºC is accompanied by sintering, which causes the destruction of the pore structure and consequently an appreciable decrease of the specific surface area. Besides, the isolated hydroxyl groups become closer due to the silica sintering which enables further dehydroxylation of the material. Complete dehydroxylation is only achieved above 1200ºC. The progressive lack of surface hydroxyl groups confers hydrophobicity to the sample.[37]

Our porous silica particles have approximately 2.5 ± 0.9 wt.% of physically adsorbed water (below 240ºC), 2.6 ± 0.9 wt.% of water derived from the condensation of vicinal hydroxyl groups (240 to 470ºC) and about 2.9 ± 0.8 wt.% of water derived from the condensation of isolated hydroxyl groups after sintering of silica (over 470ºC) (see **Figure 3.26**). The sintering can be identified between 470 and 570ºC by the higher slope in the TGA curve accompanied by the negative peak in the derivative curve. The sample weight tends to stabilize around 92 wt.%, which corresponds to the net mass of silicon and oxygen.
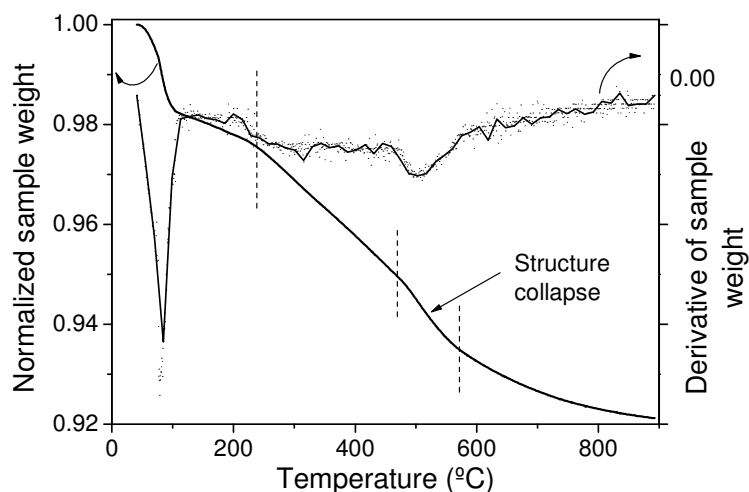
Figure 3.26. Thermal gravimetric analysis of a representative sample (Si_07_13; argon atmosphere, 5ºC/min).

The hydroxyl surface coverage can be determined by the TGA analysis. The mass loss over 240ºC corresponds to water molecules derived from the condensation of OH- groups, not directly to the mass of hydroxyl groups. Then, each desorbed water molecule comes from two hydroxyl groups. Taking into account the experimental desorbed water and the experimental surface area (section 3.3.2), the OH- number per surface area unit can be obtained with the following calculation:

$$n^o \, OH^-/nm^2 = \frac{gH_2O}{100gSiO_2} \cdot \frac{1molH_2O}{18gH_2O} \cdot \frac{2molOH^-}{1molH_2O} \cdot 6.022 \cdot 10^{23} \frac{OH^- groups}{molOH^-} \cdot \frac{1}{S_{BET}} \frac{gSiO_2}{m^2} \cdot \frac{1m^2}{10^{18}nm^2}$$

For sample Si_07_13:

$$n^o \, OH^-/nm^2 = \frac{5.5gH_2O}{100gSiO_2} \cdot \frac{1molH_2O}{18gH_2O} \cdot \frac{2molOH^-}{1molH_2O} \cdot 6.022 \cdot 10^{23} \frac{OH^- groups}{molOH^-} \cdot \frac{gSiO_2}{307m^2} \cdot \frac{1m^2}{10^{18}nm^2}$$

$$\boxed{n^o \, OH^-/nm^2 \approx 12}$$

The number of hydroxyl groups per surface area is a useful piece of information to plan a synthetic approach for a post-functionalization of the particles. Considering the particle size, 204 nm in this case, the particle surface is then 130740 nm², and consequently there are 1555806 hydroxyl groups per silica particle of sample Si_07_13.

The hydroxyl groups are also related to the hydrophilic character of the samples, both associated with the water molecules or to the silanol groups. A comparison of the hydrophilic character of different samples can be estimated by IR spectroscopy by considering the relative intensity of the bands associated to the adsorbed water (1635 cm^{-1}), hydroxyl (3400 cm^{-1}) and silanol groups (960 cm^{-1}) (see **Figure 3.27**).

Samples synthesized with TEOS/ethanol seemed to be more hydrophilic than the ones synthesized with TEOS or TMOS in acetone. This might be attributed to the ability of ethanol to produce transesterification reactions with the siloxane bonds and to the higher hydrophilicity of alkoxy groups vs. siloxane bonds. On the contrary, acetone has no alkoxy groups for transesterification reactions and consequently, the formation of a siloxane bond is not reversible. The lower hydrophilicity of silica particles synthesized in acetone might be due to a higher degree of precursor condensation and siloxane bond formation. Nevertheless, alkoxy groups can act also as hydrophobic agents since they are more hydrophobic than hydroxyl groups. Actually, methoxylation is an old known method for hydrophobization of silica gels.[38]
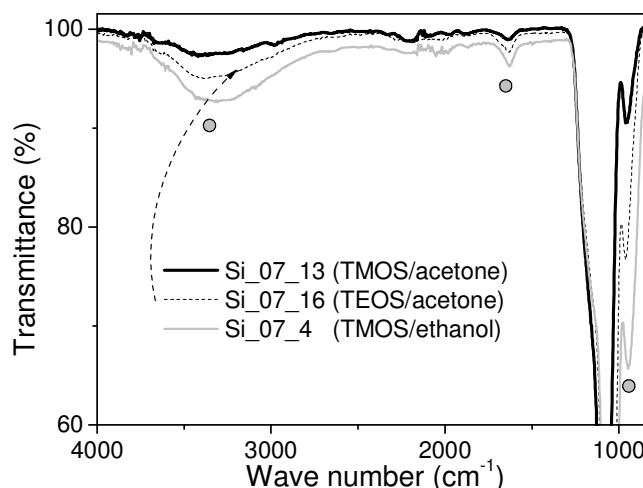
Figure 3.27. IR spectra of several samples with different hydrophilicity. The spectra are normalized to the most intense peak at 1050 cm^{-1}. Bands related to the hydrophilicity of the samples are indicated with empty circles.

3.4. Conclusions of Chapter 3

Silica micro- and nanoparticles were synthesized combining sol-gel chemistry and supercritical fluids technology. The objective of synthesizing these particles was to get the required knowledge to later coat with silica the maghemite nanoparticles described in Chapter 2 and develop a new synthetic method to stabilize magnetic nanoparticles and obtain an efficient contrast agent.

The silica particles were both synthesized and dried under supercritical conditions. The whole synthesis constituted a one-pot reaction, including the extraction of the organic solvent. In that sense, this approach reduces the number of steps compared to other sol-gel processing approaches. The particles were obtained as dry and light powder. Particles were spherical when the reaction solvent was acetone and heterogeneous in shape when using ethanol. This shape difference was attributed to the higher solubility of acetone in carbon dioxide compared to ethanol. The particles from TMOS as the silicon precursor had narrow particle size distributions as low as 5%). On the contrary, TEOS produced necking between particles. We were able to tune the particle size ranging from 200 nm to 4 microns. Concerning porosity, all the samples were microporous (d_{pore} < 2 nm), regardless of the silicon precursor. The BET surface areas oscillated between 120 and 380 m^2/g without the use of porogenic agents. No traces of organic residues were detected by IR spectroscopy, what is especially interesting for the biomedical applications. TGA was used to study the chemical composition of the particles: 3.1wt.% of adsorbed water, 4.7 wt.% of hydroxyl groups and 92 wt.% of SiO$_2$. The hydroxyl number per surface area resulted to be 12 OH$^-$/nm.

3.5.   Bibliography and notes of Chapter 3

1. Moner-Girona, M. Silica Aerogels: synthesis and characterization. *PhD Thesis*. Institut de Ciència de Materials de Barcelona (ICMAB-CSIC) and Universitat Autònoma de Barcelona, **2002.**

2. Moner-Girona, M.; Roig, A.; Molins, E.; Llibre, J. Sol-gel route to direct formation of silica aerogel microparticles using supercritical solvents. *Journal of Sol-Gel Science and Technology* **2003,** 26, (1-3), 645-649.

3. van Raap, MBF; Sanchez, FH; Torres, CER; Casas, L; Roig, A; Molins, E. Detailed magnetic dynamic behaviour of nanocomposite iron oxide aerogels *Journal of Physics-Condensed Matter* **2005** 17 (41) 6519-6531.

4. Gich, M; Casas, L; Roig, A; Molins, E; Sort, J; Surinach, S; Baro, MD; Muñoz, JS; Morellon, L; Ibarra, MR; Nogués, J. High-coercivity ultralight transparent magnets *Applied physics letters* **2003** 82 (24) 4307-4309.

5. Casas, L; Roig, A; Rodriguez, E; Molins, E; Tejada, J; Sort, J. Silica aerogel-iron oxide nanocomposites: structural and magnetic properties *Journal of non-crystalline solids* **2001** 285 (1-3) 37-43.

6. Dominguez, M; Taboada, E; Molins, E; Llorca, J. Co-SiO$_2$ aerogel-coated catalytic walls for the generation of hydrogen *Catalysis Today*, **2007** 138 (3-4) 193-197.

7. Martinez, S; Vallribera, A; Cotet, CL; Popovici, M; Martin, L; Roig, A; Moreno-Manas, M; Molins, E. Nanosized metallic particles embedded in silica and carbon aerogels as catalysts in the Mizoroki-Heck coupling reaction *New journal of chemistry* **2005** 29 (10) 1342-1345.

8. Soler, R; Cacchi, S; Fabrizi, G; Forte, G; Martin, L; Martinez, S; Molins, E; Moreno-Manas, M; Petrucci, F; Roig, A; Sebastian, RM; Vallribera, A. Sonogashira cross-coupling using carbon aerogel doped with palladium nanoparticles; a recoverable and reusable catalyst *Synthesis-Stuttgart* **2007** (19) 3068-3072.

9. Moner-Girona, M; Roig, A; Benito, M; Molins, E. Aerogel thin film synthesis by a supercritical fluid-assisted sol-gel route in a single processing unit *Journal of materials chemistry* **2003** 13 (9)2066-2068.

10. Roig A, Molins E, Rodriguez E, Martinez S, Moreno-Manas M, Vallribera A. Superhydrophobic silica aerogels by fluorination at the gel stage *Chemical communications* **2004** 20 2316-2317.

11. Costela, A; Moreno, IG; Gomez, C; Garcia, O; Sastre, R; Roig, A; Molins, E. Polymer-filled nanoporous silica aerogels as hosts for highly stable solid-state dye lasers *Journal of physical chemistry B* **2005** 109 (10) 4475-4480.

12. Costela, A; Garcia-Moreno, I; Gomez, C; Garcia, O; Sastre, R; Molins, E; Roig, A Highly stable solid-state dye laser based on polymer-filled nanoporous silica aerogels *Solid state lasers and amplifiers* **2004** 54, 6044-50.

13. Gich, M.; Roig, A.; Taboada, E.; Molins, E.; Bonafos, C. and E. Snoeck, Stabilization of metastable phases in spatially restricted fields: the case of the Fe$_2$O$_3$ polymorphs. *Faraday Discussions*, **2007**, 136, 345-354.

14. Alvarez-Arenas, TEG; de Espinosa, FRM; Moner-Girona, M; Rodriguez, E; Roig, A; Molins, E. Viscoelasticity of silica aerogels at ultrasonic frequencies *Applied physics letters* **2002** 81 (7) 1198-1200.

15. Moner-Girona, M; Martinez, E; Roig, A; Esteve, J; Molins, E. Mechanical properties of silica aerogels measured by microindentation: influence of sol-gel processing parameters and carbon addition *Journal of non-crystalline solids* **2001** 285 (1-3) 244-250.

16. Taboada, E.; del Real, R.P.; Gich, M.; Roig, A. and Molins, E. Faraday rotation measurements in maghemite-silica aerogels *Journal of Magnetism and Magnetic Materials*, **2006**, 301, 175-180.

17. Cano-Sarabia, M.; Ventosa, N.; Sala, S.; Patiño, C.; Arranz, R. and Veciana, J. Preparation of uniform rich cholesterol unilamellar nanovesicles Using CO_2-expanded solvents, *Langmuir* **2008**, 24, 2433-2437.

18. Moisan, S.; Martínez, V.; Weisbecker, P.; Cansell, F.; Mecking, F.; Amonier C. General approach for the synthesis of organic-inorganic hybrid nanoparticles mediated by supercritical CO_2. *J Am Chem Soc.* **2007** 129 (34) 10602-10606.

19. Cabañas A.; Enciso, E.; Carbajo, C.; Torralvo, M.; Pando, C. and Renuncio, J. Synthesis of SiO_2-aerogel inverse opals in supercritical carbon dioxide, *Chem. Mater.* **2005**, 17, 6137-6145.

20. Brinker, C. J. and Scherer, G. W. *Sol-gel Science, the physics and chemistry of sol-gel processing*, **1991**, Academic Press, Elsevier Science, USA.

21. Hüsing, N.; Schubert, U. Aerogels - Airy Materials: chemistry, structure, and properties, *Angewandte Chemie International Edition*, **1998**, 37 22-45.

22. Pöhler, H. and Kiran, E. Volumetric properties of carbon dioxide + acetone at high pressures *J. Chem. Eng. Data* **1997** 42, 379-383.

23. Wu, W.; Ke, J. and Poliakoff, M. Phase boundaries of CO_2 + toluene, CO_2 + acetone and CO_2 + ethanol at high temperatures and high pressures *J. Chem. Eng. Data* **2006** 51, 1398-1403.

24. When collecting or manipulating the powder, it is highly advisable to wear a protection mask against particles in order not to inhale the powder which is easily dispersed all over the room. Nevertheless, the toxicity of silica has been widely studied and no signs of systemic toxicity have been observed due to skin or eye contact, inhalation or oral intake.[25]

25. Bergna, H. E.; Roberts, W. O., *Colloidal Silica. Fundamentals and applications*. **2006**; Vol. 131.

26. Chang, C.; Day, C-Y.; Ko, C-M. and Chiu, K-L, Densities and P-x-y diagrams for carbon dioxide dissolution in methanol, ethanol and acetone mixtures, *Fluid phase equilibria* **1997** 243-258.

27. Brunauer, S. *The adsorption of gases and vapours. Vol I, Physical Adsorption*, **1943** Princeton University Press, Princeton.

28. Webb, P. A. and Orr, C., *Analytical methods in fine particle technology*, **1997**, Micromeritics Instrument Corporation, USA.

29. Brunauer, S.; Emmett, P. H. and Teller, E. Adsorption of gases in multimolecular layers *J. Am. Chem. Soc.* **1938** 60, 309.

30. Barrett, E. P.; Joyner, L. G. And Halenda, P. P. The Determination of Pore Volume and Area Distributions in Porous Substances. I. Computations from Nitrogen Isotherms *J. Am. Chem. Soc.* **1951** 73, 373.

31. M. Rose, W. Bohlmann, M. Sabo, S. Kaskel, Element-organic frameworks with high permanent porosity *Chemical Communications* **2008**, 2462.

32. Groen, J. C.; Peffer, L. A.; Pérez-Ramírez, J. Pore size determination in modified micro- and mesoporous materials. Pitfalls and limitations in gas adsorption data analysis, *Microporous and mesoporous materials*, **2003**, 60, 1-17.

33. Hinterstein, M. Unpublished data from short stay at the Institut de Ciència de Materials de Barcelona (ICMAB-CSIC), FAME exchange program, **2005**.

34. Ghanem, B.; Msayib, K.; McKeown, N.; Harris, H.; Pan, Z.; Budd, P.; Butler, A.; Selbie, J.; Book, D. and Walton, A. A triptycene-based polymer of intrinsic microposity that displays enhanced surface area and hydrogen adsorption *Chem. Commun.*, **2007**, 67–69.

35. K. Sing, Physisorption of nitrogen by porous materials *Journal of Porous Materials* **1995**, 2, 5.

36. Esquena, C. Solans, J. Llorens, Nitrogen sorption studies of silica particles obtained in emulsion and microemulsion media *Journal of Colloid and Interface Science* **2000**, 225, 291.

37. Unger, K. K. *Porous silica; its properties and use as support in column liquid chromatography* **1979** Elsevier Scientific Publishing Company, Amsterdam.

38. Mertens, G. and Fripiat, J. The methanol-silica gel system, *J. Coll. Interf Sci,* **1973**, 42 (1) 169-180.
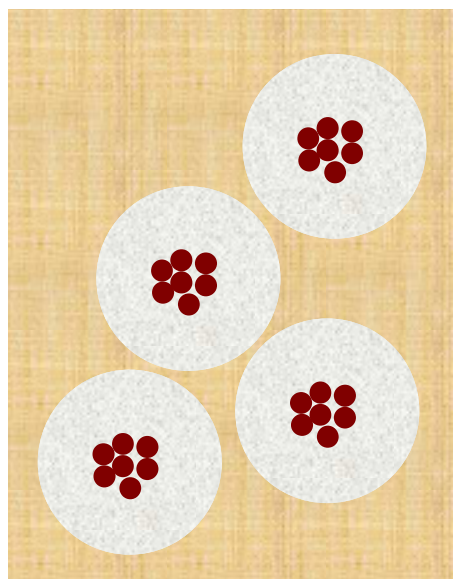
4. COMPOSITE MAGHEMITE@SILICA NANOPARTICLES

This chapter describes the novel synthesis of the composite core(γ-Fe$_2$O$_3$)@shell(SiO$_2$) nanoparticles, their characterization, the similarities and differences with the silica particles described in Chapter 3 and a proposed synthetic mechanism of the silica growth in supercritical conditions. It also describes the transformation of the multi-core(γ-Fe$_2$O$_3$)@shell(SiO$_2$) particles into single-core(ε-Fe$_2$O$_3$)@shell(SiO$_2$) ones. The evaluation as contrast agents for MRI and as mediators for magnetic hyperthermia will be addressed in Chapter 5.

4.1. Synthesis in supercritical media

The iron oxide nanoparticles described in Chapter 2 (synthesis type B) were used as nucleation sites for the synthesis of the silica under supercritical conditions following the same procedure described in Chapter 3. **Figure 4.1** illustrates the general experimental

pathway. The main steps of the protocol are labelled in the same manner as in Chapter 3. The solution of reactants was prepared (step i; now including iron oxide nanoparticles) and then pressurized with CO_2 up to 50 bar (step ii) and heated up to 250ºC (step iii) to reach the supercritical conditions of the organic solvent/CO_2 mixture. These conditions were kept for a given time named the residence time. An extra step was included before step iv: circulation of fresh CO_2 for 2 hours at supercritical conditions, as exemplified in **Figure 4.2**. Afterwards, the system was depressurized (step iv) and allowed to cool down to room temperature (step v). The dry composite particles remained in the reaction chamber. For details on the supercritical facilities see annex 7.3.8.
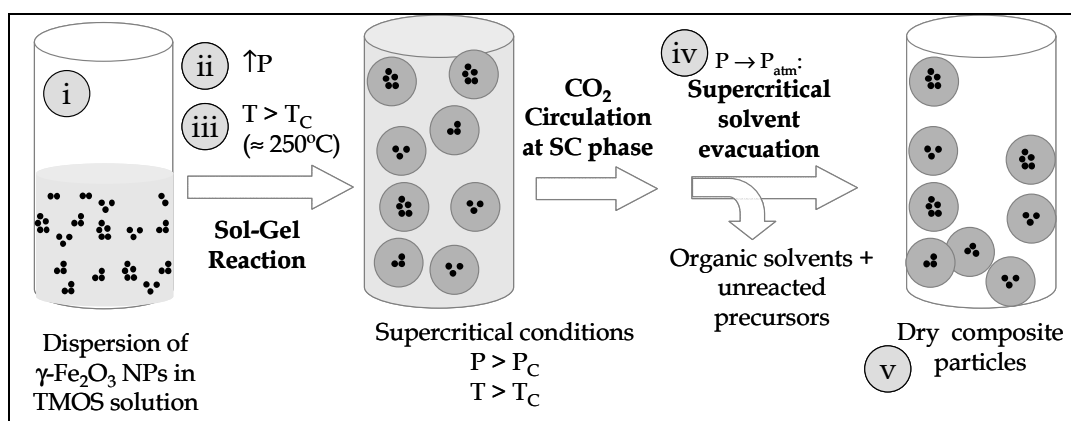
Figure 4.1. Reaction pathway for the synthesis of composite particles.

Carbon dioxide was circulated at supercritical conditions to optimize the extraction of the solvent and to flush out any unreacted species. The circulating flux had to be low enough to avoid a significant decrease of the temperature, i.e. to avoid reaching the liquid + vapour phase. During step iv, the temperature was maintained over the critical temperature to guarantee the change from supercritical to gas phase.
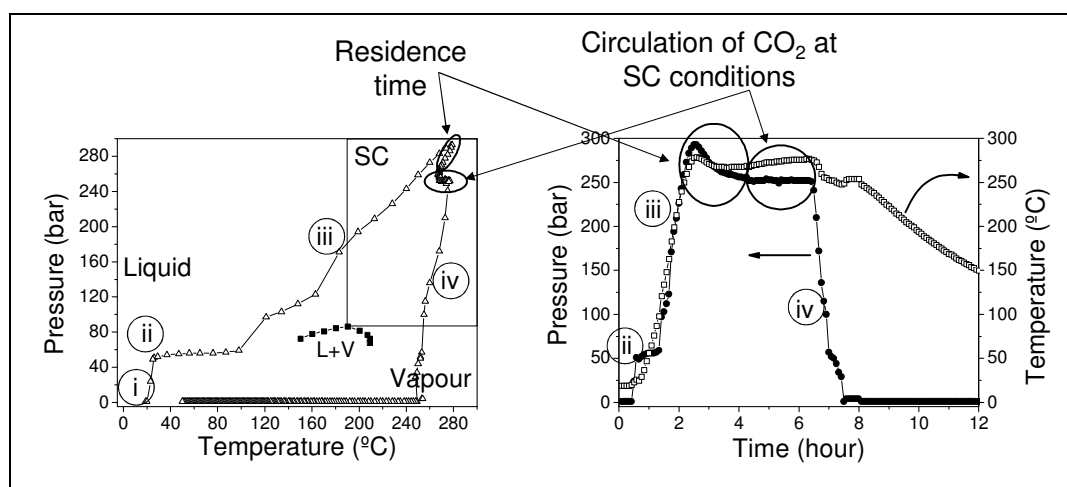
Figure 4.2. Left figure: reaction pathway of a representative experiment, pressure vs. temperature (triangles) and phase diagram of acetone/CO_2 mixture (squares; molar fraction of CO_2 = 0.30).

Right figure: pressure and temperature vs. time. The regions corresponding to the residence time and circulation of CO_2 at supercritical conditions are encircled in both images.

A technical modification was tested in some experiments, that consisted of bubbling the CO_2 (step ii) directly into the reactants solution. In the standard experiments the gas injection was done through the lower valve to the empty space around the Pyrex vessel (see **Figure 4.3**).
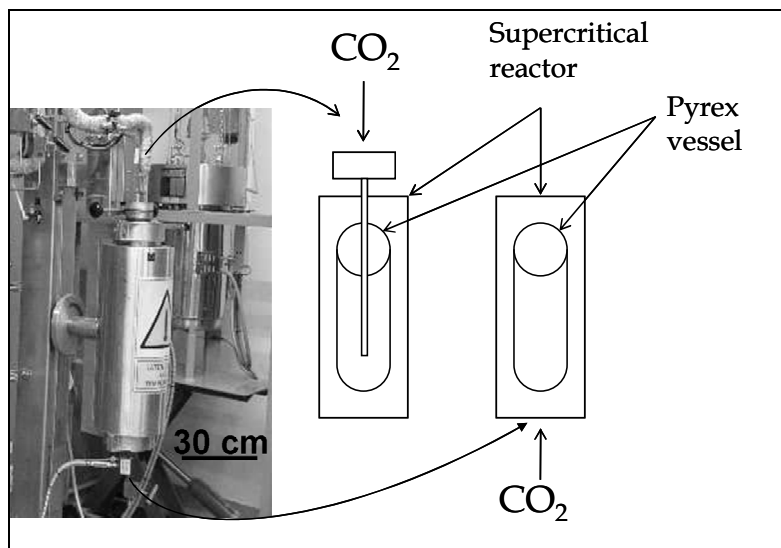
Figure 4.3. Scheme showing the two options to pressurize the autoclave with carbon dioxide: the standard one, through the lower valve, and an alternative one, directly into the reactants solution through a pipe connected to an upper valve.

The motivation of this alternative pressurization was to obtain still narrower dispersion of the particle size and the reduction of the necking degree between particles (see section 4.2.2). This alternative allowed dissolving a higher amount of CO_2 during the initial pressurization. Considering a total solubility of CO_2 in acetone, the molar fraction of CO_2 after the initial pressurization, at 50 bar, was 0.85 (see **Figure 4.4**); the critical point for an acetone/carbon dioxide mixture with a molar composition 0.15-0.85 is 87ºC and 112 bar (see **Figure 3.10**).
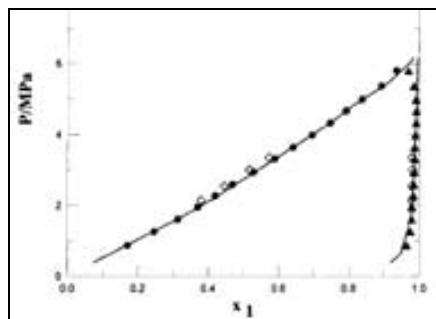
Figure 4.4. Vapour-liquid equilibrium for carbon dioxide (1) + acetone (2) at 298.16 K. Pressure is referred in MPa (1 MPa = 10 bar); x(1) represents molar fraction of carbon dioxide.[1]

4.1.1. Stability of Fe$_2$O$_3$ nanoparticles in the initial sol

Considering the results from Chapter 3, the silica coating was done using TMOS and acetone. Initial solutions contained TMOS, acetone, water and the iron oxide nanoparticles (see numerical data in **Table 4.3**). <u>The stability of these new colloidal systems was essential for the homogeneity of the final composite particles</u>.

The addition of the iron oxide nanoparticles to the TMOS/acetone solution was done in colloidal state, not in powder form. Two different approaches were tested (see **Figure 4.5**): i) neutral aqueous dispersions of iron oxide nanoparticles electrostatically stabilized with sodium citrate (labelled as *Fe$_2$O$_3$_water*) were used. The required amount of water was then substituted by the aqueous dispersion of nanoparticles. This approach failed. We attribute the failure to two facts: the water is a reactant with a substequiometric quantity. Therefore, the amount of iron oxide nanoparticles that could be added to the TMOS solution was restricted to the volume of water, which was very low (less than 1% in volume; see **Table 4.3**). Besides and essential, the iron oxide nanoparticles were unstable in the initial TMOS/acetone solution. And ii) iron oxide nanoparticles dispersed in hexane with oleic acid as surfactant (labelled as *Fe$_2$O$_3$_hexane*) were added. Because the hexane is not a reactant, but only a solvent, different amounts of hexane could be essayed without altering the reactant ratios.
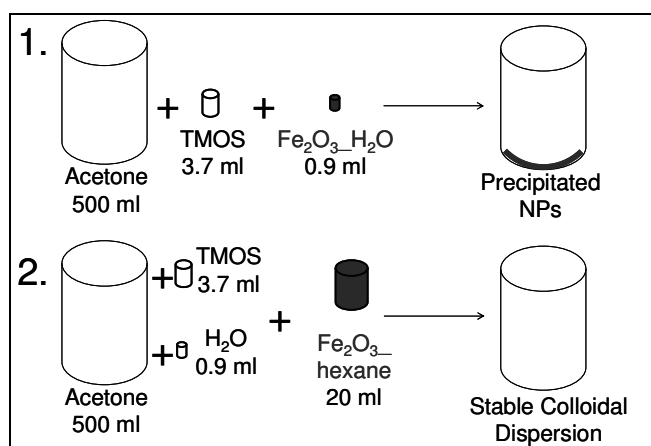
Figure 4.5. Scheme for the two approaches to prepare the initial solutions by adding the iron oxide nanoparticles dispersed in water (first approach, above) or in hexane (second approach, below).

Several tests to find the optimum composition of the initial sol were done before carrying experiments in the autoclave. For that, the stability of the iron oxide nanoparticles in the sols was monitored by dynamic light scattering (DLS). It was observed that the hydrodynamic diameter of the nanoparticles was smaller in hexane than in the TMOS/acetone/water solutions. A study on the influence of each component and their order of addition on the hydrodynamic size was undertaken. The ratio between the acetone and the hexane volume was also considered. **Table 4.1** lists the values for different solutions and **Figure 4.6** shows the DLS size distribution curves.
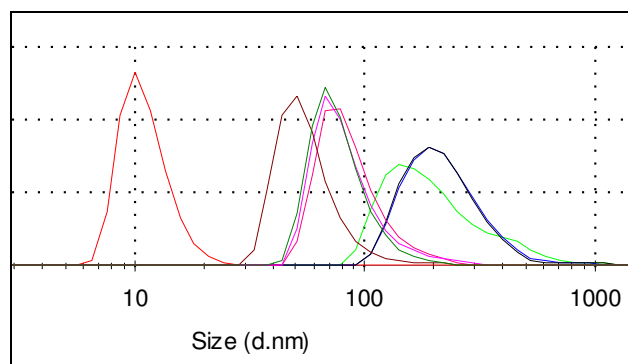
Table 4.1. Hydrodynamic diameters ($\varnothing_{HYD}$) of testing reactant solutions with different composition. The sample name indicates the composition and the ordering of the component addition. The component volumes were fixed: 10 ml acetone, 37 μl TMOS (0.025 M), 9 μl H_2O (0.05 M), 250 μl $Fe_2O_3\_hexane$ (5.9 mg Fe_2O_3/ml). The mass ratio SiO_2/Fe_2O_3 was also fixed to 10. The measurements were done just after preparing each solution. Magnetic stirring was used. Each solution was prepared with fresh components; no previous solutions were used to follow the addition sequence. All the DLS measurements are an average of 3 consecutive measurements.

	Solution indicating the order of addition	$\varnothing_{HYD}$ (by number; nm)	PdI	$Z_{average}$ (nm)
1	**$Fe_2O_3\_hexane$**	10.9	0.137	58.9
2	**Acetone / $Fe_2O_3\_hexane$**	238	0.398	376
3	**Acetone / $Fe_2O_3\_hexane$ / TMOS**	230	0.520	390
4	**Acetone / $Fe_2O_3\_hexane$ / TMOS / water**	226	0.498	477
5	**Acetone / TMOS / $Fe_2O_3\_hexane$**	87.2	0.116	122
6	**Acetone / water / $Fe_2O_3\_hexane$**	57.2	0.258	138
7	**Acetone / TMOS / water / $Fe_2O_3\_hexane$**	80.1	0.081	108
8	**Acetone / water / $Fe_2O_3\_hexane$ / TMOS**	79.6	0.090	106

The iron oxide nanoparticles dispersed in hexane are individually stabilized. The mean hydrodynamic size corresponds to the particle diameter plus the oleic acid coating ($\approx 6 + 2*2.3$ nm). When these particles are dispersed in acetone (solution 2) they have higher polidispersity index and higher mean size indicating that they form clusters. After some minutes the clusters aggregate and precipitate. This was expected since the oleic acid is not soluble in acetone. A fresh solution composed of acetone, $Fe_2O_3\_hexane$ and TMOS was prepared (number 3) to check if the later addition of TMOS could stabilize the nanoparticles in acetone. The PdI is even larger and the mean size number did not change. Solution 4 gave similar results as the previous one: the further addition of water did not stabilize the particles. Solutions 3 and 4 precipitated within minutes.

In solutions 5 and 6 the iron oxide nanoparticles were added after dissolving either TMOS or water in acetone. Both showed smaller polidispersity indexes and smaller mean sizes. Solutions 7 and 8 showed the lower PdI and mean size values. Solutions 5 to 8 were stable during the day (afterwards they were no longer monitored). Stability of the iron oxide nanoparticles in acetone with TMOS can be attributed to the adsorption of TMOS onto the iron oxide surface, due to the high affinity of silicon to iron oxide. Therefore, it can be concluded that the iron oxide nanoparticles capped with oleic acid can be stabilized in clusters when they are added to acetone/TMOS or acetone/water/TMOS solutions.

Volume ratio between acetone and hexane was identified as another important parameter. **Figure 4.7** and **Figure 4.6** gather the results. Since the $Fe_2O_3\_hexane$ nanoparticles are very stable in hexane and totally unstable in acetone, increasing the amount of acetone, the instability of the dispersion increases and the system compensates it by increasing the cluster size.
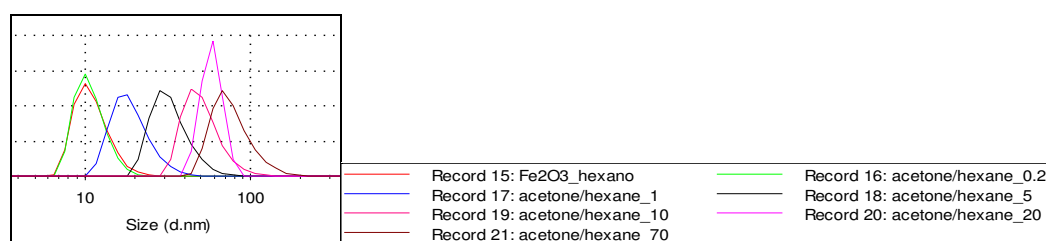
Figure 4.6. Hydrodynamic size distribution by number of colloidal dispersions with different composition and order of addition (details in **Table 4.1**). From left to right: 1-7-8-6-5-2-3-4.

Table 4.2. Hydrodynamic diameters ($\varnothing_{HYD}$) of initial sols with different acetone/hexane volume ratios. The iron oxide concentration was constant. The component volumes were fixed: 37 µl TMOS (0.025 M), 9 µl H_2O (0.05 M), 115 µl *Fe$_2$O$_3$_hexane* (13 mg Fe_2O_3/ml), x ml acetone, y ml hexane ($VolumeRatio \dfrac{acetone}{hexane} = \dfrac{x}{y+0.115}$; $x+y+0.115=10ml$). The mass ratio SiO_2/Fe_2O_3 was also fixed to 10. The measurements were done just after preparing each solution. Magnetic stirring was used. Each solution was prepared with fresh components; no previous solutions were used to follow the addition sequence. The DLS measurements are an average of 3 consecutive measurements.

	Solution	$\varnothing_{HYD}$ **(nm; by number)**	**PdI**	$Z_{average}$ **(nm)**
1	**Fe$_2$O$_3$_hexane**	10.9	0.137	59
2	**Acetone/hexane = 0.2**	10.9	0.233	287
3	**Acetone/hexane = 1**	19.3	0.197	35
4	**Acetone/hexane = 5**	33.5	0.166	60
5	**Acetone/hexane = 10**	51.7	0.156	86
6	**Acetone/hexane = 20**	58.7	0.686	1145
7	**Acetone/hexane = 70**	78.1	0.161	129

Figure 4.7. Hydrodynamic size distribution by number of colloidal dispersions with different acetone/hexane volume ratio. From left to right: red = pure hexane; green = 0.2; blue = 1; black = 5; red (after black) = 10; pink = 20 and brown = 70.

Figure 4.8 displays how to control the cluster size by varying the acetone/hexane ratio. Nevertheless, the reproducibility of the cluster formation is difficult, since we understand the speed and time of magnetic stirring can affect it. Another important consideration is the order of addition of the hexane. When the particles are first dispersed in the total amount of hexane and then added to the acetone/TMOS/water solution, they formed

small clusters. On the contrary, when they were first dispersed in a small amount of hexane, then added to the acetone/TMOS/water solution and then the hexane left was added to reach the nominal acetone/hexane volume ratio, the final clusters were bigger.
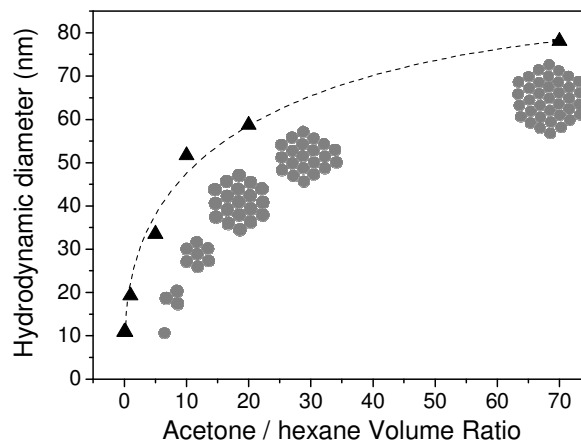
Figure 4.8. Hydrodynamic magnetic cluster size vs. volume ratio of solvents. Dots are experimental values. The dashed line is a guide for the eye.

Similar to the silica particles described in Chapter 3, none of the previous approaches used porogenic agents. Nevertheless, since larger porosity could broaden the scope of applications for drug delivery opportunities, some experiments were also performed by adding a porogenic agent, the cetyl trimethylammonium bromide ($C_{16}H_{33}N(CH_3)_3Br$; CTAB). The stabilization of the initial solutions was complicated since the CTAB is not soluble in acetone. It was first dissolved in methanol. Methanol does not alter the silica growth since the transesterification reactions with TMOS do not chemically change the reactant. The concentration of CTAB was 5 mM, 10 times lower than the TMOS concentration. When the CTAB/methanol solution was added to a just prepared acetone/TMOS/water/Fe_2O_3_hexane solution, the nanoparticles precipitated in a few minutes. It is attributed to a displacement of the TMOS adsorbed onto the iron oxide surface by the CTAB. On the contrary, if the acetone/TMOS/water/Fe_2O_3_hexane solution was allowed to rest for one day, the addition of CTAB/methanol did not destabilize the system. In fact, it was stable for months. It may be attributed to a strengthening of the TMOS-Fe_2O_3 interaction during the night and the later adsorption of CTAB onto this stabilized cluster.

Summarizing, three approaches were tested for the stabilization of the iron oxide nanoparticles in the initial sols. In the first one, the iron oxide nanoparticles were added to the TMOS/water/acetone solution as a neutral aqueous dispersion. In the second one, *Fe₂O₃_hexane* dispersion was used and in the third approach a porogenic agent, CTAB dissolved in methanol, was added to acetone/TMOS/water/Fe_2O_3_hexane dispersion. The size of the magnetic clusters formed in the acetone solutions was monitored by DLS

paying attention to the order of the components addition and the acetone/hexane volume ratio.

4.1.2. Data on experimental parameters for the synthesis of composite particles

This section gives details on the chemical composition and the technical parameters for the synthesis of composite particles. Data on experiments with *Fe₂O₃_water* particles are not included because they yielded heterogeneous materials. Data on selected experiments with composition acetone/TMOS/water/Fe₂O₃_hexane and acetone/TMOS/water/Fe₂O₃_hexane/CTAB_MeOH are listed in **Table 4.3** and **Table 4.4**. These two main groups of samples are labelled as *SiFe_hexane* and *SiFe_hexane_CTAB*, respectively. Identification of single experiments will be as follows: *SiFe_year_number of experiment.*

The reactant solutions were always prepared just before the experiments. An aliquot was kept to measure the hydrodynamic size and the time stability of the dispersions. Few aliquots were analyzed by DLS some months after their preparation to monitor the evolution of the magnetic cluster size. **Figure 4.9** shows two examples of aliquots measured 2.5 and 9 months after their preparation, respectively. No variations in the hydrodynamic size were observed indicating that the size of the iron oxide clusters was constant and also that no silica shell was formed at ambient conditions.
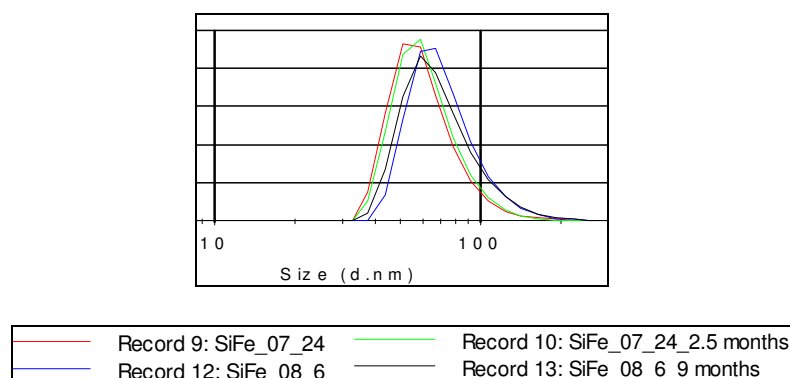
Figure 4.9. Hydrodynamic size distribution by number of two reactant solutions, SiFe_07_24 and SiFe_08_6, measured just after preparation and a few months later, 2.5 and 9 months, respectively.

The common features in all experiments were: TMOS as silicon precursor, acetone as the solvent, double concentration of water to TMOS, pressure higher than 200 bar (maximum 280 bar), temperature 250°C and 2 hours of residence time. The use of CTAB and catalysts was eventual.

Table 4.3. Experimental conditions for *SiFe_hexane* selected experiments. The circulation of CO_2 at supercritical conditions was implemented from experiment SiFe_08_1 on. The hydrodynamic diameter ($\varnothing_{HYD}$) is taken from the number distribution. pH = 5. Extra info: *$[NH_3]$ = 32 mM, **CO_2 injection by the alternative method (see **Figure 4.3**).

Synthesis ID	TMOS		Acetone volume (ml)	H$_2$O vol. (ml)	*Fe$_2$O$_3$_ hexane* volume (ml)	Mass ratio SiO$_2$/ Fe$_2$O$_3$	V$_{acet}$/ V$_{hex}$	$\varnothing_{HYD}$ (nm)
	Conc. (M)	Vol. (ml)						
SiFe_07_23	0.05	1.49	190	0.36	10	10	19	-
SiFe_07_26	0.05	1.49	197	0.36	2.8	10	70	97
SiFe_07_27	**0.025**	2.98	394	0.36	6.0	10	66	64
SiFe_07_28	0.05	1.49	197	0.36	2.7	**20**	73	69
SiFe_07_29	0.05	1.49	199	0.36	1.1	**50**	183	67
SiFe_08_1	0.05	3.72	478	0.90	22	10	22	20
SiFe_08_2	0.05	3.72	475	0.90	25	10	19	16
SiFe_08_3	0.05	3.72	474	0.90	26	10	18	59
SiFe_08_6	0.05	3.72	493	0.90	7	10	70	73
SiFe_08_7	0.05	3.72	250	0.90	250	10	1	19
SiFe_08_8	0.05	3.72	250	0.90	250	5	1	25
SiFe_08_9	0.05	3.72	250	0.90	250	10	1	30
SiFe_08_10*	0.05	3.72	478	0.90	22	10	20	125
SiFe_08_11	0.05	3.72	476	0.90	24	5	20	35
SiFe_08_12**	0.05	3.72	476	0.90	24	10	20	8
SiFe_08_13**	0.05	3.72	476	0.90	24	10	20	50
SiFe_08_17**	0.05	3.72	493	0.90	7	10	70	95
SiFe_08_18**	0.05	3.72	497	0.90	3.3	10	150	104
SiFe_08_19	0.05	3.72	497	0.90	3.3	10	150	-
SiFe_08_20	0.05	3.72	497	0.90	3.3	20	150	114

Table 4.4. Experimental conditions for *SiFe_hexane_CTAB* selected experiments. 50 ml of CTAB in methanol 50 mM; final concentration in sol was 5 mM. pH = 5. Circulation of carbon dioxide at supercritical conditions by default.

Synthesis ID	TMOS		Acetone volume (ml)	H$_2$O volume (ml)	*Fe$_2$O$_3$_hexane* volume (ml)	Mass ratio SiO$_2$/ Fe$_2$O$_3$	V$_{acet}$/ V$_{hex}$
	Conc. (M)	Vol. (ml)					
SiFe_08_21	0.05	3.72	476	0.90	24	40	20
SiFe_08_22	0.05	3.72	476	0.90	24	20	20
SiFe_08_23	0.05	3.72	476	0.90	24	10	20
SiFe_08_24	0.05	3.72	481	0.90	19	10	25

The mass ratio SiO_2/Fe_2O_3 corresponds to the nominal mass of silica (100% conversion of TMOS to SiO_2) over the mass of iron oxide in the initial solution. As an example, in experiment SiFe_08_1 the initial amount of TMOS was 3.72 ml = 0.025 mol TMOS. Assuming 100% yield the final amount of silica would be 0.025 mol SiO_2 = 1.50 g SiO_2

(molecular weight of SiO_2 = 60.1 g/mol). Therefore 0.15 g Fe_2O_3 was added to the initial solution to have a mass ratio of 10.

As we noted in Chapter 3 and we checked further in some composite particle experiments, the glass wool cover induced a heterogeneous particle size distribution, where the bigger particles were caught inside the Pyrex vessel and the smaller ones were able to cross it. To better homogenize the product all over the autoclave such cover was no longer used from experiment SiFe_08_8 onwards.

The hexane is a new component of the sol and its solubility in CO_2 was checked: it is very similar to acetone. Its critical point is 29.7 bar and 233.7 °C. The experimental reaction conditions described in Chapter 3 also guarantee the supercritical conditions of all the possible CO_2/hexane mixtures, since the highest critical pressure is around 130 bar (see **Figure 4.10**).
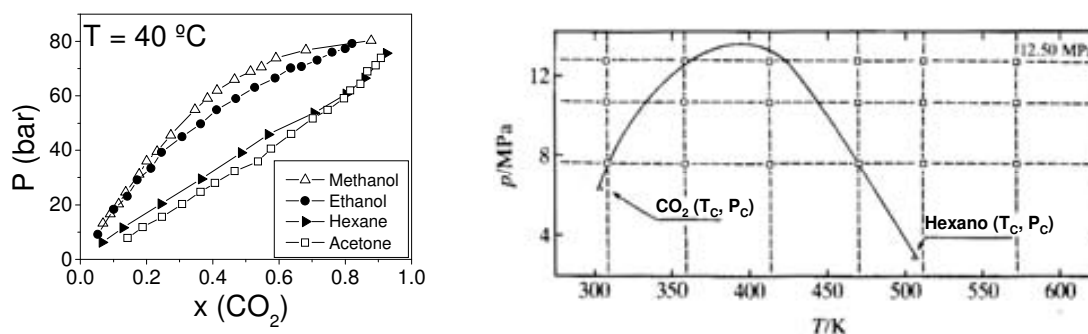
Figure 4.10. Solubility of methanol, ethanol, hexane and acetone in CO_2 at 40°C (pressure vs. molar fraction of CO_2) (left graph).[2,3] Critical conditions of CO_2 + hexane mixtures, whose maximal pressure is 130 bar (right graph; 1MPa = 10 bar).[4]

4.2.   Results and discussion

4.2.1. Morphological characterization of the materials

SiFe_hexane particles were obtained as solvent free powders dispersed all over the autoclave and the Pyrex vessel walls. They were dry, sponge-like, light and brown powders which could be attracted by a 0.5 Tesla magnet without observing phase segregation (see **Figure 4.11**). Some of the general characteristics of *SiFe_hexane* particles are listed in **Table 4.5**. The spherical samples highlighted in the shape column did not present necking between particles. The rest of spherical samples showed a small degree of it.

Figure 4.11. Photographs of *SiFe_hexane* products before being collected from the autoclave (left image), onto the Pyrex walls (middle image) and being attracted by a 0.5 Tesla magnet (right image).

Table 4.5. Results on characterization of *SiFe_hexane* particles. The size values are complemented with the particle size distribution. H stands for the homogeneity at the nanoscale checked by TEM. The size of worm-like particles corresponds to their diameter. Hydrodynamic diameter ($\varnothing_{HYD}$) corresponds to the number distribution. Magnetic cluster size will be defined later; it is schematized in **Figure 5.7**. Sample SiFe_08_10 is divided in two: *b* stands for brown and *w* stands for white; it will be clarified later. *Elemental analysis by inductively coupled plasma mass spectrometry (ICP-MS; see section 4.2.3). **Small particles adsorbed onto the bigger ones.

Synthesis ID	Mass (g) Yield (%)	H	Fe_2O_3 wt. %*	Shape	Particle Size (nm) (P)	$\varnothing_{HYD}$ (nm)	Magnetic cluster size (nm)
SiFe_07_23	0.25 42%	Yes	6.6	Spherical	163 (12%)	244	55
SiFe_07_26	0.50 76%	Yes	7.2	Spherical	173 (14%)	272	52
SiFe_07_27	0.08 12%	No	8.6	Worms**	170	299	-
SiFe_07_28	0.33 52%	No	3.3	Worms	-	499	-
SiFe_07_29	0.08 13%	No	4.0	Worms/ sphere	-	-	-
SiFe_08_1	0.99 59%	Yes	5.0	**Spherical**	71 (14%)	163	23
SiFe_08_2	1.09 66%	No	-	Spherical**	100	268	-
SiFe_08_3	1.25 76%	Yes	7.4	**Spherical**	82 (11%)	120	29
SiFe_08_6	1.01 61%	Yes	5.9	**Spherical**	152 (16%)	313	53
SiFe_08_7	1.24 75%	Yes	5.4	Worms	155	350	-
SiFe_08_8	1.15 64%	Yes	8.9	Worms	152	384	-
SiFe_08_9	1.02 62%	Yes	7.7	Worms	74	-	-

Synthesis ID	Mass (g) Yield (%)	H	Fe$_2$O$_3$ wt. %*	Shape	Particle Size (nm) (P)	Ø$_{HYD}$ (nm)	Magnetic cluster size (nm)
SiFe_08_10b	0.64 36%	No	-	Worms	50	123	-
SiFe_08_10w		Yes	0	**Spherical**	686 (10%)	-	-
SiFe_08_11	0.80 44%	Yes	10.9	Spherical	91 (12%)	232	40
SiFe_08_12	0.30 19%	Yes	-	Worms	55	-	-
SiFe_08_13	0.48 29%	No	20.2	Worms	-	284	-
SiFe_08_17	0.67 41%	No	-	Worms/ sphere	-	500	-
SiFe_08_18	-	No	-	Worms/ sphere	-	372	-
SiFe_08_19	1.15 70%	Yes	6.5	Spherical	162 (17%)	308	47
SiFe_08_20	0.79 50%	Yes	4.9	Spherical	176 (13%)	647	50

The mass yield is calculated by the ratio:

$$\%Yield = \frac{Experimental \, \Pr oductMass}{Theoretical \, 100\% \, \Pr oductMass} = \frac{Experimental \, \Pr oductMass}{mol(TMOS) \cdot MW(SiO_2) + mass(Fe_2O_3NPs)}$$

where MW(SiO$_2$) is the molecular weight of silica (60.1 g/mol).
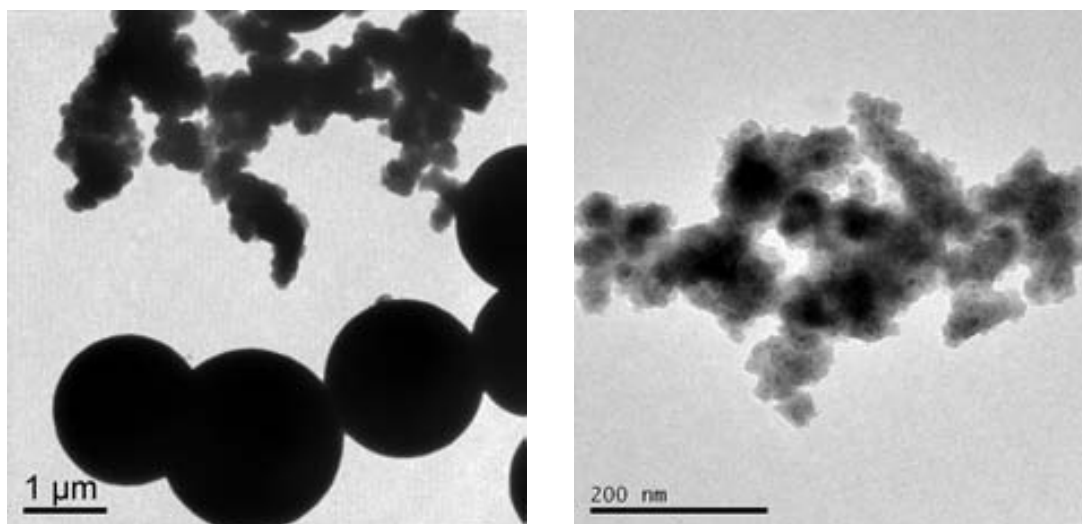
Figure 4.12. TEM images of samples SiFe_08_23 (left image) and SiFe_08_24 (right image).

The powder corresponding to the third group of samples, *SiFe_hexane_CTAB*, was not macroscopically homogeneous. Dark powder was found at the bottom of the Pyrex vessel and a lighter one, and even white, was deposited onto the upper part of the Pyrex walls.

Table 4.6 lists some characterising data. Samples SiFe_08_23 and SiFe_08_24 presented better macroscopic homogeneity although they were also heterogeneous at the microscopic level (see **Figure 4.12**).

Table 4.6. Results on characterization of *SiFe_hexane_CTAB* particles.

| Synthesis ID	Mass (g) Yield (%)	Homogeneity	Shape
SiFe_08_21	0.39 (25%)	No	-
SiFe_08_22	0.62 (39%)	No	-
SiFe_08_23	0.84 (53%)	No	Spherical and irregular
SiFe_08_24	1.1 (69%)	No	Spherical and irregular

4.2.2. Shape and size determination

Electron microscopy

Microscopically, *SiFe_hexane* particles are homogeneous in composition and size. They are composite particles with a magnetic core built up of several grouped iron oxide nanoparticles surrounded by a silica shell. These homogeneous composites can exhibit two different shapes: spherical or worm-like (see **Figure 4.13**).
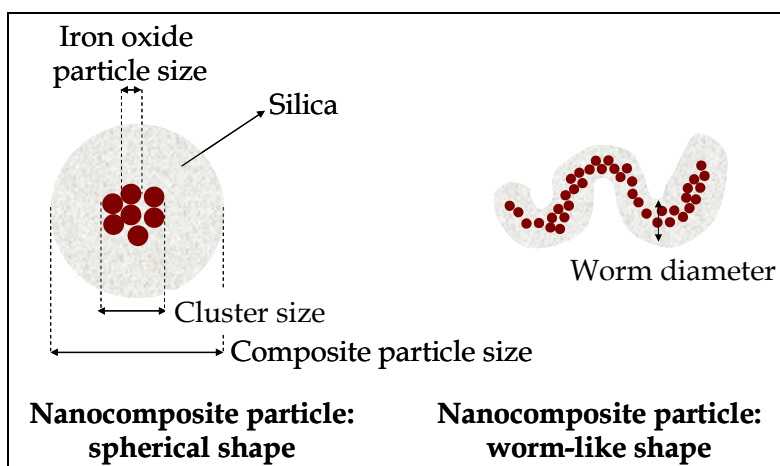
Figure 4.13. Cartoon scheme on the morphology of composite *SiFe_hexane* particles.

The spherical ones are built up of iron oxide nanoparticles grouped in clusters with spherical or elliptical shape which are then surrounded by the silica coating, as shown in **Figure 4.14**. In some cases two neighbouring particles can be partially merged by the formation of necking which reduces the monodispersity of the system. The common experimental parameters to obtain these nice particles are SiO_2/Fe_2O_3 mass ratio 10 or 5, acetone to hexane volume ratio equal or higher than 20, standard CO_2 injection and circulation flux of fresh CO_2 at supercritical conditions lower than 2 kg CO_2/h.
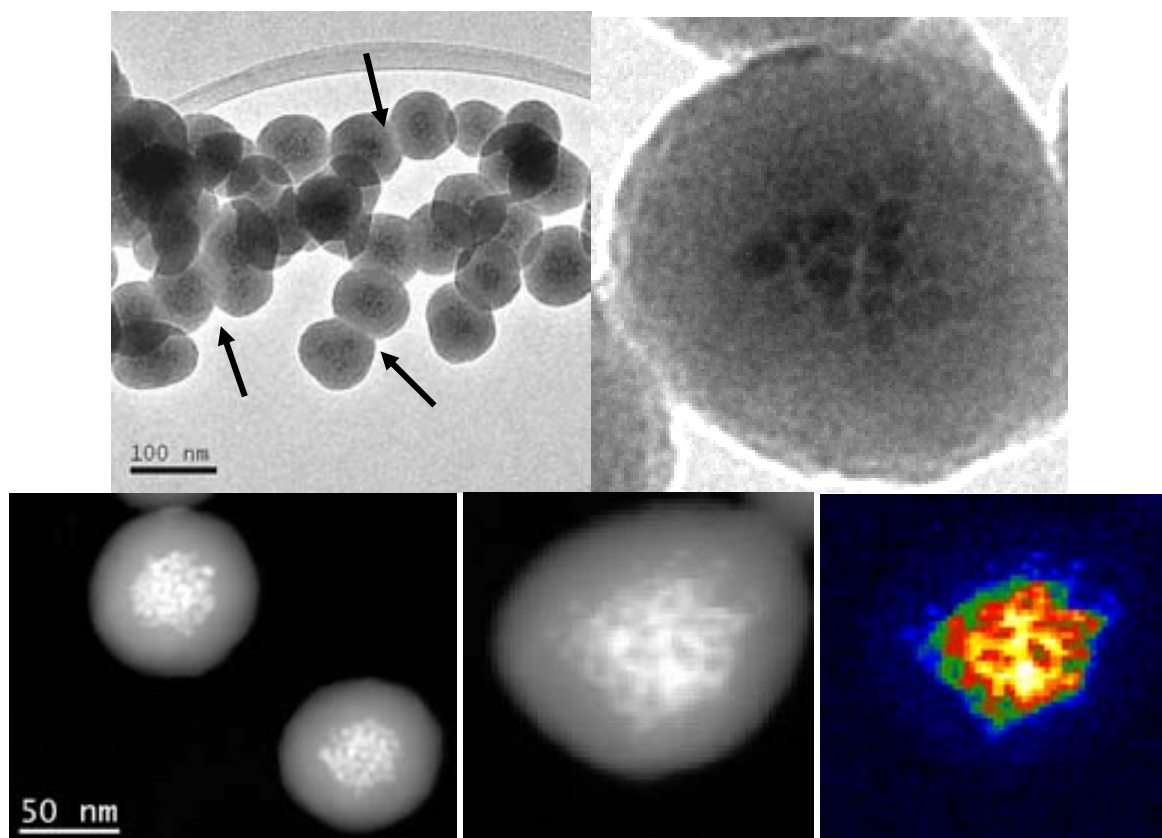
Figure 4.14. TEM images of spherical homogeneous *SiFe_hexane* particles. Above left: group of composite particles with a small degree of necking indicated by arrows. Above right: single composite particle where the original iron oxide nanoparticles can be observed in the centre of the image. The three images in the lower row are dark contrast images. The left one shows two spherical particles with non-interacting iron oxide nanoparticles in the middle. The figures in the middle and right side show a single composite particle and its corresponding EELS elemental map of iron: the concentration of iron is maximal in the centre (yellow area) and minimum in the shell (blue area).

Figure 4.15 shows two TEM images of representative homogeneous worm-like particles. Contrary to the spherical ones, the iron oxide nanoparticles are not grouped in isolated clusters, but they are arranged in continuous rows. This shape was found in the samples with acetone to hexane volume ratio equal to 1. It is attributed to the better dispersability of the iron oxide nanoparticles in the initial hexane-rich reactant solutions, where the particles do not aggregate in big clusters. Also the samples synthesized with the alternative CO_2 injection procedure resulted in worm-like particles or even heterogeneous ones.
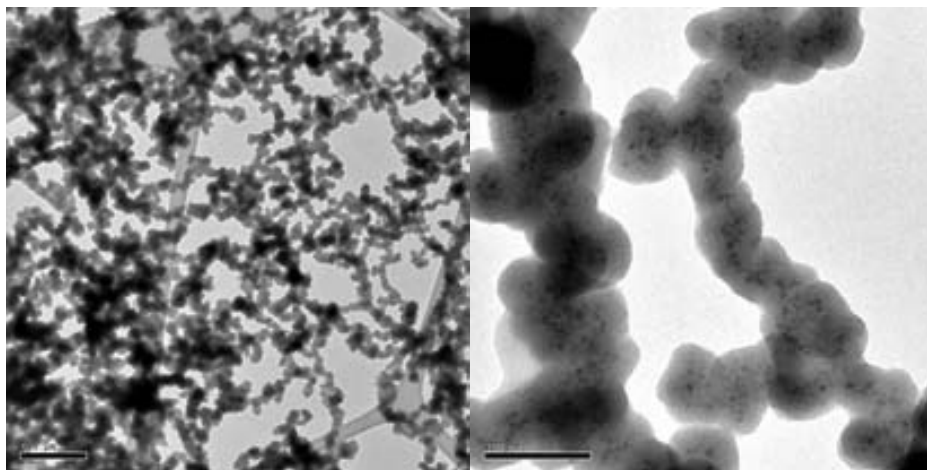
Figure 4.15. TEM images of worm-like homogeneous *SiFe_hexane* particles. The scale bars measure 500 nm (left) and 100 nm (right).

For some initial conditions heterogeneous products were obtained: worms with different shapes, perfectly spherical particles together with irregular ones and also spherical composite particles with small particles attached to their surface. The first two cases were found in experiments with small amount of iron oxide nanoparticles (SiO_2/Fe_2O_3 mass ratio = 20 or 50), with basic catalyst and with the alternative CO_2 injection. The perfectly spherical particles resulted to be composed of pure silica; their nucleation and growth are derived from an insufficient amount of iron oxide surface area to act as nucleation site or to the effect of the basic catalyst. The third case, with tiny particles attached to the surface of homogeneous spherical composite particles is attributed to a high circulation flux of CO_2 (2 kg CO_2/h), which may had shattered some still soft gel particles.
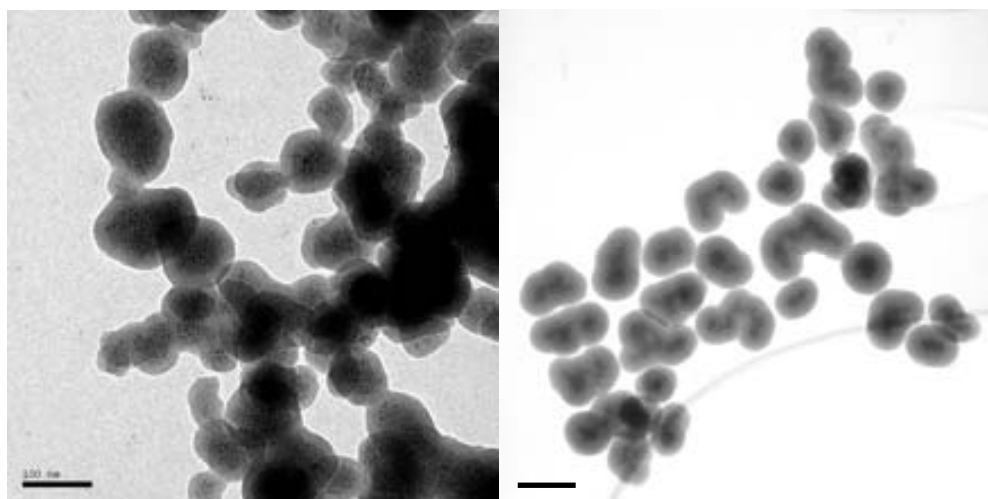
Figure 4.16. TEM images of composite particles with irregular shape mimicking the magnetic cluster shape. Scale bar = 100 nm (left image) and 200 nm (right image).

It was observed that, in general, the shape of the composite particles simulated the shape of the inner magnetic cluster of iron oxide nanoparticles (see **Figure 4.16**). This fact confirms the importance of the preparation of the initial sol.

It was also observed that the composite particle size was directly dependent on the magnetic cluster size in the sol, which in turn depended on the acetone to hexane volume ratio. It is schematized in **Figure 4.17**. Although it is not a linear relationship, the larger the initial cluster size, the larger the composite particles, as shown in **Figure 4.18**.
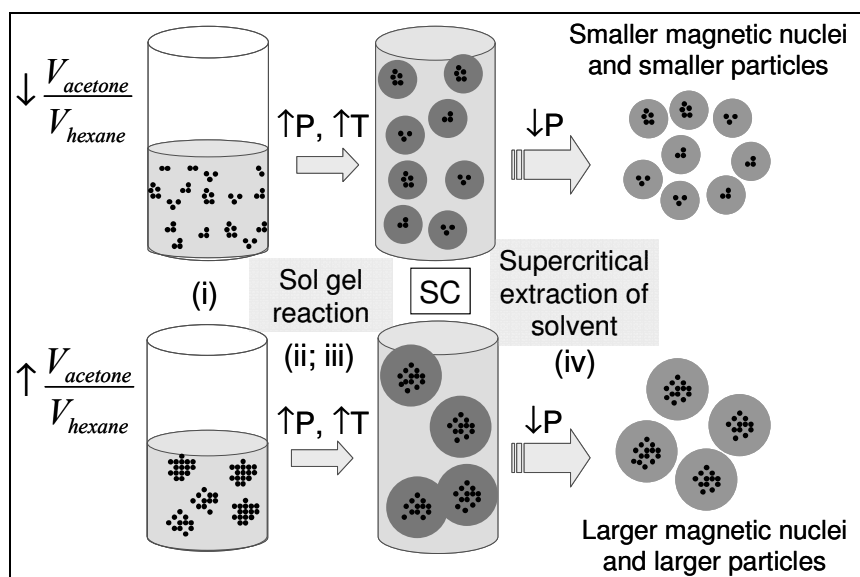
Figure 4.17. Scheme for the synthetic pathway highlighting the relationship between the size of the initial magnetic clusters and the final composite particle size.
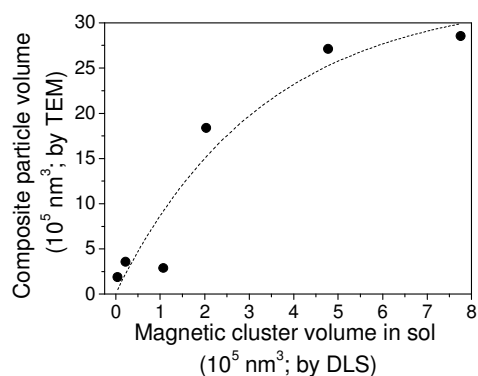
Figure 4.18. Composite particle volume of homogeneous spherical particles vs. the hydrodynamic volume of the magnetic clusters in the sol. The dashed line is a guide for the eyes.

Figure 4.19 shows selected images on spherical composite *SiFe_hexane* particles of different sizes, ranging from 70 to 200 nm. Not to be forgotten is the fact that the silica synthesis is done with no stirring (due to technical incompatibilities in the pilot plant with high temperature and pressure) and still spherical particles are obtained.
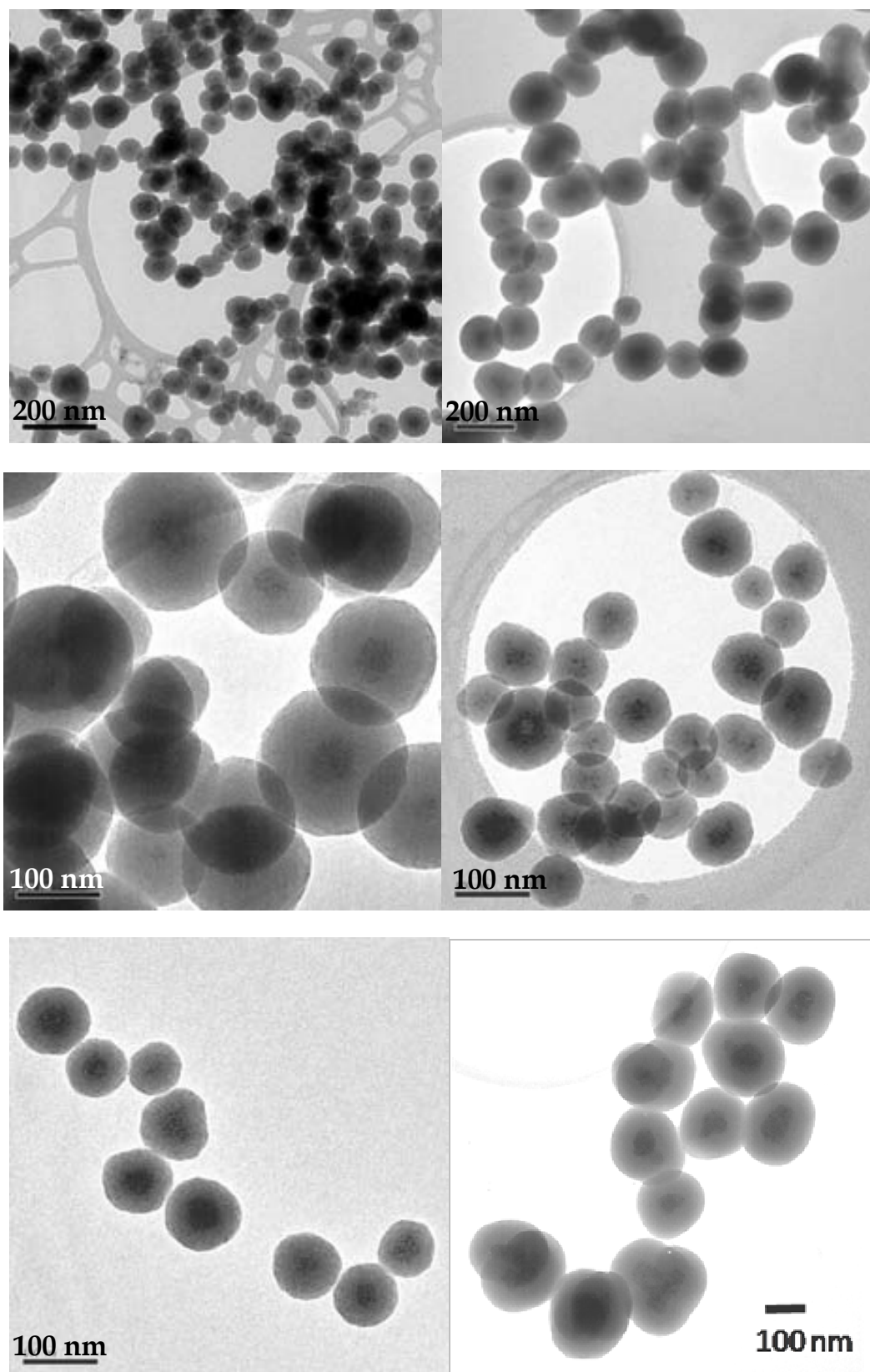
Figure 4.19. TEM images of homogeneous composite *SiFe_hexane* samples.

Although our first intention was to individually coat the iron oxide nanoparticles with a silica shell, after characterising the composite particles, we observed that the clustering of several iron oxide nanoparticles in each composite particle was much favourable from the point of view of the relaxometric properties, which will be described in Chapter 5.

Atomic force microscopy

Atomic force microscopy (AFM) images show how the particles are dispersed individually when supported onto a mica substrate as a solid powder (see **Figure 4.20**).
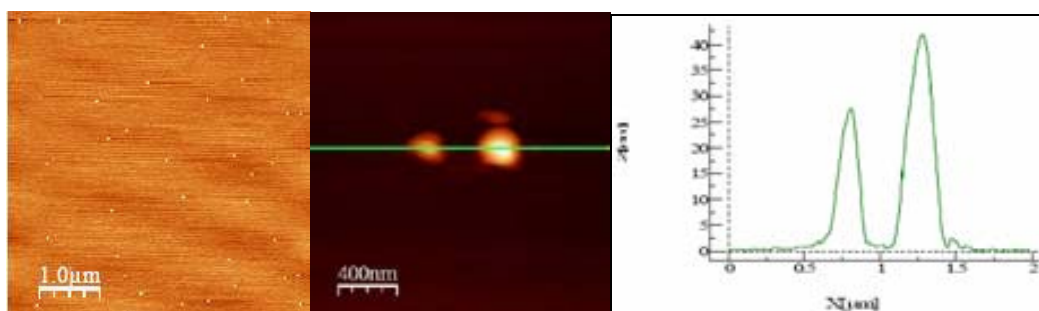
Figure 4.20. AFM images. Left image: tapping mode. Middle and right images: contact mode image and profile shown with green line in the central image. The *x*-values are not reliable, since they contain the deconvolution effect of the tip.

Dynamic light scattering

The composite particles were first stabilized at a given concentration to be analyzed by DLS. They remained stable for some days in water, acetone and ethanol. On the contrary, they were undispersible in hexane. **Figure 4.21** shows a photograph of stable dispersions in different solvents with clear colour.

Figure 4.21. Photograph of sample SiFe_08_3 stabilized in several solvents at 1 mg composite/ml.

The hydrodynamic size of composite *SiFe_hexane* particles stabilized in water is larger than twice the value obtained by TEM in both spherical and worm-like particles. Data are listed in **Table 4.5**. These values are confusing because there is no quantitative difference regarding shape and because, generally, the hydrodynamic particle size is only some

nanometres larger than the physical particle size (depending on the surfactant and the solvent). The DLS distribution shows only one peak with polydispersion indexes (PdI) of low to medium values (0.1-0.3) (see **Figure 4.22**). We tried to find an explanation for these results. Silica is almost insoluble in water, only a small amount dissolves to give monosilicic acid ($Si(OH)_4$), which confers the weak acidity to the silica dispersions (pH ≈ 5-6). From pH 1 to 8 the colloidal dispersions of silica are stable. At pH higher than 8 the dissolution of silica, and therefore, its destabilization, is accelerated. It is well-known that colloidal silica presents a characteristic stability behaviour which is higher than the predictions from DLVO theory (see section 1.3). It has been explained in the bibliography by the formation of a hydration or solvation layer of water molecules strongly bound to the surface hydroxyl groups which exerts a steric repulsion between those particles getting close to each other.[5] It is sometimes defined as "structured water" or "ice-like water"; its thickness is around 2.5-10 nm (10-40 water molecules). Israelachvili et al. claim the existence of a thick gel-like layer of protruding silanol and silicic acid groups that grows on the surface of silica in the presence of water. It is around 1 nm thick, and exerts a polymer-like steric repulsion.[6] Neither of these theories could explain the large hydrodynamic diameter of our particles compared to the observed TEM values. Maybe, the composite particles dispersed in a liquid media have a certain degree of agglomeration which could not be identified in the TEM, neither in AFM images.

The hydration layer is also found in silica colloidal dispersions of polar organic solvents which are able to form hydrogen bonds. Ren et al. states that generally the thicker the solvation layer, the stronger the disjoining pressure and thereby the higher the stability of the suspensions.[7] They observed thicker layers for particles dispersed in ethanol (27 nm) than in water (18 nm), and even thicker in the water/ethanol mixture 1:1 (36 nm). We studied the behaviour of our composite material dispersed in different solvents, and no significant differences between acetone, water and ethanol were found (see **Table 4.7** and **Figure 4.22**). However, the particles showed a higher mean size in the water/ethanol mixture 1:1, what would mean a better stability.

Table 4.7. Data on hydrodynamic size ($\varnothing_{HYD}$) of sample SiFe_08_3 dispersed in different solvents. Concentration = 1 mg composite/ml. Particle size measured by TEM is 82 nm.

Solvent	$\varnothing_{HYD}$ (by intensity; nm)	$\varnothing_{HYD}$ (by number; nm)	PdI
Acetone	226	181	0.138
Water	248	136	0.189
Ethanol	234	163	0.146
Water/ethanol (1:1)	588	383	0.173
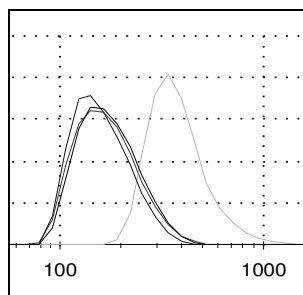
Figure 4.22. Hydrodynamic size distribution by number of sample SiFe_08_3 dispersed in different solvents (1 mg/ml): water, acetone and ethanol superimpose (left curves) and water/ethanol 1:1 (grey curve at higher values). The *x*-axis is expressed in nm.

Concluding, the *SiFe_hexane* colloidal dispersions in water, ethanol and acetone are stable for some days. The measured hydrodynamic size is larger than twice the values observed by TEM, what could be attributed to a small degree of particle aggregation.

4.2.3. Structural and functional characterisation of the materials

X-Ray diffraction

X-Ray diffraction showed that the composite particles are formed of amorphous silica and nanocrystallites of one single crystalline phase which could be indexed to magnetite and maghemite (see **Figure 4.23**). Nevertheless, the diffractogram allowed discarding the presence of any other crystalline phase and therefore the formation of any new phase during the supercritical process.
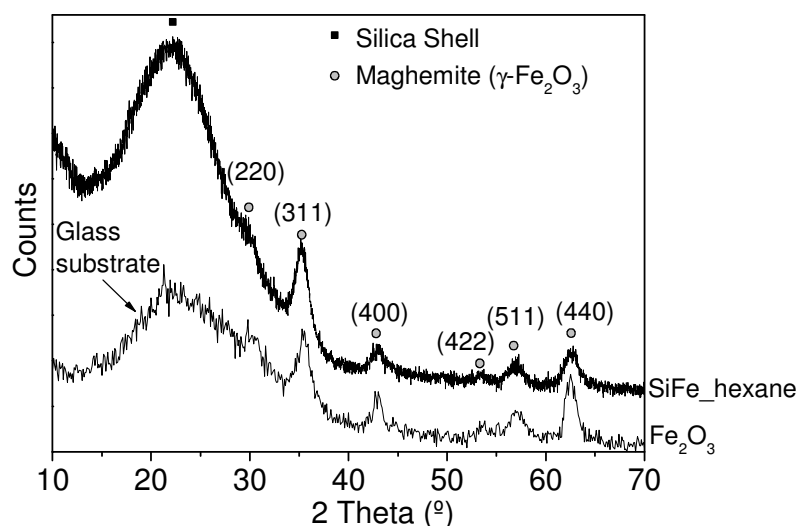
Figure 4.23. X-Ray diffractogram of a composite *SiFe_hexane* sample (upper curve) compared to the initial iron oxide nanoparticles (lower curve).

Concerning crystallite size, its calculation with the MAUD program and with the Scherrer's formula (see annex 7.3.5) was not accurate since the most intense peak of iron

oxide (35°) overlaps with the typical amorphous silica hump (22°). Besides, the noise to signal ratio was very high due to the amorphous silica matrix. The crystallite sizes obtained with Scherrer's formula from several peaks in the same diffractogram ((400), (511) and (440)) were significantly different (they differed from 1 to 3 nm). Qualitatively, it can be observed in **Figure 4.23** that the peak width in Fe_2O_3 diffractogram and in the composite sample diffractogram is similar. Then, no significant particle size change could have taken place during the supercritical conditions.

Magnetometry (for crystalline phase identification)

Magnetic measurements were used for the identification of the iron oxide phase. Magnetite has higher saturation magnetization than maghemite (see **Table 2.1**)[8] and it has been reported that magnetite nanoparticles ($2Fe^{3+}Fe^{2+}4O^{2-}$) are totally oxidized to maghemite ($3Fe^{3+}2O^{2-}$) when they are calcined in air at 300°C.[9] We calcined sample SiFe_08_1 in air at 550°C for 6 hours and we checked the magnetic properties. **Figure 4.24** shows that the magnetization curves of the as-synthesized and calcined samples at different temperatures (5 and 298 K) superimpose: there was no magnetic change during the calcination, implying that the crystalline phase of the composite particles was maghemite (γ-Fe_2O_3) before and after the calcination, discarding the presence of magnetite in composite samples.
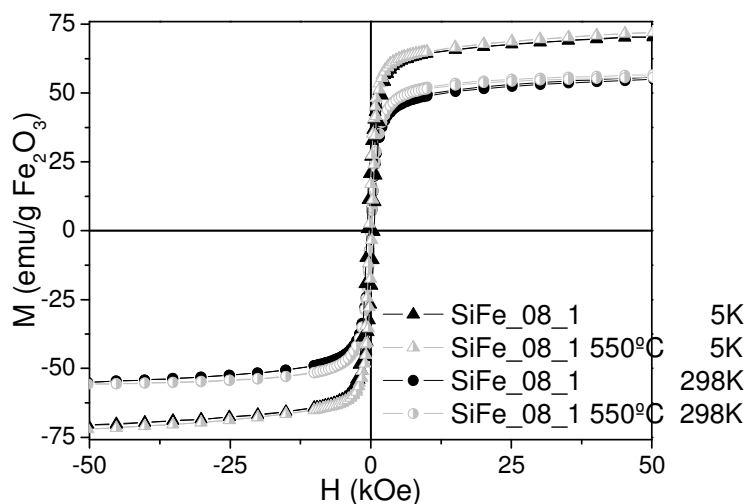
Figure 4.24. Magnetometry curves of sample SiFe_08_1 before and after calcination in air at 550°C, measured at 298 and 5K.

Elemental analysis

The elemental iron and silicon mass content of the *SiFe_hexane* particles was analyzed by inductively coupled plasma mass spectrometry (ICP-MS) at the Universitat Autònoma de

Barcelona (UAB) (see details in annex 7.3.12). To convert the **iron** mass percentage to the **iron oxide** mass percentage it was considered that all the iron atoms form maghemite:

2 Fe atoms (2x55.8 g/mol) form 1 Fe_2O_3 molecule (159.6 g/mol) $\Rightarrow$

Fe_2O_3 weight% $\equiv$ 1.4 x Fe weight%

Table 4.5 includes the iron oxide mass percentages in composite *SiFe_hexane* samples. Experimental SiO_2/Fe_2O_3 mass ratio obtained by ICP-MS in homogeneous composite particles was compared to the nominal 10% of SiO_2/Fe_2O_3 mass ratio (see page 107 for definition). As observed by TEM, no pure silica particles were formed neither uncoated iron oxide nanoparticles. However, the experimental SiO_2/Fe_2O_3 mass ratio of composite particles is higher than the nominal value, suggesting that not all the iron oxide nanoparticles were used as nucleation sites. Although no isolated iron oxide nanoparticles were observed in the TEM images we cannot rule out that a fraction of initial iron oxide was vented out.

Infrared spectroscopy

Infrared spectra of the composite samples were compared to the spectra of silica particles and no new bands at low wave number (450-650 cm^{-1}) associated to iron oxide bonds were identified (see **Figure 4.25**). Actually, it has been reported that infrared spectroscopy is a useful technique to differentiate between maghemite (630, 590, 570 and 450 cm^{-1}) and magnetite (590 cm^{-1}),[10] but we were unable to identify any new band at that region. Bruni et al. observed a new band at 590 cm^{-1} due to the Fe-O-Si bond in iron oxide-silica composite materials after calcination at 700°C.[11] However, neither did we identify this one after calcination at 550°C, nor at 1100°C (see **Figure 4.25**). Most likely the lack of this bands is due to the small amount of Fe-O bonds and even lower of Fe-O-Si bonds compared to the high amount of Si-O bonds (due to the low weight % of iron oxide in the samples).

The whole infrared spectra did not show typical bands of organic groups, such as C-H bonds, whose most intense bands appear around 3000 cm^{-1} (see **Figure 4.26**). This is a satisfying result since it means that no significant organic traces due to solvents or unreacted species are left in the solid particles after the supercritical extraction of the solvents and that the only components of the particles are silica and iron oxide, both biocompatible compounds. Besides, no extra steps for purification neither drying of the samples are needed. They are synthesized in one-pot reaction, being the final product solvent-free.
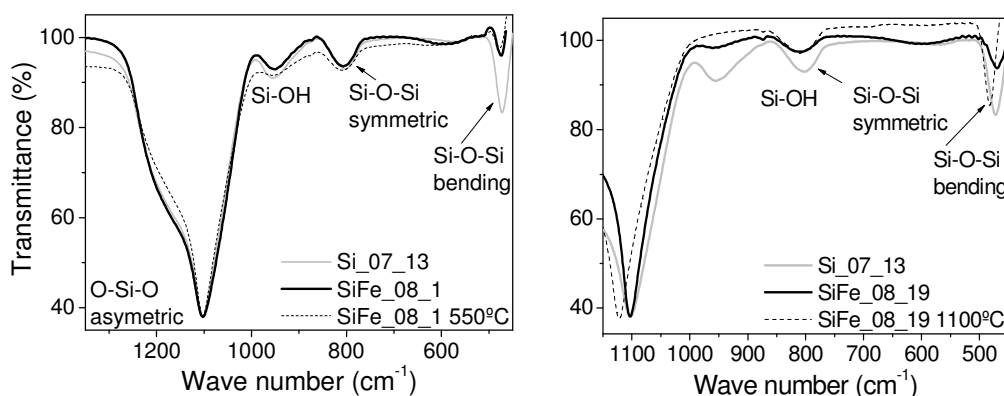
Figure 4.25. IR spectra of two *SiFe_hexane* composite samples (SiFe_08_1 and SiFe_08_19) before and after calcination compared to a silica sample (Si_07_13).

Regarding oleic acid, in section 4.2.5 it is shown that the mass composition of the pre-formed iron oxide nanoparticles is ≈ 41 wt.% Fe_2O_3 and ≈ 59 wt. % of oleic acid. As an illustrating example, the weight % of iron oxide in sample SiFe_08_1 is 5.0% (**Table 4.5**). If the oleic acid would have remained in the composite sample after the supercritical synthesis, then its weight % would have been ≈ 7%. This significant fraction of oleic acid might have been identified in the infrared spectra. Since no C-H bands around 3000 cm^{-1} are observed we rule out the presence of oleic acid. Its boiling point is 360ºC, higher than the temperature at supercritical conditions. Then, we assume that the oleic acid is extracted together with the solvents during the depressurization step.
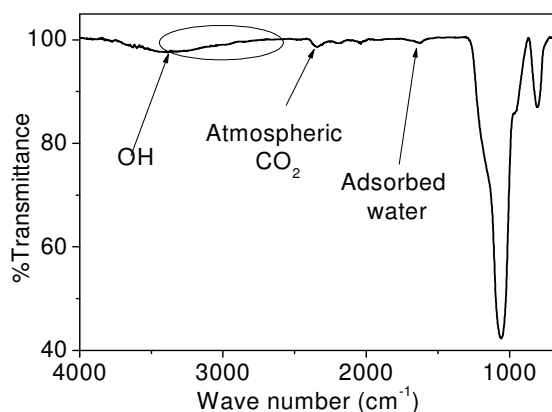
Figure 4.26. IR spectrum of sample SiFe_08_1 highlighting the absence of bands around 3000 cm^{-1}, typical region of bands related to C-H bonds.

Samples *SiFe_hexane_CTAB* were also analyzed by IR in order to determine if CTAB was left in the particles. The characteristic bands of CTAB are located around 2800-3050 cm^{-1} and 1400-1500 cm^{-1}. IR spectra of samples *SiFe_hexane_CTAB* showed either no bands or very weak bands in these ranges, attributed to small traces of the reactive. Most of it must had been vented out during the depressurization of the system but not completely.

Contact angle measurements

Contact angle measurements can provide information on the relative liophilicity of a series of samples. Especially important for biomedical applications is the hydrophilicity. To perform these analyses, the particles were first compacted into pellets following the protocol described in annex 7.3.13 and then a droplet of the analyte was placed onto the surface while video recording. If the sample has a high affinity to the solvent (liophilicity) then it is quickly absorbed. On the contrary, if it shows liophobicity, the droplet of solvent will stay onto the surface for a given time. **Table 4.8** lists some data. In *SiFe_hexane* samples water is quickly absorbed (less than 12'') showing a high hydrophilicity, as expected from silica. If measuring the contact angle at the very first seconds, we obtain values around 20°. On the contrary, when evaluating a *SiFe_hexane_CTAB* sample, water is not absorbed at all, it forms a stable droplet. The contact angle is around 72°, showing a significant hydrophobicity. These data are directly related to the surface properties of the particles (chemical composition and physical structure). The surface of *SiFe_hexane* samples is covered of silanol groups, which can bond to water molecules through hydrogen bonds. The lack of affinity of sample *SiFe_hexane_CTAB* to water may come from hydrophobic carbon chains located at the surface of the particles, the ones identified by infrared spectroscopy around 3000 cm^{-1}.

Table 4.8. Results on contact angle measurements.

Sample	Solvent	Contact Angle (°)	Observations
SiFe_08_13	water	23	Quickly absorbed (9''); almost no droplet formation
SiFe_08_20	water	16	Quickly absorbed (12''); almost no droplet formation
	ethanol	-	Quickly absorbed (3'')
	acetone	-	Quickly absorbed (2'')
	hexane	-	Quickly absorbed (3'')
SiFe_08_24 (*SiFe_hexane_CTAB*)	water	72	Stable droplet

Ethanol, acetone and hexane were also tested in the SiFe_08_20 sample. The three solvents were absorbed in scarcely 2-3 seconds, faster than water. These results on ethanol and acetone compared to water are expected from the DLS data. Regarding hexane, the sample was expected to be more liophobic.

4.2.4. Porous structure

As mentioned in section 3.3.2, bulk silica aerogels are interesting materials due to, among other properties, their high values of surface area and accessible pore volume. Porous materials are widely used as substrates for drug delivery, especially silica.[12-14] One of the main reasons for choosing silica as the coating material and for choosing supercritical

technology as the processing technique was the interest in fabricating a biocompatible porous shell in one-step while avoiding the use of the frequently toxic porogenic agents and thus avoiding costly purification steps in the process.

Nitrogen adsorption/desorption isotherms (BET model)

The initial surface area values of composite materials obtained were not as high as we had expected keeping in mind the values obtained for the silica particles (section 3.3.2). A summary of the porosity data on *SiFe_hexane* samples is listed in **Table 4.9**. The experimental values of BET surface area can be referred to the total mass of composite or only to the mass of silica (as expressed in **Table 4.9**), which is the material bearing the intrinsic porosity. The surface area referred to silica mass is a more realistic value to be compared with the silica samples, since the iron oxide nanoparticles have no inner porosity. Its calculation is the following:

Equation 4.1 $$S_{BET}(m^2/gSiO_2) = S_{BET}\left(\frac{m^2}{gcomposite}\right) \cdot \frac{1 gcomposite}{(1-x)gSiO_2}$$

where x is the mass fraction of Fe_2O_3, listed in **Table 4.5**.

Table 4.9. Porosity data on composite *SiFe_hexane* samples.[15] Samples degasified at 100°C during 24 hours. Surface area values in brackets and grey colour are referred to mass of composite and not to the mass of silica due to the lack of chemical analysis.

Synthesis ID	Surface area $(m^2/g\ SiO_2)$	% Micropore area	C	Pore volume $(cm^3/g\ composite)$	Mean pore size (nm)
SiFe_07_23	28	0	14	0.073	11.2
SiFe_07_26	25	12	131	0.034	5.9
SiFe_07_27	30	0	15	0.040	5.9
SiFe_07_28	85	15	22	0.064	3.1
SiFe_07_29	169	45	100	0.104	2.6
SiFe_08_1	102	19	62	0.136	5.6
SiFe_08_2	(46)	8	54	0.075	6.6
SiFe_08_3	52	17	80	0.021	1.8
SiFe_08_6	78	26	38	0.031	1.7
SiFe_08_7	97	49	176	0.041	1.8
SiFe_08_8	33	20	48	0.013	1.7
SiFe_08_9	46	13	63	0.019	1.7
SiFe_08_10b	(23)	0	63	0.010	1.7
SiFe_08_10w	(7)	1	25	0.003	1.6
SiFe_08_11	60	5	31	0.022	1.7
SiFe_08_12	(53)	23	64	0.023	1.7
SiFe_08_13	64	31	672	0.023	1.8
SiFe_08_17	(48)	0	55	0.021	1.7
SiFe_08_18	(33)	0	43	0.014	1.7
SiFe_08_19	34	8	75	0.014	1.8
SiFe_08_20	42	0	50	0.017	1.7

Surface area values of composite samples are lower than 100 m²/g SiO₂ (the higher value of sample SiFe_07_29 is attributed to its heterogeneous composition including pure silica spheres). The C value is positive in all the cases, indicating low or even no micropore area: the average value of micropore area fraction is 15%. However, the mean pore size is lower than 2 nm in most of the samples, although some of them bear mesopore average size.

Figure 4.27 shows a representative isotherm curve (for sample SiFe_08_13) with a scheme of several porosities. The first steep increase at low pressures is attributed to the intraparticular micropore area (i). The gentle rise at intermediate pressures corresponds to the external surface area of the particles (ii). The abrupt increase of adsorbed volume at high pressures is attributed to the interparticular voids which are meso- or macrometric in size (iii); they do not correspond to the inner particle structure. Note that the calculation of BET surface area only considers the adsorption data between 0.05 and 0.30 P/P₀. Once more, we obtained open isotherms.
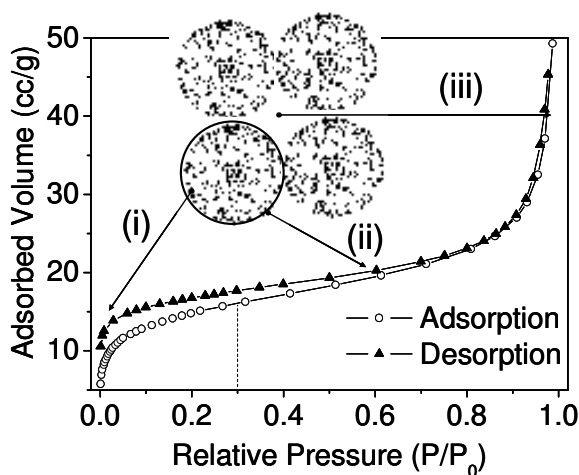
Figure 4.27. Representative isotherm of a composite sample with a clarifying scheme (sample SiFe_08_13). P/P₀ = 0.30 is highlighted to show the maximum value of pressures used to calculate the BET surface area.

Figure 4.28 shows a representative pore size distribution profile of samples *SiFe_hexane*. There is no well defined peak suggesting that there is no defined monomodal size pore population. The high increase in adsorbed volume in **Figure 4.27** at high pressures can be correlated to the high incremental volume found at pore sizes over 25 nm in **Figure 4.28**. The inset in the figure zooms the lowest pore size area. A broad peak is found around 8 nm. Although there is no well defined peak at the micropore range (< 2 nm), the mean pore size of several samples *SiFe_hexane* is within this range. As observed in the inset of **Figure 4.28**, the adsorbed volume increases as the pore size decreases below 3 nm, but the instrument does not reach enough low pressures (minimum value = 0.0001 P/P₀) to give more information about the micropore range.
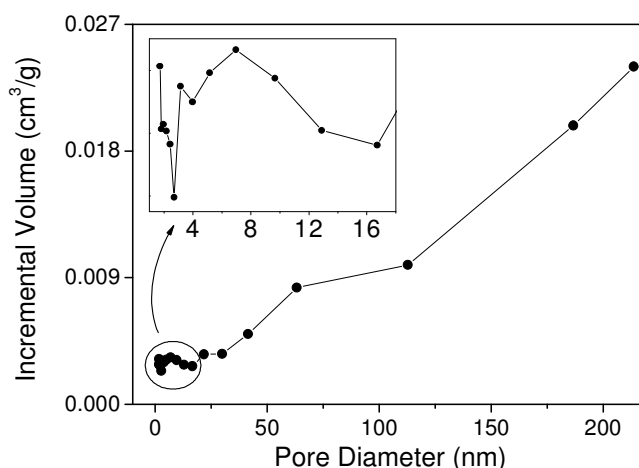
Figure 4.28. Pore size distribution of a representative *SiFe_hexane* sample (SiFe_08_6). The inset corresponds to a zoomed area at low pore size.

Some samples were calcined to study the porosity evolution with temperature. The surface areas vs. calcination temperature are shown in **Figure 4.29**. Firstly, sample SiFe_08_8 was calcined at 200ºC, 300ºC, 500ºC and 700ºC. The highest value appeared after heating the sample at 300ºC and then decayed progressively. These results match the expected sintering of the material around 500ºC (see **Figure 3.6**) with the consequent decrease of surface area. Samples SiFe_08_1 and SiFe_08_11 corroborate the highest surface area after calcination at 300ºC. In the three samples the increase of surface area is 50%. The same behaviour of surface area evolution with temperature was found by Martí Gich in bulk silica xerogels with dispersed maghemite nanoparticles.[16]

The isotherms of calcined samples also presented open cycles. These samples are no longer flexible gels, but rigid solids, especially the ones calcined at the highest temperatures. In that scenario, the explanation of open isotherms due to flexible silica networks should be neglected.
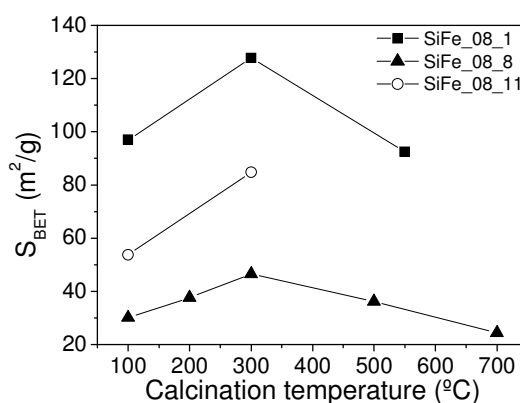
Figure 4.29. Surface area vs. calcination temperature of *SiFe_hexane* samples.

125

To calculate the degree of porosity of a given material, the values of the bulk density (the density of the material, including the pores) and the skeletal density (considering only the solid structure density) are needed. Since our material is nanoparticulated, the measurement of its bulk density is not straightforward and therefore, some estimated calculations were done. Besides, we calculated the surface areas in case of compact spherical particles. These values were compared to the experimental surface areas to estimate the inner surface area of the particles (see **Figure 4.30** for clarifying scheme).

$$S_{BET} = \frac{SphereSurface}{ParticleMass} \qquad S_{BET} = \frac{Sphere + InnerSurface}{ParticleMass}$$
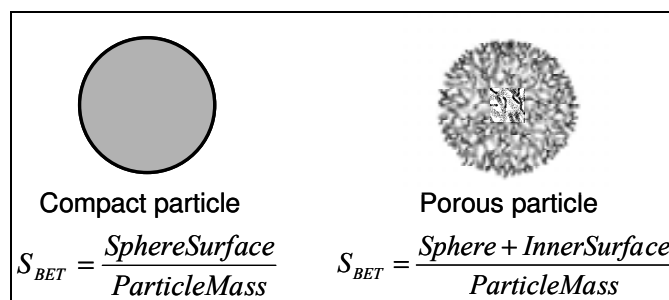
Figure 4.30. Scheme highlighting the difference in surface area of two particles of the same size, being the first one compact (left drawing) and the second one porous (right drawing).

The skeletal density was calculated considering the chemical composition of the particles, as exemplified in **Equation 4.2**:

Equation 4.2 $\qquad \rho \text{ (composite particle)} = 5.24*x(Fe_2O_3) + 2.2*(1- x(Fe_2O_3))$

where ρ stands for density, 5.24 g/cm^3 is the iron oxide density, 2.2 g/cm^3 is the compact silica density (which we consider the skeletal density of pure silica) and $x(Fe_2O_3)$ stands for weight fraction of iron oxide measured by chemical analysis (data in **Table 4.5**). The percentage of porosity was calculated with **Equation 4.3**:

Equation 4.3 $\qquad \%Porosity = 100 \cdot \dfrac{V_{pore}}{V_{pore} + V_{skeletal}} = 100 \cdot \dfrac{V_{pore}}{V_{pore} + \dfrac{1}{\rho_{ptle}}}$

where V_{pore} is the experimental pore volume obtained from the nitrogen isotherm (cm^3/g) and $V_{skeletal}$ corresponds to the inverse of the particle skeletal density calculated with **Equation 4.2**. Only spherical particles were considered. **Table 4.10** lists the results. Values on silica particles are also included to be compared with the composite ones. Pure silica particles showed values of porosity percentage among 16 and 30%, higher than the ones shown by the composite particles. In fact, the values of %porosity for most of the composite samples were lower than 10%. Besides, the ratio of experimental surface area over the calculated one was higher than 20, even 236, for pure silica particles. On the contrary, this ratio for the composite particles hardly reached 4. These data indicate that pure silica particles have a high inner surface area but the composite ones have only a small amount of porosity, although both materials were synthesized in the same way.

Table 4.10. Values of calculated surface area considering compact spherical particles compared to the experimental ones, as well as the calculated percentage of porosity. Abbreviations: *Exp* stands for experimental, *Calc* stands for calculated and *Vol* stands for volume.

Sample	$\varnothing_{TEM}$ (nm)	Fe_2O_3 wt. fraction	ρ (ptle.) (g/cm³)	Calc surface area (m²/g)	Exp Surface area (m²/g)	Exp Area Calc Area	Exp Pore Vol (cm³/g)	% Porosity
Si_07_1	2000	0	2.20	1.4	322	236	0.151	**25**
Si_07_13	210	0	2.20	13.0	307	24	0.106	**29**
Si_07_14	642	0	2.20	4.3	197	46	0.077	**19**
Si_08_4	2400	0	2.20	1.1	183	161	0.085	**16**
Si_08_5	480	0	2.20	5.7	181	32	0.085	**16**
SiFe_07_23	163	0.066	2.40	15.3	26	1.7	0.073	15
SiFe_07_26	173	0.072	2.42	14.3	23	1.6	0.034	8
SiFe_08_1	76	0.050	2.35	33.6	97	2.9	0.136	24
SiFe_08_3	82	0.074	2.42	30.2	48	1.6	0.021	5
SiFe_08_6	157	0.059	2.38	16.1	73	4.5	0.031	7
SiFe_08_11	91	0.109	2.53	26.0	54	2.1	0.022	5
SiFe_08_19	162	0.050	2.35	15.8	32	2.0	0.014	3
SiFe_08_20	176	0.050	2.35	14.5	40	2.8	0.017	4

Different strategies were carried out to try to increase the surface area and the intrinsic porosity of the composite particles by modifying the synthetic conditions. They are listed below.

- Improvement of the supercritical extraction of the organic solvent by introducing an extra step of circulation of CO_2 at supercritical conditions (from experiment SiFe_08_1 onwards). This step also intended to separate the silica shell growth process from the drying process, to decrease the necking formation. The porous structure did not suffer any clear change compared to the previous samples, neither the degree of necking.

- The different acetone to hexane volume ratio did not influence the porous structure.

- Influence of catalyst was also investigated. It was considered that the oleic acid (adsorbed onto the iron oxide nanoparticles) could act as a weak acid catalyst influencing the nucleation and growth of the silica. For that, experiment Si_08_14 was planned: addition of oleic acid to the reactants solution without iron oxide nanoparticles ([TMOS] = 0.05 M, [oleic acid] = 6.3 M; see Chapter 3). Unfortunately, oleic acid was not homogeneously distributed in the product, since it was found at the bottom of the Pyrex vessel as an oily substance. The surface area (120 m²/g SiO_2) decreased compared to silica particles, but it was still higher than the one for composite samples. It was also observed that Si_08_14 particles were smaller in size (370 nm) than silica particles synthesized in the same

conditions without oleic acid (Si_07_22: 1000 nm; Si_08_4: 2400 nm). Nevertheless, they were bigger than composite particles with the same experimental conditions (the biggest spherical composite particles are 200 nm in diameter). Then, oleic acid may influence the silica growth and its porous properties.

- Another experiment using hydrochloric acid as a strong acid catalyst was undertaken (experiment Si_08_15: [TMOS] = 0.05 M; [HCl] = 0.02 M; see Chapter 3). The resulting surface area, 286 m^2/g, is very similar to the ones in silica particles (as well as the particle size). Then, the acid catalysis does not alter the porous structure of the silica particles. Besides, if oleic acid influences the silica growth it is not due to its acidic character.

- Basic catalysis was also tested, in this case with iron oxide nanoparticles (sample SiFe_08_10, [NH$_3$]). The powder found inside the Pyrex vessel was brown, whereas the powder on the autoclave walls was white (although the initial reactants solution was stable for months). They were separately analyzed by TEM: the brown powder was made of composite worm-like particles and the white one contained perfectly spherical silica particles. Regarding porosity they had different surface area values, 23 and 6.5 m^2/g for the brown and white powder, respectively. In this experiment, the iron oxide nanoparticles acted as nucleation sites forming worm-like composite particles, similar to other *SiFe_hexane* experiments. However, NH$_3$ catalyzed the formation of silica nuclei without the need of the iron oxide nanoparticles. The resulting pure silica particles were compact, 6.5 m^2/g, suggesting that the basic catalyst dramatically affects the porous properties of the silica network.

- Finally, we added a porogenic agent, CTAB, to the initial reactants solution. The experimental data are listed in **Table 4.4** and the porosity data of *SiFe_hexane_CTAB* samples are listed in **Table 4.11**. All the products were macroscopically heterogeneous, although only sample SiFe_08_22 could be separated in two different aliquots (silica-rich product labelled *w* for *white* and composite-rich product labelled *b* for *brown*). BET surface areas of the most homogeneous samples, SiFe_08_23 and SiFe_08_24, were similar to *SiFe_hexane* samples. The higher BET values of the heterogeneous sample SiFe_08_22 showed microporosity and BET surface areas more similar to the silica particles (due to its enrichment in silica particles). Then, no improvement in the surface area of the composite particles was obtained with the addition of CTAB to the initial reactant solution.

Table 4.11. Porosity data of *SiFe_hexane_CTAB* samples. Samples degasified at 100ºC during 24 hours.

Synthesis ID	Surface area (m²/g)	% Micropore area	C	Pore volume (cm³/g)	Mean pore size (nm)
SiFe_08_21	-	-	-	-	-
SiFe_08_22w	219.96	80	-76	0.106	1.4
SiFe_08_22b	126.67	39	-640	0.058	1.3
SiFe_08_23	83.83	0	42	0.035	1.7
SiFe_08_24	55.27	0	21	0.022	1.6

Concluding, several approaches were tested in order to increase the particle surface area and inner porosity of the composite particles but we did not succeeded in it.

HCl accessibility

Selected *SiFe_hexane* samples were dispersed in concentrated HCl (35 wt.%) to dissolve the iron oxide nanoparticles and quantify its concentration by titration with potassium dichromate (for protocol details see annex 7.3.1). Composite samples dispersions were brown (see **Figure 4.21**) whereas iron ions solutions are lemon-yellow. To our surprise we observed no colour change in most samples after several days of the acid attack. Just a few of them showed a very weak yellow coloration. These results mean that there is no accessibility of the protons through the silica shell to the iron oxide particles, or, in case the protons reach the iron oxide surface, the generated free iron ions cannot get out of the silica to reach the bulk solution. We think that the first silica layer synthesized directly onto the iron oxide nanoparticles is non-porous and the shell left bears some inner porosity, the one observed in the nitrogen isotherms. The fact that iron oxide nanoparticles are not accessible to protons is a positive result for the toxicity of the material, since only one material, the silica, would be in contact with the biological material when used *in vivo* or *in vitro*.

4.2.5. Magnetic properties

Special interest was devoted to understand the magnetic properties of the composite particles, since these are the properties to be later exploited in the biomedical applications. Chapter 5 will follow the discussion about them. In this section, only homogeneous *SiFe_hexane* samples will be considered. The main results are listed in **Table 4.12**. All the analyzed samples have the same magnetic behaviour, and therefore only representative graphs will be shown. Magnetization values can be referred to the total mass of composite or only to the mass of the magnetic material, the iron oxide. The last one is preferred to be compared with other magnetic materials (i.e. maghemite bulk saturation magnetization is 76 emu/g Fe_2O_3 at room temperature[17]).

Table 4.12. Magnetic data on selected homogeneous *SiFe_hexane* samples. H_C = coercitive field, M_R = remanence magnetization, M_S = saturation magnetization. M_S values are considered at 5 T (1 T = 10 kOe). χ = magnetic susceptibility in cgs units (calculated at 298 K at low field (-400 – 400 Oe)), $\varnothing_{MAG}$ = magnetic particle diameter (calculated from χ with **Equation 4.4**), T_B = blocking temperature at 100 Oe.

Sample	Fe$_2$O$_3$ wt %	H$_C$ 5K (Oe)	$\frac{M_R}{M_S}$ 5K	M$_S$ (emu/g composite)		M$_S$ (emu/g Fe$_2$O$_3$)		χ (cgs)	Ø$_{MAG}$ (nm) (± 0.7 nm)	T$_B$ (K)
				5K	298K	5K	298 K			
SiFe_07_23	6.6	568	0.34	4.9	4.1	73.9	61.5	0.189	7.5	61
SiFe_07_26	7.2	556	0.33	5.1	4.0	71.3	56.0	0.104	6.6	41
SiFe_07_27	8.6	532	0.33	6.1	4.9	70.1	57.0	0.150	7.3	57
SiFe_08_1	5.0	655	0.38	3.6	2.8	72.0	55.6	0.197	8.1	60
SiFe_08_3	7.4	627	0.38	5.4	4.4	72.8	58.8	0.121	6.7	39
SiFe_08_6	5.9	639	0.38	4.4	3.7	75.3	62.2	0.174	7.4	61
SiFe_08_7	5.4	677	-	-	3.2	-	59.8	0.168	7.4	55
SiFe_08_8	8.9	583	0.38	7.0	5.8	78.2	65.1	0.189	7.3	57
SiFe_08_9	7.7	654	0.38	6.9	5.6	89.1	73.0	0.154	6.3	41
SiFe_08_11	10.9	598	0.37	8.4	6.7	77.2	61.4	0.142	6.8	47
SiFe_08_13	20.2	604	0.36	9.2	7.9	45.5	39.3	0.010	8.2	55
SiFe_08_19	6.5	-	-	-	3.7	-	56.7	0.136	7.5	-
SiFe_08_20	4.9	-	-	-	2.5	-	51.0	0.084	6.5	-

M(H) curves

Figure 4.31 shows magnetization curves at room temperature and 5 K. At low temperature there is small coercivity (values between 550 and 680 Oe) and small M_R/M_S ratio (lower than 0.5), typical of soft magnetic materials. At room temperature the curve has no coercivity and can be adjusted to a Langevin equation (**Equation 1.5**): the material is then superparamagnetic at room temperature.

The magnetization curves do not fully saturate even at 5 T. This behaviour is attributed to the existence of a magnetic outer dead layer in the iron oxide nanoparticles, due to the lower crystalline order of the external shell. A much accurate method to measure the particle size has recently been reported by Chen et al. where the outer layer has been considered and computed.[18] As expected, saturation magnetization values are higher at lower temperature.
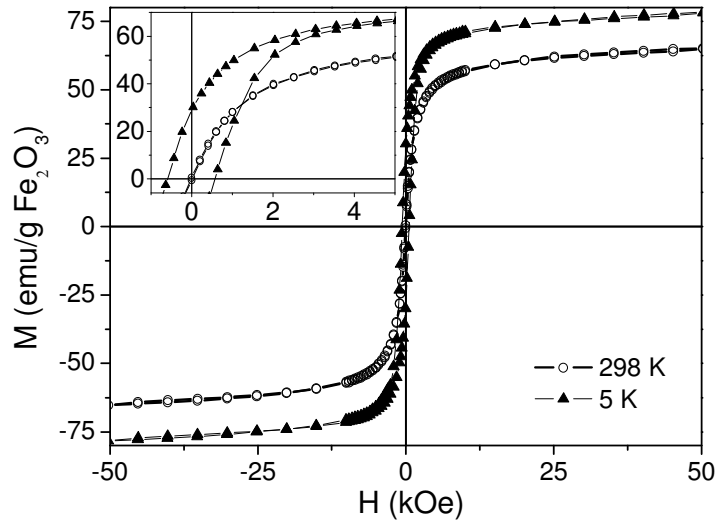
Figure 4.31. Representative magnetization curves vs. external applied field, M(H), at room temperature and 5 K of sample SiFe_08_8. The magnetization is referred to the mass of iron oxide. Inset: zoom at low magnetic field to show the coercive field at 5 K and the lack of it at 298 K.

Equation 1.5
$$M = M_S \cdot (\coth \alpha - \frac{1}{\alpha}) \qquad \alpha = \frac{m_0 \cdot H}{k_B \cdot T} \qquad \mathbf{m_0 = M_S \cdot V_{ptle}}$$

The magnetic particle size can be calculated by fitting the whole magnetic curve (M(H)) to a Langevin equation (**Equation 1.5**) or by measuring the magnetic susceptibility at low field and applying **Equation 4.4**:

Equation 4.4
$$\chi = \frac{n \cdot \mu_0 \cdot m_0^{\,2}}{3 \cdot k_B \cdot T}$$

where χ is the volume susceptibility in SI units; n (1/m³) is the number density of particles, μ_0 is $4\pi \cdot 10^{-7}$ H/m, $m_0 = M_S \cdot v$, where m_0 is the magnetic moment per particle (A·m²), M_S is the saturation magnetization per volume unit (A/m) and v is the particle volume (m³), k_B is $1.38 \cdot 10^{-23}$ J/K and T is the temperature (K).

The magnetic susceptibility in cgs units was obtained from the slope of the magnetization curves at very low fields (-400 – 400 Oe). **Figure 4.32** shows an example of the linear fitting with the appropriate units: M as the volume magnetization of iron oxide in cgs units (emu/cm³ Fe₂O₃) and H as the applied magnetic field in cgs units (Oe). Then, the susceptibility was converted to the SI units with **Equation 4.5**. The values of susceptibility and magnetic diameter calculated from the magnetization curves are listed in **Table 4.12**. The mean iron oxide particle size for the studied samples is 7 ± 1 nm.

Equation 4.5
$$\chi(cgs) = \frac{M}{H} = \frac{\frac{emu}{cm^3}}{Oe} = \frac{1000 \frac{A}{m}}{\frac{1000 \cdot A}{4\pi \cdot m}} = 4\pi (SI)$$
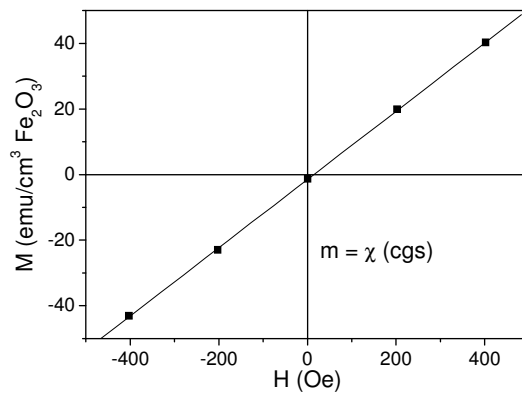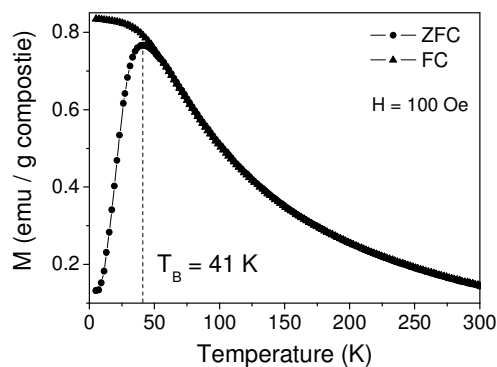
Figure 4.32. Representative magnetization data at low fields (scatter) and linear fitting (straight line) of a composite sample (298 K). The magnetization is referred to volume of magnetic material (cm^3) vs. field (Oe). The slope of the linear fitting corresponds to the magnetic susceptibility in cgs units (R = 0.99995).

Despite of the clustering of the iron oxide nanoparticles and the high pressure and temperature conditions during the silica synthesis, the iron oxide nanoparticles did not sinter neither they became ferromagnetic at room temperature. This is an important result for the biomedical applications to avoid embolism when administered via intravenously *i.v.*

ZFC-FC curves

Zero field cooling-field cooling curves (ZFC-FC) of a representative sample are shown in **Figure 4.33**. The ZFC curve presents a well defined narrow peak at low temperature. Its position is defined as the blocking temperature (T_B). The FC curve decays with increasing temperature. This is a typical profile of a superparamagnetic material. Since the maximum in ZFC is a sharp peak and the field-cooling curve separates from the zero field-cooling one just above the blocking temperature, it is confirmed that the system has a narrow magnetic particle size distribution. T_B ranges from 40 to 60 K in the composite particles. Below T_B the systems behave ferrimagnetically and superparamagnetically above it.

Figure 4.33. Representative ZFC-FC curves at 100 Oe of a composite sample.

AC measurements

Magnetic measurements in alternating current mode (ac mode) were performed to calculate the effective magnetocrystalline anisotropy constant (K_{eff}). The magnetization in an ac field is a complex number with a real component, the amplitude (in-phase magnetization, M'), and an imaginary component, the delay in the orientation of the magnetic spins with respect to the external applied field (out-of-phase magnetization, M''). The amplitude corresponds to the magnetization in dc mode. The experiments were done at different frequencies (f = 10, 100, 1000 and 10000 Hz) in the temperature range 5 - 150 K. These curves are analogous to the ZFC curves in dc mode. A low enough ac field was used to avoid non-linear magnetizing effects (0.137 Oe). A dc field of 10 Oe was also applied. The effective magnetocrystalline anisotropy constant (K_{eff}, J/m^3) can be calculated with **Equation 4.6**:

Equation 4.6
$$\ln f = \ln f_0 - \frac{K_{eff} \cdot V}{k_B \cdot T_{max}}$$

where V is the magnetic particle volume (m^3), k_B is the Boltzmann constant ($1.38 \cdot 10^{-23}$ J/K) and T_{max} is the temperature value at the maximal magnetization (K).

The left panel in **Figure 4.34** shows the out-of-phase (M'', above) and the in-phase (M', below) magnetization curves in ac field at different frequencies. Both sets of data clearly show maxima, attributed to the superparamagnetic character of the particles. The in-phase magnetization intensity (M') decreases with the frequency, because the particles have a shorter time to align with the external field. Shorter times facilitate observing the blocking of the spins in a given orientation. Then, the blocking temperature increases with frequency. On the other hand, the out-of-phase magnetization intensity (M'') increases with frequency. The right panel in **Figure 4.34** represents the ln frequency vs. the inverse of the maximal temperatures and their linear fitting. Data are listed in **Table 4.13**.

According to **Equation 4.6**, the slope of the straight line (m) is proportional to the volume of the magnetic entity and the magnetocrystalline anisotropy constant: m = - $K_{eff} \cdot V/k_B$. Since the magnetic size of the particle is known from the M(H) curves (see **Table 4.12**), which is 7.5 nm in diameter for sample SiFe_07_23, the anisotropy constant (K_{eff}) can be calculated: K_{eff} (M'') = $0.93 \cdot 10^5$ J/m^3 and K_{eff} (M') = $1.96 \cdot 10^5$ J/m^3. These values are of the same order of magnitude of previously reported ones around 10^5 J/m^3,[10] although there is some controversy about the real anisotropy values at the nanometric range. Another controversy lies on the value of anisotropy constant to be used, the one derived from the in-phase magnetization or the one from the out-of-phase one.[19]
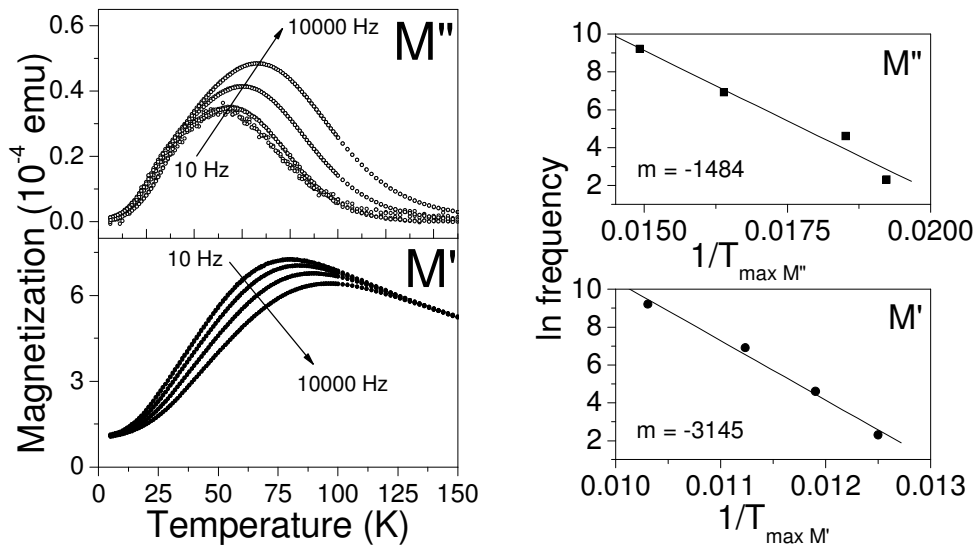
Figure 4.34. Left panel: magnetization vs. temperature in ac field at different frequencies of sample SiFe_07_23 (above: out-of-phase; below: in-phase). Right panel: ln frequency vs. inverse of maximum temperature (scatter) and lineal fittings (line) (above: values from out-of-phase measurements; below: in-phase).

Table 4.13. Numerical data on ac measurements of sample SiFe_07_23 (see **Figure 4.34**) used to calculate the effective anisotropy constant.

Frequency (Hz)	Ln f	T_{max} M' (K)	$1/T_{max}$ M' (1/K)	T_{max} M" (K)	$1/T_{max}$ M" (1/K)
10	2.303	80	0.01250	52	0.01923
100	4.605	84	0.01190	54	0.01852
1000	6.908	89	0.01124	61	0.01639
10000	9.210	97	0.01031	67	0.01493

Comparison between composite and iron oxide nanoparticles

The magnetic properties of the composite particles were compared to the magnetic properties of the original iron oxide nanoparticles finding interesting similarities and differences. **Table 4.14** gathers such data.

The ratio between the remanence and the saturation magnetization (M_R/M_S) is related to the interparticle interactions. A value of 0.5 is attributed to non-interacting superparamagnetic particles. A ratio higher than 0.5 corresponds to interacting FM particles and a ratio lower than 0.5 to SPM particles with demagnetizing interactions.[20] Then, the as-synthesized iron oxide nanoparticles in powder have stronger demagnetizing interactions than their composite counterparts (M_R/M_S = 0.24 vs. 0.37, respectively). The dipole-dipole interactions between superparamagnetic particles at room temperature with no external applied magnetic field may be negligible. However, in the presence of an external magnetic field, these interactions may become significant. The dipole-dipole

interaction energy (E_{d-d}) of two magnetic particles decays with the third power of the distance between their centres (r) as shown in **Equation 4.7**:

Equation 4.7
$$E_{d-d} = \frac{-2 \cdot m^2}{4\pi \cdot \mu_0 \cdot r^3}$$
(SI units)

where *m* is the magnetic moment per particle, $m = \mu_0 \cdot M \cdot V$, *M* is the magnetization per volume and *V* is the particle volume. **Equation 4.7** can be rewritten as:

Equation 4.8
$$E_{d-d} = \frac{-2 \cdot \mu_0^2 \cdot M_{vol}^2 \cdot V_{ptle}^2}{4\pi \cdot \mu_0 \cdot r^3}$$
**(SI units)**

Table 4.14. Magnetic properties of composite samples and the original iron oxide nanoparticles. Units: $[M_R/M_S]$ = adimensional in cgs units at 5 K, $[M_S]$ = emu/g Fe_2O_3 at 298 K, $[\chi]$ = adimensional in cgs units, $[\varnothing_{MAG}]$ = nm and $[T_B]$ = K.

Sample	Composite					Fe_2O_3 nanoparticles					$\dfrac{M_S \text{ comp}}{M_S Fe_2O_3}$
	$\dfrac{M_R}{M_S}$	M_S	χ	$\varnothing_{MAG}$	T_B	$\dfrac{M_R}{M_S}$	M_S	χ	$\varnothing_{MAG}$	T_B	
SiFe_07_26	0.33	56.0	0.104	6.6 ± 0.7	41	0.24	43.6	0.077	7.0 ± 0.7	41	1.3
SiFe_08_1	0.38	55.6	0.197	8.1 ± 0.8	60	0.26	35.4	0.063	7.6 ± 0.7	61	1.6
SiFe_08_3	0.38	58.8	0.121	6.7 ± 0.7	39	0.22	31.7	0.039	6.9 ± 0.7	48	1.9
SiFe_08_6	0.38	62.2	0.174	7.4 ± 0.7	61	0.27	26.2	0.042	8.1 ± 0.8	61	2.3
SiFe_08_7	0.39	59.8	0.168	7.4 ± 0.7	55	0.23	35.2	0.045	6.8 ± 0.7	57	1.7
SiFe_08_8	0.38	65.1	0.189	7.3 ± 0.7	57	0.24	-	-	-	61	-
SiFe_08_9	0.38	73.0	0.154	6.3 ± 0.6	41	0.23	26.8	0.032	7.3 ± 0.7	47	2.7
Average	**0.37**	**61.5**	**0.158**	**7.1**	**51**	**0.24**	**33.1**	**0.050**	**7.3**	**54**	**1.92**

Therefore, the coating of the iron oxide nanoparticles and their spatial distribution play a significant role in the dipole-dipole interparticle energy. If the particles align forming chains, the interparticle interactions generate an increase of magnetic susceptibility and coercivity.[21] But, if the particles form clusters, the interparticle interactions will act as a demagnetizing factor.[20] The larger the interparticle distance, the smaller the contribution of the dipole-dipole interaction to the total energy of the system. In some TEM images it can be clearly observed how the iron oxide nanoparticles inside the composite ones are not directly in contact, probably due to the existence of a thin shell of silica around each iron oxide nanoparticle (see **Figure 4.14**). However, the preformed iron oxide nanoparticles were analyzed in powder form (precipitated from colloidal dispersions

stabilized with electrolytes). In powder form, the electrolytes do not repel the particles and then demagnetizing interactions might be generated between them.

Saturation magnetization (M_S) is an intrinsic property of each material which varies with temperature and size at the nanometric range. The values of the composite samples are significantly higher than those of the iron oxide counterparts, even though the magnetic size has not increased during the supercritical conditions of the silica synthesis, as shown in **Table 4.14**. The average magnetic susceptibility (χ) at room temperature is three times larger in the composite samples. χ depends on the magnetization and also on the interparticle interactions. **Figure 4.35** illustrates a representative example of the higher susceptibility in composite samples compared to iron oxide ones. Since the net magnetization has increased significantly after the synthesis of the silica coating, the difference in susceptibility cannot be simply attributed to different interparticle interactions.
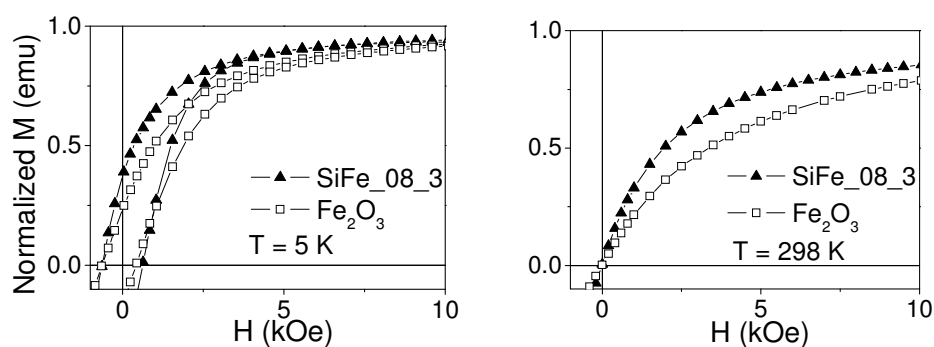
Figure 4.35. Normalized magnetization vs. magnetic field of a composite particle and its iron oxide counterpart. T = 5 K (left panel) and T = 298 K (right panel). The curves are normalized at 50 kOe.

The last parameter to be compared is the blocking temperature. It can be observed that this temperature does not change after the silica coating synthesis. The average value for all the original iron oxide nanoparticles and the composite ones are 54 and 51 K, respectively (see **Table 4.14**). When overlapping the ZFC-FC curves of a composite sample and its iron oxide counterpart new information is acquired (**Figure 4.36**). Although the T_B is very similar, 55 and 57 K for the composite and iron oxide, respectively, the net magnetization over 30 K is lower for the preformed iron oxide nanoparticles. This behaviour is once more attributed to higher dipole-dipole demagnetizing interactions in the iron oxide nanoparticles, in accordance with their lower M_R/M_S value.[22,23]
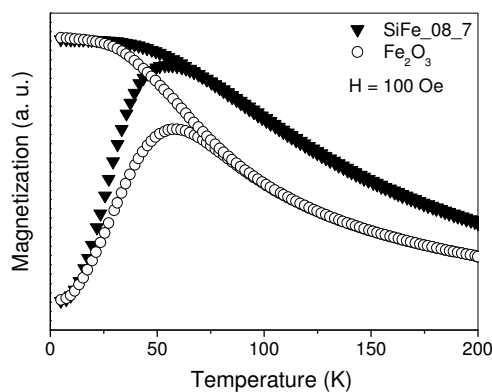
Figure 4.36. ZFC-FC curves of a composite sample and its iron oxide nanoparticles counterpart normalized at 5 K.

Increase of saturation magnetization after silica coating

Beside the above discussion, the most interesting result was the increment of saturation magnetization after synthesizing the silica core. We performed some extra analysis to find out its origin.

- Our first assumption was that the particle size increased during the supercritical conditions of the silica synthesis (250 $^{\circ}$C and 250 bar) due to the sintering of the original iron oxide nanoparticles. But, as it was proved with the magnetization measurements (see **Table 4.14**) the magnetic size did not change.

- Another hypothesis was the change of crystalline phase from maghemite to magnetite, since the last one has a higher bulk saturation magnetization, as shown in **Table 2.1**. This assumption was also proved wrong (see section 4.2.3).

- At present we believe that the increase of magnetization is due to an improvement in the crystallinity of the particles during the supercritical conditions of the silica coating. To check if the high temperature was responsible for the crystallinity improvement we performed two different experiments.

(a) The first one consisted of synthesizing two batches of iron oxide nanoparticles (synthesis type A): one standard batch (labelled as *Fe₂O₃_standard*) and another one with modified cooling procedure. In the standard batch the cooling lasted around 1 hour (see **Figure 2.1**). For the second batch, the cooling process took approx. 8 hours (labelled as *Fe₂O₃_slow*). The new procedure pretended to simulate the thermal treatment of the silica coating synthesis in supercritical media: the composite particles were cooled down slowly in 16 hours (see **Figure 3.8**). We hypothesized that the longer cooling time would induce a better crystallinity of

the outer shell of the iron oxide nanoparticles reducing the magnetic dead layer, and therefore increasing the saturation magnetization. We performed TGA analyses: sample *Fe₂O₃_slow* had a higher amount of oleic acid and it needed higher temperature to desorb it (see **Table 4.15**). The magnetic properties were measured finding no difference in the magnetization curves vs. magnetic applied field (see **Figure 4.37_left**). Consequently, the magnetic particle size was the same, 6.5 nm in diameter. The FC curves were similar (**Figure 4.37_right**) but the ZFC curves differed: sample *Fe₂O₃_standard* had higher blocking temperature than sample *Fe₂O₃_slow*. Since the particle size was the same, the lower blocking temperature of sample *Fe₂O₃_slow* may be attributed to a lower degree of interparticle interactions derived from the higher amount of oleic acid coating. **Table 4.15** lists the quantitative data derived from the TGA and the magnetometry analyses.
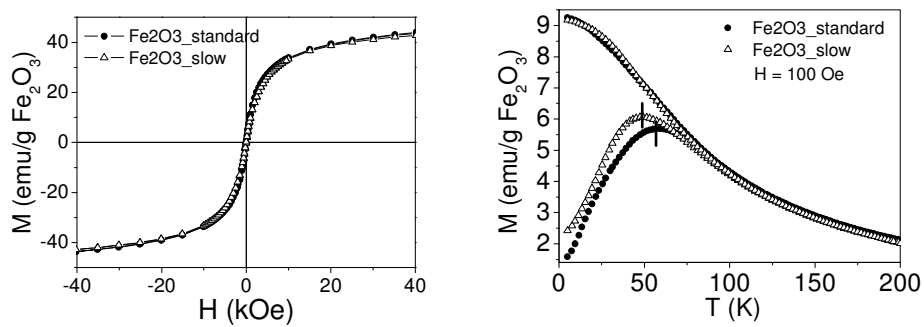
Figure 4.37. Magnetization curves for samples *Fe₂O₃_standard* and *Fe₂O₃_slow* vs. applied magnetic field (left panel) and ZFC-FC curves (right panel).

Table 4.15. TGA and magnetometry data on samples *Fe₂O₃_standard* and *Fe₂O₃_slow*.

Iron oxide sample	TGA			Magnetometry		
	Wt. % 1st Oleic acid (T)	Wt. % 2nd Oleic acid (T)	Wt. % Fe_2O_3	M_S (emu/g Fe_2O_3) (298 K)	$\varnothing_{MAG}$ (nm)	T_B (K)
Fe₂O₃_standard	42 (183°C)	10 (204°C)	41	45	6.5	59
Fe₂O₃_slow	66 (214°C)	16 (234°C)	13	43	6.5	49

Concluding, the longer cooling time did not change the saturation magnetization of the iron oxide nanoparticles, although the blocking temperature decreased, probably due to a better oleic acid coating.

(b) The second experiment to test if the increase of saturation magnetization was due to the temperature consisted in preparing the composite nanoparticles in bulk form: iron oxide nanoparticles dispersed in a bulk silica gel. The synthesis reads as follows: a methanol solution containing TMOS and water was cooled down in an

ice bath before adding an aqueous dispersion of iron oxide nanoparticles (the final molar ratio was TMOS/H_2O/methanol 1:4:12.25 and 1 wt.% Fe_2O_3). NH_3 was added as a catalyst to begin the hydrolysis and condensation reactions of the silicon precursor ([NH_3] = 0.065 M). The solution was distributed in small plastic boxes (4 ml in volume) before it gelified in a few minutes. Some gels were dried by evaporation of the solvent (identified as xerogels, XG) and some of them were supercritically dried (identified as aerogels, AG) following the same pressure and temperature conditions used in the synthesis of composite samples. The aerogel and xerogel samples were chemically equivalent to the composite and iron oxide nanoparticles, respectively. In addition, one of the xerogel samples was calcined at 250ºC under air for 24 h (XG-250ºC), simulating only the temperature conditions of the supercritical drying, but at atmospheric pressure. It has been reported that such calcination improves the crystallinity of the particles.[24]

Table 4.16. Main magnetic data on aerogel and xerogel composites. Saturation magnetization at 20 kOe (2 Tesla).

Sample	M_S (emu/g Fe_2O_3)	χ (cgs, adimensional)	$\emptyset_{MAG}$ (nm)
XG	35.6	0.048	6.9 ± 0.7
XG-250ºC	43.4	0.070	6.8 ± 0.7
AG	67.4	0.135	6.4 ± 0.7

The magnetization curves at 298 K are shown in **Figure 4.38**. After supercritical conditions, the saturation magnetization almost doubles, the susceptibility is three times bigger and the particle size is unaltered. The calcined xerogel also had higher M_S and χ than the xerogel, but the increase was not comparable to the one of the aerogel. Therefore, the temperature conditions in supercritical drying played a role in the improvement of the magnetization, although it was not the only determining factor.

We attribute the improvement in crystallinity to the growing of silica onto the iron oxide nanoparticles. It is well-known the high affinity of silica to iron oxide and we propose that it might contribute to considerably decrease the magnetic dead layer. At atomic level, the magnetization in maghemite is due to the superexchange interactions between iron ions through the oxygen atoms. This phenomenon is strongly dependent upon the Fe-O-Fe bond angle.[20] Consequently, the degree of crystallinity of the solid strongly influences its magnetic properties. The outer layer in iron oxide nanoparticles which is called dead layer (where the iron ions are not fully coordinated and the angle of the Fe-O-Fe becomes distorted) decreases the saturation magnetization of the nanoparticle. We postulate that, when silica grows around the iron oxide particles, the outer iron ions recover their full coordination state favouring the magnetic superexchange. Then, the dead layer thickness is reduced and the saturation magnetization increases.
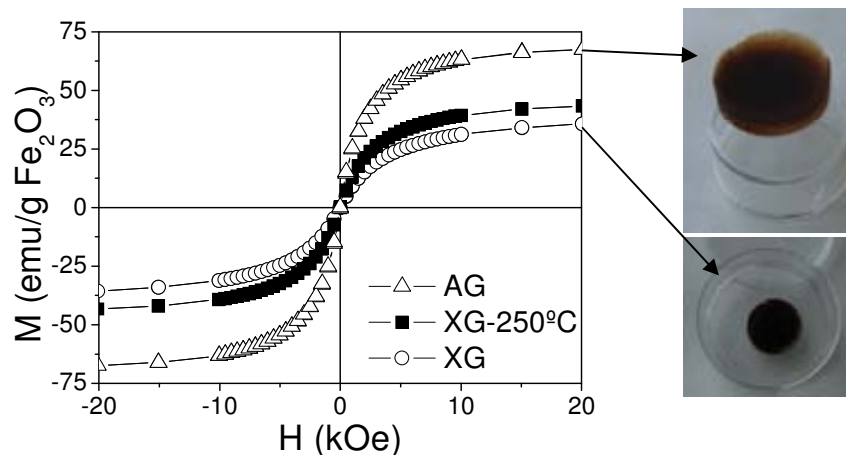
Figure 4.38. Magnetization curves vs. applied magnetic field at 298 K of xerogel (empty circles), calcined xerogel (full squares) and aerogel samples (empty triangles). The photographs at the right correspond to an aerogel (upper) and a xerogel monolith (lower). Note the volume difference, due to the different drying method: supercritical extraction (AG) vs. evaporation (XG).

4.3.   Comparison to pure silica particles

Chapter 3 reports on the synthesis of pure silica particles. This knowledge was later applied to coat iron oxide nanoparticles with a silica shell. We observed that the silica synthesized in the presence and absence of iron oxide nanoparticles showed some differences. This section is dedicated to summarize the similarities and differences between silica and composite particles, which will be used to propose a synthetic mechanism.

- The reactants (TMOS, acetone and water; except for the iron oxide) and the synthetic protocol are the same.

- The silica and composite particles were collected as dry powder dispersed all over the reactor volume.

- The chemical composition of the silica is equivalent in silica and in composite materials. It is composed of amorphous silica with no traces of organic residues, as observed by IR spectroscopy.

- The average yield of silica and composite particles was 32% and 47%, respectively. These values are in accordance with the concept of stabilization of the iron oxide nanoparticles in the initial sols by adsorption of TMOS molecules (as explained in section 4.1.1). It results a gradient of TMOS concentration, maximal at the iron oxide surface and minimal in the bulk solution. In this sense, the kinetics of the reaction is faster than in the absence of nanoparticles: TMOS starts hydrolyzing and condensating onto the iron oxide nanoparticles sooner than the formation of

140

the first pure silica nuclei (consequently, only composite particles are formed). The faster reaction kinetics leads to higher product yields in composite particles synthesis.

- The shape of the particles is different: silica particles are perfectly spherical with no necking at all, independently of their size, whereas composite particles can be spherical (with and without necking), worm-like or even heterogeneous in shape. Their shape is directly dependent on the magnetic cluster shape.

- The size range is also different: silica particles cover from 200 nm in diameter up to 4 microns, with a wide range of particle size distributions (from 5 to 50%). On the contrary, composite particles cover only from 70 to 200 nm in diameter and the particle size distribution varies from 10% to 17%. Some heterogeneous products were composed of small composite particles and bigger silica particles. Then, the reduction in size may be attributed to the addition of the iron oxide nanoparticles to the system. The higher number of nucleation sites might be the cause for the smaller composite particle size.

- Porosity. **Table 4.17** lists the average values of porous properties of the silica and composite particles. The silica particles have larger surface area, mainly microporous, and larger pore volume. The heterogeneous composite particles which were stored in two separate batches due to macroscopic heterogeneity showed two different pore properties: the brown powder was similar to the composite particles and the white powder similar to the silica ones. Then, it may be concluded that the introduction of iron oxide nanoparticles in the reactants solution lowers the silica surface area and pore volume, as well as the percentage of micropore area.

Table 4.17. Comparison of average porous properties of silica and composite samples.

Synthesis ID	Surface area (m^2/g SiO_2)	% Micropore area	C	Pore volume (cm^3/g)	Mean pore size (nm)
SiO_2	241	78	< 0	0.105	1.5
Composite	54	15	> 0	0.040	3.2

The common features are the open isotherms at low pressures and the ratio between percentage of micropore area and total surface area (**Figure 4.39**). Even the calcined samples follow this behaviour, what makes us think that all the particles share the same inner pore structure, independently on the total inner pore volume.
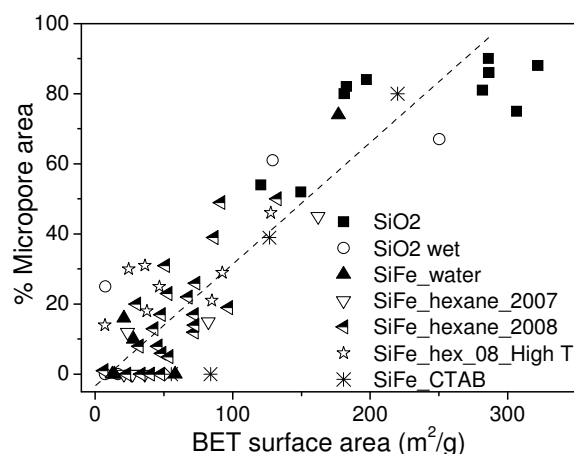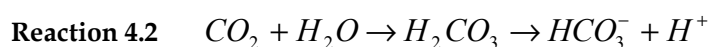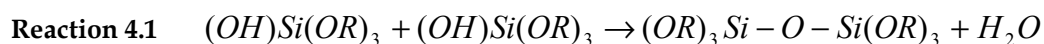
Figure 4.39. Relationship between micropore area and total BET surface area of all the silica and composite samples, including the calcined ones. The dashed line is a guide for the eye.

4.4. Proposed mechanism of silica formation in composite particles

The difference in product yield, particle shape and size between silica and composite particles has already been justified by the adsorption of TMOS onto the iron oxide surface, what creates a gradient of TMOS concentration. In this section a synthetic mechanism for the silica is formulated to justify the different porous properties.

Firstly, a short note on carbon dioxide is included. Carbon dioxide plays an active role in the synthetic process, besides being a co-solvent and pressurizing agent. Carbon dioxide speeds up the silica condensation reaction (**Reaction 4.1**) because it shifts the reaction to the right side (to the products) since it uses the water to form carbonic acid (**Reaction 4.2**).

Reaction 4.1 $\quad (OH)Si(OR)_3 + (OH)Si(OR)_3 \rightarrow (OR)_3 Si - O - Si(OR)_3 + H_2O$

**Reaction 4.2** $\quad CO_2 + H_2O \rightarrow H_2CO_3 \rightarrow HCO_3^- + H^+$

A consequence is the acidification of the medium. Irina Smirnova proved that the acidic medium does not catalyze the formation of silica by testing different acids.[25] We performed an experiment repeating the synthetic conditions of experiment SiFe_08_23 but with no CO_2 pressurization, only temperature increase. Only 2% of mass yield was obtained. There was almost no silica formation. We also performed experiments in a small autoclave (10 ml) with a small glass window and a video camera to record the experiments (THAR autoclave; see annex 7.3.8). We observed that only the combination of high temperature and carbon dioxide injection caused silica particle formation. Only temperature or only pressure increase did not produce particles. We concluded then that CO_2 plays an active role in the silica synthesis.

Based on the relationship shown in **Figure 4.39**, we hypothesize that the silica shell in composite particles grows as porous as the silica particles, but it collapses due to an inappropriate supercritical drying. Then, our hypothesis is as follows: the pure silica particles nuclei are formed in the liquid acetone and are dispersed all over the volume when the acetone changes to the supercritical phase. They grow further in the supercritical phase and then, they are supercritically dried by the extraction of the supercritical solvent to the gas phase (see **Figure 3.19**). They end to be microporous particles. The medium inside the autoclave follows the phase pathway: liquid → supercritical → gas (**Figure 3.5_b**).

We observed experimentally that the Pyrex vessel in composite particles syntheses showed iron oxide rings after the experiments. These tracks indicate that the liquid acetone is solubilized progressively in the gaseous carbon dioxide, in such a way that the liquid volume is reduced and the gas volume is increased up to the total change to supercritical phase. Then, we hypothesize the composite particles formation as follows (see **Figure 4.40**): the sol is prepared (step i) and pressurized (step ii) with increase of temperature. Nucleation of silica takes place at the iron oxide surface, faster than in the absence of iron oxide (white corona around the black dots; step iii_a). As the temperature increases, the particles grow (step iii_b). While the gas phase becomes richer in acetone there is no liquid phase enough to cover the composite particles: they are found in the gaseous phase (step iii_c). At this step the silica network collapses and the porous structure is partially destroyed. Later, the system reaches the supercritical conditions (step iii_d) but the supercritical drying of the particles (step iv) can not compensate the network collapse. The final composite particles are less porous than the silica ones (step v). The medium inside the autoclave follows the phase pathway: liquid → gas → supercritical → gas. This more compact structure of composite particles matches the non-accessibility of HCl to the iron atoms through the silica shell.

Concluding, the reason for the different porous properties may lie on their different reaction kinetics what may have altered the optimum phase pathway liquid → supercritical → gas (silica particles) to the non-desirable liquid → gas → supercritical → gas (composite particles). Further experiments to fully prove this hypothesis are needed.
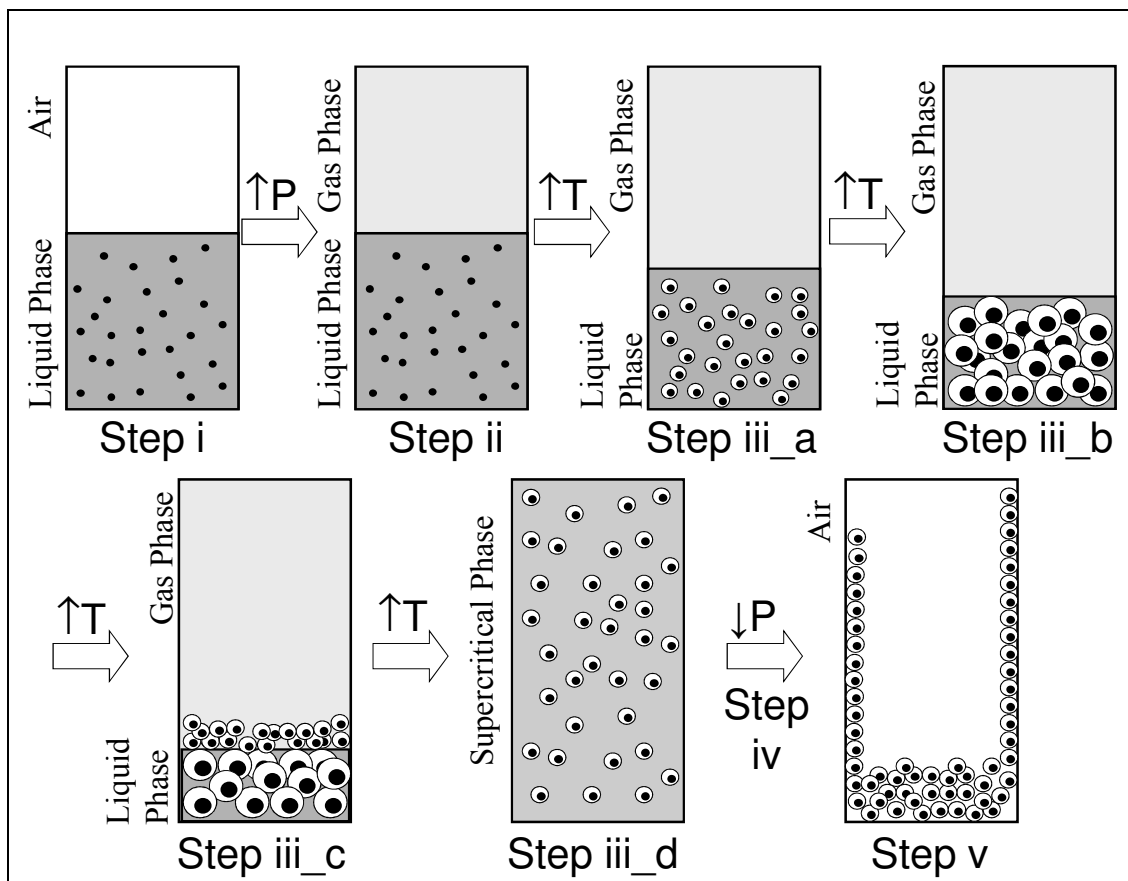
Figure 4.40. Scheme of proposed synthetic mechanism of composite particles. The black dots represent the magnetic clusters formed of several iron oxide nanoparticles; the white shells around the black dots represent silica.

4.5.   Synthesis of composite ε-Fe₂O₃@SiO₂ nanoparticles

A new route to produce single crystals of ε-Fe$_2$O$_3$@SiO$_2$ individually wrapped in a silica shell was also developed. Formation of ε-Fe$_2$O$_3$@SiO$_2$ composite nanoparticles was achieved by controlled recrystallization of γ-Fe$_2$O$_3$@SiO$_2$ nanoparticles.

Epsilon iron-oxide (ε-Fe$_2$O$_3$) is a metastable ferric oxide which has been stabilized as a pure nanophase in the form of nanoparticles,[26,27] nanorods[28] or nanowires[29]. Spherical particles, nanowires and nanorods were produced in silica matrices via sol-gel inspired methods followed by heat treatments at relatively high temperatures. This polymorph is ferrimagnetic and presents an uncommon high coercivity of 2 Tesla at room temperature (20 kOe), low saturation magnetization (15 emu/g) and moderate anisotropy (5·10⁵ J/m³). In addition, its magnetic and dielectric properties are coupled.[30]

It is well known that maghemite (γ-Fe$_2$O$_3$) is a metastable polymorph at the nanoscale that transforms to hematite (α-Fe$_2$O$_3$) around 400°C. However, the stability of γ-Fe$_2$O$_3$ can be maintained up to 1000°C when the nanoparticles are confined in a silica matrix. Above this

temperature, and for a given range of crystallite sizes, the transformation into ε-Fe$_2$O$_3$ begins. This has been explained in terms of a lower bulk free energy and higher surface energy values of the epsilon phase as compared to maghemite.[31,32]

The interest in ε-Fe$_2$O$_3$ is owed to its rich magnetic phase diagram and magnetoelectric properties not found in other simple ferric oxides. However, the potential of this material has not been fully exploited because of the difficulties encountered, initially obtaining the material as a pure phase, and lately producing it in a suitable shape useful to be integrated in devices. The majority of systems investigated up to now have been nanocomposite powders of ε-Fe$_2$O$_3$ nanoobjects in a silica matrix or aggregates of epsilon particles or nanowires without supporting matrix. Nanocomposite spheres have recently been reported[33] although the shape of the reported magnetic loops reveals that ε-Fe$_2$O$_3$ only represented a minor fraction of the ferric oxide phases. We have moved a step further and we have obtained single crystals of ε-Fe$_2$O$_3$ with high purity (90 wt.%) stabilized with a silica coating.

Synthesis

Composite ε-Fe$_2$O$_3$@SiO$_2$ nanoparticles were obtained by calcination of γ-Fe$_2$O$_3$@SiO$_2$ nanoparticles in air at 1100ºC following a stepwise heating protocol: 3 hours of calcination every 100ºC from 300ºC to 1100ºC. Extra experiments modifying the highest calcination temperature (T$_{max}$) and the calcination time at T$_{max}$ were performed in order to increase the fraction of ε-Fe$_2$O$_3$. Results on sample SiFe_08_19 will be presented. It belongs to the composite *SiFe_hexane* group. The experiments will be labelled with T$_{max}$ and time at T$_{max}$ (i.e. SiFe_08_19_1100ºC_6h).

The crystalline phase and the magnetic properties were determined by XRD and magnetic measurements. TEM images were used to monitor the shape and size change of the inner iron oxide nanoparticles and the composite particles. Colloidal stability and hydrodynamic size were also studied.

XRD and magnetometry: follow-up of crystalline phase transformation

The calcination of sample SiFe_08_19 up to 1100ºC for 6 hours already transformed maghemite into epsilon iron oxide, as observed by XRD (see **Figure 4.41**). Measurements of magnetization vs. magnetic field indicate that the original maghemite, which could not be identified by XRD, is still present in a greater or lesser extent in the annealed materials. This is evidenced by the shape of the curves (truncated hysteresis loop), the value of the saturation magnetization (in between that one of maghemite and ε-Fe$_2$O$_3$) and the value of the coercive field (lower than the one of ε-Fe$_2$O$_3$) (see **Figure 4.42**). Knowing that the saturation magnetization of the starting material is 57 emu/g Fe$_2$O$_3$ and the room

temperature magnetization of pure ε-Fe$_2$O$_3$ at 50 kOe is 15 emu/g, we can intrapolate the magnetic composition of the sample annealed at 1100°C for 6 h to be about 90 wt.% ε-Fe$_2$O$_3$ and 10 wt.% γ-Fe$_2$O$_3$.
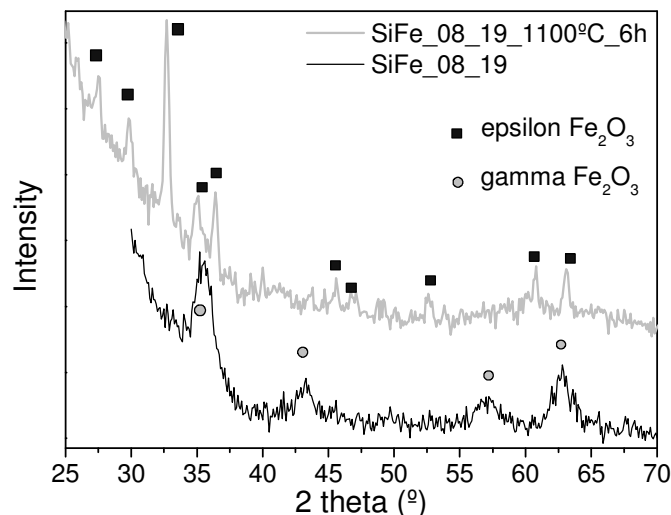

**Figure 4.41.** X-Ray diffractograms of samples SiFe_08_19 (black line) and SiFe_08_19_1100°C_6h (grey line).
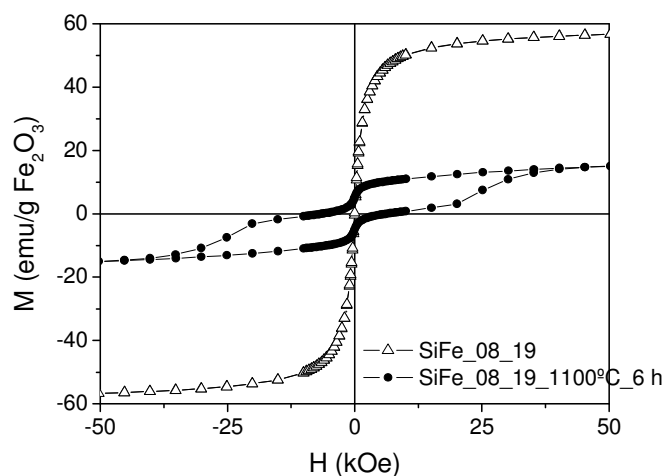
Figure 4.42. Magnetization curves of samples SiFe_08_19 (empty triangles) and SiFe_08_19_1100°C_6h (full circles) at 298K.

New experiments with longer calcination times at 1100°C were performed. The objective was to favour the formation of epsilon phase at the sacrifice of maghemite and reach the huge coercitive field of ε-Fe$_2$O$_3$ (20 kOe) while still maintaining the spherical shape of the composite particles. **Figure 4.43** shows the x-ray diffractogram of samples calcined at 1100°C for 6, 30 and 96 hours, respectively. The left graph zooms the low 2θ area. The broad hump centred at 22° in sample SiFe_08_19 corresponds to the amorphous silica. As the sample was calcined for longer times, this broad peak became more intense and narrower, indicating the crystallization of the amorphous silica into cristobalite.

146
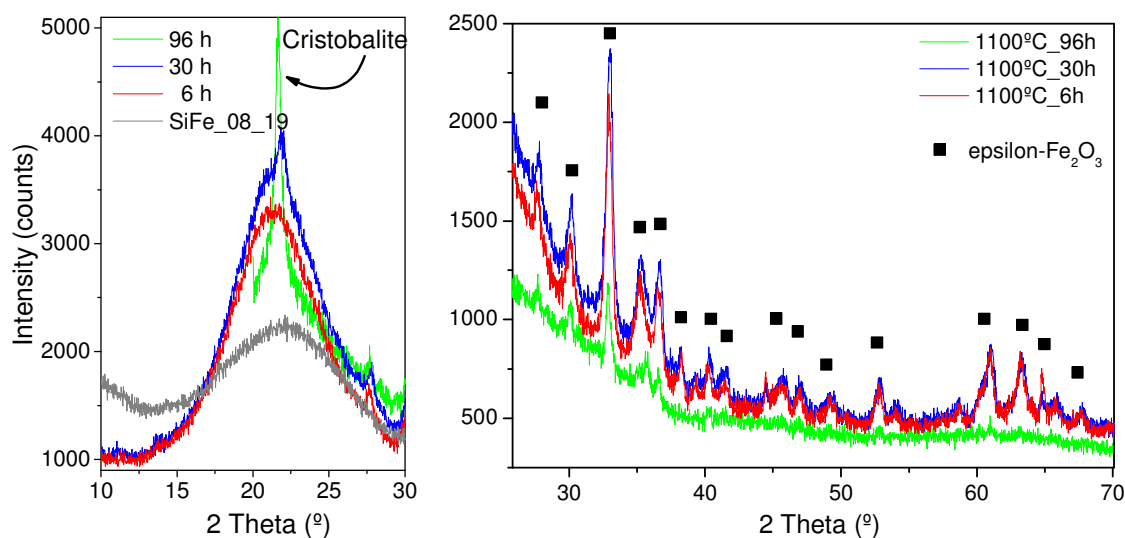
Figure 4.43. XRD of sample SiFe_08_19 calcined at 1100ºC for different times. Left graph: zoom on the most representative peak of silica. Right graph: most representative peaks of epsilon.

The diffraction peaks corresponding to the epsilon iron oxide are easily identified in samples 1100ºC_6h and 1100ºC_30h (see right graph in **Figure 4.43**). In sample 1100ºC_96h the identification of ε-Fe$_2$O$_3$ phase was difficult due to the low sample signal intensity. **Figure 4.44** shows the magnetization curves of samples calcined at 1100ºC for 10, 30 and 96 h, respectively. It was also tested the annealing at 1000ºC for 96h. The lowest coercive field and higher saturation magnetization corresponded to this last sample, indicating that it beard the highest amount of maghemite. Coercive fields increased in samples calcined at 1100ºC with increasing calcination time, reaching up to 20.1 kOe, which corresponds to the value of pure epsilon. The optimised material in terms of the smaller amount of maghemite is found for the sample annealed at 1100ºC during 30 hours. The M$_s$ value for the sample annealed during 96 h is slightly lower than for pure epsilon pointing out to a small amount of hematite (less than 5%) as a consequence of the onset of silica crystallisation, as seen in **Figure 4.43**.
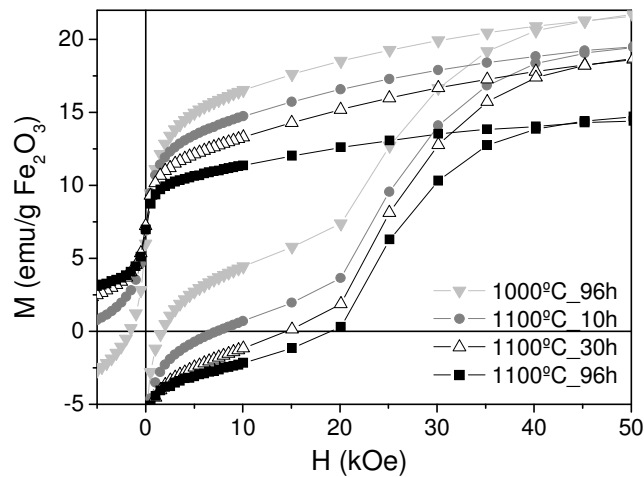
Figure 4.44. Magnetization curves of sample SiFe_08_19 calcined at different temperatures and times.

Another experiment consisted in annealing the sample up to 1300ºC. Silica was totally transformed into cristobalite, as shown in **Figure 4.45_left**. When zooming the lower intensity area (right graph) a mixture of epsilon iron oxide, hematite and magnetite was identified. Then, the stabilization temperature of epsilon iron oxide was surpassed at 1300ºC.
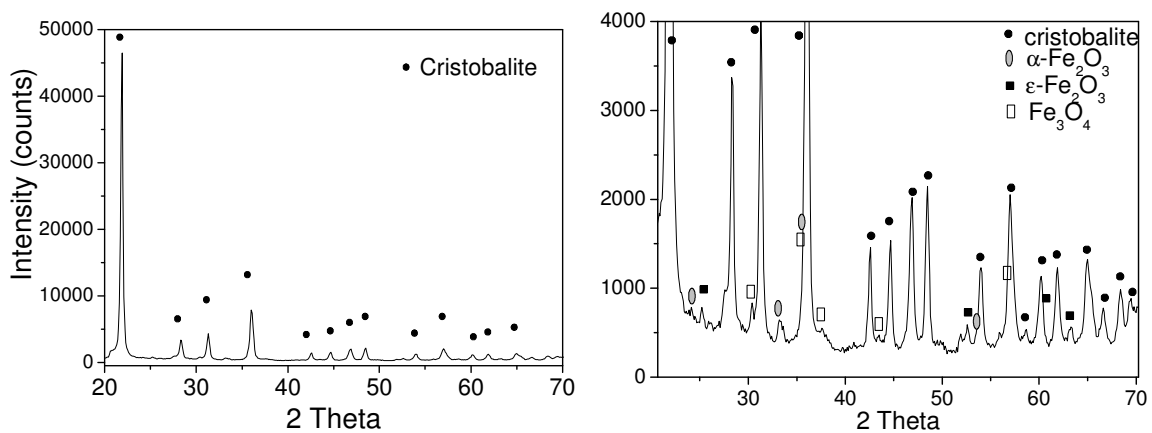

Figure 4.45. XRD of sample SiFe_08_19_1300ºC. Left graph: whole diffractogram. Right graph: zoom at low intensities (note the difference in intensity count number between the graphs).

TEM analysis: evolution of particle size and shape

Particle morphology was checked by TEM. The original material SiFe_08_19 was formed by spherical composite γ-Fe$_2$O$_3$@SiO$_2$ nanoparticles with several iron oxide nanoparticles clustered in the centre. After calcination at 1100ºC for 6 h the composite particle shape did not change. On the contrary, the clustered γ-Fe$_2$O$_3$ nanoparticles sintered in one single

ε-Fe$_2$O$_3$ nanoparticle, also placed at the centre of the silica shell, with diameters ranging from 20 to 100 nm (see **Figure 4.46**).
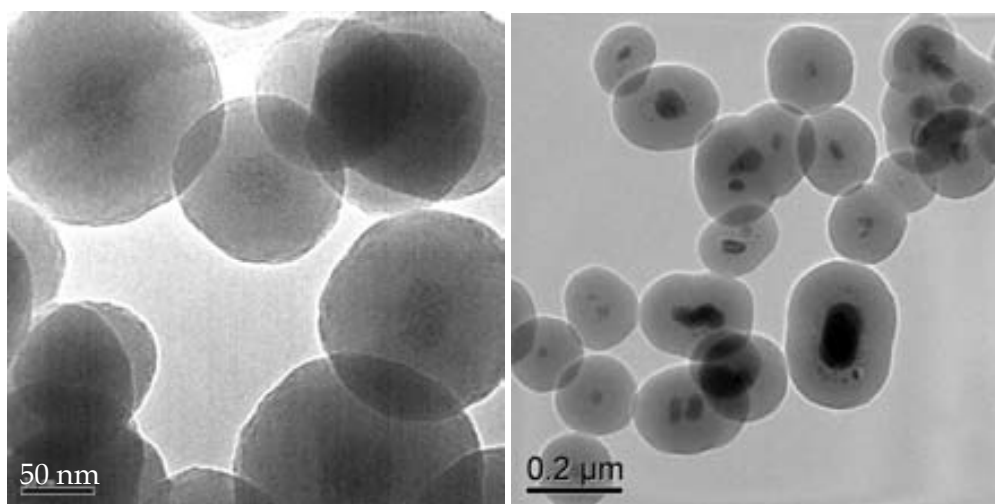
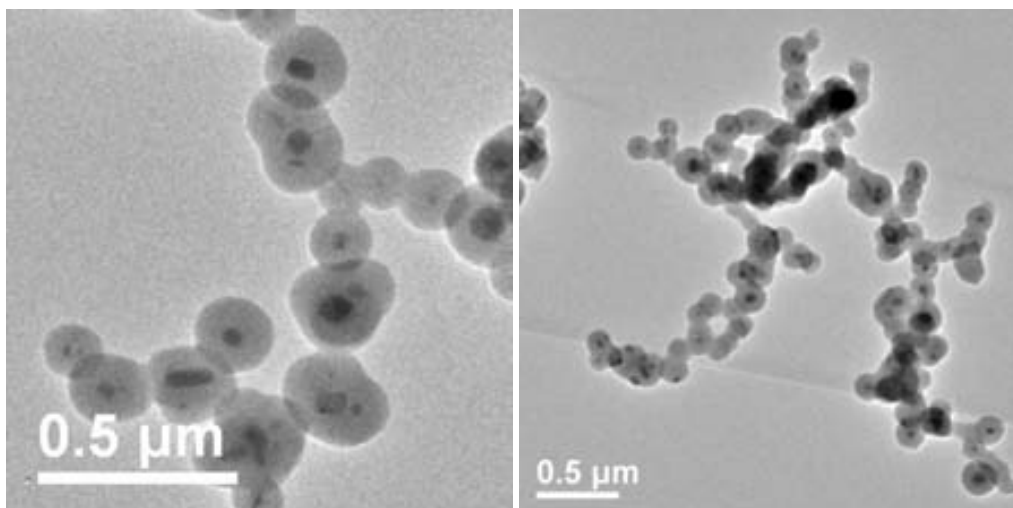
Figure 4.46. TEM images of samples SiFe_08_19 (left) and SiFe_08_19_1100°C_6h (right).

Figure 4.46_right and **Figure 4.47** show the "satellites" of what we assume are maghemite nanoparticles around the central epsilon particle. As assessed from magnetization measurements, maghemite is less than 10 wt.%. **Figure 4.47** zooms one single ε-Fe$_2$O$_3$ particle showing the interplanar distances corresponding to the zone axis [411].
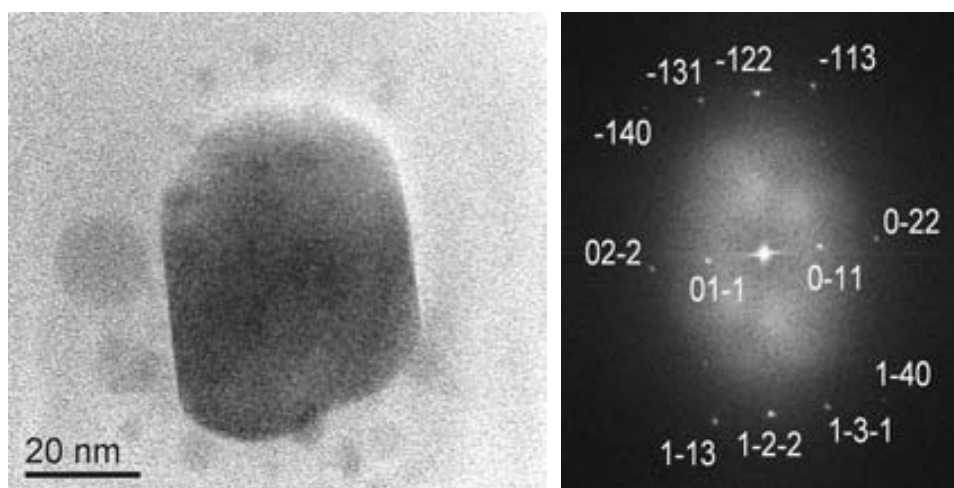
Figure 4.47. Left: TEM image zoomed in the centre of a composite sample showing an epsilon iron oxide particle and maghemite "satellite" smaller particles around it. Right: electron diffraction image with indexation of the planes, corresponding to the zone axis [411].

Annealing at 1100°C for 30 hours caused the silica shell to begin to sinter and, even though the spherical shape was well maintained, some necking between the particles started to appear. This is more pronounced for the sample annealed at 96 h, as shown in **Figure 4.48**.

Figure 4.48. TEM images of samples SiFe_08_19_1100ºC_30h (left image) and SiFe_08_19_1100ºC_96h (right image).

Finally, the particles annealed up to 1300ºC, whose silica was completely crystallized to cristobalite, showed irregular shapes (see **Figure 4.49**).
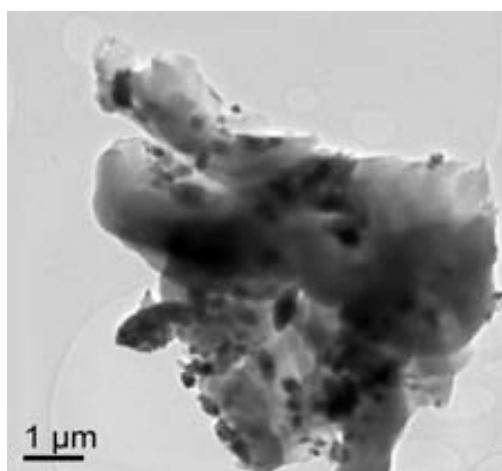
Figure 4.49. TEM image of sample SiFe_08_19_1300ºC.

The most relevant data on ε-Fe$_2$O$_3$@SiO$_2$ particles described above is listed in **Table 4.18**. Data on samples SiFe_08_19 and SiFe_08_19_700ºC have been added for completeness.

**Table 4.18.** Characterization data on selected samples derived from the calcination of SiFe_08_19. α stands for α-Fe$_2$O$_3$(hematite), γ stands for γ-Fe$_2$O$_3$(maghemite), ε stands for ε-Fe$_2$O$_3$, C stands for cristobalite. Magnetic data were measured at 298K.

Sample ID	XRD phase	Magnetic phase	H$_C$ (kOe)	M$_S$ (emu/g Fe$_2$O$_3$)	TEM observations
SiFe_08_19	γ	γ	0	56.7	Spherical composite particles; γ-Fe$_2$O$_3$ nanoparticles 7 nm
SiFe_08_19 _700°C	γ	γ	0	56.0	-
SiFe_08_19 _1000°C_96h	-	ε + γ	1.5	21.7	-
SiFe_08_19 _1100°C_6h	ε	ε + γ	-	-	Spherical composite particles; ε-Fe$_2$O$_3$ NPs in the centre > 20 nm + γ-Fe$_2$O$_3$ NPs
SiFe_08_19 _1100°C_10h	ε	ε + γ	7.5	19.5	-
SiFe_08_19 _1100°C_30h	ε + C	ε + γ	15.1	18.7	Spherical composite particles with a small degree of necking; ε-Fe$_2$O$_3$ NPs in the centre > 20 nm + γ-Fe$_2$O$_3$ NPs
SiFe_08_19 _1100°C_96h	ε + C	ε + γ	20.1	14.4	Spherical composite particles with a higher degree of necking; ε-Fe$_2$O$_3$ NPs in the centre > 20 nm + γ-Fe$_2$O$_3$ NPs
SiFe_08_19 _1300°C	C + α + Fe$_3$O$_4$	-	-	-	Irregular shape

Colloidal stability and DLS measurements

The composite particles could be easily dispersed as colloids in several polar solvents (water, ethanol and acetone) and they were undispersible in hexane. **Figure 4.50_left** displays the dispersions for the γ-Fe$_2$O$_3$/SiO$_2$ (a), Fe$_2$O$_3$_1100°C_6h (b) and Fe$_2$O$_3$_1100°C_30h (c) samples (0.5 mg/ml). Such dispersions are stable for around 12 h although they get easily re-dispersed by a short sonication. Colloidal suspensions of materials calcined for shorter time periods (6 h to 10 h) are more stable than the ones treated for longer times (30 h to 96 h). In the later case, necking formation within the particles produces larger aggregates and induces faster sedimentation. Dispersion light scattering (DLS) measurements were also performed (see **Figure 4.50_right**). In our case, the DLS size is about double than the one determined by TEM. This concerns to both the as-obtained materials and the calcined ones and we ascribe it to the formation of dimmers. Such result does not prevent the colloidal stability of the system.
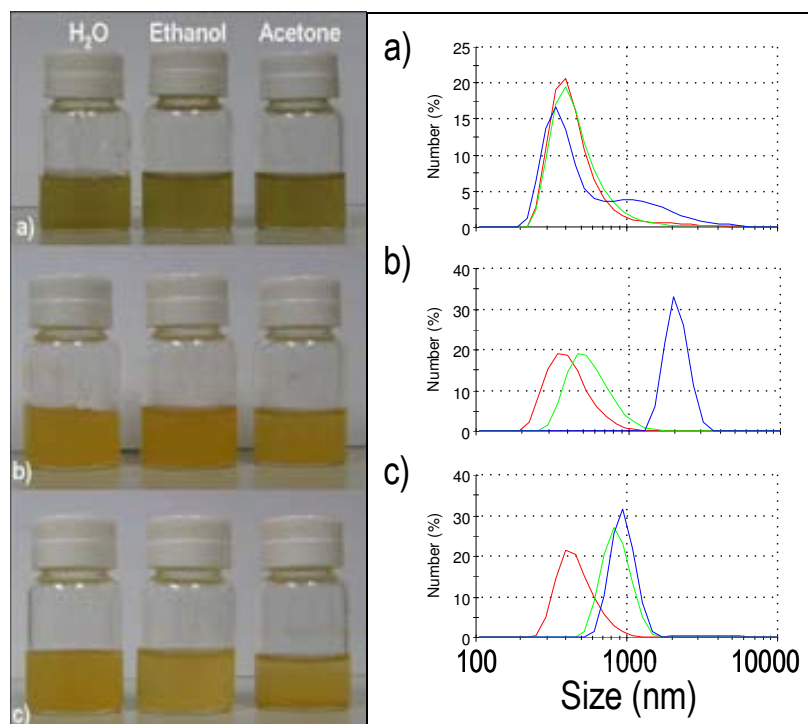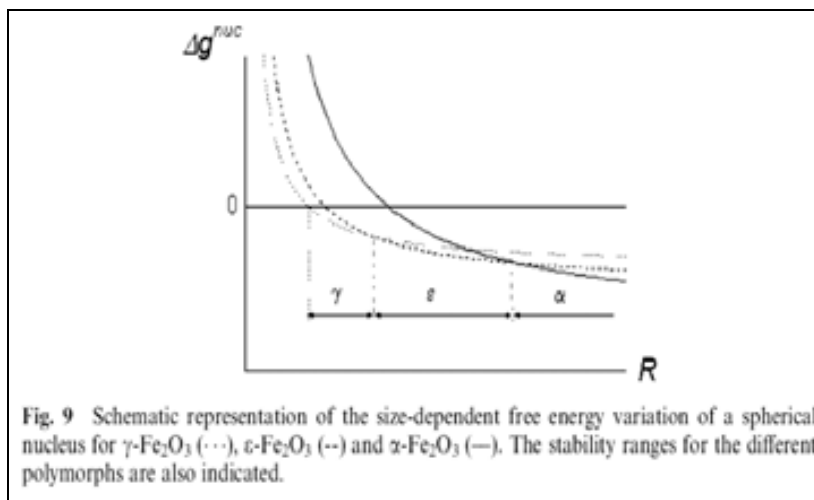
Figure 4.50. Left panel: photographs of the colloidal dispersions in water, ethanol and acetone for the a) γ-Fe$_2$O$_3$/SiO$_2$, b) Fe$_2$O$_3$_1100ºC_6h and c) Fe$_2$O$_3$_1100ºC_30h samples (0.5 mg/ml). Right panel: DLS size distribution by number of γ-Fe$_2$O$_3$/SiO$_2$ (red), Fe$_2$O$_3$_1100ºC_6h (green) and Fe$_2$O$_3$_1100ºC_30h (blue) samples in a) water, b) ethanol and c) acetone for a concentration of 0.5 mg/ml.

Discussion

The crystalline phase of the magnetic nanoparticles in composite *SiFe_hexane* samples did not change by annealing in air up to 1000ºC. Between 1000ºC and 1100ºC took place the formation of epsilon iron oxide through the sintering of the small maghemite nanoparticles into bigger epsilon ones. The crystalline phase conversion was not complete, probably due to maghemite particle hindrances to migrate through the silica matrix. In **Figure 4.46** and **Figure 4.47** it is clearly visible the "satellite" small nanoparticles around the central epsilon particle which are attributed to maghemite traces.

As mentioned in the introduction and confirmed by this work, the stability of γ-Fe$_2$O$_3$ nanoparticles can be maintained up to 1000ºC when the particles are confined in a silica matrix. Above this temperature, and for a given range of crystallite sizes, the transformation into ε-Fe$_2$O$_3$ starts. This has been explained in terms of a lower bulk free energy and higher surface energy values of the epsilon phase as compared to that of maghemite (see **Figure 4.51**).[31,32] Our nanocomposite particles follow this same pattern. The silica coating limits the particle growth and enables the formation of epsilon iron oxide single crystals except for the outermost maghemite crystals unable to migrate close

enough to the large epsilon crystal. At 1300°C the amorphous silica shell crystallizes to cristobalite and the iron oxide phase segregates and grows further, forming hematite and magnetite.

Fig. 9 Schematic representation of the size-dependent free energy variation of a spherical nucleus for γ-Fe$_2$O$_3$ (···), ε-Fe$_2$O$_3$ (--) and α-Fe$_2$O$_3$ (—). The stability ranges for the different polymorphs are also indicated.

Figure 4.51. Schematic representation of the size-dependent (R ≡ radius) free energy (Δg_{nuc}) variation of a spherical nucleus for γ-Fe$_2$O$_3$ (…), ε-Fe$_2$O$_3$ (- - -) and α-Fe$_2$O$_3$ (----). The stability intervals for the different polymorphs are also indicated.[31]

An advantage of this synthetic method over the already known is the possibility of synthesizing non-aggregated single ε-Fe$_2$O$_3$ crystals. The thick silica shell weakens the dipole-dipole interactions between composite particles avoiding aggregation due to magnetostatic attraction thus facilitating their stability in powder form as well as in aqueous and alcoholic solutions which in turn broadens its potential. The size of the epsilon crystallites might be modulated by selecting maghemite@silica composite particles with different magnetic cluster size, as described in section 4.2.2.

4.6.   Conclusions of Chapter 4

We have developed a novel method to coat iron oxide nanoparticles with silica combining sol-gel chemistry and supercritical fluid technology. The stabilization of the initial sol was achieved by following the reactive addition sequence: acetone-TMOS-water-Fe$_2$O$_3$_hexane. Other orders of addition resulted in unstable colloidal dispersions. The iron oxide nanoparticles formed clusters in the reactants sol. The cluster size depended on the acetone to hexane volume ratio. Few experiments were performed with the addition of a porogenic agent, following the addition sequence: acetone-TMOS-water-Fe$_2$O$_3$_hexane (one night still)-CTAB_methanol. Stability of the reactant colloidal dispersion resulted essential for the homogeneity of the final composite particles.

SiFe_hexane samples were obtained as dry and light powders. They were solvent-free, with no traces of unreacted species, as seen from IR. This fact constitutes an advantage

compared to other sol-gel methods, because it avoids the time consuming purification and drying steps. The particles were then redispersible in polar solvents, such as water, ethanol and acetone.

SiFe_hexane particles were built up of a magnetic core composed of clustered iron oxide nanoparticles surrounded by the silica shell. The shape was spherical or worm-like, depending on the initial magnetic cluster shape. The composite size, which was directly dependent on the magnetic cluster size, ranged from 70 to 200 nm with particle size dispersions lower than 17%. Consequently, the composite particle size could be modulated by the acetone to hexane volume ratio in the reactant solution.

XRD analyses revealed the presence of amorphous silica and iron oxide. There was no change of crystallite size compared to the initial iron oxide nanoparticles, meaning that no particle sintering took place during the supercritical conditions. By magnetometry the iron oxide phase was identified as maghemite, discarding the presence of magnetite.

Porous properties of composite samples were analyzed by nitrogen adsorption/desorption isotherms. The resulting BET surface areas were lower than expected when compared with the silica particles, with values lower than 100 m^2/g SiO_2 and low degree of microporosity (< 15%). Calcined samples showed a maximum of S_{BET} at 300ºC. The decrease of S_{BET} above this temperature is related to the collapse of the silica network at high temperatures. Considering the external surface area, estimations on the internal porosity of the particles were done, obtaining low values for the composite particles and high values for the silica ones. Different strategies were tested to increase the porosity, including the addition of a porogenic agent (*SiFe_hexane_CTAB* samples), without much success. It was observed with an HCl test that the iron oxide nanoparticles were scarcely accessible through the silica shell.

Composite particles are superparamagnetic at room temperature, with small coercivity at 5K (550-680 Oe) and blocking temperature between 40 and 60K. The mean magnetic particle size calculated from the susceptibility at low field at RT is 7 ± 1 nm. These results indicate that the particles have not grown during the supercritical conditions, neither sintered nor become ferromagnetic. This is an important result for the biomedical applications to avoid embolism when administered via intravenously *i.v.* The anisotropy constant was calculated from the magnetization vs. temperature curves in ac-field, resulting in $0.93 \cdot 10^5$ J/m^3 when calculated from the out-of-phase magnetization (M″) and $1.96 \cdot 10^5$ J/m^3 when calculated from the in-phase magnetization (M′). The comparison of the magnetic properties with the original iron oxide nanoparticles showed that the composite particles have lower demagnetizing interactions (M_R/M_S = 0.24 vs. 0.37, for iron oxide and composite particles, respectively), attributed to a lower dipole-dipole interaction energy due to a thin silica shell coating each iron oxide nanoparticle. The blocking temperature did not change, but the ZFC-FC curves also showed the higher

dipole-dipole demagnetizing interactions in iron oxide nanoparticles. The saturation magnetization (M_S) in composite samples almost doubled the one in iron oxide nanoparticles (61.5 vs. 33.1 emu/g Fe_2O_3), the susceptibility was tripled (0.158 vs. 0.050, adimensional in cgs units) and the magnetic particle size remained the same (7 ± 1 nm). We attribute the increase of M_S to an improvement of the iron oxide crystallinity due to the silica growing onto its surface at high temperature. The dead layer thickness is reduced with a consequent increase in the net magnetization of the particles.

The silica and composite particles showed several differences when using the same reaction conditions: product yield, particle shape and size and the porous properties. The three first differences were attributed to a selective adsorption of TMOS onto iron oxide nanoparticles what induces faster kinetics of hydrolysis and condensation of silica, giving rise to higher yield, smaller particles and particle shape dependent on the iron oxide cluster shape. A reaction mechanism was proposed to explain the lower porosity of the composite particles. It was attributed to an inefficient supercritical drying. The different reaction kinetics altered the optimum phase pathway liquid → supercritical → gas (silica particles) to the non-desirable liquid → gas → supercritical → gas (composite particles) which produced the collapse of the porous silica shell. Further experiments are needed to confirm this hypothesis.

Epsilon iron oxide@silica nanospheres were synthesized by calcination in air of maghemite@silica composite particles at different temperature and time. This is the first time, to the extent of our knowledge, that ε-Fe_2O_3@SiO_2 nanospheres with 90 wt.% of ε-Fe_2O_3 (wt.% of magnetic phase) are synthesized. The ε-Fe_2O_3 phase was identified by XRD and magnetometry measurements. TEM images showed one ε-Fe_2O_3 particle (20 to 100 nm in size) in each composite particle. By annealing up to 1100ºC for different times we obtained 90% of epsilon-Fe_2O_3, with coercivity up to 20 kOe and saturation magnetization around 15 emu/g Fe_2O_3, similar to the bulk phase. The 10% mass left corresponded to γ-Fe_2O_3 nanoparticles, which appeared as "satellites" around the ε-Fe_2O_3 particle. The spherical shape of the original composite particles was maintained up to 96 h of annealing at 1100ºC, although some necking appeared from 30 h on and silica began to crystallize into cristobalite. At 1300ºC the particle shape was completely lost due to the total formation of cristobalite; hematite and magnetite were formed. Particles were dispersible in water, ethanol and acetone, making them more versatile for technological applications. It is envisaged that the crystal size of ε-Fe_2O_3 could be controlled by starting from composite γ-Fe_2O_3@SiO_2 particles with different cluster size.

4.7.   Bibliography and notes of Chapter 4

1. Day, C.; Chang, C.; Chen, C. Phase equilibrium of ethanol + CO_2 and acetone + CO_2 at elevated pressures *J. Chem. Eng. Data* **1996** 41, 839-843.

2. Nemati Lay, E.; Taghikhani, V. And Ghotbi C.; Measurement and correlation of CO_2 solubility in the systems of CO_2 + toluene, CO_2 + benzene and CO_2 + hexane at near-critical and supercritical conditions, *J. Chem. Eng. Data* **2006** 51, 2197-2200

3. Chang, C.; Day, C.; Ko, C.; Chiu, K. Densities and P-x-y diagrams for carbon dioxide dissolution in methanol, ethanol and acetone mixtures. *Fluid phase equilibria* **1997** (131) 243-258.

4. Christensen, J. J.; Zebolsky, D. M. and Izatt R. M. The excess enthalpies of (carbon dioxide + hexane) at 470.15, 510.15 and 573.15 K from 7.50 to 12.50 MPa. *J. Chem. Thermodynamics* **1985** (17) 183-192.

5. Allen, L and Matijevic, E. Stability of colloidal silica. *J. Coll. Interf. Sci.* **1969**, 31 (3) 287-296.

6. Vigil, G.; Xu, Z.; Steinberg, S. And Israelachvili, J. Interactions of silica surfaces, *J. Coll. Interf. Sci.* **1994**, 165, 367-385.

7. Ren, J.; Song, S.; Lopez-Valdivieso, A.; Shen, J. and Lu, S. Dispersion of silica fines in water-ethanol suspensions, *J. Coll. Interf. Sci.* **2001** 238, 279-284.

8. Schwertmann, U.; Cornell. R. M. *Iron oxides in the laboratory: preparation and characterization.* VCH, Weinheim **2000**.

9. Vereda, F.; Vicente, J.; Morales, M.; Rull, F. and Hidalgo-Álvarez, R. Synthesis and characterization of single-domain monocrystalline magnetite particles by oxidative aging of $Fe(OH)_2$, *J Phys Chem C*, **2008**, 112, 5843-49.

10. Ayyub, P.; Multani, M.; Barma, M.; Palkar, V. R.; Vijayaraghavan, R. Size-induced structural phase transitions and hyperfine properties of microcystalline Fe_2O_3. *J. Phys. C: Solid State Phys.* **1998**, 21, 2229-45.

11. Bruni, S.; Cariati, F.; Casu, M.; Lai, A.; Musinu, A.; Piccaluga, G. And Solinas, S. IR and NMR study of nanoparticle-support interactions in a Fe_2O_3-SiO_2 nanocomposite prepared by a sol-gel method, *Nanostructured Materials*, **1999**, 11 (5), 573-586.

12. K. Gupta and Gupta, M. Synthesis and surface engineering of iron oxide nanoparticles for biomedical applications, *Biomaterials* **2005**, 26, 3995-4021.

13. Rigby, S.P.; Fairhead, M. and van der walle, C. F. Engineering silica particles as oral drug delivery vehicles, *Current Pharm Design*, **2008** 14, 1821-1831.

14. Wu, S.; Lin, Y.; Hung, Y.; Chou, Y.; Hsu, Y.; Chang, C. and Mou, C. Multifunctional mesoporous silica nanoparticles for intracellular labeling and animal magnetic resonance imaging studies, *ChemBioChem* **2008** 9, 53-57.

15. Regarding *SiFe_hexane* samples synthesized with the use of glass wool cover (before experiment SiFe_08_8). The powder all over the autoclave was stored separately from the powder set inside the Pyrex vessel. The nitrogen isotherm was measured separately in three samples and it was found no significant differences in the pore analysis. In **Table 4.9** they are referred as single samples.

16. Gich, M. Nanopartícules magnètiques en matrius de sílice, *PhD Thesis*, **2006**, Institut de Ciència de Materials de Barcelona, ICMAB-CSIC and Universitat Autònoma de Barcelona (UAB).

17. Zhang, L.; Papaefthymiou, G. C.; Ying, J. Y. Size quantization and interfacial effects on a novel γ-Fe$_2$O$_3$/SiO$_2$ magnetic nanocomposite via sol-gel matrix-mediated synthesis *J. Appl. Phys.* **1997**, 81 (10), 6892.

18. Chen, D.-X.; Sanchez, A.; Taboada, E.; Roig, A.; Sun, N. and Gu, H.-C. Size determination of superparamagnetic iron oxide nanoparticles from magnetization curve, *Journal of Applied Physics* **2009**, 105, 083924.

19. Fernández van Raap, M. B.; Sánchez, F, H.; Rodríguez Torres, C. E.; Casa, Ll.; Roig, A. and Molins, E. Detailed magnetic dynamic behaviour of nanocomposite iron oxide aerogels, *J. Phys.: Condens Matter* **2005** (17) 6519-6531.

20. Blundell, S. *Magnetism in Condensed Matter*, Oxford Master Series in condensed matter physics, Oxford University Press, **2001**, Oxford.

21. Gross, A.; Diehl, M.; Beverly, K.; Richman, E. and Tolbert, S. Controlling magnetic coupling between cobalt nanoparticles through nanoscale confinement in hexagonal mesoporous silica. *J. Phys. Chem. B* **2003**, 107. 5475-5482.

22. Nakata, K.; Hu, Y.; Uzun, O.; Bakr, O. and Stellaci, F. Chains of superparamagnetic nanoparticles, *Advanced Materials* **2008** 20 4294-4299.

23. Murray, C. B.; Sun, S.; Doyle, H. and Betley, T. Monodisperse 3d Transition-Metal (Co, Ni, Fe) Nanoparticles and Their Assembly into Nanoparticle Superlattices, *MRS Bulletin* **2001** 985.

24. Millan, A.; Urtizberea, A.; Silva, N. J. O.; Palacio, F.; Amaral, V. S.; Snoeck, E. and Serin, V. Surface effects in maghemite nanoparticles, *J. Magn. Magn. Mater.* **2007** 312 L5-L9.

25. Smirnova, I. Synthesis of silica aerogels and their application as a drug delivery system, *PhD Thesis*, **2002**, Technischen Universität Berlin.

26. Jin, J.; Ohkoshi, S. and Hashimoto, K. Giant coercive field of nanometer-sized iron oxide, *Adv. Mater.* **2004** 16 (1) 48-51.

27. Popovici, M.; Gich, M.; Nižňanský, D.; Roig, A.; Savii, C.; Casas, Ll.; Molins, E.; Zaveta, K.; Enache, C.; Sort, J.; de Brion, S.; Chouteau, G.; J. Nogués, J. Optimized synthesis of the elusive epsilon-Fe$_2$O$_3$ phase via sol-gel chemistry. *Chem. Mater.* **2004**, 16, 5542-5548.

28. Jin, J.; Hashimoto, K. and Ohkoshi, S. Formation of spherical and rod-shaped ε-Fe$_2$O$_3$ nanocrystals with a large coercive field, *J. Mater. Chem.* **2005** 15, 1067.

29. Ding, Y.; Morber, J. R.; Snyder, R. L. and Wang, Z. L. Nanowire structural evolution from Fe$_3$O$_4$ to ε-Fe$_2$O$_3$, *Adv. Funct. Mater.* **2007**, 17 (7) 1172-1178.

30. Gich, M.; Frontera, C.; Roig, A.; Fontcuberta, J.; Molins, E.; Bellido, N.; Simon, Ch.; Fleta, C. Magnetoelectric coupling in epsilon-Fe$_2$O$_3$ nanoparticles. *Nanotechnology* **2006**, 17, 687-691.

31. Gich, M.; Roig, A.; Taboada, E.; Molins, E.; Bonafos, C. and E. Snoeck, Stabilization of metastable phases in spatially restricted fields: the case of the Fe$_2$O$_3$ polymorphs. *Faraday Discussions*, **2007**, 136, 345-354.

32. Ohkoshi, S.; Sakurai, S.; Jin, J.; Hashimoto, K. The additions effects of alkaline earth ions in the chemical synthesis of epsilon-Fe$_2$O$_3$ nanocrystals that exhibit a huge coercive field. *J. Appl. Phys.* **2005**, 97, 10K312_1-10K312_3.

33. Nakamura, T.; Yamada, Y.; Yano, K. Novel synthesis of highly monodispersed gamma-Fe$_2$O$_3$/SiO$_2$ and epsilon-Fe$_2$O$_3$/SiO$_2$ nanocomposite spheres. *J. Mater. Chem.* **2006**, 16, 2417-2419.
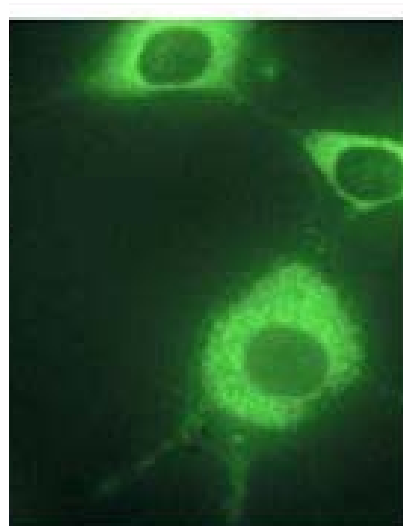
5. BIOMEDICAL APPLICATIONS OF MAGHEMITE AND COMPOSITE NANOPARTICLES

This chapter deals with the evaluation of the materials described in Chapters 2 and 4 as contrast agents for magnetic resonance imaging (MRI) and as mediators for magnetic hyperthermia.

5.1. Toxicity evaluation

The toxicity of a material is defined as the degree to which the material is toxic to living organisms. The evaluation of the toxicity in cells is defined as cytotoxicity. By toxic it is understood the ability of a substance to alter the normal functioning of the cells (reproduction, growth, breathing, etc.) or even to kill them. Toxicity of nanomaterials is an emerging discipline. Since their size is comparable to biological functional units within cells there are new interactions with living matter that should be considered when evaluating the use of nanomaterials in humans.

There is an urgent need to standardize the evaluation protocols to facilitate the comparison of data.[1] It is still not well understood which parameters involved in toxicity at the nanoscale are relevant: is it the large surface area, the absolute mass of nanomaterial, is it the mass/surface area ratio, the chemical nature of the surface or is it the particle size...? There are also other non-resolved issues such as the sterilization tools, time of evaluation, serum addition or not, etc. In the meantime, the published results are mostly referred to the mass.[1]

Iron oxide nanoparticles have been reported to be biologically safe.[2,3] They are metabolized into elemental iron species by either hydrolytic enzymes or the acidic conditions found inside lysosomes. The iron is then merged in normal body stores and is subsequently incorporated in haemoglobin. The toxicity of silica has been widely studied and no signs of systemic toxicity have been observed due to skin or eye contact, inhalation or oral intake.[4] Actually, silica is being extensively used in drug administration (oral or parenteral) and many studies proof its biocompatibility.[5-9]

Experimental results

Some preliminary tests on the cytotoxicity of the iron oxide colloidal dispersions were done in fibroblast NIH3T3 cells (a common line used to test toxicity) with 3-(4,5-Dimethylthiazol-2-yl)2,5-diphenyl-tetrazoilum bromide (MTT) reduction assays[10] by Dr. Elisenda Rodríguez (see annex 7.3.15 for protocol details). Data for incubation times at 2, 6 and 12 hours are presented. Results are expressed by means of cell viability, which is defined as the percentage of living cells compared to a reference cell culture free of particles. Materials can be considered biocompatible when the cell viability is higher than 90%, i.e. when only 10% of cells have died in the presence of such material. Below 90% they are considered as toxic.[11]

The *Fe₂O₃_citrate* nanoparticles are biocompatible at concentrations below 1 mM Fe and only slightly toxic up to 5 mM Fe when incubated for 12 hours (see **Figure 5.1**).

It is difficult to compare these results with the bibliographic data due to the lack of standardized units to report the results.[1] Nevertheless, we chose the same order of magnitude of iron concentration than the ones described in the review in reference 11 and we observed that the toxicity of our nanoparticles is comparable to other published values for iron oxide systems.
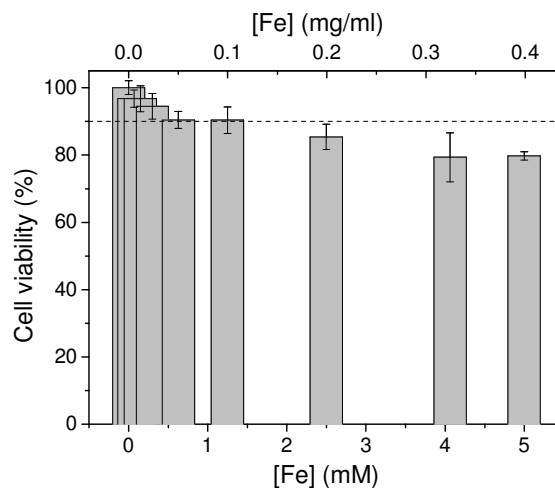
Figure 5.1. Cell viability of *Fe₂O₃_citrate* nanoparticles (Ø = 7 nm) at 12 hours. The iron concentration is indicated in millimolar and micrograms per millilitre units. The dashed line at 90% cell viability is a guide for the eye.

Toxicity of porous silica particles was also tested, as shown in **Figure 5.2**. It has been reported that its toxicity at the nanometric range depends inversely on the particle size.[12] We observed that our particles showed a much lower toxicity than the ones presented in reference 12: they were non-toxic up to 150 μg/ml and only slightly toxic up to 1250 μg/ml. On the contrary, particles in reference 12 were toxic from 50 μg/ml on. Nevertheless, the MTT analyses in reference 12 were done at 24 hours, so they are not directly comparable.

The toxicity of the composite particles was expected to be only derived from the silica surface, since we observed previously with an HCl test (see page 129) that there is no release of iron ions.
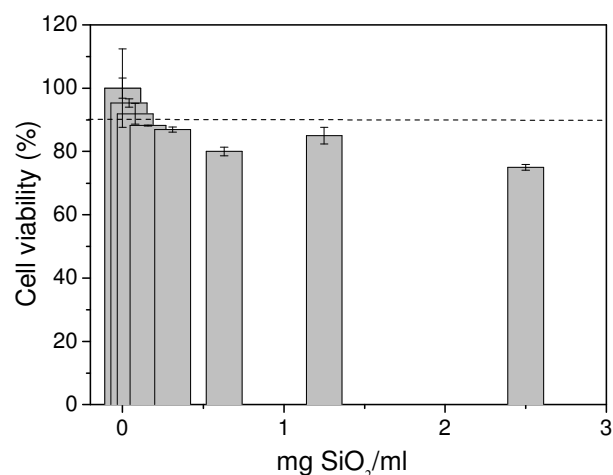
Figure 5.2. Cell viability of pure silica particles (sample Si_07_13; ∅ = 204 nm) at 12 hours. The dashed line at 90% cell viability is a guide for the eye.

As it is illustrated in **Figure 5.3**, the composite particles were slightly toxic from 0.5 mM Fe on and their toxicity increased further as the particles were more concentrated. Interestingly, they were more toxic than the pure silica particles, attributed to their smaller size. A similar result was also reported in reference 12. And not only that, but also the biggest spherical composite particles (sample SiFe_08_6, 152 nm) showed the best cell viability. Concerning the other spherical particles (samples SiFe_08_1 and SiFe_08_3, 71 and 82 nm, respectively), their toxicity was very similar as it was their size. Sample SiFe_08_8 was worm-like and showed the same behaviour as the smallest particles. Regarding the incubation time, **Figure 5.4** shows the evolution of the cell viability of sample SiFe_08_6 at 2, 6 and 12 hours, showing no significant differences.
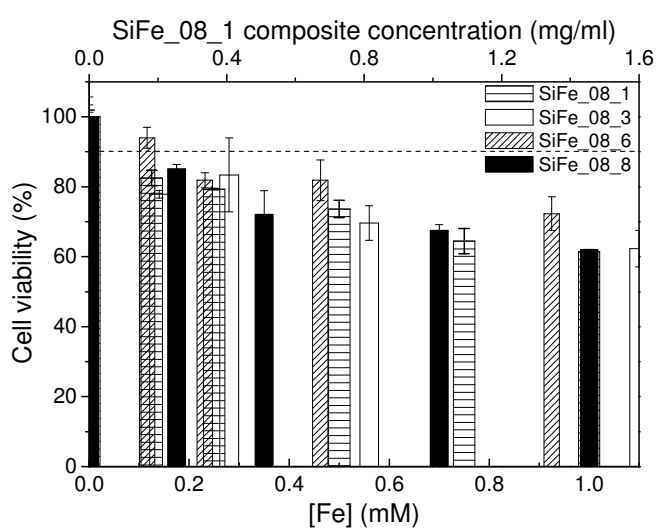
Figure 5.3. Cell viability of four *SiFe_hexane* samples dispersed in water at 12 hours. The lower horizontal axis represents the molar concentration of iron. The upper horizontal axis

indicates the composite concentration of sample SiFe_08_1 (considering the iron oxide mass fraction) as a reference to the total composite mass content. The dashed line at 90% cell viability is a guide for the eye.
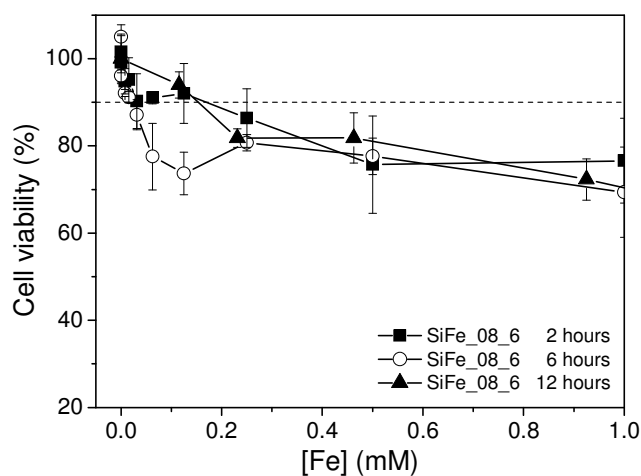

Figure 5.4. Cell viability of composite sample Si_08_6 at different incubation times. The dashed line at 90% cell viability is a guide for the eye.

5.2. Magnetic Resonance Imaging (MRI)

Magnetic resonance imaging is a non-invasive medical technique to obtain tomographic images of any part of the body, taking profit of the resonant radiofrequency (rf) energy and enabling the differentiation of tissues according to their water content. Consequently, it allows for distinguishing pathological tissues from healthy ones. It is considered as a biologically safe technique. The physical bases are described in section 1.1.4.1. Briefly, a sample is placed in a magnetic field parallel to the z axis. The sample has then a net magnetization, m. Following a given sequence, a radiofrequency pulse is applied perpendicular to the magnetic field with equal or similar frequency than the Larmor frequency of protons (**Figure 5.5**). During the rf pulse the protons in the sample are excited and their magnetic spins precess in the x-y plane (there is no net magnetization in the z-axis). When the rf pulse ends, the protons relax to their equilibrium state where the spins precess back around the z axis. The longitudinal relaxation is the recovery of the magnetization in the z axis. The time needed to recover the 63% of the initial longitudinal magnetization is defined as T_1 (s). The transversal relaxation corresponds to the coherence loss of the spins in the x-y plane. Its characteristic time, T_2 (s), is the time needed to lose 63% of transversal magnetization. The inverse of these times are defined as the relaxation rates, R_1 (s^{-1}) and R_2 (s^{-1}).[13]
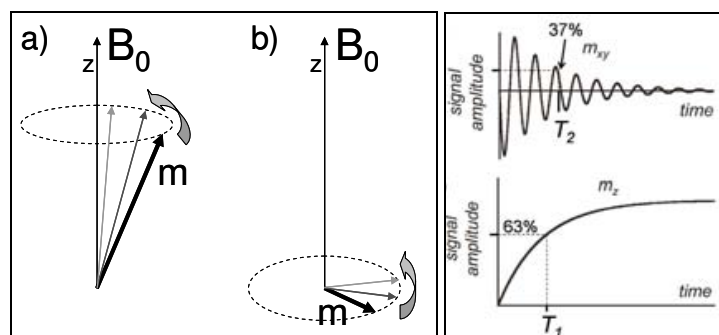
Figure 5.5. Left image: scheme of proton magnetic moments which precess around the direction of an external magnetic field (a), and their precession in the *x-y* plane while excited with a perpendicular radiofrequency pulse (b). Right image: magnetic moment vs. time after removal of the rf pulse. Upper figure: *x-y* plane values; lower figure: *z* values.

MRI is characterized by high spatial resolution but also by its intrinsically low sensitivity. As a result, large doses of contrast agents are typically administered to alter the water protons relaxation times in order to enhance image contrast of specific tissues. Approximately half of clinical MR images are performed with the aid of contrast agents to detect multiple diseases, including cancer lesions. The use of contrast agents (CA) accelerate the relaxation processes and consequently, increase the relaxation rates producing an enhancement in signal intensity. To evaluate and compare the efficiency of magnetic materials as contrast agents for MRI their relaxation rates are referred to their concentration. The new value is called **relaxivity**, r_1 and r_2 (s^{-1} mM^{-1}). The higher the r_i values, the better the contrast will be in the images. Depending on the ratio r_2/r_1, the materials can be defined as positive contrast agents, T_1-CA ($r_2/r_1 < 2$), or as negative contrast agents, T_2-CA ($r_2/r_1 > 2$). Both relaxivity values depend on the contrast agent magnetization. However, there is an important difference between the relaxation processes: regarding the longitudinal one, the protons need to be in contact with the magnetic contrast agent in order to increase their relaxation rates. On the other hand, the transversal relaxivity can be accelerated even if there is no physical contact between the protons and the contrast agent.

Positive contrast agents have been the most used in clinical diagnosis.[13] They are based on paramagnetic ions, such as manganese (II), dysprosium (III), iron (III), and mainly gadolinium (III). Since paramagnetic ions bear low magnetization they show very small sensitivity. Due to the high toxicity of these ions, they need to be chelated with biocompatible ligands. Some examples are DTPA (diethylenetriaminepentaacetic acid), DTPA-BMA (5,8-bis(carboxymethyl)-11-[2-(methylamino)-2-oxoethyl]-3-oxo-2,5,8,11-tetraazatridecan-13-oic acid), DOTA (1,4,7,10-tetraazacyclododecane-1,4,7,10-tetraacetic acid), etc. The chelation must always assure the accessibility of the water molecules to the lanthanide ion.

Iron oxide nanoparticles have been widely evaluated as negative contrast agents due to their high magnetization and their tuneable particle size.[14-19] They mainly differ in the iron oxide phase, the magnetic core size or their coating material (dextran, albumin, silicones, polymers, electrolytes, silica, etc.). For those systems, the reported hydrodynamic mean diameter ranges from 10 to 3500 nm. Very few cases of iron oxide colloidal dispersions with very small particle size (5-10 nm) have been reported to act as T_1-CAs.[20] To achieve that, one should try to maximize r_1 while keeping r_2 as small as possible.[21-22]

Experimental results

We first evaluated the iron oxide nanoparticles stabilized with TMAOH and sodium citrate described in Chapter 2. The results listed in **Table 5.1** include the magnetization at 5 K as a reference value, the relaxivities at 20 and 60 MHz and also the stability at 24 hours (which was confirmed by repeating the relaxivity values 24 hours after the first measurement to check if there were significant differences; if different values were measured, the sample was considered as unstable). Samples A, B, C and D correspond to 5.5, 7.0, 5-12 and 10.0 nm in diameter, respectively. Those nanoparticles present ratio r_2/r_1 smaller than 2 and should be considered as useful positive contrast agents,[22] contrary to the most observed behaviour of iron oxide nanoparticles.[14-19] This is mainly due to the small size of the particles favouring a closer interaction between the protons of the water molecules and the iron ions, resulting in an increase of the longitudinal relaxivity. These results are very interesting due to the potentiality of avoiding the highly toxic gadolinium-based contrast agents and taking profit of the biocompatible iron oxide nanoparticles.

Regarding the unstable particles, the stability seems to be lowered due to the multiple manipulations of the samples prior to the relaxivity measurements (see annex 7.3.16). The unstable samples are highlighted in grey to show how the relaxivity values are affected by the clustering of the particles: r_1 values decrease while r_2 values increase. Due to the lower interaction of the water protons with the iron ions the clustering induces a decrease in r_1. On the other hand, the new magnetic cluster has a higher magnetization which induces faster decoherence of spins and then r_2 increases. The highest values of r_1 and r_2 within the stable basic samples correspond to sample A*_TMAOH. These results are attributed to the smallest size with narrow size distribution and to the highest magnetization.

When the samples were stabilized at neutral pH with sodium citrate the r_2 values increased. The increase of the transversal relaxivity matches the observed bigger hydrodynamic size by DLS (see page 57) which is approximately twice the size. The

resultant magnetic moment per cluster might also be twice the value of the individually stabilized particles.

Table 5.1. Relaxivity values of samples *Fe₂O₃_TMAOH* (basic pH) and *Fe₂O₃_citrate* (neutral pH) at 37°C. $M_S \equiv$ magnetization at 5 K, a = stability at 24 hours. 20 MHz ≡ 0.47 Tesla, 60 MHz = 1.4 Tesla.

Synthesis ID	M_S (emu/g Fe_2O_3; 298 K)	r_1 (s⁻¹mM⁻¹) (20 MHz)	r_2 (s⁻¹mM⁻¹) (20 MHz)	r_2/r_1 (20 MHz)	r_1 (s⁻¹mM⁻¹) (60 MHz)	r_2 (s⁻¹mM⁻¹) (60 MHz)	a
A*_TMAOH	80	16.5	108.3	6.6	-	-	No
A*_TMAOH	70	21.7	35.3	**1.6**	-	-	Yes
A*_TMAOH	68	20.8	28.6	**1.4**	17.6	35.8	Yes
B_TMAOH	45	8.4	80.0	9.6	-	-	No
B_TMAOH	41	9.0	16.5	**1.8**	-	-	Yes
C_TMAOH	29	10.2	25.8	2.5	9.5	47.2	Yes
D_TMAOH	42	16.4	68.5	4.2	9.4	85.3	No
A*_citrate	70	25.8	89.9	3.5	-	-	No
A*_citrate	68	20.8	51.0	2.5	14.5	66.9	Yes
C_citrate	29	14.5	40.2	2.8	9.4	55.1	Yes

To understand the mechanisms governing the relaxation phenomenon of the system, an NMRD profile was recorded and fitted according to the usual model.[23] The NMRD profile displays r_1 over a wide range of magnetic fields and provides the information necessary to asses the properties of a contrast agent at any field strength. It also gives information on the particle diameter (*d*) and the value of the saturation magnetization (M_S). The relaxivity profile (r_1) of Fe_2O_3-water nanoparticles is represented in **Figure 5.6**. The relaxivity of this complex behaves as expected for ultrasmall superparamagnetic particles. The maximum of the relaxativity is placed between 30 and 60 MHz and only diminishes by a factor of 2 at 200 MHz, meaning that very good performance is expected at the conditions used in clinical imaging (fields of 100-200 MHz). The NMRD profile was analyzed quantitatively according to eq 31 from ref 23. It should be pointed out that the theoretical values of particle size and saturation magnetization obtained from the fitting[22] are in good agreement with those obtained by the other employed techniques (TEM, XRD, and magnetometry), pointing out once more to a very narrow distribution of the particle size and showing consistency within all the used characterization techniques.
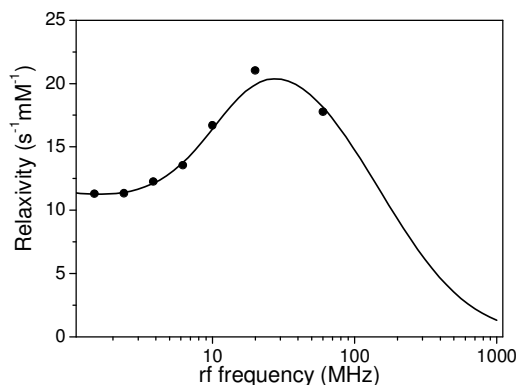
Figure 5.6. NMRD profile of longitudinal relaxivity of sample A*_citrate at 37°C. The dots correspond to the experimental values and the continuous line to the fitting according to equation 31 in reference 23.

The previous results on the synthesis and relaxometric evaluation of iron oxide nanoparticles were gathered in reference 22. The whole text is included in annex 7.1.

Table 5.2 lists the relaxivity values of the composite samples dispersed in water. The first relevant aspect of the composite particles is their low values of longitudinal relaxivities, generally lower than 1 (the T_1 values are similar to that one of water, 1500 ms). These results are in accordance with the lack of accessibility of the water molecules to the iron oxide surface as evidenced with the HCl test (see page 129). The iron oxide surface seems to be completely covered with compact silica hindering its accessibility. Consequently, the composite particles have no effect as positive contrast agent.

Table 5.2. Relaxivity values of composite samples. 20 MHz ≡ 0.47 T.

Synthesis ID	Particle shape	r_1 (s^{-1}mM^{-1}) (20 MHz)	r_2 (s^{-1}mM^{-1}) (20 MHz)	r_2/r_1 (20 MHz)
Fe$_2$O$_3$_citrate	Spherical	2.89	15.5	5.4
SiFe_07_23	Spherical	-	250	-
SiFe_07_26	Spherical	-	199	-
SiFe_08_1	Spherical	0.29	148	510
SiFe_08_3	Spherical	0.27	164	607
SiFe_08_6	Spherical	0.17	326	1917
SiFe_08_8	Worms	0.07	160	2285
SiFe_08_11	Spherical	0.81	238	294
SiFe_08_13	Worms	0.66	203	308
SiFe_08_19	Spherical	1.54	190	123
SiFe_08_20	Spherical	2.17	130	60
Endorem®	-	40	160	4
Resovist®	-	25.4	151	5.9
Lumirem®	-	3.4	3.8	1.1

On the contrary, the transversal relaxation is a distance effect. The composite particles showed very high r_2 values ranging from 130 to 326 s^{-1}mM^{-1}. The ratio r_2/r_1 was much larger than 2. Then the composite particles were classified as negative contrast agents, as iron oxide based contrast agents generally behave. The data of Endorem®, Resovist® and Lumirem® have been added as reference values to show the promising results obtained with our particles. These materials are commercial contrast agents based on iron oxide nanoparticles stabilized with dextran, carboxydextran and siloxane, respectively. They are currently used worldwide for liver and gastrointestinal clinical diagnosis.[24] Up to the extent of our knowledge the transversal relaxivity values obtained with our composite particles are the highest published ones on iron oxide based contrast agents measured at 0.47 T (20 MHz).[14,15,25,26] Coming back to the toxicity evaluation, the slightly higher toxicity observed for the composite samples compared to the maghemite nanoparticles would be compensated with their outstanding r_2 values, since a lower dose of material would be necessary to increase the contrast when performing magnetic resonance images.

The composite particles increased importantly the r_2 values compared to the iron oxide nanoparticles (130-326 vs. 15-50 s^{-1}mMFe^{-1}), even though the magnetic phase was maghemite in both materials. The increment of r_2 is due to the clustering of the iron oxide nanoparticles.[27-29] We found a dependence of relaxivity with the magnetization per composite particle. The calculation of the magnetization per composite particle is explained below and the results are listed in **Table 5.3**. Only spherical particles were considered.

The main idea of the following calculation is to know the magnetization of an iron oxide nanoparticle (M(Fe$_2$O$_3$ particle)) and the number of iron oxide nanoparticles per composite particle (N), to finally obtain the magnetization per composite particle (M(cluster), which corresponds to the magnetization of the central magnetic cluster). For the sake of clarity **Figure 5.7** shows a scheme of the diameters involved in this calculation.
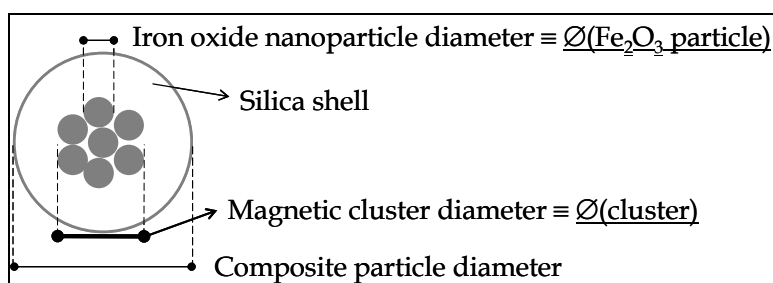
Figure 5.7. Scheme of a composite particle highlighting the different diameters involved in the calculation of magnetization per composite particle.

The magnetic iron oxide particle size ($\varnothing$(Fe$_2$O$_3$ particle)) was already calculated for each sample from the magnetization curves at room temperature (see **Table 4.12**) and therefore, its volume could be calculated (V(Fe$_2$O$_3$ particle)). Considering the maghemite density (5.24 g/cm³), the particle weight was then obtained (mass(Fe$_2$O$_3$ particle)). Now, with the experimental value of magnetization at 0.47 T (the applied magnetic field in the relaxivity measurements) and room temperature expressed in emu/g Fe$_2$O$_3$, the value of magnetization per iron oxide nanoparticle at 0.47 T is available (M(Fe$_2$O$_3$ particle)). Making use of the TEM images, the average size of the central magnetic cluster in the composite particles was measured ($\varnothing$(cluster)). Then, the volume of the magnetic cluster was calculated considering spherical shape (V(cluster)). Now, considering that the packing of the iron oxide nanoparticles inside the silica shell may have no specific order, we considered a packing factor of 0.5 (lower than the packing factor for bcc arrangement, 0.64). The ratio V(cluster)/V(Fe$_2$O$_3$ particle) multiplied by the 0.5 packing factor will give us an average number of magnetic particles per magnetic cluster, N (equivalent to the average number of particles per composite particle). Finally, multiplying N by M(Fe$_2$O$_3$ particle), the magnetization of a composite particle at 0.47 T and RT is obtained (M(cluster)). Special attention must be paid to the unit conversions. As an example, the calculation for sample SiFe_08_1 is detailed below:

$$M(Fe_2O_3\,particle) = M(SiFe\_08\_1)\frac{emu}{gFe_2O_3}\cdot mass(Fe_2O_3\,particle)gFe_2O_3 =$$

$$= M(SiFe\_08\_1)\frac{emu}{gFe_2O_3}\cdot V(Fe_2O_3\,particle)cm^3\cdot \rho\,\frac{gFe_2O_3}{cm^3} =$$

$$= M(SiFe\_08\_1)\frac{emu}{gFe_2O_3}\cdot \frac{4}{3}\pi\left(\frac{\phi(particle)}{2}\right)^3\frac{cm^3}{10^{21}nm^3}\cdot \rho\,\frac{gFe_2O_3}{cm^3}$$

$$M(Fe_2O_3\,particle) = 45.5\,\frac{emu}{gFe_2O_3}\cdot \frac{4}{3}\pi\left(\frac{8.2}{2}\right)^3\frac{cm^3}{10^{21}nm^3}\cdot 5.24\,\frac{gFe_2O_3}{cm^3} = 6.9\cdot 10^{-17}\,emu$$

$$N = PackingFactor\cdot\frac{V(cluster)}{V(Fe_2O_3\,particle)} = 0.5\cdot\frac{(4/3)\pi(\phi(cluster)/2)^3}{(4/3)\pi(\phi(Fe_2O_3\,particle)/2)^3} =$$

$$= 0.5\cdot\frac{\phi(cluster)^3}{\phi(Fe_2O_3\,particle)^3} = 0.5\cdot\frac{23^3}{8.2^3} = 11$$

$$M(cluster) = M(Fe_2O_3\,particle)\cdot N = 6.9\cdot 10^{-17}\,emu\cdot 11 = 7.6\cdot 10^{-16}\,emu$$

Table 5.3. Magnetic data of spherical composite samples and their transversal relaxivity (see **Figure 5.7** for clarification, $\varnothing$(Fe_2O_3 particle) from **Table 4.12**, N stands for calculated mean number of iron oxide nanoparticles per composite particle).

| Sample	$\varnothing$(Fe_2O_3 particle) (nm)	$\varnothing$(cluster) (nm)	N	M(cluster) (emu) 298K, 0.47T	r_2 (s^{-1} mMFe^{-1}; 310K, 0.47T)
Fe_2O_3_citrate	7	7	1	$1.1 \cdot 10^{-17}$	15.5
SiFe_07_23	7.5	55	197	$1.1 \cdot 10^{-14}$	250
SiFe_07_26	6.6	52	245	$8.1 \cdot 10^{-15}$	199
SiFe_08_1	8.2	23	11	$7.6 \cdot 10^{-16}$	148
SiFe_08_3	6.7	29	41	$1.5 \cdot 10^{-15}$	164
SiFe_08_6	7.4	53	184	$9.8 \cdot 10^{-15}$	326
SiFe_08_11	6.8	40	102	$4.0 \cdot 10^{-15}$	238
SiFe_08_19	7.3	47	133	$6.3 \cdot 10^{-15}$	190

The relationship between the calculated magnetization per cluster and the number of iron oxide particles per cluster is graphically represented in **Figure 5.8**. The higher the content in iron oxide nanoparticles, the higher the composite particle magnetization.
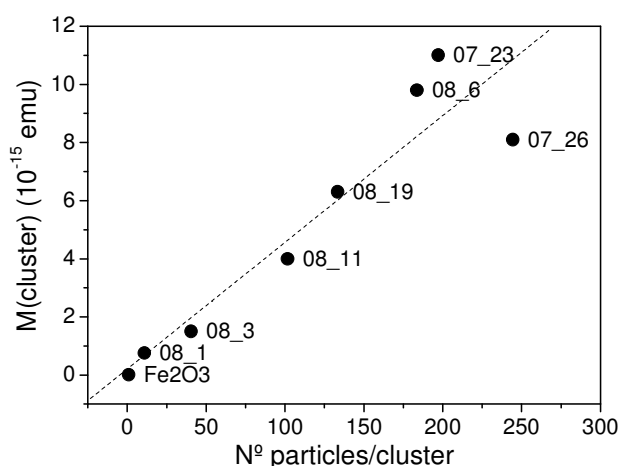
Figure 5.8. Calculated magnetization per cluster vs. calculated number of particles per cluster (dots) and linear fitting (dashed line). The labels indicate the synthesis ID.

From the data in **Table 5.3** we expected a relationship between the experimental transversal relaxivity values and the calculated magnetization per cluster. We observed a clear trend to higher values of relaxivity as the magnetization of the cluster increased (see **Figure 5.9**), although there was a high degree of dispersion considering a linear relationship (R = 0.752).
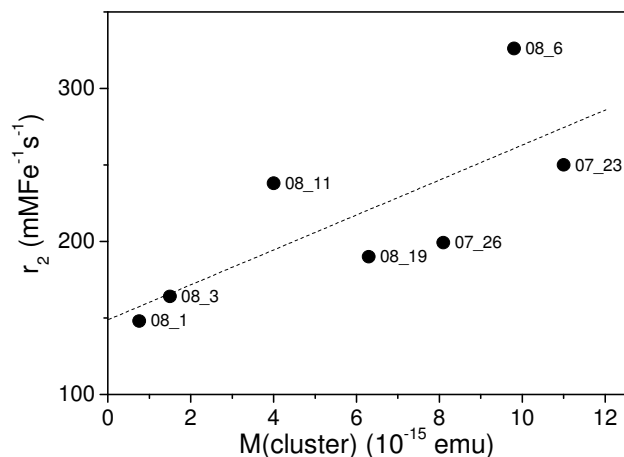
Figure 5.9. Transversal relaxivity vs. cluster magnetization at 0.47 T. Dots correspond to the experimental values and dashed line correspond to the linear fitting. The labels indicate the synthesis ID. R = 0.752.

The intensity of the magnetic field sensed by the water protons decays with the distance to the magnetic nanoparticles. Then, the total size of the composite particle might also play an active role in the relaxivity process. **Figure 5.10** shows the dependence of the relaxivity with the cluster magnetization over the composite particle radius. The new linear fitting has a higher linear regression factor (R = 0.870) than the one in **Figure 5.9**.
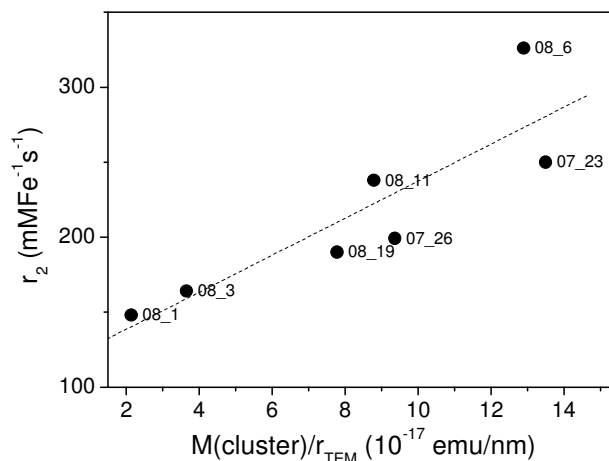
Figure 5.10. Transversal relaxivity vs. cluster magnetization over composite radius (measured by TEM) at room temperature and 0.47 T. Dots correspond to the experimental values and dashed line corresponds to the linear fitting. The labels indicate the synthesis ID. R = 0.870.

But, if the composite particle size and the distance from the magnetic cluster to the protons seemed to play a role, then the silica shell thickness might play it, too. Defining the silica shell thickness as (composite particle diameter - $\varnothing$cluster)/2, we obtained a better linear relationship (R = 0.897), as shown in **Figure 5.11** (the fitting would reach R = 0.978 if sample 08_6 were not considered).
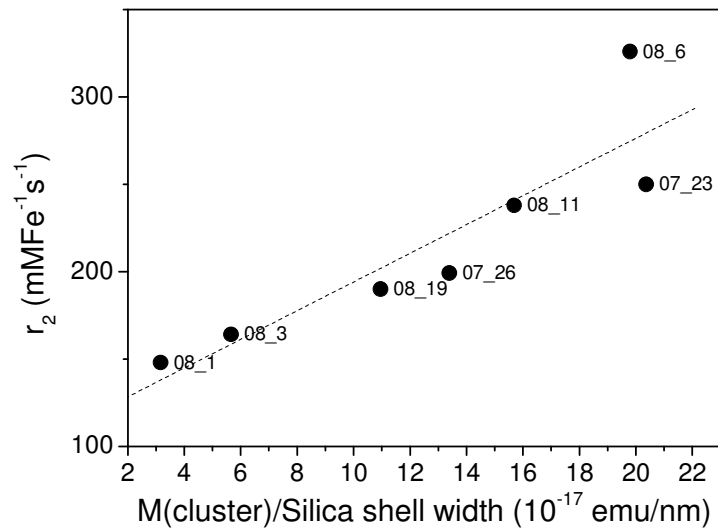
Figure 5.11. Transversal relaxivity vs. cluster magnetization over silica shell thickness (measured by TEM) at room temperature and 0.47 T. Dots correspond to the experimental values and dashed line corresponds to the linear fitting. The labels indicate the synthesis ID. R = 0897.

Then, in general, the relaxivity values increase with the magnetization of a composite particle and decrease with their silica shell thickness. The preliminary results on relaxivity of composite particles together with their synthesis were gathered in reference 25. The whole text is included in annex 7.1.

As a general conclusion, we observed that the same original material, iron oxide nanoparticles 7 nm in size, could act as positive and negative contrast agents for magnetic resonance imaging. The original iron oxide nanoparticles, individually stabilized, acted as positive contrast agents. On the contrary, the composite particles acted as negative contrast agents. The different behaviour between both systems was attributed to the stabilizing agent and the iron oxide particles clustering. These conclusions are illustrated in **Figure 5.12**.
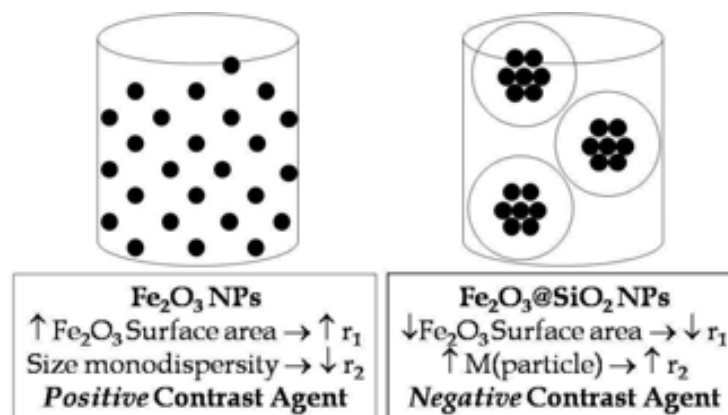
Figure 5.12. Summarizing scheme on the relaxivity properties of our particles.

5.3. Magnetic Hyperthermia

Magnetic hyperthermia is a physical effect consisting of heating a magnetic material with the application of an alternating magnetic field (ac field). This effect is very useful in medicine since it is known that the cancerous cells die when they are heated around 41-48°C, whereas the healthy cells can stand higher temperatures. It is thought that the high temperature induces a modification of many structural and enzymatic functions within cells, which can induce apoptosis.[30] Generally, it is used in combination with standard treatments like surgery, irradiation or chemotherapy.

When the size of the magnetic material is within the nanometric range, the amount of generated heat by means of an ac-field depends on the size and the magnetic properties of the particles. For multidomain ferro- or ferrimagnetic particles, heating is due to hysteresis losses. The orientation of the magnetic moments inside the material takes place through the displacements of the domain walls. On the other hand, in single-domain superparamagnetic nanoparticles, the heating is due to two relaxation mechanisms: Neél relaxation and Brownian relaxation. Neél relaxation transforms magnetic energy into thermal one when the magnetized particles come back to their equilibrium state. Its characteristic time (t_N) is defined in **Equation 5.1** and depends on the magnetocrystalline anisotropy of the material (K) and the particle volume (V). The Brownian relaxation mechanism involves the physical movement of the whole particle in the carrier liquid due to the rotational Brownian motion. The heat is generated due to the viscous friction between rotating particles and surrounding medium. Its characteristic time (t_B) depends on the hydrodynamic size of the particles (d_{HYD}), the viscosity of the solvent (η) and the temperature (T), as defined in **Equation 5.2**.

Equation 5.1
$$t_N = t_0 \cdot \exp\frac{K \cdot V}{k_B \cdot T}$$
Neél relaxation time

Equation 5.2
$$t_B = \frac{3 \cdot \eta \cdot d_{HYD}}{k_B \cdot T}$$
Brownian relaxation time

The frequency (f) dependence of the relaxation of the particle system is related to its complex susceptibility. The imaginary part $\chi''(f)$ (i.e. the de-phasing between magnetization and external field), which is defined by **Equation 5.3**, is in turn related to magnetic losses by **Equation 5.4**.

Equation 5.3 $\chi''(f) = \chi_0 \phi / (1 + \phi^2)$ $\phi = f \cdot t_{N,B}$, $\chi_0 = \mu_0 \cdot M_S^2 \cdot V / (k_B \cdot T)$

where M_S is saturation magnetization.

Equation 5.4 $P(f,H) = \mu_0 \pi \chi''(f) \cdot H^2 \cdot f$

where P is the loss power density and H is the applied field. Then, the higher the H·f product, the more efficient the heat generation. However, the ac magnetic field is limited by deleterious physiological effects of high frequency magnetic fields, i.e. stimulation of skeletal muscles, possible arrhythmia, etc. Hergt et al. estimated that exposure to fields where the product (H·f) exceeds $5 \cdot 10^9$ Am^{-1} s^{-1} can be harmful to humans.[31] Accounting for these data, superparamagnetic nanoparticles are a better choice for magnetic hyperthermia than ferromagnetic ones since ferromagnetic materials need high magnetic field amplitudes to fully saturate. Another advantage of superparamagnetic nanoparticles is the possibility of directing them with external magnetic fields to a specific target within the body, avoiding potential embolism when the external field is removed. The selection of the optimal product of magnetic field amplitude and frequency depends on the kind of material to be heated.[32] Besides, every material bears an own Curie temperature, which enables a self-limitation of the temperature enhancement. The Curie temperature depends on the material itself as well as on the particle volume. An optimal Curie temperature would be around 41-48°C to ensure the destruction of tumoral cells reducing the damage to the surrounding healthy cells. Gazeau et al. described several colloidal dispersions of iron oxide and cobalt ferrite nanoparticles with different average sizes which could reach a broad range of temperatures, from 38 to more than 100°C.[33] Duguet et al. have also studied the heating power and the Curie temperature dependence with particle size of manganese perovskite nanoparticles.[34] Iron oxide nanoparticles have been widely investigated for this application due to their biocompatibility and high magnetization.[35]

The efficiency of a magnetic material as a hyperthermia mediator is defined by the specific absorption rate (SAR), the power of heating of a magnetic material per gram. The evaluation consists of measuring the temperature increase of a colloidal dispersion of nanoparticles with a given volume and concentration with respect to time. The specific absorption rate (SAR) is defined by **Equation 5.5**:

Equation 5.5
$$SAR = \frac{C(H_2O)}{x(Fe)} \cdot \frac{\Delta T}{\Delta t}$$

where C is the specific heat capacity of water (4.184 J/°C·g), x(Fe) is the mass fraction of iron in the sample (gFe/gH$_2$O $\equiv$ gFe/ml, equivalent to the mass concentration) and $\Delta T / \Delta t$ is the initial slope of the temperature vs. time curve (°C/s). After a given time, the temperature reaches a plateau which corresponds to the Curie temperature of the system at the experimental conditions of field amplitude and frequency. As defined in **Equation 5.5**, SAR values are independent of the magnetic material concentration.

174

Experimental results

We evaluated the efficiency of our particles as mediators for magnetic hyperthermia at the Institut de Chimie de la Matière Condensée de Bordeaux (ICMCB-CNRS), at the group of Prof. Etienne Duguet. The details of the experimental set-up are described in annex 7.3.17. The experiments consisted of placing a given volume of the magnetic aqueous colloidal dispersion inside an induction coil, with a fluoroptic thermometer inside the liquid phase. Then the generator was switched on and the temperature was monitored and registered every half second up to the temperature plateau. Firstly, we studied the dispersions of the iron oxide nanoparticles described in Chapter 2. Several *Fe₂O₃_citrate* samples stabilized at neutral pH with sodium citrate with different particle size and different concentrations were evaluated at 107 kHz and 88 mT (sample volume = 1 ml). The results are listed in **Table 5.4**. Special attention must be paid to the units when calculating the SAR values:

$$SAR = \frac{C(H_2O)}{x(Fe)} \cdot \frac{\Delta T}{\Delta t} = \frac{4.184 \frac{J}{°C \cdot gH_2O}}{[Fe] \frac{mgFe}{mlH_2O}} \cdot \frac{1000mgFe}{1gFe} \cdot \frac{\Delta T}{\Delta t} \frac{°C}{min} \cdot \frac{1\min}{60s} = \frac{4184}{60 \cdot [Fe]} \frac{W}{gFe}$$

Table 5.4. SAR values for *Fe₂O₃_citrate* samples at different concentrations. Sample volume = 1 ml. f = 107 kHz and H = 88 mT ($\equiv$ 70 kA/m). H f = 7.5 $\cdot 10^9$ Am^{-1}s^{-1}. The conversion from mT to kA/m is: 1 mT = 0.795 kA/m.

Sample ID	[Fe] (mg/ml)	Slope (°C/ min)	SAR (W/g Fe)
A_citrate	2.2	0.211	**6.59**
	93.6	0.403	0.30
	129.9	0.347	0.19
	151.1	0.520	0.24
A*_citrate	2.7	0.282	**7.33**
B_citrate	1.3	0.393	**20.44**
	13.4	0.518	2.69
	119.7	0.431	0.25
	153.2	0.370	0.17
	162.8	0.386	0.17
D_citrate	1.0	0.252	**17.48**
	1.3	0.219	11.39
	10.0	0.477	3.31
	13.4	0.504	2.62
	101.5	0.356	0.24
	113.8	0.393	0.24

The SAR values of the most diluted dispersions are comparable to those found in the bibliography for iron oxide nanoparticulated systems measured at the same or similar conditions.[33,35,36] However, we found no direct relationship of the SAR values with the particle size and, contrary to what we theoretically expected, SAR

values decreased as the colloidal dispersions were concentrated. **Figure 5.13** clearly shows the linear relationship between the logarithm of SAR and the logarithm of iron concentration with a high regression coefficient (R = 0.992).
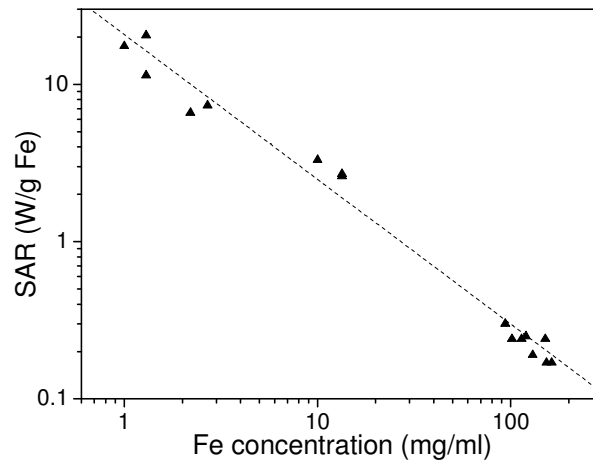
Figure 5.13. SAR dependence on the iron concentration of *Fe₂O₃_citrate* samples. Full triangles correspond to the experimental values and dashed line to the linear fitting.

We attribute this dependence of the SAR values with the iron oxide concentration to an increase of the liquid viscosity, due to the tendency of the iron oxide to gelify when being concentrated in aqueous media. In that sense, we would assume that the heating process is governed by the Brownian relaxation mechanism over the Neél one.

The composite samples were evaluated at different combinations of frequency and field amplitude in order to find the right conditions to obtain the highest SAR values, always bearing in mind the safety limits. As a graphical example, the temperature vs. time curves measured at 107 kHz with varying field amplitude are shown in **Figure 5.14**. The whole set of experimental conditions and calculated SAR values is listed in **Table 5.5**.
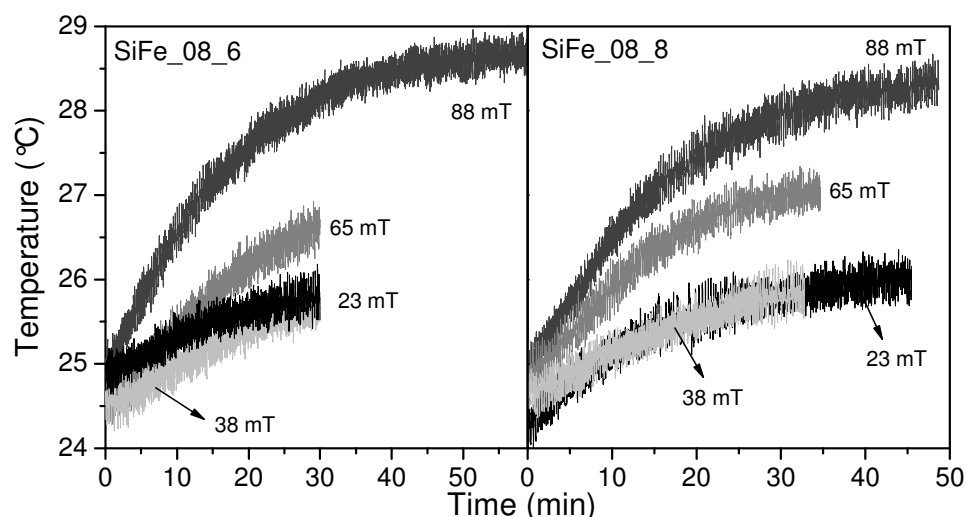
Figure 5.14. Temperature vs. time curves for samples SiFe_08_6 (left graph) and SiFe_08_8 (right graph) measured at 107 kHz and variable field amplitude, indicated by the labels.

Table 5.5. SAR values for composite samples at different combinations of frequency (f) and amplitude of applied magnetic field (H). Sample volume = 1 ml. *The conversion from mT to kA/m is: 1 mT = 0.795 kA/m.

Sample ID	[composite] (mg/ml)	Fe_2O_3 wt.%	[Fe] (mg/ml)	f (kHz)	H (mT)	H f (A/m·s)*	Slope (ºC/min)	SAR (W/gFe)
SiFe_08_6	83	5.9	3.4	**107**	23	$2.0 \cdot 10^9$	0.045	0.92
					38	$3.2 \cdot 10^9$	0.051	1.04
					65	$5.5 \cdot 10^9$	0.095	1.93
					88	**$7.5 \cdot 10^9$**	**0.157**	**3.20**
				500	5.28	$2.1 \cdot 10^9$	0.067	1.36
				1000	1.76	$1.4 \cdot 10^9$	-0.013	-0.26
					3.52	$2.8 \cdot 10^9$	0.014	0.29
					5.28	$4.2 \cdot 10^9$	0.015	0.31
SiFe_08_8	100	8.9	6.2	**107**	23	$2.0 \cdot 10^9$	0.079	0.89
					38	$3.2 \cdot 10^9$	0.055	0.62
					65	$5.5 \cdot 10^9$	0.109	1.22
					88	**$7.5 \cdot 10^9$**	**0.159**	**1.78**
				500	5.28	$2.1 \cdot 10^9$	-0.010	-0.11
				1000	1.76	$1.4 \cdot 10^9$	-0.019	-0.21
					3.52	$2.8 \cdot 10^9$	0.074	0.82
					5.28	$4.2 \cdot 10^9$	0.025	0.28

We could corroborate that the best SAR values were obtained with the highest H f product, which corresponded to the combination of 107 kHz and 88 mT, the same conditions as used for the *Fe₂O₃_citrate* samples. SAR values of composite samples at these conditions and iron concentrations of 3.4 and 6.2 mg Fe/ml were the same order of magnitude than the ones obtained for *Fe₂O₃_citrate* samples with iron concentration around 10 mg Fe/ml. Then, the silica shell did not induce an insulating effect avoiding the heat transfer from the magnetic cluster to the bulk

solution. The SAR values showed a clear dependence on the field amplitude. On the contrary, the relationship with frequency and H·f product was not straightforward.

We performed new experiments with the composite samples at different concentration with the highest H·f product of the former experiments, shown in **Table 5.6**. Although the SAR values are theoretically independent of the magnetic material concentration, we found once more a well-defined relationship with iron concentration (see **Figure 5.15**). These values are similar to some others published for composite systems of iron oxide coated with silica. Duguet et al. have reported a SAR value of 18.8 W/g Fe at the same measurement conditions[37] and Hofmann et al. reported 2.9 W/g Fe at 140 kHz and 6 mT.[38]

Table 5.6. SAR values for composite samples at different concentrations. Sample volume = 1 ml. f = 107 kHz and H = 88 mT.

Sample ID	[composite] (mg/ml)	Fe_2O_3 wt.%	[Fe] (mg/ml)	Slope (ºC/ min)	SAR (W/gFe)
SiFe_07_23	**20**	6.6	0.9	0.250	**18.9**
SiFe_08_1	74	5.0	2.6	0.286	7.7
	40		1.4	0.197	9.8
	20		0.7	0.233	**23.2**
SiFe_08_6	83	5.9	3.4	0.157	3.2
	40		1.7	0.207	8.7
	20		0.8	0.179	**15.1**
SiFe_08_8	100	8.9	6.2	0.159	1.8
	40		2.5	0.192	5.4
	20		1.2	0.185	**10.4**
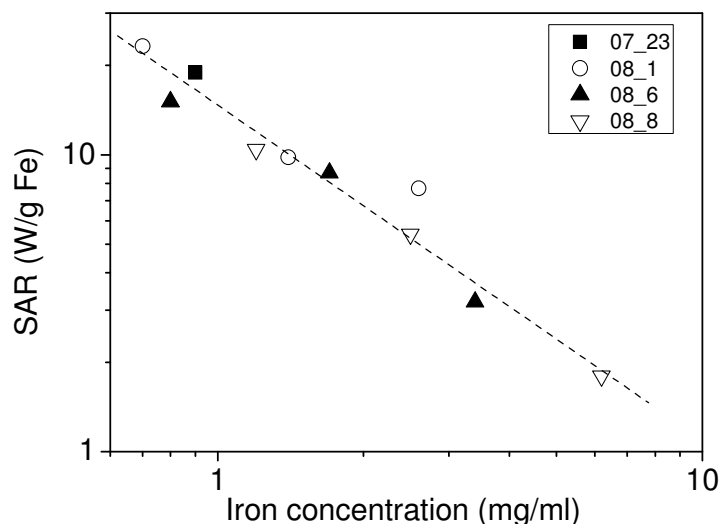
Figure 5.15. SAR of composite samples vs. iron concentration. The dashed line corresponds to the linear fitting (R = 0.978).

When plotted against the composite concentration we found that each sample showed an own linear relationship. Considering the hydrodynamic particle size of

each sample we found that the higher the SAR values of every sample, the smaller their particle size, as plotted in **Figure 5.16**.
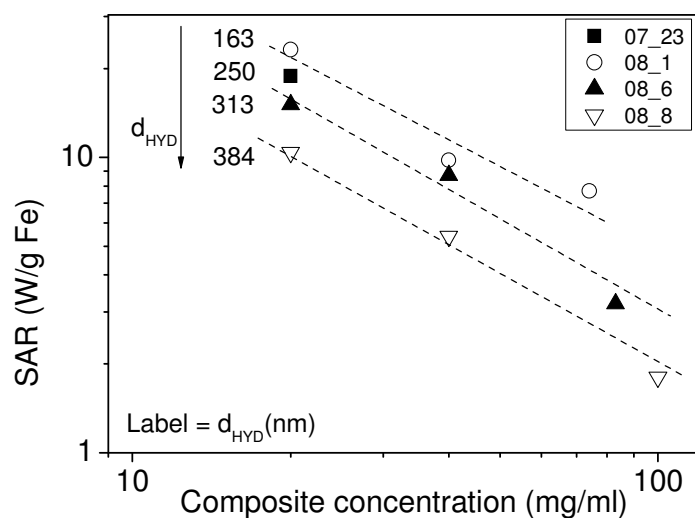
Figure 5.16. SAR of composite samples vs. composite concentration. The dashed lines are a guide for the eye.

Both relationships of the SAR values we have observed with, on the one hand, the iron concentration and, on the other hand, the hydrodynamic particle size, were attributed to a predominance of the Brownian relaxation process over the Néel one in the generation of heat. The concentration of our samples, both the iron oxide nanoparticles and the composite ones, might induce an increase of the liquid phase viscosity in such a way, that the Brownian motion of the particles is hindered and with it, the conversion of magnetic energy to thermal one. This increase in viscosity was attributed to the tendency of iron oxide and silica to gelify when concentrated.

5.4. Conclusions of Chapter 5

Cytotoxicity evaluation of iron oxide nanoparticles, silica and composite particles was performed with the MTT test. The iron oxide nanoparticles were biocompatible up to 100 μg/ml and only slightly toxic up to 400 μg/ml, similar results to the ones found in the bibliography on iron oxide nanoparticles. Silica particles were non-toxic up to 150 μg/ml and only slightly toxic up to 1250 μg/ml. The toxicity of composite particles was attributed only to the silica shell, since the HCl tests showed no iron leakage in highly acid conditions. The toxicity of the composite particles was higher than the pure silica ones, attributed to the smaller size of the former ones. Evaluation of composite samples at different incubation times from 2 to 12 hours gave no significant differences on cell viability.

Regarding magnetic resonance imaging, we observed how the same magnetic phase (maghemite) can act as positive or negative contrast agent depending on its size and shape, spatial distribution and stabilizing agent. When the maghemite nanoparticles were individually stabilized with TMAOH or sodium citrate, they could act as positive contrast agents, which is an unusual but promising behaviour for iron oxide nanoparticles. This behaviour was attributed to: a) the high amount of available particle surface area to the water protons due to the small size of the nanoparticles; this fact favours high values of longitudinal relaxivity (r_1); b) the high magnetization of the nanoparticles (directly related to the increment of relaxivity) and c) size monodispersity of the system which implies a better homogeneity of the magnetic field induced by the nanoparticles; this fact favours a decrease of the transversal relaxivity (r_2). On the other hand, when the particles were stabilized with silica by the method developed by us based on supercritical fluids, the local concentration of magnetic particles due to their clustering and their low accessibility due to the silica coating enlarged the transversal relaxivity while sharply lowering the longitudinal one. The particles acted then as negative contrast agents. The obtained transversal relaxivities for the composite particles are, to the best of our knowledge, the highest ones published for iron oxide based contrast agents at 0.47 T, and considerably higher than several commercial products currently used for clinical diagnosis. We found a relationship between the relaxivity of composite material and the magnetization per composite particle together with the silica shell thickness. In that sense, we might expect higher values of relaxivity for particles with a higher amount of iron oxide nanoparticles and a thinner silica shell. The higher transversal relaxivity of composite particles compensated their higher cytotoxicity, since a lower dose may be necessary to obtain quality contrast.

Finally, concerning magnetic hyperthermia, the SAR values obtained for diluted iron oxide nanoparticles ($\approx$ 1-2 mg Fe/ml) were comparable to data found in the bibliography. However, contrary to the theoretical expectations, the SAR values decreased while increasing iron concentration. This trend was also observed in the composite samples as well as an increase in SAR with decreasing the hydrodynamic size. We attributed the dependence of SAR with iron concentration to an increase of the medium viscosity, due to a tendency of oxides to gelify. In that sense, we hypothesized that the conversion of magnetic energy into heat is governed by the Brownian relaxation process against the Néel one.

5.5. Bibliography and notes of Chapter 5

1. Hussain, S.; Braydich-Stolle, L.; Schrand, A.; Murdock, R.; Yu, K.; Mattie, D.; Schlager, J. and Terrones, M. Toxicity evaluation for safe use of nanomaterials: recent achievements and technical challenges, *Adv. Mater.* **2009**, 21, 1-11.

2. Lawrence, R. Development and comparison of iron dextran products, *PDA J. Pharm. Sci. Technol.* **1998** 52 190-198.

3. Wang, Y.; Hussain, S.; Drestin, G. *Eur. Radiol.* **2001**, 11, 2319-2331.

4. Bergna, H. E.; Roberts, W. O., *Colloidal Silica. Fundamentals and applications.* **2006**; Vol. 131.

5. K. Gupta and Gupta, M. Synthesis and surface engineering of iron oxide nanoparticles for biomedical applications, *Biomaterials* **2005**, 26, 3995-4021.

6. Hernández-Ruiz, E.; López-Noriega, A.; Arcos, D.; Izquierdo-Barba, I.; Terasaki, O. and Vallet-Regí, M. Aerosol-assisted synthesis of magnetic mesoporous silica spheres for drug targeting, *Chem. Mater.* **2007** 19, 3455-3463.

7. Rigby, S.P.; Fairhead, M. and van der walle, C. F. Engineering silica particles as oral drug delivery vehicles, *Current Pharm Design*, **2008** 14, 1821-1831.

8. Radin, S.; El-Bassyouni, G.; Vresilovic, E.; Schepers, E. and Ducheyne, P. In vivo tissue response to resorbable silica xerogels as controlled-release materials, *Biomaterials* **2005**, 26, 1043-1052.

9. Wu, S.; Lin, Y.; Hung, Y.; Chou, Y.; Hsu, Y.; Chang, C. and Mou, C. Multifunctional mesoporous silica nanoparticles for intracellular labeling and animal magnetic resonance imaging studies, *ChemBioChem* **2008** 9, 53-57.

10. Mosmann, T. Rapid colorimetric assay for cellular growth and survival: Application to proliferation and cytotoxic assay, *J. Immunol. Method.* **1993**, 95, 55-63.

11. Lewinski, N.; Colvin, V. and Drezeck, R. Cytotoxicity of nanoparticles, *Small*, **2008**, 4 (1), 26-49.

12. Yu, K.; Grabinski, C.; Schrand, A.; Murdock, R.; Wang, W; Gu, B.; Schlager, J. And Hussain, S. Toxicity of amorphous silica nanoparticles in mouse karatinocytes, *J. Nanopart. Res.* **2009** 11, 15-24.

13. Rinck, P. A., Magnetic Resonance in Medicine. Vienna **2001**. Blackwell Science.

14. Laurent, S.; Forge, D.; Port, M.; Roch, A.; Robic, C.; Elst, L. and Muller, R. Magnetic iron oxide nanoparticles: synthesis, stabilization, vectorization, physicochemical characterization and biological applications. *Chemical Reviews* **2008**, 108, 2064-2110.

15. Jun, Y.; Lee, J. and Cheon, J. Chemical design of nanoparticle probes for high-performance magnetic resonance imaging, *Angewandte Chemie Int. Ed.*, **2008**, 47, 5122-5135.

16. Josephson, L.; Lewin, j.; Jacobs, P.; Hanh, P. F.; Stark, D. D. The effects of iron oxides on proton relaxivity *Magn. Reson. Imaging*, **1988**, 6, 647.

17. Weissleder, R.; Elizondo, G.; Wittenberg, J.; Rabito, C. A.; Bengele, h.; Josephson, L. Ultrasmall superparamagnetic iron oxide: characterization of a new class of contrast agents for MR imaging *Radiology* **1990**, 175, 489.

18. Laurent, S.; Quakssim, A.; Nicotra, C.; Goussin, Y.; Roch, A.; Vander Elst, L.; Cornant, M.; Soleil, P.; Muller, R. N. Influence of the length of the coating molecules on the nuclear magnetic relaxivity of superparamagnetic colloids *Phys. Status Solidi C* **2004**, 1, 3644.

19. Muller, R. N.; Vander Elst, L.; Roch, A.; Peters, J. A.; Csajbok, E.; Gillis, P.; Goussin, Y. *Adv Inorg. Chem*. Relaxation by metal-containing nanosystems **2005** 57, 239.

20. Cunningham, C. H.; Arai, T.; Yang, P. C., McConnell, M. V.; Pauly, J. M.; Conolly, S. M. Positive contrast magnetic resonance imaging of cells labeled with magnetic nanoparticles *Magn. Reson. Med*. **2005**, 53, 999.

21. Kellar, K. E.; Fuji, D. K.; Gunther, W. H. H.; Briley-Saebo, K.; Bjornerud, A.; Spiller, M.; Koening, S. H. NC100150 injection, a preparation of optimized iron oxide nanoparticles for positive-contrast MR angiography *J. Magn. Reson. Imaging* **2000**, 11, 488.

22. Taboada, E.; Rodriguez, E.; Roig, A.; Oro, J.; Roch, A.; Muller, R. N., Relaxometric and magnetic characterization of ultrasmall iron oxide nanoparticles with high magnetization. Evaluation as potential T_1 magnetic resonance imaging contrast agents for molecular imaging. *Langmuir* **2007,** 23, (8), 4583-4588.

23. Roch, A.; Muller, R. N. and Gillis, P. Theory of proton relaxation induced by superparamagnetic particles. *J. Chem. Phys*. **1999** 110 (11) 5403-5411.

24. Qiao, R.; Yang, C. and Gao, M. Superparamagnetic iron oxide nanoparticles: from preparation to in vivo MRI applications. *J. Mater. Chem.* **2009** 19, 6274-6293.

25. Taboada, E.; Solanas, R.; Rodríguez, E.; Weissleder, R. and Roig, A. Supercritical fluid assisted one-pot synthesis of biocompatible core(γ-Fe_2O_3)@shell(SiO_2) nanoparticles as high relaxivity T_2-contrast agents for magnetic resonance imaging. *Advanced Functional Materials,* **2009** 19, 2319-2324**.**

26. Corot, C.; Robert, P.; Idée, J. and Port, M. Recent advances in iron oxide nanocrystal technology for medical imaging. *Advanced Drug Delivery Reviews*, **2006**, 58, 1471-1504.

27. Matsumoto, Y. and Jasanoff, A. T_2 relaxation induced by clusters of superparamangetic nanoparticles: Monte Carlo simulations, *Magnetic Resonance Imaging* **2008**, 26, 994-998.

28. Tromsdorf, U.; Bigall, N.; Kaul, M.; Bruns, O.; Nikolic, M.; Mollwitz, B.; Sperling, R.; Reimer, R.; Hohenberg, H.; Parak, W.; Förster, S.; Beisiegel, U.; Adam, G. And Weller, H. Size and surface effects on the MRI relaxivity of manganese ferrite nanoparticle contrast agents. *Nanoletters*, **2007**, 7 (8) 2422-2427.

29. Berret, J.; Schonbeck, N.; Gazeau, F.; El Kharrat, D.; Sandre, O.; Vacher, A. And Airiau, M. Controlled clustering of superparamangetic nanoparticles using block copolymers: design of new contrast agents for magnetic resonance imaging. *J. Am. Chem. Soc*. **2006** 128, 1755-1761.

30. Moroz, P.; Jones, S. K.; Gray, B. N., Status of hyperthermia in the treatment of advanced liver cancer. *Journal of Surgical Oncology* **2001,** 77, (4), 259-269.

31. Hergt, R. and Dutz, S. Magnetic particle hyperthermia-biophysical limitations of a visionary tumour therapy. *J. Magn. Magn. Mater*. **2007**, 311, 187-192.

32. Glöckl, G.; Hergt, G.; Zeisberger, M.; Dutz, S.; Nagel, S. And Weitschies, W. The effect of field parameters, nanoparticle properties and immobilization on the specific heating power in magnetic particle hyperthermia. *J. Phys.: Condens. Matter* **2006** 18 S2935-S2949.

33. Fortin, J.; Wilhelm, C.; Servais, J.; Ménager, C.; Bacri, J. and Gazeau, F. Size-sorted anionic iron oxide nanomagnets as colloidal mediators for magnetic hyperthermia. *J. Am. Chem. Soc.* **2007** 129, 2628-2635.

34. Pollert, E.; Knizek, K.; Marysko, M.; Kaspar, P.; Vasseur, S. and Duguet. E. New T_C-tuned magnetic nanoparticles for self-controlled hyperthermia, *J. Magn. Magn. Mater.* **2007**, 316, 122-125.

35. Mornet, S.; Vasseur, S.; Grasset, F.; Duguet, E. Magnetic nanoparticle design for medical diagnosis and therapy. *J. Mater. Chem.* **2004**, 14, 2161-217.

36. Sonvico, F.; Mornet, S.; Vasseur, S.; Dubernet, C.; Jaillard, D.; Degrouard, J.; Hoebeke, J.; Duguet, E.; Colombo, P. and Couvreur, P. Folate-conjugated iron oxide nanoparticles for solid tumor targeting as potential specific magnetic hyperthermia mediators: synthesis, physicochemical characterization and in vitro experiments, *Bioconjugate Chemistry*, **2005**, 16, 1181-1188.

37. Julián-López, B.; Boissière, C.; Chanéac, C.; Grosso, C.; Vasseur, S.; Miraux, S.; Duguet, E. and Sanchez, C. Mesoporous maghemite–organosilica microspheres: a promising route towards multifunctional platforms for smart diagnosis and therapy. *J. Mater. Chem*. **2007**, 17, 1563-1569.

38. Chastellain, M.; Petri, A.; Gupta, A.; Rao, K.V. and Hofmann, H. Superparamagnetic silica-iron oxide nanocomposites for application in hyperthermia, *Adv. Engin. Mater.* **2004**, 6 (4) 235-241.
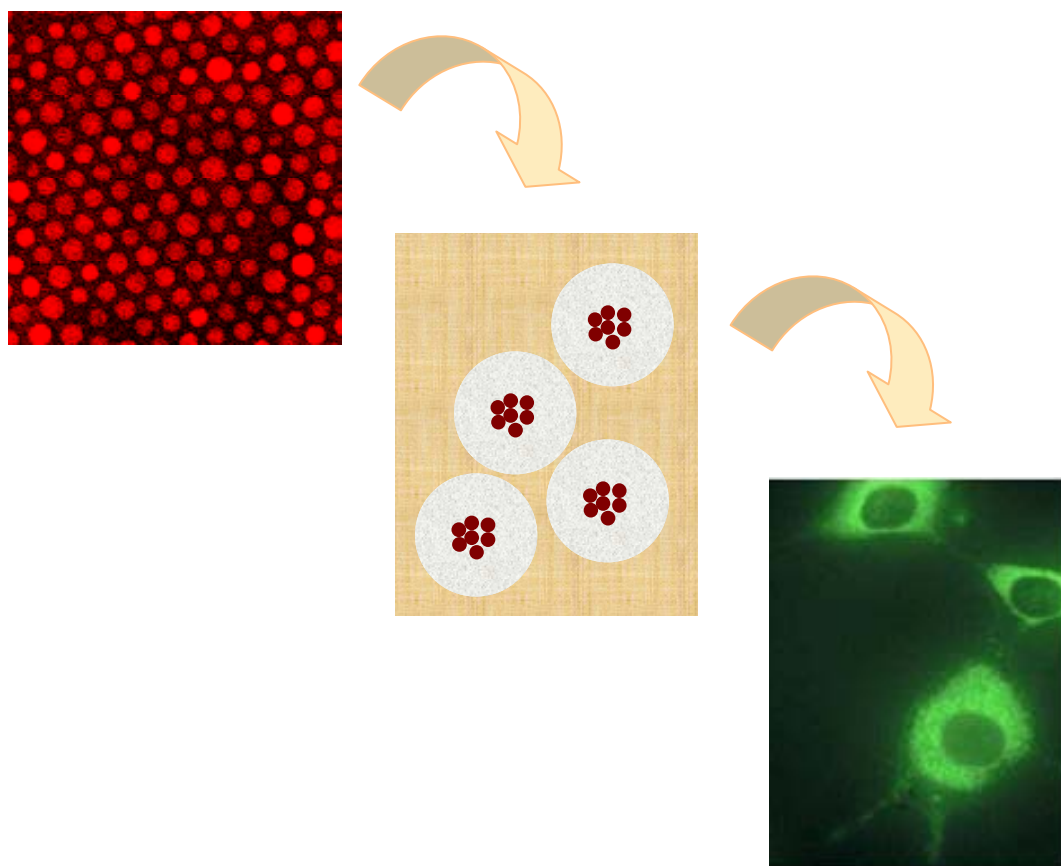
6. CONCLUSIONS

6.1.   Conclusions (English)

The main goal from the present thesis has been the development of a novel synthetic method to coat iron oxide nanoparticles with silica by sol-gel chemistry using supercritical fluid technology. A second objective has been the assessment of those materials in two different biomedical applications namely, as contrast agents for magnetic resonance imaging and as mediators for magnetic hyperthermia. The conclusions are divided into three sections:

i)   Synthesis and characterization of maghemite nanoparticles.

ii)   Coating of maghemite nanoparticles with silica by sol-gel chemistry under supercritical conditions.

iii)   Evaluation of the maghemite nanoparticles before and after the silica coating as contrast agents for magnetic resonance imaging and mediators for magnetic hyperthermia.

i) Synthesis and characterization of maghemite nanoparticles.

-   Monocrystalline maghemite nanoparticles have been successfully synthesized by thermal decomposition of iron pentacarbonyl in octyl ether in the presence of oleic acid and stabilized in hexane.

-   The mean particle size is tuned by the amount of oleic acid. Very narrow particle size distributions are obtained, as demonstrated by their self-assembling into 2D and 3D superlattices with hexagonal closed packing arrangements when deposited onto flat surfaces.

-   The system presents superparamagnetism at room temperature and high saturation magnetization values. Surprisingly, some of the smallest particles, 5 nm in size, show very high saturation magnetization (68 emu/g Fe_2O_3), close to the bulk value (76 emu/g Fe_2O_3 at RT). This observation is attributed to a higher degree of crystallinity with a smaller contribution of the magnetic dead layer.

-   The stabilization of nanoparticles in water at physiological pH is achieved via electrostatic repulsion with TMAOH and sodium citrate.

ii) Coating of maghemite nanoparticles with silica by sol-gel chemistry under supercritical conditions.

-   A novel synthetic protocol has been developed to coat the previous maghemite nanoparticles with silica by sol-gel chemistry under supercritical conditions of the solvent.

-   The synthesis of the silica coating as well as the extraction of the solvents (what constitutes the drying of the silica) are carried out under supercritical conditions in one-pot and one-step reaction.

-   This novel mechanism allows for the reduction of synthetic steps compared to other methods of silica coating, namely, the drying of the particles, the removal of porogenic agent and the purification. It also allows producing a fair amount of material, up to 3 g in one batch. We believe the process has good potentiality as to be easily scaled up.

-   In the initial sol the iron oxide nanoparticles self-arrange in clusters. The stability of these clusters depends on the order of addition of the reactants. The cluster size was dependent on the acetone to hexane volume ratio in the initial sol.

-   The final material is composed of solvent free magnetic-core@silica-shell nanoparticles, with no traces of unreacted precursors.

-   The resulting particles are spherical with diameters ranging from 70 to 200 nm. The magnetic cores are built up of groups of non-interacting maghemite nanoparticles clustered in the centre of every composite nanoparticle. For some experimental conditions, worm-like particles are obtained.

-   The silica shell is porous, with BET surface areas up to 100 m^2/g SiO_2.

-   The composite particles are superparamagnetic at room temperature. The size of the iron oxide nanoparticles forming the magnetic cluster does not change during the supercritical conditions, implying that no particle sintering takes place. Blocking temperature also remained unchanged.

-   The saturation magnetization of the composite particles is significantly larger compared to the original maghemite nanoparticles (61.5 vs. 33.1 emu/g Fe_2O_3). It is attributed to an improvement in the crystallinity of the iron oxide surface induced by the growing of the silica at high temperature.

-   Epsilon iron oxide@silica composite nanoparticles are synthesized by calcination in air of maghemite@silica composite particles at different temperatures and times. The formation of epsilon iron oxide is favoured by the physical confinement inside the silica shell. This is the first time, to the extent of our knowledge, that epsilon iron oxide@silica nanospheres with 90 wt.% of epsilon iron oxide (wt.% of magnetic phase) are obtained.

-   The magnetic phase in ε-Fe_2O_3@SiO_2 nanoparticles calcined up to 1100ºC for 30 h has 90 wt.% of epsilon phase. The spherical composite size is maintained up to 30 h of annealing. For longer annealing times some necking appears. At 1300ºC the silica crystallizes into cristobalite and epsilon phase is transformed to hematite and magnetite. The particle shape is then completely lost.

- Pure silica particles are also synthesized using the same synthetic protocol when no maghemite nanoparticles are added to the initial reactant solution.

- Particles are spherical when the reaction solvent is acetone and heterogeneous in shape when using ethanol due to the higher solubility of acetone in carbon dioxide. We are able to tune the particle size ranging from 200 nm to 4 microns. All the samples are microporous without use of porogenic agents: S_{BET} = 120-380 m²/g and d_{pore} < 2 nm. No traces of organic residues are detected by IR spectroscopy.

- The size and shape differences between the pure silica and composite particles, as well as the higher product yield of composite particles, is attributed to faster reaction kinetics for the composite particles (due to the selective adsorption of TMOS onto the maghemite nanoparticles, acting then as nucleation sites for silica). The lower porosity of composite particles is attributed to an inefficient supercritical drying of the silica shell.

iii) Evaluation of the maghemite nanoparticles before and after the silica coating as contrast agents for magnetic resonance imaging and mediators for magnetic hyperthermia.

- In vitro cellular cytotoxicity studies showed that: the iron oxide nanoparticles are biocompatible up to 100 µg/ml and only slightly toxic up to 400 µg/ml. Silica particles are non-toxic up to 150 µg/ml and only slightly toxic up to 1250 µg/ml. The toxicity of the composite particles is higher than that one of pure silica ones attributed to their smaller size.

- Maghemite can act as positive or negative contrast agent depending on its size, spatial distribution and stabilizing agent.

- Maghemite nanoparticles individually stabilized with sodium citrate act as positive contrast agents. This is an unusual but promising behaviour for iron oxide nanoparticles. This behaviour is attributed to: a) the high amount of available particle surface area to the water protons due to the small size of the nanoparticles (high longitudinal relaxivity), b) the high magnetization of the nanoparticles (high relaxivity) and c) size monodispersity of the system which implies a better homogeneity of the magnetic field induced by the nanoparticles (low transversal relaxivity).

- Composite particles act as negative contrast agents due to their high magnetization per particle (high transversal relaxivity) and the low accessibility to the iron oxide surface (low longitudinal relaxivity).

- The transversal relaxivities for the composite particles are, to the best of our knowledge, the highest ones published for iron oxide based contrast agents at 0.47 T, and considerably higher than several commercial contrast agents currently used for clinical diagnosis.

- We have found a relationship between the relaxivity of composite material and the magnetization per composite particle together with the silica shell thickness. In that sense, we expect higher values of relaxivity for particles with a higher amount of iron oxide nanoparticles and a thinner silica shell.

- The higher transversal relaxivity of composite particles compensates their higher cytotoxicity, since a lower dose might be necessary to obtain quality contrast.

- Concerning magnetic hyperthermia and contrary to the initial expectations, the SAR values decrease while increasing iron concentration, both in maghemite and composite nanoparticles.

- In the composite samples there is also an increase in SAR with decreasing the hydrodynamic size.

- We attribute the dependence of SAR with iron concentration to an increase of the medium viscosity, due to a tendency of oxides to gelify. In that sense, we hypothesize that the conversion of magnetic energy into heat is governed by the Brownian relaxation process against the Néel one.

Prospective of future research

Regarding prospective of future research the results presented in this thesis allow for further research in different directions. About the chemical aspect of the novel method, we expect this synthetic approach could be extended as a general protocol to coat other crystalline phases or even a mixture of two. For each new material, optimal conditions of reactants and solvents should be found to prepare a stable initial colloidal dispersion. Regarding the biomedical applications, the dependence of the relaxivity values with the magnetization per composite particle encourages synthesizing new particles with increasing iron oxide content and thinner silica shell. The modulation of the magnetic core size could also enable the synthesis of ε-Fe$_2$O$_3$@SiO$_2$ nanoparticles with tuneable ε-Fe$_2$O$_3$ particle size. Parallel, the increase of the silica shell porosity and new surface functionalization could broaden the application scope of the material for drug delivery applications.

6.2. Conclusiones (Español)

El objetivo principal de esta tesis ha sido el desarrollo de un nuevo método sintético para recubrir nanopartículas de óxido de hierro con sílice mediante química sol-gel y tecnología de fluidos supercríticos. El segundo objetivo ha sido la evaluación del material como agente de contraste para resonancia magnética de imagen (RMI) y como mediador de hipertermia magnética. Las conclusiones se dividen en tres secciones:

i)   Síntesis y caracterización de nanopartículas de maghemita.

ii)   Recubrimiento de nanopartículas de maghemita con sílice mediante química sol-gel en condiciones supercríticas.

iii)   Evaluación de las nanopartículas de maghemita antes y después del recubrimiento con sílice como agentes de contraste para resonancia magnética de imagen (RMI) y como mediadores de hipertermia magnética.

i) Síntesis y caracterización de nanopartículas de maghemita.

-   Hemos sintetizado nanopartículas de maghemita monocristalinas por descomposición térmica de pentacarbonilo de hierro y las hemos estabilizado en hexano con ácido oleico.

-   El tamaño medio de partícula se moduló con la cantidad de ácido oleico. Obtuvimos distribuciones de tamaño de partícula muy estrechas, que permite el auto ordenamiento de las nanopartículas en superestructuras 2D y 3D con empaquetamiento hexagonal compacto al depositarlas en superficies planas.

-   El sistema es superparamagnético a temperatura ambiente, con valores de magnetización de saturación (M_S) altos. Sorprendentemente, algunas de las partículas más pequeñas, de 5 nm, mostraron los valores de M_S más altos (68 emu/g Fe_2O_3), cercanos al valor másico (76 emu/g Fe_2O_3 a 298 K). Este comportamiento se atribuyó a una mejor cristalinidad de las partículas y por tanto, a una "dead layer" magnética más fina.

-   Las nanopartículas se estabilizaron en agua a pH neutro con electrolitos (TMAOH y citrato sódico).

ii) Recubrimiento de nanopartículas de maghemita con sílice mediante química sol-gel en condiciones supercríticas.

-   Hemos desarrollado un nuevo método sintético para recubrir las nanopartículas de maghemita con sílice por medio de química sol-gel en condiciones supercríticas.

- La síntesis de la capa de sílice y la extracción de los disolventes de reacción (secado de la sílice) se llevaron a cabo en condiciones supercríticas en un solo paso y en un único recipiente.

- Este nuevo método permite reducir el número de etapas experimentales comparado con otros métodos de recubrimiento de sílice: evita el secado de las partículas, la extracción del agente porogénico y la purificación del material. También permite sintetizar una cantidad considerable de producto, hasta 3 gramos por tanda. Creemos que el proceso tiene potencialidad para ser fácilmente escalado.

- Las nanopartículas de maghemita se organizan en clústeres en el sol inicial, antes de la reacción. La estabilidad de las nanopartículas en este sol depende del orden de adición de los reactivos. El tamaño de clúster depende de la relación de volúmenes entre la acetona y el hexano.

- El material obtenido son nanopartículas compuestas con un núcleo magnético y una capa de sílice, sin restos de disolvente ni de precursores iniciales.

- Las partículas compuestas son esféricas, con diámetros entre 70 y 200 nm. Los núcleos magnéticos están formados de nanopartículas de maghemita agrupadas en el centro, sin contacto entre ellas, formando un clúster. El tamaño de clúster se puede modular mediante la relación de volúmenes entre la acetona y el hexano en el sol inicial. Para algunas condiciones experimentales se obtienen partículas con forma de gusano.

- La capa de sílice es porosa, con áreas superficiales (S_{BET}) hasta 100 m^2/g SiO_2.

- Las partículas compuestas son superparamagnéticas a temperatura ambiente. El tamaño de las partículas de óxido de hierro del núcleo magnético no cambia durante las condiciones supercríticas, implicando que no hay sinterización. La temperatura de bloqueo tampoco cambia.

- La M_S de las partículas compuestas aumenta considerablemente respecto a las partículas de maghemita (61.5 vs. 33.1 emu/g Fe_2O_3). Se atribuyó a una mejora de la cristalinidad de la superficie de las nanopartículas de maghemita inducida por el crecimiento de sílice.

- Mediante la calcinación de las partículas compuestas a diferentes temperaturas y tiempos obtuvimos partículas compuestas de ε-Fe_2O_3. La formación de la fase épsilon se favoreció por el confinamiento físico en la sílice.

- La fase magnética de las partículas compuestas ε-Fe_2O_3@SiO_2 calcinadas a 1100ºC durante 30 h contiene 90% en peso de fase épsilon. Tiempos de calcinación más largos inducen "necking" entre partículas. A 1300ºC, la sílice cristaliza en

cristobalita y la fase épsilon se transforma en hematita y magnetita. La esfericidad de las partículas se pierde completamente.

- También sintetizamos partículas de sílice pura mediante el mismo método sintético, sin añadir óxido de hierro al sol inicial.

- Las partículas de sílice son esféricas si el disolvente usado es acetona y de forma heterogénea usando etanol, debido a la mayor solubilidad de la acetona en dióxido de carbono. Es posible modular el tamaño de partícula desde 200 nm a 4 micras. Todas las muestras son microporosas sin necesidad de usar agentes porogénicos: S_{BET} = 120-380 m^2/g y d_{poro} < 2 nm. No se detectaron restos orgánicos por espectroscopia IR.

- Las diferencias de tamaño y forma entre las partículas de sílice y las compuestas, así como el mayor rendimiento de reacción de las partículas compuestas, se atribuyó a una cinética de reacción más rápida en las partículas compuestas (debido a la adsorción específica del TMOS sobre las partículas de maghemita, que entonces actuaban como puntos de nucleación para la sílice).

- La menor porosidad de las partículas compuestas se atribuyó a un secado supercrítico ineficiente de la capa de sílice.

iii) Evaluación de las nanopartículas de maghemita antes y después del recubrimiento con sílice como agentes de contraste para resonancia magnética de imagen (RMI) y como mediadores de hipertermia magnética.

- Las nanopartículas de óxido de hierro muestran biocompatibilidad hasta 100 µg/ml y una cierta toxicidad hasta 400 µg/ml. Las partículas de sílice no presentan toxicidad hasta 150 µg/ml y una cierta toxicidad hasta 1250 µg/ml. La toxicidad de las partículas compuestas es mayor que la de las partículas de sílice, atribuido a su menor tamaño.

- Las nanopartículas de maghemita pueden actuar como agente de contraste positivo o negativo, dependiendo del tamaño, distribución espacial y agente estabilizante.

- Las nanopartículas de maghemita estabilizadas con citrato sódico se comportan como agentes de contraste positivo. Éste es un comportamiento inusual pero muy interesante. Se atribuyó a: a) gran área superficial de óxido de hierro disponible para los protones de agua, debido al pequeño tamaño de las partículas (alta relajatividad longitudinal), b) alta magnetización de las nanopartículas (alta relajatividad) y c) monodispersidad de tamaño del sistema, que implica una mejor homogeneidad del campo magnético inducido por las nanopartículas (baja relajatividad transversal).

- Las partículas compuestas se comportan como agentes de contraste negativo debido a la alta magnetización por partícula (alta relajatividad transversal) y baja o nula accesibilidad de los protones al núcleo magnético (baja relajatividad longitudinal).

- La relajatividad transversal de nuestras partículas compuestas es mayor que los valores que hemos encontrado en la bibliografía hasta ahora, para sistemas de óxido de hierro a 0.47 T. Además, son considerablemente mayores que la relajatividad de los agentes de contraste comerciales utilizados de forma rutinaria para diagnóstico clínico.

- La relajatividad transversal de las partículas compuestas aumenta con la cantidad de óxido de hierro por partícula compuesta y disminuye con el grosor de la capa de sílice.

- Por tanto, la toxicidad relativa de las partículas compuestas es menor debido a sus mayores valores de relajatividad, ya que se necesitaría menos cantidad para obtener imágenes bien contrastadas.

- Respecto a la hipertermia magnética y contrariamente a lo esperado, los valores de SAR disminuyen con la concentración de hierro, tanto en las partículas de maghemita como en las compuestas.

- En las partículas compuestas también observamos una disminución de SAR con el tamaño hidrodinámico de las partículas.

- Atribuimos la dependencia de SAR con la concentración de hierro a un aumento de la viscosidad del medio, debido a la tendencia de los óxidos a gelificar. En este sentido, postulamos que la conversión de energía magnética en térmica está gobernada por la relajación Browniana frente a la relajación de Néel.

6.3. Conclusions (Català)

L'objectiu principal d'aquesta tesi ha estat el desenvolupament d'un nou mètode sintètic per tal de recobrir nanopartícules d'òxid de ferro amb sílice mitjançant química sol-gel i tecnologia de fluids supercrítics. El segon objectiu ha estat l'avaluació dels materials com a agents de contrast per a ressonància magnètica d'imatge (RMI) i com a mediadors d'hipertèrmia magnètica. Les conclusions es divideixen en tres seccions:

i) Síntesi i caracterització de nanopartícules de maghemita.

ii) Recobriment de nanopartícules de maghemita amb sílice mitjançant química sol-gel en condicions supercrítiques.

iii) Avaluació de les nanopartícules de maghemita abans i després del recobriment amb sílice com a agents de contrast per a ressonància magnètica d'imatge (RMI) i com a mediadores d'hipertèrmia magnètica.

i) Síntesi i caracterització de nanopartícules de maghemita.

- Hem sintetitzat nanopartícules de maghemita monocristal·lines per descomposició tèrmica de pentacarbonil de ferro i les hem estabilitzat en hexà amb àcid oleic.

- La mida de les partícules es va poder modular amb la quantitat d'àcid oleic. S'han obtingut distribucions de mida molt estretes i per tant, les nanopartícules s'auto-ordenen en superestructures i empaquetament hexagonal compacte quan es dipositan en superfícies planes de silici.

- El sistema és superparamagnètic a temperatura ambient, amb valors de magnetització de saturació (M_S) alts. Sorprèn que algunes de les partícules més petites, 5 nm, presentin els valors més alts de M_S (68 emu/g Fe_2O_3), propers al valor del 'bulk' (76 emu/g Fe_2O_3 a 298 K). Hem atribuït aquest comportament a una millor cristal·linitat de les partícules i potser a una capa superficial magnèticament desordenada més fina.

- Les nanopartícules van estabilitzar-se en aigua, a pH neutre, desplaçant l'àcid olèic amb electròlits (TMAOH i citrat sòdic).

ii) Recobriment de nanopartícules de maghemita amb sílice mitjançant química sol-gel en condicions supercrítiques.

- Hem desenvolupt una nova metodologia sintètica per a recobrir les nanopartícules de maghemita amb sílice mitjançant química sol-gel en condicions supercrítiques.

- La síntesi de la capa de sílice i l'extracció dels dissolvents (assecatge de la sílice) es van portar a terme en condicions supercrítiques en un sol pas i en un únic recipient.

- Aquest nou mètode permet reduir el nombre d'etapes experimentals en comparació amb d'altres mètodes de recobriment de sílice: estalvia l'assecatge de les partícules, l'extracció de l'agent porogènic i la purificació del material resultant. També permet sintetitzar una quantitat considerable de material, fins a 3 grams per experiment. Creiem doncs, que el procés té potencialitat per a ser escalat.

- En el sol inicial, les nanopartícules de maghemita s'organitzen en clústers. L'estabilitat de les nanopartícules en aquest sol depèn de l'ordre d'adició dels reactius. La mida de clúster és controlable i depèn de la relació de volums entre acetona i hexà.

- El material obtingut són nanopartícules compostes amb un nucli magnètic i una capa de sílice, sense restes de dissolvent ni precursors inicials.

- Les partícules nanocompostes són esfèriques amb diàmetres d'entre 70 i 200 nm. Els nuclis magnètics estan formats de nanopartícules de maghemita no interaccionant agrupades al centre. Per algunes condicions sintètiques el material resultant té forma de cuc.

- La capa de sílice és porosa, amb àrees superficials (S_{BET}) fins a 100 m^2/g SiO$_2$.

- Les partícules compostes són superparamagnètiques a temperatura ambient. La mida de les partícula magnètiques del nucli no canvia durant el tractament en condicions supercrítiques, per tant no s'ha produït sinterització. La temperatura de bloqueig tampoc no ha canviat durant el procés.

- El valor de la magnetització de saturació de les partícules compostes augmenta considerablement respecte al valor de les partícules de maghemite (61.5 vs. 33.1 emu/g Fe$_2$O$_3$). Ho atribuïm a una millora de la cristal·linitat de la superfície de les nanopartícules de maghemita induïda pel recobriment de sílice.

- Mitjançant un tractament tèrmic de les partícules compostes (a diferents temperatures i temps) vam obtenir partícules compostes amb un nucli de ε-Fe$_2$O$_3$. L'estabilització de la fase èpsilon s'aconseguix pel confinament físic que exerceix la sílice.

- La fase magnètica de les partícules compostes ε-Fe$_2$O$_3$@SiO$_2$ calcinades a 1100ºC durant 30 h conté 90% en pes de fase èpsilon. Temps de calcinació més alts indueixen "necking" entre les partícules. A 1300ºC, la sílice cristalitza en cristobalita i la fase èpsilon es transforma en hematita i magnetita. La esfericitat de les partícules es perd completament.

- També hem sintetitzat partícules de sílice pura fent servir el mateix mètode sintètic, sense afegir òxid de ferro al sol inicial. Les partícules resultants són esfèriques quan el dissolvent utilitzat és acetona i de forma heterogènia quan es fa servir etanol. Això s'explica degut a la major solubilitat de l'acetona en el diòxid de carboni. Hem aconseguit modular la mida de partícula des de 200 nm fins a 4 micres. Malgrat no fer servir agents porogènics, les partícules són microporoses (S_{BET} = 120-380 m²/g i d_{porus} < 2 nm) i fent servir espectroscòpia IR no s'han detectat restes de compostos orgànics.

- Les diferències de mida i forma entre les partícules de sílice i les compostes, així com el major rendiment de reacció de les partícules compostes, s'ha atribuit a una cinètica de reacció més ràpida en les partícules compostes (degut a l'adsorció específica del TMOS sobre les partícules de maghemita, que actuen com a punts de nucleació per a la sílice). La menor porositat de les partícules compostes ho atribuïm a aquesta diferència en la cinètica de reacció que pot implicar un assecatge supercrític menys òptim de la capa de sílice en comparació a les partícules de sílice.

iii) Avaluació de les nanopartícules de maghemita abans i després del recobriment amb sílice com a agents de contrast per a ressonància magnètica d'imatge (RMI) i com a mediadores d'hipertèrmia magnètica.

- Hem demostrat que les nanopartícules d'òxid de ferro són biocompatibles fins a una concentració de 100 µg/ml i presenten una baixa toxicitat fins a 400 µg/ml. Les partícules de sílice són biocompatibles fins a una concentració de 150 µg/ml i una baixa toxicitat fins a 1250 µg/ml. Per una mateixa concentració, la toxicitat de les partícules compostes és més gran que la de les partícules de sílice.

- Les nanopartícules de maghemita poden actuar com a agent de contrast positiu o negatiu, depenent de la mida, distribució espaial i agent estabilitzant.

- Les nanopartícules de maghemita estabilitzades amb citrat sòdic actuen com a agents de contrast positiu. Aquest és un comportament poc comú però molt interessant. Ho atribuim a: a) degut a la mida petita de partícules, hi ha una gran àrea superficial d'òxid de ferro disponible pels protons de l'aigua (alta relaxativitat longitudinal), b) alta magnetització de les nanopartícules (alta relaxativitat) i c) monodispersitat de mida que implica una millor homogeneïtat del camp magnètic induït per les nanopartícules (baixa relaxativitat transversal).

- Les partícules compostes actuen com a agents de contrast negatiu degut a la l'alta magnetització per partícula (alta relaxativitat transversal) i baixa o nul·la accessibilitat dels protons al nucli magnètic (baixa relaxativitat longitudinal).

196

- La relaxativitat transversal de les nostres partícules compostes és més gran que els valors reportats a la bibliografia fins ara, per a sistemes d'òxid de ferro a 0.47 T. I són considerablement més grans que la relaxativitat dels agents de contrast comercials utilitzats en diagnosi clínica.

- Hem trobat una relació entre la relaxativitat de les partícules compostes i la magnetització per partícula pesat pel gruix de la capa de sílice. Així doncs, esperem que la relaxativitat augmenti a l'augmentar la quantitat d'òxid de ferro per partícula composta i al disminuir el gruix de la capa de sílice.

- Respecte a les mesures de hipertèrmia magnètica, i contràriament a l'esperat, els valors de velocitat específica d'absorció (SAR) disminueixin amb la concentració de ferro, en les partícules de maghemita i també en les compostes.

- Per les partícules compostes també s'observa una disminució del valor de SAR amb la mida hidrodinàmica de les partícules.

- Atribuïm la dependència del valor de SAR amb la concentració de ferro a un augment de la viscositat del medi, degut a la tendència dels òxids a gelificar. D'aquesta manera, postulem que la conversió d'energia magnètica a tèrmica està governada fonamentalment per la relaxació Browniana i no per la relaxació de Néel.

7. ANNEXES

7.1. Publications derived from the main subject of this thesis

- Taboada, E.; Rodríguez, E.; Roig, A.; Oró, J.; Roch, A. and Muller, R. N. Relaxometric and magnetic characterization of ultra-small iron-oxide nanoparticles with high magnetization. Evaluation as potential T_1 Magnetic Resonance Imaging contrast agents for Molecular Imaging *Langmuir*, **2007**, 23, 4583-4588. Citations (Sept. 2nd 2009): 18.

- Taboada, E.; Solanas, R.; Rodríguez, E.; Weissleder, R. and Roig, A. Supercritical fluid assisted one-pot synthesis of biocompatible core(γ-Fe$_2$O$_3$)@shell(SiO$_2$) nanoparticles as high relaxivity T_2-contrast agents for magnetic resonance imaging. *Advanced Functional Materials*, **2009**, 19, 2319-2324.

- Chen, D.-X.; Sanchez, A.; Taboada, E.; Roig, A.; Sun, N. and Gu, H. C. Size determination of superparamagnetic iron oxide nanoparticles from magnetization curve, *Journal of Applied Physics* **2009**, 105 (8) 083924-083924-6.

- Taboada, E.; Roig A.; Gich M. Nanospheres of silica with a ε-Fe$_2$O$_3$ single crystal nucleus, submitted for publication.

202

Relaxometric and Magnetic Characterization of Ultrasmall Iron Oxide Nanoparticles with High Magnetization. Evaluation as Potential T_1 Magnetic Resonance Imaging Contrast Agents for Molecular Imaging

Elena Taboada,[†] Elisenda Rodríguez,[†,‡] Anna Roig,*,[†] Judit Oró,[†] Alain Roch,[‡] and Robert N. Muller[‡]

Institut de Ciència de Materials de Barcelona, Consejo Superior de Investigaciones Científicas (ICMAB-CSIC), Esfera de la UAB, 08193 Bellaterra, Catalunya, Spain, and NMR and Molecular Imaging Laboratory, Department of General, Organic and Biomedical Chemistry, University of Mons-Hainaut, B-7000 Mons, Belgium

Here we report on the synthesis of ultrasmall γ-Fe_2O_3 nanoparticles (5 nm) presenting a very narrow particle size distribution and an exceptionally high saturation magnetization. The synthesis has been carried out by decomposition of an iron organometallic precursor in an organic medium. The particles were subsequently stabilized in an aqueous solution at physiological pH, and the colloidal dispersions have been thoroughly characterized by complementary techniques. Particular attention has been given to the assessment of the mean particle size by transmission electron microscopy, X-ray diffraction, dynamic light scattering, magnetic, and relaxometric measurements. The good agreement found between the different techniques points to a very narrow particle size distribution. Regarding the magnetic properties, the particles are superparamagnetic at room temperature and present an unusually high saturation magnetization value. In addition, we describe the potential of these particles as specific positive contrast agents for magnetic resonance molecular imaging.

Introduction

Magnetic resonance imaging (MRI) is a medical technique widely employed in many clinical practices due to its capability to enhance contrast differences between healthy and pathological tissues. Images of body sections precisely reflect the variation in the proton density and longitudinal (T_1) or transversal (T_2 or T_2*) relaxation times of the tissues. Despite the inherent versatility of this imaging modality, researchers and clinicians are dedicating huge efforts to develop safer and more effective contrast agents (CAs) that will expand the diagnostic utility and improve the precision of MRI.[1] The main application of CAs relies on the shortening of the relaxation times of the water protons. Positive contrast agents reduce T_1, resulting in a brighter signal, while negative contrast agents reduce T_2 (or T_2*), resulting in a darker signal. The reciprocals of the relaxation times are called the relaxation rates, R_1 and R_2, with the effectiveness of a CA expressed as relaxivities, r_1 and r_2, i.e., the rate enhancement(s) brought per millimolar concentration of metal.

A large number of compounds, mostly paramagnetic substances, have been assayed as potential MRI contrast agents.[2,3] Gadolinium chelates, such as Gd−DTPA, constitute the largest group of paramagnetic MR T_1 contrast agents and are considered to be safe and effective.[4−6] Up to now, iron oxides (magnetite and maghemite) have played an important role as negative MR

T_2 contrast agents due to their sizes and magnetic properties. Various iron oxide nanoparticles have been synthesized and evaluated as T_2 CAs.[7−10] They mainly differ in the iron oxide phase, the magnetic core size, or the coating material used (dextran, albumin, silicones, poly(ethylene glycol), etc.). For those systems, the reported hydrodynamic mean diameter ranges from 10 to 3500 nm. Very few cases of iron oxide colloidal dispersions with very small particle size (5−10 nm) have been reported to act as T_1 CAs.[11] To achieve that, one should try to maximize r_1 while keeping r_2 as small as possible.[12]

In the past few years, considerable advances have been made in high-resolution in vivo imaging methods for monitoring specific molecular or cellular processes. For this purpose and due to the limited number of targets, high relaxivity values and high specificity of the CAs are necessary. When using Gd-based materials, a large number of paramagnetic centers (high concentration of metal) are often needed to reach a sufficient detection level.[13−16] Owing to the large number of iron atoms per crystal, superparamagnetic nanoparticles of iron oxide have

---

* To whom correspondence should be addressed. E-mail: roig@icmab.es.

† ICMAB-CSIC.

‡ University of Mons-Hainaut.

(1) Rodríguez, E.; Roig, A.; Molins, E.; Arús, C.; Quintero, M. R.; Cabañas, M. E.; Cerdán, S.; Lopez-Larrubia, P.; Sanfeliu, C. *NMR Biomed.* **2005**, *18*, 300.

(2) Lauffer, R. B. *Chem. Rev.* **1987**, *87*, 901.

(3) Merbach, A. E.; Toth, E. *The Chemistry of Contrast Agents in Medical Magnetic Resonance Imaging*; Wiley: Chichester, U.K., 2001.

(4) Aime, S.; Frullano, L.; Crich, S. G. *Angew. Chem., Int. Ed.* **2002**, *41*, 1017.

(5) Caravan, P. J.; Ellison, J.; McMurry, J.; Lauffer, R. B. *Chem. Rev.* **1999**, *99*, 2293.

(6) Rink, P. A.; Muller, R. N. *Eur. Radiol.* **1999**, *9*, 998.

(7) Josephson, L.; Lewis, J.; Jacobs, P.; Hahn, P. F.; Stark, D. D. *Magn. Reson. Imaging* **1998**, *6*, 647.

(8) Weissleder, R.; Elizondo, G.; Wittenberg, J.; Rabito, C. A.; Bengele, H.; Josephson, L. *Radiology* **1990**, *175*, 489.

(9) Muller, R. N.; Vander Elst, L.; Roch, A.; Peters, J. A.; Csajbok, E.; Gillis, P.; Goussin, Y. *Adv. Inorg. Chem.* **2005**, *57*, 239.

(10) Laurent, S.; Ouakssim, A.; Nicotra, C.; Goussin, Y.; Roch, A.; Vander Elst, L.; Cornant, M.; Soleil, P.; Muller, R. N. *Phys. Status Solidi C* **2004**, *1*, 3644.

(11) Cunningham, C. H.; Arai, T.; Yang, P. C.; McConnell, M. V.; Pauly, J. M.; Conolly, S. M. *Magn. Reson. Med.* **2005**, *53*, 999.

(12) Kellar, K. E.; Fuji, D. K.; Gunther, W. H. H.; Briley-Saebo, K.; Bjornerud, A.; Spiller, M.; Koening, S. H. *Magn. Reson. Mater. Phys., Biol. Med.* **1999**, *8* (3), 207. Kellar, K. E.; Fuji, D. K.; Gunther, W. H. H.; Briley-Saebo, K.; Bjornerud, A.; Spiller, M.; Koening, S. H. *J. Magn. Reson. Imaging* **2000**, *11*, 488.

(13) Modo, M.; Mellodew, K.; Cash, D.; Fraser, S. E.; Meade, T. J.; Price, J.; Williams, S. C. *Neuroimage* **2004**, *21*, 311.

(14) Querol, M.; Chen, J. W.; Weissleder, R.; Bogdanov, A. *Org. Lett.* **2005**, *7* (9), 1719.

(15) Cabella, C.; Geninatti Crich, S.; Corpillo, D.; Barge, A.; Ghirelli, C.; Bruno, E.; Lorusso, V.; Uggeri, F.; Aime, S. *Contrast Med. Mol. Imaging* **2006**, *1*, 23.

strong T_2 and T_2^* effects and therefore can be useful to image low concentrations of a specific molecular process.[17,18] Negative T_2 CAs from the iron oxide particles sometimes extend well beyond their immediate surroundings, leading to distorted or obscure adjacent anatomy.[19] In that context, positive iron oxide T_1 CAs, once adequately functionalized, can be useful for applications, such as tracking of stem cells or transplanted cells, where the exact location and extent of the cells are important parameters.[20] Alternatively, ultrasmall particles of iron oxides have also been used to develop blood pool contrast media for magnetic resonance angiography.[21]

In spite of their widespread use, inherent problems of iron oxide systems remain unsolved or difficult to address, especially for ultrasmall particle sizes. The most prominent ones are a broad particle size distribution, lack of crystal phase identification, low value of the saturation magnetization of the nanoparticles as compared to the bulk materials, particle aggregation in a magnetic field, and particle sedimentation in physiological media. Moreover, as we have previously mentioned, the negative contrast agents induce signal voids (darkening) in the image, and then the CA enhanced area cannot be distinguished from naturally dark areas. In such contexts, very small (5–10 nm) and well-characterized particles are needed.

The aim of this work is to investigate the physical-chemical, magnetic, and relaxometric behavior of ultrasmall maghemite nanoparticle aqueous dispersions with very narrow particle size distribution and high magnetization, stabilized at basic and physiological pH, to assess the homogeneity of the system by measuring the mean particle size by complementary techniques, and to give a preliminary estimation of its potential as a positive contrast agent for MRI. The synthesis of the nanoparticles was adapted from a previously reported one based on the decomposition of $Fe(CO)_5$ in hydrocarbon solvents.[22] To stabilize the particles in a physiological environment, they have been transferred to an aqueous medium using an ammonium salt and sodium citrate. The particle size distribution remained narrow, as characterized by transmission electron microscopy (TEM), X-ray diffraction (XRD), and magnetic measurements, as well as superparamagnetic at room temperature. The performed relaxometric characterization is in good agreement with magnetic and TEM results, pointing also to a very narrow distribution of the particle sizes. As a consequence of the high magnetization of our particles at clinical field strengths and their ultrasmall size, the system acts as a positive T_1 contrast agent with a very small r_2/r_1 ratio, and the stabilizer used will enable further functionalization of these particles. After functionalization with specific biological ligands these nanoparticles could be used as magnetic reporters for molecular imaging probes.

Materials and Methods

Materials. Iron pentacarbonyl ($Fe(CO)_5$; 99.999%), oleic acid (99%), dioctyl ether (99%), tetramethylammonium hydroxide ((TMA)OH; 25 wt % in H_2O), sodium citrate, potassium dichromate

($K_2Cr_2O_7$; 1/25 M in H_2O), tin(II) chloride ($SnCl_2$; 98%), mercury-(II) chloride ($HgCl_2$; 99.5%), sodium diphenylamine 4-sulfonate, and chloric acid (HCl; 37%) were purchased from Sigma-Aldrich (Spain) and used as received without further purification.

Synthesis of Hexane-Dispersed Maghemite Nanoparticles. Maghemite nanoparticles were synthesized by decomposition of iron pentacarbonyl in dioctyl ether, in the presence of oleic acid, a nonpolar surfactant. Briefly, 0.32 mL (1 mmol) of oleic acid was added to 20 mL of dioctyl ether (solvent) and heated under an argon atmosphere to 90 °C. Then, 0.1 mL (0.75 mmol) of $Fe(CO)_5$ was added to the reaction mixture. The temperature was raised to 340 °C and kept constant for 30 min. Afterward, the mixture was allowed to cool to room temperature. To isolate the nanoparticles from the reaction medium, 40 mL of ethanol was added to precipitate the particles. The mixture was centrifuged, and the black precipitate was recovered in 20 mL of hexane, followed by another centrifugation to allow the precipitation of any insoluble impurities. The solution was recovered and stored tightly closed and hereafter is referred to as Fe_2O_3–hexane.

Stabilization of Maghemite Nanoparticles at Physiological pH. To stabilize the particles in an aqueous solution, the organic nonpolar surfactant was displaced by an electrolyte, (TMA)OH. A 5 mL portion of an aqueous solution of (TMA)OH (1.71 wt % in water) was added to 5 mL of the hexane iron oxide dispersion. The mixture was stirred for 12 h. The nanoparticles were recovered by precipitation with acetone, followed by centrifugation. The supernatant was then discarded, the precipitate was resuspended in 0.02 mL of (TMA)-OH, and water was added to bring the total volume to 5 mL. The material was stored and hereafter is referred to as Fe_2O_3–water. After addition of 0.02 mL of (TMA)OH (25 wt % in water) and 8 mg (0.03 mmol) of sodium citrate to a 0.5 mL of Fe_2O_3-water solution, the pH was brought to neutral pH by adding 0.1 M HNO_3 dropwise. The sample then got clear and stable and hereafter is referred to as Fe_2O_3-citrate.

Characterization of Magnetic Nanoparticles. *TEM and Electron Diffraction*. A JEOL JEM-1210 electron microscope, operating at 120 keV, was used for the electron diffraction analysis and transmission electron microscopy. The samples for electron microscopy were prepared by deposition of a droplet of the nanoparticle solution onto a carbon-coated film supported on a copper grid and allowed to dry.

XRD. The Fe_2O_3–water sample (after freeze-drying) was characterized by X-ray diffraction with a Siemens D5000 X-ray powder diffractometer using Cu Kα incident radiation. XRD patterns were analyzed by Rietveld refinement with the MAUD program.[23]

Dynamic Light Scattering (DLS) and ζ Potential. Dynamic light scattering and ζ potential measurements were performed with a Zetasizer Nano ZS (Malvern Instruments), provided with a He/Ne laser of 633 nm wavelength. The determination of the isoelectric point, IEP, was performed using the MPT-2 autotitrator, an accessory of the Zetasizer Nano ZS. The samples were further dissolved 20 times before the measurements of the isoelectric point.

Infrared (IR) Spectroscopy. IR spectra (4000–400 cm^{-1}) from KBr disks of Fe_2O_3 aqueous solutions (after freeze-drying of the aqueous solution) and of Fe_2O_3 in hexane solution (after evaporation of the solvent) were recorded on a Fourier transform Perkin-Elmer spectrometer.

Magnetic Measurements. Hysteresis loops of the Fe_2O_3 aqueous solutions at room temperature were performed in a magnetometer, VSM-NUVO, MOLSPIN, Newcastle Upon Tyne, U.K. For the frozen Fe_2O_3–water sample, hysteresis loops at 5 K and the zero-field cooling–field cooling (ZFC–FC) curves were measured with a superconducting quantum interference device (SQUID) magnetometer (Quantum Design MPMS5XL). The experimental results were corrected for the holder contribution and for a temperature-independent diamagnetic contribution. All the magnetization data are presented in units of (A m^2)/kg of Fe_2O_3.

Relaxometric Measurements. The NMRD (nuclear magnetic resonance dispersion) profiles were recorded from 10 kHz to 10

(16) Deboutière, P.-J.; Roux, S.; Vocanson, F.; Billotey, C.; Beuf, O.; Favre-Réguillon, A.; Lin, Y; Pellet-Rostaing, S.; Lamartine, R; Perriat, P.; Tillement, O. *Adv. Funct. Mater.* **2006**, *16*, 2330.

(17) Montet, X.; Montet-Abou, K.; Reynolds, F.; Weissleder, R.; Josephson, L. *Neoplasia* **2006**, *8* (3), 214.

(18) Boutry, S.; Laurent, S.; Vander Elst, L.; Muller, R. N. *Contrast Med. Mol. Imaging* **2006**, *1*, 15.
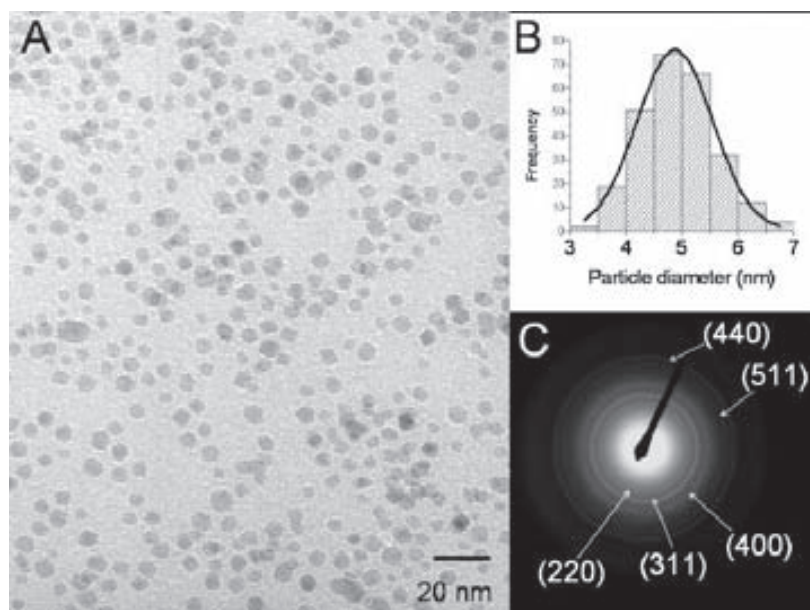
(19) Could, P. *Nanotoday* **2006,** *1* (4), 31.

(20) Hauger, O.; Frost, E.; Heeswijk, R.; Deminière, C.; Xue, R.; Delmas, Y.; Combe, C.; Moonen, C.; Grenier, N.; Bulte, J. *Radiology* **2006**, *238*, 200.

(21) Wagner, S.; Schnorr, J.; Pilgrim, H.; Hamm, B.; Taupitz, M. *Invest. Radiol.* **2002**, *37* (4), 167.

(22) Hyeon, T.; Lee, S. S.; Park, J.; Chung, Y.; Bin Na, H. *J. Am. Chem. Soc.* **2001**, *123*, 12798.

(23) Lutterrotti, L.; Gialanella, S. *Acta Mater.* **1997**, *46*, 101.

Figure 1. (A) TEM images of Fe_2O_3−hexane. (B) Particle size distribution histogram. (C) Selected area electron diffraction (SAED) pattern with indexed planes.

MHz on a Stelar field cycling relaxometer (Stelar, Mede, Italy). Additional measurements at 20 and 60 MHz were performed on a Bruker Minispec system (Bruker, Karlsruhe, Germany). The stability of the T_1 and T_2 relaxation times was assessed by repeating the T_1 and T_2 measurements of one sample at several times (24, 48, and 36 h). No relaxivity changes were detected.

Total Iron Concentration. The iron concentration in 0.2 mL for the Fe_2O_3 aqueous solutions was determined by relaxometry measurements at 20 MHz and 330 K after mineralization in acidic conditions (0.6 mL of HNO_3 and 0.3 mL of H_2O_2) by microwaves (Milestone MSL-1200, Sorisole, Italy). The evidence of the Fe^{2+} ion in the Fe_2O_3−water solution was determined by titration with potassium dichromate ($K_2Cr_2O_7$).

Results and Discussion

Characterization of Fe_2O_3−Hexane Nanoparticles. Iron oxide nanoparticles, crystalline and with very narrow particle size distribution, have been synthesized from the decomposition of the $Fe(CO)_5$ in an organic solvent. Oleic acid creates a shell around the inorganic iron oxide core through the carboxylate oxygens, resulting in a steric repulsion between the particles and thus preventing their aggregation and precipitation. Transmission electron microscopy images of the Fe_2O_3−hexane solution show rather spherical, well-formed nanocrystals with narrow particle size distribution (see Figure 1A). By measuring more than 260 particles, the mean diameter obtained is 4.9 ± 0.7 nm, with a standard deviation of 14% (see Figure 1B), where 94% of the particles display sizes between 3.5 and 5.75 nm, and none of them are larger than 8 nm. It has to be assumed that for very small particle sizes (∼5 nm) a difference of 0.5 nm in diameter already means a standard deviation of 10%. High crystallinity of the magnetic particles is deduced from the good definition of the electron diffraction ring pattern (see Figure 1C). It corresponds to a polycrystalline diffraction pattern (the electron beam is larger than a single particle). The diffraction rings can be equally well indexed considering any of the two iron oxide crystal structures: maghemite (γ-Fe_2O_3) or magnetite (Fe_3O_4). Complementary analyses have been carried out to discern which one of the structures is present in our sample (results shown in the next section).

Characterization and Stabilization of Fe_2O_3−Water Nanoparticles. Before these particles can act as contrast agents, they
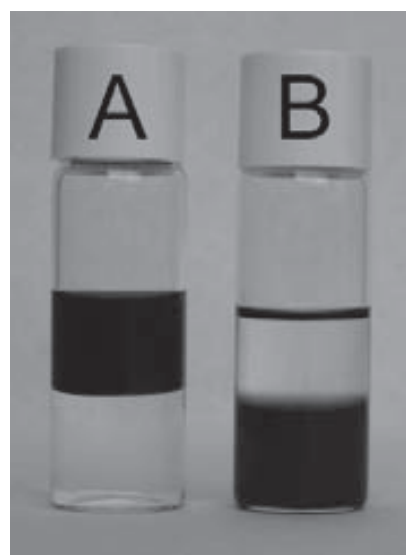
Figure 2. Photograph of two-phase mixtures with Fe_2O_3 nanoparticles dispersed in hexane (A) and in water (B).

must be first stabilized in water at physiological pH. The redispersion of Fe_2O_3−hexane nanoparticles in water requires the removal of the surfactant layer, oleic acid, and subsequent replacement with (TMA)OH. Figure 2 shows a photograph of Fe_2O_3−hexane (top of the two-phase mixture, Figure 2A) and of Fe_2O_3−water (bottom of the two-phase mixture, Figure 2B), that is, before and after the phase transfer. In both cases the iron concentration was measured, obtaining the same value in hexane and in water solution, pointing to an exchange yield of 100%.

X-ray diffraction was performed on a lyophilized aliquot of the Fe_2O_3−water sample. Because of the modest amount of available sample and the small size of the crystalline particles, the peaks of the diffractogram are not very well defined (see the Supporting Information). They can be indexed either to maghemite or magnetite. The calculated crystallite size, according to the Rietveld refinement of the pattern, was 5 ± 1 nm, for both maghemite and magnetite, a value which is in agreement with the one obtained by TEM (results not shown).
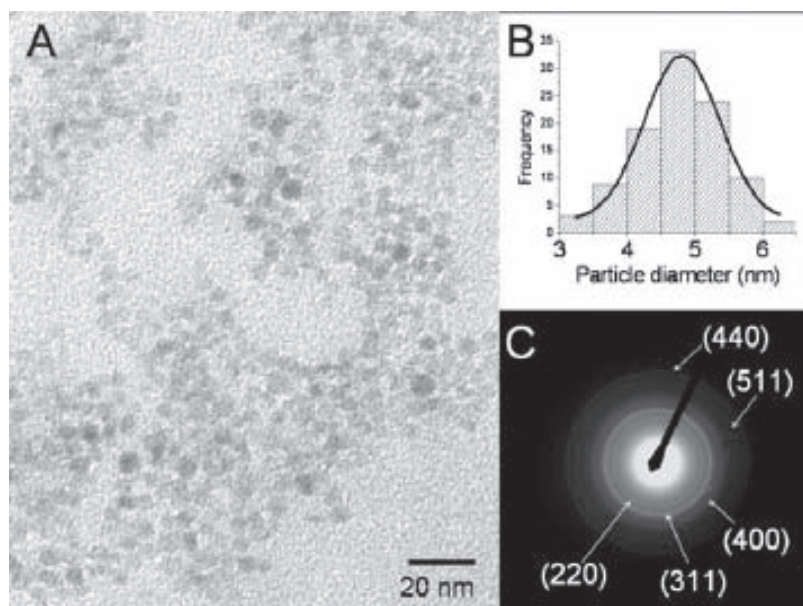
Figure 3. (A) TEM images of Fe_2O_3−citrate. (B) Particle size distribution histogram. (C) SAED pattern with indexed planes.

To discern whether our iron oxide particles are built up of magnetite ($Fe_3O_4 \equiv 2Fe^{3+}Fe^{2+}4O^{2-}$) or maghemite ($Fe_2O_3 \equiv 2Fe^{3+}3O^{2-}$), the existence of Fe^{2+} ions was determined by the titration with potassium dichromate. No significant Fe^{2+} ion concentration was determined, suggesting the maghemite phase as the crystalline phase. Moreover, the solution presents a red-brown color, as is expected for maghemite solutions, and not black, which would correspond to magnetite nanoparticle dispersions.[24]

Keeping in mind the biological applications, it was necessary to decrease the pH value from basic to neutral pH. For this purpose, nitric acid (HNO_3) was also used in the presence of sodium citrate to avoid the agglomeration and precipitation of the nanoparticles at pH lower than 7.5 (the stable pH range of the aqueous samples was further determined with ζ potential measurements, results shown below).

TEM images were also obtained for Fe_2O_3−citrate, resulting in the same particle characteristics as before (see Figure 3A). The mean particle diameter was 4.8 ± 0.6 nm, with a standard deviation of 12%, where 98% of the particles display sizes between 3.25 and 5.75 nm (see Figure 3B), the largest particles being 6.25 nm in diameter. The electron diffraction pattern (see Figure 3C) displays the same diffraction rings as before. The results suggest that no physical-chemical changes occurred during the organic solvent−water exchange.

The hydrodynamic diameter, d_{HYD}, is a useful measurement that will define the final biological application of the studied material. Dynamic light scattering size measurements were performed for the three samples: Fe_2O_3−hexane, Fe_2O_3−water, and Fe_2O_3−citrate, resulting in hydrodynamic diameters of 12 ± 2, 8 ± 2, and 18 ± 4 nm, respectively. We interpret the increase in size for the Fe_2O_3−citrate sample with regard to the Fe_2O_3−water one as due to the incorporation of the citrate anions at the surface of the iron particles, which may induce some aggregation between pairs of particles.

Subsequently, the ζ potential and the IEP for the Fe_2O_3 aqueous solutions were estimated. The ζ potential value can be used as an indicator of the stability of a colloidal system. The higher the ζ absolute values, the higher the net electrical charge on the
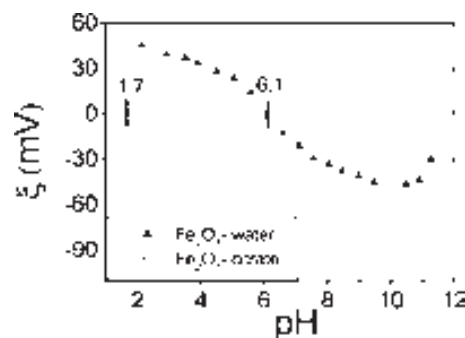
Figure 4. Behavior of the ζ potential versus pH for the Fe_2O_3−water and Fe_2O_3−citrate samples.

surface of the particles and, therefore, the larger the electrostatic repulsion between particles. The theoretical limit of stability is $|30|$ mV; i.e., a colloidal system will be stable if its ζ potential is higher than 30 mV or lower than −30 mV. The IEP specifies the pH at which the net electrical charge on the surface of the particles is zero, i.e., the pH of lowest stability of the system.[25] In Figure 4, the behavior of the ζ potential for Fe_2O_3−water and for Fe_2O_3−citrate versus the pH is shown. For Fe_2O_3−water, ζ is lower than −30 mV for pH > 7.5 and higher than 30 mV for pH < 4.3, with an isoelectric point of 6.1, suggesting a lack of stability in the range of physiological pH. The addition of citrate shifts the isoelectric point down to 1.7. This system is then stable at pH higher than 4.1, up to which the citrate anions are negatively charged and no longer neutralized by the protons of the medium, ensuring the electrostatic repulsion between the particles.

Finally, clear evidence of the removal of the organic layer from the surface of the particles was also provided by FTIR spectroscopy measurements of dried samples mixed with KBr. In the case of the hydrophobic particles, oleic acid is observed, while in aqueous solution, for Fe_2O_3−water and for Fe_2O_3−citrate, the organic ligand has been replaced by (TMA)OH. Further, the spectrum of Fe_2O_3−citrate shows clearly the adsorption of citrate anions but still conservation of some of the (TMA)OH molecules (see the Supporting Information).

(24) Bruce, I. J.; Taylor, J.; Todd, M.; Davies, M. J.; Borioni, E.; Sangregorio, C.; Sen, T. *J. Magn. Magn. Mater.* **2004**, *284*, 145.

(25) Malvern Instruments. *Zetasizer Nano Series User Manual*; Worcestershire, U.K., 2004; Nano 317 Issue 2.1, 16.1−16.3.
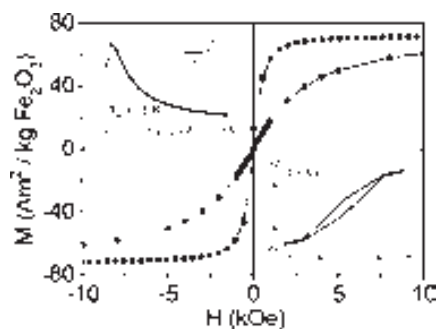
Figure 5. Main panel: magnetization curves at 298 K (circles) and 5 K (squares) for the Fe_2O_3−water sample. Upper inset: ZFC−FC curves. Lower inset: enlargement of the magnetization loop at 5 K.

Magnetic measurements of the Fe_2O_3−water sample are shown in Figure 5. The magnetization curve at room temperature plotted in Figure 5 shows that the Fe_2O_3−water sample exhibits superparamagnetic behavior deduced by the zero coercitive field and the zero remanent magnetization values. At 5 K, the maghemite nanoparticles show the expected ferrimagnetic behavior with a coercive field of 96 Oe (see the lower inset in Figure 5). The sample is already saturated at 10 kOe, with a saturation magnetization value (M_S) of 74 (A m^2)/kg of Fe_2O_3. Data at room temperature were fitted to a Langevin function, obtaining the following values: M_S = 68 (A m^2)/kg and d_{mag} = 5 nm, results which are in good agreement with TEM measurements and a magnetization saturation value only 10% lower than the value for the bulk material (lit.[26] M_S = 76 (A m^2)/kg of Fe_2O_3 at 298 K). Interestingly enough, our iron oxide nanoparticles exhibit a strong induced magnetization, close to the bulk value, even after their size is decreased to 5 nm, contrasting with the low saturation magnetization reported in many other maghemite particulated systems[27−29] (a detailed magnetic study is currently being carried out).

The ZFC−FC curves of the Fe_2O_3−water sample (upper inset in Figure 5) describe the temperature dependence of the magnetization. The ZFC curve gives information about the ferri-superparamagnetic transition of the system, which occurs at the temperature of the maximum magnetization value, the blocking temperature (T_B). For our system a T_B value of 15 K was obtained. The splitting of the curves just below T_B and the sharp maximum of the ZFC curve once more stand for a very narrow particle size distribution.

No significant changes in the magnetic behavior were detected when the above-described results were compared with the ones obtained for the Fe_2O_3−citrate system (see the Supporting Information). The shape of the magnetization loop at room temperature for the Fe_2O_3−citrate system is characteristic of a superparamagnetic system with a saturation magnetization value of 65 (A m^2)/kg of Fe_2O_3, confirming the magnetic stability of the sample at different pH values.

Some physical properties of Fe_2O_3−water and of Fe_2O_3−citrate are summarized in Table 1.

As previously mentioned, MR contrast agents act by shortening the relaxation times of the surrounding protons, T_1 and T_2, because of their inherent magnetic properties. The effectiveness of a CA

Table 1. Physical Properties of Fe_2O_3−Water and Fe_2O_3−Citrate Solutions[a]

physical property	Fe_2O_3−water	Fe_2O_3−citrate
d_{TEM} (nm)	4.9 ± 0.6	4.8 ± 0.6
d_{XRD} (nm)	5 ± 1	
d_{HYD} (nm)	8 ± 2	18 ± 4
crystalline phase	γ-Fe_2O_3	γ-Fe_2O_3
color of solution	red	red
IEP (pH unities)	6.1	1.7
pH	12.5	7.4
M_S ((A m^2)/kg) at 298 K	68	65
H_C (Oe) at 5 K	96	73
T_B (K)	15	11

[a] d = average particle diameter, TEM = transmission electron microscopy, XRD = X-ray diffraction, HYD = hydrodynamic, IEP = isoelectric point, M_S = saturation magnetization, H_C = coercive field, and T_B = blocking temperature.

Table 2. Relaxivity Values of Fe_2O_3−Water Solutions at Basic pH and 310 K

	r_1 (mM^{-1} s^{-1})	r_2 (mM^{-1} s^{-1})	r_2/r_1
20 MHz	20.81	28.61	1.38
60 MHz	17.59	35.75	2.03

Table 3. Relaxivity Values of Fe_2O_3−Citrate Solutions at Neutral pH and 310 K

	r_1 (mM^{-1} s^{-1})	r_2 (mM^{-1} s^{-1})	r_2/r_1
20 MHz	20.76	51.02	2.46
60 MHz	14.50	66.90	4.61

is usually expressed as relaxivities, r_1 and r_2, per millimolar concentration of metal. Relaxivities of Fe_2O_3−water nanoparticles placed in water with TMAOH are shown in Table 2. r_1 values are higher than those observed for the paramagnetic complexes, such as Gd−DTPA, due to its high magnetization, while r_2 values are much lower than values observed for the superparamagnetic particles of larger size. The magnitude of r_1 is dependent on the magnetization of the CA, the electron spin relaxation, the size of the magnetic crystal, and the accessibility to the CA of bearing nuclear spins of the tissue. The magnitude of r_2 reflects the ability of the CA to produce local magnetic inhomogeneities. At high field r_1 decreases while r_2 increases when the diameter of the crystal is larger. The ratio r_2/r_1 is therefore an indicator of the relaxometric properties of a CA, and it is used to classify a given type of MR CA as a T_1 or T_2 CA.[6] In general, for paramagnetic chelates, r_2/r_1 varies between 1 and 2, and for the superparamagnetic colloids it can be as large as 50. In our system, due to the small size of the iron oxide particles together with its high magnetization, the ratio r_2/r_1 corresponds to the typical values expected for paramagnetic complexes (T_1 CA), thus enlarging the diagnosis possibilities of the iron oxide systems. In the case of Fe_2O_3−water, r_2/r_1 = 1.38 at 20 Hz, which is a value much smaller than 1.64 reported in ref 12 and as far as we are aware the smallest reported to date.

Relaxivity measurements of Fe_2O_3−citrate were also performed (see Table 3). In comparison with relaxivity values of Fe_2O_3−water, the r_1 value for Fe_2O_3−citrate is similar but the r_2 value is larger due to a larger hydrodynamic ratio; then r_2/r_1 = 2.46, comparable to the value reported for MION particles.[12] This increase of the ratio r_2/r_1 can be considered as an indicator of the clustering or pairing between particles,[30] which could be avoided by precisely controlling the amount of citrate.

(26) Zhang, L.; Papaefthymiou, G. C.; Ying, J. Y. *J. Appl. Phys.* **1997**, *81* (10), 6892.

(27) Martínez, B.; Roig, A.; Obradors, X.; Molins, E.; Rouanet, A.; Monty, C. *J. Appl. Phys.* **1996**, *79* (5), 2580.

(28) Morales, M. P.; Veintemillas-Verdaguer, S.; Montero, M. I.; Serna, C. J.; Roig, A.; Casas, Ll.; Martínez, B.; Sandiumenge, F. *Chem. Mater.* **1999**, *11* (11), 3058.

(29) Monte, F.; Morales, M. P.; Levy, D.; Fernandez, A.; Ocaña, M.; Roig, A.; Molins, E.; O'Grady, K.; Serna, C. J. *Langmuir* **1997**, *13* (14), 3627.

Figure 6. ^{1}H NMRD profile of the Fe_2O_3−water sample at 310 K.

Table 4. Comparison of the Parameters Obtained from the Fitting of the NMRD Profile at 310 K and from other Techniques for the Fe_2O_3−Water Sample

d^a (nm)	$M_S{}^a$ ((A m^2)/kg of Fe$_2$O$_3$)	d^b (nm)	$M_S{}^c$ ((A m^2)/kg of Fe$_2$O$_3$)	d^c (nm)
5.7	73	4.9	68	5

^{a} Diameter and M_S from NMRD profile. ^{b} Diameter from TEM measurements. ^{c} Diameter and M_S from magnetic measurements.

To understand and quantify the mechanisms governing the relaxation phenomenon of the system, an NMRD profile was recorded and fitted according to the usual model.[31] The NMRD profile displays r_1 over a wide range of magnetic fields and provides the information necessary to asses the properties of a contrast agent at any field strength. It also gives information on the particle diameter (d) and the value of the saturation magnetization (M_S). The relaxivity profile (r_1) of Fe_2O_3−water nanoparticles is represented in Figure 6. The relaxivity, r_1, of this complex behaves as expected for ultrasmall superparamagnetic particles. The maximum of the relaxativity is placed between 30 and 60 MHz and only diminishes by a factor of 2 at 200 MHz, meaning that very good performance is expected at the conditions used in clinical imaging (fields of 100−200 MHz). The high-field inflection point called "dispersion of the longitudinal relaxation profile" is roughly given by the condition $\omega_i\tau_D = 1$ in which $\tau_D = r^2/D$, with r being the radius of the crystal and D the relative diffusion coefficient of water with respect to the particle. τ_D is the diffusion correlation time, which defines the time during which the diffusing proton is influenced by the superparamagnetic particle. After the high-field dispersion, the longitudinal relaxation decreases rapidly to zero. The NMRD profile was analyzed quantitatively according to eq 31 from ref

31, and the values obtained from the fitting are summarized in Table 4. It should be pointed out that theoretical values obtained from the fitting are in good agreement with those obtained by the other employed techniques (TEM, XRD, and magnetometry), pointing once more to a very narrow distribution of the particle size and showing consistency within all the used characterization techniques.

Conclusions

The present investigation focuses on an extensive chemical and physical characterization of a colloidal iron oxide dispersion. Ultrasmall iron oxide nanoparticles with narrow particle size distribution and a high saturation magnetization value have been obtained. They have been stabilized in water at physiological pH and proved to be useful as positive T_1 MRI contrast agents. After functionalization with specific biological ligands, these iron oxide nanoparticles could be used as molecular imaging probes for cell tracking. Cytotoxicity of those particles is currently being investigated on the basis of intracellular uptake.

Supporting Information Available: Figure 1, X-ray diffraction pattern for the Fe_2O_3−water sample, Figure 2, magnetic measurements for the Fe_2O_3−citrate sample, and Figure 3, IR spectra of all the samples. This material is available free of charge via the Internet at http://pubs.acs.org.

LA063415S

(30) Roch, A.; Gossuin, Y.; Muller, R. N.; Gillis, P. *J. Magn. Magn. Mater.* **2005**, *293*, 532.
(31) Roch, A.; Muller, R. N.; Gillis, P. *J. Chem. Phys.* **1999**, *110* (11), 5403.

Supercritical-Fluid-Assisted One-Pot Synthesis of Biocompatible Core(γ-Fe$_2$O$_3$)/Shell(SiO$_2$) Nanoparticles as High Relaxivity T_2-Contrast Agents for Magnetic Resonance Imaging

By *Elena Taboada, Raul Solanas, Elisenda Rodríguez, Ralph Weissleder,* and *Anna Roig**

Monodisperse iron oxide/microporous silica core/shell composite nanoparticles, core(γ-Fe$_2$O$_3$)/shell(SiO$_2$), with a diameter of approximately 100 nm and a high magnetization are synthesized by combining sol–gel chemistry and supercritical fluid technology. This one-step processing method, which is easily scalable, allows quick fabrication of materials with controlled properties and in high yield. The particles have a specific magnetic moment (per kg of iron) comparable to that of the bulk maghemite and show superparamagnetic behavior at room temperature. The nanocomposites are proven to be useful as T_2 MRI imaging agent. They also have potential to be used in NMR proximity sensing, theranostic drug delivery, and bioseparation.

1. Introduction

Surface control of magnetic nanoparticles is gaining in importance since surface modification has been proven useful in a wide range of technological applications including electronics and photonics, heterogeneous catalysis, chemical sensing, water remediation, information storage and medical diagnosis.[1] A large number of biomedical applications make use of magnetic nanoparticles; these include magnetic resonance imaging (MRI), controlled drug delivery, tissue repair, detoxification of biological fluids, immunoassays, and biological targeting or separation. Among those, we have chosen MRI as a testing ground of the novel materials processing approach presented here. MRI is a non-invasive and wide-spread diagnostic imaging technique used to obtain high-resolution tomographic images of the body without the need of employing ionizing radiation or radiopharmaceuticals. The actual trend is towards visualization of events at cellular and even sub-cellular levels, particularly those that are key targets in disease processes and require very high-detection sensitivity (up to the nanomolar level). For that purpose, a new generation of MRI agents is critical for targeting highly specific receptors and cells. Moreover, one needs suitable amplification strategies to increase sensitivity of the technique, biocompability and optimized pharmacodynamics.[2,3] It is believed that in the near future, iron-based imaging agents will play an increasing significant role in this area, and thus, special attention is given to the fabrication of novel systems with higher relaxivity values.[4–6] Specific target iron oxide probes,[7] theranostic applications,[8] as well as, the detection of molecular interactions,[9] are other aspects where fast advances are being reported. In addition, libraries of nanoparticles are being generated.[10] Such libraries should facilitate the development of effective therapies by for example, using magnetofluorescent nanoparticles.

Compared to polymer coatings, silica-coated nanoparticles represent one alternative to increase relaxivity and expand modularity through different chemistries.[11] Here, we report on a straightforward synthesis for highly monodispersed core/shell particles with iron oxide cores and microporous silica shells in the nanometer range (approximately 100 nm) and their performance as a very high-relaxivity T_2 imaging agent. No toxic effects were observed up to 1 m$_M$ Fe for 12 h incubation in a cell line.[12] Each nanoparticle is formed by a well-defined magnetic nucleus consisting of several non-contacting maghemite particles (7 nm), guaranteeing a high volume magnetic moment and at the same time safeguarding the superparamagnetic behavior of ultrasmall iron oxide particles at room temperature. The magnetic nucleus is surrounded by a microporous silica shell ensuring the system's biocompatibility, which should eventually lead to potential applications of the material as a nanocarrier. A therapeutic agent could be encapsulated in the silica shell, and surface functionalization with small molecules could be

[*] Dr. A. Roig, E. Taboada
Institut de Ciència de Materials de Barcelona (ICMAB-CSIC)
Campus de la UAB, 08193, Bellaterra (Spain)
E-mail: roig@icmab.es
R. Solanas
MATGAS 2000 AIE and Institut de Ciència de Materials de Barcelona (ICMAB-CSIC)
Campus de la UAB, 08193, Bellaterra (Spain)
Dr. E. Rodríguez, Prof. R. Weissleder
Center for Molecular Imaging Research
Massachusetts General Hospital – Harvard Medical School
Room 5406 CNY-149 13th Street, Charlestown, MA 02129 (USA)

performed via silanol groups to target specific body sites. There are a number of examples where mesoporous silica materials have been used as a delivery matrix of water-insoluble drugs,[11,13] but magnetic biocompatible versions have been less explored.

The fabrication of size-controlled porous silica particles usually comprises several separate synthetic steps, the use of structure-directing agents, and consequently, long processing times.[14] The same applies, and still is more relevant, when referring to well-defined core/shell morphologies. Multi-step reactions often require intermediate separation or purification steps (very important when targeting biomedical applications) that not only reduce the net material yield but seriously impede the up-scaling of the material's production. Here, we report on a novel one-pot method. It can be described as a combination of sol–gel chemistry and clean supercritical fluid technology, and it is based on the common approach of fabricating silica aerogels. Shortly, after a gel is formed by hydrolysis and condensation of a silicon precursor, the solvent trapped inside the gel pores can be removed at supercritical conditions preventing the strong capillary forces in the walls of the nanopores and consequently, the collapse of the structure.[15] The synthetic route presented here has several important advantages over previously described methods for obtaining porous magnetic nanoparticles since it allows control over the particle size (from 50 to 200 nm), a narrow particle size distribution without a particle size separation step ($\sigma < 15\%$), relatively fast processing time (maximum overall processing time of 8 h), high material yield (batches of approximately 1 g), and microporosity without the use of structure-inducing agents (no traces of harmful reagents in the final product). In addition, the method can be generalized to any other magnetic nucleus, and the nanocomposite particles can be easily stabilized as an aqueous colloidal dispersion.

2. Results and Discussion

The chemical process to fabricate the material is thoroughly described in the Experimental Section, and it is visually summarized in Scheme 1. The material collected from the autoclave was a light and dry brown powder, macroscopically homogeneous in color and consistency. It readily follows a magnet and is very easily dispersable in water (see Fig. 1). As seen from the transmission electron microscopy (TEM) images of Figure 2, the material is homogeneous at the nanometer scale. The powder is formed by nanocomposite particles with a magnetic core of grouped iron oxide nanoparticles surrounded by a silica shell. It can be observed that the magnetic particles are not in contact with each other suggesting that their oleic acid capping is still present. This is quite expected since the maximum temperature reached during the supercritical process was 260 °C, well below the boiling point of oleic acid (360 °C). Adjusting the acetone/hexane volume ratio in the initial sol, the resulting material is either spherical in shape (for acetone/hexane volume ratio ≥ 20) or wormlike (for acetone/hexane volume ratio ≈ 1). Particle size is also related to the volume ratio of acetone/hexane in the initial sol. The reason is that oleic acid–iron oxide particles are very stable in hexane, but unstable in acetone/hence. They tend to self-assemble into clusters in a mixture of solvents. This is observed when measuring the hydrodynamic radius of the initial sols by dynamic light scattering
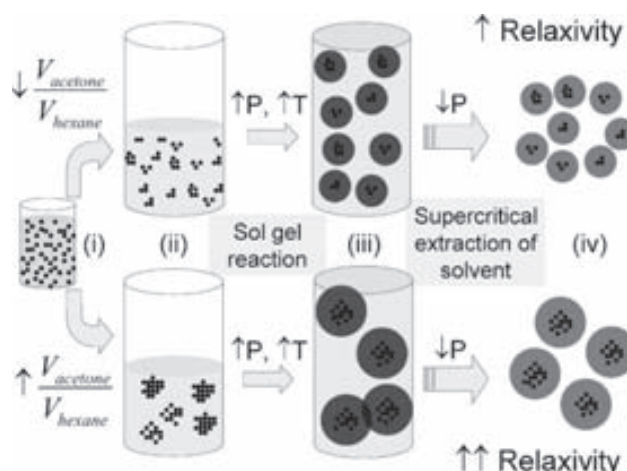

Scheme 1. Processing pathway for obtaining the nanocomposite material. i) Colloidal dispersion of γ-Fe$_2$O$_3$ nanoparticles in hexane. ii) Initial sol with silicon precursor, water, solvents and iron oxide NPs at ambient conditions. iii) Expanded sol under supercritical conditions with gel composite particles. iv) Dry composite particles.

(DLS). The magnetic clusters serve as nucleation sites for hydrolyzed tetramethoxy silane (TMOS) to condensate, leading to the construction of the silica shell. The larger the magnetic core, the larger the composite particle. The overall particle size could also be adjusted by varying the amounts of TMOS and water in the original sol, the amount of the iron oxide, the use of catalysts, and the other experimental conditions (pressure, temperature, reaction time, etc.).

Four representative materials were selected to be further characterized, and they were evaluated as MRI agents. The physico-chemical parameters and the relaxivity measurements are gathered in Table 1. Samples S1, S2, and S3 refer to spherical nanocomposite particles of different sizes; W1 refers to the
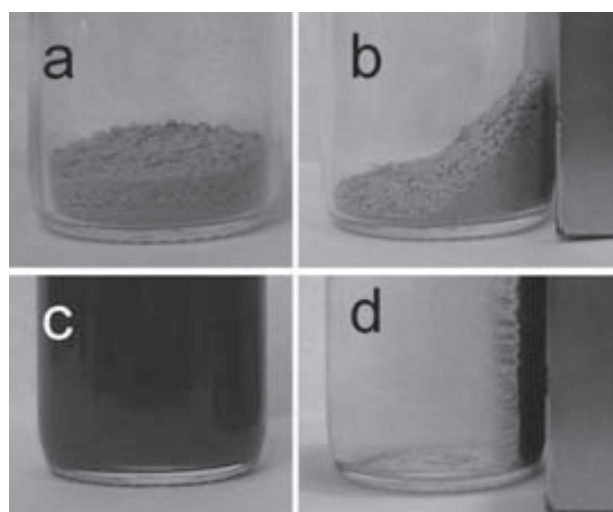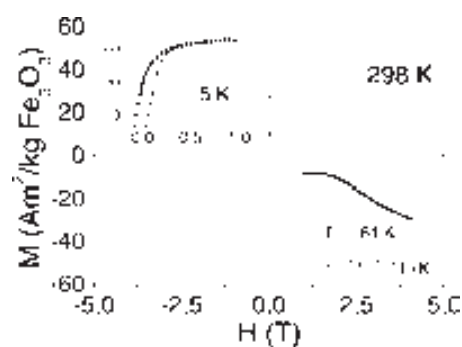

Figure 1. Photographs of the as-synthesized composite dry powder a) without and b) with a magnet. Photographs of the aqueous dispersion c) without and d) with a magnet.
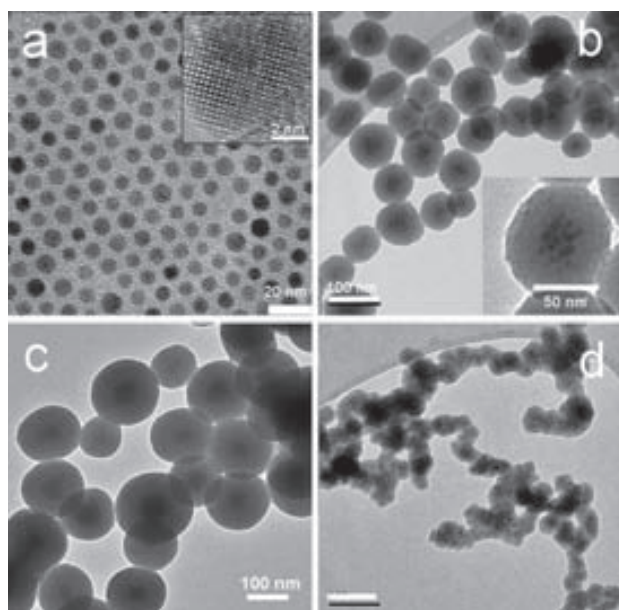
Figure 2. TEM images of a) γ-Fe$_2$O$_3$ nanoparticles, b) S1 composite particles, c) S3 composite particles, and d) W1 composite particles. Images a and b include a zoom to show the crystallinity of the iron oxide nanoparticles (inset a) and the presence of separated iron oxide nanoparticles inside a composite particle (inset b).

Figure 3. Magnetization as a function of the applied field for sample S1. The curve shows no coercivity nor remanence, as expected for a superparamagnetic system. In the lower inset, ZFC-FC magnetization curves as a function of temperature is presented ($H = 100$ Oe). The ZFC curve shows a distinctive peak with a maximum at the blocking temperature of 61 K; both curves separate from each other at the peak cusp indicating that the particles do not form aggregates. The upper inset shows $M(H)$ at 5 K and the presence of remanence and coercivity, typical of a blocked state.

wormlike nanocomposite, while γ-Fe$_2$O$_3$ refers to the as-synthesized maghemite particles (see Fig. 2). Data of a commercial iron oxide system, Endorem^{TM}, which has a similar hydrodynamic size, was added for comparison. Nanoworms were included because recently Park et al. have reported that elongated structures improve the ability of the nanoparticles to circulate, target, and image tumors.[16]

Herein, we detail the main features for the smallest particles, sample S1. They are characterized by a mean diameter of 70 nm with 14% size dispersion (see Fig. 2b) and a hydrodynamic diameter of 160 nm. The measured zeta potential (ζ) is negative as expected from the surface silanol groups. Nevertheless, the colloidal stability of silica does not conform to DLVO (Derjaguin–Landau–Verwey–Overbeek) theory as most of colloids do. Colloidal silica can be stabilized both at pH = 2 (isoelectric point) and at neutral pH with high salt concentration.[17] Therefore, the ζ

absolute value is not useful for predicting its stability. For S1, the iron oxide mass portion in the composite is of 5.0 wt% and the mean number of original iron oxide nanoparticles per composite particle is 40.

Biocompatibility and high magnetization are two essential requirements for in vivo use. To ensure biocompatibility, special consideration were made at the synthetic and processing stages. Firstly, even though methanol is the most frequently used solvent in TMOS sol–gel reactions, acetone was chosen as the solvent rather than the more toxic methanol.[18,19] Secondly, the supercritical extraction of the solvent not only serves to dry the material, but also to extract any unreacted reagents out of the processing vessel. Furthermore, no porogenic agents were used.

Maghemite spherical particles under 35 nm in diameter behave as superparamagnets at room temperature.[20] In the composite particles, the magnetic cores formed by the grouped maghemite nanoparticles have diameters between 20 and 60 nm. $M(H)$ curves at 298 K for all the composite materials (see Fig. 3 for detailed data on sample S1) were measured; they all behave as superparamagnets with high magnetization saturation (approximately 60 A m^2 kg^{-1} Fe$_2$O$_3$ at 300 K) comparable to the value of the bulk material. Zero-field-cooled–field-cooled (ZFC-FC) curves (lower

Table 1. Physico-chemical parameters and relaxivity values of characteristic samples.

Sample	Physical properties					M_s (298 K, 5 T)		Relaxometry values (37 °C, 0.47 T)	
	d_{TEM} [nm]	σ [%]	d_{HYD} [nm]	S_{BET} [m^2 g^{-1} SiO$_2$]	Fe$_2$O$_3$ content [wt%]	A m^2 kg^{-1} composite	A m^2 kg^{-1} Fe$_2$O$_3$	r_1 (s^{-1} mM Fe^{-1})	r_2 (s^{-1} mM Fe^{-1})
S1	70	14	160	134	5.0	2.8	55.6	0.29	148
S2	82	11	120	68	7.4	4.4	58.8	0.27	164
S3	157	13	313	100	5.9	3.7	62.2	0.17	326
W1	–	–	–	43	8.9	5.8	57.9	0.07	159
Fe$_2$O$_3$	6.1	8	8.6	–	100	–	20.0	2.89	16
Endorem^{TM}			120–180	–	–	–	–	40	160

inset of Fig. 3) confirm the superparamagnetic character of the system. The ZFC portion presents a well-defined narrow peak (indicative of a narrow particle size distribution) and the maximum magnetization value at 60 K, which corresponds to the blocking temperature. At 5 K (upper inset of Fig. 3), the hysteresis loop shows remanence and hysteretic behavior, typical of the blocked ferromagnetic state. These results confirm that supercritical drying has not induced sintering or particle growth, which would have led to undesirable ferromagnetic behavior at room temperature. Ferromagnetic particles irreversibly aggregate in the presence of an external magnetic field and could induce embolism when administered intravenously. It is worth mentioning that the value of the saturation magnetization (M_s) per kilogram of Fe_2O_3 for the nanocomposite material is much larger than for the as-synthesized Fe_2O_3 particles. We believe that it is related to an improvement of the crystallinity of the nanoparticles resulting from the high-temperature treatment during the silica shell fabrication (further analysis is currently underway).

Nitrogen adsorption/desorption isotherms were measured to determine the surface area of the silica shell, as well as the average pore diameter. This porosity can be used to enlarge the application scope of the material by further loading the particles with therapeutic agents or by functionalizing the silica through the surface silanol groups. A typical adsorption isotherm is shown in Figure 4. A steep slope at very low pressures, representative of microporosity, can be observed. We ascribe the soft slope for relative pressures, P/P_0, between 0.1 and 0.9 to the external area of the particles, and the high volume uptake at $P/P_0 > 0.9$ to the meso- and macropores formed by the interparticular space.[21] To be highlighted is the fact that the isotherms do not form closed curve even at very low relative pressures. Several mechanisms may be responsible for such behavior (e.g., pores blocked by narrow openings,[21] slit-shaped pores,[22] or a fractal structure expected for silica gels dried under supercritical conditions[23]). The overall surface area values determined by BET (Brunauer–Emmett–Teller) measurements, which are summarized in Table 1, are much larger than the calculated surface area for compact spherical particles of the same size (36, 30, and 16 $m^2 g^{-1}$ SiO_2 for S1, S2, and S3 samples, respectively; density 2.2 g cm^{-3}). Concerning pore size, the adsorption BJH (Barrett–Joyner–Halenda) pore size
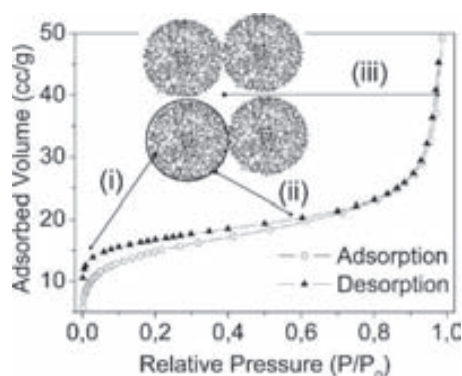
distribution shows the presence of micropores, smaller than 2 nm in diameter.

To test the efficacy of our materials as imaging agents for MRI, relaxivity measurements were performed at 0.47 T and 37 °C in water. The results are shown in Table 1. The as-synthesized iron oxide nanoparticles were transferred to water using TMAOH (tetramethylammonium hydroxide) and sodium citrate to stabilize them as an aqueous dispersion at neutral pH. They showed a longitudinal relaxivity (r_1) of 2.89 s^{-1} mM Fe^{-1}, a transversal relaxivity (r_2) of 16 s^{-1} mM Fe^{-1}, and the r_2/r_1 ratio of 6. These are typical values for very small superparamagnetic iron oxide nanoparticles.[24] As expected, they behave quite differently when coated with the silica shell. It is to be pointed out that the longitudinal relaxation rate ($R_1 = 1/T_1$) values of the composite materials are similar to the values for water indicating that the protons in the media do not have access to the inner magnetic core. The most interesting relaxivity results are the r_2 values: those of the composite particles are 20 times that of the as-synthesized maghemite nanoparticles, and that of sample S3 is twice that of commercial Endorem™. The highest r_2 value, observed for sample S3, is due to the fact it has the largest magnetic nucleus; larger magnetic nuclei induce larger magnetic inhomogeneities and thus faster decoherence in the hydrogen spins.[25]

Summarizing, the iron oxide and the iron oxide/microporous silica core/shell nanoparticles can be applied differently in MRI, i.e., as T_1 and T_2 contrast agents, respectively. Smaller nanoparticles have higher residence times in blood circulation providing the advantage that when they are specifically functionalized, they can be delivered to the target organs. Their main drawback is that their detection requires the uptake of a large number of particles due to their weak magnetic responsiveness. Composite particles with higher volume magnetic moment, which would lead to an enhancement of T_2 contrast, but with a reasonable particle size (smaller than 200 nm), which would avoid quick opsonization, may be a solution. Moreover, because of the amphiphilic properties of the silica coating, the circulation time of the nanocomposites will be extended from minutes to hours, allowing better internalization into the target organ once they have been functionalized.[26] In that direction, Dunning et al. have reported that even micrometer-sized magnetic microspheres were useful to track labeled glial cells in vivo by MRI after their implantation into demyelinated lesions in the rat spinal cord.[27] In addition, the composite system, due to its high magnetization, could be moved towards the organ of interest using an external magnet and avoid particle aggregation once the magnetic field is removed.[28] The major benefit one can envisage of this approach is the targeting of the probes to the tumor environment reducing toxic consequences arising from free drugs in the body.

Cytotoxicity studies were done in a fibroblast cell line (NIH3T3) using the 3-(4,5-dimethylthiazol-2-yl)2,5-diphenyl-tetrazoilum bromide (MTT) assay (see Fig. 5). Cells were treated for 12 h with the different materials (see Fig. 5c). None of them presented important toxic effects in the range of concentrations studied (<1 mM Fe). Toxicity of pure silica nanoparticles was also evaluated (Fig. 5a), and no toxic effects were observed for concentrations lower than 1.2 mg mL^{-1}. It has been reported that surface charge also plays a role in toxicity, with cationic surfaces being more toxic than anionic ones and neutral surface being the most biocompatible. This was explained by the affinity of cationic particles to the
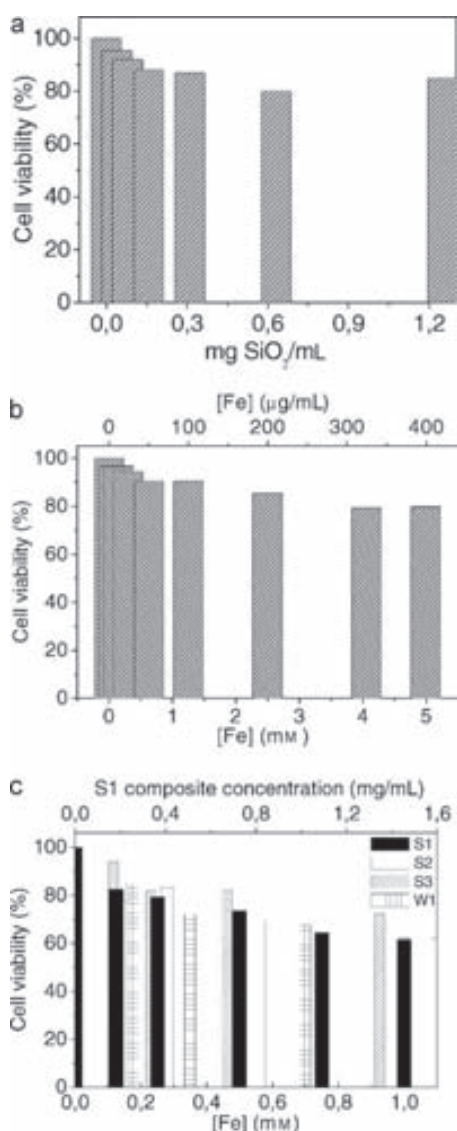

Figure 4. Typical nitrogen adsorption/desorption isotherm with a representative scheme showing the particles surface structure. i) Inner microporosity. ii) External surface area. iii) Interparticle meso- and macroporosity.

Figure 5. Cytotoxicity studies at 12 h performed with NIH3T3 cells using the MTT reduction assay for silica particles (a), TMAOH–citrate-capped γ-Fe$_2$O$_3$ (b), and nanocomposites S1, S2, S3, and W1 (c). All of the values in c refer to the bottom axis of millimolar concentration of iron. Additionally, the top axis shows the corresponding concentration in milligram of composite per milliliter for sample S1; it is added to help the reader compare these data with those in a for pure silica particles.

negatively charged cell membranes. Due to surface silanol groups, the nanocomposite silica particles are moderately negatively charged at pH = 7 and thus low toxicity is expected.[29] Finally, cytotoxicity studies were also performed for aqueous dispersions of as-synthesized iron oxide nanoparticles (TMAOH–citrate-capped) (Fig. 5b) showing a mild toxic effect for concentrations lower than 5 mM. As it can be seen in Fig. 5, the toxicity behavior of the composite particles is more similar to that of pure silica particles than that of iron oxide. This observation matches the low r_1 values, suggesting the non-accessibility of the protons to the magnetic core. Considering the high relaxivities of the composites,

it is worthy to point out that the dose administered in vivo could be much lower than that administered for other T_2 agents.[24]

3. Conclusions

In this work, we have attempted to address one of the outstanding problems mentioned in the review by C. Corot et al.[24] ''The synthesis of iron oxide crystalline structures requires a reproducible industrial process resulting in a monodisperse population of magnetic grains of controlled size without laborious purification steps. New processes should also provide iron oxides characterized by a high degree of crystallinity and consequently high magnetization saturation.'' Monodisperse iron oxide/microporous silica core/shell nanocomposite particles, around 100 nm in diameter and with a high magnetization were synthesized by combining sol–gel chemistry and supercritical fluid technology. Such a one-step processing methodology, which should be easily scalable, allows the quick fabrication of materials with a high yield and controlled properties. Moreover, porosity was induced without the need of porogenic agents. The nanocomposite was shown to be biocompatible and may be particularly useful as an enhanced T_2 imaging agent, as NMR proximity sensors,[30] as theranostic agents, or as a bioseparating agent.

4. Experimental

Synthesis: Maghemite nanoparticles (γ-Fe$_2$O$_3$-NPs) were synthesized by a modification of the method first described by Hyeon et al. [31]. We previously reported their use as T_1 MRI contrast agents [32]. Iron pentacarbonyl (Fe(CO)$_5$) is thermally decomposed in organic media in the presence of oleic acid, which acts as surfactant. After centrifugation and washing, the oleic-acid-coated particles are re-dispersed in hexane. In a typical experiment, the resulting particles are 7 nm in mean diameter, with a very narrow particle size dispersion (typically <10%), and they remain stable in hexane for months and even years. They are superparamagnetic at room temperature. The coating of the maghemite nanoparticles with silica was done in a novel one-pot approach, combining sol–gel hydrolysis and condensation of a silicon precursor and supercritical evacuation of the solvent inside an autoclave. The chemical process is exemplified in Scheme 1. Typically, initial reagents with a TMOS/H$_2$O/acetone/Fe$_2$O$_3$/hexane mass composition of 0.92/0.22/95.63/0.04/3.19 wt% were placed in a Pyrex vessel at ambient conditions; the TMOS/H$_2$O molar ratio was kept fixed at 0.5 and the acetone/hexane volume ratio varied from 70 to 1. Nether catalysts nor porogenic agents were used. The vessel was then introduced into the 2 L supercritical reactor, and the pressure inside the reactor was increased up to 50 bar using carbon dioxide (CO$_2$). Afterwards, the temperature was raised up to 250 °C, with the pressure correspondingly increasing up to 250 bar. The final P and T values were over the critical point of any possible CO$_2$/acetone solvent mixture (P_c(max) = 120 bar and T_c (max) = 235 °C) [33]. After 2 h of reaction at supercritical conditions, the system was depressurized down to 150 bar and fresh CO$_2$ was recirculated for 1 h with a flow of 0.5 kg$_{CO2}$·h^{-1} and for another 1 h at 1.5 kg$_{CO2}$·h^{-1}. The recirculation served to extract any unreacted silicon precursor out of the vessel, and thus, minimized the necking formation between particles. Finally, the autoclave was depressurized and cooled down to room temperature. The resulting material was a dry powder homogeneously distributed around the reactor walls. For completeness, several batches of pure silica nanoparticles were fabricated following our previously reported method [34].

Transmission Electron Microscopy (TEM): A JEOL JEM-1400 operating at 200 keV was used for the microstructure analysis. To observe the materials, a drop of diluted acetone dispersion was deposited onto a TEM carbon grid

and allowed to dry. Aqueous dispersions were avoided to prevent the formation of silica necking at the contact area between particles when exposed to the high-energy electron beam.

Dynamic Light Scattering (DLS) and Zeta Potential (ζ): Dynamic light scattering and zeta potential measurements were performed with a Zetasizer Nano ZS (Malvern Instruments, Ltd., UK), provided with a He/Ne laser of 633 nm wavelength. The determination of the isoelectric point, IEP, was performed using the MPT-2 autotitrator, an accessory of the Zetasizer Nano ZS.

Chemical Analysis: The elemental composition was measured by inductively coupled plasma mass spectroscopy (ICP-MS). The samples were first digested with a mixture of nitric acid (HNO_3) and hydrofluoric acid (HF) in a microwaves oven. Digestion of control samples were also performed and analyzed.

XRD: The composite samples were characterized by X-ray diffraction with a Siemens D5000 X-ray powder diffractometer using Cu Kα incident radiation. Crystallite size determination was done by applying the Scherrer's formula to the 400 or 440 peaks. The 311 peak of maximum intensity could not be used because it overlapped with the typical broad peak of amorphous silica, which is situated at $2\theta = 22°$.

Magnetic Measurements: Magnetization versus applied magnetic field at 5 and 298 K and the ZFC-FC curves with a 100 Oe applied field were measured with a superconducting quantum interference device (SQUID) magnetometer (Quantum Design MPMS5XL, USA). All the magnetization data were presented in units of A m^2 kg^{-1} γ-Fe$_2$O$_3$.

BET: Nitrogen adsorption data were taken at 77 K using an ASAP 2000 surface area analyzer (Micromeritics Instrument Corporation, USA) after degasification at 300 K under vacuum for 24 h to remove the adsorbed species. Surface area and mean pore diameter determinations were carried out following BET and BJH models, respectively.

Relaxivity Measurements: T_1 and T_2 relaxation times were measured using an inversion-recovery pulse sequence with a Bruker Minispec (Bruker Analytics, North Bellirica, MA) at 37 °C and 0.47 T (20 MHz).

Cytotoxicity Experiments: In vitro toxic effects of the iron oxide nanoparticles as well as the silica nanocomposites were studied using the fibroblast cell line NIH3T3. Cells seeded in 96-well plates (1.5×10^4 cells/ 100 μL) were treated with the nanoparticles dissolved in Dulbecco's Modified Eagle's Medium (DMEM) with 10% fetal bovine serum for 12 h. Toxicity was evaluated using the 3-(4,5-dimethylthiazol-2-yl)2,5-diphenyl-tetrazoilum bromide (MTT) reduction assay, which measures cell metabolic activity. After the incubation period, optical density was measured at 570 nm to subtract any possible interference from the nanoparticle solution, and then the cells were incubated with 0.5 mg · mL^{-1} MTT for 2 h. A lysing buffer that dissolves the blue formazan crystals was added to each well, and the plates were incubated overnight at 37 °C. Optical density was again measured at 570 nm, and values were expressed as a percentage of control-well values (wells containing cell culture medium without nanoparticles).

Acknowledgements

[1] U. Jeong, X. W. Teng, Y. Wang, H. Yang, Y. N. Xia, *Adv. Mater.* **2007**, *19*, 33.

[2] R. Weissleder, M. J. Pittet, *Nature* **2008**, *452*, 580.

[3] D. E. Sosnovik, R. Weissleder, *Curr. Opin. Biotechnol.* **2007**, *18*, 4.

[4] N. Nasongkla, E. Bey, J. Ren, H. Ai, C. Khemtong, J. S. Guthi, S. F. Chin, A. D. Sherry, D. A. Boothman, J. Gao, *Nano Lett.* **2006**, *6*, 2427.

[5] J. B. Williams, Q. Ye, T. K. Hitchens, C. L. Kaufman, C. Ho, *J. Magn. Reson. Imaging* **2007**, *25*, 1210.

[6] E. Rodriguez, R. V. Simoes, A. Roig, E. Molins, N. Nedelko, A. Slawska-Waniewska, S. Aime, C. Arus, M. E. Cabanas, C. Sanfeliu, S. Cerdan, M. L. Garcia-Martin, *Magn. Reson. Mater. Phys. Biol. Med.* **2007**, *20*, 27.

[7] C. Riviere, M.-S. Martina, Y. Tomita, C. Wilhelm, A. Tran-Dinh, C. Menager, E. Pinard, S. Lesieur, F. Gazeau, J. Seylaz, *Radiology* **2007**, *244*, 439.

[8] J. R. McCarthy, F. A. Jaffer, R. Weissleder, *Small* **2006**, *2, 983.*

[9] J. M. Perez, L. Josephson, T. O'Loughlin, D. Högemann, R. Weissleder, *Nat. Biotechnol.* **2002**, *20*, 816.

[10] R. Weissleder, K. Kelly, E. Y. Sun, T. Shtatland, L. Josephson, *Nat. Biotechnol.* **2005**, *23*, 1418.

[11] C. Barbé, J. Bartlett, L. Kong, K. Finnie, H. Q. Lin, M. Larkin, S. Calleja, A. Bush, G. Calleja, *Adv. Mater.* **2004**, *16*, 1959.

[12] S. Y. Shaw, E. C. Westly, M. J. Pittett, A. Subramanian, S. L. Schreiber, R. Weissleder, *Proc. Natl. Acad. Sci. USA* **2008**, *105*, 7387.

[13] J. Lu, M. Liong, J. I. Zink, F. Tamanoi, *Small* **2007**, *3*, 1341.

[14] S. Huh, J. W. Wiench, J. C. Yoo, M. Pruski, V. S. Y. Lin, *Chem. Mater.* **2003**, *15*, 4247.

[15] N. Husing, U. Schubert, *Angew. Chem. Int. Ed.* **1998**, *37*, 23.

[16] J. H. Park, G. von Maltzahn, L. L. Zhang, M. P. Schwartz, E. Ruoslahti, S. N. Bhatia, M. J. Sailor, *Adv. Mater.* **2008**, *20*, 1630.

[17] P. Mulvaney, L. M. Liz-Marzán, M. Giersig, T. Ung, *J. Mater. Chem.* **2000**, *10*, 1259.

[18] K. Yano, Y. Fukushima, *J. Mater. Chem.* **2003**, *13*, 2577.

[19] L. Martin, J. O. Osso, S. Ricart, A. Roig, O. Garcia, R. Sastre, *J. Mater. Chem.* **2008**, *18*, 207.

[20] Note: This value has been calculated from the Langevin equation: $KV = 25k(B) \times T(b)$, where K, V, $k(B)$, and $T(b)$ refer to the magnetocrystalline anisotropy, particle volume, Boltzmann constant, and blocking temperature, respectively.

[21] M. Rose, W. Bohlmann, M. Sabo, S. Kaskel, *Chem. Commun.* **2008**, 2462.

[22] K. Sing, *J. Porous Mater.* **1995**, *2*, 5.

[23] J. Esquena, C. Solans, J. Llorens, *J. Colloid Interface Sci.* **2000**, *225*, 291.

[24] C. Corot, P. Robert, J. M. Idee, M. Port, *Adv. Drug Delivery Rev.* **2006**, *58*, 1471.

[25] L. L. Josephson, J. Lewis, P. Jacobs, P. Hahn, D. Stark, *Magn. Reson. Imaging* **1988**, *6*, 647.

[26] D. L. J. Thorek, A. Chen, J. Czupryna, A. Tsourkas, *Ann. Biomed. Eng.* **2006**, *34*, 23.

[27] M. D. Dunning, M. I. Kettunen, C. F. Constant, R. J. M. Franklin, K. Brindle, *NeuroImage* **2006**, *31*, 172.

[28] P. Gould, *Nano Today* **2006**, *1*, 34.

[29] N. Lewinski, V. Colvin, R. Drezek, *Small* **2008**, *4*, 26.

[30] H. Lee, E. Sun, D. Ham, R. Weissleder, *Nat. Med.* **2008**, *14*, 869.

[31] T. Hyeon, S. S. Lee, J. Park, Y. Chung, H. B. Na, *J. Am. Chem. Soc.* **2001**, *123*, 12798.

[32] E. Taboada, E. Rodriguez, A. Roig, J. Oro, A. Roch, R. N. Muller, *Langmuir* **2007**, *23*, 4583.

[33] H. Pohler, E. Kiran, *J. Chem. Eng. Data* **1997**, *42*, 379.

[34] M. Moner-Girona, A. Roig, E. Molins, J. Llibre, *J. Sol–Gel Sci. Technol.* **2003**, *26*, 645.

Size determination of superparamagnetic nanoparticles from magnetization curve

D.-X. Chen,[1,a] A. Sanchez,[2] E. Taboada,[3] A. Roig,[3] N. Sun,[4] and H.-C. Gu[4,b]

[1]*ICREA and Departament de Física, Universitat Autònoma de Barcelona, 08193 Bellaterra, Spain*
[2]*Departament de Física, Universitat Autònoma de Barcelona, 08193 Bellaterra, Spain*
[3]*Institut de Ciència de Materials de Barcelona (ICMAB), CSIC, 08193 Bellaterra, Spain*
[4]*Nano Biomedical Research Center, Med-X Research Institute, Shanghai Jiaotong University, Shanghai 200030, China*

The size distribution of superparamagnetic iron oxide nanoparticles in two powder samples is determined from the measured magnetization curve fitted by a core-shell model and a uniform model, both based on the Langevin function with a log-normal particle volume distribution. Different average sizes are evaluated from the fitting parameters and compared to those determined by other techniques. Conceptual discussions are presented on different models and approaches, from which the core-shell model fitting is recommended for the magnetic size determination of superparamagnetic nanoparticles. © *2009 American Institute of Physics.* [DOI: 10.1063/1.3117512]

I. INTRODUCTION

Iron oxide nanoparticles serve as a key element in many technologies, including recent developments in fields such as magnetic separation, drug delivery, hyperthermia treatments, and magnetic resonance imaging contrast agents,[1] which have followed earlier applications in magnetic recording. In many cases, an accurate knowledge on the average size and size distribution of each assembly of nanoparticles is crucially important for the proper working of the particular application.

Such a size distribution may be determined from the measurements of magnetization curve based on the theory of superparamagnetism first proposed by Bean and co-workers.[2–4] This theory considers a dilute assembly of ferromagnetic particles as superparamagnetic if the particles are single domain and when the thermal energy at the temperature of the experiment is sufficient to equilibrate the magnetization of the assembly in a time short compared to that of the experiment. The reduced magnetization $M(H)$ curve of the superparamagnetic assembly is expressed by the Langevin function $L(x) = \cosh x - 1/x$, where $x = \mu_0 m_0 H / k_B T$, with m_0, k_B, and T being the particle magnetic moment, the Boltzmann constant, and temperature, respectively.[4] Thus, the particle moment may be determined by magnetic measurements, from which the particle volume may be obtained as m_0 / M_s if saturation magnetization M_s is known.

This M_s was first thought to be the M_s for the bulk material that has the same composition and structure as the particles. However, the saturation magnetization M_s of many acicular γ-Fe$_2$O$_3$ polycrystalline particles was measured at room temperature, and it was found that M_s decreases with decreasing the average crystallite size determined from x-ray diffraction (XRD) line broadening measurements using the Scherrer relation.[5] This phenomenon was explained by as-suming the crystallites to be separated by a nonmagnetic grain shell of the order of 0.6 nm thick. A similar effect was found by Kaiser and Miskolczy for single-domain superparamagnetic Fe$_3$O$_4$ particles in ferrofluids; their magnetization curve may be correlated to the superparamagnetic theory only when the size distribution of the suspended particles is considered with their volumetric concentration corrected for the formation of a nonmagnetic surface mantle 1-unit-cell thick.[6] Such surface mantle was later called the magnetically dead layer with respect to the magnetic core.[7] The difference in magnetic structure between the surface layer and the core has been an interesting topic in physics.[8–11]

Assuming the particle M_s to be the same as that of the bulk with a log-normal size distribution, Chantrell *et al.* proposed a method to determine the median particle diameter and standard deviation from the low and high field magnetizations.[12] They named the thus-determined size as "magnetic size" since it was different from and significantly smaller than the physical size obtained from transmission electron microscopy (TEM) data, consistent with the observation of Kaiser and Miskolczy. Such a relation between magnetic size and dead surface layer has been studied by other researchers.[13–17]

In recent years, research on superparamagnetic particles has revived owing to their potential applications. In the determination of particle sizes by magnetic measurements, a paramagnetic susceptibility has been incorporated to the superparamagnetic particles, and the magnetically determined sizes of Fe$_3$O$_4$ or γ-Fe$_2$O$_3$ nanoparticles are found to be in agreement with the sizes determined by TEM or x-ray techniques.[18–20] It is unclear why this magnetically determined size becomes the physical size different from the magnetic size mentioned above.

In the present work, we will study two superparamagnetic iron oxide systems by careful measurements and model fits. We will use a core-shell model and a uniform model, both considering a log-normal particle volume distribution and a paramagnetic contribution. We will show that the mea-

[a]Electronic mail: duxing.chen@uab.es.
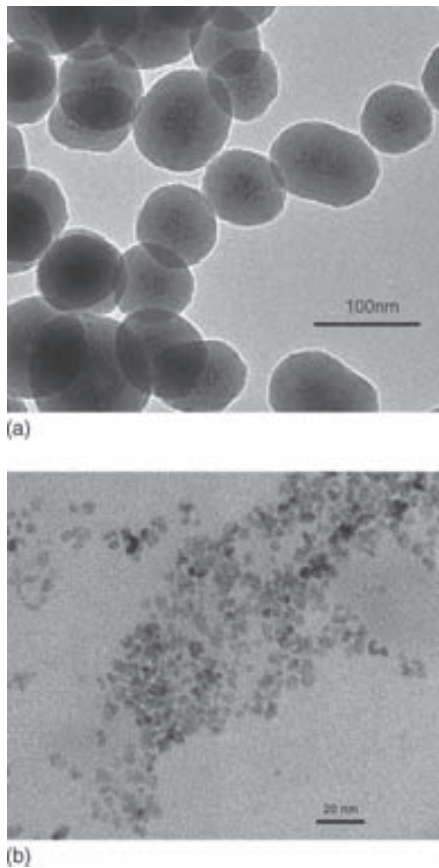[b]Electronic mail: hcgu@sjtu.edu.cn

FIG. 1. TEM images for (a) sample 1 and (b) sample 2.

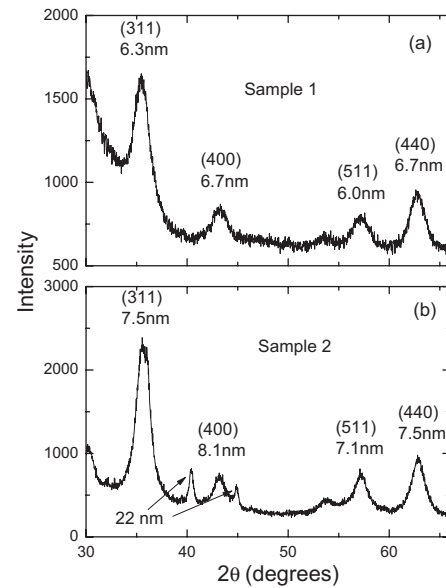

FIG. 2. The XRD patterns for (a) sample 1 and (b) sample 2. Peak indices with corresponding Sherrer particle diameters are indicated.

sured magnetization curves may be equally well fitted by the core-shell model and uniform model and that the median diameter and standard deviation obtained from the former model are smaller than those from the latter. We will derive different average sizes from the fitting parameters so that the magnetically determined sizes can be correctly compared to those determined from TEM observations, XRD patterns, or dynamic light scattering measurements. We will explain that the abovementioned magnetic size smaller than the physical size is a consequence of self-inconsistent approaches and this magnetic size is not the size of the particle core but smaller than it. We will emphasize the necessity of the core-shell model fits for a correct particle size determination.

II. SAMPLES AND MEASUREMENTS

Two powder samples are studied in this work. Sample 1 was produced at the ICMAB, Barcelona, Spain, and consisted of silica spheres with mean diameter of 82 nm, each containing around 130 γ-Fe$_2$O$_3$ nanoparticles, as shown by the TEM image in Fig. 1(a). Its preparation will be described elsewhere.[21] Sample 2 was SH U555C, a commercial product of Schering, Berlin, Germany, used as magnetic resonance imaging contrast agents.[22] It is an optimized formulation of carboxydextran-coated γ-Fe$_2$O$_3$/Fe$_3$O$_4$ nanoparticles (Resovist).[23] A TEM image of sample 2 is shown in Fig. 1(b). For both samples, the particle sizes observed by TEM are about 6 nm, but there is a larger size distribution for sample 2. The XRD patterns of both samples are presented in

Fig. 2. Average particle sizes of 6.4 ± 0.4 and 7.6 ± 0.5 nm for samples 1 and 2, respectively, are determined using the Scherrer relation from the (311), (400), (511), and (440) peaks at $2\theta \approx 36°$, $43°$, $57°$, and $63°$ with a spherical shape factor of $4/3$.[24] Compared to sample 1, there are two extra peaks for sample 2 centered at $2\theta = 40.4°$, and $44.9°$, corresponding to certain crystallites (not γ-Fe$_2$O$_3$/Fe$_3$O$_4$) with an average grain size of about 22 nm.

The magnetization curves were measured by a superconducting quantum interference device (SQUID) (sample 1) or vibrating-sample magnetometer (sample 2). In order to get magnetization in SI units, the total volume of γ-Fe$_2$O$_3$ particles in sample 1 was calculated from the measured mass, the weight fraction of 0.074 of γ-Fe$_2$O$_3$ chemically analyzed by atomic spectroscopy, and the density of 5074 kg/m^3 of Fe$_2$O$_3$.[25] The same was done for sample 2, with a weight fraction of 0.34 determined by thermogravimetric analysis technique and a density of 5150 kg/m^3 taken for the mixture of γ-Fe$_2$O$_3$/Fe$_3$O$_4$ considering the density of Fe$_3$O$_4$ to be 5240 kg/m^3.[26]

The measured room-temperature magnetization $\mu_0 M$ versus applied field $\mu_0 H$ curves for samples 1 and 2 are plotted by open circles in Figs. 3 and 4, respectively. In order to see clearly the model fits to the measured data in the entire field range, logarithmic and linear scales are used in plots (a) and (b), respectively.

III. MODEL FITS

To fit the $\mu_0 M$ versus $\mu_0 H$ curves, we assume that all the particles are spherical without mutual interaction and use two models. For the core-shell model, each particle has an inner single-domain core with the spontaneous magnetization M_s of the bulk material and an outer paramagnetic shell of susceptibility χ_{pm} and thickness δ, if the particle diameter is $D > 2\delta$. Writing the volumes of a particle, its core, and its shell as v, v_c, and v_s, respectively, we have in general v
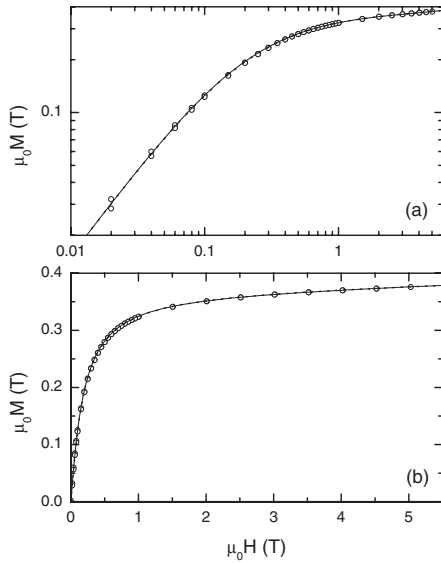
FIG. 3. The measured room-temperature magnetization curve of sample 1 (symbols) and its fitting by the core-shell model (solid lines) and the uniform model (dotted lines). Logarithmic and linear scales are used in plots (a) and (b), respectively.

$= v_c + v_s = \pi D^3 / 6$ and $v_c = 0$ if $D < 2\delta$ and $v_c = \pi (D - 2\delta)^3 / 6$ otherwise. We further assume a particle volume distribution with the log-normal probability density function

$$p(v; \mu, \sigma) = \frac{1}{\sqrt{2\pi} \sigma v} \exp \left[-\frac{(\ln v - \mu)^2}{2\sigma^2} \right], \qquad (1)$$

where μ and σ are the mean and standard deviation of $\ln v$. For convenience, we define

$$\mu \equiv \ln v_0 = \ln(\pi D_0^3 / 6), \qquad (2)$$

where v_0 and D_0 are the median volume and its corresponding diameter, respectively.
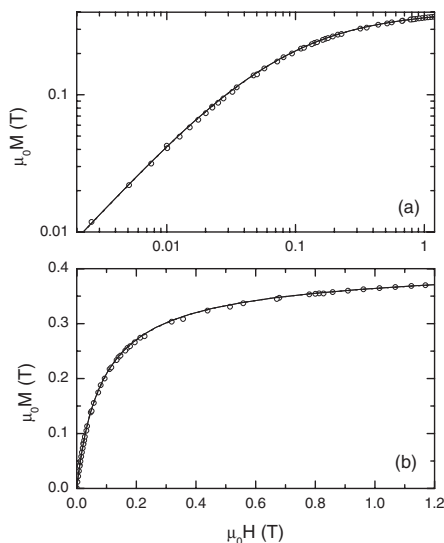
FIG. 4. Same as Fig. 3 but for sample 2.

TABLE I. Fitting parameters D_0 (the diameter corresponding to the median particle volume v_0), σ (the standard deviation of logarithmic particle volume $\ln v$), δ (the paramagnetic shell thickness), χ_{pm} (the paramagnetic susceptibility), and M_s (the spontaneous magnetization) and deduced average particle diameters D_{vv}, D_{vd}, D_{nd}, and D_z for samples 1 and 2 in the core-shell and the uniform models.

| | Model | | | |
| | Core-shell | | Uniform | |
Sample	1	2	1	2
D_0 (nm)	6.27	7.7	6.42	8.2
σ	0.65	0.95	0.69	1.0
δ (nm)	0.295	0.41	.	.
χ_{pm}	0.013	0.024	0.0035	0.011
$\mu_0 M_s$ (T)	0.500	0.553	0.368	0.382
D_{vv} (nm)	6.73	8.9	6.95	9.7
D_{vd} (nm)	6.42	8.1	6.59	8.7
D_{nd} (nm)	5.59	5.9	5.63	6.1
D_Z (nm)	7.39	10.9	7.72	12.1

In this model, magnetization M as a function of field H is contributed by the core superparamagnetism and the shell paramagnetism of all the particles with a volume distribution $p(v; \mu, \sigma)$ and is expressed by

$$M(H) = \int_0^\infty p(v; \mu, \sigma) v^{-1} [M_s v_c L(x) + v_s \chi_{pm} H] dv, \qquad (3)$$

where the Langevin function[4]

$$L(x) = \coth x - 1/x \qquad (4)$$

with

$$x = \mu_0 M_s v_c H / k_B T. \qquad (5)$$

Using Eq. (3) to calculate the modeling magnetization curve numerically, we fix values as the Boltzmann constant $k_B = 1.38 \times 10^{-23}$ J/K, the measurement temperature $T = 298$ K, the permeability of free space $\mu_0 = 4\pi \times 10^{-7}$ H/m, and the spontaneous magnetization of the core $\mu_0 M_s = 0.5$ T for sample 1 (a value close to the theoretical and measured $\mu_0 M_s$ of bulk γ-Fe$_2$O$_3$ at room temperature[25]) and 0.55 T for sample 2 (a value between 0.5 and 0.6 T for bulk γ-Fe$_2$O$_3$ and Fe$_3$O$_4$, respectively[25]), and change the values of parameters σ, D_0, δ, and χ_{pm} iteratively until the measured $\mu_0 M$ versus $\mu_0 H$ curve is best fitted. The fitting curves are plotted as solid lines in Figs. 3 and 4 for samples 1 and 2, respectively. The optimum fitting parameters are listed in Table I.

For the uniform model, the same particle size distribution [Eq. (1)] is assumed with all the particles having the same spontaneous magnetization M_s (equal to the average saturation magnetization of the superparamagnetism for the entire particle assembly and less than M_s of the bulk) and the same paramagnetic susceptibility χ_{pm}. Thus, Eq. (3) is replaced by

$$M(H) = \int_0^\infty p(v;\mu,\sigma)[M_s L(x) + \chi_{pm}H]dv. \tag{6}$$

The fitting is done by changing iteratively the values of σ, M_s, D_0, and χ_{pm}. The fitting curves are plotted by dotted lines in Figs. 3 and 4 for samples 1 and 2, respectively. The optimum fitting parameters are listed in Table I.

We can see that both fitting curves collapse perfectly with the measured data points. We note that small hysteresis in Fig. 3 between the measured ascending and descending data points, owing to the irreversibility of the superconducting magnet in SQUID measurements, is corrected by their average.

IV. AVERAGE SIZES

Different average particle diameters, as defined in Refs. 27 and 28, may be deduced from the fits. To simplify the expressions, we write the particle diameter as a function of its volume,

$$D(v) = (6v/\pi)^{1/3}. \tag{7}$$

The average diameter corresponding to the particle-volume-weighted average volume is

$$D_{vv} = D(v_v), \tag{8}$$

where

$$v_v = \int_0^\infty p(v;\mu,\sigma)v dv = v_0 \exp(\sigma^2/2). \tag{9}$$

This D_{vv} is the average size directly deduced from magnetic measurements since magnetization is contributed by moments of particles, which are proportional to particle volume. D_{vv} should also be relevant for suspended particles in nuclear magnetic resonance measurements, where the relaxation rates influenced by the particles are proportional to the particle volume fraction.[29]

The particle-volume-weighted average diameter is

$$D_{vd} = \int_0^\infty p(v;\mu,\sigma)D(v)dv. \tag{10}$$

This D_{vd} may be directly determined from XRD patterns using the Scherrer relation since the x-ray intensity is proportional to the total particle volume and the peak width is directly related to the particle size.

The particle-number-weighted average diameter is

$$D_{nd} = \frac{\int_0^\infty p(v;\mu,\sigma)v^{-1}D(v)dv}{\int_0^\infty p(v;\mu,\sigma)v^{-1}dv}. \tag{11}$$

This D_{nd} may be directly determined from TEM observation by counting the particle number within a group of size intervals.

The Z-average diameter, i.e., the particle-volume-square-weighted average diameter, is

$$D_Z = D_{v^2 d} = \frac{\int_0^\infty p(v;\mu,\sigma)v D(v)dv}{\int_0^\infty p(v;\mu,\sigma)v dv}. \tag{12}$$

This D_Z is the magnetic counterpart of the hydrodynamic D_Z of particles in a suspension, directly determined by dynamic light scattering techniques based on the Stokes–Einstein equation, for which the light intensity is proportional to v^2. We note that there are different definitions for D_Z in literature, and Eq. (12) follows Ref. 27 but not Ref. 28, where D_Z is defined as our D_{vd}.

The values of all these average diameters are listed in Table I for both samples. There is a relation among these average diameters and D_0: $D_Z > D_{vv} > D_{vd} > D_0 > D_{nd}$. The difference among them increases with increasing σ. It is useful to note that if the distribution is not defined with respect to particle volume v as in Eq. (1) but with respect to particle diameter D as $p(D;\mu,\sigma)$, then the resulting new σ equals one third of σ in the present treatment.

V. DISCUSSION

A. Error analysis and demagnetizing effects

The superparamagnetism theory requires the magnetostatic interaction energy between adjacent particles to be smaller than $k_B T$. This requirement corresponds to a particle size less than 8 nm if the iron oxide particles are dense packed. In the present work, sufficiently small particles in each cluster are dense packed for sample 1, whereas slightly large particles are loose packed in sample 2, so that this condition is satisfied for both samples.

The correctness of the deduced particle sizes relies not only on the correctness of measurements and the assumed parameter values but also on the correctness of the assumed log-normal distribution. The excellent fits to magnetization curves by both models suggest that the assumed log-normal particle volume distribution correctly reflects the reality at least for the two samples studied. All the instruments used are standard, and the SQUID magnetometer has been well calibrated with standard samples. If the assumed $\mu_0 M_s$ for the bulk iron oxides has been overestimated, then the resulting core size will be smaller than the actual one with an overestimated δ since the difference between the bulk and the measured M_s is artificially augmented in this case. If the assumed mass density is overestimated, then the measured M_s is artificially increased, so that the estimated core size increases at expenses of δ.

Special care must be taken for demagnetizing effects. If the overall initial susceptibility of the sample is not negligibly smaller than the shape susceptibility defined by $1/N_m$, where N_m is the magnetometric demagnetizing factor, a demagnetizing correction is necessary.[30,31] Nonmagnetic coating in samples 1 and 2 has reduced the overall initial susceptibility to about 10% and 5%, respectively, of those shown in Figs. 3 and 4 for iron oxides, so that the required demagnetizing correction is negligible. For powders of superparamagnetic particles without a thick nonmagnetic coating, a large demagnetizing correction is definitely necessary since the diameters deduced from magnetization curve will be very much underestimated otherwise. In this case, using liquid

samples with suspended particles or using particle powders mixed with additional nonmagnetic particles may be good choices, as long as the total mass of the particles can be accurately measured. Note that there may be a strong diamagnetic contribution if the liquid is water.

B. Comparison between both models

A core-shell model was originally proposed for particles with a size distribution and a nonmagnetic dead layer[6,7] and was recently incorporated with a paramagnetic shell but without a size distribution.[18] We have completed this model and used it to perform careful fits to experimental data. The uniform model has recently been used in particle size determination.[19,20] It is relatively approximate in nature since the same entire particle cannot be both ferrimagnetic and significantly paramagnetic, and the ferrimagnetic spontaneous magnetization cannot be appreciably smaller than that for the bulk material with the same composition and structure. We have used it here to fit the data of the same sample as that fitted by the core-shell model in order to compare both models.

Independent of the accuracy of the particle size determination, we see from Table I that for each sample, σ, D_0, and all the average D's resulting from the core-shell model are smaller than those from the uniform model. The results of the core-shell model should be more reliable, and the systematic difference in results between both models should arise from the systematic error of the uniform model itself. This is in agreement with a fact found in Ref. 19, i.e., the particle size distribution determined using the uniform model was slightly wider than that from TEM observation.

The magnetic structure and property of the shell have been intensively studied, as briefly summarized in Ref. 18. The paramagnetism assumed in the core-shell model should be related to them. With the help of this model, the shell thickness and susceptibility may be studied for many samples in a wide temperature range, providing more information for the understanding of the nature of the shell.

C. Comparison with other techniques

We compare the magnetically determined sizes, D_{nd}, D_{vd}, and D_Z, using the core-shell model, with those determined by TEM, XRD, and dynamic light scattering techniques. From Table I and Figs. 1 and 2, we see for both samples that only small difference occurs between D_{nd} and the average size of most particles in TEM pictures and between D_{vd} and the averaged size determined from XRD patterns. We have made dynamic light scattering measurements for water suspension of particles corresponding to sample 2, resulting in the hydrodynamic $D_Z = 19$ nm. This value is larger than $D_Z = 10.9$ nm determined magnetically, suggesting an effective thickness of 4 nm for the total solid and liquid nonmagnetic hydrodynamic attachment.

We have proposed a method of the core-shell model fit to the measured magnetization curve as an independent way to determine the physical sizes of superparamagnetic nanoparticles. The sizes determined by this method can be consistent with those determined by conventional XRD and

TEM techniques. Since magnetization measurements have been frequently performed in research on nanoparticles to check the weakness of irreversibility in technical magnetization and to determine saturation magnetization, the application of the proposed method does not require extra measurements but carefulness in the measurements and a model fit to the results. As a result, the size distribution and average sizes in different definitions are obtained altogether. Besides the overall size, which may be also measured by other techniques, this method can also give the sizes of core and shell with different properties for further study. The good agreement with other techniques shown in the present work indicates the smallness of the interactions among the particles in the two systems, and it will be interesting to study other systems with larger or densely aggregated particles even at low temperatures with enhanced effects of magnetic interactions or magnetocrystalline anisotropy. In this case, disagreement in particle sizes between different techniques may occur, from which the nature of such effects may be better understood.

D. Magnetic size

Finally, we discuss the concept of magnetic size. In literature, the magnetically determined particle size is referred to as the magnetic size if there is a nonmagnetic dead surface layer for the particles.[12–17] This is obviously contradicted by the technique presented here, by which the actual physical size is determined magnetically. We will see below that such a contradiction comes from a self-inconsistency in the particle size determination in Refs. 12–17. Although certain particle size distributions are involved in those works, the problem may be simplified by assuming all particles to have the same volume without loosing conceptual generality. In this case with a dead layer, the initial susceptibility is derived from the Langevin function as

$$\chi_0 = \frac{n\mu_0 M_s^2 v^2}{3k_B T}, \tag{13}$$

where n is the particle number per cubic meter.

For a self-consistent treatment, if v defined as the total volume of the particle, then M_s should be defined as the average magnetization in this volume. For example, in the case of sample 1 with $\chi_0 = 1.52$, using the averaged $\mu_0 M_s = 0.368$ T and converting Eq. (13) into

$$\chi_0 = \frac{\mu_0 M_s^2 v}{3k_B T} \tag{14}$$

by noticing $nv = 1$, one obtains $v = 174$ nm³, leading to a diameter $D = 6.93$ nm. Since this v is actually the particle-volume-weighted average v when there is a distribution, such a D is actually D_{vv} for our uniform model obtained by fitting the entire magnetization curve. This is a reason for us to have stated that D_{vv} is the average size directly deduced from magnetic measurements.

There may be different kinds of self-inconsistent treatments. A usually applied one is to use Eq. (14) with the physical meaning of its premise $nv = 1$ being overlooked. For the above example and regarding M_s and v in Eq. (14) as the

spontaneous magnetization for the bulk and the magnetic volume of the particle core, one obtains the magnetic volume and diameter to be $v_{mag}=94.3$ nm^3 and $D_{mag}=5.65$ nm. Although this D_{mag}, smaller than the physical particle size, is qualitatively consistent with the presence of a dead layer, it is a significantly underestimated diameter of the core, which is $D_{vv}-2\delta=6.14$ nm from our core-shell model fit. The explanation for this discrepancy can be as follows. The quantity n in Eq. (13) is the number of particles per unit volume and $n=1/v$ occurs only when v is defined as the total volume but not the core volume of the particle. In this self-inconsistent treatment, the factor v^2 in Eq. (13) has been regarded as the total particle volume multiplied by the core volume. As a consequence, the determined magnetic size is neither that of the total particle nor that of the core. It is a size even smaller than that of the core.

Different from our method, M_s is determined in some other techniques by a linear extrapolation of M versus $1/H$ to $1/H=0$ as early proposed by Bean and Jacobs when the maximum applied field was not high enough.[3] We have tested this approach for our samples and found a M_s consistent with that obtained by model fitting, as long as a certain field range is chosen for the extrapolation. In fact, the paramagnetism has a negligible contribution to the low field portion of the curve and especially to χ_0, so that even if $\chi_{pm}=0$ with a dead surface layer, the self-consistently determined particle size will be the actual physical size but not the core size.

VI. CONCLUSION

The magnetization curves of two powder samples consisting of superparamagnetic iron oxide nanoparticles with a nonmagnetic coating layer are measured and fitted by a core-shell model and a uniform model. For the former model, particles have a ferrimagnetic core with the spontaneous magnetization for the bulk material and a paramagnetic shell with the same thickness and susceptibility, whereas for the latter, all particles have the same spontaneous magnetization and the same paramagnetic susceptibility. Both models are based on the Langevin function and consider a log-normal particle volume distribution. It is found that both experimental curves can be perfectly fitted by either model, so that the log-normal distribution is a good approximation of the actual case. Different average particle sizes are deduced and evaluated from the fitting parameters. The standard deviation and all average sizes determined from the core-shell model are shown to be smaller than those from the uniform model; the former is more reliable since the core-shell model is physically more sound. The magnetically determined average sizes by the core-shell model are reasonably in agreement with those determined from TEM and XRD experiments and reasonably smaller than the hydrodynamic size determined by dynamic light scattering. The magnetic size determination

without using a core-shell model is shown to be self-inconsistent, leading to results even smaller than the core size.

[1]Q. A. Pankhurst, J. Connolly, S. K. Jones, and J. Dobson, J. Phys. D: Appl. Phys. **36**, R167 (2003).
[2]C. P. Bean, J. Appl. Phys. **26**, 1381 (1955).
[3]C. P. Bean and I. S. Jacobs, J. Appl. Phys. **27**, 1448 (1956).
[4]C. P. Bean and J. D. Livingston, J. Appl. Phys. **30**, 120S (1959).
[5]A. E. Berkowitz, W. J. Schule, and P. J. Flanders, J. Appl. Phys. **39**, 1261 (1968).
[6]R. Kaiser and G. Miskolczy, J. Appl. Phys. **41**, 1064 (1970).
[7]R. E. Rosensweig, *Ferrohydrodynamics* (Cambridge University Press, Cambridge, 1985), p. 60.
[8]J. M. D. Coey, Phys. Rev. Lett. **27**, 1140 (1971).
[9]R. H. Kodama, A. E. Berkowitz, E. J. McNiff, Jr., and S. Foner, Phys. Rev. Lett. **77**, 394 (1996).
[10]B. Martinez, X. Obradors, Ll. Balcells, A. Rouanet, and C. Monty, Phys. Rev. Lett. **80**, 181 (1998).
[11]H. Kachkachi and M. Dimian, Phys. Rev. B **66**, 174419 (2002).
[12]R. W. Chantrell, J. Popplewell, and S. W. Charles, IEEE Trans. Magn. **14**, 975 (1978).
[13]J. Popplewell and L. Sakhnini, J. Magn. Magn. Mater. **149**, 72 (1995).
[14]N. S. Kommareddi, M. Tata, V. T. John, G. L. McPherson, M. F. Herman, Y.-S. Lee, C. J. O'Connor, J. A. Akkara, and D. L. Kaplan, Chem. Mater. **8**, 801 (1996).
[15]J. F. Hochepied, P. Bonville, and M. P. Pileni, J. Phys. Chem. B **104**, 905 (2000).
[16]D. Caruntu, G. Caruntu, and C. J. O'Connor, J. Phys. D: Appl. Phys. **40**, 5801 (2007).
[17]K. Simeonidis, S. Mourdikoudis, I. Tsiaoussis, M. Angelakeris, C. Dendrinou-Samara, and O. Kalogirou, J. Magn. Magn. Mater. **320**, 1631 (2008).
[18]A. Millan, A. Urtizberea, N. J. O. Silva, F. Palacio, V. S. Amaral, E. Snoeck, and V. Serin, J. Magn. Magn. Mater. **312**, L5 (2007).
[19]R. C. Woodward, J. Heeris, T. G. St. Pierre, M. Saunders, E. P. Gilbert, M. Rutnakornpituk, Q. Zhang, and J. S. Riffle, J. Appl. Crystallogr. **40**, s495 (2007).
[20]P. P. Vaishnava, U. Senaratne, E. C. Buc, R. Naik, V. M. Naik, G. M. Tsoi, and L. E. Wenger, Phys. Rev. B **76**, 024413 (2007).
[21]E. Taboada, R. Solanas, E. Rodrguez, R. Weissleder, and A. Roig, Adv. Funct. Mater. (unpublished).
[22]P. Reimer, C. Bremer, T. Allkemper, M. Engelhardt, M. Mahler, W. Ebert, and B. Tombach, Radiology **231**, 474 (2004).
[23]P. Reimer, E. J. Rummeny, H. E. Daldrup, T. Balzer, B. Tombach, T. Berns, and P. E. Peters, Radiology **195**, 489 (1995).
[24]J. I. Langford, D. Louër, and P. Scard, J. Appl. Crystallogr. **33**, 964 (2000).
[25]G. Bate, in *Ferromagnetic Materials*, edited by E. P. Wohlfarth (North-Holland, Amsterdam, 1980), Vol. 2, p. 432.
[26]D.-X. Chen, A. Sanchez, H. Xu, H.-C. Gu, and D.-L. Shi, J. Appl. Phys. **104**, 093902 (2008).
[27]R. Finsy and N. De Jaeger, Part. Part. Syst. Charact. **8**, 187 (1991).
[28]D. C. Blackley, *Polymer Latices: Science and Technology* (Chapman and Hall, London, 1997), Vol. 1, p. 44.
[29]S. H. Koenig and K. E. Kellar, Magn. Reson. Med. **34**, 227 (1995).
[30]D.-X. Chen, J. A. Brug, R. B. Goldfarb, IEEE Trans. Magn. **27**, 3601 (1991).
[31]D.-X. Chen, E. Pardo, and A. Sanchez, J. Magn. Magn. Mater. **306**, 135 (2006).

7.2.   Complementary projects

Parallel to the main scope of this thesis I have been involved in other projects collaborating with several research groups. I include here a very brief introduction to each subject and the corresponding publications. I am very grateful for their contributions and their knowledge.

Three other collaborations with groups at the ICMAB have been carried out which have not resulted in publication, for the moment. The first one, with Josep Puigmartí and David Amabilino, dealt with the synthesis of organic tetrathiafulvalene (TTF) gels composed with our maghemite nanoparticles. The second one, with Carlos García and Concha Domingo dealt with the post-synthesis surface hydrophobization of the silica particles with organosilanes. And the third one, with Jordi Faraudo, Juan Camacho (UAB) and Sepmag Tecnologies, dealt on the study of the magnetophoretic properties of our composite nanoparticles.

7.2.1. Maghemite nanoparticles confined in silica matrices and their magneto-optical properties

Two different projects were undertaken regarding magneto-optical properties of maghemite nanoparticles. The first one consisted of synthesizing the magnetic nanoparticles in silica aerogel matrices. The resulting material, which was synthesized by us, combined the transparency and high porosity of silica aerogel and the magnetic properties of the maghemite nanoparticles, enabling the characterization of the Faraday rotation of the monolithic samples. The Faraday measurements were performed by Rafael Pérez del Real at the Instituto Nacional de Técnica Aeroespacial (INTA), in Madrid, Spain.

The second project consisted of filling an inverse silica opal with maghemite nanoparticles. Good quality opals with adjustable magnetic characteristics were obtained by this method. Preliminary analyses showed that Kerr rotation may not be proportional to the overall magnetization pointing to non-linear magneto-optical effects. The opals were synthesized at the Insituto de Ciencia de Materiales de Madrid (Spain) by Martín López, Álvaro Blanco and Cefe López, as well as the optical characterization. We performed the synthesis of maghemite nanoparticles. The magneto-optical measurements were performed at the ICMAB by Jose Manuel Caicedo, David Hrabovsky, Gervasi Herranz and Josep Fontcuberta.

Publications:

- Taboada, E.; del Real, R.P.; Gich, M.; Roig, A. and Molins, E. Faraday rotation measurements in maghemite-silica aerogels *Journal of Magnetism and Magnetic Materials*, **2006**, 301, 175-180. Citations (Sept. 2nd 2009): 6.

- Caicedo, J.M.; Taboada, E.; Hrabovský, D.; López-García, M.; Herranz, G.; Roig, A.; Blanco, A.; López, C. and Fontcuberta, J. Facile route to magneto-photonic crystals by infiltration of 3D-inverse opals with magnetic nanoparticles *Journal of Magnetism and Magnetic Materials,* **In Press.** DOI: 10.1016/j.jmmm.2009.02.139.

Faraday rotation measurements in maghemite-silica aerogels

E. Taboada[a], R.P. del Real[b], M. Gich[a], A. Roig[a],*, E. Molins[a]

[a]*Institut de Ciència de Materials de Barcelona—Consejo Superior de Investigaciones Científicas (ICMAB—CSIC), Esfera UAB, 08193 Bellaterra, Catalunya, Spain*
[b]*Laboratorio de Optoelectrónica, Instituto Nacional de Técnica Aeroespacial (INTA), Torrejón de Ardoz, 28850, Spain*

Abstract

Faraday rotation measurements have been performed on γ-Fe_2O_3/SiO_2 nanocomposite aerogels which are light, porous and transparent magnetic materials. The materials have been prepared by sol–gel polymerization of a silicon alkoxide, impregnation of the intermediate silica gel with a ferrous salt and supercritical drying of the gels. During supercritical evacuation of the solvent, spherical nanoparticles of iron oxide, with a mean particle diameter of 8.1 ± 2.0 nm, are formed and are found to be homogenously distributed within the silica matrix. The specific Faraday rotation of the composite was measured at 0.6 T using polarized light of 810 nm, being 29.6°/cm. The changes in the plane of polarization of the transmitted light and the magnetization of the material present similar magnetic field dependencies and are characteristic of a superparamagnetic system.
© 2005 Elsevier B.V. All rights reserved.

1. Introduction

The development of composites that combine selected functional properties of various materials is nowadays one of the major challenges of materials science. Nanocomposites formed by particles trapped in inorganic porous media are a subject of interest since the structural confinement of the particles allows tailoring of the electronic [1], magnetic [2] and optical properties of the nanocomposite [3]. Moreover, the use of an open-pore inorganic matrix provides from one side, enough nucleation sites for the particle formation [5] and on the other, an effective way for the de-aggregation and confinement of air-borne nanoparticles while still maintaining the particle accessibility necessary in various applications such as magnetic separation or heterogeneous catalysis [6].

---

*Corresponding author. Tel.: +34 9358 01853x325; fax: +34 9358 05729.

E-mail address: roig@icmab.es (A. Roig).

Silica aerogels fulfil most of the required conditions demanded from a host matrix; chemical inertness, a large accessible surface area, high porosity, pores in the nanometer range and a high degree of transparency. Adequate magneto-optical properties of the final nanocomposite would make such material a suitable candidate for applications in magnetic data storage [7], optical fiber sensors [8] and optical isolators [9], among others.

In general, magnetic materials are neither porous nor transparent. The lack of transparency hinders the evaluation of their specific Faraday rotation, which is an important property that couples the optical and the magnetic behaviour of a material. However, a material consisting of magnetic nanoparticles embedded in a silica matrix with a high degree of optical transparency allows to overcome this difficulty and facilitates, for instance, the study of the relationship between particle size and Faraday rotation [9]. The Faraday rotation is defined as the change produced in the plane of polarization of the light transmitted through a material when a magnetic field is applied. It depends on the strength of the applied magnetic field, the length of sample crossed by the light and the wavelength of the beam source.

Here, we report on the synthesis of γ-Fe$_2$O$_3$/SiO$_2$ nanocomposite aerogels formed by impregnation of a wet silica gel with an anhydrous ferrous acetate salt, Fe(ac)$_2$, and subsequent supercritical drying of the material. During the supercritical drying of the gel, the ferrous salt converts into nanoparticles of γ-Fe$_2$O$_3$ homogeneously distributed in the matrix. The material has been characterized by structural and magnetic techniques. The specific Faraday rotation was evaluated, being 29.6°/cm at 0.6 T. It is observed that the magnetization curve ($M = f(H)$) is proportional to the Faraday rotation as a function of the applied magnetic field.

2. Experimental

Silica aerogel nanocomposites were obtained through sol–gel chemistry and supercritical drying of the wet gel. The resulting materials have been described elsewhere [11]. Shortly, the synthesis was as follows: to obtain the initial sol, tetraethoxysilane (TEOS), water, ethanol and nitric acid were mixed in the 1:4:1:0.1 molar ratios. The reaction starts with the hydrolysis of the silica precursor (TEOS) which is followed by a condensation process catalyzed by nitric acid that causes the formation of the siloxane bonds and yields the silica network. Ethanol acts as the co-solvent of both TEOS and water. The sol, which was kept tightly closed in the recipients to avoid the evaporation of the solvent, needed 3 days to gellify. The gels were aged in a hydroethanolic solution for 2 days and washed with fresh ethanol to remove the residual water for two more days. Then, a supersaturated ethanolic solution of iron (II) acetate was used to impregnate the gels during 4 days. Finally, the gels were dried inside an autoclave under ethanol supercritical conditions at 277 °C and 110 bar. Supercritical drying avoids the occurrence of very large capillary forces in the matrix preserving the solid gel structure. Ambient drying of the gel would result in the collapse of the pores, an increase of their bulk density and the loss of monolithcity and transparency of the material.

The material was characterized by X-ray diffraction (XRD) with a Siemens D5000 X-ray powder diffractometer using Cu Kα incident radiation. XRD patterns were analysed by Rietveld refinement with the MAUD program [12]. Transmission electron microscopy (TEM and HRTEM), electron diffraction analysis and energy dispersive spectrometry (EDX) were performed using a Hitachi H-7000 microscope operating at 125 keV and a Philips CM30 operating at 300 keV. The iron content of the composite was determined by flame atomic absorption spectrometry. The total surface area and the porosity of the sample were measured using the N$_2$ adsorption/desorption analysis, with a BET single point surfaces area-meter ASAP 2000 (Micrometrics Inst. Co.).

The magnetic properties were studied by Mössbauer spectroscopy with a Mössbauer spectrometer bearing a ^{57}Co/Rh source. For the measurement of the magnetization curves a superconducting quantum interference device (SQUID) magnetometer (Quantum Desing, MPMS5XL) was used.

To carry out the magneto-optical measurements a block of the aerogel nanocomposite was embedded inside an epoxy resin and polished to obtain a plate with final thickness of 0.43 mm.

The set up to measure the Faraday rotation is based on a light emission diode (LED) Hitachi 8811 with peak wavelength of 810 nm, a HP 8153A optical power meter and two near infrared polarizers (Polarcor) with their axes at 45°. This spectral band has been selected because of the figure of merit of the material, the specific Faraday rotation, F, divided by the absorption, as it was estimated in Ref. [3] for a material of very similar characteristics. As it can be seen in Fig. 1 of Ref. [3], F shows a narrow peak centred around 765 nm and three secondary peaks at 734, 789 and 825 nm. F is above 80°/cm for the 730–825 nm spectral region and since the absorption coefficient, α, (Fig. 2) diminishes with the wavelength, the optical measurements at low frequency are favoured. The figure of merit, $2F/\alpha$, is above 3 in the spectral region 760–820 nm. On the other hand, in the seminal work on the subject by Ziolo et al. [4] it was shown that the absorption coefficient of γ-Fe_2O_3 in nanocomposite materials is one order of magnitude lower than the value measured for "bulk material", suggesting that the diffusive scattering of light can improve the optical properties of nanocomposite materials.

An electromagnet was used with two tapered pole pieces filled in with a bundle of optical fibers of 50 µm of core, to carry the light from the emitter to the sample and from this to the optical power meter. The pole pieces were placed 1 cm apart to allow the positioning of a sample-holder and the two polarizers (the analyser had capacity to rotate). In this configuration, the electromagnet could supply up to 0.8 T. All the measurements were made at room temperature.

3. Results and discussion

The as-obtained nanocomposite aerogels are disc-shaped monoliths, with diameters around 1.8 cm and 0.1–0.2 cm width. The material has a brownish-reddish colour and partially transmits the 650 nm wavelength light. Table 1 summarizes the nanocomposite main chemical and physical properties. The low bulk density, $0.66 \pm 0.1 \, g/cm^3$, arises from the high porosity of the silica aerogel matrix revealed by the large surface area, calculated using the BET method, $597 \pm 20 \, m^2/g$. The total pore volume is $0.36 \, cm^3/g$. Flame atomic absorption spectrometry was performed, and a value of 7.3 wt% of iron was obtained. The corresponding wt% of iron oxide was 10.4. The X-ray diffractogram could be indexed as maghemite (γ-Fe_2O_3) (pattern not shown), as has been reported elsewhere [10]. The calculated crystallite size, according to the Rietveld refinement of the pattern, was 6 ± 2 nm.
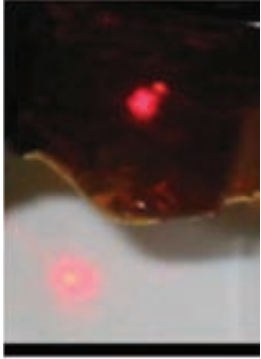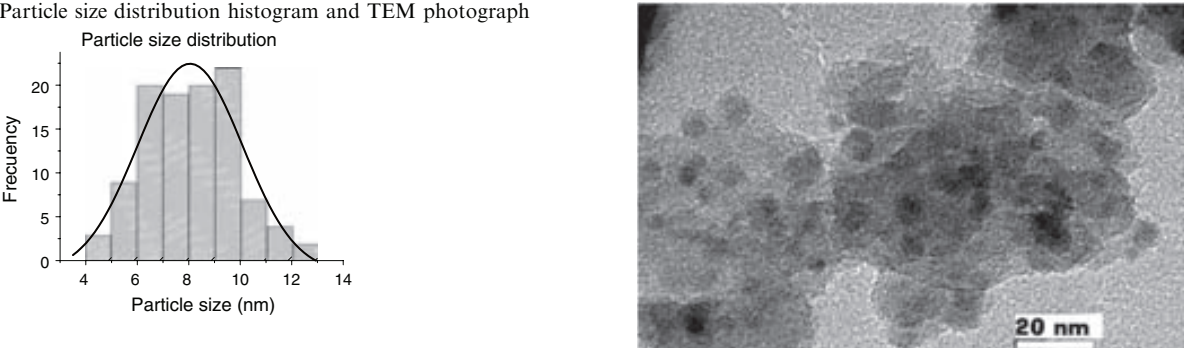
In the TEM images (see Table 1) the contrast between the two different phases is evidenced; the silica matrix as the lighter background and the iron oxide nanoparticles with darker contrast. These are rather spherical, well dispersed all over the matrix, with a size distribution that can be adjusted to a Gaussian function with a mean diameter value of 8.1 nm and a standard deviation $\sigma = 2.0$ nm.

In the electron diffractogram (not shown) five bright rings were clearly observed. The interplanar distances, d, correspond to the higher diffraction intensities of the gamma iron oxide phase, the same as in the X-ray diffractogram. Energy dispersive spectrometry revealed the presence of silicon, oxygen and iron.

When a laser beam is directed to the aerogel, some of the radiation is reflected, some dispersed and some is transmitted. The bare matrix is transparent to visible light ($\approx 60\%$ transmittance at 650 nm). It loses part of its transparency when nanoparticles are dispersed or synthesized in it [13]. In our material, a degree of transparency of the nanocomposite is preserved, although the final colour changes to reddish-brown. Due to the magnetic character of the nanoparticles, and the transparency of the matrix, the magneto-optical properties of this material, i.e. Faraday rotation, can be studied and related to other magnetic properties. These were studied by Mössbauer spectrometry [10], magnetometry and Faraday rotation. The Mössbauer spectra were recorded at 300 and 80 K. In the former, a single doublet was observed associated to the superparamagnetic

Table 1
Physical properties of the nanocomposite

Physical property	Magnitude
ρ_b (bulk density)	$0.66 \pm 0.1 \, \text{g/cm}^3$
S_{BET}	$597 \pm 20 \, \text{m}^2/\text{g}$
Total pore volume	$0.36 \, \text{cm}^3/\text{g}$
Fe, wt%	$7.3 \pm 1 \, \text{g Fe/100 g nanocomposite}$
Fe_2O_3, wt%	$10.4 \pm 1 \, \text{g Fe}_2\text{O}_3/100 \, \text{g nanocomposite}$
Photograph: a laser beam ($\lambda = 650 \, \text{nm}$) passing through the aerogel	
Particle size distribution histogram and TEM photograph	
d_{XRD} (nm)	$6 \pm 2 \, \text{nm}$
d_{TEM} (nm)	$8.1 \pm 2.0 \, \text{nm}$

character of the particles at room temperature. At 80 K the doublet transformed into a sextet, meaning that at 80 K the iron oxide particles are below their blocking temperature ($T_B^{\text{Möss}}$) and the thermal energy is not sufficient to overcome the anisotropy barrier of the magnetic moment of each particle, therefore, presenting a blocked magnetic behaviour.

The superparamagnetic character of the maghemite nanoparticles at room temperature is evidenced by the characteristic temperature dependence of the magnetization, $M(T)$, recorded after zero-field-cooling (ZFC) and field-cooling (FC) the sample (see upper inset of Fig. 1a). The maximum of $M_{ZFC}(T)$ indicates the blocking temperature measured by DC magnetometry, $T_B^{\text{DC}} \sim 40 \, \text{K}$, which is below $T_B^{\text{Möss}}$, as expected from the longer characteristic times of this measurement ($\sim 10 \, \text{s}$) as compared to the Mössbauer spectroscopy ones ($\sim 10^{-7} \, \text{s}$). It can be noticed that the increase of $M_{ZFC}(T)$ until it reaches the maximum at T_B^{DC} is rather sharp and it overlaps with $M_{FC}(T)$ for temperatures just above T_B^{DC}. This behaviour results both from the fact
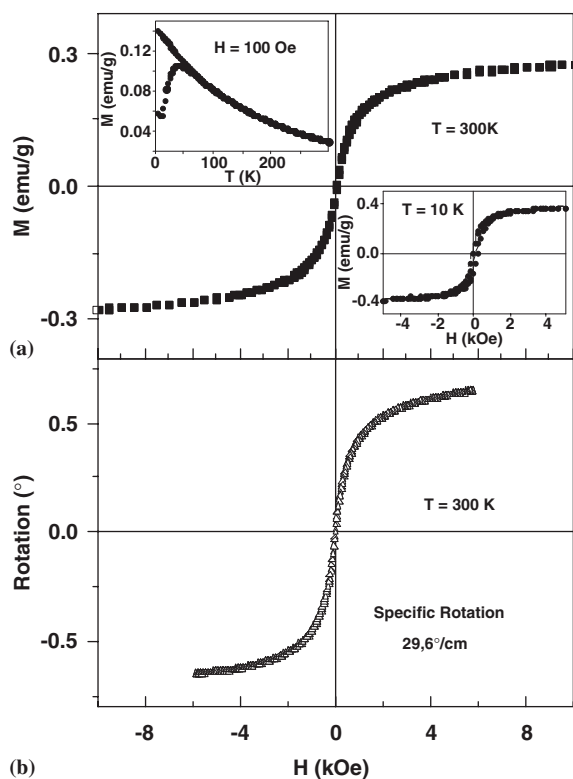
Fig. 1. (a) Magnetization curve at 300 K. Insets: upper inset: magnetization vs. temperature measured at 100 Oe in the zero-field cooled (ZFC) and field cooled (FC) states. Lower inset: magnetization curve at 10 K. (b) Faraday rotation vs. applied magnetic field at 300 K. (Both curves fully overlap. The emu/g unities are referred to grams of sample.)

that the sample consists of non-interacting maghemite particles, well-dispersed in the aerogel matrix, among which the dipolar interactions that would oppose the thermal fluctuations are negligible, but also because its size distribution is rather narrow. The DC measurement of the magnetization vs. the applied magnetic field, $M(H)$, at 10 K (lower inset of Fig. 1a) presents a hysteretic behaviour (coercivity ~100 Oe and remanence ~0.09 emu/g) expected for a thermally blocked ferro/ferrimagnetic system. In contrast, the $M(H)$ measurement at 300 K, well above T_B^{DC}, shows no hysteresis (Fig. 1a).

The curve of rotation vs. applied magnetic field (Fig. 1b) fully overlaps with the magnetization curve (Fig 1a). The value of the specific Faraday rotation of the sample was 29.6°/cm for an applied

field of 0.6 T. This value is in agreement with the results obtained by Rosa et al. [9] for γ-Fe_2O_3 dispersed in a SiO_2 matrix with different particle sizes. In that work the samples showed a theoretical molar ratio Fe/Si of 18% (19.3 wt% of Fe_2O_3) and the measurements were made at 0.8 T. The specific Faraday rotation for particles with a diameter between 6 and 8 nm ranged between 27° and 40°/cm. The specific Faraday rotation for the reported sample at 0.8 T, obtained from the overlapping with the SQUID measurements, would be 31.1°/cm, that is, roughly twice the value in Ref. [9] taking into account the Fe concentration of the samples. We argue that such differences can be attributed to the different synthetic routes used, which in turn yields nanoparticles with a different degree of crystallinity as well as different thickness of the magnetically disorder surface layer.

4. Conclusions

We have synthesized a γ-Fe_2O_3/SiO_2 nanocomposite, a very light solid, magnetic material, with some degree of optical transparency in the visible region. The synthesis method was via sol–gel by impregnation of the wet silica gels with an anhydrous ferrous salt. During the supercritical drying of the gel, the ferrous salt was converted into γ-Fe_2O_3 nanoparticles, homogeneously distributed in the aerogel matrix. The composite, with 10.4 wt% of iron oxide, has a specific Faraday rotation of 29.6°/cm at 0.6 T. It is observed that the magnetization curve ($M = f(H)$) is proportional to the Faraday rotation as a function of the applied magnetic field. This relation between the magnetic and optical properties of the material can be used for scientific and industrial purposes, such as optical fibre sensors, optical isolators and magnetic data storage.

References

[1] S.K. Poznyak, D.V. Talapin, A.I. Kulak, Thin Solid Films 35 (2002) 405.

[2] M. Gich, Ll. Casas, A. Roig, E. Molins, J. Sort, S. Suriñach, M.D. Baró, J.S. Muñoz, L. Morellon, M.R. Ibarra, J. Nogués, Appl. Phys. Lett. 82 (2003) 4307.

[3] H. Guerrero, G. Rosa, M.P. Morales, F. del Monte, E.M. Moreno, D. Levy, R. Perez del Real, T. Belenguer, C.J. Serna, Appl. Phys. Lett. 71 (1997) 2698.

[4] R.F. Ziolo, E.P. Giannelis, B.A. Weinstein, M.P. O'Horo, B.N. Ganguly, V. Mehrotra, M. Russell, D.R. Huffman, Science 257 (1992) 219.

[5] F. del Monte, M.P. Morales, D. Levy, A. Fernandez, M. Ocaña, A. Roig, E. Molins, K. O'Grady, C.J. Serna, Langmuir 13 (1997) 3627.

[6] S. Martinez, M. Meseguer, Ll. Casas, E. Rodriguez, E. Molins, M. Moreno-Manas, A. Roig, R.M. Sebastian, A. Vallribera, Tetrahedron 59 (2003) 1553.

[7] J.I. Martín, J. Nogués, K. Liu, J.L. Vicent, I.K. Schuller, J. Magn. Magn. Mater. 256 (2003) 449.

[8] G.W. Day, A.H. Rose, Proc. SPIE 985 (1988) 138.

[9] G.E. Lano, C. Pinyan, Laser Focus World 31 (1995) 125.

[10] G. Rosa, H. Guerrero, D. Levy, A. Álvarez-Herrero, R.P. del Real, J. Appl. Phys. 97 (2005) 64314.

[11] M. Popovici, M. Gich., A. Roig, Ll. Casas, E. Molins, C. Savii, D. Becherescu, J. Sort, S. Suriñach, J.S. Muñoz, M.D. Baro, J. Nogues, Langmuir 20 (2004) 1425.

[12] L. Lutterrotti, S. Gialanella, Acta Mater. 46 (1997) 101.

[13] G.M. Pajonk, P.B. Wagh, D. Haranath, J. Mater. Synth. Process. 5 (1997) 403.

Facile route to magnetophotonic crystals by infiltration of 3D inverse opals with magnetic nanoparticles

J.M. Caicedo [a], E. Taboada [a], D. Hrabovský [a], M. López-García [b], G. Herranz [a,*], A. Roig [a], A. Blanco [b], C. López [b], J. Fontcuberta [a]

[a] Institut de Ciència de Materials de Barcelona (ICMAB-CSIC), Campus UAB, E08193, Bellaterra, Spain
[b] Instituto de Ciencia de Materiales de Madrid (ICMM-CSIC), Campus UAM, Madrid 28049, Spain

ARTICLE INFO

ABSTRACT

We report here on the fabrication and characterization of magnetophotonic crystals obtained by infiltrating magnetic nanoparticles (maghemite) into silica-based inverse opals. Good quality opals, with adjustable photonic and magnetic characteristics have been obtained by this method. Magnetic and magneto-optic measurements, performed by using SQUID magnetometry and Kerr and Faraday effects, have been used to monitor the magnetic filling of the opals. It is observed that the Kerr rotation is not proportional to the overall magnetization of the magnetophotonic crystal. Possible scenarios for this unexpected result are discussed.

© 2009 Elsevier B.V. All rights reserved.

1. Introduction

Photonic crystals (PCs) are composite systems in which two or more dielectric materials are periodically structured [1–3] to modulate the dielectric constant. When the period of the structure is comparable to the optical wavelength a photonic band gap (PBG) for electromagnetic waves, analogous to the band gap in semiconductor materials, appears, and light propagation inside the PBG is forbidden. This feature makes PCs suitable for several applications such as sensors, lasers, optical fibers, optical filters or photonic components in telecommunication devices. A very promising subclass of PCs includes magnetophotonic crystals (MPCs) which bear magnetic materials in their structure. It has been proposed that in MPCs the photonic band structure is controllable magnetically [1]; moreover, the strong photon confinement in the MPCs should promote a large enhancement of the linear and nonlinear magneto-optical response in these materials, as demonstrated in one-dimensional (1D) MPCs composed of a magnetic garnet thin film sandwiched between dielectric Bragg mirrors [4]. These effects have been also investigated in three-dimensional (3D) MPCs, which present many advantages for several applications. For instance, an enhancement of the Faraday rotation within the photonic band gap was observed in 3D-MPCs impregnated with a Faraday-active liquid [5]. These are built up by dielectric spheres that self-assemble in ordered fcc crystalline arrangements, leaving holes

between the spheres which may be filled with magnetic material to form the MPCs [6]. Here we report on MPCs based on inverse opals [7]. First, a direct opal is synthesized and then its interparticular voids are filled with a dielectric material. After subsequent removal of the opal spheres, the resulting spherical voids are loaded with the magnetic material. This route has the advantage of a potential major degree of magnetic material filling with respect to the direct opal MPCs.

2. Experimental

Inverse opals were prepared using silica (SiO_2) as host material and then filled with maghemite (γ-Fe_2O_3) nanoparticles (NPs). The synthesis can be shortly described as follows: direct opals were built up of polystyrene (PS) spheres of different size assembled by vertical deposition onto hydrophilic glass substrates. They constitute the template for the inverse opal preparation. Afterwards, the host materials (SiO_2) were infiltrated between the PS spheres by chemical vapor deposition (CVD) and the original organic spheres were removed by dissolution with toluene leaving behind spherical voids in the structure [6]. These inverse opals were subsequently infiltrated with the magnetic NPs by immersion in an aqueous dispersion of maghemite NPs. The opal was then pulled out of the solution using a vertical stepping motor to precisely control the speed. This step can be repeated several times to increase the magnetic loading. By proceeding in this way, the magnetic NPs filled up the spherical voids in the inverse opal. The maghemite NPs were previously synthesized in organic media by thermal decomposition of iron pentacarbonyl
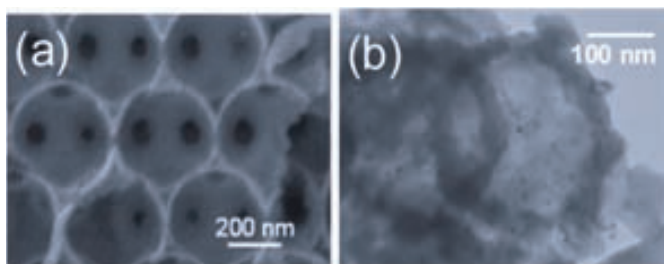
Fig. 1. (a) SEM image of a silica inverse opal infiltrated with maghemite nanoparticles; (b) TEM image of the same sample showing the regular distribution of magnetic nanoparticles.

[8,9] and transferred to water using sodium citrate as the stabilizer. They are 10 nm in diameter, with narrow particle size distribution ($\sigma < 10\%$) and superparamagnetic at room temperature, with a saturation magnetization at 300 K of 30 emu/g and a blocking temperature lower than 60 K.

Here we will restrict ourselves to the characterization of two silica-based inverse opals. They differ in the spherical void sizes (the original PS particles were 467 nm for MPC1 and 380 nm for MPC2). Thus the corresponding PBGs will occur at different wavelengths. They also differ in the fact that they were infiltrated with different amounts of NPs by cycling the NP filling process twice (sample MPC1) and once (MPC2). Thus one expects that the loading of magnetic material of MPC1 will be higher than that of MPC2. A scanning electron microscopy (SEM) image of sample MPC2 is shown in Fig. 1a, where it can be appreciated the high quality of the SiO$_2$ inverse opal, with wall widths less than 20 nm. In Fig. 1b, where we show the transmission electron microscopy (TEM) image of an inverse opal infiltrated in the same conditions as MPC2, we appreciate the regular distribution of the NPs. One notices that the magnetic NPs have not clustered significantly during the infiltration and thus it is to be expected (see below) that their superparamagnetic characteric is preserved in the MPCs.

3. Results

Room temperature measurements by SQUID magnetometry of MPC1 and MPC2 revealed superparamagnetic behaviour of the material (Fig. 2) with saturation fields about 3 kOe, thus confirming that the magnetic NPs do not magnetically interact with each other once being infiltrated in the opal. SEM images were used to estimate the sample thickness, and thus the opal's volume. Saturation magnetization values were 3.05 emu/cm^3 for MPC1 and 1.07 emu/cm^3 for MPC2. These values correspond to a magnetic loading of 1.9% and 0.7%, respectively (volume percentages). The higher magnetization of sample MPC1 is in agreement with its higher magnetic filling. The larger voids in MPC1 may have relation with the observation that with only two NP loading cycles for MC1 the magnetization value and the NP load of MPC1 is three times higher than that of MPC2.

Now we turn to the magnetophotonic properties of our two MPCs. PBG were measured by standard normal reflectance as a function of the wavelength of the excitation light. In Fig. 3 it can be observed that the PBG for MPC1 is centred at $\lambda = 830$ nm, whereas for MPC2 it is centred at $\lambda = 572$ nm. Kerr magneto-optical characterization was performed using two lasers, with wavelengths $\lambda = 542$ nm (green) and $\lambda = 633$ nm (red) in polar Kerr geometry at normal incidence. In Fig. 3 the positions of these wavelengths with respect to the PBGs of our MPCs are indicated (both wavelengths fall outside the range of the gap). The Faraday rotation of MPC1 and MPC2 was measured with the green laser
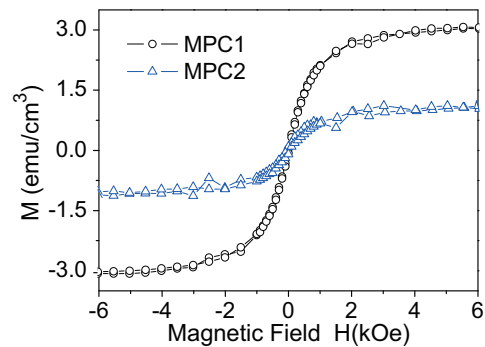
**Fig. 2.** Magnetization loops of MPC1 and MPC2 samples.
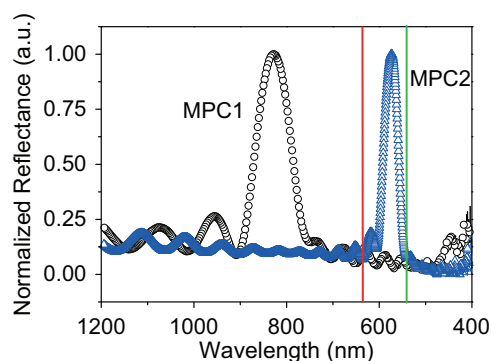
Fig. 3. Reflectivity spectrum as a function of the wavelength of the samples MPC1 and MPC2. Red ($\lambda = 542$ nm) and green ($\lambda = 633$ nm) wavelength are indicated by the vertical lines (for interpretation of the references to color in this figure legend, the reader is referred to the web version of this article).
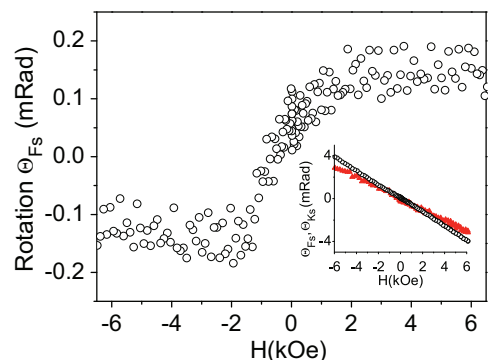
Fig. 4. Faraday rotation of sample MPC1 obtained with green laser ($\lambda = 542$ nm). *Inset*: Faraday and Kerr rotations of MPC1 before the correction of the linear glass substrate contribution.

(see Fig. 4), whereas the Kerr rotation was measured with the red laser (see Fig. 5). To obtain the magneto-optical response specific of our MPCs, we subtracted the glass substrate linear contribution from the raw data measurements (shown in the inset of Fig. 4). Inspection of results in Fig. 5 shows that the hysteresis loops by magneto-optical Kerr effect are in a good agreement with those obtained by SQUID magnetometry (Fig. 2). This fact indicates that the infiltration of inverse opals with magnetic NPs is a very convenient way to fabricate MPCs and also that the magnetization and Kerr rotation can be controlled by the filling factor. Indeed, the Kerr rotation of sample MPC1 is significantly higher than that of MPC2, which, as noted above, is consistent with a higher degree of magnetic NP filling of MPC1 with respect to MPC2. Moreover,
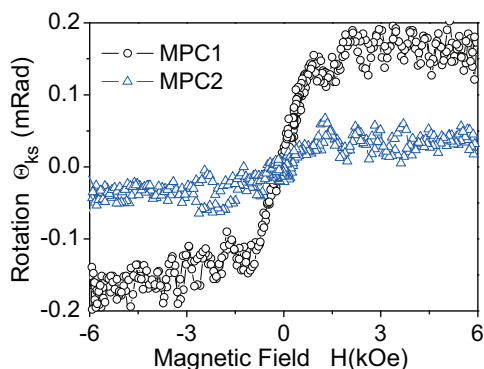
Fig. 5. Kerr rotation of samples MPC1 and MPC2 obtained with red laser ($\lambda = 633\,\text{nm}$).

we note that the ratio of the Kerr rotation measured for MPC1 and MPC2 (0.2/0.05 mRad, see Fig. 5) is larger than the the magnetization ratio ($3.05/1.07\,\text{emu cm}^3$, see Fig. 2). This may indicate that the Kerr rotation is not simply proportional to the overall magnetization of the MPCs. This behaviour, which contrasts with results in bulk materials, could indicate the existence of a certain enhancement in the magneto-optical response of the MPCs [10]. However, it cannot be excluded that inhomogeneous magnetic filling at the mm scale (the size of the laser beam) could cause this unexpected observation. Further investigations are currently underway to address this issue.

Finally, we would like to note that the linear slope coming from the substrate in the Faraday configuration is of the same order than the one of the Kerr configuration (see the inset of Fig. 4). In principle, one should not expect such a strong effect from the substrate in Kerr measurements since the signal is coming from the reflection on the sample. This can be understood since just a small fraction of the beam is attenuated by the infiltrated opal and hence, the largest fraction of the light propagates through the glass substrate and it is reflected back to the substrate/air

interface. This hypothesis was confirmed by doing experiments on raw glass substrates.

4. Conclusions

In summary, we have reported on the preparation and characterization of MPCs obtained by infiltration of magnetic nanoparticles inside 3D inverse silica opals. Our preparation technique allows obtaining good quality MPCs with PBGs adjustable by the synthetic conditions and can be extended to a variety of materials improving their versatility. Our samples showed superparamagnetic-like behaviour at room temperature and PBGs in the near infrared–visible spectrum of light. The Kerr and Faraday rotation have been measured as a function of the degree of magnetic filling. Surprisingly enough it is observed that the Kerr rotation does not scale linearly with the magnetization. We have argued that this unexpected feature, which may be originated by an inhomogeneous infiltration of the NPs, could also be an indication of an enhanced magneto-optical response in MPCs.

References

[1] M. Inoue, et al., J. Phys. D: Appl. Phys. 39 (2006) R151–R156.
[2] M Inoue, et al., Proceedings of the Second International Symposium on Frontiers in Magnetism (Stockholm, August 1999)
[3] C. López, J. Opt. A: Pure Appl. Opt. 8 (2006) R1.
[4] B. Byron, et al., Adv. Mater. 13 (2001) 21.
[5] C. Koerdt, et al., Appl. Phys. Lett. 82 (2003) 1538.
[6] A. Blanco, et al., J. Mater. Chem. 16 (2006) 2969–2971.
[7] A. Blanco, et al., Nature 405 (2000) 437–440.
[8] E. Taboada, et al., Langmuir 23 (2007) 4583.
[9] T. Hyeon, et al., J. Am. Chem. Soc. 123 (2001) 12798.
[10] V.V. Pavlov, et al., Appl. Phys. Lett. 93 (2008) 072502.

7.2.2. Epsilon-iron oxide nanoparticles (ε-Fe$_2$O$_3$)

Epsilon iron oxide is a metastable polimorph of ferric oxide that presents difficulties to be stabilized in bulk form. The interest of the phase is owed to its high coercive field at room temperature as well as its rich magnetic phase diagram. In our case, the epsilon iron oxide phase was synthesized by controlled thermal treatments (up to 1100ºC) of maghemite nanoparticles dispersed in silica xerogel matrices. In bulk form, maghemite transforms to hematite when annealed in air but when maghemite is nanometric and is physically confined, the particle growth is hindered and the formation of epsilon iron oxide is favoured due to its lower surface energy. Martí Gich dedicated huge efforts to the study of this iron oxide phase during his thesis at our group. I participated in the synthesis of the materials. A thorough structural and magnetic characterization was performed by Martí Gich. We have later applied this knowledge to synthesize ε-Fe$_2$O$_3$@SiO$_2$ nanoparticles from γ-Fe$_2$O$_3$@SiO$_2$ (see section 4.5).

Publications:

- Gich, M.; Roig, A.; <u>Taboada, E.;</u> Molins, E.; Bonafos, C. and E. Snoeck, Stabilization of metastable phases in spatially restricted fields: the case of the Fe$_2$O$_3$ polymorphs. *Faraday Discussions*, **2007**, 136, 345-354. Citations (Sept. 2nd 2009): 1.

- Gich, M.; Frontera, C.; Roig, A.; <u>Taboada, E.;</u> Molins, E.; Rechenberg, H. R.; Ardisson, J. L.; Macedo, W. A. A.; Ritter, C.; Hardy, V.; Sort, J.; Skumryev, V. and Nogués, J. High-and low- temperature crystal and magnetic structures of ε-Fe$_2$O$_3$ and their correlation to its magnetic properties *Chemistry of Materials*, **2006**, 18, 3889-3897. Citations (Sept. 2nd 2009): 13.

Stabilization of metastable phases in spatially restricted fields: the case of the Fe_2O_3 polymorphs

Martí Gich,†*[a] Anna Roig,[a] Elena Taboada,[a] Elies Molins,[a] Caroline Bonafos[b] and Etienne Snoeck[b]

In this work we show how the confinement of particles in a silica matrix with pores, acting as nano-vessels, plays an important role in the formation of pure ε-Fe_2O_3 nanoparticles and their thermal stability. In particular, a HRTEM study of a series of Fe_2O_3–SiO_2 xerogels annealed at different temperatures reveals that, at low temperatures, γ-Fe_2O_3 nanoparticles are formed and only transform to ε-Fe_2O_3 after subsequent annealing at higher temperatures. These data are complemented by measurements of the SiO_2 matrix porosity as well as with calorimetric and structural analysis of the nanoparticles after matrix removal. The gathered data indicate that the SiO_2 matrix acts as a barrier, hindering thermal diffusion and particle growth even at the high temperatures where the formation of ε-Fe_2O_3 appears to be favoured, thereby preventing its transformation to α-Fe_2O_3.

1. Introduction

Size-dependent properties are a distinctive characteristic of nanoscopic objects. Among the reasons that account for this behaviour is the fact that at the nanometric scale there is a significant fraction of the atoms that are located at the surfaces or interfaces and consequently, some of the material characteristics such as, for instance, the catalytic activity, melting point or stability of a given polymorph are strongly dependent on the particle size. It is generally accepted that surface energy and surface stress play important roles in the formation and stability of crystalline phases. This was already pointed out more than twenty years ago when it was realised that zirconia microcrystals tended to grow in a metastable tetragonal form rather than in the usual monoclinic crystals.[1] Similar behaviours have been reported thereafter in a variety of systems: metals,[2] semiconductors,[3] organics[4] or the well-studied C allotropes.[5] In the case of the Fe_2O_3 system in the form of nanoparticles it is well known that maghemite (γ-Fe_2O_3) tends to be the stable phase which transform to hematite (α-Fe_2O_3), the stable Fe(III) oxide polymorph, around 400 °C.[6] However, the stability of γ-Fe_2O_3 nanoparticles can be increased up to about 1000 °C when those particles are confined in a silica matrix and above this

[a] *Institut de Ciència de Materials de Barcelona-CSIC, Campus de la UAB, Bellaterra, 08193, Catalonia, Spain. E-mail: roig@icmab.es; Fax: +34 935805729; Tel: +34 935801853*
[b] *Centre d'Élaboration de Materiaux et Études Structurales-CNRS, NanoMat group, 29 rue Jeanne Marvig, BP 94347, 31055, Toulouse Cedex 4, France*

† Current address: Saint-Gobain Recherche, 39 quai Lucien Lefranc, 93303, Aubervilliers, France.

temperature, the transformation into ε-Fe$_2$O$_3$ starts.[7] In this context, we have recently reported how pure ε-Fe$_2$O$_3$ can be prepared by a controlled sol–gel synthesis inside the pores of a SiO$_2$ xerogel.[8] ε-Fe$_2$O$_3$ is one of the rarest and less studied Fe$_2$O$_3$ polymorphs due to the difficulty in synthesizing it as a single phase. In this work we discuss how the particle confinement in the silica pores, that act as nano-vessels, plays an important role in the formation and the high thermal stability of pure ε-Fe$_2$O$_3$ nanoparticles. In particular, a HRTEM study of a series of Fe$_2$O$_3$–SiO$_2$ xerogels annealed at different temperatures reveals that, initially, γ-Fe$_2$O$_3$ nanoparticles are formed at low temperatures which are then transformed into ε-Fe$_2$O$_3$ after subsequent annealing at higher temperatures. This has been comple-mented by Brunauer–Emmett–Teller (BET) N$_2$ adsorption experiments aiming to evaluate the evolution of the SiO$_2$ matrix porosity upon annealing as well as with calorimetric and structural analysis of the nanoparticles after matrix removal. All these measurements indicate that the amorphous SiO$_2$ matrix acts as a barrier, hindering thermal diffusion and particle growth even at the high temperatures where the formation of ε-Fe$_2$O$_3$ appears to be favoured, thereby preventing its transforma-tion to α-Fe$_2$O$_3$. The interest in exploring phase transformations in spatially restricted fields as a new approach to controlling polymorphism and searching for unknown polymorphs will also be discussed in a more general context.

2. Experimental

Synthesis

SiO$_2$–Fe$_2$O$_3$ nanocomposites are prepared by sol–gel chemistry using iron nitrate (Aldrich, 96%) and tetraethoxysilane (TEOS) (Aldrich, 98%) as precursors with a targeted composition of 30 wt% Fe$_2$O$_3$ in the final SiO$_2$–Fe$_2$O$_3$ composite. First, a gel is obtained through hydrolysis and condensation processes occurring in an acidic hydroethanolic medium at TEOS : H$_2$O : EtOH = 1 : 6 : 6 mole ratio and the appropriate amount of iron nitrate, being the reaction pH ∼0.9. These reactions are self-catalyzed by the nitric acid resulting from the hydrolysis of iron nitrate. The solution is then placed in a beaker covered with pin-holed parafilm to allow the evaporation of the solvent, gelation takes place at room temperature in a time ranging from two weeks to several months depending on the laboratory temperature and humidity. Wet gels are then dried at 60–80 °C for 14 h, crushed in an agate mortar and the resulting xerogels are annealed in air atmosphere for three hours every 100 °C between 300–1100 °C with a 600 °C min^{-1} heating rate between the isotherms. Four different composites, labelled S700, S900, S1000 and S1100 were obtained according to the different temperatures of the final thermal treatment at 700, 900, 1000 and 1100 °C. In addition, part of S1100 was treated in a 12 M NaOH aqueous solution at 80 °C to remove the SiO$_2$ amorphous matrix. After two days the solution was centrifuged and washed several times with distilled water until achiev-ing a neutral pH and finally dried at 60 °C. X-Ray diffraction analysis performed after this treatment revealed that the SiO$_2$ had been efficiently removed while the iron oxide phases present in S1100 remained unaltered. The material containing no silica is labelled S1100B and consists of ε-Fe$_2$O$_3$ nanoparticles.

Transmission electron microscopy (TEM)

Observations were carried out using a Philips CM 30 microscope operating at 300 kV. Before the TEM observations, the samples were crushed and ultrasonically dispersed in ethanol. Drops of the solution were subsequently deposited onto Cu TEM grids that were coated with a conductive polymer, and the ethanol was allowed to evaporate.

Powder X-ray diffraction (XRD)

The formation of the crystalline phases was studied by X-ray diffraction (XRD) in a θ–2θ Bragg–Brentano geometry using a Siemens D5005 powder diffractometer with diffracted beam monochromator and a Brüker D8 diffractometer equipped with a microdiffraction stage. In both cases Cu Kα radiation was used (λ = 1.5406 Å). To quantitatively analyze the structural parameters, e.g. phase percentages, crystallite sizes or cell parameters, Rietveld refinements were performed using the *MAUD* program.[9] The orthorhombic (space group $Pna2_1$) structure, described by Tronc et al.,[10] and the usual defect inverse spinel structure (space group Fd-$3m$) were adopted for ε-Fe_2O_3 and γ-Fe_2O_3, respectively. Modeling of the silica glass is based on the assumption that from the X-ray diffraction pattern it is not possible to distinguish if the structure is completely amorphous or nanocrystalline SiO_2.[11] This method approximates the SiO_2 amorphous phase as a nanocrystalline solid (cubic structure with space group $P2_13$) in which crystallite size is taken to be of the same order of magnitude as the cell parameters and the disorder is statistically introduced by the microstrain effect.[12]

Surface area measurements

Nitrogen adsorption data were taken at 77 K using an ASAP 2000 surface area analyzer (Micromeritics Instrument Corporation) after heating the samples at 180 °C under vacuum for 24 h to remove the adsorbed species. Surface area determinations were carried out following the BET method.

Thermal analysis

Phase stability in the 300–1800 K range was studied by differential thermal analysis (DTA) on a Perkin-Elmer DTA 7 apparatus at several heating rates under an air atmosphere.

3.   Results and discussion

Typically, from the gels prepared by mixing an aqueous solution of a metal salt and an alcoholic solution of a Si–alkoxide, one can obtain a composite of amorphous silica and nanoparticles of the metal oxide by means of appropriate thermal treatments. Thus, it is worth considering both the evolution of the SiO_2 matrix and the nanoparticles and trying to correlate them. In Fig. 1, the thermal treatments
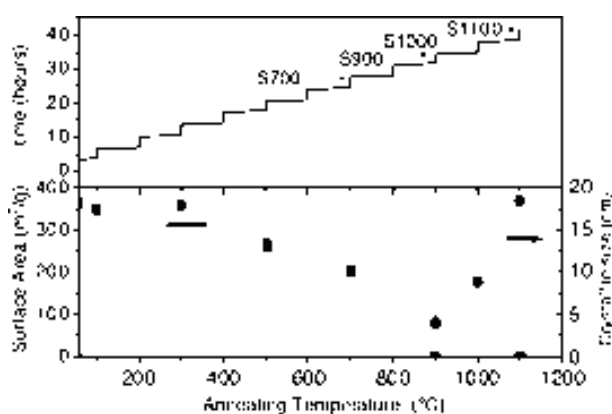
Fig. 1   Thermal treatment of the xerogels yielding the composites studied in this work (upper panel) and its influence on the amorphous SiO_2 porosity (■) and the crystallite size of the nanoparticles (●) (lower panel).
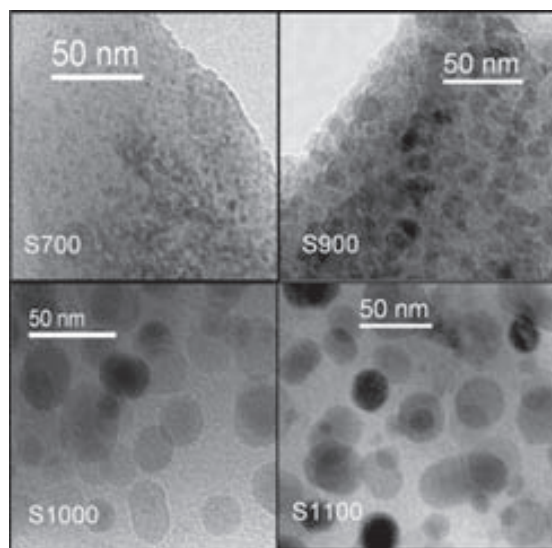
Fig. 2 TEM images of the different SiO_2–Fe_2O_3 composites.

of the different SiO_2–Fe_2O_3 composites that have been studied are represented with the corresponding evolution of the silica matrix porosity, which is considered to be proportional to the surface area measured by nitrogen adsorption. The matrix porosity gradually decreases between 300 and 900 °C, where it vanishes. In the figure we can also observe that for the S900, S1000 and S1100 composites, the mean crystallite size $\langle d \rangle_{XRD}$ of the iron oxide nanoparticles, as obtained from the broadening of the diffraction peaks, increases with the annealing temperature coinciding with the range of annealing temperatures where the silica matrix has no porosity. For S700 it has not been possible to obtain $\langle d \rangle_{XRD}$, since only the characteristic silica glass hump centred around $2\theta = 22°$ was observed in the diffraction pattern of this composite. In Fig. 2, the TEM images of the different composites show a dispersion of nanoparticles in the silica matrix and it can be observed that the nanoparticles coarsen as the annealing temperature is increased. However, in this case the increase in the nanoparticle diameter is especially important between S700 and S1000 and not so evident between S1000 and S1100. Indeed, histograms of the particle size distributions were obtained from several TEM images of S1000 and S1100. The histograms were fitted to log-normal distribution functions which gave average particle sizes of 22 ± 2 nm and 26 ± 4 nm, respectively. Thus, by increasing the annealing temperature between 700 and 1000 °C the nanoparticles grow but this trend is not extended at higher temperatures and a subsequent annealing at 1100 °C has almost no effect on the particle size and its main effect is to increase the crystallinity of the nanoparticles. In fact, $\langle d \rangle_{XRD}$ is to be interpreted as the size of the coherent domains of diffraction within the particles and in general is lower than the particle size observed by TEM. These results combined with the temperature dependence of the silica matrix porosity indicate something which is indeed quite intuitive, namely, that the growth of nanoparticles is favoured by the presence of a porous matrix but hindered as the matrix densifies when decreasing its porosity.

The composites were also studied by high resolution TEM (HRTEM). These experiments revealed interesting features of the crystallisation process and the different iron(III) oxides polymorphs. Fig. 3 presents HRTEM images of nanoparticles corresponding to the S1100 and S1000 composites. The Fourier transform of an HRTEM image allows us to identify the crystallographic phase of the nanoparticle and its orientation. For instance, in Fig. 3 we can see HRTEM images of the
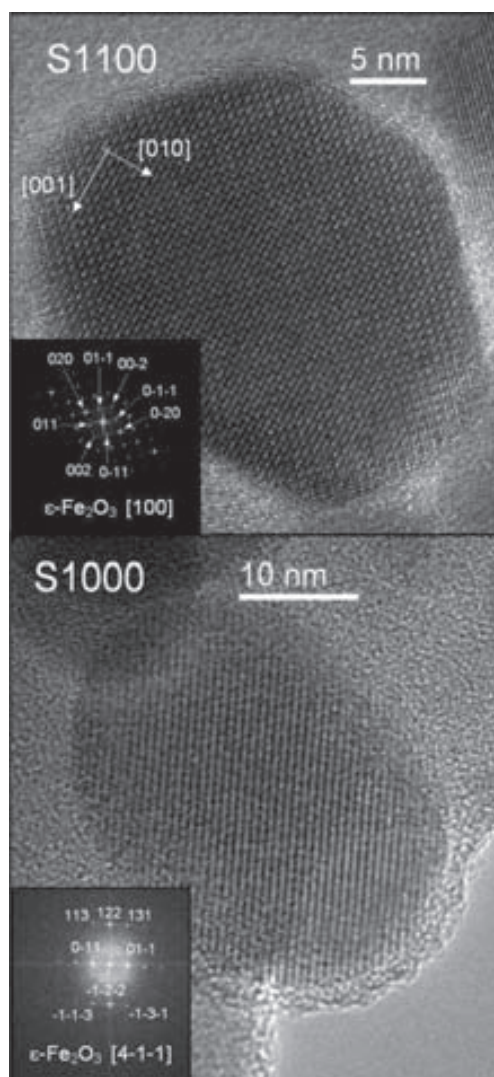
Fig. 3 HRTEM images of nanoparticles from S1100 and S1000 composites. The Fourier transform of the images (insets) corresponds to the [100] and [4-11] zone axes of ε-Fe$_2$O$_3$, respectively.

S1100 and S1000 composites corresponding to ε-Fe$_2$O$_3$ nanoparticles taken along the [100] and [4-1-1] zone axes, respectively. Analysing the HRTEM images of these composites we have only observed the presence of ε-Fe$_2$O$_3$ in accordance with previous XRD results[8] showing that the iron oxide present in composites equivalent to S1100 and S1000 was also ε-Fe$_2$O$_3$ and less than 10 wt% of α-Fe$_2$O$_3$. In that study, relying on the fact that the only XRD patterns with reflections due to the presence of ε-Fe$_2$O$_3$ nanoparticles were those annealed at temperatures above 900 °C, we assumed that the nucleation of the ε-Fe$_2$O$_3$ nanoparticles should occur below this temperature. In particular, the magnetic and Mössbauer spectroscopy measurements indicated that the composite annealed at 700 °C already presented crystalline clusters. However, the analysis of the HRTEM images of composite S700 proves that this first hypothesis was wrong. Indeed, S700 contains γ-Fe$_2$O$_3$ rather than ε-Fe$_2$O$_3$ nanoparticles (see Fig. 4). Thus, it is between 700 and 1000 °C that a
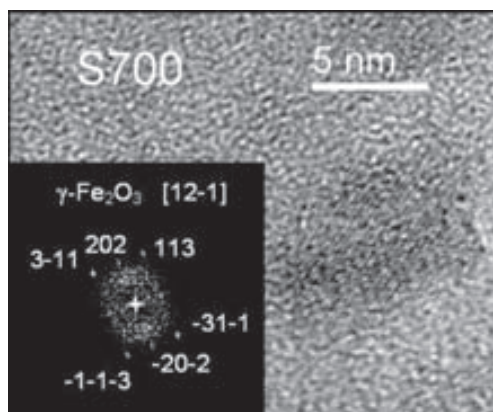
Fig. 4 HRTEM image of a nanoparticle from S700 composite. The Fourier transform of the image (inset) corresponds to the [12-1] zone axis of γ-Fe$_2$O$_3$.

γ → ε phase transformation must occur. In fact, the Fourier transforms of the HRTEM images of S900 could not be ascribed to any of the zone axes of either γ-Fe$_2$O$_3$ or ε-Fe$_2$O$_3$. However, the XRD pattern of S900 is best fitted by assuming that ε-Fe$_2$O$_3$ instead of γ-Fe$_2$O$_3$ is the major iron oxide phase in the composite (see Fig. 5), suggesting that the γ → ε transformation takes place gradually. In fact, many attempts were made to detect the transformation by DTA analysis which turned out to be unfruitful since no distinct exothermal signal could be detected between 700 and 1000 °C. This behaviour would be in accordance with a phase transformation in which the release of energy occurs along a broad temperature range indicating that the transformation consists of a continuous process characterised by the emergence of disorder bringing about a gradual disappearance of the γ polymorph and the subsequent appearance of the ε structure. Interestingly, this
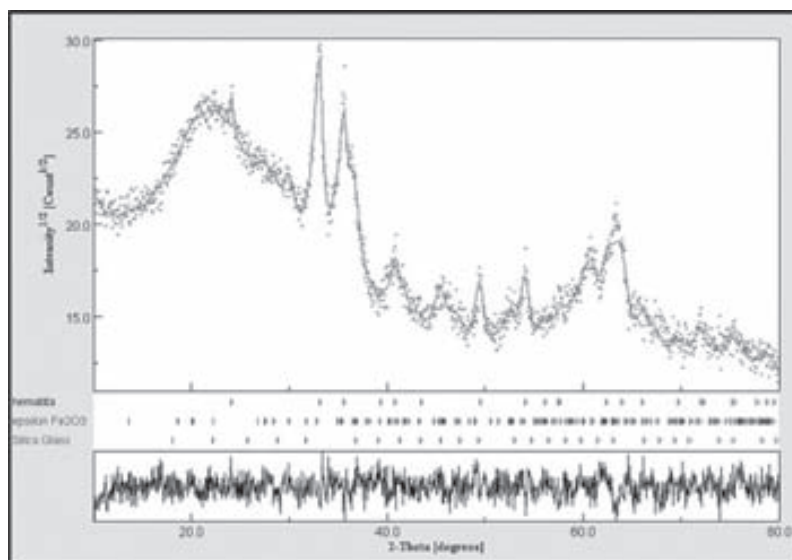
Fig. 5 Experimental (dots), calculated (solid line) and difference plot (lower panel line) for the Rietveld refinement of S900 considering ε-Fe$_2$O$_3$, α-Fe$_2$O$_3$ and amorphous SiO$_2$. Reflection positions of the different phases are indicated by vertical lines.
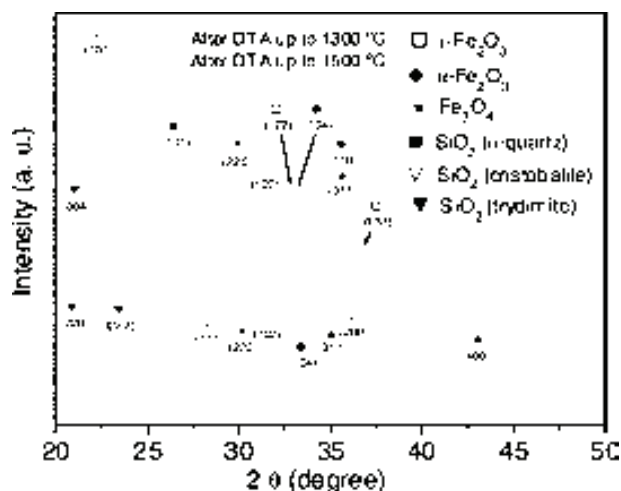
Fig. 6 XRD patterns of composite S1100 collected after heating it up to 1300 °C and 1500 °C in a DTA apparatus under air atmosphere.

kind of processes have been observed in oxide systems such as zirconia[13] or the Fe_2O_3 itself,[14] in which the size-reduction by milling of a stable structure yields a metastable polymorph. Alternatively, one could think of a particular energy landscape presenting local minima between the γ and ε structures in which the phase transition would involve the formation of well defined intermediate polymorphs.

The DTA experiments have also revealed the remarkable thermal stability of the amorphous SiO_2–ε-Fe_2O_3 composite. Actually, the transformation of ε-Fe_2O_3 nanoparticles into stable oxide phases such as hematite or magnetite is preceded by the devitrification of the silica matrix which starts at above 1200 °C. Fig. 6 shows the XRD patterns of the composites recorded after heating the material to 1300 and 1500 °C in DTA runs. It can be observed that after heating the material to 1300 °C, the amorphous silica matrix has been partially transformed into quartz and cristobalite while ε-Fe_2O_3 transforms to α-Fe_2O_3 and Fe_3O_4 (solid curve). Upon further annealing the material to 1500 °C, the crystallisation of amorphous silica occurs, which is stabilised into cristobalite and trydimite, and the disappearance of ε-Fe_2O_3 is completed (dotted curve). These results indicate that the transformation of ε-Fe_2O_3 to the stable Fe oxides is indeed triggered by the devitrification–crystallisation of the silica matrix and points to the prominent role of the latter in both the formation and stability of the ε polymorph. Stronger evidence to support this interpretation is given by the DTA experiment performed with sample S1100B, only containing ε-Fe_2O_3 nanoparticles, in which an exothermic process starting at about 750 °C is clearly detected (see Fig. 7). As expected, the XRD pattern of S1100B collected after the DTA run (see Fig. 8) shows that the ε-Fe_2O_3 nanoparticles have transformed mainly into the α-Fe_2O_3 stable polymorph, a small fraction of Fe_3O_4 has also been detected. Thus, the thermal stability limit of ε-Fe_2O_3 is increased from 750 °C to about 1200 °C by the presence of the silica amorphous matrix, although even in the absence of the latter, the ε-Fe_2O_3 nanoparticles exhibit a better stability at high temperatures compared to γ-Fe_2O_3 nanoparticles which are known to transform to hematite at about 400 °C.[6]

The relative stability of the γ, ε and α polymorphs of Fe_2O_3 can be understood in the framework of a simple model for small-particle phase transformations, *i.e.* one that only considers the surface energies and bulk free energies of the phases involved and neglects other contributions such as stress. In such a model, the size-dependence of the free energy variation per unit volume for the nucleation of a phase b from a phase a, Δg_b^{nuc}, is expressed in the relation (1), where R is the radius of the nucleus,
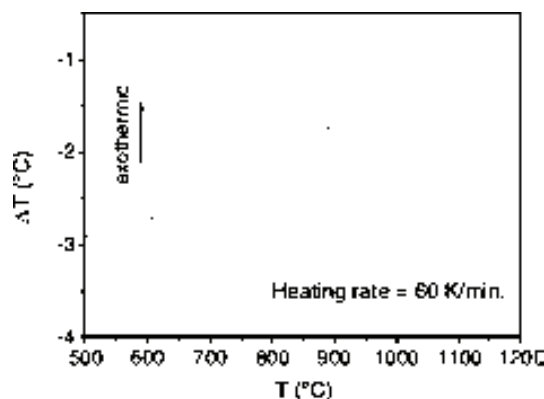
Fig. 7 DTA curve under an air atmosphere of sample S1100B only containing ε-Fe_2O_3 nanoparticles.

Δg_b is negative and represents the bulk free energy variation per unit volume of the transformation and γ_b is the surface energy of an a–b interface. Relation (1) is schematically represented in Fig. 9 for the γ, ε and α Fe_2O_3 polymorphs for a state in which the conditions (i) $\gamma_\gamma < \gamma_\varepsilon < \gamma_\alpha$ and (ii) $\Delta g_\gamma < \Delta g_\varepsilon < \Delta g_\alpha$ are fulfilled. The figure shows that it is the particle size that determines which is the stable polymorph. In this scenario, ε-Fe_2O_3 would form at intermediate sizes from those that stabilise maghemite or hematite. There are several reasons to believe that condition (i) is true. Navrotsky *et al.* have extensively studied the energetics of nanocrystalline aluminas which present polymorphs isostructural with those encountered for Fe_2O_3 and they experimentally established that the surface energy of α-Al_2O_3 is higher than that of γ-Al_2O_3.[15] On the other hand, the ε-Fe_2O_3 structure presents features that are common to both γ-Fe_2O_3 (*e.g.* the presence of tetrahedrally coordinated Fe^{3+} ions) and of the α-Fe_2O_3 (*e.g.* the hexagonal stacking of O planes). In that context one can expect that the surface energy of the ε phase is also intermediate between that of γ and α polymorphs. Regarding condition (ii), although at standard conditions the formation enthalpy of γ-Fe_2O_3 is slightly more negative than that of ε-Fe_2O_3 (-808 and -798 kJ mol^{-1}, respectively),[16] there are no thermodynamic data for ε-Fe_2O_3 available at temperatures above 700 °C. Moreover, at high temperatures the entropic
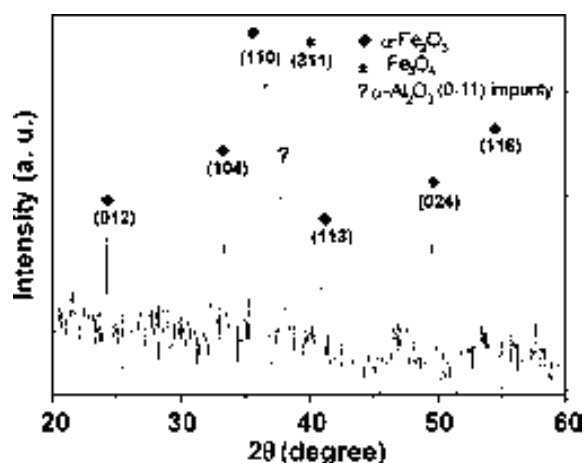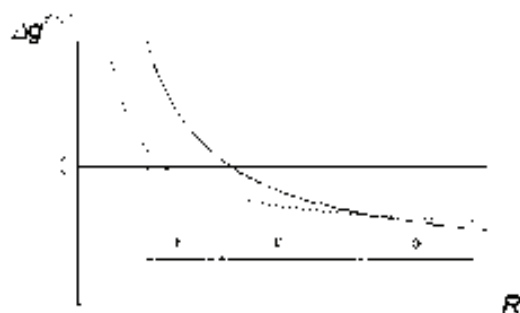

Fig. 8 XRD pattern of material S1100B after a DTA run in an air atmosphere up to 1200 °C.

Fig. 9 Schematic representation of the size-dependent free energy variation of a spherical nucleus for γ-Fe_2O_3 ($\cdots$), ε-Fe_2O_3 (--) and α-Fe_2O_3 (—). The stability ranges for the different polymorphs are also indicated.

term in the free energy becomes more important and a large entropy should be expected for ε-Fe_2O_3 since its asymmetric unit contains four non-equivalent Fe^{3+}.[6] Still, since eqn (1) is more sensitive to surface energy γ_b than to the bulk free energies, (ii) is not a necessary condition for the relative stabilities of Fig. 9 to hold. Somehow, temperatures above 700 °C are necessary for the $\gamma \rightarrow \varepsilon$ transformation to occur and we don't have means of knowing if that is because there is a crossover for the $\Delta g_\gamma < \Delta g_\varepsilon$ condition or because a high activation energy is needed.

$$\Delta g_b^{nuc} = \Delta g_b + \frac{3\gamma_b}{R} \tag{1}$$

The point that we would like to emphasise here is that the role of the silica matrix is essential to ensure that the somehow antagonistic conditions required for the ε-Fe_2O_3 formation, namely a small particle size and a high temperature, are simultaneously satisfied. Thermal treatments at increasingly higher temperatures provoke an increase in the nanoparticle size which allows the $\gamma \rightarrow \varepsilon$ transformation. However, the gradual reduction in the silica matrix porosity hinders diffusion and ensures that the Fe_2O_3 nanoparticles do not reach the critical size to transform to hematite. The possibility that a significant role is played by the silica matrix due to its interaction with the surface atoms of the Fe oxide nanoparticles has to be ruled out according to the conclusions of an X-ray absorption spectroscopy study on amorphous SiO_2–Fe_2O_3 nanocomposites.[17]

4. Conclusions

The results presented herein for the Fe_2O_3 system show how the confinement of nanoparticles in a matrix yields a polymorphic form otherwise impossible to stabilise. In general, for a phase transition involving the occurrence of a (re)crystallisation, a change in temperature, pressure or pH is needed, usually accompanied by a process of crystalline growth. However, one can imagine for instance a number of nanocrystalline phases or polymorphs that can only be prepared at high temperatures and in a restricted range of particle sizes. In other words, there are probably new nanocrystalline phases and polymorphs that could be prepared if one is able to control the intensive thermodynamic variables by keeping the particle size constant or small enough. As has been shown here for the Fe_2O_3 polymorphs, this can be carried out by performing the nanoparticle synthesis in a matrix and a similar approach has been used to control the synthesis of polymorphs of an organic compound.[4] It is also worth noting that producing the nanoparticles in a matrix offers the advantage of avoiding their agglomeration but at the same time the matrix represents a useful and safe support to keep, manipulate and transport the nanoparticles. In conclusion, the exploration of phase transformations in spatially

restricted fields is a new approach to controlling polymorphism and searching for unknown polymorphs is especially appealing at the nanoscale.

References

1 (*a*) R. C. Gravie, *J. Phys. Chem.*, 1965, **69**, 1238; (*b*) R. C. Gravie, *J. Phys. Chem.*, 1978, **82**, 218.
2 (*a*) H. He, G. T. Fei, P. Cui, K. Zheng, L. M. Liang, Y. Li and L. D. Zhang, *Phys. Rev. B*, 2005, **72**, 073310; (*b*) P. Taneja, R. Banerjee, P. Ayyub and G. K. Dey, *Phys. Rev. B*, 2001, **64**, 033405; (*c*) M. Gich, E. A. Shafranovsky, A. Roig, A. Ślawska-Waniewska, K. Racka, Ll. Casas, E. Molins, Yu. I. Petrov and M. F. Thomas, *J. Appl. Phys.*, 2005, **98**, 024303.
3 S. H. Tolbert and A. P. Alivisatos, *Science*, 1994, **265**, 373.
4 J.-M. Ha, J. H. Wolf, M. A. Hillmyer and M. D. Ward, *J. Am. Chem. Soc.*, 2004, **126**, 3382.
5 Q. Jiang and Z. P. Chen, *Carbon*, 2006, **44**, 79.
6 P. Ayyub, M. Multani, M. Barma, V. R. Palkar and R. Vijayaraghavan, *J. Phys. C: Solid State Phys.*, 1988, **21**, 2229.
7 C. Chaneac, E. Tronc and J. P. Jolivet, *Nanostruct. Mater.*, 1995, **6**, 715.
8 M. Popovici, M. Gich, D. Nižňanský, A. Roig, C. Savii, Ll. Casas, E. Molins, K. Zaveta, C. Enache, J. Sort, S. de Brion, G. Chouteau and J. Nogués, *Chem. Mater.*, 2004, **16**, 5542.
9 L. Lutterrotti and S. Gialanella, *Acta Mater.*, 1997, **46**, 101.
10 E. Tronc, C. Chanéac and J. P. Jolivet, *J. Solid State Chem.*, 1998, **139**, 93.
11 A. Le Bail, *J. Non-Cryst. Solids*, 1995, **183**, 32.
12 L. Lutterotti, R. Ceccato, R. Dal Maschio and E. Pagani, *Mater. Sci. Forum*, 1998, **278–281**, 87.
13 J. Balley, P. Bills and D. Lewis, *Trans. J. Br. Ceram. Soc.*, 1975, **74**, 247.
14 N. Randrianantoandro, A. M. Mercier, M. Hervieu and J. M. Grenèche, *Mater. Lett.*, 2001, **47**, 150.
15 J. M. McHale, A. Auroux, A. J. Perrotta and A. Navrotsky, *Science*, 1997, **277**, 788.
16 (*a*) J. Majzlan, K.-D. Grevel, A. Navrotsky and B. F. Woodfield, *Am. Mineral.*, 2003, **88**, 855; (*b*) J. Majzlan, A. Navrotsky and U. Schwertmann, *Geochim. Cosmochim. Acta*, 2004, **68**, 1049.
17 A. Corrias, G. Ennas, G. Mountjoy and G. Paschina, *Phys. Chem. Chem. Phys.*, 2000, **2**, 1045.

High- and Low-Temperature Crystal and Magnetic Structures of ε-Fe₂O₃ and Their Correlation to Its Magnetic Properties

M. Gich,* C. Frontera, A. Roig, E. Taboada, and E. Molins

*Institut de Ciència de Materials de Barcelona, Consejo Superior de Investigaciones Científicas,
Campus de la UAB, 08193 Bellaterra, Catalunya, Spain*

H. R. Rechenberg

Instituto de Física, Universidade de São Paulo, Caixa Postal 66318, 05315-970 São Paulo, Brazil

J. D. Ardisson and W. A. A. Macedo

*Laboratório de Física Aplicada, Centro de Desenvolvimento da Tecnologia Nuclear,
31270-901 Belo Horizonte, Brazil*

C. Ritter

Institut Laue-Langevin, 6 rue Jules Horowitz, BP 156, 38042 Grenoble Cedex, France

V. Hardy

Laboratoire CRISMAT/ENSICAEN, UMR 6508 du CNRS, 6 Bd Marechal Juin, 14050 Caen, France

J. Sort, V. Skumryev, and J. Nogués

*Institució Catalana de Recerca i Estudis Avançats (ICREA) and Departament de Física,
Universitat Autònoma de Barcelona, 08193 Bellaterra, Catalunya, Spain*

The crystal and magnetic structures of orthorhombic ε-Fe₂O₃ have been studied by simultaneous Rietveld refinement of X-ray and neutron powder-diffraction data in combination with Mössbauer spectroscopy, as well as magnetization and heat-capacity measurements. It has been found that above 150 K, the ε-Fe₂O₃ polymorph is a collinear ferrimagnet with magnetic moments directed along the *a* axis, whereas the magnetic ordering below 80 K is characterized by a square-wave incommensurate structure. The transformation between these two states is a second-order phase transition and involves subtle structural changes mostly affecting the coordination of the tetrahedral and one of the octahedral Fe sites. The temperature dependence of the ε-Fe₂O₃ magnetic properties is discussed in light of these results.

I. Introduction

Despite being known since 1934,[1] ε-Fe₂O₃ has been much less studied than other iron(III) oxides, such as the α and γ polymorphs. For instance, it was not until quite recently that an agreement was reached on describing its crystalline structure with an orthorhombic cell in the *Pna*2₁ space group.[2] The structure is isomorphous to GaFeO₃ and AlFeO₃ and presents four different Fe sites, three in octahedral and one in tetrahedral oxygen coordination. From the magnetic point of view, ε-Fe₂O₃ has long been known to be paramagnetic above 510 K and to present below this temperature an antiparallel arrangement of the Fe³⁺ cations,[2–5] characterized by a rather large anisotropy.[5] However, no in-depth studies

have been carried out up to now to determine its magnetic structure. The interest in the magnetic properties of this material has been revived because the scenario disclosed by recent studies is unexpectedly rich and complex. Indeed, this oxide exhibits a huge room-temperature coercivity of about 20 kOe,[6,7] and a magnetic transition at low temperature.[8,9] This low-temperature transition leads to about 5% diminution in the saturation magnetization, M_s, and a reduction in the squareness ratio, M_r/M_s, from 0.5 to 0.2 on cooling from 150 to 85 K, where M_r is the remanent magnetization. Moreover, a large decrease in the coercivity, H_c, from 22.5 to 0.8 kOe is observed between 200 and 100 K[9] (see Figure 1). In

* To whom correspondence should be addressed. E-mail: mgich@icmab.es.
(1) Forrestier, H.; Guiot-Guillain, G. C. *C. R. Acad. Sci.* **1934**, *199*, 720.
(2) Tronc, E.; Chanéac, C.; Jolivet, J. P. *J. Solid State Chem.* **1998**, *139*, 93.
(3) Trautmann, J.-M.; Forestier, H. C. *C. R. Acad. Sci.* **1965**, *261*, 4423.
(4) Schrader, R.; Buttner, G. *Z. Anorg. Allg. Chem.* **1963**, *320*, 220.
(5) Dézsi, I.; Coey, J. M. D. *Phys. Status Solidi A* **1973**, *15*, 681.

(6) Jin, J.; Ohkoshi, S.; Hashimoto, K. *Adv. Mater.* **2004**, *16*, 48.
(7) Popovici, M.; Gich, M.; Nižňanský, D.; Roig, A.; Savii, C.; Casas, Ll.; Molins, E.; Zaveta, K.; Enache, C.; Sort, J.; de Brion, S.; Chouteau, G.; Nogués, J. *Chem. Mater.* **2004**, *16*, 5542.
(8) Kurmoo, M.; Rehspringer, J.-L.; Hutlova, A.; D'Órleans, C.; Vilminot, S.; Estournès, C.; Nižňanský, D. *Chem. Mater.* **2005**, *17*, 1106.
(9) Gich, M.; Frontera, C.; Roig, A.; Savii, C.; Casas, Ll.; Molins, E.; Zaveta, K.; Enache, C.; Sort, J.; de Brion, S.; Chouteau, G.; Nogués, J. *J. Appl. Phys.* **2005**, *98*, 044307.

Figure 1. Temperature dependence of the coercive field H_C, the squareness ratio M_R/M_S, and the saturation magnetization M_S; (inset) in ϵ-Fe$_2$O$_3$ (taken from ref 9).

addition, the material presents a magnetoelectric coupling at about 100 K.[10]

Tronc et al. studied the ϵ-Fe$_2$O$_3$ magnetic structure at 9 K by means of in-field Mössbauer spectroscopy and proposed a nearly collinear ferrimagnetic order at the octahedral sites and a misalignment with possible disorder at the tetrahedral sites.[2] However, the presence of a magnetic transition, which is not observed in the GaFeO$_3$ and AlFeO$_3$ ferrimagnetic isomorphous systems,[11,12] was somehow overlooked in their work, and the large thermal dependence presented by the hyperfine field of the Fe tetrahedral site was ascribed to dynamical phenomena. The two groups that first reported on this low-temperature transition have interpreted it quite differently.[8,9] On the one hand, according to Kurmoo et al., all Fe^{3+} cations in ϵ-Fe$_2$O$_3$ carry the same magnetic moment and its room-temperature magnetic structure is that of a canted antiferromagnet that, on cooling to below 150 K, would undergo a Morin-like transition resulting in a second canted antiferromagnetic phase with smaller canting angles.[8] A similar interpretation to the transition has been given by Sakurai et. al, who also studied the ϵ-Fe$_2$O$_3$ structure by X-ray diffraction in a 60−293 K temperature range, although they were not able to reveal any structural change along the transition.[13] In contrast, we have proposed that at room-temperature, ϵ-Fe$_2$O$_3$ is a collinear ferrimagnet with the net magnetization arising from the lower magnetic moment of the Fe^{3+} in tetrahedral coordination; we have related the anomalies in the magnetic properties at low temperatures to the appearance of an incommensurate magnetic order, already indicated by preliminary neutron-diffraction experiments.[9] In the context described above, besides clarifying the nature of the ϵ-Fe$_2$O$_3$ magnetic structure below 100 K, we need to investigate a second question of whether the eventual occurrence of structural changes is associated with the transition. Indeed, understanding the relationship between the structural and magnetic properties of ϵ-Fe$_2$O$_3$ can be crucial to comprehending both the magnetic softening[9] and

the coupling between magnetic and dielectric properties[10] that are observed in this oxide.

Thus, the aim of this work is to elucidate the high temperature (HT) and low temperature (LT) structures of ϵ-Fe$_2$O$_3$ and to shed some light into the nature of this transition. We present here a refinement of the crystal and magnetic structures of ϵ-Fe$_2$O$_3$ from X-ray and neutron powder-diffraction data that is complemented by Mössbauer spectroscopy, magnetization, and heat-capacity measurements.

II. Experimental Details

For the present study, we have used the ϵ-Fe$_2$O$_3$/amorphous SiO$_2$ nanocomposite sample that was already investigated in our previous work.[9] For the powder-diffraction measurements, new batches were prepared following the same procedure that has been described in detail elsewhere.[7] In some of these samples, small amounts (<10 wt %) of α-Fe$_2$O$_3$ were detected. To optimize the material structural characterization using diffraction, we removed the SiO$_2$ amorphous matrix by continuously stirring the sample in a concentrated NaOH solution ($\sim$12 M) at 80 °C. After 2 days, the solution was centrifuged; the sample was washed several times with distilled water until it achieved a neutral pH and was finally dried at 60 °C. X-ray diffraction analysis performed after this treatment revealed the complete removal of the SiO$_2$ amorphous matrix, whereas the ϵ-Fe$_2$O$_3$ phase remained unaltered. Neutron powder-diffraction (NPD) patterns were collected in the D20 instrument at the Institut Laue Langevin (Grenoble, France) using a 2.42 Å wavelength on heating at 1.7 K/min between 10 and 300 K. Synchrotron X-ray powder-diffraction (SXRPD) measurements were performed at fixed temperatures on heating in the same temperature range using the ID31 diffractometer of ESRF (Grenoble, France) with a 0.500 Å wavelength. The patterns were refined by the Rietveld method using the FullProf[14] program suite. The presence of small amounts of α-Fe$_2$O$_3$ was considered in the refinements, taking into account its different magnetic structure above and below the Morin transition (at about 240 K). However, this magnetic transition has not been further considered, because it takes place in a temperature well above the temperature range discussed herein. Mössbauer spectra were acquired at different temperatures between 10 and 300 K using a conventional transmission Mössbauer spectrometer with a ^{57}Co/ Rh source. Velocity calibration was done using a 6 μm foil of metallic iron, and the Mössbauer parameters are given relative to this standard at room temperature. The program package NORMOS[15] was used to fit the spectra. Magnetization measurements were performed using a Quantum Design MPMS SQUID magnetometer. Measurements of the ac susceptibility (1 Oe, 33− 1000 Hz) and heat capacity C_p, using a 2τ relaxation method, were carried out in a Quantum Design PPMS.

III. Results and Discussion

A. Neutron and X-ray Diffraction. In Figure 2, the NPD patterns of ϵ-Fe$_2$O$_3$ recorded at 200, 160, 80, and 10 K evidence a change in magnetic structure taking place between 160 and 80 K that is characterized by the disappearance of the (011), (110), (111), and (120) magnetic reflections and the development of satellites at either sides of these reflec-

(10) Gich, M.; Frontera, C.; Roig, A.; Fontcuberta, J.; Molins, E.; Bellido, N.; Simon, Ch.; Fleta, C. *Nanotechnology* **2006**, *17*, 687.
(11) Berthaut, E.; F.; Bassi, G.; Buisson, G.; Chappert, J.; Delapalme, A.; Pauthenet, R.; Rebouillat, H. P.; Aleonard, R. *J. Phys. (Paris)* **1966**, *7*, 28.
(12) Bouree, F.; Badour, J. L.; Elabraoui, E.; Musso, J.; Laurent, C.; Rousset, A. *Acta Crystallogr., Sect. B* **1996**, *52*, 217.
(13) Sakurai, S.; Jin, J.; Hashimoto, K.; Ohkoshi, S. *J. Phys. Soc. Jpn.* **2005**, *74*, 1946.

(14) Rodriguez-Carvajal, J. *Physica B* **1993**, *192*, 55.
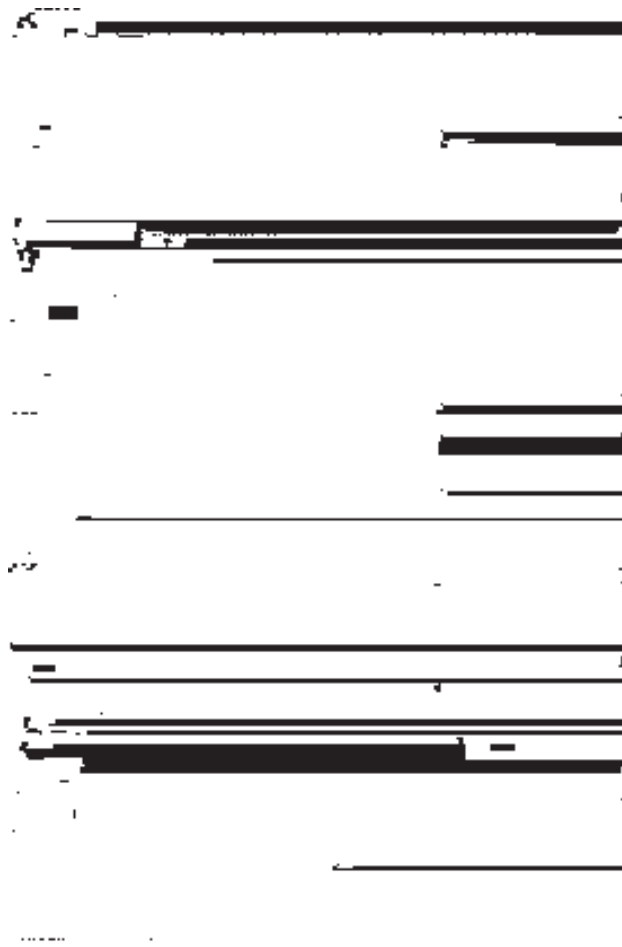(15) Brand, R. A. *Nucl. Instrum. Methods Phys. Res., Sect. B* **1987**, *28*, 398.

Figure 2. NPD patterns corresponding to the HT (200 and 160 K) and LT (80 and 10 K) phases of ϵ-Fe$_2$O$_3$. The up arrows indicate the satellites emerging in the LT phase.

tions. The changes observed in the NPD patterns of Figure 2 affect only some of the magnetic reflections, suggesting that the transformation does not involve major structural changes. Whereas the HT phase of ϵ-Fe$_2$O$_3$ (200 and 160 K patterns) can be refined using the magnetic and nuclear structures of AlFeO$_3$ as a starting model,[12] the new peaks that characterize the magnetic structure of the LT phase can be indexed with an incommensurate propagation vector **k** = (0, 0.1047, 0).

The small crystallite size of the ϵ-Fe$_2$O$_3$ nanoparticles (less than 20 nm) causes a peak broadening and therefore a strong peak overlap, which reduces the number of effective reflections. A multipattern approach using both NPD and SXRPD patterns recorded at 200 and 10 K was used to attempt a reliable refinement of nuclear and magnetic structures of the HT and LT phases of ϵ-Fe$_2$O$_3$, respectively. Besides ϵ-Fe$_2$O$_3$, the nuclear and magnetic structures of α-Fe$_2$O$_3$, representing less than 10 wt % of the sample, were also considered in the refinements. The comparisons between the experimental and calculated data obtained with the joint Rietveld refinement of the SXRPD and NPD patterns at 200 and 10 K are presented in Figures 3 and 4, respectively. The refined atomic coordinates for the 10 nonequivalent atomic sites at 200 and 10 K, together with the standard reliability factors, are given in Table 1. As is found for isostructural phases GaFeO$_3$, AlFeO$_3$, and κ-Al$_2$O$_3$, which have been previously refined,[16,12,17] the cation coordination polyhedra are two distorted[18] and one regular octahedra and one tetrahedron. Therefore, the different Fe^{3+} sites are hereafter referred as Fe$_{DO1}$, Fe$_{DO2}$, Fe$_{RO}$, and Fe$_T$ (where DO stands for distorted octahedral, RO for regular octahedral and T for tetrahedral

(16) Abrahams, S. C.; Reddy, J. M. Bernstein, J. L. *J. Chem. Phys.* **1965**, *42*, 3957.
(17) Smrèok, L.; Langer, V.; Halvarsson, M.; Ruppi, S. *Z. Kristallogr.* **2001**, *216*, 409.
(18) The distortion of a coordination polyhedron of a cation is defined as $1/n\sum_{i=1}^{n}[(d_i - \langle d\rangle)/\langle d\rangle]^2$, where d_i is the distance to a given neighbor, $\langle d\rangle$ the average distance to the first neighbor, and n is the coordination number. At 200 K, the distortions of Fe$_{DO-1}$, Fe$_{DO-2}$, Fe$_{RO}$, and Fe$_T$ have been found to be 71.3 × 10^{-4}, 58.4 × 10^{-4}, 2.4 × 10^{-4}, and 4.6 × 10^{-4}, respectively.

Figure 3. Experimental (■), calculated (solid line), and difference (lower line) plots for the joint refinement of SXRPD and NPD patterns of ϵ-Fe$_2$O$_3$ collected at 200 K (upper and lower panels, respectively). Reflection positions of the different phases are indicated by vertical bars in the following descending order: ϵ-Fe$_2$O$_3$, α-Fe$_2$O$_3$ for the upper panel and ϵ-Fe$_2$O$_3$, ϵ-Fe$_2$O$_3$ magnetic, α-Fe$_2$O$_3$ and α-Fe$_2$O$_3$ magnetic for the lower panel.

coordinations). In Figure 5, the coordination octahedra of Fe$_{DO1}$ and Fe$_{DO2}$ are represented in black and dark gray, respectively, whereas the Fe$_{RO}$ and Fe$_T$ environments are represented in light gray. As expected, the changes between the asymmetric units of the HT and LT phases are in general small, although the z coordinate of O2 significantly increases on cooling from 200 to 10 K (see Table 1). As can be seen from Figure 5 (black spheres), the 0.3 Å displacement of O2 along c is responsible for the increased tilting of the Fe$_{DO1}$ and Fe$_T$ coordination polyhedra in the LT structure. The bonding distances and angles calculated from cell parameters and asymmetric units reported in Table 1 (see Tables 2 and 3) reveal other features that can be relevant to understanding the HT $\rightarrow$ LT magnetic transition. On one hand, it is found that on cooling from 200 to 10 K, there is an increase in the bonding distances of both Fe$_T$ with O4, O6 and Fe$_{DO2}$, Fe$_{RO}$ with O2, the latter showing an average expansion of about 1%. In the case of the tetrahedral site, the elongation of the apical Fe$_T$–O4 distance shows a 2.2% variation. On the other hand, the distortions of the Fe$_T$ and Fe$_{DO1}$ polyhedra, which are more affected by the HT $\rightarrow$ LT transition, increase from 2.4 × 10^{-4} to 6.8 × 10^{-4} and from 71.3 × 10^{-4} to 84.3 ×

Table 1. Cell Parameters and Asymmetric Units of ϵ-Fe$_2$O$_3$ at 200 and 10 K, Together with the Reliability Parameters of the Multipattern Rietveld Refinement Expressed in Percent (except for χ^2)

	$T = 200$ K[a]				$T = 10$ K[b]		
atom	x/a	y/b	z/c	atom	x/a	y/b	z/c
O1	0.978(2)	0.3282(15)	0.4314(11)	O1	0.978(4)	0.331(3)	0.4288(17)
O2	0.515(2)	0.4907(17)	0.4187(16)	O2	0.512(3)	0.4871(20)	0.4489(14)
O3	0.650(3)	0.9979(13)	0.1883(9)	O3	0.646(4)	0.9943(20)	0.1871(14)
O4	0.160(3)	0.1637(15)	0.1956(7)	O4	0.159(4)	0.162(2)	0.2002(11)
O5	0.841(3)	0.1680(15)	0.6669(7)	O5	0.858(3)	0.157(3)	0.6685(12)
O6	0.527(2)	0.1637(19)	0.9362(9)	O6	0.523(4)	0.161(3)	0.9257(15)
Fe$_{DO1}$	0.1928(11)	0.1506(6)	0.5807(3)	Fe$_{DO1}$	0.1931(17)	0.1514(10)	0.5820(4)
Fe$_{DO2}$	0.6826(6)	0.0291(3)	0.7897(5)	Fe$_{DO2}$	0.6867(10)	0.0283(4)	0.7938(8)
Fe$_T$	0.1858(10)	0.1519(6)	0.0000	Fe$_T$	0.1852(15)	0.1526(9)	0.0000
Fe$_{RO}$	0.8104(7)	0.1580(4)	0.3071(3)	Fe$_{RO}$	0.8098(10)	0.1592(6)	0.3079(5)

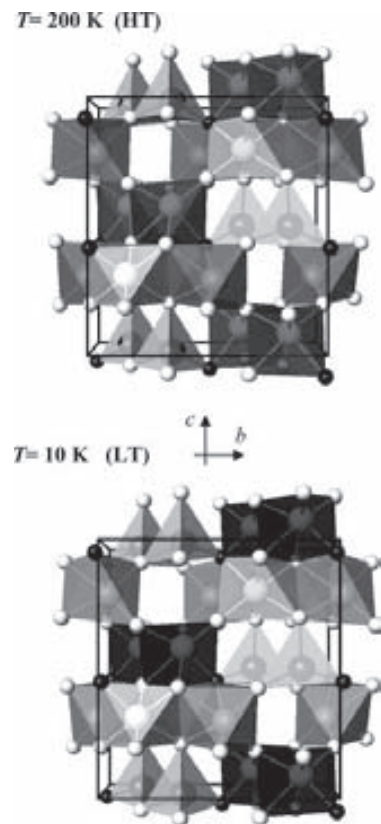[a] Parameters: $a = 5.0885(5)$ Å, $b = 8.7802(14)$ Å, $c = 9.4709(13)$ Å. Reliability parameters (in % except for χ^2): SXRPD $R_B = 2.26$, $R_{wp} = 3.59$, $R_{exp} = 1.94$, $\chi^2 = 3.43$; NPD $R_B = 1.41$, $R_{Mag} = 1.89$, $R_{wp} = 4.00$, $R_{exp} = 1.33$. [b] Parameters: $a = 5.085(1)$, $b = 8.774(2)$, $c = 9.468(2)$. Reliability parameters (in % except for χ^2): SXRPD $R_B = 2.98$, $R_{wp} = 7.33$, $R_{exp} = 3.66$, $\chi^2 = 4.015$. NPD $R_B = 3.85$, $R_{Mag} = 6.33$, $R_{wp} = 7.60$, $R_{exp} = 1.40$.
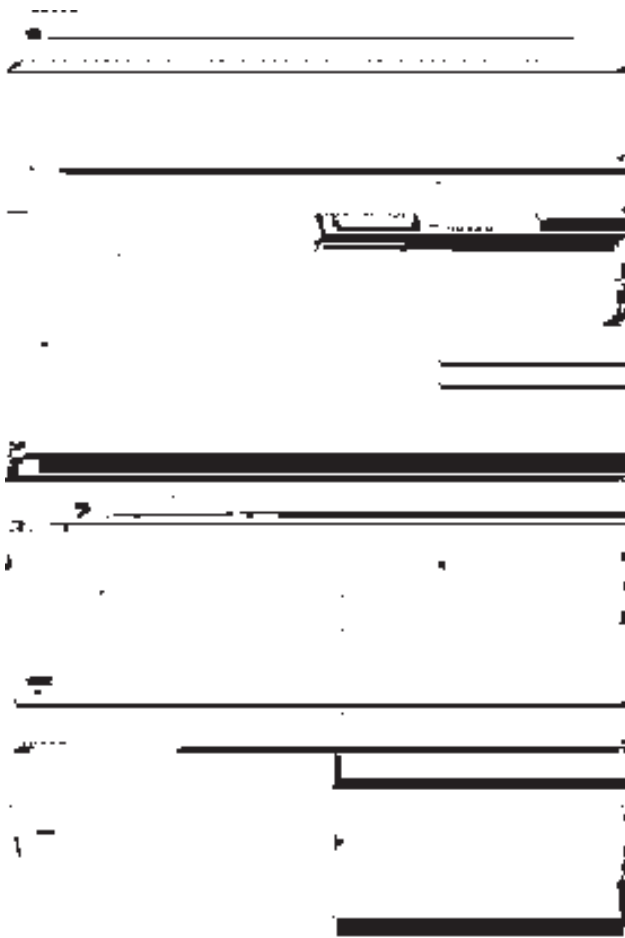
Figure 4. Experimental (■), calculated (solid line), and difference (lower line) plots for the joint refinement of SXRPD and NPD patterns of ϵ-Fe$_2$O$_3$ collected at 10 K (upper and lower panels, respectively). Reflection positions of the different phases are indicated by vertical bars in the following descending order: ϵ-Fe$_2$O$_3$ and α-Fe$_2$O$_3$ for the upper panel and ϵ-Fe$_2$O$_3$, ϵ-Fe$_2$O$_3$ magnetic, α-Fe$_2$O, and α-Fe$_2$O$_3$ magnetic for the lower panel.

Figure 5. Perspective view of the ϵ-Fe$_2$O$_3$ HT and LT structures along the [100] direction (upper and lower panels, respectively). The coordination octahedra of Fe$_{DO1}$, Fe$_{DO2}$, and Fe$_{RO}$ are black, gray, and light gray, respectively, and the oxygen atoms are represented by small spheres. The main structural changes concern the orientations of the coordination polyhedra of Fe$_{DO1}$ (black octahedron) and Fe$_T$ (light gray tetrahedron) due to the displacement of O2 (in black) along c.

10^{-4}, respectively, with the Fe$_{DO1}$−O2 distance decreasing by about 10%.

Regarding the magnetic structures, the model that yielded the best fits for the HT phase is one in which the magnetic moments m are along the a axis with $m_{HT}(\text{Fe}_{DO1}) = -3.9\mu_B$, $m_{HT}(\text{Fe}_{DO2}) = 3.9\mu_B$, $m_{HT}(\text{Fe}_T) = -2.4\mu_B$, and $m_{HT}(\text{Fe}_{RO}) = 3.7\mu_B$. The refinement was performed using the constraint $m_{HT}(\text{Fe}_{DO1}) = -m_{HT}(\text{Fe}_{DO2})$ suggested by Mössbauer spec-

troscopy measurements (see section B below). Thus, the ϵ-Fe$_2$O$_3$ HT magnetic structure presents the $m'm2'$ point group and is represented in Figure 6. The antiferromagnetic coupling between the different magnetic moments yields a net magnetization of $0.3\mu_B$ per Fe^{3+}, in agreement with the M_s values of ϵ-Fe$_2$O$_3$ at 200 K.[9] It is interesting to note that the NPD data can be also simulated allowing small y and z components for the Fe$_T$ and Fe$_{RO}$ moments (i.e., a small canting), although this did not result in any improvement in the fit. However, the fact that the NPD data do not exclude small canting of the Fe$_T$ and Fe$_{RO}$ spins would be in agreement with the thermal fluctuations in these sites,

Table 2. Coupling Angles between the Different Fe Sites and Fe−O Distances (given in Å) at 200 K and 10 K (italics)

O1

	Fe$_{DO1}$	Fe$_{DO1}$b	Fe$_{DO2}$a	Fe$_{RO}$	Fe$_{RO}$b
Fe$_{DO1}$	2.372(13), *2.41(2)*				
Fe$_{DO1}$b	88.5(5), *86.8(9)*	2.035(11), *2.056(20)*			
Fe$_{DO2}$a	171.5(5), *171.9(9)*	94.6(5), *94.5(9)*	2.362(13), *2.31(2)*		
Fe$_{RO}$	93.1(5), *92.5(9)*	99.6(5), *98.8(9)*	94.2(5) *95.1(9)*	2.085(12), *2.08(2)*	
Fe$_{RO}$b	90.1(5), *89.4(8)*	167.2(5), *167.2(9)*	85.2(5), *87.6(8)*	93.2(5), 93.5(9)	2.064(11), *2.041(20)*

O2

	Fe$_{DO1}$b	Fe$_{DO2}$a	Fe$_T$a	Fe$_{RO}$b
Fe$_{DO1}$b	2.171(15), *1.976(17)*			
Fe$_{DO2}$a	102.0(6), *102.1(8)*	1.994(13), *2.149(16)*		
Fe$_T$a	111.2(7), *125.0(10)*	122.4(6), *116.0(8)*	1.908(15), *1.833(18)*	
Fe$_{RO}$b	102.7(6), *104.8(7)*	101.0(6), *91.0(7)*	115.1(7), *112.2(8)*	1.976(14), *2.121(16)*

O3

	Fe$_{DO1}$c	Fe$_{DO2}$c	Fe$_{RO}$
Fe$_{DO1}$c	1.838(12), *1.817(19)*		
Fe$_{DO2}$c	124.2(7), *126.6(10)*	1.960(14), *1.976(20)*	
Fe$_{RO}$	129.8(6), *128.6(9)*	*99.4(6), 97.8(8)*	1.977(12), *2.026(18)*

O4

	Fe$_{DO2}$c	Fe$_T$	Fe$_{RO}$	Fe$_{RO}$b
Fe$_{DO2}$c	2.074(13), *2.047(18)*			
Fe$_T$	110.8(5), *111.7(7)*	1.860(7), *1.902(11)*		
Fe$_{RO}$	95.3(6), *96.1(8)*	124.6(5), *123.8(7)*	2.069(14), *2.048(19)*	
Fe$_{RO}$b	105.0(5), *105.6(7)*	122.2(5), *120.6(7)*	94.4(6), *95.0(8)*	2.038(13), *2.022(17)*

O5

	Fe$_{DO1}$	Fe$_{DO1}$b	Fe$_{DO2}$
Fe$_{DO1}$	1.973(15), *1.891(17)*		
Fe$_{DO1}$b	104.0(7), *102.5(10)*	1.942(14), *2.05(2)*	
Fe$_{DO2}$	126.8(7), *133.2(10)*	129.0(6), *124.2(10)*	1.868(12), *1.855(20)*

O6

	Fe$_{DO2}$	Fe$_T$	Fe$_T$b
Fe$_{DO2}$	1.987(13), *1.90(2)*		
Fe$_T$	124.8(6), *129.0(10)*	1.841(11), *1.86(2)*	
Fe$_T$b	123.9(7), *124.2(11)*	110.1(7), *106.6(11)*	1.908(16), *1.96(3)*

[a] Transformations: a = ($^1/_2 - x$, $y - ^1/_2$, $z - ^1/_2$); b = ($^1/_2 - x$, $^1/_2 - y$, z); c = ($-x$, $-y$, $z + ^1/_2$).

recently reported by Tronc et al.[19] For the LT phase, different helimagnetic and sine-modulated structures have been tested to account for the magnetic structure associated with **k**. The best fit has been obtained for a sine-modulated structure with a periodicity of about 10 crystalline unit cells and with all the magnetic moments lying in the *xy* plane. As in the HT structure, m_{LT}(Fe$_{DO1}$) and m_{LT}(Fe$_{DO2}$) were constrained to be antiparallel and directed along the *x* direction, whereas m_{LT}(Fe$_T$) and m_{LT}(Fe$_{RO}$) are mainly oriented in opposite directions along *x* and present small *y* components. However, for the LT structure, the symmetry analysis imposes that all the magnetic atoms are split into two orbits, and the fact that the structure is sine-modulated introduces magnetic phases. This results in an increased number of refinable magnetic parameters that increase the difficulty of finding an appropriate model for the magnetic structure from the small number of measurable magnetic reflections. All the magnetic moments obtained in our best fit of the NPD pattern at LT using a simple sine-wave-modulated structure increase with respect to those of the HT structure. The values of some

of them are, however, clearly nonphysical, exceeding the 5μ_B expected for an Fe^{3+} cation.

B. Mössbauer Spectroscopy. Mössbauer spectroscopy gives additional information that can be complementary to the NPD data. In Figure 7, it can be observed that the Mössbauer spectra of ϵ-Fe$_2$O$_3$ change on cooling through the HT → LT transition, especially because of the evolution of the Fe$_T$ subspectrum (dotted line). According to the crystalline structure of ϵ-Fe$_2$O$_3$, the spectra were fitted assuming that each of the four Fe sites contributed to the spectra with a sextet. In particular, the spectra could be fitted by constraining the hyperfine fields, B_{hf}, and the widths of the Fe$_{DO1}$ and Fe$_{DO2}$ contributions to be equal, in accordance with the NPD results. Figure 8a shows the temperature dependence of the hyperfine parameters for the different Fe sites in the 10−200 K range. Between 150 and 80 K, most of the hyperfine parameters of the different Fe sites deviate from the thermal dependence displayed at higher temperatures. These anomalies are particularly important for Fe$_T$, which displays a 20% increase in B_{hf} between 140 and 100 K and a shift in both the isomer shift, δ, and the quadrupole splitting, Δ, in the same temperature range. Below 150 K,

(19) Tronc, E.; Chanéac, C.; Jolivet, J. P.; Grenèche, J. M. *J. Appl. Phys.* **2005**, *98*, 053901.

Table 3. Bonding Angles in the Coordination Polyhedra for the four Fe Sites of ϵ-Fe$_2$O$_3$ at 200 and 10 K[a]

	200 K	10 K		200 K	10 K
O2a−Fe$_T$−O4	113.9(10)	105.0(12)	O1−Fe$_{DO1}$−O1b	81.6(7)	81.1(13)
O2a−Fe$_T$−O6	114.5(10)	116.1(17)	O1−Fe$_{DO1}$−O2b	76.2(8)	78.9(13)
O2a−Fe$_T$−O6b	106.0(13)	109.5(18)	O1−Fe$_{DO1}$−O3c	175.9(10)	175.8(17)
O4−Fe$_T$−O6	113.0(8)	116.1(13)	O1−Fe$_{DO1}$−O5	77.2(7)	80.5(12)
O4−Fe$_T$−O6b	103.8(9)	107.0(13)	O1−Fe$_{DO1}$−O5b	83.7(7)	83.7(12)
O6−Fe$_T$−O6b	104.3(10)	102.7(18)	O1b−Fe$_{DO1}$−O2b	81.9(8)	85.6(13)
			O1b−Fe$_{DO1}$−O3c	98.0(8)	96.9(13)
O1−Fe$_{RO}$−O1b	88.3(7)	90.0(15)	O1b−Fe$_{DO1}$−O5	158.0(11)	159.8(15)
O1−Fe$_{RO}$−O2b	87.5(9)	83.8(14)	O1b−Fe$_{DO1}$−O5b	86.6(8)	86.1(13)
O1−Fe$_{RO}$−O3	179.5(10)	179.0(18)	O2b−Fe$_{DO1}$−O3c	99.7(10)	97.3(12)
O1−Fe$_{RO}$−O4	85.4(8)	84.8(12)	O2b−Fe$_{DO1}$−O5	87.6(9)	82.8(11)
O1−Fe$_{RO}$−O4b	84.0(7)	82.6(12)	O2b−Fe$_{DO1}$−O5b	158.1(12)	161.6(17)
O1d−Fe$_{RO}$−O2b	99.5(9)	94.3(13)	O3c−Fe$_{DO1}$−O5	102.7(11)	100.9(15)
O1d−Fe$_{RO}$−O3	91.6(8)	90.3(12)	O3c−Fe$_{DO1}$−O5b	100.4(10)	100.0(17)
O1d−Fe$_{RO}$−O4	173.7(11)	174.7(17)	O5−Fe$_{DO1}$−O5b	96.6(11)	100.0(15)
O1d−Fe$_{RO}$−O4b	86.7(7)	86.4(12)			
O2c−Fe$_{RO}$−O3	93.0(9)	97.2(11)	O1a−Fe$_{DO2}$−O2a	78.0(7)	75.7(11)
O2c−Fe$_{RO}$−O4	80.6(9)	84.2(10)	O1a−Fe$_{DO2}$−O3c	83.6(7)	84.2(12)
O2c−Fe$_{RO}$−O4b	169.3(12)	166.4(14)	O1a−Fe$_{DO2}$−O4c	76.6(7)	76.5(11)
O3−Fe$_{RO}$−O4	94.7(10)	94.9(14)	O1a−Fe$_{DO2}$−O5	172.1(10)	168.7(19)
O3−Fe$_{RO}$−O4b	95.5(9)	96.5(13)	O1a−Fe$_{DO2}$−O6	84.8(9)	86.4(17)
O4−Fe$_{RO}$−O4b	92.3(10)	93.9(14)	O2a−Fe$_{DO2}$−O3c	161.1(12)	159.9(15)
			O2a−Fe$_{DO2}$−O4c	80.1(8)	83.5(10)
			O2a−Fe$_{DO2}$−O5	99.1(10)	101.9(12)
			O2a−Fe$_{DO2}$−O6	88.9(9)	88.0(13)
			O3c−Fe$_{DO2}$−O4c	91.4(10)	91.4(14)
			O3c−Fe$_{DO2}$−O5	98.4(11)	97.8(15)
			O3c−Fe$_{DO2}$−O6	94.0(9)	91.3(13)
			O4c−Fe$_{DO2}$−O5	95.7(10)	92.3(16)
			O4c−Fe$_{DO2}$−O6	159.9(11)	162.3(18)
			O5−Fe$_{DO2}$−O6	102.6(8)	104.7(13)

[a] Transformations: a = ($^1/_2$ − x, y − $^1/_2$, z − $^1/_2$); b = ($^1/_2$ − x, $^1/_2$ − y, z); c = (−x, −y, z + $^1/_2$).
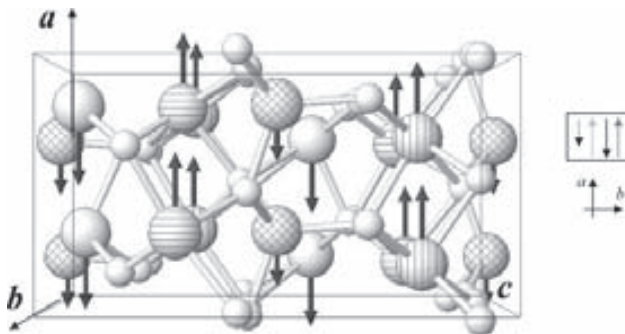
Figure 6. Magnetic structure of the ϵ-Fe$_2$O$_3$ HT phase, where the Fe$_{DO1}$, Fe$_{DO2}$, Fe$_{RO}$, and Fe$_T$ atoms are distinguished by plain, horizontal stripes, vertical stripes, and cross-hatch patterns, respectively. The magnetic moments of the Fe$_{DO1}$, Fe$_{DO2}$, Fe$_{RO}$, and Fe$_T$ sites are schematically represented in the figure by black, gray, light gray, and dotted arrows, respectively.

B_{hf} decreases by ∼4% for Fe$_{RO}$ between 150 and 110 K and by ∼3.5% for Fe$_{DO1}$ and Fe$_{DO2}$ between 150 and 130 K. Note that for Fe$_{DO1}$, Δ changes from negative to positive values in this interval of temperatures and that below 130 K, δ decreases with temperature for this particular site, in contrast with the usual temperature dependence of the isomer shift. The latter results suggest that on cooling below 150 K, some structural changes would affect the Fe$_{DO1}$ coordination octahedron, which, subsequently, would induce changes in the coordination of the Fe$_T$ site. Indeed, this interpretation is compatible with the results obtained from the diffraction experiments, which revealed that the HT → LT transition results in an increased tilting and distortion of the Fe$_{DO1}$ and Fe$_T$ coordination polyhedron. It is worth pointing out that large changes in Δ can be also due to spin reorientations. Although the NPD results seem to indicate that the HT →
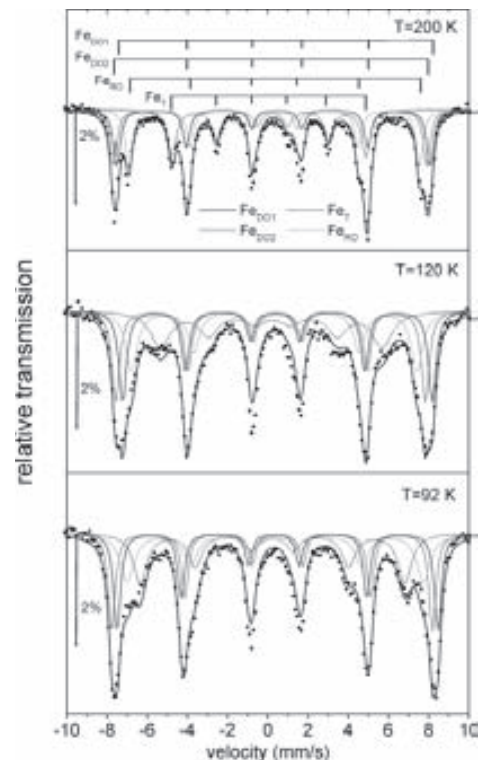
Figure 7. Mössbauer spectra of ϵ-Fe$_2$O$_3$ at 200, 120, and 92 K. The subspectra correspond to the different Fe sites in the ϵ-Fe$_2$O$_3$ structure and are schematically presented at the top of the figure.

LT transition has little effect in the direction of the Fe$_{DO1}$ magnetic moment, the LT magnetic structure would be needed to ascribe the sign change in Δ for this site exclusively to structural changes.
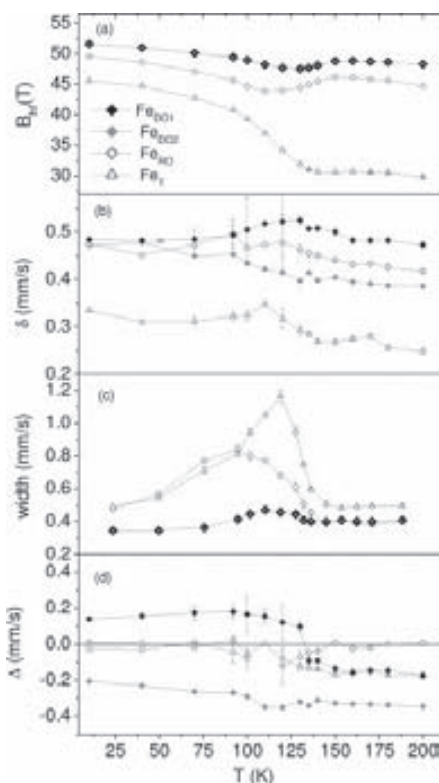
Figure 8. Temperature dependence of the (a) hyperfine field (B_{hf}), (b) isomer shift (δ), (c) sextet line width (width), and (d) quadrupolar splitting ($\triangle$) of the different Fe sites of ϵ-Fe$_2$O$_3$ obtained from Mössbauer spectra.


Figure 9. Simplified schematic representation of the square-wave magnetic structure of the LT phase of ϵ-Fe$_2$O$_3$. The magnetic moments of the Fe$_{DO1}$, Fe$_{DO2}$, Fe$_{RO}$, and Fe$_T$ sites are schematically represented by black, gray, light gray, and dotted arrows, respectively.

The structural transformations occurring below 150 K might be responsible for the magnetic softening of the system that is reported in Figure 1. Interestingly, the changes observed in Δ for both the Fe$_{DO1}$ and Fe$_T$ sites can be related to modifications in the spin−orbit coupling of the Fe cations, which are responsible for the magnetic anisotropy of a magnetic system. In contrast, in the case of the Fe$_T$ site, the substantial elongation of the apical Fe$_T$−O4 occurring along the HT → LT transformation could be responsible for the large increase in B_{hf} observed at this site, which in turn indicates an increment of the Fe$_T$ magnetic moment,[20] also deduced from the analysis of the NPD data at 10 K. This can explain the M_s diminution observed below 150 K (see Figure 1 inset), because the Fe$_T$ and Fe$_{RO}$ are antiferromagnetically coupled and the increase in B_{hf} at the Fe$_T$ site is larger than the B_{hf} increase experienced by Fe$_{RO}$. Regarding the hyperfine fields, it is also interesting to note that the ratio between the B_{hf} values for different Fe sites at 200 K (i.e., $B_{hf}(\text{Fe}_{DO1})/B_{hf}(\text{Fe}_T) = 1.63$, $B_{hf}(\text{Fe}_{RO})/B_{hf}(\text{Fe}_T) = 1.56$) is in good agreement with the corresponding ratio of magnetic moments obtained from the analysis of the NPD data. Assuming that the proportionality between B_{hf} and m still holds for the LT phase and combining the m_{HT} values obtained from the NPD pattern at 200 K with the B_{hf} at 10 K, we can estimate the magnetic moments for the LT phase to be $m_{LT}(\text{Fe}_{DO1}) = -4.2\mu_B$, $m_{LT}(\text{Fe}_{DO2}) = 4.2\mu_B$, $m_{LT}(\text{Fe}_T) = -3.7\mu_B$, and $m_{LT}(\text{Fe}_{RO}) = 4.1\mu_B$, in clear disagreement with the unrealistic values obtained from our best-fit model.

In this regard, the temperature dependence of the Mössbauer subspectra line width (see Figure 8c) can shed some light on the deficiencies of our preliminary model for the LT magnetic structure of ϵ-Fe$_2$O$_3$. On cooling below 150 K, a sextet line width broadening is observed for all Fe sites but specially for Fe$_T$, which is due to the appearance of some disorder at the different crystallographic sites and indicates that the transformation is rather broad and that several phases can coexist in the 150−92 K interval. However, as T is further decreased, the line width values decrease progressively. Interestingly, at about 10 K, the line width values for all the sites are only slightly larger than those at 200 K, implying that the Mössbauer components for all the sites are quite narrow and, consequently, that the corresponding magnetic moments throughout the structure should be almost constant in modulus. However, this is not what one would expect if the LT magnetic structure of ϵ-Fe$_2$O$_3$ is supposed to be sine-modulated with a periodicity of about 10 unit cells. In this case, because for the $Pna2_1$ space group there is only one Wyckoff position of 4-fold multiplicity, an average of 40 atoms for every Fe site with magnetic moments ranging from zero to a maximum value are involved in one period of the amplitude-modulated structure, which would yield a broad hyperfine field distribution. Because the helical or spiral structures with constant m modulus that could account for the narrow Mössbauer lines of the LT phase are not consistent with the NPD data, the only magnetic structure that can make both the Mössbauer and the diffraction data compatible is a square-wave-modulated structure, i.e., the superposition of a series of sine-modulated structures having the harmonics of **k** as propagation vectors. In fact, the exceedingly large magnetic moments obtained when a single sine wave was considered might be reduced by taking into account the amplitudes of the different Fourier components. Thus, to determine the exact magnetic structure, it would be necessary to identify the higher-order reflections and determine the new propagation vectors, but this cannot be carried out because of the peak overlapping and the low intensity of the harmonic reflections. However, on the grounds of the above discussion, one may consider the structure represented in Figure 9 to be a simplified schematic model of the LT magnetic cell.

C. Magnetization and Heat-Capacity Measurements. The results presented in section B indicate that the HT → LT transformation in ϵ-Fe$_2$O$_3$ takes place in a broad temperature range and suggest that it consists of a succession of magnetic and structural changes. In this section, we present magnetic and heat-capacity measurements that give some details about the nature of the transition. Figure 10a shows the temperature dependence of the ϵ-Fe$_2$O$_3$ zero-field-cooling (ZFC) magnetization under 100 and 1000 Oe applied fields,

(20) Preston, R. S.; Hanna, S. S.; Heberle, J. *Phys. Rev.* **1962**, *128*, 2207.
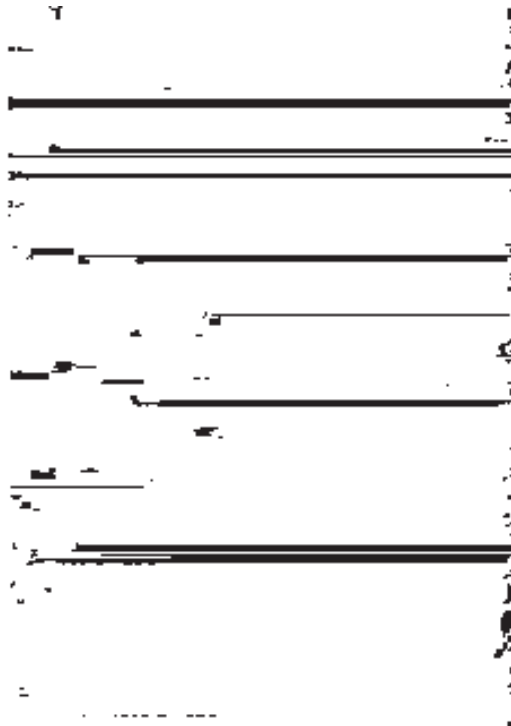
Figure 10. (a) Zero-field cooling (ZFC) and field cooling (FC) measurements of the temperature dependence of the magnetization in 100 and 1000 Oe applied fields. (b) Temperature dependence of the in-phase (▲) and out-of-phase (△) components of ϵ-Fe$_2$O$_3$ ac-susceptibility measured at 1000 Hz and 10 Oe field amplitude. The solid line is the temperature derivative of the $M_{100}^{ZFC}(T)$ curve presented in panel (a).

$M_{100}^{ZFC}(T)$ and $M_{1000}^{ZFC}(T)$, respectively, together with the field-cooling (FC) measurement in 1000 Oe, $M_{1000}^{FC}(T)$. Upon heating from 10 K, $M_{100}^{ZFC}(T)$ presents an important increase between 85 and 150 K that takes place in three stages, if one considers the changes of the $M_{100}^{ZFC}(T)$ slope, in three temperature ranges ΔT_1 (85 K < T < 95 K), ΔT_2 (95 K < T < 110 K) and ΔT_3 (110 K < T < 147 K), the slope being much steeper in ΔT_1 and ΔT_2 than in ΔT_3. When the ZFC magnetization is measured in a field 10 times larger (see the $M_{1000}^{ZFC}(T)$ curve), the larger magnetization step starts at a lower temperature and is more gradual; it is also no longer possible to clearly distinguish between the first two stages. In contrast, no shift is observed for the magnetization stage in ΔT_3, which now presents a somewhat larger slope. Moreover, the FC measurement (see $M_{1000}^{FC}(T)$ curve) shows that the magnetic behavior below 110 K is irreversible even for small fields such as 1000 Oe, in contrast to the reversibility observed above this temperature. These measurements suggest that on heating, the transition from the LT to the HT magnetic structure of ϵ-Fe$_2$O$_3$ takes place in three consecutive stages occurring in ΔT_1, ΔT_2, and ΔT_3, hereafter referred as S1, S2, and S3, respectively. The measurements of Figure 10a evidence a distinct magnetic character of S1 and S2 as compared to S3, which is also confirmed by the temperature dependence of the magnetic AC susceptibility, χ. Namely, in Figure 10b, the temperature dependence of both the in-phase, $\chi'(T)$, and out of phase, $\chi''(T)$, components of ac susceptibility present sharp peaks at about 91 and 101 K, signaling the S1 and S2 transformations, respectively. Indeed, the susceptibility peaks coincide
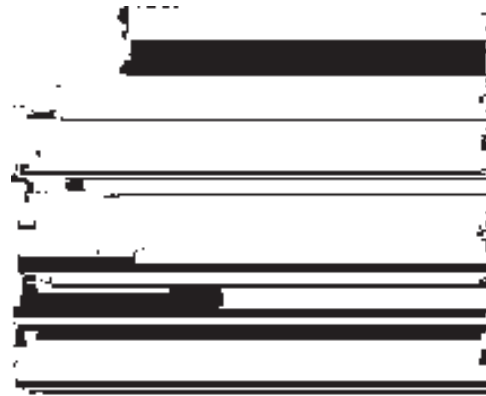
Figure 11. Temperature dependence of the (120) magnetic reflection and its satellites of ϵ-Fe$_2$O$_3$.
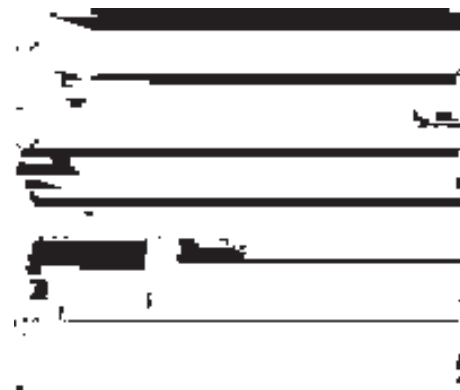
Figure 12. Temperature dependence of the ϵ-Fe$_2$O$_3$ heat capacity vs temperature.

with the maxima in the temperature derivative of $M_{100}^{ZFC}(T)$ (solid line in Figure 10b), i.e., with the maximum slopes of $M_{100}^{ZFC}(T)$ in ΔT_1 and ΔT_2. On the other hand, for ΔT_3, only a barely observable shoulder occurs in $\chi'(T)$, whereas $\chi''(T)$ is zero. The magnetic measurements presented in Figure 10 are in agreement with the occurrence of magnetic and structural changes along ΔT_3 that can be inferred from the anomalies in the Mössbauer hyperfine parameters in this temperature interval. Thus, S3 is to be associated to the latter transformation, which in turn induces S2 and S1 at lower temperatures, which are predominantly related to a magnetic transition displaying a field-dependent behavior. The distinct magnetic nature of S3 on the one hand and S2 + S1 on the other is also revealed in Figure 11 by the temperature dependence of the NPD patterns. On cooling below 200 K, the intensity of the (120) magnetic reflection slightly decreases, with this diminution becoming much more pronounced below 150 K, coinciding with the gradual appearance of the satellites that characterize an incommensurate order (S3). Below 110 K, the intensity of the satellites suddenly increases (S2 + S1), resulting in the LT magnetic structure of ϵ-Fe$_2$O$_3$, which is fully developed at about 80 K. Heat-capacity measurements provide an additional evidence of the different characteristics of S3 with respect to S2 and S1. The temperature dependence of C_p/T represented in Figure 12 shows an anomaly around 130 K (i.e., in S3) and two distinct regimes above and below this temperature. Because $C_p/T = -\partial^2 G/\partial T^2$, where G is the free

energy, the anomaly in C_p/T suggests that S3 is related with a second-order magnetic and structural transition, which is supported by the absence of thermal hysteresis both in the magnetic (Figure 10) and dielectric[10] measurements.

IV. Conclusion

In conclusion, the HT magnetic structure of ϵ-Fe₂O₃ is that of a collinear ferrimagnetic material with the Fe^{3+} magnetic moment antiferromagnetically coupled along a. The Fe^{3+} magnetic moments in the Fe_{DO1} and Fe_{DO2} distorted octahedral positions mutually cancel, and the net magnetization of this phase results from the uncompensated magnetic moment of the atoms in tetrahedral (Fe_T) and regular octahedral (Fe_{RO}) positions. Between 150 and 80 K, ϵ-Fe₂O₃ undergoes magnetic and structural phase transformations that bring about a gradual decrease in the magnetic anisotropy. This transition takes place in at least three stages. Between 150 and 110 K, there are evidences of a second-order structural transition presumably involving the changes in the coordination of the Fe_{DO1} and Fe_T sites, occurring simultaneously with the emergence of an incommensurate magnetic order. The magnetic structure undergoes several transformations as the temperature is further decreased, but no additional changes are observed below 80 K. The combination of powder-diffraction and Mössbauer spectroscopy measurements indicate that ϵFe₂O₃ presents a square-wave incommensurate magnetic structure at LT.

CM060993L

7.2.3. Cobalt nanoparticles confined in silica aerogel as catalysts for hydrogen generation

Silica aerogel are materials with high porosity (up to 99%) and high accessible surface area. The combination of these properties with the enhanced catalytic activity of cobalt nanoparticles lead to the fabrication of an excellent catalyst for the generation of hydrogen from steam reforming of ethanol. The new catalyst had a low activation temperature (307-317°C), resistance to oxidation, chemical and physical stability and fast response to hydrogen production with respect to conventional catalytic monoliths based on Co–SiO$_2$ xerogel. A patent has been filled for this invention. This collaboration was carried out with Montse Domínguez and Jordi Llorca, from the Universitat Politècnica de Catalunya (UPC). In this project I was supervised by and Elies Molins, from the ICMAB. The synthesis and some of the physical characterization of the material was performed at the ICMAB, whereas further characterization on the material and the study of the reforming reaction was performed at the UPC.

Publications:

- Domínguez, M.; <u>Taboada, E.;</u> Molins, E.; Llorca, J. Co–SiO$_2$ aerogel-coated catalytic walls for the generation of hydrogen. *Catalysis Today*, **2008**, 138,193-197. Citations (Sept. 2nd 2009): 1.

- Domínguez, M.; <u>Taboada, E.;</u> Idriss, I.; Molins, E.; Llorca. Fast and efficient hydrogen production over aerogel-dispersed cobalt-talc nanolayers.

- Catalytic device, fabrication process and application for the production of hydrogen. Llorca, J.; Domínguez, M.; Molins, E. and <u>Taboada, E.</u> Spanish Patent and Trade Marks Office. N°: P200702066. Published patent. WO2009010621.

- Press Release: "Investigadores del CSIC y la UPC desarrollan un catalizador que podría ser una solución definitiva para el coche de hidrógeno", El Mundo, **14/07/2008**.

Co–SiO₂ aerogel-coated catalytic walls for the generation of hydrogen

Montserrat Domínguez [a], Elena Taboada [b], Elies Molins [b], Jordi Llorca [a,*]

[a] Institut de Tècniques Energètiques, Universitat Politècnica de Catalunya, Av. Diagonal 647, Ed. ETSEIB, Barcelona 08028, Spain
[b] Institut de Ciència de Materials de Barcelona (ICMAB-CSIC), Campus UAB, Bellaterra 08193, Spain

ARTICLE INFO

ABSTRACT

Cobalt–silica (Co–SiO₂) aerogel coatings were successfully grown on the walls of ceramic monolith channels, thus resulting in structured catalytic wall materials useful for gas–solid reactions. The preparation involved the synthesis *in situ* of SiO₂ gels by the sol–gel hydrolysis and condensation of tetraethylorthosilicate (TEOS), quenching at the gelation point, incorporation of Co by impregnation, and extraction of the solvent by supercritical drying. Characterization of the aerogel-coated monoliths revealed an excellent dispersion and homogeneity of the aerogel and good adherence properties. The catalytic performance of these materials in the ethanol steam reforming reaction addressed to obtain hydrogen was studied at atmospheric pressure by carrying out consecutive cycles at 473–773–473 K with a $C_2H_5OH:H_2O \sim 1:3$ (molar) mixture and stability tests, and the results were compared with those obtained over monoliths prepared by conventional washcoating methods from Co–SiO₂ xerogel. Co–SiO₂ aerogel catalytic walls were about four times more active for hydrogen generation at 623 K than conventional monoliths. An unusual rapid activation of aerogel-coated monoliths was attained at 580–590 K, even after several cycles and oxidation treatments at 563–613 K, which was attributed to highly dispersed cobalt particles and higher effective diffusivity of reaction species due to high porosity and larger average pore size. The reproducible low-temperature activation of Co–SiO₂ aerogels supported on ceramic monoliths may be useful for the practical application of fuel reformers to the on-site generation of hydrogen from ethanol.

1. Introduction

Aerogels are extremely light and porous materials obtained by removing the solvent from gels under supercritical conditions to avoid the capillary pressures, responsible for the porous collapse. The result is an open porous material with very high surface area and excellent mass transfer properties, becoming attractive in application as catalysts or catalytic supports [1–10]. High porosity and high surface area are interesting properties for catalytic chemisorption since they favor the accessibility to the active centers. However, given the low tensile strength of aerogels, the direct use of aerogel particles in a catalytic reactor may result in reactor blocking and pressure drop. In this work we have grown Co–SiO₂ aerogel coatings on the walls of ceramic monolith channels and studied their catalytic performance for the generation of hydrogen through the ethanol steam reforming reaction. The results are compared with conventional materials obtained by washcoating methods, i.e. xerogel coatings, synthesized by drying the gels at atmosphere pressure. Currently, the search for an active and selective catalyst for the generation of hydrogen through ethanol steam reforming at low temperature constitutes an active research area since ethanol is a renewable, liquid fuel with low toxicity and high energy density that is easy to handle and distribute [11,12].

Cobalt-based catalysts exhibit good performance for the generation of hydrogen from steam reforming of ethanol (1) at low temperature [13–25]:

$$C_2H_5OH + 3H_2O \rightarrow 6H_2 + 2CO_2 \qquad (1)$$
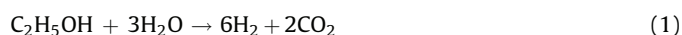
Other catalysts have been tested for ethanol steam reforming as well [26–28], but the requirement of higher temperatures to achieve reasonable activity values results in poor selectivity towards hydrogen and therefore, in accumulation of secondary products. In particular, as the reaction temperature increases, the reverse water gas shift reaction (2) is favored, thus hydrogen is consumed and the concentration of carbon monoxide in the product mixture increases. It is well known that carbon monoxide is a serious poison for polymeric fuel cells and its presence in the reactor effluent should be avoided in order to suppress costly

additional purification processes in auxiliary units.

$$H_2 + CO_2 \leftrightarrow H_2O + CO \qquad (2)$$

Other undesired products of the reaction are mainly ethylene (originated from ethanol dehydration onto acidic sites of catalysts), methane (formed either by decomposition of ethanol or by methanation reactions) and condensation products such as dimethylketone [29]. Over cobalt-based catalysts, it has been demonstrated with *in situ* magnetic studies coupled to reaction tests and with diffuse reflectance infrared spectroscopy [30,31] that the simultaneous presence of metallic cobalt and cobalt oxide is required for the progress of the reaction. Two steps of the reaction have been identified. First, ethanol dehydrogenates into acetaldehyde and hydrogen (3) over cobalt oxide (Co_3O_4):

$$C_2H_5OH \xrightarrow{Co_3O_4} CH_3CHO + H_2 \qquad (3)$$

Hydrogen partly reduces the surface of cobalt particles into metallic cobalt and then, the second step, the reforming of acetaldehyde into the final products H_2 and CO_2, takes place (4).

$$CH_3CHO + 3H_2O \xrightarrow{Co} 5H_2 + 2CO_2 \qquad (4)$$
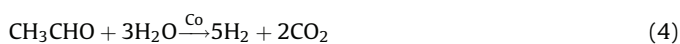
In powdered samples, cobalt oxide slowly reduces into metallic cobalt under ethanol steam reforming conditions and long induction times (typically of various hours) are necessary before enough metallic cobalt is present on the surface of the cobalt particles for the reaction to be completed [32]. In addition, as the temperature is lowered, metallic cobalt rapidly re-oxidizes into cobalt oxide under the ethanol:water reaction mixture and, again, the catalyst needs a slow reactivation before being catalytically active for reforming. In this work we demonstrate that cobalt particles in Co–SiO_2 aerogels supported on ceramic monoliths are activated very fast under ethanol steam reforming reaction conditions, even after warming up of the reformer in air, and furthermore, that high and stable yields of hydrogen can be obtained at temperatures as low as 598 K.

2. Experimental methods

2.1. Preparation of aerogels and catalytic walls

Silica gels were first synthesized by the sol–gel method, through hydrolysis and condensation of the silica precursor, tetraethylorthosilicate (TEOS), dissolved in ethanol and catalyzed with HNO_3–HF [33,34]. Cordierite ($Al_4Mg_2Si_5O_{18}$) monoliths of ca. 2 cm diameter and 2 cm long (Corning Inc., 400 cells per square inch) were immersed into the resulting sol and removed at the gelation point. Gelation was completed under continuous rotation (75 rpm) in liquid ethanol for ca. 30 min. Cobalt was then incorporated by impregnation of the gels with a $Co(NO_3)_2$ (0.57 M) ethanolic solution for 3 days. Finally, the gels were dried under supercritical conditions of ethanol (6.28×10^6 Pa, 516 K). On the other hand, conventional catalytic monoliths were obtained following the previously explained procedure, but allowing the solvent to evaporate at atmosphere pressure instead of under supercritical conditions. Afterwards, the Co–SiO_2 xerogel was calcined at 673 K for 2 h.

2.2. Characterization techniques

The morphology and composition of the interior of monolith channels were studied by scanning electron microscopy (SEM) and energy dispersive X-ray analysis (EDX). Images were taken at 15–20 kV with JEOL JSM 6400 and Hitachi S-2300 microscopes. Surface area measurements (BET) of powders were carried out with a Micromeritics ASAP 2000 apparatus. Samples were degassed at 443 K before surface measurements. Mechanical stability was evaluated by exposing monoliths directly to mechanical vibration. The vibration frequency was raised progressively from 20 to 50 Hz at a fixed acceleration value of 2 G, and at 50 Hz at acceleration values between 5 and 15 G. Weight loss was monitored after 30 min at each frequency, and after 3 h under the most severe vibration conditions (50 Hz, 15 G). G levels were controlled directly on the vibration test board with a Brüel & Kjaer 4370 accelerometer.

2.3. Catalytic studies

Catalytic tests were carried out at atmospheric pressure in a tubular, stainless-steel reactor. A C_2H_5OH:$H_2O \sim$ 1:3 (molar) vapor mixture balanced with inert gas was passed through the reactor at 25 STP mL min^{-1} (0.26 mL min^{-1} C_2H_5OH). Prior to catalytic tests, the temperature of the reactor was raised up to 473 K in air and held at this temperature for 30 min. Thermal cycles at 473–773–473 K were performed at 2 K min^{-1} as well as stability tests at 598–673 K. In some experiments, the temperature of the reactor was raised up to 563 or 613 K in air before the catalytic test. The reactor effluent was monitored continuously on-line either by mass spectrometry (Cirrus MKS) taking 14 scans per minute (1–60 u), or by gas chromatography (Agilent 3000 A) using MS 5 Å, PlotU and Stabilwax columns.

3. Results and discussion

3.1. Coating monolith walls with catalytic aerogels

No previous attempts have been reported in the literature concerning the growth of catalytic aerogels on monolith walls. Here we have developed a method for coating cordierite monoliths with a Co–SiO_2 aerogel. The most critical point of the procedure described in Section 2.1 for avoiding the blocking of the monolith channels was the control of the gelation point during the condensation of the silica precursor inside them. Different mixtures of HF:HNO_3 (HF/NHO_3 from 1.1 to 4.2) were investigated in order to control the gelation point and to obtain reproducible results. Using a H_2O:C_2H_5OH:TEOS:HF:HNO_3 = 16:6:1:0.11:0.03 (molar) mixture and heating up to 313 K, an advantageous gelation point at 18 ± 1 min was obtained for sample manipulation. Fig. 1a corresponds to a low-magnification SEM image of the inner part of a monolith channel coated with Co–SiO_2 aerogel. The homogeneity and distribution of the aerogel layer were excellent and energy dispersive X-ray analysis performed at various locations yielded constant Co/Si atomic ratios of about 0.36. Fig. 1b–d shows SEM images at higher magnification corresponding to cordierite before coating (Fig. 1d) and after coating with Co–SiO_2 aerogel (Fig. 1b) or xerogel (Fig. 1c). The porous structure of the cordierite walls was not recognizable after coating due to the thickness of the aerogel and xerogel layers. The microstructure of the xerogel and aerogel coatings was strongly different. Aerogel-coated monoliths showed high porosity and a typical cluster-of-grape morphology [8], whereas xerogel-coated monoliths were constituted by agglomerated particles of varying size. According to their morphology at the microscale level, the surface area of aerogel samples was considerably higher than that of xerogel samples, 645 vs. 280 m^2 g^{-1}. The average BJH pore sizes (Barret–Joyner–Halenda method) of aerogel and xerogel samples were 18.9 and 8.2 nm, respectively. Concerning mechanical stability, it was found that the adherence of aerogels onto the monolith walls was similar to that of washcoated xerogels. At increasing vibration
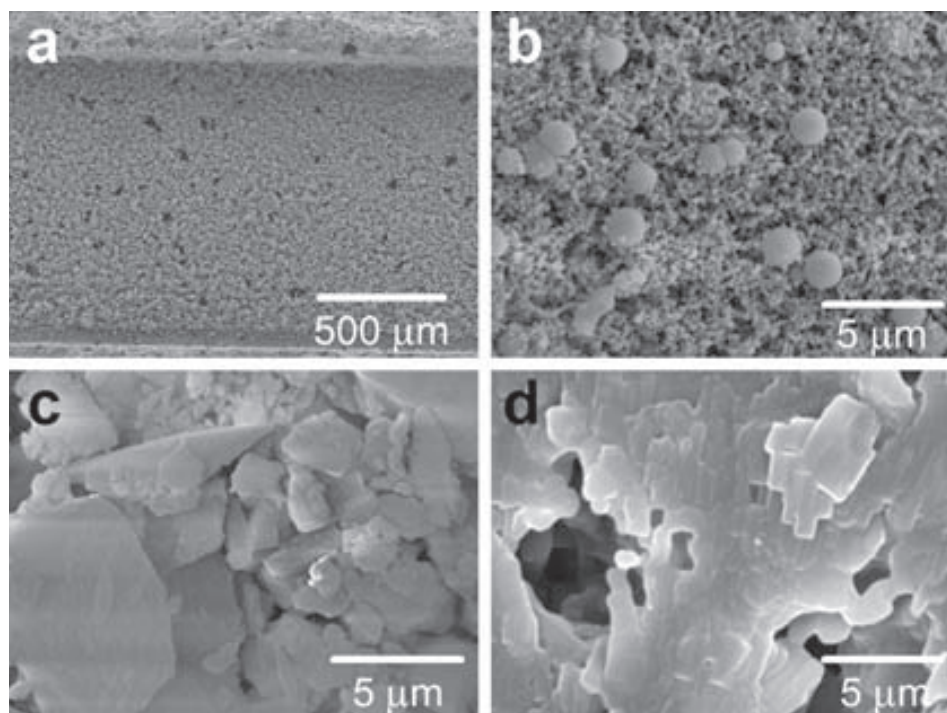
Fig. 1. Scanning electron microscopy images of Co–SiO$_2$ aerogel (a, b) and xerogel (c) coatings over cordierite monolith walls (d).

frequencies (20–50 Hz) and acceleration values (2–15 G) for 5.5 h the weight loss of both coatings was only ca. 20%. The amount of aerogel or xerogel deposited on the inner part of the monolith channels was 4–6% (w/w) and the amount of Co (measured by X-ray fluorescence) was ca. 20 wt.% with respect to SiO$_2$.

3.2. Ethanol steam reforming reaction

The catalytic behavior of catalysts was continuously monitored during several temperature cycles of 473–773–473 K. Fig. 2 shows some of such cycles for the monolith washcoated with xerogel and
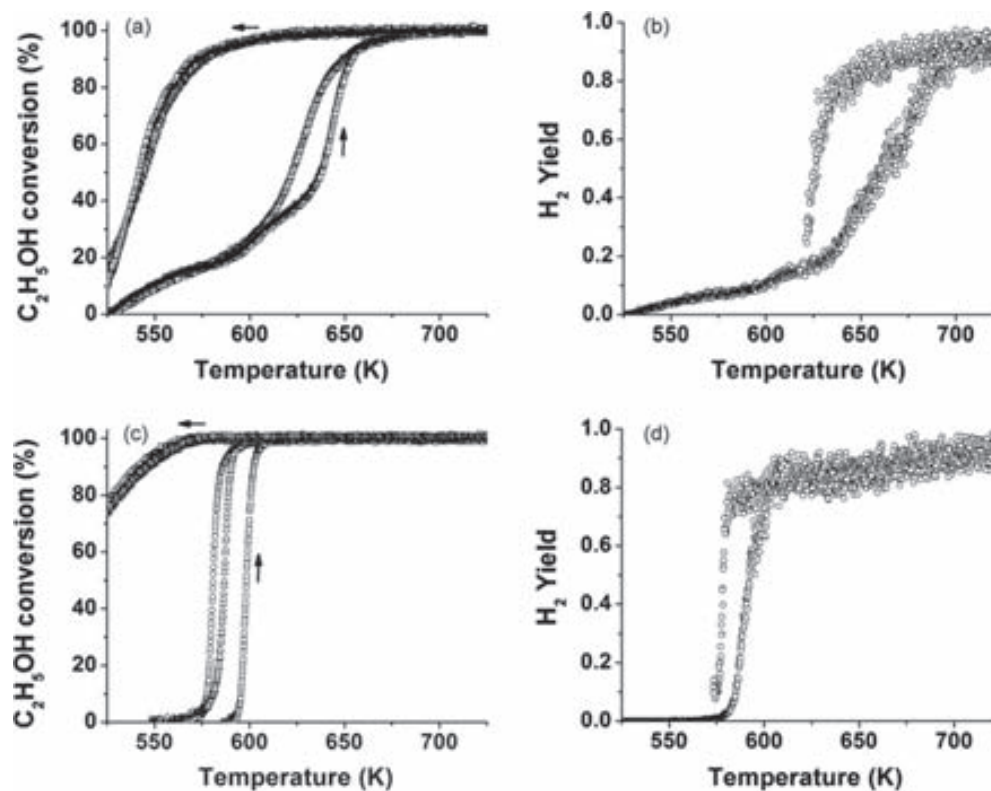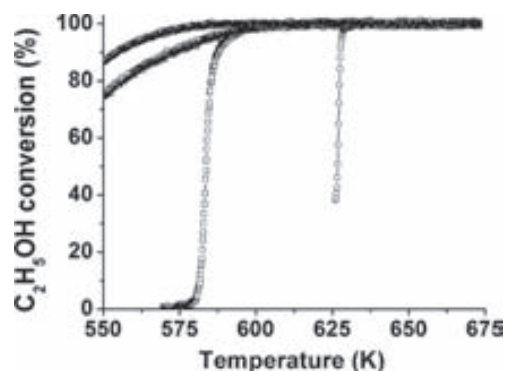

Fig. 2. Variation of ethanol conversion and hydrogen fractional yield under various 473–773–473 K cycles over monoliths coated with Co–SiO$_2$ xerogel (a, b) and aerogel (c, d). □ = cycle 2, △ = cycle 3, ○ = cycle 6. Hydrogen yield is reported for cycle 2. 0.26 mL min^{-1} C$_2$H$_5$OH, C$_2$H$_5$OH:H$_2$O $\sim$ 1:3 (molar), total flow 25 mL min^{-1}.

for the monolith coated with aerogel in terms of ethanol conversion and hydrogen yield. Cycles corresponding to the monolith wash-coated with xerogel (cycles 2 and 3) showed a slow increase of ethanol conversion (Fig. 2a) and hydrogen production (Fig. 2b) in a wide range of temperature as the temperature was raised. 40–50% of ethanol was converted at 623 K whereas a temperature of at least 698 K was required in order to obtain total conversion of ethanol and a good hydrogen yield. In contrast, as the temperature was lowered, ethanol conversion was maintained at temperatures higher than 623 K. This large hysteresis of ethanol conversion and hydrogen yield following temperature cycles is ascribed to the progressive reduction of cobalt oxide under ethanol steam reforming conditions at increasing temperature and the oxidation of metallic cobalt when the temperature is lowered, as has been discussed earlier [32]. On the contrary, the performance of aerogel-coated monoliths under exactly the same reaction conditions was strongly different (Fig. 2c and d). During the first part of cycle 2, there was a sudden increase of ethanol conversion from 10 to 100% in a temperature interval of only 13–14 K, accompanied by a rapid increase of hydrogen production. Ethanol conversion and hydrogen yield were maintained at higher temperatures, and in the second part of the cycle (as the temperature was lowered) the yield of hydrogen started to decrease only at 583 K. Exactly the same shape was observed for cycle 3, but now the temperature at which 50% of ethanol conversion was attained decreased from $T_{1/2}$ = 599 to 587 K (Fig. 2c), resulting even in a better performance at a lower temperature. The activation temperature progressively decreased during the following cycles until a constant value of ca. $T_{1/2}$ = 581 K was reached after cycle 5. 17.3 mol H_2/mol C_2H_5OH g^{-1} min^{-1} were produced over the aerogel-coated monolith at 623 K, being the composition at the reactor outlet 68.7% H_2, 23.2% CO_2, 1.0% CO and 7.1% CH_4. For comparison, 5.0 mol H_2/mol C_2H_5OH g^{-1} min^{-1} were produced over the xerogel-coated sample at this temperature.

The better catalytic performance and fast activation of Co–SiO$_2$ aerogels with respect to their homologue xerogels is attributed to highly dispersed cobalt particles and higher effective diffusivity of reaction species due to high porosity and larger average pore size of the aerogel. In order to further test this hypothesis, we carried out additional temperature cycles under ethanol steam reforming conditions after oxidizing the aerogel-coated monolith under air at 563 K (before the activation temperature) and 613 K (after activation). Fig. 3 shows the ethanol conversion corresponding to these cycles. In both cases the aerogel-coated monolith was activated almost immediately and hydrogen was obtained at the same time. In addition, the second part of the cycle, from 773 to 473 K, was indistinguishable from the previous cycles without the
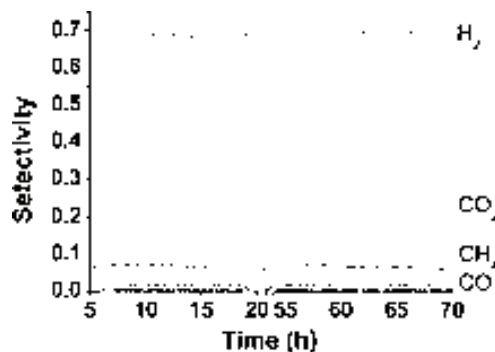
Fig. 4. Product selectivity obtained at 623 K during long term catalytic tests. The break between 21 and 54 h corresponds to an aging treatment at 673 K. 0.26 mL min^{-1} C_2H_5OH, $C_2H_5OH:H_2O$ ~ 1:3 (molar), total flow 25 mL min^{-1}.

oxidation treatment (Fig. 2c). These results show that cobalt particles in the aerogel become easily activated under ethanol steam reforming conditions even after oxidation at high temperature or, in other words, cobalt particles in the aerogel undergo rapid redox equilibrium under reaction, irrespectively of their initial state.

Long term catalytic runs were carried out over monoliths coated with aerogel in order to study their stability. The samples were subjected to continuous ethanol steam reforming at 623–673 K for several days and no deactivation was observed. Fig. 4 shows the selectivity results for a 3-day experiment. Successfully, the selectivity towards the reforming products, H_2 + CO_2, was maintained between 92 and 94%.

4. Conclusions

Ceramic monoliths have been coated with catalytic aerogel layers and used as structured materials for gas–solid reactions. Excellent homogeneity, dispersion and adherence were obtained with Co–SiO$_2$ aerogel coatings over the cordierite monoliths. The catalytic performance of Co–SiO$_2$ aerogel-coated monoliths for the generation of hydrogen from ethanol steam reforming was outstanding in terms of catalyst activation at low temperature (580–590 K), resistance to oxidation (563–613 K), stability and fast response to hydrogen production with respect to conventional catalytic monoliths washcoated with Co–SiO$_2$ xerogel. On-board reformers may benefit from monoliths coated with catalytic aerogels since they can be heated to the reaction temperature in air, they do not require long activation treatments prior to use and they are stable under start-up/shut down-cycles.

Fig. 3. Ethanol conversion and hydrogen fractional yield over Co–SiO$_2$ aerogel supported on cordierite monoliths after heating up the reactor in air at 563 K ($\square$) and 613 K ($\bigcirc$). 0.26 mL min^{-1} C_2H_5OH, $C_2H_5OH:H_2O$ ~ 1:3 (molar), total flow 25 mL min^{-1}.

References

[1] G.M. Pajonk, Catal. Today 35 (1997) 319.
[2] B.C. Dunn, P. Cole, D. Covington, M.C. Webster, R.J. Pugmire, R.D. Ernst, E.M. Eyring, N. Shah, G.P. Huffman, Appl. Catal. A 278 (2005) 233.
[3] K.M.K. Yu, C.M.Y. Yeung, D. Thompsett, S.C. Tsang, J. Phys. Chem. B 107 (2003) 4515.
[4] Z. Xu, Y. Li, J. Zhang, L. Chang, R. Zhou, Z. Duan, Appl. Catal. A 213 (2001) 65.
[5] A. Orlovic, D. Janackovic, D. Skala, Catal. Commun. 3 (2002) 119.
[6] L. Piao, Y. Li, J. Chen, L. Chang, J.Y.S. Lin, Catal. Today 74 (2002) 145.

[7] H. Rotter, M.V. Landau, M. Carrera, D. Goldfarb, M. Herskowitz, Catal. Appl. B (2004) 111.

[8] C.-T. Wang, S.-H. Ro, Appl. Catal. A 285 (2005) 196.

[9] Y. Guo, W. Meyer-Zaika, M. Muhler, S. Vukojevic, M. Epple, Eur. J. Inorg. Chem. 23 (2006) 4774.

[10] S. Martínez, A. Vallribera, C. Cotet, M. Popovici, L. Martín, A. Roig, M. Moreno-Mañas, E. Molins, New J. Chem. 29 (2005) 1342.

[11] G.A. Deluga, J.R. Salge, L.D. Schmidt, X.E. Verykios, Science 303 (2004) 993.

[12] F. Frusteri, S. Freni, J. Power Sources 173 (2007) 200.

[13] J. Llorca, N. Homs, J. Sales, P. Ramírez de la Piscina, J. Catal. 209 (2002) 306.

[14] J. Llorca, P. Ramírez de la Piscina, J.A. Dalmon, J. Sales, N. Homs, Appl. Catal. B 43 (2003) 355.

[15] J. Llorca, N. Homs, J. Sales, J.L.G. Fierro, P. Ramírez de la Piscina, J. Catal. 323 (2004) 470.

[16] J.A. Torres, J. Llorca, A. Casanovas, M. Domínguez, J. Salvadó, D. Montané, J. Power Sources 169 (2007) 158.

[17] S. Freni, S. Cavallaro, N. Mondello, L. Spadaro, F. Frustreri, Catal. Commun. 4 (2003) 259.

[18] J. Sun, X.-P. Qiu, F. Wu, W.-T. Zhu, Int. J. Hydrogen Energy 30 (2005) 437.

[19] F. Mariño, G. Baronetti, M. Jobbagy, M. Laborde, Appl. Catal. A 238 (2003) 41.

[20] M.S. Batista, R.K.S. Santos, E.M. Assaf, J.M. Assaf, E.A. Ticianelli, J. Power Sources 134 (2004) 27.

[21] H. Song, L. Zhang, R.B. Watson, D. Braden, U.S. Ozkan, Catal. Today 129 (2007) 346.

[22] H. Wang, J.L. Ye, Y. Liu, Y.D. Li, Y.N. Qin, Catal. Today 129 (2007) 305.

[23] M. Benito, R. Padilla, L. Rodríguez, J.L. Sanz, L. Daza, J. Power Sources 169 (2007) 167.

[24] A. Kaddouri, C. Mazzocchia, Catal. Commun. 5 (2004) 339.

[25] F. Haga, T. Nakajima, H. Miya, S. Mishima, Catal. Lett. 48 (1997) 223.

[26] P.D. Vaidya, A.E. Rodrigues, Chem. Eng. J. 117 (2006) 39.

[27] A. Haryanto, S. Fernando, N. Murali, S. Adhikari, Energy Fuels 19 (2005) 2098.

[28] M. Ni, Y.C. Leung, M.K.H. Leung, Int. J. Hydrogen Energy 32 (2007) 3238.

[29] J. Llorca, P. Ramírez de la Piscina, J. Sales, N. Homs, Chem. Commun. (2001) 641.

[30] J. Llorca, J.A. Dalmon, P. Ramírez de la Piscina, N. Homs, Appl. Catal. A 243 (2003) 261.

[31] J. Llorca, N. Homs, P. Ramírez de la Piscina, J. Catal. 227 (2004) 556.

[32] J. Llorca, P. Ramírez de la Piscina, J.A. Dalmon, N. Homs, Chem. Mater. 16 (2004) 3573.

[33] R.F. Silva, W.L. Vasconcelos, Mater. Res. 2 (1999) 197.

[34] R. Ramió, M. Moner-Girona, A. Roig, E. Molins, J. Torres, Proceedings of the 6th Meet. Supercr. Fluids: Chem. Mater., Nottingham (1999) 58.
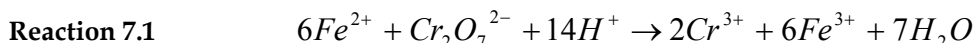
## 7.3. Brief description of the characterization techniques and the supercritical facilities

7.3.1. Iron titration with potassium dichromate

The method used to measure the iron content of the colloidal dispersions is the redox titration of ferrous ions with potassium dichromate. The full redox reaction is:

Reaction 7.1 $6Fe^{2+} + Cr_2O_7^{2-} + 14H^+ \rightarrow 2Cr^{3+} + 6Fe^{3+} + 7H_2O$

and the protocol to perform the titration is as follows:

a) Dissolution of the iron oxide nanoparticles to iron ions with hydrochloric acid 37% (HCl). The brown colloidal dispersion changes to a bright lemon-yellow solution.

Reaction 7.2 $Iron \cdot oxide + HCl \rightarrow Fe^{3+} ions$
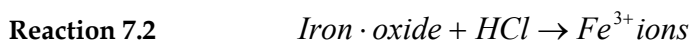
b) Addition of a few drops of tin chloride 0.25 M (SnCl$_2$) to reduce the ferric ions (Fe(III)) to ferrous ones (Fe(II)). The yellow solution turns colourless.

Reaction 7.3 $2Fe^{3+} + Sn^{2+} \rightarrow 2Fe^{2+} + Sn^{4+}$
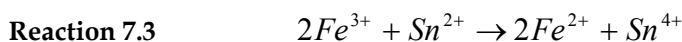
c) Quick addition of mercury chloride (HgCl$_2$) 5 wt. % to oxidize the excess of Sn(II) ions to Sn(IV). Sn(II) ions interfere the redox reaction between potassium dichromate and iron ions. The solution changes from colourless to cloudy white.

Reaction 7.4 $Sn^{2+} + 2HgCl_2 \rightarrow Hg_2Cl_2 + Sn^{4+} + 2Cl$
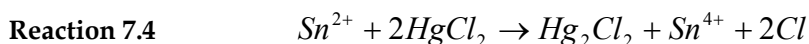
d) Addition of 4-5 drops of the indicator, sodium diphenylaminosulphonate 2 wt. % (C$_{12}$H$_{10}$NNaO$_3$S).

e) Titration with potassium dichromate (K$_2$Cr$_2$O$_7$). The equivalent volume is reached when the solution turns from olive green to bright violet.

Reaction 7.1 $6Fe^{2+} + Cr_2O_7^{2-} + 14H^+ \rightarrow 2Cr^{3+} + 6Fe^{3+} + 7H_2O$
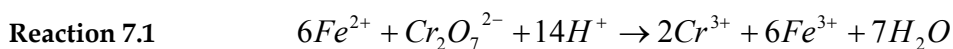
The concentration of iron ions in the initial solution is calculated with **Equation 7.1**:

**Equation 7.1** $$[Fe] = \frac{6 \cdot [K_2Cr_2O_7] \cdot V_{eq}}{V_{sample}}$$

Each sample was titrated three times and an average concentration was considered. The method has associated a significant error due to the difficulty in determining the moment of colour change since the reaction is reversible (the solution goes back from violet to green in seconds if no more potassium dichromate is added).

7.3.2. Dynamic light scattering (DLS) and Laser Doppler velocimetry (LDV)

Dynamic light scattering (also known as PCS - Photon Correlation Spectroscopy) measures Brownian motion and relates it to the size of the particles. It does this by illuminating the particles with a 633 nm laser and analysing the intensity fluctuations in the scattered light at 173°. The calculated hydrodynamic size is defined as the diameter of a sphere which has the same Brownian motion as the analyzed particle, independently of the particle shape. This diameter corresponds not only to the particle, but also to the molecules strongly adsorbed onto its surface (surfactants, electrolytes and solvent.). Therefore, the hydrodynamic size is always larger than the size observed by TEM. Furthermore, the scattering intensity depends on the sixth power of the particle radius (intensity $\propto r^6$) meaning that the larger particles contribute more to the average size than the smaller ones.

DLS technique is very sensitive to any particle in suspension, such as dust. Therefore to obtain reliable data, it is very important to have a well purified sample in order to avoid interferences during the DLS measurements. Since the iron oxide nanoparticles are so small, dust particles or whichever other impurity can severely affect the measurement. **Figure 7.1** shows the raw correlation data of the sample before and after sample purification (purification was performed by multiple centrifugation cycles at 4400 rpm of the colloidal dispersions to discard the solid precipitates until no solid was observed for two consecutive cycles).
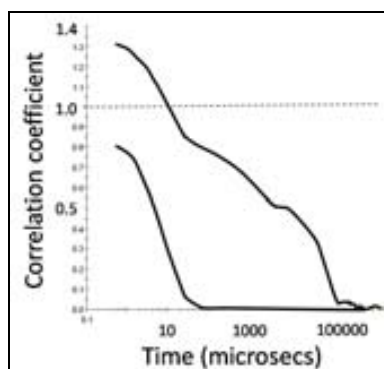
Figure 7.1. Raw correlation data of as-synthesized iron oxide nanoparticles sample (upper curve) and after thorough purification (lower curve).

The correlation curve of the as-synthesized sample in **Figure 7.1** shows three different bumps which correspond to three populations of particle size. Its Z average value is almost 5000 nm. The polydispersion index reached the highest value, 1.0. Nevertheless, when considering the mean hydrodynamic size by number, the value corresponds to the iron oxide nanoparticles, 10.5 nm. The large particles must be dust particles, in a very small number, which contribute largely to the Z average value but almost nothing to the

number distribution. The purified sample shows only one decay slope at very low microseconds, what means that there is only one population of particles with small size. The numerical values show a narrow particle size distribution (PdI = 0.185) centred at 13.4 nm (Z average value), very close to the mean size by number, 10.4 nm. Then, the nanoparticles can be identified both in pre and post purified samples with the number distribution but a high quality analysis can be only achieved after a thorough purification process.

Laser Doppler Velocity (LDV) measures the electrophoretic mobility of the particles and uses it to calculate the zeta potential (ζ) of charged colloidal particles (see **Figure 7.2**).
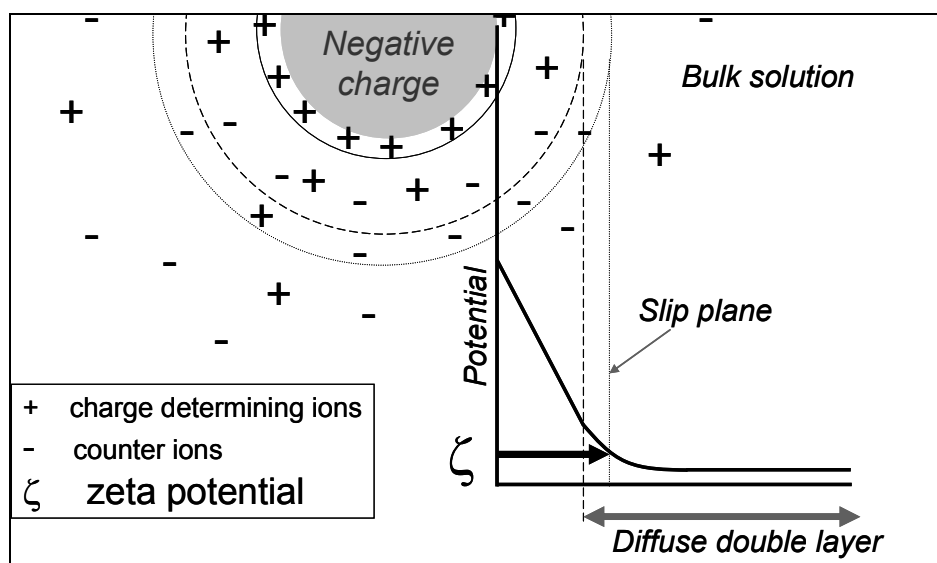
Figure 7.2. Zeta potential scheme.

A cell with electrodes is filled up with the colloidal sample and then a potential is applied. The particles move towards the electrode of opposite charge while they are illuminated with a 633 nm laser. The scattering light at 170° is combined with the reference beam and the rate of fluctuation of the signal intensity is used to calculate the speed of the particles. In turn, zeta potential can be calculated from the speed. Zeta potential depends on the pH of the system. By changing the pH, the isoelectric point (IEP; point of zero charge) can be determined.

The measurements of hydrodynamic size and zeta potential were performed at MATGAS 2000 AIE with a Zetasizer Nano ZS from Malvern Instruments, equipped with a He/Ne 633 nm laser. The isoelectric point determination was performed with the MPT-2 Autotitrator attachment (see **Figure 7.3**). Each sample was measured three times and each measurement was in turn composed of 10 to 20 runs, depending on the solvent and concentration. An average value was obtained.

Figure 7.3. Photograph of the Zetasizer Nano ZS instrument (Malvern) (left) and the MPT-2 Autotitrator (right).

7.3.3. Transmission electron microscopy (TEM) / Electron diffraction (ED)

Transmission electron microscopy allows for the direct observation of objects with nanometric resolution. An electron beam is directed with electromagnetic lenses to the sample, located in a high-vacuum column. The sample must be very thin (< 200 - 300 nm) in order to let the electron beam pass through it. The transmitted electrons are projected onto a fluorescent screen creating a temporal image or onto a photographic substrate to obtain a permanent image. This technique provides information about the morphology, size and constitution of the sample. High resolution TEM allows for atomic resolution.

The preparation of solid thick samples for TEM analysis is very tedious, but the preparation of nanoparticles in colloidal suspensions is quite simple: a droplet of sample is deposited onto a carbon-coated film supported onto a copper grid (or the grid is directly immersed into the sample). Then, the solvent is allowed to evaporate. The dispersion has to be highly diluted. On the contrary the beam would not be transmitted through the grid. In our case, the colour of the iron oxide dispersions had to be just slightly yellow (< 0.01 mg Fe_2O_3/ml). The particles are observed in dry state, therefore the information about interactions and ordering of the particles cannot be extrapolated to the colloidal state. Several images from different positions of the grid were taken in each analysis in order to get representative information of the whole material. Particle size distributions were plotted considering the diameter values of at least 200 nanoparticles, directly measured from different digital images. No specific software was used for that purpose. The nanoparticles can self-assemble in ordered arrangements once the solvent has evaporated.

Electron diffraction provides information about the crystalline structure of the sample. If the sample is monocrystalline, the electron diffractogram is formed by the diffraction

spots corresponding to the zone axis perpendicular to the electron beam. In case of polycrystalline samples, the diffractogram shows diffraction rings. The reticular spaces (d_{hkl}) are calculated by measuring the distance (r) from the centre of the diffractogram to the diffraction rings or spots using the **Equation 7.2**:

Equation 7.2
$$d_{hkl}\left(\text{Å}\right) = \frac{L(mm \cdot \text{Å})}{r(mm)}$$

where L is the camera length.

Transmission electron microscopy images were obtained with two different instruments: a JEOL JEM-1400 operating at 200 keV (Universitat Autònoma de Barcelona) and a JEOL JEM-1210 operating at 120 keV (ICMAB). High resolution images (HRTEM) were taken with a JEOL JEM 1010 equipped with a high resolution digital camera. Electron diffraction was performed with the microscope JEOL JEM-1210 with 23.1 mm·Å camera length (L). Dr. Jaume Gázquez performed preliminary STEM and EELS analyses of the composite samples.

7.3.4. Scanning electron microscopy (SEM)

Scanning electron Microscopy (SEM) analyses were performed at the ICMAB with a PHILIPS SEM 515 microscope operating at 0.2-30 kV. It is equipped with secondary and backscattering electrons detectors. The isolating silica samples were previously coated with gold at the Universitat Autònoma de Barcelona (Servei de Microscòpia) with a K550 Sputter Coater (Coating Attachment Emitech. Ashford, UK). The gold film thickness depends on the intensity, voltage and coating time, following the relationship:

Equation 7.3 $d(\text{A}) = I(mA) \cdot V(kV) \cdot t(\min) \cdot K$

where d is the film thickness in Angstrom, I is the intensity, V is the voltage, t is time and K is a constant related to the ambient gas (K(argon) = 5). The used experimental values of intensity, voltage and K were constant, 25 mA, 1 kV and K=5, respectively. Time was changed. For t = 0.5 min, the coating thickness was $\approx$ 6 nm.

7.3.5. X-ray diffraction (XRD)

X-Ray diffraction is a non-destructive analytical technique to study the crystalline structure of solids, their chemical composition and some physical properties. When x rays interact with matter which is composed of ordered arrangements of atoms and/or molecules the x rays diffract at different angles (θ) depending on the distance between the crystalline planes (d_{hkl}) of the solid. Bragg's law relates these parameters with the wavelength of the incident radiation (λ):

Equation 7.4 $\lambda = 2 \cdot d_{hkl} \cdot sen\,\theta_{hkl}$

The diffractograms represent the double of the diffracted angle (2θ) vs. the diffraction intensity. The experimental information regarding the peaks position and intensity is compared to standard patterns of known compounds in order to identify the crystalline species of the sample. When the crystalline size is reduced to the nanometric range, the peaks broaden. The peak width can be related to the crystallite size ($d_{particle}$) by the Scherrer's Formula.[1]

MAUD program[2] (Materials analysis using diffraction) uses the Rietveld refinement method to fit experimental diffractograms and extract information from the material such as crystallite size, crystalline cell dimensions, proportions of phases in case of mixtures, etc.

The x-ray diffractograms of powder samples were performed with the two different diffractometers at the ICMAB: a Siemens D5000 and a Rigaku Rotaflex RU-200 B, both with cupper Kα incident radiation (λ = 1.54 Å). The experiment parameters step time, step size and 2theta range were tuned depending on the sample. The amount of sample for analysis with the Siemens and Rigaku diffractometers has to be enough to cover a circular glass substrate of 2.5 cm in diameter. For a lower amount of sample, the contribution of the glass substrate appears in the diffractogram.

The analyses of colloidal dispersions were performed in a Bruker D8 Advance diffractometer (ICMAB). It is a GADDS (General Area Detector Diffraction System) bi-dimensional detector with cupper Kα incident radiation. The higher sensitivity of this instrument allows measuring very small amounts of sample. It is commonly named microdiffractometer. The experimental time is much shorter than with the Siemens and Rigaku diffractometers (seconds vs. minutes/hours). It measures discrete frames of 30 2θ degrees. To study larger ranges of 2θ, several frames are measured and then they are overlapped (that is why the background may not be constant). Borosilicate capillary tubes are preferred compared to silicate ones, because they absorb less amount of radiation (boron has a lower atomic number than silicon). The tube width for microdiffraction has to be small enough not to disturb significantly the diffraction intensity but at the same time, it has to be wide enough so it can be filled with the liquid overcoming the capillary pressures. We selected tubes 0.5 mm in diameter. The capillary tubes were analyzed without sample and it was obtained a peak around 30-34 2θ degrees.

Several aqueous dispersions with different particle size and different iron oxide concentration were analyzed. Just hundreds of microlitres were needed for analysing each sample. A borosilicate capillary tube 0.5 mm in diameter was used as the holder. The first diffractograms showed no defined peak. Several parameters such as iron oxide concentration, exposure time and collimator diameter were varied to find the optimum experimental conditions. They resulted to be:

- 1 hour exposure: although this diffractometer usually takes seconds or minutes to perform one analysis, our samples had too little amount of crystalline matter and needed longer times. Analyses one hour long showed representative peaks of iron oxide. Longer times did not significantly improve the results.
- 0.5 mm collimator (instead of the routinely used 0.3 mm) to diffract a higher area of sample and increase the intensity of the signal.
- The higher iron oxide concentration as possible. It was tested up to 0.5 M iron oxide.

Figure 7.4 shows two diffractograms obtained with different collimator diameters. The upper one (black line) also fulfils the optimum conditions of experiment time (1 hour) and iron oxide concentration (0.5 M). The main peaks of maghemite/magnetite at 35º, 43º, 53º, 57º and 63º 2θ are clearly identified. The opening of the collimator allows an increase in the intensity of the diffracted signal.
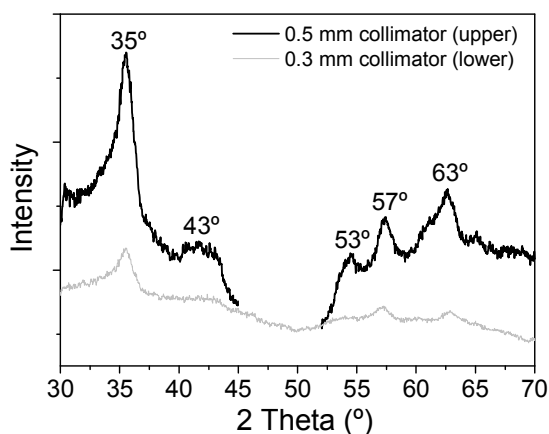
Figure 7.4. Diffractograms acquired in colloidal state to compare two different collimator diameters (0.3 vs. 0.5 mm). The break of the upper diffractogram is related to the measuring conditions of this instrument.

7.3.6.   Small angle x-ray scattering (SAXS)

Small angle x-ray scattering is a non-destructive analytical technique for the structural characterization of solid and fluid materials in the nanometre range. Parameters like the size, shape and characteristic distances of partial ordering between the entities are obtained. The nanometric objects can be colloidal particles, pores, macromolecules, proteins, polymers, etc., either crystalline or amorphous, in solid phase or in liquid dispersion. The analysis is performed by irradiating the sample with a well-defined, monochromatic x-ray beam and collecting the diffracted intensity at very low angles (typically 0.1 - 10º). The experimental curves are then fitted to different theoretical models in order to obtain the particle size and size distribution, interparticle distance and type of ordering. The models which have been used in the present thesis consider polydisperse

spherical entities or particles with different interactions. They are (i) non-interacting spheres; (ii) Percus-Yevick approximation for short-range interacting spheres without crystalline order; (iii) interacting spheres with a body centred cubic arrangement (bcc); (iv) interacting spheres with a face centred cubic arrangement (fcc); and (v) interacting spheres with a hexagonal compact packing (hcp). The position of the first minimum in the scattering curves is dependent on the particle size and the position of the peaks depends on the kind of ordering and interparticle distances. As mentioned for DLS, the scattering intensity depends on the sixth power of the particle radius (intensity $\propto$ r^6) and thus the bigger particles contribute more to the average size than the smaller ones.

The iron oxide nanoparticles were analysed both in powder form and in colloidal dispersion of water and hexane. Only a few miligrams or 1 microlitre were necessary. The experimental time was tuned from 1 to 30 h to reduce the noise level and to obtain a sufficiently high scattering intensity. Colloidal samples in hexane were also deposited onto silicon wafers and calcined under air atmosphere up to different temperatures (200-450 ºC, every 50ºC) to study the ordering of the particles. All the samples were calcined at the same time; the heating rate was 1.6ºC/min and the heating time at each calcination temperature was 10 minutes. One piece of silicon buffer was taken out of the oven at each defined temperature. The silicon wafers were previously hydrophobized with solutions of hydrogen peroxide (H_2O_2) and sulphuric acid (H_2SO_4), and washed with water and ethanol, to favour the adhesion of the nanoparticles coated with oleic acid.

Small angle X-ray scattering (SAXS) curves were performed with a rotating anode with pinhole collimation. A Nonius rotating anode device (P = 4 kW, Cu Kα) and an image-plate detector system were used. With the image plates placed at a distance of 40 cm from the sample, a scattering vector range from s = 0.05 - 1.6 nm-1 (s = 2·sinθ/λ) was available. The 2D isotropic diffraction patterns were transformed into a 1D radial average of the scattering intensity. The SAXS experiments were performed at the Max-Planck Institute of Colloids and Interfaces in Potsdam, Germany, at Prof. Antonietti's group, under the supervision of Bernd Smarsly.

7.3.7. Magnetometry

The evaluation of the magnetic properties comprises the measurement of the magnetization vs. the applied magnetic field at a constant temperature (M(H) curves) and vs. the temperature at a constant applied magnetic field (ZFC-FC curves). A brief explanation on the magnetic properties of nanostructured materials is described in section 1.1.2.

The magnetization curves vs. temperature are called zero field cooling-field cooling curves (ZFC-FC). Each sample is measured twice consecutively from low to high temperature: the first run starts when the sample has been cooled without applying the

magnetic field (ZFC). For the second one, on the contrary, the temperature is decreased with an external magnetic field.

The use of colloidal samples is preferred to the use of solid powder since the amount of iron oxide nanoparticles synthesized per batch is small (100 – 120 mg) and it is usually difficult to redisperse the already precipitated particles. This is the reason why we looked for means of directly measuring colloidal dispersions with all techniques. The commonly used sample holders for solid samples are gelatin capsules (1.5 cm length and 0.5 cm diameter; water soluble) where the solid is immobilized by adding pressed cotton (diamagnetic material). Since the available magnetometers do not have a reliable sample holder for liquids and the gelatin capsules are water soluble at room temperature we first froze down the capsules with liquid nitrogen (78 K), quickly add a known volume of colloidal dispersion (of known concentration) and measure its magnetization in solid state at 253 K (-20 ºC). Because the risk of sample leaking inside the magnetometer is high and it is not possible to measure up to room temperature which is essential for biomedical applications this protocol was dismissed. The second and more secure approximation is to use some cotton as substrate for a known volume of the colloidal dispersion. The cotton is kept inside a gelatin capsule with no risk of contamination to the instrument and the experiment is performed in the same way as for solid samples in the whole temperature range.

The magnetization curves with continuous magnetic field were performed at the ICMAB with a magnetometer VSM-NUVO MOLSPIN, Newcastle Upon Tyne, UK (at room temperature) and with a superconducting quantum interference device (SQUID) magnetometer (Quantum Design MPMS5XL) (5–300 K). This last magnetometer was also used to measure the zero field cooling-field cooling (ZFC-FC) curves at 100 Oe. The measurements in alternating field (ac) were performed with a PPMS device at room temperature with a continuous field of 10 Oe and an alternating field of 0.137 Oe at the frequency range 10-10000 Hz.

7.3.8. Supercritical facilities

The supercritical experiments were performed in the Pilot Plant of the Laboratory of Supercritical Fluids sited at MATGAS 2000 AIE. Raul Solanas is the engineer in charge of the supercritical facilities who controls and manipulates the pilot plant during the experiments at supercritical conditions.

Figure 7.5. Supercritical pilot plant at MATGAS 2000 AIE used for the supercritical experiments.

The pilot plant, shown in **Figure 7.5**, can be operated up to 500 bar and 400ºC. Flexibility is one of the more important aspects of this plant, so temperature, pressure and flow rate can be easily tuned at different points allowing getting different working conditions in each of the four reactors. All the plant is controlled by a Programmable Logic Controller (PLC) through a software control. This software shows the pressure, temperature and flows at the dynamic conditions. The drying and synthesis of silica and composite particles used the 2-litre reactor as the synthesis reactor. The 1-litre reactor was used as the collector for the extracted solvents. The pressurization was performed by injection of compressed carbon dioxide with a Lewa pump or heating the reactor to the experimental conditions. The depressurization was automatically controlled by a flow rate control valve. No mechanical stirring was used during the synthesis because of technical incompatibilities with the applied high pressures and temperatures. The reactor has no refrigeration system and consequently it cools down by inertia. The reproducibility of the experimental pressure profile is very difficult, since the system allows the control of the pressure, but not the amount of CO_2 injected into the autoclave.

Some tests on the reaction mechanism were performed in an autoclave Thar System Phase Monitor SPM20-2P with PAL Camera, Thar Technologies, Inc. Pittsburgh. The reactor volume is variable, from 5 to 15 ml. The CO_2 pump is Thar P-50. It is equipped with a mechanical stirrer PPI Dyna/Mag MIXERS SCALE TYPE model MM-006 up to 2500 rpm.

7.3.9. Infrared spectroscopy

Infrared spectra were recorded at the ICMAB on a Fourier transform Perkin-Elmer Spectrum one spectrometer. The samples were measured with KBr disks (4000-400 cm^{-1}) or directly as solid powder by using UATR accessory (universal attenuated total reflectance; 4000-650 cm^{-1}).

7.3.10. Nitrogen adsorption/desorption isotherms (BET method)

Nitrogen adsorption/desorption data were taken at 77 K using an ASAP 2000 surface area analyzer (Micromeritics Instrument Corporation) after degasification at 100ºC or 300ºC under vacuum for 24 h to remove the adsorbed species. Surface area and mean pore diameter determinations were carried out following BET (Brunauer, Emmett and Teller) and BJH (Barrett, Joyner and Halenda) models respectively.

### 7.3.11. Thermal gravimetric analysis (TGA)

Thermal gravimetric analyses were performed at the ICMAB with an ATG 7 Perkin Elmer device. The maximum temperature is 900ºC. Atmosphere can be air, nitrogen or argon, the heating rate can be modulated between 0.1 and 200 ºC/min.

7.3.12. Chemical analysis

The elemental composition was measured at the Universitat Autònoma de Barcelona (Servei d'Anàlisi Química) by inductively coupled plasma mass spectroscopy (ICP-MS). The samples were first digested with a mixture of nitric acid (HNO_3) and hydrofluoric acid (HF) in a microwaves oven. Digestion of control samples were also performed and analyzed.

7.3.13. Contact angle measurements

Contact angle is defined as the angle at which a liquid/vapour interface meets a solid surface (see **Figure 7.6**). It depends on the nature of the three components. The measurements were performed with a Krüss DSA 100 instrument. Powder samples were compacted in disk shape and a solvent drop of 7 μl was poured onto them while video recording. The contact angle was calculated by using the device software.
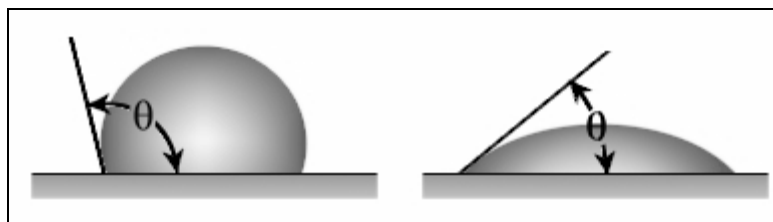
Figure 7.6. Scheme of contact angle (θ). The left image corresponds to a liophobic solid and the right image to a liophilic one.

7.3.14. Atomic force microscopy (AFM)

Atomic force microscopy analyses were done at the ICMAB by Marcos Paradinas (Dr. Carmen Ocal's group) with a Nanotec Electrónica® AFM device equipped with a Dulcinea control system and combined with WSxM software for Real Time Data Acquisition. A budgetsensors cantilever with nominal force constant K = 0.06 N/m was used under ambient conditions.

7.3.15. Cytotoxicity evaluation

The 3-(4,5-Dimethylthiazol-2-yl)2,5-diphenyl-tetrazoilum bromide (MTT) reduction assay for cell viability evaluation has been described as a suitable method for the evaluation toxicity. The MTT assay relies on the mitochondrial activity of fibroblasts and represents a parameter for their metabolic activity.[3] The toxicity evaluation was performed by Dr. Elisenda Rodríguez at the Massachusetts General Hospital (MGH) in USA (Professor R. Weissleder's group). The possible cytotoxic effects of the iron oxide nanoparticles as well as the silica composites were evaluated in NIH3T3 cells using the 3-(4,5-Dimethylthiazol-2-yl)2,5-diphenyl-tetrazoilum bromide (MTT) reduction assay. The nanoparticles were dissolved in Dulbecco's modified Eagle's medium (DMEM) plus 10% fetal bovine serum (FBS). NIH3T3 cells planted in 96-well cell culture plate (1.5×10^4/100 mL) were treated with the particles and with the controlled medium for 12 hours. After the incubation period, optical density was measured at 570 nm as a blank and the cells were incubated with 0.5 mg/ml MTT for 2 h. Then, a lysing buffer that dissolves the blue formazan crystals was added and the plates were incubated overnight at 37ºC. Optical density was again measured at 570 nm and values were expressed as a percentage of control well values.

7.3.16. Relaxivity measurements

Relaxivity measurements were done by Dr. Elisenda Rodríguez at the Mons_Hainaut University in Belgium (Professor R. Muller's group) and at the Massachusetts General Hospital in USA (Professor R. Weissleder's group). The NMRD (Nuclear Magnetic Resonance Dispersion) profiles were recorded from 10 kHz to 10 MHz on a Stelar field

cycling relaxometer (Stelar, Mede, Italy). Additional measurements of the relaxation times at 20 and 60 MHz were performed on a Bruker Minispec system (Bruker, Karlsruhe, Germany) at 37°C. T_1 values were obtained by using an inversion-recuperation sequence and T_2 values with a cpmg sequence. Each sample was measured three times to calculate the average value. The stability of the dispersion was reduced due to their multiple manipulations prior to the relaxivity measurements, including the mailing to Belgium or USA, dilutions and several changes of vials.

7.3.17. Hyperthermia measurements

The magnetic heating of the iron oxide colloidal dispersions were done at the Institut de Chimie de la Matière Condensée de Bordeaux (ICMCB-CNRS), at the group of Prof. Etienne Duguet. **Figure 7.7** shows a scheme of the experimental set-up for the monofrequency device composed of an inductor Celes C97104 with an alternating magnetic field of 88 mT and 108 kHz. The temperature was monitored with a fluoroptic thermometer Luxtron m 600 with a specific optic fibre STF-2 for liquid contact. No metallic thermopar was used in order to avoid any possible extra-heating of the sample. The system collects data every 0.5 seconds.
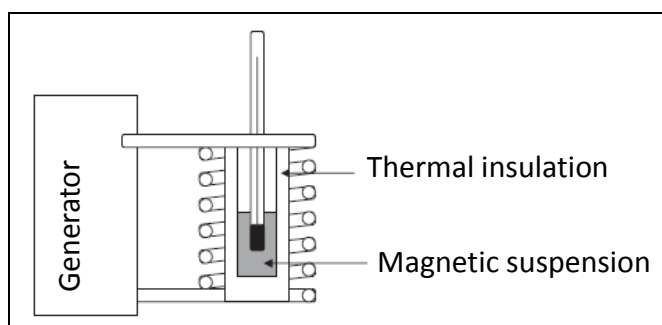
Figure 7.7. Experimental set-up for the hyperthermia magnetic measurements.[4]

The multifrequency inductor operates at 50, 100, 200, 500 and 1000 kHz (coil description: 28 loops, length = 0.2 m, steps of 0.7 cm). The field strength is adjustable from 2 to 10 mT thanks to a range of condensators (Celem Passive Components, Israel). The AC electric signal is delivered by a generator FI1202 (Française d'Instrumentation, France) and this electric signal is amplified by an amplifier (AR Worldwide 800A3, 10 kHz - 3 MHz, EMV, France).

7.3.18. Bibliography of Annexes

1. Bermúdez-Polonio, J. Métodos de difracción y de rayos X. Principios y aplicaciones. Ed. Pirámide S. A., **1981** Madrid**.**

2. Lutterrotti, L., Gialanella. S. X-ray diffraction characterization of heavily deformed metallic specimens. *Acta Mater*. **1997** 46, 101-110.

3. Mosmann, T. Rapid colorimetric assay for cellular growth and survival: Application to proliferation and cytotoxic assay, *J. Immunol. Method*. **1993**, 95, 55-63.

4. Vasseur, S.; Duguet, E.; Portier, J.; Goglio, G.; Mornet, S.; Hadová, E.; Knízek, K.; Marisco, M.; Veverka, P. and Pollert, E. Lanthanum manganese perovskite nanoparticles as possible in vivo mediators for magnetic hyperthermia *J. Magn. Magn. Mater*. **302** (2006) 315-320.